



STRONG MICROWAVES IN PLASMAS

2000

Volume 1

*Institute of Applied Physics
Nizhny Novgorod*

RUSSIAN ACADEMY OF SCIENCES
INSTITUTE OF APPLIED PHYSICS

STRONG MICROWAVES IN PLASMAS

PROCEEDINGS
OF THE INTERNATIONAL WORKSHOP
*Nizhny Novgorod,
2 – 9 August 1999*

**Edited by
A.G. Litvak**

**In two volumes
Volume 1**

Nizhny Novgorod – 2000

© Institute of Applied Physics
Russian Academy of Sciences, 2000

ISBN 5-8048-0007-8

Editor's Preface

The 4th International Workshop on Strong Microwaves in Plasmas, 3–9 August 1999, was held on board the “Nizhny Novgorod” river ship cruising from Nizhny Novgorod to Saratov and back. This Workshop had an essentially interdisciplinary character; its objective was to gather developers of high-power microwave devices and researchers who study interaction of microwaves with matter (primarily, with plasma, both fusion and low-temperature plasmas). The three-year cycle chosen for holding the Workshop provides the participants with the possibility to accumulate, between the Workshops, a considerable research material. Thus, another objective of the Workshop is actually to sum up the results of three years of research activity. This makes participation in it especially attractive for representatives of leading scientific centers and laboratories of the world, in spite of a great number of yearly conferences in the related fields. Success of the Workshop is also conduced by its form: a weeklong stay in the closed space of a comfortable ship makes it possible to combine presentations at Workshop sessions with actually unlimited discussions in the participants' free time.

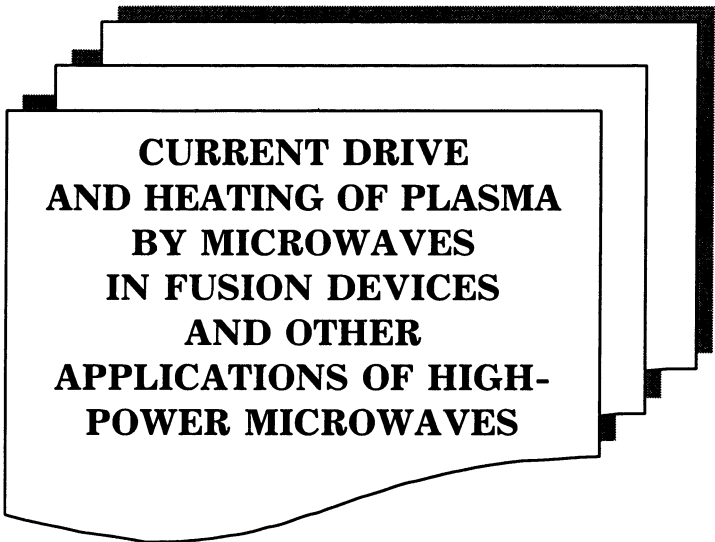
The Workshop hosted 131 scientists from 14 countries. Its scientific program comprised 20 invited plenary lectures, 16 invited topical talks and 76 original presentations. Four traditional topical sections were working at the Workshop:

- *Current drive and heating of magnetically confined plasma by microwaves (electron cyclotron and low-hybrid frequency ranges).*

- *Microwave discharges in gases and their applications.*
- *Nonlinear processes in plasmas (theory and microwave-plasma interaction experiments).*
- *Development of high-power microwave sources.*

This book is the collection of invited lectures and original contributions delivered at the Fourth International Workshop on Strong Microwaves in Plasmas. The material gives a sufficiently detailed idea of the state-of-the-art and new trends in the field of development high-power microwave sources and their applications. It will be certainly useful for professionals working in this area.

A. G. Litvak



**CURRENT DRIVE
AND HEATING OF PLASMA
BY MICROWAVES
IN FUSION DEVICES
AND OTHER
APPLICATIONS OF HIGH-
POWER MICROWAVES**

ECRH AND ECCD AT HIGH POWER DENSITY AT W7-AS

*H. Maaßberg, C.D. Beidler, V. Erckmann, U. Gasparino,
J. Geiger, H. Laqua, S.V. Kasilov[†], N.B. Marushchenko[†],
S. Murakami[‡], and the W7-AS Team*

Institut für Plasma Physik, EURATOM Association,
Garching, Germany

[†] Institute of Plasma Physics, NSC-KhPTI, Kharkov, Ukraine

[‡] National Institute for Fusion Science, Toki, Japan

ECRH at high power level (up to 1.3 MW) significantly affects the confinement properties at the W7-AS stellarator. The neoclassical prediction of the “electron root”, i.e., a strongly positive radial electric field, E_r (being the solution of the ambipolarity condition of the particle fluxes), is driven by ripple-trapped suprathermal electrons generated by the ECRH. The reduction of the neoclassical transport coefficients for this “electron root” feature leads to peaked T_e profiles (with $T_e(0)$ up to 6 keV) which disappear nearly immediately after the ECRH is switched off. The radial polarization current is estimated by a neoclassical simulation of the transient E_r profile (from the electron energy balance) when the ECRH is switched off and is consistent with the “convective” ECRH-driven electron flux obtained from Monte Carlo simulations in 5D phase space. The current balance is analyzed in high power (1.3 MW) ECCD experiments at low density. The ECCD predicted from linear theory exceeds by a factor of about 2 the “experimental” one consisting of bootstrap and inductive currents (for net current free operation) which are calculated from neoclassical theory by using the measured density and temperature profiles. Nonlinear Fokker-Planck simulations with a loss-cone modelling of the power sink (∇B -drift of ripple-trapped electrons) cannot explain this degradation.

Introduction

At W7-AS the ECRH launching system is located very close to the “elliptical” plane with a magnetic field topology corresponding to an vertically elongated tokamak cross section. The strong elongation (factor of about 2) in this symmetry plane with the main (local) toroidal curvature leads both to the reduction of the Pfirsch-Schlüter currents and to improved neoclassical confinement properties. The EC waves are launched highly focused from the low-field side by means of a flexible mirror system allowing for off-axis deposition as well as for EC current drive. The beam width is about

5 cm leading (due to the elongation) to a highly peaked power deposition profile (of about 2 cm in the effective radius) as is predicted by ray-tracing calculations with an absorption coefficient from quasi-linear theory based on a Maxwellian distribution function. In the experiments described here, only 2nd harmonic X-modes at 140 GHz (corresponding to $B \simeq 2.5$ T) with a power level of up to 1.3 MW (3 gyrotrons) were launched. Furthermore, the magnetic field strength changes along the field line within the absorption zone leading to a significant amount of trapped particles in the “standard” configuration. By changing the current in the coils located in the “elliptical” plane, the fraction of ripple-trapped electrons absorbing the wave power can be controlled (at a sufficiently high current, a “maximum- B ” scenario without trapped particles in the ECRH launching plane can be realized).

The confinement properties of stellarators in the long-mean-free-path (*lmfp*) regime are determined by the radial ∇B -drift of particles trapped in local ripples and by the poloidal $E \times B$ -drift which reduces the radial excursions. Therefore, the neoclassical transport coefficients depend themselves on the radial electric field, E_r . The effect of E_r on reducing the neoclassical transport coefficients is much stronger for ions than for electrons. Together with the E_r -driving term in the “thermodynamic force” ($\propto q_{e,i} E_r / T_{e,i}$ where q and T are the particle charge and temperature), the ambipolarity condition of the particle fluxes, i.e., vanishing radial current, gives an equation for the ambipolar radial electric field with an odd number of roots [1, 2].

The stellarator-specific “electron root” with strongly positive E_r , decreasing significantly also the electron transport coefficients, seems to be very promising: improved confinement compared to the “ion root”, and, most important, prevention of impurity accumulation. However, the existence of the “electron root” has not been clearly indicated experimentally in the past. Only recently strong indications for an “electron root” feature both in CHS and W7-AS were found; see Refs. [3, 4]. In extremely low-density (some 10^{18} m^{-3}) ECRH discharges at CHS, highly peaked electrostatic potential profiles were measured by the heavy ion beam probe diagnostic. At CHS, the resultant peaking of the central T_e profile (quite similar to the potential profile) is attributed to the formation of an ITB (internal transport

barrier) at the position where the E_r profile changes strongly[5]. At W7-AS, an “electron root” feature was inferred from the electron power balance analysis and the comparison with the neoclassical predictions for low-density ($2 \cdot 10^{19} \text{ m}^{-3}$) ECRH discharges. In this more conservative interpretation, the improved electron confinement is obtained by the strong E_r itself, in contrast to a strong poloidal rotation shear (i.e. E_r').

The strongly positive radial electric field within the region of the “electron root” feature leads to complex effects on the flux surfaces. In the continuity equation, the inhomogeneity of the magnetic field strength, B , on a flux surface ($\nabla \cdot \underline{v}_{E \times B} = -2 \underline{v}_{E \times B} \cdot \nabla \ln B$) drives a parallel flow (which is the equivalent of the Pfirsch-Schlüter current) as well as a (1st order) density inhomogeneity, n_1 . In the ion force balance equation, the $(\underline{v} \cdot \nabla) \cdot \underline{v}$ term is approximately given by the gradient of the kinetic energy related to the poloidal rotation as well as to the parallel flow. Viscous damping of this parallel flow by ripple-trapped particles leads to an enhanced density disturbance n_1 which, in turn, has to be compensated by a (1st order) potential, Φ_1 , in the electron force balance equation. These effects can play an essential role in the poloidal component of the force balance equations, however, they are disregarded in the traditional neoclassical theory, e.g., in the estimation of the transport coefficients with “strong” E_r by Monte Carlo technique (e.g. Refs. [6, 7]) or by the DKES code (Refs. [8, 9]).

Both by the viscous damping of the parallel flow within the “electron root” region and by the poloidal friction force due to the shear viscosity term within the transition region, the rotation energy is dissipated. From this point of view, a direct drive by a sufficient suprathreshold ripple-trapped electron population generated by the ECRH may be essential for establishing the “electron-root” feature. The time-scale for the appearance and for the vanishing of the ECRH-driven “electron-root”, however, is determined by the ion dynamics, in particular by the polarisation current and by the parallel ion flow which compensates the torus effect in the poloidal rotation. For example, the damping of the poloidal rotation (described by the ion inertia term in the force balance equation) is equivalent for the “electron root” feature and for the L- and H-mode transitions.

In the ECCD scenarios at larger toroidal launch angles, where

the power is dominantly absorbed by passing particles, the “electron-root” is not established. Nevertheless, the ∇B -drift of the ripple-trapped electrons leads to the stellarator-specific power loss in the electron energy balance which determines the shape of the distribution function together with the power source which is described by the quasi-linear diffusion term in the nonlinear Fokker-Planck simulations[10]. In agreement with the neoclassical treatment (i.e., the $1/\nu$ regime at moderate E_r), where the radial ∇B -drift of ripple-trapped electrons dominates the thermal electron transport, a pure loss-cone modelling of the power sink is used in the Fokker-Planck calculations. Consequently, with the quasi-linear heating located outside of the loss-cone for the ECCD scenarios at larger launch angles, very steep gradients in the electron distribution function close to the loss cone boundary are obtained at high heating power and low density, which drives the high energy flux in this collisional Fokker-Planck modelling.

For a strong deviation of the distribution function from the Maxwellian (i.e. for high ECCD scenarios at high power level and at low density) kinetic instabilities may be driven by the domains where $\partial f / \partial v_{\parallel}^2 > 0$ representing free energy in the distribution function. These conditions are found close to the loss cone boundary. The frequency of these unstable modes is of the order of the electron cyclotron frequency, and the growth yields a much shorter time-scale than the collisional one in the supra-thermal range where the deviation from the Maxwellian is maximum. In a preliminary analysis, the roots of the dispersion relation with the full non-Maxwellian distribution function obtained from the Fokker-Planck simulations are calculated yielding this kind of kinetic instability. Then, the distribution function is affected by these instabilities and the deviation from the Maxwellian is limited by the condition of marginal stability. Consequently, the ECCD efficiency may be degraded under these conditions.

The experimental analysis of the ECCD efficiency is very important for the current control scenarios of W7-X which is under construction at Greifswald, Germany. W7-X is also a low shear stellarator, but without inductive current control. Although the bootstrap current is predicted to be fairly small due to the optimisation of the magnetic configuration [11], the position of the island divertor x-point

depends sensitively on the plasma current. In addition to a desirable experimental flexibility, advanced ECCD scenarios, e.g. with launching from the high-field side in order to absorb the power first by the high-energy electrons, are needed as “technical tools” for current control. In this context, the high-power ECCD experiments at W7-AS must provide access to the relevant physics and confidence for their application to W7-X.

The ECRH-driven “electron-root”

The additional peaking of the central T_e profile (measured by the ECE and the Thomson diagnostics) in low-density discharges with fairly high ECRH power level indicated for the first time an “electron root” feature in W7-AS [12]. The “experimental” electron heat diffusivity from the power balance was found to be significantly smaller than the neoclassical prediction for small E_r in this central region. Consequently, poloidal rotation measurements by the Doppler shift of impurity lines from active charge exchange recombination spectroscopy (CXRS) were carried out [13] in order to check the radial electric field predicted for the neoclassical “electron root”. In these discharges, strongly positive E_r have been obtained in the central region with the peaked T_e profile.

Electron energy balance:

After upgrading the ECRH power to 1.3 MW, central electron temperatures up to 6 keV have been found. This is illustrated in Figure 1 by an ECRH power scan at low density (on the left) and by a density scan at full power (on the right) in the “standard” configuration with a significant fraction of trapped particles in the ECRH launching plane. At lowest ECRH power at low density (on the left), this “electron root” feature is not established (no peaking and no strong $E_r > 0$) yielding a power threshold at fixed density. On the other hand, only a marginal “electron root” feature is found at the highest density at full power (on the right) indicating a density threshold. The T_e profiles in the “ion root” region ($r \geq 6$ cm) are nearly independent of density. This finding directly confirms the $1/\nu$ dependence of the neoclassical transport coefficients, i.e., the electron heat flux being independent of density. For the strongly positive radial electric field of the “electron root” region, the thermal electron transport coefficients are mainly determined by the $\sqrt{\nu}$ -regime scal-

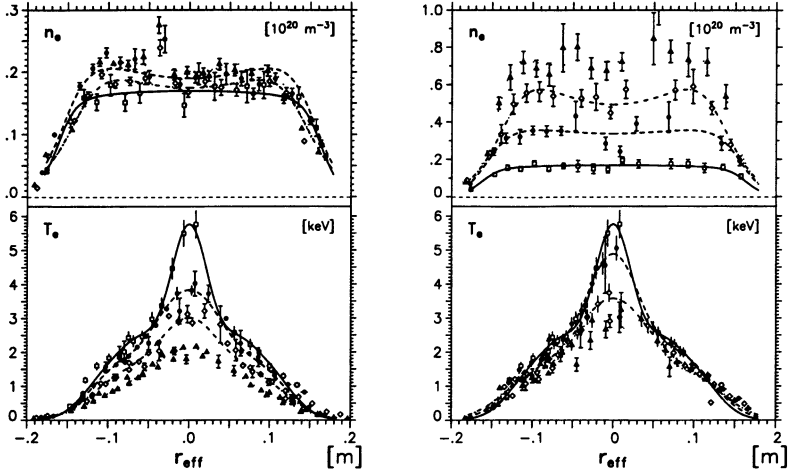


Figure 1: ECRH power scan (on the left; 0.2, 0.4, 0.8 and 1.2 MW) and density scan (on the right) at 1.2 MW.

ing, and the expected fairly strong density dependence is in agreement with the density dependence of the highly peaked T_e profile. The equivalent experiments in the “maximum B ” configuration (nearly without trapped particles) show neither the central peaking of the T_e profile (except for the highest ECRH power at lowest density) nor the strongly positive E_r (confirmed by shifting the diagnostic neutral beam over the central region). Consequently, the thresholds depend sensitively on the magnetic configuration.

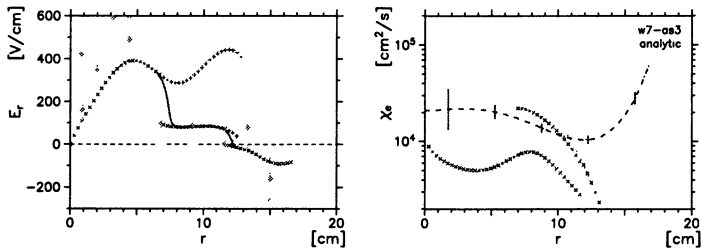


Figure 2: Radial electric fields (on the left) and electron heat diffusivities (on the right) vs. radius for the 800 kW ECRH discharge of Fig. 1. The “experimental” E_r (symbols with error bars) is derived from the poloidal plasma rotation measured by active CXRS.

The electron heat diffusivity profile, $\chi_e(r)$, is estimated from the power balance and compared with the diagonal term of the neoclassical transport matrix, D_{22}^e , with the ambipolar E_r taken into account.

As an example, the ambipolar E_r , the χ_e from the power balance (dot-dashed line) and the neoclassical predictions for the discharge with 800 kW ECRH of Fig. 1 are shown in Figure 2. The $E_r(r)$ is estimated from the roots of the ambipolarity condition of only the neoclassical particle fluxes (\times). The ambipolar E_r shows the “electron root” feature (the position of the poloidal rotation shear layer, i.e., the transition between the roots is $r_{sl} \simeq 7.2$ cm). By solving the diffusion equation[14] for the radial electric field, this transition is smoothed (solid line). Since the ion temperature ($\simeq 400$ eV) is flat, also the E_r of the “ion root” is positive at the intermediate radii, and becomes negative only in the density gradient region. The radial electric fields obtained from the active CXRS poloidal rotation measurements [13] are consistent with the neoclassical prediction. The neoclassical $D_{22}^e(r)$ with the ambipolar E_r (\times , the D_{22}^e with $E_r = 0$ (dotted line) is given for reference) are compared with the χ_e from the power balance analysis (estimated by least-squares fitting of the power balance to the measured T_e ; see Ref. [14]) where only the temperature gradient drives the heat flux (flat n_e profile). Only in the outer 30% of the plasma radius is the “experimental” χ_e much larger than the neoclassical one (all neoclassical transport coefficients become small with temperature). For the intermediate radii, the “ion root” E_r are sufficient to reduce the neoclassical D_{22}^e and these are fairly consistent with χ_e .

The “electron root” feature with the highly peaked T_e profile is only found for ECRH deposition close to the magnetic axis. The accurate estimation of the deposition profile, however, turns out to be a complex problem. Both the Shafranov shift of the magnetic axis due to the highly peaked pressure profile (also the rotational transform is reduced by the peaked inductive current density for compensating the bootstrap current) as well as the “inward” shift of the absorption layer due to the relativistic effect in the resonance condition play an important role for this “electron root” feature. Even with the Shafranov shift taken into account, the cold resonance (i.e., $B = 2.5$ T at 140 GHz for perpendicular launching) must be significantly off-axis on the low-field side to allow for central absorption. Using the quasi-linear absorption coefficient[15] for a Maxwellian, the maximum absorption is obtained at a (perpendicular) energy corresponding to $2T_e$. For $T_e \simeq 5$ keV, the relativistic mass correction leads to an “in-

ward” shift of the resonance, i.e. the hot resonance for a Maxwellian with maximum (linear) absorption is at $B = 2.55$ T. For the W7-AS launching conditions, this difference corresponds to an “inward” shift in the effective radius of 4 cm. Both the formation of a “quasi-linear plateau” in the electron distribution function and the violation of the assumptions for linear absorption will increase this shift.

Finally, neither at half field ($B_0 \simeq 1.25$ T) nor for O-mode launching at 2.5 T was a similarly pronounced “electron root” feature indicated. For the 70 GHz heating scenarios, however, the available ECRH power was less than 700 kW.

The X-mode with high optical depth has (for perpendicular launching) maximum linear absorption for $v_{\parallel} \simeq 0$, the quasi-linear diffusion coefficient, $Q_{\perp\perp}$, therefore has its maximum for the deeply trapped particles in the launching plane, and the wave power is absorbed close to the resonance layer by the thermal bulk. For the coherent ECRH power densities, however, the assumption of linear absorption may fail and electron trapping in the wave field at low v_{\parallel} may become important. The ECRH power at fundamental O-mode launching is more efficiently absorbed by the barely trapped particles ($Q_{\perp\perp}(v_{\parallel} = 0) = 0$), but at higher energy since the lower optical depth allows the launched wave to penetrate deeper behind the resonance layer. For both heating scenarios, a broadening of the “effective” heating profile was found in ECRH power modulation experiments. This broadening is attributed to the radial ∇B -drift of ripple-trapped suprathermal electrons; see Refs. [16, 17, 18]. The equivalent conclusion, that these ripple-trapped suprathermal electrons generated by the ECRH absorption are responsible for establishing the “electron root” feature is discussed in the followings.

Decay of the “electron-root”:

With the *hypothesis* that the non-local (convective) radial flux of ripple-trapped suprathermal electrons contributes significantly to the ambipolarity condition, thus forming the “electron root” feature with strongly positive E_r , it should be possible to identify two time scales. The radial ∇B -drift time of the ripple-trapped suprathermal electrons is much shorter than the neoclassical diffusion time of, e.g., “ion root” confinement. Without the ECRH-driven convective flux, the E_r in the “electron root” region would drop on the fast time scale and nearly instantaneously the neoclassical D_{22}^e should increase to

the “ion root” level. Consequently, the highly peaked “electron root” T_e should drop much faster than the “ion root” T_e after the ECRH power is switched off (or decreased under the power threshold). These different times can be identified from the ECE electron temperature traces with high sampling rate (typically 25 kHz).

Close to the thresholds, both stimulated and spontaneous transitions are observed indicating that the “electron root” feature may be described in a bifurcation picture. Spontaneous transitions into the “electron root” feature and back are found by shifting the ECRH deposition slightly off-axis in a B_0 scan, even coherent transitions with a frequency of about 500 Hz are observed. Also the outer ECE channels (with non-thermal emission) show an increased emission during the time of the highly peaked central T_e profile whereas no indication of an increased temperature exists for the equivalent high-field side channels. These findings support the premise that at least a part of this non-thermal ECE signal is related to the relativistically down-shifted emission of highly energetic electrons.

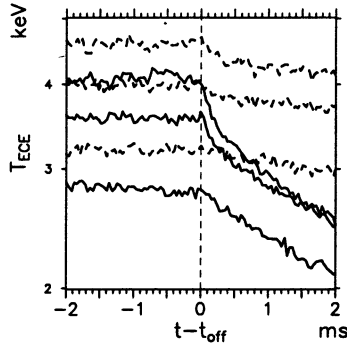


Figure 3: Time traces of the electron temperature for central ECE channels (on the high-field side, at 144.1 GHz, 143.1 GHz and 142.1 GHz with increasing T_e which covers the range $0 \leq r \leq 4$ cm) for the $n_e \simeq 3.5 \cdot 10^{19} \text{ m}^{-3}$ discharge (see Fig. 1 on the right) when the ECRH power is switched from 1200 to 800 kW (dashed lines) and switched-off from 800 kW (solid lines).

The example in Figure 3 shows the dependence of the “electron root” feature on the ECRH power; compare Fig. 1 (on the right, dashed lines). “standard” configuration (on the left), After one gyrotron is switched off, i.e., the ECRH power is reduced from 1.2 MW to about 800 kW (dashed lines), the electron temperatures are only

slightly decreased, and no fast transition is found. The central T_e profile remains highly peaked. After the other gyrotrons are switched off, the central peaking of the T_e profiles and the “electron root” feature disappears within 0.3 ms which is much faster than the thermal decay after this transition. In this context, the effect of a significant local Shafranov shift due to the highly peaked central pressure profile must be taken into account: this effect increases the changes in the central ECE channels resonant on the low field side, but reduces the changes in the high field side channels (only high field side channels are shown in Fig. 3. The E_r data are deduced from Doppler shift measurements by active CXRS, and the time resolution of these measurements is fairly poor. Thus, no direct experimental information (in contrast to the heavy ion beam probe data at CHS [5]) is available as to how fast the “electron root” E_r disappears.

The estimate of $E_r(r, t)$ by means of the ambipolarity condition of purely neoclassical fluxes is not very reliable since the neoclassical ordering is violated for the ions in case of the “electron root” E_r and the ERCH-driven fluxes are disregarded. A more conservative approach is based on the electron energy balance with purely neoclassical transport coefficients, i.e., the broadening of the “effective” power deposition profile due to the radial drift of suprathermal electrons is neglected. For the low density discharges, radiation losses as well as the collisional electron-ion coupling can be omitted. With the density profile assumed to be stationary with respect to the fast time scale, only the evolution of the E_r profile determines $T_e(r, t)$ in the neoclassical simulation of the electron energy balance.

Figure 4 gives the results of this neoclassical simulation for the decay of the “electron root” feature in the late phase of the discharge shown in Fig. 3 (solid lines). The $E_r(r, t)$ is modelled by a stationary contribution (simulating the slow time scale of the “ion root”) and an additional strongly positive contribution in the “electron root” region with an exponential time decay $\propto \exp(-t/\tau_{E_r})$ (with $\tau_{E_r} = 0.3$ ms) after the ECRH (at 800 kW) is switched-off; see the upper left plot. With this $E_r(r, t)$ profile, the neoclassical $T_e(r, t)$ calculated from the electron energy balance fits fairly well both the stationary and the strongly transient phase of the discharge of Fig. 3; see the lower left and the right plot. An equivalent simulation with $\tau_{E_r} = 0$ (corresponding to “jumping” neoclassical transport coefficients) leads to a

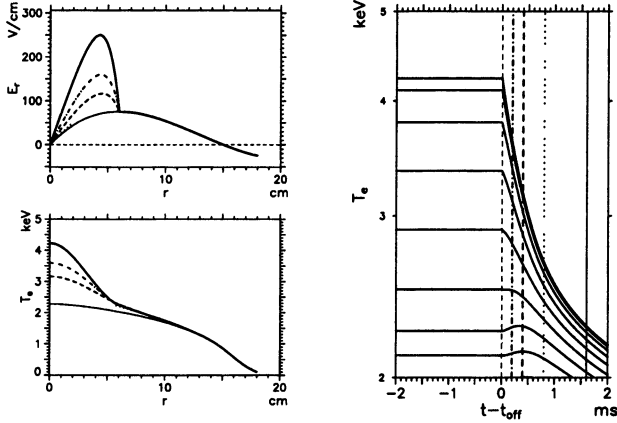


Figure 4: Neoclassical simulation of the electron energy balance. Upper left plot: $E_r(r, t)$ with a stationary (thick solid line) and a transient part (at $t = 0.2, 0.4, 0.8$ and 1.6 ms after the ECRH at 800 kW is switched-off; see the right plot). Lower left plot: $T_e(r, t)$ profiles based on neoclassical transport coefficients (only at the outer 3 cm an “anomalous” contribution dominates). On the right: Time traces of the calculated $T_e(r, t)$ (with an increment of $\delta r = 1$ cm); compare the solid lines in Fig. 3.

nearly discontinuous crash in the central T_e (there is no damping mechanism in the neoclassical electron energy balance). Consequently, this procedure allows for an estimate of the transient behaviour of the E_r profile, however, the magnitude of E_r is roughly a factor of 2 lower than the one obtained from the ambipolarity condition with purely neoclassical fluxes.

A radial polarization current density, $j_r(r, t)$, is directly connected with this transient radial electric field[19]

$$M_{eff} \epsilon_{\perp} \epsilon_0 \frac{\partial E_r}{\partial t} = j_r(r, t),$$

where $\epsilon_{\perp} = 1 + (\omega_{pi}/\omega_{ci})^2$ (here ω_{pi} (ω_{ci}) is the ion plasma (cyclotron) frequency) and M_{eff} is an enhancement factor resulting mainly from the toroidal curvature ($M_{eff} = 1$ for a homogeneous magnetic field). As discussed in the previous Section, a parallel flow (equivalent to the Pfirsch-Schlüter current) is driven by the variation of the $E_r \times B$ -drift in the flux surfaces. As long as the parallel viscous damping (due to trapped particles) is small, an axisymmetric treatment may be used;

see Refs. [20, 21]. Otherwise, a self-consistent neoclassical treatment is necessary.

Following Ref. [21], the enhancement factor M_{eff} depends on the ion poloidal Mach number, $M_p \simeq RE_r / \tau r B v_{th,i}$, which is of the order of 10 for the “electron root” feature. In the limit $M_p \gg 1$, $M_{eff} = 1 + (\beta_{10}^*/\tau)^2$ is obtained where the normalized toroidal curvature, $\beta_{10}^* \simeq 0.7$ for W7-AS, reflects the optimization based on an “averaged elongation” (equivalent to the reduction of the Pfirsch-Schlüter currents). The bootstrap current in these W7-AS discharges was feedback controlled by the transformer. The positive E_r strongly reduces the electron bootstrap current density in the “electron root” region (the ion bootstrap current is negligible). Consequently, the central τ profile is dominated by the ohmic current density profile and significantly reduced compared to the edge value, τ_a . For the simulation of Fig. 4, $\tau \leq 0.2$ for $r \leq 5$ cm ($Z_{eff} = 3.5$) is obtained ($\tau_a \simeq 0.35$). This strongly increases M_{eff} in the “electron root” region.

In this procedure, a lower limit for the radial polarisation current density is obtained which corresponds for the simulation of Fig. 4 to a particle flux of $3.5 \cdot 10^{19} \text{ s}^{-1}$ at $r = 4$ cm (the ambipolarity condition with purely neoclassical fluxes yields $0.9 \cdot 10^{19} \text{ s}^{-1}$ with E_r nearly 600 V/cm).

The ECRH-driven electron flux:

The crucial point for establishing the “electron root” feature is the radial electric field profile which is determined by the ambipolarity condition of both the thermal (diffusive) and the ECRH-driven (convective) particle fluxes. The latter depend on ECRH power, density and the fraction of trapped particles in the launching plane, and may be comparable to the “diffusive” neoclassical fluxes depending only on the local E_r . Based on fits to the measured density and temperature profiles, the neoclassical particle fluxes are calculated and the radial electric fields are estimated by the (multiple) roots of the ambipolarity condition. This approach is valid if the ECRH-driven electron fluxes are small compared to the ambipolar neoclassical ones. In a first step, these ECRH-driven electron fluxes are calculated with the Monte-Carlo technique [18] with an assumed E_r profile. In principle, a self-consistent approach with all fluxes taken into account may be obtained by iteration.

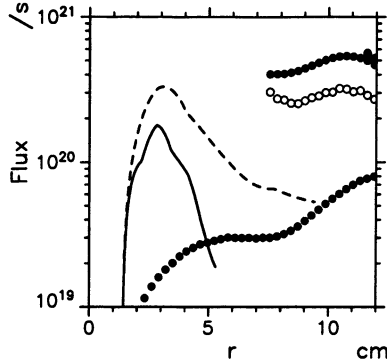


Figure 5: The ambipolar neoclassical particle fluxes (circles) and the ECRH-driven electron flux from the Monte-Carlo simulation with E_r corresponding to the neoclassical prediction (solid line) and with $E_r = 0$ (dashed line) vs. radius for the 800 kW ECRH discharge of Fig. 1 (on the left) and Fig. 2.

In Figure 5, the particle fluxes are shown for the 800 kW ECRH discharges of Figs. 1 and 2. An “electron root” feature (lower solid circles) is obtained from the ambipolarity condition with only the neoclassical fluxes. In the central region, the ECRH-driven electron fluxes obtained from the Monte-Carlo simulation with a E_r profile roughly corresponding to the “electron root” solution (solid line) significantly exceed the ambipolar neoclassical ones, but are consistent with the extrapolation of the ambipolar “ion root” fluxes (upper solid circles, the open circles represent the unstable E_r root). The ECRH-driven electron fluxes are less sensitive to the inner radial electric field profile (dashed line for a Monte-Carlo simulation with $E_r = 0$). As a consequence, the non-local ECRH-driven electron fluxes are significantly larger than the neoclassical ones in the central “electron root” region and must to be taken into account when estimating the radial electric field.

Consequently, the different contributions to the ambipolarity condition of all particle fluxes must be discussed in more detail, in particular for the large E_r of the “electron root” region. Quasi-linear and non-linear [22] effects become important if a significant fraction of the wave power is absorbed by resonant trapped electrons. At very high power levels, the distribution function flattens, i.e. $\partial f_e / \partial v_\perp$ is reduced in the region of the resonance $\omega - k_{\parallel} v_{\parallel} - l\omega_c / \gamma = 0$ (with

$l = 2$ for 2nd harmonic and γ being the relativistic mass factor), and the wave absorption is shifted to higher fields and higher energies. As both the collisional detrapping ($\propto v^{-3}$) is decreased and the ∇B -drift is increased ($\propto v^2$) whereas the $E \times B$ -drift is less effective for reducing these non-local fluxes, the simplified linear estimate given in Fig. 5 is a lower bound for the ECRH-driven electron flux.

Comparing this result with the values of the polarisation current estimated from the simulation of the transient decay of the $E_r(r, t)$ after the ERCH is switched off (see Fig. 4 at equivalent power but higher density) yields reasonable agreement. This equivalence of the ECRH-driven electron flux and the polarisation current, i.e. the fast transient behaviour of the “electron-root” E_r , supports the hypothesis that the “electron-root” feature is driven by suprathermal electron generated by the ERCH absorption.

High power ECCD

No direct access to the ECCD densities, j_{ECCD} , is experimentally available, and estimates from the current balance must rely on an accurate calculation of both the bootstrap, j_{bt} , and the inductive current densities, j_{oh} , which depend on the n_e , T_e and Z_{eff} profiles. In addition, an estimate of the ECCD density from linear theory, j_{lin} , is obtained by using the adjoint approach with the trapped particles included [23] (implemented in the ray-tracing code) and compared with the current balance. Furthermore, the rotational transform profile, $\tau(r)$, is calculated based on these current densities and low order rational values (e.g. $\tau = \frac{1}{2}$) can be identified in local mode activity (e.g. from ECE and SX diagnostics).

ECCD launching angle scan

Driven currents up to ± 20 kA are obtained from the current balance of bootstrap (I_{bt}) and ohmic currents (I_{oh}), i.e. $I_{bt} + I_{\text{ECCD}} = -I_{oh} \equiv -U_{loop}/R$, in the net-current free discharges assuming stationary conditions. The electron densities are in the range of $2.5 \cdot 10^{19} \text{ m}^{-3}$ and the central T_e are of up to 5 keV. Pronounced differences in the T_e profiles were found for co- and counter current drive (positive φ_{inj} leads to co-current drive). For co-ECCD the profiles are peaked displaying the ECRH-driven “electron root” at small launching angles (for higher φ_{inj} the beam becomes defocused leading to broader deposition profiles). In the counter ECCD cases the profiles are very

flat in the central region which is attributed to the strong decrease of the τ -profile due to the high central ECCD densities. Equilibrium considerations would exclude an $\tau = 0$ -surface, but both ECRH and the ECCD are coupled with the B-field resonance and should be localized. The assumption of field ergodisation in the central region (where the profiles are flat) with high radial transport of energy and current would lead to a much broader deposition profile.

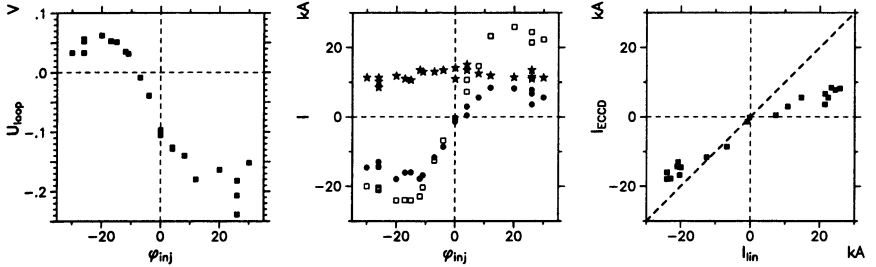


Figure 6: 1.2 MW ECCD scan of launching angle φ_{inj} (shots 43023-62): Loop voltage (left), bootstrap (\star) and ECCD (\bullet) current and I_{lin} (\square) (middle), and experiment vs linear prediction (right).

Fig. 6 shows that the linear theory (I_{lin}) overestimates the ECCD efficiency for higher launching angles, where its maximum is expected from theory. The deviation is more severe for co- than for the counter-ECCD which shows reasonable agreement. The current densities in these discharges are at least marginally stationary at the times where the current balance is analyzed. Furthermore, $U_{loop}(t)$ develops in the start-up phase and becomes stationary.

A problem to be discussed is the accuracy of the current balance. In the case of ctr-ECCD the main contributions are the bootstrap current and the ECCD, and a small inductive current is sufficient for compensation. On the other hand, for the co-ECCD case I_{bt} and I_{ECCD} are compensated by a strong I_{oh} , and I_{ECCD} is obtained from the difference of large numbers. In the neoclassical calculation of j_{bt} the radial electric field becomes important, especially in the “electron-root” region where the j_{bt} is strongly reduced. Thus, the neoclassical estimation of the bootstrap current density depending on the ambipolar E_r yields some uncertainty in the current balance for I_{ECCD} . However, since the current balance seems to be reliable at small φ_{inj} (only small ECCD) and the variation of I_{bt} with φ_{inj} is fairly small (j_{bt} dominates at outer radii), the estimation of I_{ECCD}

from current balance should also be reliable at larger φ_{inj} .

Fokker-Planck modelling

Two main approaches are available to solve the Fokker-Planck equation in the 5D-phase space: the Monte-Carlo technique [18] used to describe the ECRH-driven electron fluxes and the direct Fokker-Planck modelling [10]. Whereas the effect of a complex magnetic field topology on the quite different types of trapped particles and their drift motion is correctly described in the Monte-Carlo technique, the diffusion in velocity space due to the non-linear collision term as well as the quasi-linear diffusion term (modelling the ECRH and the ECCD source) are insufficiently described. On the other hand, the non-linear Fokker-Planck modelling with the fully self-consistent collision term is better suited for high heating power levels since the velocity space diffusion is correctly treated. However, the high phase space dimension demands some simplifications with respect to real space. The high power ECCD scenarios with highly localized power deposition close to the axis are modelled by using the Fokker-Planck approach.

The Fokker-Planck modelling is restricted to the near vicinity of the magnetic axis where the power is absorbed. Here, radial and poloidal variations of the magnetic field can be neglected, the toroidal variation is taken into account. In the *lmfp*-limit (being justified for the scenarios under investigation), bounce-averaging leads to a further reduction of the relevant phase-space dimension. In the bounce-averaged Fokker-Planck code [10] used, the magnetic field is represented by several (5 for W7-AS) independent mirrors, i.e., the equivalence of the trapped-particle distribution functions is broken by the localized heating. In this approach, the radial transport has to be formulated as an energy sink. Two different models are used: an isotropic energy and momentum sink roughly simulating an “anomalous” transport (e.g., by magnetic fluctuations) and a stellarator-specific loss-cone model where the energy sink is described by the ∇B -drift of the ripple-trapped particles. Note, that this loss-cone modelling can only describe the “convective” energy loss of suprathreshold ripple-trapped electrons generated by the ECRH. This approach is reasonable since for the low n_e , high T_e discharges both the “diffusive” neoclassical transport ($1/\nu$ -regime) and the “convective” Monte-Carlo simulation are confirmed by the experimental

findings; see the previous section.

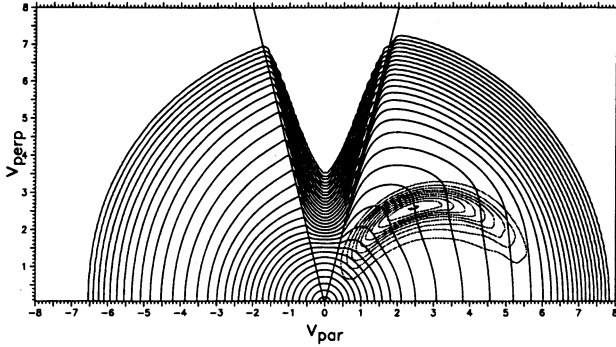


Figure 7: Contour levels of the distribution function at the minimum B-location from Fokker-Planck modelling, and contour levels of quasi-linear diffusion coefficient, $Q_{\perp\perp}$, from ray-tracing: $n_e = 2.5 \cdot 10^{19} \text{ m}^{-3}$, $T_e = 3 \text{ keV}$ and 50 W/cm^3 absorbed power density.

Figure 7 shows the electron distribution function obtained from the Fokker-Planck modelling of an ECCD scenario corresponding to Fig. 6. The 1.2 MW ECRH power being highly locally absorbed (estimated by ray-tracing calculations) corresponds in the averaged Fokker-Planck calculations to a toroidally averaged power density of about 50 W/cm^3 , a very high averaged power density. Since collisional power loss to the ions as well as radiative losses are negligible, the energy sink located in the loss cone (due to ∇B -drift) is equivalent to the energy source which is for this ECCD scenario outside of the loss cone (see the quasi-linear diffusion coefficient $Q_{\perp\perp}$ in Fig. 7). As a consequence, steep gradients in the electron distribution function develop allowing strong collisional power flux from the heating zone into the loss cone. Note the quasi-linear “plateau” formation in the heating zone ($\partial f / \partial v_{\perp}$ becomes small). Non-linear absorption effects [22] are negligible for this scenario at almost maximum ECCD.

Although the deviation of the electron distribution function from the Maxwellian is very strong, the effect on the ECCD efficiency turns out to be fairly small. Figure 8 gives the Fokker-Planck results of an ECCD-power scan corresponding roughly to the simulation of Fig. 7. For the “convective” loss-cone modelling of the energy sink, the ECCD efficiency only slightly increases with power. In contrast, the isotropic energy sink modelling leads to a significant loss of momentum and consequently to strongly degraded ECCD ef-

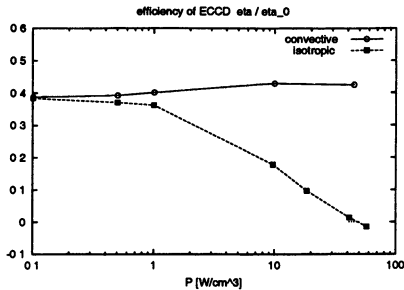


Figure 8: ECCD efficiency (normalized to that in the homogeneous field) vs. absorbed power density: $n_e = 2.5 \cdot 10^{19} \text{ m}^{-3}$, $T_e = 3 \text{ keV}$.

efficiency. Note that the ECCD efficiency at very low power is in full agreement with the linear prediction (adjoint approach); see Ref. [10]. Consequently, the experimentally found degradation of the EC driven current may be simply attributed to an “anomalous” transport effect.

Furthermore, the strong deviation of the electron distribution function from the Maxwellian may also affect the electric conductivity and, consequently, the estimation of I_{ECCD} from the current balance. For the typical loop voltages (of the order of 0.2 V) the electric conductivity as function of ECRH power was calculated, and an increase of only 6% at 50 W/cm^3 was obtained. Thus, the estimation of the inductive current in the current balance is not affected.

Finally, the problem of kinetic instabilities in the electron cyclotron frequency range must be treated. A first preliminary analysis based on the roots of the dispersion relation with the dielectric tensor calculated with the electron distribution function from the Fokker-Planck simulations shows potential instabilities which may be responsible for a degradation of the ECCD efficiency. For these kinds of instabilities the strong drive in regions where $\partial f / \partial v_{\parallel}^2 > 0$ is counteracted by strong Landau damping. As a consequence, the deviation of the distribution function from the Maxwellian (i.e. roughly proportional to the ECCD power) leads to a sensitive threshold for instability. This kind of analysis needs further investigations.

Conclusions

The “electron root” feature with highly peaked electron temperature profiles ($T_e(0)$ up to 6 keV) found at W7-AS is driven by the radial “convective” flux of ripple-trapped suprathermal electrons generated by the ECRH at high power densities. This additional ECRH-

driven electron flux drives strongly positive E_r , which significantly reduce the traditional (“diffusive”) neoclassical electron heat flux.

In the switch-off phase of the ECRH, the electron energy balance with purely neoclassical transport coefficients is solved yielding the transient T_e profile which depends on the decay of the radial electric field in the “electron-root” region. By comparison with the experimental $T_e(r, t)$ (obtained from ECE), the time-constant of the decaying E_r as well as the related radial polarisation current is obtained which is in reasonable agreement with 5D Monte Carlo simulations of the ECRH-driven flux. These findings at W7-AS do not support the *hypothesis* of an *internal transport barrier* [5] used for the interpretation of fairly similar experimental findings at CHS.

In high power (1.2 MW) ECCD experiments with detailed scan of the launching angle from co- to counter-current drive, the currents obtained from the current balance (with bootstrap and inductive currents for net-current free operation) are less than the predictions from linear theory (adjoint approach) based on Maxwellian distributions. Bounce-averaged Fokker-Planck calculations based on the fully self-consistent collision operator (mandatory for toroidally averaged power densities of up to 50 W/cm^3) and with the stellarator-specific loss-cone modelling of radial “convective” transport of ripple-trapped electrons (∇B drift) even show a slightly increased current drive efficiency. However, very steep gradients in the electron distribution function close to the loss-cone boundary are obtained. Kinetic instabilities in the electron cyclotron range of frequency may be driven which can reduce these steep gradients and, as a consequence, also the ECCD efficiency at very high power level. This topic is presently under investigation.

ECCD experiments at W7-AS as well as kinetic modelling is of high relevance for the current control of W7-X which will have no inductive current control. Especially at moderate densities, the ECCD efficiency (roughly scaling with n_e^{-1}) found in W7-AS at low-field side launching may be not sufficient to control the bootstrap current expected in W7-X. However, advanced ECCD scenarios with, e.g., high-field side launching are very promising since the absorption starts at the high-energetic electrons before the cold resonance is reached. The upgraded ECRH system of W7-AS allows with its flexibility a detailed analysis of all the ECCD scenarios.

References

- [1] H.E. Mynick and W.N.G. Hitchon, *Nucl. Fusion* **23**, 1053 (1983).
- [2] D.E. Hastings, W.A. Houlberg, and K.C. Shaing, *Nucl. Fusion* **25**, 445 (1985).
- [3] A. Fujisawa, S. Kubo, H. Iguchi, and H. Idei *et al.*, *16th International Conference Fusion Energy*, Montreal 1996, (International Atomic Energy Agency, Vienna, 1997), *Fusion Energy 1996*, Vol. 2, p. 41.
- [4] V.Erckmann, H.P. Laqua, and J. Geiger *et al.*, *16th International Conference Fusion Energy*, Montreal 1996, (International Atomic Energy Agency, Vienna, 1997), *Fusion Energy 1996*, Vol. 2, p. 119.
- [5] A. Fujisawa *et al.*, *Phys. Rev. Lett.* **82**, 2669 (1999).
- [6] A.H. Boozer and G. Kuo-Petravic, *Phys. Fluids* **24**, 851 (1981).
- [7] W. Lotz and J. Nührenberg, *Phys. Fluids* **31**, 2984 (1988).
- [8] S.P. Hirshman *et al.*, *Phys. Fluids* **29**, 2951 (1986).
- [9] W.I. van Rij and S.P. Hirshman, *Phys. Fluids B* **1**, 563 (1989).
- [10] N. Marushchenko, U. Gasparino, H. Maaßberg, and M. Romé, *Comp. Phys. Comm.* **103**, 145 (1997).
- [11] H. Maaßberg, W. Lotz, and J. Nührenberg, *Phys. Fluids B* **5**, 3728 (1993).
- [12] R. Brakel *et al.*, *Plasma Phys. Control. Fusion* **39**, B273 (1997).
- [13] J. Baldzuhn, M. Kick, H. Maaßberg, and the W7-AS Team, *Plasma Phys. Control. Fusion* **40**, 967 (1998).
- [14] H. Maaßberg *et al.*, *Phys. Fluids B* **5**, 3627 (1993).
- [15] M. Bornatici, R. Cano, O. De Barbieri, and F. Engelmann, *Nucl. Fusion* **23**, 1153 (1983).
- [16] M. Romé *et al.*, *Plasma Phys. Control. Fusion* **39**, 117 (1997).
- [17] S. Murakami *et al.*, *J. Plasma Fusion Res. SERIES* **1**, 122 (1998).
- [18] S. Murakami *et al.*, *17th IAEA Fusion Energy Conference*, Montreal 1996, paper IAEA-CN-69/TH 2/1.
- [19] K. Itoh and S-I. Itoh, *Plasma Phys. Control. Fusion* **38**, 1 (1996).
- [20] S.P. Hirshman, *Nucl. Fusion* **18**, 917 (1978).
- [21] K.C. Shaing, H.D. Hazeltine, and H. Sanuki, *Phys. Fluids B* **4**, 404 (1992).
- [22] M.F. Heyn, S.V. Kasilov, and W. Kernbichler *et al.*, *Proc. 26th EPS Conf. Contr. Fusion Plasma Phys.*, Maastricht, 1999.
- [23] M. Romé, V. Erckmann, U. Gasparino, and N. Karulin, *Plasma Phys. Controlled Fusion* **40**, 511 (1998).

ELECTRON CYCLOTRON PLASMA PRODUCTION AND HEATING ON LHD: SYSTEM AND ITS APPLICATION

K. Ohkubo, S. Kubo, T. Shimozuma, H. Idei, M. Sato, Y. Yoshimura, Y. Mizuno, S. Ito, S. Kobayashi, Y. Takita, O. Kaneko, K. Kawahata, A. Komori, N. Ohyabu, H. Yamada, K. Ikeda, Y. Oka, M. Osakabe, K. Takeiri, K. Tsumori, R. Kumazawa, T. Mutoh, K. Saito¹, T. Seki, T. Watari, N. Ashikawa², M. Emoto, P. C. de Vries, H. Funaba, M. Goto, K. Ida, S. Inagaki, M. Isobe, S. Kado, T. Kobuchi², S. Masuzaki, T. Minami, J. Miyazawa, T. Morisaki, S. Morita, S. Murakami, S. Mutoh, Y. Nagayama, Y. Nakamura, H. Nakanishi, K. Narihara, K. Nishimura, N. Noda, S. Ohdachi, T. Ozaki, R. O. Pavlichenko, B. J. Peterson, A. Sagara, S. Sakakibara, R. Sakamoto, H. Sasao², M. Sasao, K. Sato, M. Shoji, S. Sudo, H. Suzuki, M. Takechi, K. Tanaka, K. Toi, T. Tokuzawa, I. Yamada, S. Yamaguchi, S. Yamamoto¹, K. Yamazaki, M. Yokoyama, K. Y. Watanabe, O. Motojima, M. Fujiwara

National Institute for Fusion Science, Toki, 509-5292, Japan

¹Nagoya University, Faculty of Engineering, Nagoya, 464-8603, Japan

²Graduate University for Advanced Studies, Dept. Fusion Study, Toki, 509-5292, Japan

The electron cyclotron heating system on LHD is overviewed. Electromagnetic characteristics on the sliding waveguide are analyzed by using the mode-matching method and scattering matrix technique. It is confirmed that the small power decrease of $< 0.1\%$ in HE_{11} transmission of 168 GHz is obtained in the sliding length of 2 cm and that transmission and reflection powers change slightly with the period of a half wavelength in the sliding length. The result from first electron cyclotron heating on LHD is described. By using three gyrotrons, the maximum injected power of 0.45 MW at 82.6/84 GHz is injected into LHD and experiments on the on-axis and off-axis heating are performed. The obtained maximum plasma parameters are line-averaged density of $3 \times 10^{19} \text{ m}^{-3}$, electron temperature of 2.0 keV and energy content of 36 kJ. The trial toward the CW operation of LHD by ECH is introduced.

1 Introduction

The construction of a large helical device (LHD)¹ with superconducting and cryogenic technology realizes net current-free plasmas by helical system and progresses physics and technology for helical fusion plasmas. The principal aim of the LHD is to realize plasmas with high $n\tau T$ and to study transport applicable to fusion plasma, to demonstrate high β plasmas, to develop important physics and technology for steady state operation using the divertor, to simulate α particle behavior and to understand the physics of toroidal plasmas with complementary study on tokamak. The LHD is designed to enable operation of a local island divertor, which controls the islands and corrects the error fields with low mode. For the plasma heating method, three kinds of electron cyclotron heating (ECH), ion cyclotron range of frequency (ICRF) heating and neutral beam injection (NBI) heating are being prepared. Electron cyclotron plasma production/heating and control of electric field by electron cyclotron waves are important as target plasmas for NBI and transport study. From the viewpoint of steady state operation, ECH as well as ICRF are a good candidates for plasma heating. In January 1998, the LHD was completed and cooled down to superconducting state. At the end of March 1998, the first plasma was produced by second ECH in $B_t=1.5$ T.

In this paper we report the design, installation and application of ECH-system to LHD. A brief description of LHD and an outline of ECH-system are presented in section 2 and section 3. In section 4, a recent analysis of sliding waveguide by mode-matching method and scattering matrix technique is described. Finally, the first application of ECH to LHD is given.

2 The LHD

The magnetic configuration of LHD is $l=2$ heliotron type of $m=10$ and $A_p=6-7$. The major radius, coil minor radius of the machine and plasma radius a_p are 3.9 m, 0.975 m and 0.6 m, respectively. The maximum toroidal field B_t is 3 T for phase I and 4 T for phase II in the operation of 1.8 K such as superfluid helium cooling. The helical coils of NbTi stabilized Al are cooled by boiling type, while cooling of three poloidal coils of NbTi conductor are forced flow type. The LHD has various flexibilities such as control of helical winding pitch, magnetic axis and elongation and also local-island-divertor coil. Final

heating power of ECH, NBI and ICRF is specified to be 10, 20 and 12 MW. As for ECH in $B_t=3$ T, two kinds of 82.6/84 GHz gyrotron and 168 GHz gyrotron are prepared to operate in comparably wide range of B_t near the fundamental resonance and to obtain high density plasmas in the vicinity of second harmonic resonance. In the first and second experimental campaigns, production and heating of plasmas are performed by 82.6/84 GHz gyrotrons, mainly in the range of $B_t=1.4 - 2.7$ T. In the helical system without ohmic heating, a role of ECH or ICRF as plasma start-up is important. In the second campaign, it is found that toroidal plasma is initiated by high-power NBI with long pulse alone and grows to high temperature. This technique² is specific for an external confining magnetic structure. For NBI one has to wait several hundreds ms until plasma initiation and employ a tough beam armor. But there is no such constraint for cyclotron harmonic resonance in ECH.

3 Electron Cyclotron Heating System

An 84 GHz, two 82.6 GHz (0.5 MW/2s) and six 168 GHz (0.5 MW/1s) gyrotrons are prepared. In $B_t=3$ T, the role of 82.6/84 GHz gyrotrons is the fundamental electron cyclotron plasma production and heating, and a tool for creation of steady state plasma. The 84 GHz gyrotron with an anode was operated for 1 hour with 50 kW in R&D in 1994. The 82.6 GHz gyrotron is a diode-type one. The 168 GHz gyrotrons are used for the second electron cyclotron heating of high density plasma. The cutoff density of ordinary(O) mode and extraordinary(X) mode is $8.8 \times 10^{19} \text{m}^{-3}$ and $1.8 \times 10^{20} \text{m}^{-3}$, respectively. The gyrotron with depressed potential collector realizes an increase in efficiency, a decrease in X-ray radiation and only requires low-voltage power supplies. Regulation of the collector voltage is not so critical. But the regulation of the body/anode power supplies with small current is important. Present 168 GHz gyrotron is of the depressed potential collector type. Here, the regulation of collector, body and anode power supplies is $\sim 5\%$, $< 0.3\%$ and $< 0.3\%$, respectively.

For 168 GHz gyrotrons, the solid state power supply without a tetrode is adopted due to the simplification of maintenance, limit of anode current in the tetrode and construction of an inexpensive system. In Fig.1, the block diagram is shown. The power supply system consists of three clusters. In a cluster, three gyrotrons with each body (90 kV/0.1 A), anode (50 kV/0.3 A) and heater power supplies are

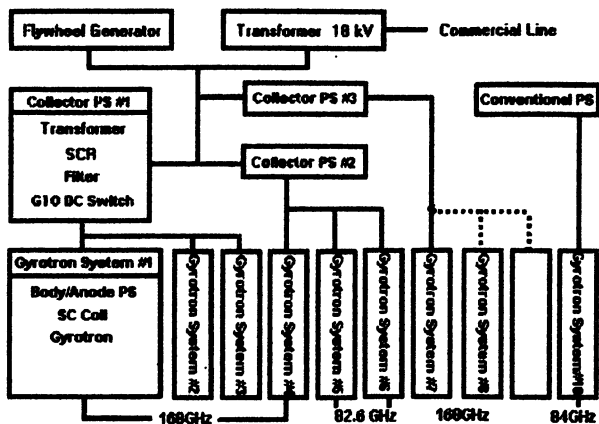


Figure 1: Block diagram of ECH system for LHD

connected to the main collector power supply with maximum voltage/current of 66.2 kV/126 A. Three collector power supplies with a transformer, a SCR, a filter, and a GTO DC switch are driven via commercial line or a flywheel generator. On the other hand, a conventional power supply with a tetrode can supply 80 kV/50 A and is connected to 84 GHz gyrotron. The beam current is turned off within 10 μ sec when gyrotron arcing occurs. Six sets of corrugated-waveguide transmission line of 88.9 mm in diameter are prepared via the LHD basement and the public trench from the heating equipment room. In each line, a polarizer, a circularizer, a waveguide switch, and sliding waveguides are included. To transmit power with the frequency range from 82.6 to 168 GHz, the center frequency of 126 GHz is chosen for the corrugated waveguide. A supporting structure of waveguide is built together with a catwalk for maintenance and adjustment. The catwalk is isolated from the supporting structure to prevent waveguide line from displacement. If the waveguide transmission line is tilted by 0.1 degrees, higher-order modes with 1% would be excited³. The alignment of waveguide is within the accuracy less than 0.1 degrees and 0.1 mm. In the cold test of the straight corrugated-waveguide transmission line with 64 m, low transmission loss of around 2 dB/km was confirmed⁴. In the LHD building, the length of each transmission line is around 110 m and loss around 30 ~ 40% of the system is due to mode-conversion loss in a lot of

(18 to 20) miter bends. To increase maximum withstanding voltage, dry air or nitrogen gas is always introduced in each waveguide. As a result of an arcing, the maximum pulse width of transmitted power depends on injection power into the mouth of corrugated waveguide from the MOU. The arcing problem will be able to be solved by filtering of the output from the MOU and by modifying coupling section into the waveguide. Three launcher mounts are prepared

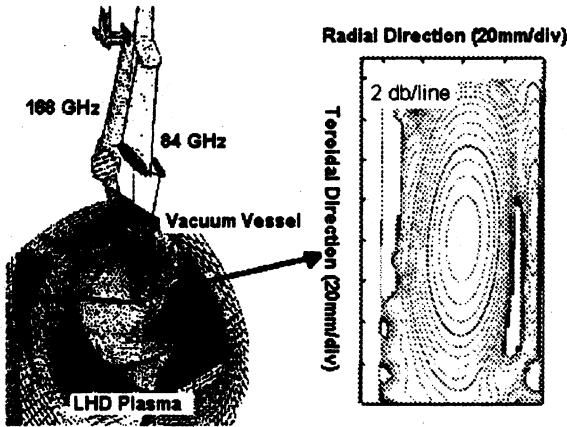


Figure 2: Vertical launcher mount and characteristics of beam at 84 GHz

on LHD. Two vertical launcher mounts are installed on the 5.5U- and 9.5U-ports of the top of LHD and the other horizontal launcher mount on the 20-port from the outside of equatorial plane. The vertical launcher mounts consists of two mirror-aligned lines as shown in Fig.2. Mirror supporting structures, cooling channels, crank shafts to scan the beam two-dimensionally are included. The first mirror with different curvature in toroidal and radial directions generates elliptical gaussian beam. The second mirror is a plane one to direct the beam to the third one. The third mirror has the focusing mirror and the fourth plane mirror can steer two-dimensionally by driving the super-sonic motors. In Fig.2, the beam profile for 84 GHz measured at the mid-plane of the LHD is shown. The radiation pattern clearly shows the well-defined elliptical gaussian beam with waist size of 15 mm in radial and 50 mm in toroidal directions. In the range of 20 cm in toroidal and 15 cm in radial directions, the beam is steered with almost no change in quality.

4 Theoretical Analysis of Sliding Waveguide

In ECH transmission lines, the sliding waveguides are used to adjust the waveguide length. As shown in Fig.3(a), the corrugated waveguides with the inner diameter $2a=88.9$ mm are inserted into the short waveguide with smooth wall with the inner diameter of $2b=110$ mm. The sliding surface is coated by MoS_2 and sealed with a silicon O-ring. By using the electromagnetic (EM) analysis on the mode

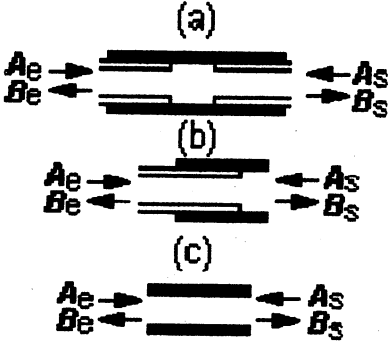


Figure 3: The sliding waveguide for the transmission line.

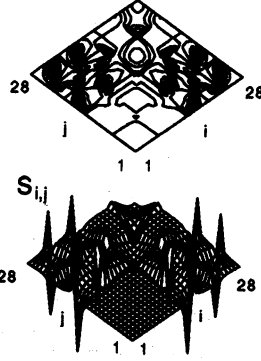


Figure 4: S-Matrix for $N = 7$.

matching method, we take reflection from the discontinuous junction planes into consideration and calculate the complex amplitude of EM-wave in transmission and reflection modes. Equations satisfying the boundary condition at the junction plane are given by

$$\mathbf{e}_0^+ + \sum_n C_n \mathbf{e}_n^- = \sum_m D_m \mathbf{E}_m^+, \quad (1)$$

$$\mathbf{h}_0^+ + \sum_n C_n \mathbf{h}_n^- = \sum_m D_m \mathbf{H}_m^+ + 2\mathbf{h}_0^+ H(a), \quad (2)$$

where the relation $\mathbf{e}_n^+ = \mathbf{e}_n^-$ and $\mathbf{h}_n^+ = -\mathbf{h}_n^-$ are satisfied. To determine the coefficients C_n and D_m , the least square method is adopted:

$$\Gamma_N = \frac{\int_S |\mathbf{e}_0^+ + \sum_n^N C_n \mathbf{e}_n^- - \sum_m^N D_m \mathbf{E}_m^+|^2 dS}{\int_S |\mathbf{e}_0^+|^2 dS} + \frac{\int_S |\mathbf{h}_0^+ + \sum_n^N C_n \mathbf{h}_n^- - \sum_m^N D_m \mathbf{H}_m^+ - 2\mathbf{h}_0^+ H(a)|^2 dS}{\int_S |\mathbf{h}_0^+|^2 dS} \quad (3)$$

where, m, n are mode number, $(+, -)$ is the traveling direction of EM-wave. EM-fields $(\mathbf{e}_0^+, \mathbf{h}_0^+)$, $(\mathbf{e}_n^-, \mathbf{h}_n^-)$ are incident and reflected waves in input waveguide and $(\mathbf{E}_m^+, \mathbf{H}_m^+)$ transmitted wave to the output waveguide. In Eq.(2) on the boundary equations, the term including the Heviside function H is the induced field at the ring-shaped metallic wall in the junction plane when the EM-wave in the smooth wall waveguide is injected into the corrugated waveguide. If $N = \infty$, Γ_∞ is equal to zero. In finite mode number N ,

$$\frac{\partial \Gamma_N}{\partial C_i} = 0, \quad (4)$$

$$\frac{\partial \Gamma_N}{\partial D_i} = 0 \quad (5)$$

are satisfied in order to minimize Γ_N . Because C_i and D_i are complex value in general, $4N$ simultaneous linear equations are solved:

$$\Re[Q_i] = - \sum_j \Re C_j T_{i,j} + \sum_j \Re D_j U_{i,j}, \quad (6)$$

$$\Im[Q_i] = - \sum_j \Im C_j T_{i,j} + \sum_j \Im D_j U_{i,j}, \quad (7)$$

$$\Re[R_i] = - \sum_j \Re C_j V_{i,j} + \sum_j \Re D_j W_{i,j}, \quad (8)$$

$$\Im[R_i] = - \sum_j \Im C_j V_{i,j} + \sum_j \Im D_j W_{i,j}, \quad (9)$$

where $T_{i,j} = \int \mathbf{e}_i^{-*} \cdot \mathbf{e}_j^- dS/K_e + \int \mathbf{h}_i^{-*} \cdot \mathbf{h}_j^- dS/K_h$, $U_{i,j} = \int \mathbf{e}_i^{-*} \cdot \mathbf{E}_j^+ dS/K_e + \int \mathbf{h}_i^{-*} \cdot \mathbf{H}_j^+ dS/K_h$, $V_{i,j} = \int \mathbf{E}_i^{+*} \cdot \mathbf{e}_j^- dS/K_e + \int \mathbf{H}_i^{+*} \cdot \mathbf{h}_j^- dS/K_h$, $W_{i,j} = \int \mathbf{E}_i^{+*} \cdot \mathbf{E}_j^+ dS/K_e + \int \mathbf{H}_i^{+*} \cdot \mathbf{H}_j^+ dS/K_h$, $Q_i = \int \mathbf{e}_i^{-*} \cdot \mathbf{e}_0^+ dS/K_e + \int \mathbf{h}_i^{-*} \cdot (\mathbf{h}_0^+ - 2\mathbf{h}_0^+ H(a)) dS/K_h$, $R_i = \int \mathbf{E}_i^{+*} \cdot \mathbf{e}_0^+ dS/K_e + \int \mathbf{H}_i^{+*} \cdot (\mathbf{h}_0^+ - 2\mathbf{h}_0^+ H(a)) dS/K_h$, $K_e = \int |\mathbf{e}_0^+|^2 dS$ and $K_h = \int |\mathbf{h}_0^+|^2 dS$.

To carry out the numerical integration, the two dimensional data files sampled with 64×64 points are provided for all the modes. Here, the radius of corrugated waveguide is 24 points. The sliding waveguide as shown in Fig.3(a) consists of the up-step waveguide (b), the straight waveguide (c) and the down-step waveguide (b). By the mode-matching method, each mode amplitude of input waves (A_{eq}, A_{sq}), and reflected waves (B_{eq}, B_{sq}) in S-matrix S of Fig.3(b) is calculated, where suffix e and s are name of ports. Although the up-step (the down-step) waveguide has real two ports, $4N$ virtual ports

with TE_{1p} , TM_{1p} , HE_{1p} and EH_{1p} transmission lines for $p = 1 \sim N$ ($p = 2 \sim N + 1$ for EH_{1p}) are considered:

$$\begin{pmatrix} B_{e1} \\ B_{e2} \\ \dots \\ B_{s1} \\ B_{s2} \\ \dots \end{pmatrix} = \left(\begin{array}{c|c} S_{11} & S_{12} \\ \hline S_{21} & S_{22} \end{array} \right) \begin{pmatrix} A_{e1} \\ A_{e2} \\ \dots \\ A_{s1} \\ A_{s2} \\ \dots \end{pmatrix}, \quad (10)$$

where input and reflected hybrid modes are denoted by A_{eq} and B_{eq} . As for input and reflected TE/TM modes, A_{sq} and B_{sq} are used: $A_{e1} = A_{eHE_{11}}, \dots, A_{e(N+1)} = A_{eEH_{12}}, \dots, A_{s1} = A_{sTE_{11}}, \dots, A_{s(N+1)} = A_{sTM_{11}}, \dots$ and $B_{e1} = B_{eHE_{11}}, \dots, B_{e(N+1)} = B_{eEH_{12}}, \dots, B_{s1} = B_{sTE_{11}}, \dots, B_{s(N+1)} = B_{sTM_{11}}, \dots$.

In Fig.4, the contour plot and wireframe of S-matrix for $N = 7$ at 168 GHz are shown. The S-matrix shows that injection power of HE_{1p} or EH_{1p} modes to the smooth waveguide in the up-step junction are almost transmitted as TE_{1p} and TM_{1p} modes. On the other hand, TE_{1p} and TM_{1p} modes at the down-step junction are partially reflected when these modes are injected into the corrugated waveguide. For example, in 28 modes of TE_{1p} , TM_{1p} , HE_{1p} and EH_{1p} for $p = 1 - 7$ ($p = 2 - 8$ for EH-mode), the calculation of $S_t S^*$ shows that the off-diagonal terms are close to zero and diagonal terms except $|S_{66}|^2$, $|S_{77}|^2$, $|S_{12,12}|^2$, $|S_{13,13}|^2$, $|S_{14,14}|^2$ are close to unity. This results from insufficient mode number in the mode conversion such as $HE_{1,7}$ to mainly (TE_{77} , TM_{77}) and more higher modes which is truncated. This S-matrix is nearly unitary and the system does not conserve energy completely due to the finite modes number considered. Even if N increases, no complete unitary matrix can be obtained. When the sliding length increases, multi-reflection of TE_{1p} and TM_{1p} modes between step junctions causes more higher modes. T-matrice U, D for the up-step and down-step waveguide component as shown in Fig.3(b) are calculated straightforward by the following relation.

$$\begin{pmatrix} B_{s1} \\ B_{s2} \\ \dots \\ A_{s1} \\ A_{s2} \\ \dots \end{pmatrix} = \left(\begin{array}{c|c} U_{11} & U_{12} \\ \hline U_{21} & U_{22} \end{array} \right) \begin{pmatrix} A_{e1} \\ A_{e2} \\ \dots \\ B_{e1} \\ B_{e2} \\ \dots \end{pmatrix}, \quad (11)$$

$$\begin{pmatrix} B_{e1} \\ B_{e2} \\ \dots \\ A_{e1} \\ A_{e2} \\ \dots \end{pmatrix} = \left(\begin{array}{c|c} D_{11} & D_{12} \\ \hline D_{21} & D_{22} \end{array} \right) \begin{pmatrix} A_{s1} \\ A_{s2} \\ \dots \\ B_{s1} \\ B_{s2} \\ \dots \end{pmatrix}, \quad (12)$$

where $U_{11} = S_{21} - S_{22}S_{12}^{-1}S_{11}$, $U_{12} = S_{22}S_{12}^{-1}$, $U_{21} = -S_{12}^{-1}S_{11}$, $U_{22} = S_{12}^{-1}$, $D_{11} = S_{12} - S_{11}S_{21}^{-1}S_{22}$, $D_{12} = S_{11}S_{21}^{-1}$, $D_{21} = -S_{21}^{-1}S_{22}$, and $D_{22} = S_{21}^{-1}$. For the straight waveguide component of Fig.3(c), T-matrix F is given by

$$\begin{pmatrix} B_{s1} \\ B_{s2} \\ \dots \\ A_{s1} \\ A_{s2} \\ \dots \end{pmatrix} = \left(\begin{array}{c|c} F_{11} & 0 \\ \hline 0 & F_{22} \end{array} \right) \begin{pmatrix} A_{e1} \\ A_{e2} \\ \dots \\ B_{e1} \\ B_{e2} \\ \dots \end{pmatrix}, \quad (13)$$

where

$$\left(F_{11} \right) = \begin{pmatrix} e^{-j\theta_1} & 0 & \dots & 0 \\ 0 & e^{-j\theta_2} & \dots & 0 \\ \vdots & \vdots & \vdots & 0 \\ 0 & 0 & 0 & e^{-j\theta_{2N}} \end{pmatrix} \quad (14)$$

and

$$\left(F_{22} \right) = \begin{pmatrix} e^{j\theta_1} & 0 & \dots & 0 \\ 0 & e^{j\theta_2} & \dots & 0 \\ \vdots & \vdots & \vdots & 0 \\ 0 & 0 & 0 & e^{j\theta_{2N}} \end{pmatrix}. \quad (15)$$

Here, θ_q is the phase angle for TE (for $q \leq N$) and TM (for $q > N$) modes. Finally, T-matrix for the sliding waveguide is obtained as

$$\begin{pmatrix} B_{s1} \\ B_{s2} \\ \dots \\ A_{s1} \\ A_{s2} \\ \dots \end{pmatrix} = D [\Re F + \Im F] U \begin{pmatrix} A_{e1} \\ A_{e2} \\ \dots \\ B_{e1} \\ B_{e2} \\ \dots \end{pmatrix}, \quad (16)$$

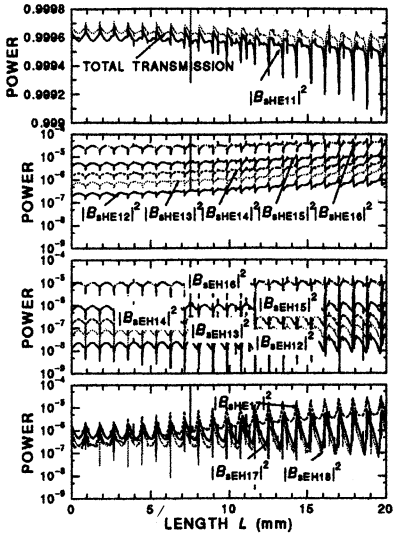


Figure 5: The transmission power.

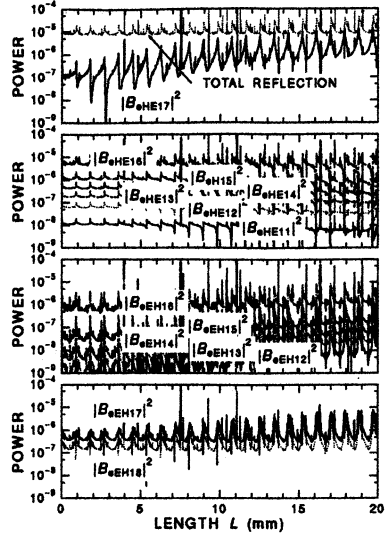


Figure 6: The reflection power.

where HE₁₁ mode of 168 GHz is injected into the sliding waveguide, and transmitted wave amplitude B_{sq} and reflected wave amplitude B_{eq} are solved numerically as a function of the sliding length L by substituting $A_{e1}=1$, $A_{eq}=0$ (for $q \neq 1$), and $A_{sq}=0$. Also, for HE₁₂ injection, B_{sq} and B_{eq} are obtained by replacing A_{e1} with A_{e2} . In Fig.5 and Fig.6, transmitted and reflected power fractions of HE_{1 p} and EH_{1 p} modes $|B_{sHE1p}|^2, \dots, |B_{sEH1p}|^2, \dots, |B_{eHE1p}|^2, \dots, |B_{eEH1p}|^2, \dots$ are plotted as a function of sliding length L for mode number of $N = 7$ when HE₁₁ mode is injected into the sliding waveguide. It is confirmed that transmission power of HE₁₁ at $L = 0$ becomes close to unity when N increases. For instance, this value for $N = 5, 7, \dots$ is 0.9991, 0.9997,.... Because phase difference between TE₁₁ and TM₁₁ modes increases with L , power fraction of transmitted HE₁₁ mode, which is a composition of TE₁₁ and TM₁₁ modes, decreases. Typically, for sliding length of $L=2$ cm the transmission loss of HE₁₁ is $< 0.1\%$. With increasing L , many periodic changes in the transmission and the reflection are observed, the depth of trough increases and the period is almost a half waveguide-wavelength. This phenomenon results from the formation of standing wave of TE and TM modes with low-order trapped partially in the sliding section. Waveguide-wavelength of low higher-mode is nearly

equal to the wavelength in free space. Up to now we can not understand why positive and negative spikes appear with the same period.

5 Plasma Production and Heating Experiments

At the end of March 1998, the plasma-production experiment started with the injection of X mode at the second electron cyclotron harmonics⁵. Here, the toroidal magnetic field is 1.5 T. Here, working gas is hydrogen. In the experiments three gyrotrons with the frequency of 82.6 and 84 GHz are operated. As in Fig.7, elliptical

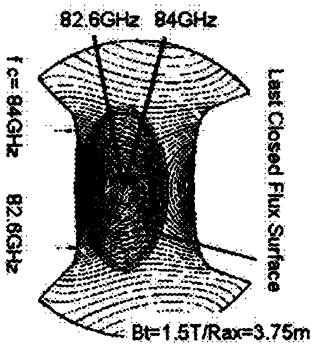


Figure 7: Magnetic field configuration

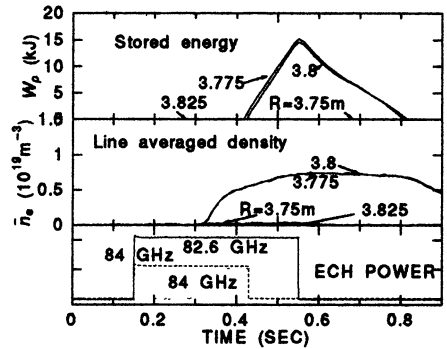


Figure 8: The waveforms of W_p , \bar{n}_e and ECH pulse

gaussian beams are injected vertically and EM-wave of the focusing rays resonates near the magnetic axis and plasma is initiated. By scanning the beam axis radially or strength of magnetic field, parameter range to initiate plasmas is examined. As in Fig.8, it was found that the radial focusing point to get to high temperature plasma is limited within 2 cm near the layer of electron cyclotron resonance where the magnetic axis is located. Here, the line-averaged density around $7 \times 10^{18} \text{m}^{-3}$ and stored energy W_p of 15 kJ are obtained for ~ 0.25 MW of input power. Because rough estimation of absorbed power by $dW_p/dt|_{-\epsilon} - dW_p/dt|_{\epsilon}$ is about 0.2 MW, it is inferred that most of EM power is deposited effectively by sharp gaussian beam without multi-reflection at the wall. During the second experimental campaign, a maximum power of 0.45 MW is injected by three gyrotrons; maximum line-averaged density, electron temperature T_e and stored energy are attained at $3 \times 10^{19} \text{m}^{-3}$, 2.0 keV and 36 kJ, respectively. The existence of a divertor may suppress production of

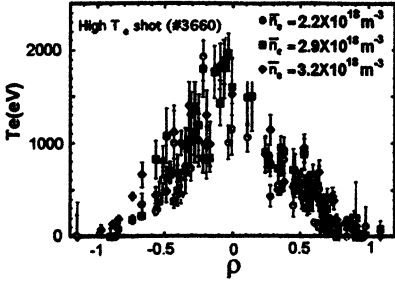


Figure 9: Temperature profile for high T_e shot.

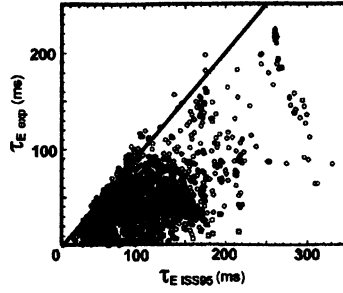


Figure 10: Comparison of τ_{EISS95} with τ_{Eexp} .

a high density plasma because the penetration of gas puffed into the plasma core is difficult without pellet injection. As for high temperature plasma, the peaked electron temperature profile with pedestals near the edge is observed by the Thomson scattering shown in Fig.9 at $\bar{n}_e = 2.2 - 3.2 \times 10^{18} \text{ m}^{-3}$.

The plasma parameters obtained in LHD are compared with a common scaling for the stellarator L -mode confinement given by the ISS95⁶

$$\tau_E^{ISS95} = 0.079 \times a^{2.21} R^{0.65} P_{tot}^{-0.59} \bar{n}_e^{-0.51} B_t^{0.83} (\iota/2\pi)_{2/3}^{0.43}. \quad (17)$$

Here, $(\iota/2\pi)_{2/3}$ is used for the confinement-relevant region with the normalized radius of $2/3$. To calculate experimental τ_{Eexp} , the plasma energy content measured by the diamagnetic flux and absorbed heating power corrected for temporal change in the energy content are needed. Figure 10 shows the data set of the experimental τ_{Eexp} with no correction for temporal change in W_p and injected power P_{inj} for P_{tot} is plotted, because accuracy of transient response for the diamagnetic flux signal is not high. Nevertheless, the upper boundary of data set for ECH is close to the ISS95 scaling. To prevent the LHD from quenching of SC-coil, careful increase in magnetic field up to 2.75 T at the magnetic axis of 3.6 m is tried during second experimental campaign. With increasing B_t , fundamental resonance layer appears at edge region. Plasmas with finite W_p are produced at 2.2 T and W_p increases with B_t . In contrast with plasma production in second electron cyclotron resonance, plasma grows up with the scattering ray at the wall when the fundamental resonance layer exists inside the last closed flux surface. In $B_t = 2.4$ T, the electron temper-

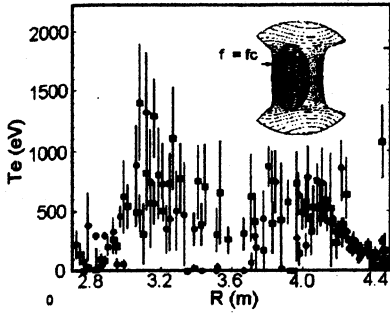


Figure 11: The temperature profile in off-axis ECH. Solid circle and square show the values at $t = 0.22$ and 0.24 sec. The fundamental resonance layer at the equatorial plane is in $r/\rho \sim 0.6$

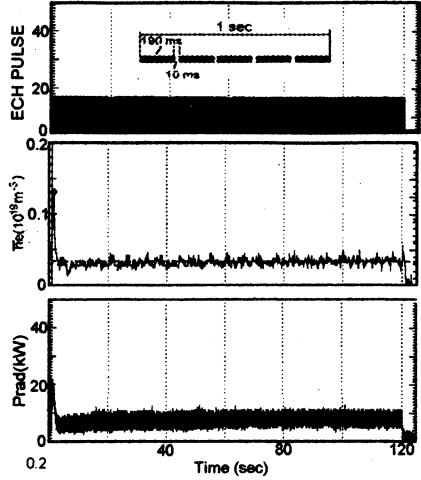


Figure 12: The waveform of ECH pulse, \bar{n}_e and P_{rad} .

ature profile is measured. The measured profile of T_e as a parameter of time is hollow as shown in Fig.11.

As the first trial on steady-state plasma production by ECH, the 84 GHz gyrotron is operated with keeping the duty factor of 95 % with 5 Hz (190 ms/ON and 10 ms/OFF) at $P_{inj} = 50$ kW as shown in Fig.12. In the long-pulse experiments, total injection time of ECH pulse is extended to 10, 20 sec and 120sec. Here, $B_t = 1.5$ T and $R_{ax} = 3.75$ m. Fig.12 shows time evolutions of He-plasma parameters during 120 sec. The steady $\bar{n}_e = 3 - 5 \times 10^{17} \text{ m}^{-3}$ and radiation signal P_{rad} measured by the bolometer system are observed except for the initial 5 sec. The ion temperature estimated by spectroscopy of CV line and electron temperature measured by soft X-ray PHA are about 300eV and the value less than 650 eV, respectively.

6 Summary

The electron cyclotron heating system on LHD is described. In this system, solid state power supply with three clusters is adopted. For fundamental and second electron cyclotron harmonic heatings at $B_t = 3$ T, 82.6/84 GHz and 168 GHz gyrotrons are prepared. Six sets of transmission lines with around 110 m is installed. In first and second experimental campaigns, two sets of vertical launcher mount

are used and injecting beams are scanned poloidally. By injecting the maximum power of 0.45 MW at 82.6/84 GHz, the obtained maximum plasma parameters are line-averaged density of $3 \times 10^{19} \text{m}^{-3}$, electron temperature of 2.0 keV and energy content of 36kJ. The theoretical analysis of sliding waveguide is performed with a combination of mode-matching and scattering matrix techniques. The result shows that small amount of higher-order modes in reflection and transmission is excited and that HE_{11} mode is transmitted with the loss of $< 0.1\%$ at the sliding length $L = 2$ cm.

Acknowledgments

The authors would like to thank the machine operation group for supporting experiments and Dr. A. Iiyoshi for his continuing encouragement.

References

1. Iiyoshi, A et al. *IAEA-F1-CN-69,EX2/3*, 1998.
2. Kaneko, O et al. submitted to *Nucl. Fusion*.
3. Ohkubo, K. et al. *International Journal of Infrared and Millimeter Waves*, **15**, 1507-1519, 1994.
4. Ohkubo, K. et al. *International Journal of Infrared and Millimeter Waves*, **18**, 23-41, 1997
5. Kubo, S. et al. to be published in *Proc. of 19th Topical Conf. of Application of Radio Frequency Power to Plasmas*, Annapolis 1999.
6. Stroth, U. et al. *Nucl. Fusion*, **36**, 1063, 1998.

POLARIZATION MEASUREMENTS DURING ELECTRON CYCLOTRON HEATING EXPERIMENTS ON THE DIII-D TOKAMAK

C.C. Petty, T.C. Luce, M.E. Austin, H. Ikezi, J. Lohr, and R. Prater*

General Atomics, P.O. Box 85608, San Diego, California, 92186-5608, USA

*University of Texas at Austin, Austin, Texas.

The polarization of the launched electron cyclotron wave has been optimized for coupling to the X-mode by adjusting the inclination of grooved mirrors located in two consecutive mitre bends of the waveguide. The unwanted O-mode component of the launched beam can be positively identified by the difference in the power deposition profiles between X-mode and O-mode. The optimal polarization for X-mode launch is in good agreement with theoretical expectations.

Electron cyclotron heating (ECH) and current drive (ECCD) experiments on the DIII-D tokamak need narrow beams in nearly pure X-mode to achieve the highly localized deposition and current drive required for advanced tokamak scenarios. The electron cyclotron waves are launched from the low-field-side of the tokamak using two 110 GHz gyrotrons ("Katya" and "Dorothy"), corresponding to the second harmonic of the electron cyclotron frequency. The two gyrotrons are capable of 1.7 MW of combined power for 1 s pulses. For current drive experiments, a toroidal launch angle of 19° is used, while perpendicular launch is also possible for pure heating applications using a different mirror geometry. The ECCD launcher is steerable in poloidal angle which allows the deposition location to be varied from the plasma center to the edge.

The polarization of the launched wave is controlled by adjusting the inclination of grooved mirrors located in two consecutive mitre bends of the evacuated waveguide.¹ This type of polarizer produces a polarization dependent phase delay since the wave is reflected from the top of the grooves when the electric field is aligned to the groove, whereas the wave is reflected from the bottom of the grooves when the electric field is perpendicular to the groove. Nearly any mixture of X-mode and O-mode power is possible using these polarizers. For perpendicular launch, the desired polarization for X-mode is linearly polarized (ellipticity = 0) with an inclination of 90° relative to the magnetic field at the plasma edge.

The power deposition profile is determined experimentally by modulating the ECH power at 100 Hz and measuring the electron temperature (T_e) response using a 32-channel heterodyne radiometer.² In the limit of infinite modulation frequency (ω), the temperature response (\tilde{T}_e) is everywhere proportional to the ECH source term with a 90° phase lag

from the injected power. For square wave modulation, the power deposition profile can be found from³

$$P_{abs} = \frac{2\omega}{\pi} \frac{3}{2} n_e \bar{T}_e \quad , \quad (1)$$

where n_e is the electron density. However, this equation places only an upper bound on the deposition profile width for the relatively low modulation frequency of 100 Hz used in these experiments.

Experimental Results

Recent experiments on DIII-D have verified the correct operation of the polarizers by scanning the mixture of X-mode and O-mode power by changing the inclination and ellipticity of the launched beam. Perpendicular launch of the ECH is used in this experiment since this allows the regions of deposition for X-mode power and O-mode power to be easily separated, as described below and shown in Fig. 1. The X-mode component is strongly absorbed off-axis at the location of the second harmonic ECH resonance, whereas the O-mode component is weakly absorbed owing to the low electron temperature off-axis. The remaining O-mode component of the wave reflects off of the graphite inner wall and makes a second pass through the plasma, this time passing close to the plasma center where the O-mode power is more strongly absorbed due to the higher electron temperature.

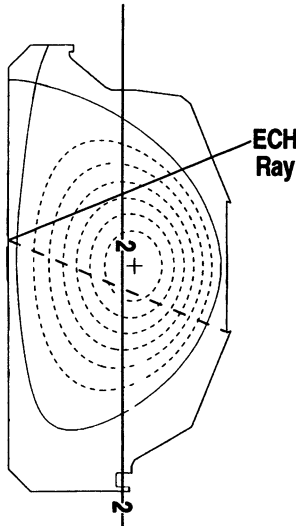


Fig. 1. Vacuum ray paths for perpendicular launch of electron cyclotron waves for these experiments.

Measurements of the power deposition profile can clearly resolve the separate X-mode and O-mode peaks, as shown in Fig. 2. In the case of Fig. 2(a) for the Katya gyrotron, the mixture of X-mode power and O-mode power is varied by changing the inclination of the linear polarized launched beam, whereas in the case of Fig. 2(b) for the Dorothy gyrotron, the ellipticity of the launched beam is changed as well. Figure 2 shows that the X-mode component is absorbed near $\rho \approx 0.55$, where ρ is the normalized toroidal flux coordinate. After reflecting off the inner wall, the O-mode component is seen to damp near $\rho \approx 0.15$. The relative size of the X-mode and O-mode peaks are in good agreement with the expected X-mode and O-mode powers based on the polarizer settings.

Scans of the wave inclination show that the launched X-mode power is optimized for an inclination near 90° , which agrees with theoretical expectations for perpendicular injection. Figure 3(a) shows the measured power deposition profiles for Katya during an inclination scan about the optimal X-mode launch point. The unwanted O-mode component is seen to increase as the inclination moves away from 90° in either direction. Conversely, the magnitude of the X-mode component increases as the inclination moves closer to 90° . A similar result is obtained for Dorothy, as shown in Fig. 3(b).

Scans of the wave ellipticity show that the unwanted O-mode power is minimized for an ellipticity near 0, in agreement with theory for perpendicular launch. This is shown in Fig. 4(a) for Katya and Fig. 4(b) for Dorothy. Since the O-mode component in Fig. 4(a) never completely

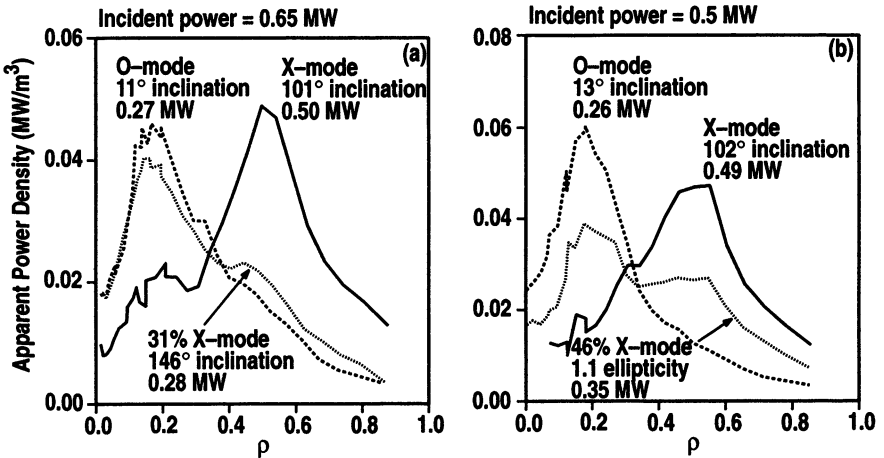


Fig. 2. Power deposition profiles for X-mode and O-mode launch for (a) Katya, and (b) Dorothy. The integrated absorbed powers are also indicated.

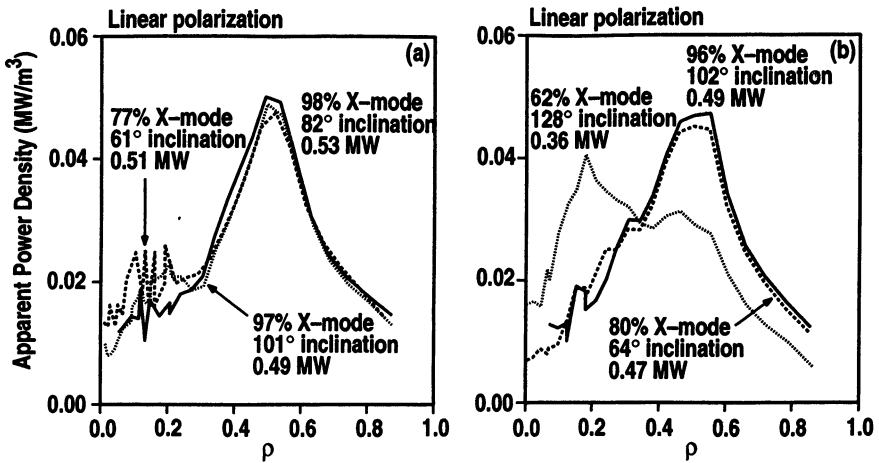


Fig. 3. Power deposition profiles for an inclination scan about the optimal X-mode point for (a) Katya, and (b) Dorothy. The integrated absorbed powers are also indicated.

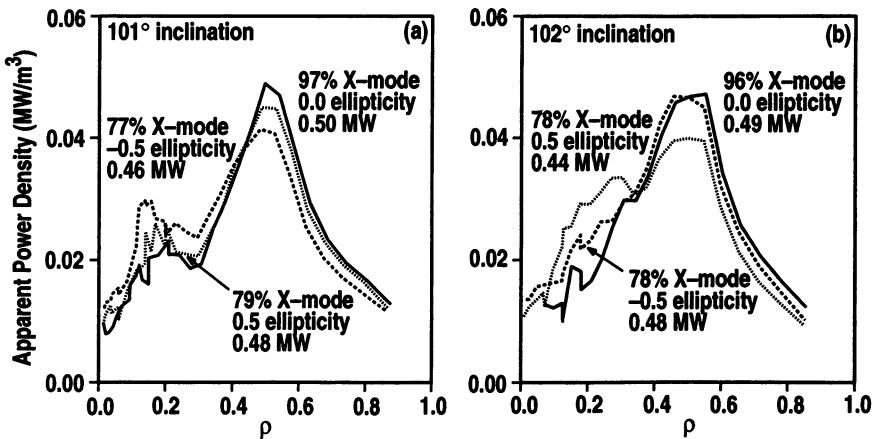


Fig. 4. Power deposition profiles for an ellipticity scan about the optimal X-mode point for (a) Katya, and (b) Dorothy. The integrated absorbed powers are also indicated.

disappears, even for an ellipticity of 0, this would indicate that the inclination has not been set to the ideal value for X-mode launch. There is also a puzzling asymmetry in the magnitude of the measured O-mode power for ellipticities of ± 0.5 . In Fig. 4(a), the O-mode peak for Katya is lower for an ellipticity of 0.5 compared to -0.5 , while in Fig. 4(b), the

O-mode peak for Dorothy is higher for an ellipticity of 0.5 compared to -0.5. Although this asymmetry is not understood presently, it may be related to the slightly different toroidal angular components for the two ECH systems since the launchers actually inject $\pm 2^\circ$ from perpendicular.

Conclusions

Experiments on DIII-D have shown that the polarization of the launched electron cyclotron waves can be controlled by adjusting the inclination of grooved mirrors located in two consecutive mitre bends of the waveguide. The X-mode and O-mode components of the launched beam can be identified by their different deposition profiles, determined by modulating the ECH power and measuring the electron temperature response. For perpendicular injection of the waves, the experimentally determined polarization for optimal X-mode launch is in agreement with theory. This gives confidence that the required polarization for X-mode launch in the more difficult situation of current drive injection can be correctly obtained.

Acknowledgment

This is a report of work supported by the U.S. Department of Energy under Contract No. DE-AC03-99ER54463 and Grant No. DE-FG03-97ER54415.

References

1. Doane, J.L., *Int. J. Infrared Millimeter Waves* 13, 1727 (1992).
2. Wang, Z., et al., *Proc. of the 9th Int. Workshop on Electron Cyclotron Emission and Electron Cyclotron Heating, Borrego Springs, California, (World Scientific, 1995) p. 427.*
3. Murakami, M., et al., *Proc. of the 10th Int. Conf. on Radiofrequency Power in Plasmas, Boston, Massachusetts (American Institute of Physics, 1993) p. 48.*

THE 110 GHz GYROTRON SYSTEM ON DIII-D: GYROTRON TESTS AND PHYSICS RESULTS

J. Lohr, P. Cahalan, R.W. Callis, T.S. Chu,* J.S. deGrassie,
I. Gorelov, H. Ikezi, R.A. Legg, T.C. Luce, C.C. Petty,
D. Ponce, R. Prater, D.I. Schuster,† S.E. Tsimring,*

General Atomics, P.O. Box 85608, San Diego, California, 92186-5608, USA

*Communications and Power Industries, Palo Alto, California, U.S.A.

†Brown University, Providence, Rhode Island, U.S.A.

The DIII-D tokamak has installed a system with three gyrotrons at the 1 MW level operating at 110 GHz. Physics experiments on electron cyclotron current drive, heating, and transport have been performed. Good efficiency has been achieved both for on-axis and off-axis current drive with relevance for control of the current density profile leading to advanced regimes of tokamak operation, although there is a difference between off-axis ECCD efficiency inside and outside the magnetic axis. Heating efficiency is excellent and electron temperatures up to 10 keV have been achieved. The gyrotron system is versatile, with poloidal scan and control of the polarization of the injected rf beam. Phase correcting mirrors form a Gaussian beam and focus it into the waveguide. Both perpendicular and oblique launch into the tokamak have been used. Three different gyrotron designs are installed and therefore unique problems specific to each have been encountered, including parasitic oscillations, mode hops during modulation and polarization control problems. Two of the gyrotrons suffered damage during operations, one due to filament failure and one due to a vacuum leak. The repairs and subsequent testing will be described. The transmission system uses evacuated, windowless waveguide and the three gyrotrons have output windows of three different materials. One gyrotron uses a diamond window and generates a Gaussian beam directly. The development of the system and specific tests and results from each of the gyrotrons will be presented. The DIII-D project has committed to an upgrade of the system, which will add three gyrotrons in the 1 MW class, all using diamond output windows, to permit operation at up to ten seconds per pulse at one megawatt output for each gyrotron.

I. Introduction

The 110 GHz ECH system on the DIII-D tokamak comprises three different gyrotrons in the 1 MW class, one Gycom gyrotron and two CPI gyrotrons. The gyrotrons are of two general types, characterized by either a diode or triode magnetron injection gun (MIG) and are further differentiated by the power handling capability of their output windows, which in turn determines the designed characteristics of the output rf beams.

The characteristics and representative gyrotron typical best performance are summarized in Table 1.

Table 1. Gyrotron Characteristics

Manufacturer	Gun type	Window	Performance	rf beam	Mfg. Type	Local name
Gycom ¹	diode MIG	BN	0.8 MW 2.0 s	broad	Centaur	Katya
CPI ²	triode MIG	sapphire	1.1 MW 0.6 s	broad	8011A	Dorothy
CPS ³	triode MIG	diamond	0.5 MW 4.2 s	Gaussian	8110	Toto

Measurements of the rf output power are made using calorimetry on the window cooling circuits. The BN window on Katya is edge cooled by water and has 3.7% absorption. The sapphire window on Dorothy is a face cooled double disk with a chloro-fluorocarbon, FC-75, as the coolant. This window has 1.7% absorption. The window on Toto is a single diamond disk. For this window the absorption, approximately 0.33%, is too low for reliable calorimetric measurements, so output power was measured directly using a black planar load with 1-octanol as the working fluid. Octanol has linear absorption of 13 dB per cm traversed⁴ and the load has minimum thickness of 2.6 cm. The output powers and rf generation efficiencies for each of the gyrotrons are presented in Fig. 1 (a,b,c).

The diode gyrotron has demonstrated somewhat better efficiency than either of the triode tubes. The triode tube produced the highest output power, 1.09 MW averaged over a 600 msec pulse, but the triode tube with the diamond output window has consistently had the worst rf efficiency, averaging 20%–25% in measurements at DIII–D. In initial tests of this gyrotron at CPI, a higher efficiency, about 30% was measured. The reason for the discrepancy is under investigation.

The internal optics systems in the gyrotrons are used to optimize the rf beams for use with the different windows. For the BN and sapphire windows, it was necessary to spread the Gaussian beams naturally produced by the internal mode converters so that the limiting power density was not exceeded on the window. For the Toto gyrotron, with its diamond window, the Gaussian beam could pass without exceeding the limiting power density, so in this gyrotron the Gaussian beam profile was maintained. The waveguide transmission lines used at DIII–D are corrugated circular aluminum tubes propagating the HE_{1,1} circular waveguide

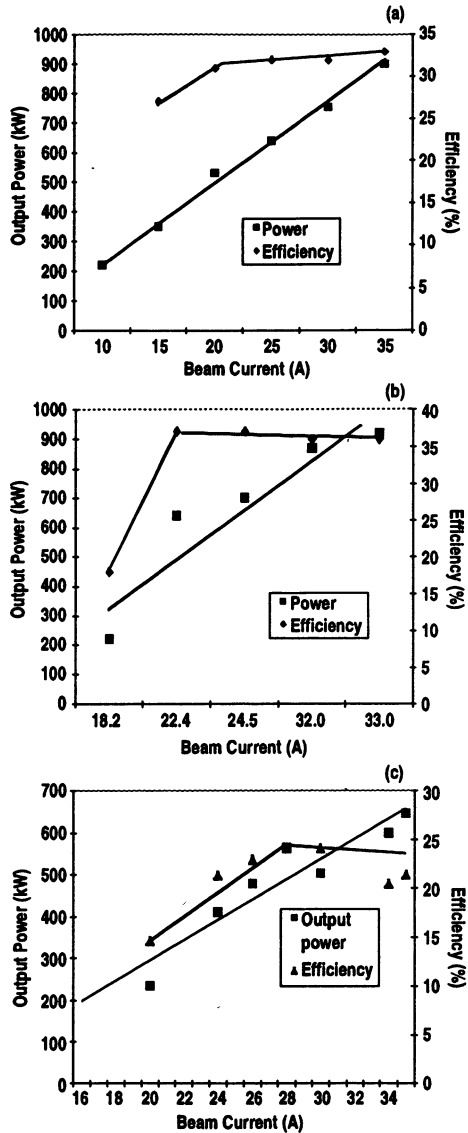


Fig. 1. The rf production efficiencies and output powers for the three gyrotrons, Katya, Dorothy, and Toto are shown in (a), (b), and (c) respectively. The highest output power, 1.09 MW averaged over a 600 msec pulse, was achieved by the triode gyrotron Dorothy, while the highest rf production efficiency was consistently achieved by the diode gyrotron Katya.

mode, which couples well to a Gaussian beam. Therefore the rf beams from Katya and Dorothy had to be restored to Gaussians by reflection from phase correcting mirrors and all three beams had to have Gaussian waists at the waveguide inputs with diameters of 20.3 mm, which is 64% of the diameter of the waveguide. Infrared camera views of the rf beam cross sections for the three gyrotrons near the output windows are shown in Fig. 2 (a,b,c), where this design requirement is clear.

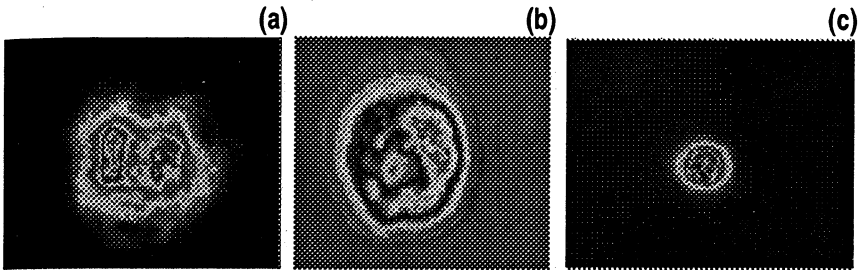


Fig. 2. Infrared camera pictures of the power profiles near the output windows for the three gyrotrons, Katya, Dorothy, and Toto are presented in (a), (b), and (c), respectively. The Toto gyrotron has a diamond output window and the internal optics are designed to produce a Gaussian output beam with a waist near the 5 cm diameter output window, but the other two gyrotrons, Katya and Dorothy, have windows with limiting power density capabilities, therefore the internal optics systems for these tubes spread the output rf beams over a large fraction of the 10 cm diameter windows.

The rf beams propagate into free space, and power profile measurements at several axial positions can be used to calculate the surfaces of phase correcting mirrors which can be used to reform Gaussian beams. This phase reconstruction technique⁵⁻⁸ has been applied to the DIII-D systems and the resulting beams at the waveguide inputs are seen in Fig. 3 (a,b,c), produced using thermally sensitive paper at the waveguide inputs, to be well suited for exciting the $HE_{1,1}$ mode.

II. System Performance and Diagnostics

The gyrotron systems installed on DIII-D collectively have demonstrated all the requirements for advanced tokamak research at fusion parameters: Unit power ≥ 1 MW; Pulse lengths ≥ 2.0 sec; Gaussian beams; Low loss transmission over lines approaching 100 m in length; Control of the trajectory and polarization of the launched rf beam; and Excellent reliability. Repairable failures were experienced in the two

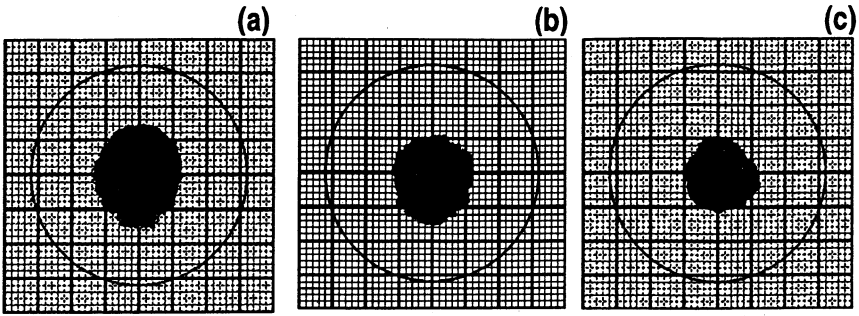


Fig. 3. The same rf beams shown in Fig 2 are shown in Fig. 3(a), (b), and (c) following reflection from pairs of mirrors especially designed to place a Gaussian waist with $w/a=0.64$ at the input to the corrugated waveguides. The mirrors both focus and phase correct the beams produced by the gyrotrons. Thermally sensitive plotter paper is used to indicate the power profiles. The waveguide diameter, indicated by the circles, is 31.75 mm.

triode development gyrotrons. On Dorothy, which had about 5,000 hours of filament operation, the filament shorted, possibly due to an incorrect startup command sent by the control system. On Toto, there was a small failure in a braze in the collector region, which partially vented the gyrotron following a normal pulse. Toto has been repaired and is in test at CPI using its original gun, and Dorothy is ready to be reassembled following its repair. In each case, the cost of the repair was about 10% of the value of the gyrotron.

Polarization of the rf beam

The second harmonic extraordinary mode plasma wave is excited by the microwave beam in the DIII-D installation. In order to generate this mode using microwave injection at arbitrary toroidal and poloidal angles to the tokamak flux surfaces, it must be possible arbitrarily to control the elliptical polarization of the injected rf beam.⁹ This is accomplished at DIII-D by use of grooved mirrors in two of the miter bends of the transmission line. The mirrors have sinusoidal grooves and rotate under remote control.

Measurement of the power deposition profile using Fourier analysis of $T_e(r, t)$ measured by the 32 channel heterodyne radiometer for modulated rf injection has been used to determine the actual injected polarization. The plasma wave excited by the rf can be viewed in the general case as a

superposition of extraordinary and ordinary mode waves. These two waves have substantially different power deposition profiles and wave refraction. The differences are particularly pronounced for off-axis injection.¹⁰ In Fig. 4, the vacuum, X-mode, and O-mode trajectories are plotted, projected to the poloidal plane at the injector, for an rf beam injected with a 19° toroidal angle for current drive and a poloidal angle such that the wave encounters the plasma second harmonic resonance above the magnetic axis but near the major radius, R_0 . For perfect X-mode, the optical depth is large enough that the absorption is essentially 100% in a single pass. For O-mode, the off-axis optical depth is small, first pass absorption is negligible and second pass absorption, where the wave trajectory crosses the resonance for the second time at a location with higher T_e , is only marginally greater. Although it was intended that the X-mode only be excited, the measured power deposition profile clearly reveals an O-mode component. These measurements indicated that determination of the injected polarization at the tokamak would be required fully to qualify the system.

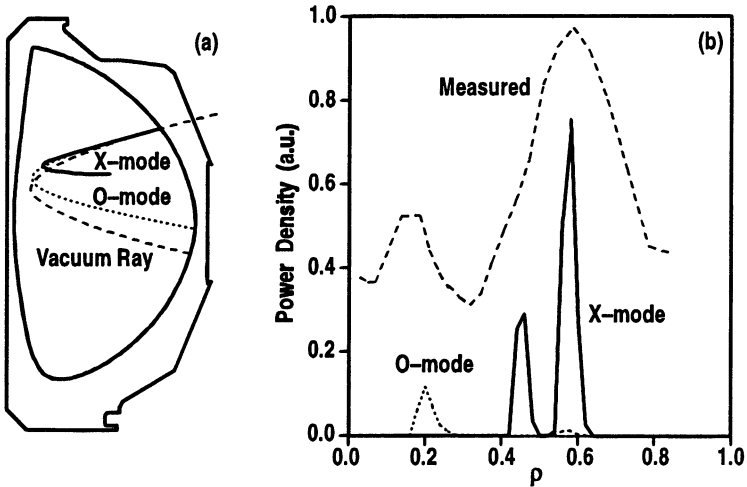


Fig. 4. The injected X-mode, O-mode, and the vacuum rf beam trajectories are shown projected to the poloidal plane of injection for a toroidal injection 19° off-perpendicular for current drive. The plasma second harmonic electron resonance is approximately on a vertical line at the major radius. The measured absorption profile has a peak associated with O-mode, although pure X-mode was intended to have been launched.

Measurements were made of the polarization of the rf beam using a polarimeter developed especially for the purpose.¹¹ Because of transient

behavior during the first few 100 msec of the gyrotron pulse, it was required that the polarimeter operate in vacuum at the full rf beam power, up to 1 MW, and for pulse lengths ≤ 300 msec.

The electric field vector of an electromagnetic wave in the general case traces out an ellipse in an $x - y$ plane perpendicular to its direction of propagation as indicated in Fig. 5. The wave polarization can be completely specified using the lengths of the elliptical axes a, b and the tilt angle α of one of the axes with respect to the laboratory reference. The special cases $b/a = -1, 0, +1$ are called, respectively, left circular, linear and right circular polarization and for $b/a = 0, \alpha = 90^\circ$ and rf injection perpendicular to the flux surfaces, the X-mode will be excited in the plasma.

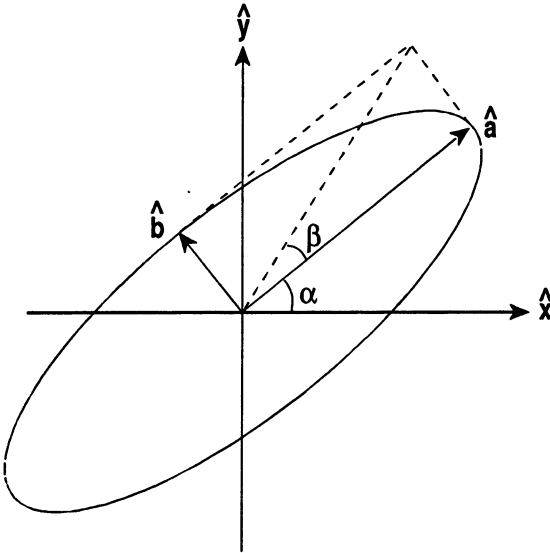


Fig. 5. Coordinate system for describing arbitrary elliptical polarization of the rf beam. The cases $b/a = -1, 0, +1$ are, respectively, left hand, linear, and right hand circular polarization. Parameters $\alpha = 90^\circ, b/a = 0$ would be used to excite X-mode for injection perpendicular to the magnetic field.

The analyzer samples the waveguide rf beam using a diamond pickoff mirror mounted in a miter bend with about -40 dB coupling coefficient. The polarimeter consists of a rotating birefringent quarter wave plate and a fundamental waveguide detection system. The analyzer is shown schematically in Fig. 6. For an 800 kW microwave beam and 300 msec pulse length, the pickoff mirror peak temperature was 150°C without

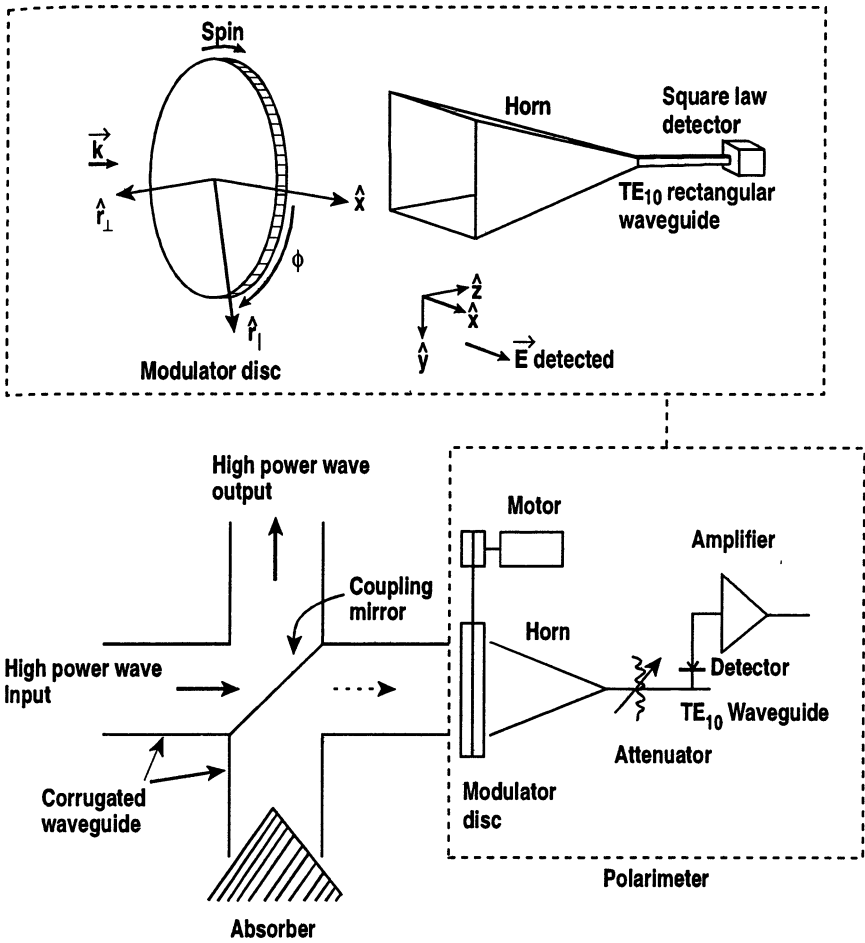


Fig. 6. Schematic diagram of the high power vacuum polarimeter. The rotating birefringent plate modulates the rf detected by a fundamental waveguide system which is then Fourier analyzed to obtain the polarization parameters.

cooling. A cooled version of this mirror is being developed for 1 MW cw operation.

Calibration of the polarimeter at low power allows the rf beam parameters to be calculated directly from the modulated signal detected as the analyzing plate is rotated during a gyrotron pulse. In Fig. 7, a typical example of the measurement at the output of Katya is shown. The polarization is nearly completely linear, but with a tilt angle of about 3°

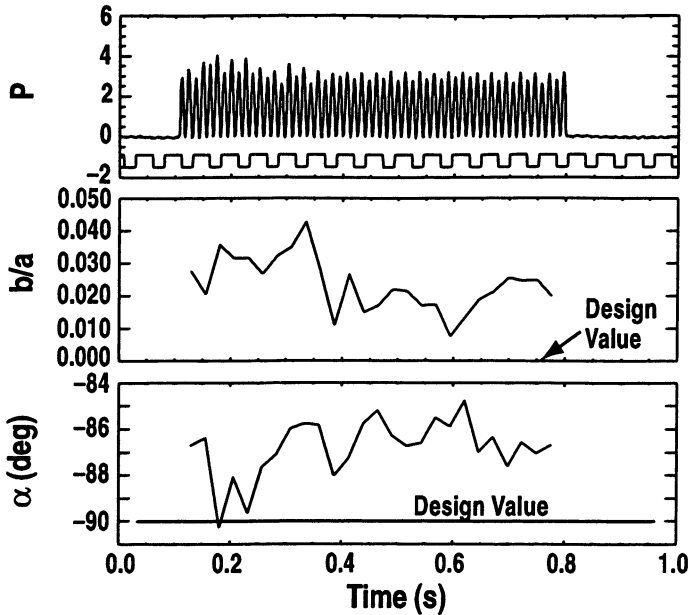


Fig. 7. Raw detected data and post processed data showing the measurements of b/a and α for the output from the Katya gyrotron. A small deviation from horizontal linear polarization of the rf from the gyrotron can result in an admixture of O-mode in the wave excited in the tokamak as indicated by the power deposition profile measurements for oblique injection.

from horizontal. This tilt propagates through the transmission line and polarizer system to appear as an undesired O-mode component in the beam injected into DIII-D, exactly as indicated in the plasma measurements of the power deposition profile.

The polarimeter has been used to characterize all the gyrotron and waveguide systems and the individual characteristics of the separate systems are taken into account in determining the settings for the polarizer mirrors for a particular DIII-D injection geometry. The accuracy of the measurement is $\pm 1^\circ$ in tilt and 1% in b/a .

Alignment of the rf beam to the waveguide

Alignment of the rf beam and the waveguide for the DIII-D system has always been an issue, since misalignment can result in coupling to lossy modes in the waveguide rather than the desired $HE_{1,1}$ and both

damage to the components and injection of waves with mixed polarizations into the tokamak can occur.

The current alignment procedure is to determine the direction in space of the axis of the rf beam emanating from the gyrotron and to place the optical axis of the two-mirror Matching Optics Unit on this axis. This guarantees that, to high accuracy, the rf beam strikes the center of the first MOU mirror. Micrometer screws on the first mirror are then used to adjust the tilt of this mirror slightly to place the centroid of the beam on the center of the second MOU mirror, which is diagnosed by infrared camera measurements of an rf absorber on the surface of the second mirror. This step is less precise, because the beam is not focused at this point. The final x, y alignment at the waveguide input is determined for short pulses using thermally sensitive paper attached to the waveguide.

This procedure can center the beam to better than 1.0 mm at the waveguide input, which is easy to measure, with coaxiality to better than 0.5° which is difficult to measure. This accuracy would yield only a few per cent mode conversion at worst.¹²⁻¹⁴ But the measured power losses to the MOU mirrors and structure have always been around 15% for all our systems, which could be due to misalignment. Furthermore, all the alignment is done for short pulses as the gyrotron is turning on, which might be atypical of the situation for longer pulses. Therefore, an independent measurement of the mode mix in the waveguide with long pulse capability was sought.

The device developed for this measurement makes use of the diamond coupling mirror designed for the polarization measurements described above. In the straight through arm of the miter bend, a corrugated waveguide initially carries the coupled low power rf beam. The weaker spurious modes must be separated from the dominant $HE_{1,1}$ mode. After an arbitrary distance, the waveguide wall corrugations end and the wall becomes smooth, causing conversion of the $HE_{1,1}$ mode to $TE_{1,1}$, $TE_{1,2}$, ..., $TM_{1,1}$, $TM_{1,2}$... modes, all of which have electric field components at the waveguide center in the \hat{y} direction and no component in the \hat{x} direction. Thus, a fundamental waveguide at the waveguide center oriented to couple to E_y can be used as the $HE_{1,1}$ detector. Spurious modes generated from misalignments either couple to modes which have E_x and E_y components at intermediate radii, say $a/2$, or have nonzero x and y components themselves. For example, the $HE_{2,1}$ mode resulting from either angular or transverse misalignment converts to $TE_{2,1}$, $TE_{2,2}$, ..., $TM_{2,1}$, $TM_{2,2}$, etc. Therefore, the analyzer incorporates two additional fundamental waveguide pickoffs at intermediate radii placed azimuthally at $\theta=0$ and $\theta=\pi/2$ where $\theta=0$ is in the horizontal plane and $\theta=\pi/2$ is in the vertical plane. For horizontal polarization incident on

the analyzer, an angular misalignment in the vertical plane excites waveguide modes with $E_x = 0$ at $\theta = 0$, $r/a = 1/2$, but $E_x \neq 0$ at $\theta = \pi/2$, $r/a = 1/2$, and an angular misalignment in the horizontal plane excites modes with $E_x = 0$ at $\theta = \pi/2$, but $E_x \neq 0$ at $\theta = 0$. Thus the central detector becomes the monitor for the $HE_{1,1}$ component and the ratio of this signal to the two off-axis signals gives the extent of the misalignment in the x and y planes. A schematic of the analyzer is shown in Fig. 8.

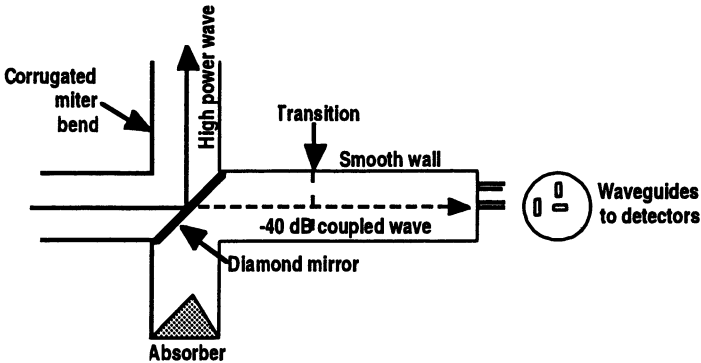


Fig. 8. The alignment analyzer relies on mode conversion from a non-coaxial or non-centered “ $HE_{1,1}$ ” beam to modes with off-axis E_x or E_y components. The pickoff mirror couples about -40 dB to the analyzer.

The device is in initial testing stages, so no positive conclusions can yet be drawn, but the preliminary indication is that spurious modes are present at low but detectable levels in the waveguide, that the analyzer behaves as designed and that the alignment procedure outlined above gives excellent axial and transverse alignment.

Parasitic oscillations in the gyrotrons

Two of the three gyrotrons installed at DIII-D exhibit parasitic oscillations.^{15,16} Although the low frequency emissions cause difficulties for circuits and nearby equipment, the effect on the gyrotron operation is not pronounced. Although some characteristics of the parasites in the two gyrotrons are the same, in some respects the behaviors are quite different.

The Katya gyrotron has a low frequency parasite at 96 MHz, the radiated intensity of which has been estimated at a few kW. For this gyrotron, the parasite is always present above a threshold electron beam current of about 4 A. At very low currents the exact frequency is not well

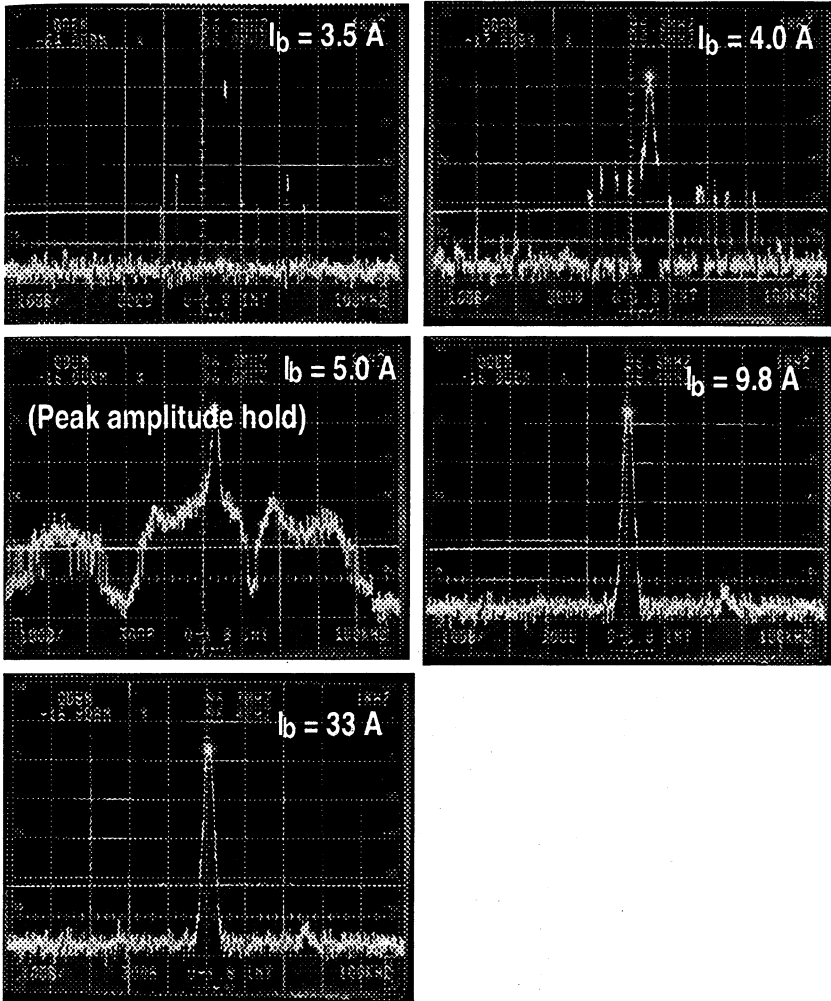


Fig. 9. The parasitic emission spectra on Katya for a range of electron beam currents. Below a threshold current, no parasite is observed. The emission begins sporadically as the beam current is increased and finally locks to a monochromatic output above about $I_b = 12 \text{ A}$.

determined and sporadic oscillations are observed over a $\pm 5 \text{ MHz}$ range centered at 96 MHz . As the beam current is increased, the averaged spectrum fills in with well defined sidebands and harmonics at least to the tenth. At the operating beam current, around 32 A , the spectrum is rather

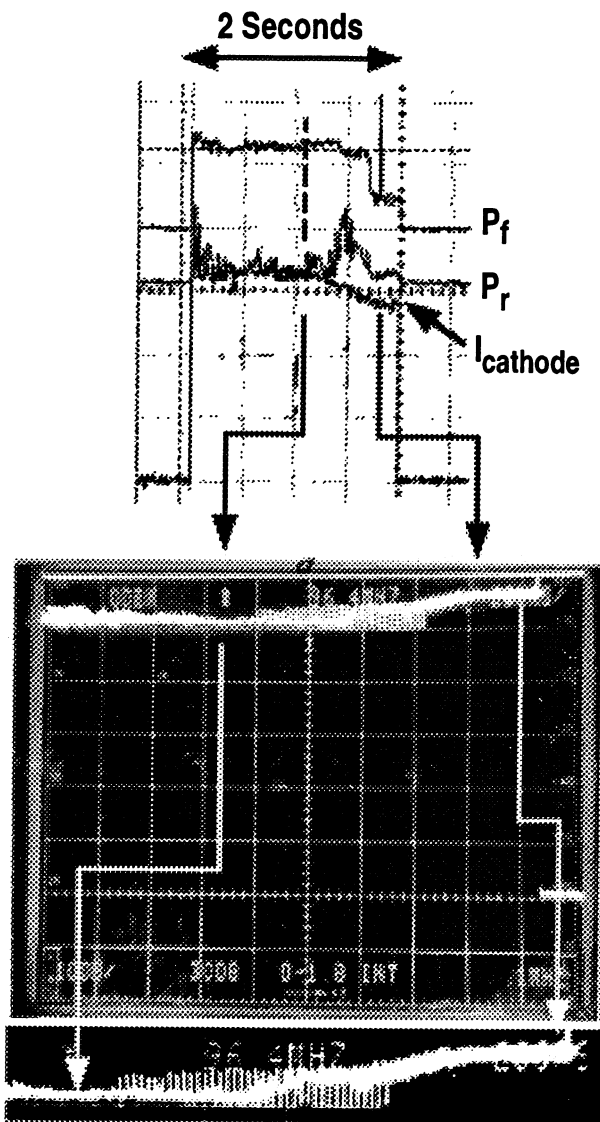


Fig. 10. The amplitude of the Katya parasite increases substantially when the cathode current drops near the end of a long pulse. The increase begins as a series of regularly spaced spikes, the peaks of which eventually define the c.w. parasite amplitude. Decreasing the gun bucking coil current can preserve the constant cathode current, without the increase in parasite amplitude, but the observation may have a bearing on operation for still longer pulses. Sensitivity is 10 dB/cm.

monochromatic. The spectra observed on an antenna near the gyrotron are shown in Fig. 9 with I_b as a parameter. For long pulses greater than about 1.5 sec, there is a clear correlation between an increase in the parasitic emission and a decrease in the electron beam current. In Fig. 10 the spectrum analyzer is tuned to 96 MHz with a 100 kHz bandwidth. When the electron beam current begins to droop, there is a regular series of 10 dB spikes in the parasitic emission, the peaks of which eventually become the new equilibrium emission level. A decrease in the gun bucking coil current decreases the electron pitch angle and restores normal operation at constant current to the end of the pulse, strongly suggesting that reflected electrons trapped in the magnetic mirror between the gun and the cavity are involved.¹⁷ The time constant for the change in beam current at the end of the pulse suggests thermal effects are involved.

Parasitic oscillations in gyrotrons with triode MIGs have rarely been encountered, but are clearly seen on Toto, the gyrotron with diamond window and Gaussian output beam. The observations, however, differ qualitatively from those for Katya. On Toto, the onset of the parasite is characterized by a rapid increase, typically about 10%, in the cathode current. The output spectrum at 110 GHz is practically not affected. In contrast with the spectrum for Katya, the parasitic spectrum for Toto is orders of magnitude less strong, closer to the strengths of broadcast signals. But the spectrum peaks at about the same frequency and similar sidebands are observed. In Fig. 11 the spectra for Toto are shown, while in Fig. 12 the cathode current is shown with the 110 GHz spectrum both before and after the step in current. The spectrum analyzer sensitivity decreases slightly in the presence of the low frequency noise associated with the parasite, but no detectable change in the output power at 110 GHz is observed calorimetrically when the parasite is present.

The Toto parasite is not as ubiquitous as for Katya. In a series of pulses some will exhibit the parasite and some will not. There is a 1:1 correlation between parasitic emission and vacuum current, pulses with the parasite having poorer gyrotron vacuum, but causality for this has not been identified.

III. Current Drive Results

The ECH system was primarily used during the 1999 experimental campaign in support of experiments requiring high T_e values, such as fast wave current drive studies. The available power from Katya alone was not sufficient for large scale advanced tokamak research and MHD suppression studies that had originally been contemplated. Nevertheless, the sophistication and sensitivity of the analysis of the $j(r)$ profile using the Motional Stark Effect diagnostic has yielded encouraging current

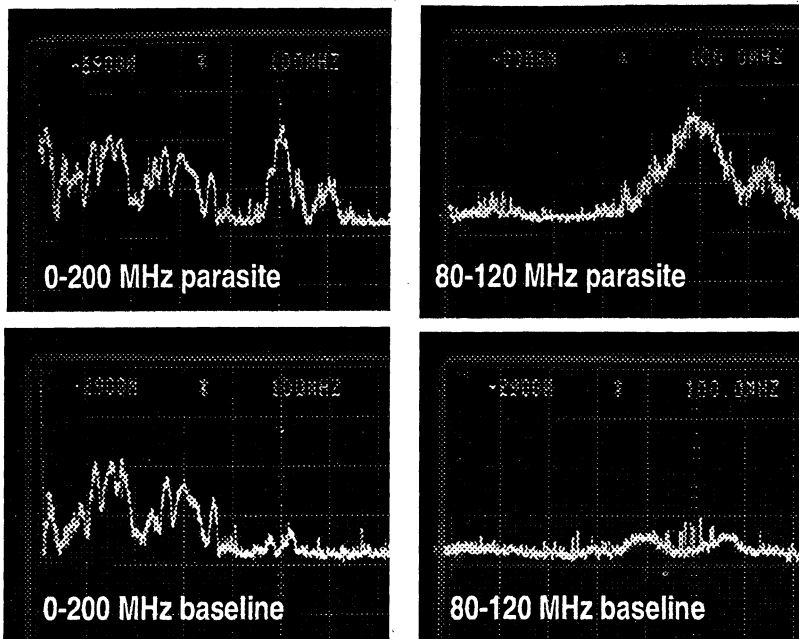


Fig. 11. The low frequency spectra near 100 MHz for Toto during parasitic oscillation. The signals are much weaker than for Katya, but the sidebands are qualitatively the same as the Katya low current spectrum. Sensitivity is 10 dB/cm.

drive results,¹⁸ particularly for off-axis current drive, which will be a critical element of the development of an advanced tokamak concept.

The analysis of non-inductive current drive makes use of the $j(r)$ reconstruction technique of Forest¹⁹ in which magnetic probe data plus the internal magnetic fields measured by Motional Stark Effect spectroscopy give a temporal series of equilibria from which the poloidal flux $\psi(r, t)$ is calculated. The spatial derivative of ψ gives the parallel current density j_{\parallel} as a function of normalized flux and the time derivatives of poloidal flux at fixed poloidal flux give the parallel electric field. In the absence of sawteeth or other strong MHD effects which redistribute the flux, the non-inductive current density $j_{\text{NI}} = j_{\parallel} - \sigma_{\text{neo}} E_{\parallel}$ can then be calculated subject to a neoclassical model for the conductivity. Performing the identical analysis for discharges with and without ECCD allows the non-inductive current density from the bootstrap effect to be separated from the ECCD for both on and off-axis cases.

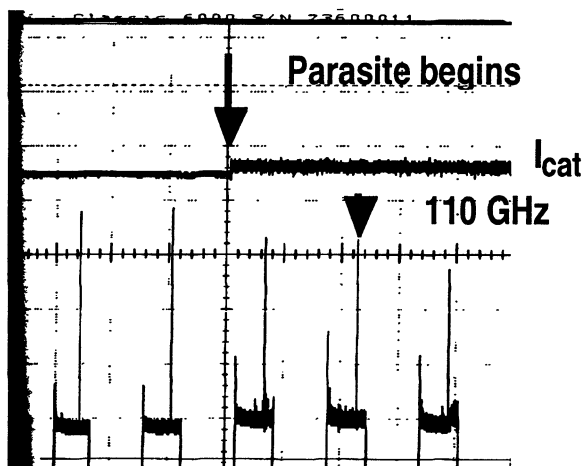
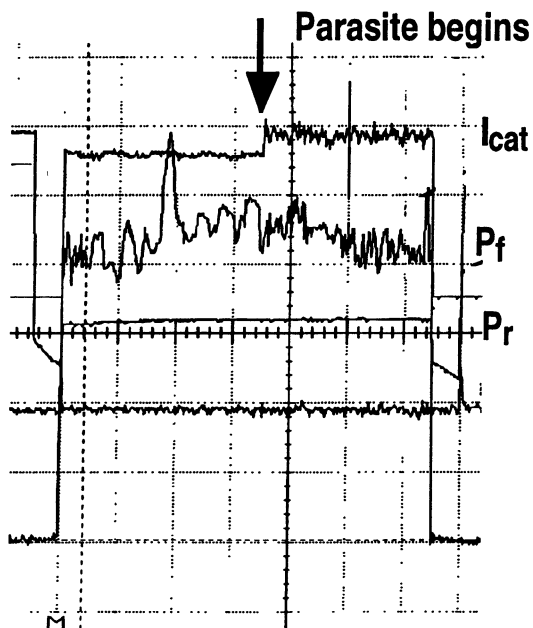


Fig. 12. The region near 110 GHz is shown for a Toto pulse which broke into parasitic oscillation at the point where the cathode current jumps. The 110 GHz output is essentially unaffected, although the additional video noise decreases the sensitivity of the receiver during the parasite.

The injected EC power for the ECCD experiments was about 1 MW. For ECCD near the discharge center, the peak current density driven by electron cyclotron waves was about 90 A/cm^2 , corresponding to an integrated driven current of $92 \pm 29 \text{ kA}$. This integrated value is in excellent agreement with a quasilinear Fokker-Planck calculation, although the profile of the EC driven current is broader than the calculation predicts. In the case of off-axis ECCD, a peak driven current density of 8 A/cm^2 and an integrated total driven current of $35 \pm 13 \text{ kA}$ were observed. This value is in agreement with the calculations regarding the peak driven current density, but again, the breadth of the EC driven profile is greater for the experiment than for the Fokker-Planck calculations and the integrated value for currents driven outside the magnetic axis are greater than the calculations predict. Experiments in which ECCD both inside and outside the magnetic axis was measured suggest that the discrepancy between measurement and calculations may be due to the way trapped particle collisionality is handled by the codes, but the initial attempts to model this have not been able to reproduce the better than expected total current drive in the off-axis case.

IV. Future Plans

The DIII-D project has committed to increasing its ECH capability substantially. An additional three 110 GHz gyrotrons in the MW class with long pulse capability, up to 10 sec, are being produced by CPI for phased delivery late in 1999 and early in 2000. These tubes employ diode guns and single disk diamond output windows with Gaussian rf beams. Modulator-regulator power supplies from the MFTF project are being modified to handle two gyrotrons each and a new addition to the DIII-D building is under construction to house the new gyrotrons. Cold test results for the first of the upgrade tubes are shown in Fig. 13 and indicate that the beam is approximately Gaussian down to the -21 dB contour. The first of the upgrade tubes will employ a single mirror external to the gyrotron to focus and direct the rf beam to the waveguide input, a compromise with completely eliminating the matching optics unit with its steering and phase correcting mirrors. The waveguide runs to the new gyrotrons are approximately 85 m, which should introduce approximately 2% additional transmission loss compared with the present installation.

In addition, the DIII-D Project has acquired two Gycom gyrotrons identical to Katya from the Tokamak de Varennes project. Present plans are for these tubes to be installed in time for the 2000 campaign. The flexibility of the ECH launchers is being enhanced in a cooperative project with the Princeton Plasma Physics Laboratory. PPPL is providing a fully articulating launcher assembly for DIII-D which can inject two rf

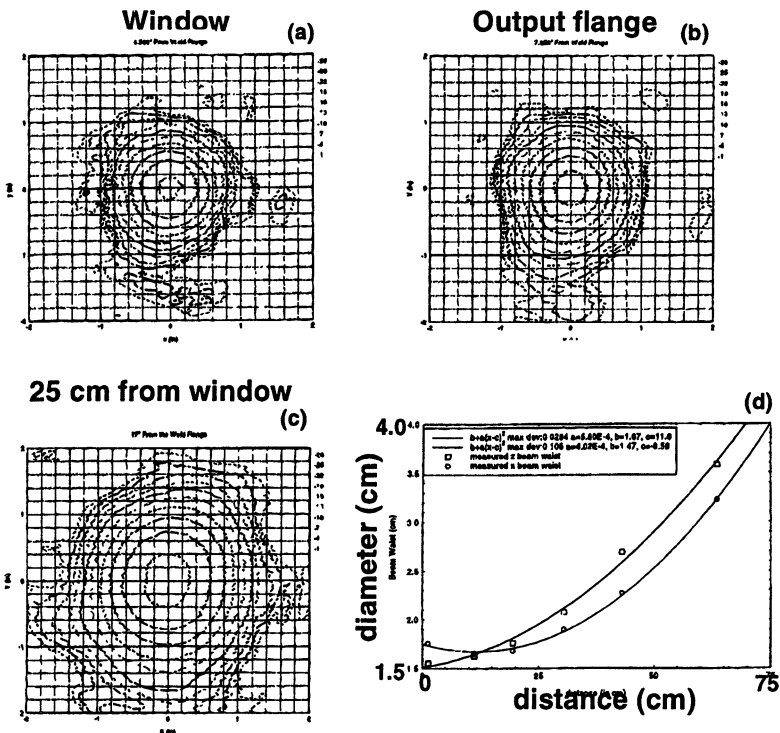


Fig. 13. The three gyrotrons which are being produced by CPI for DIII-D will have diamond output windows and Gaussian rf beams. The cold test results from the first of these gyrotrons are shown in the figure. The output is nearly Gaussian, with a waist at the window. A single mirror system will couple the beam into the waveguide.

beams at variable poloidal and toroidal angles. If the project is successful, launchers for six rf beams will be installed.

V. Conclusions

The 110 GHz gyrotron ECH system on DIII-D has demonstrated many of the key physics results upon which the future advanced tokamak program will depend: Efficient current drive both on and off axis; heating; and required performance parameters. The transmission lines, polarizers, beam steering, dummy loads and diagnostic hardware are working well. Two developmental gyrotrons, which failed in service, have been repaired and are entering a test program. In addition, two

clones of the Gycom gyrotron Katya have been purchased from the Tokamak de Varennes project. An additional group of three production gyrotrons is being produced and tested at CPI. A four-gyrotron system with unit power around 1 MW and pulse lengths of several seconds is planned for the year 2000 experimental campaign with fifth and sixth gyrotrons coming on line during the campaign.

Acknowledgment

This is a report of work supported by U.S. Department of Energy Contract DE-AC03-99ER54463.

References

1. Agapova, M.V., *et al.*, Proc. 20th Int. Conf. Infrared and Millimeter Waves, Orlando (1995) p. 205.
2. Felch, Kevin, *et al.*, IEEE Trans. Plasma Sci. **24**, 558 (1996).
3. Felch, K., *et al.*, Proc. 23rd Int. Conf. Infrared and Millimeter Waves, Colchester (1998) p. 367.
4. Stickel, H., Int J. Electronics **64**, 63 (1988).
5. Katsenelenbaum, B.Z., Semonov, V.V., Rad. Eng. and Elec. Phys. **12**, 223 (1967).
6. Chirkov, A.V., Denisov, G.G., Alexandrov, N.I., Opt. Comm. **115**, 449 (1995).
7. Denison, D.R., Chu, T.S., Shapiro, M.A., Temkin, R.J., IEEE Trans. Plasma Sci. **27**, 512 (1999).
8. Denison, D.R., Kimura, T., Shapiro, M.A., Temkin, R.J., Proc. 22nd Int. Conf. Infrared and Millimeter Waves (Freund, H.P., ed.) Wintergreen (1997) p. 81.
9. Smits, F.M.A., Proc. 8th Joint Workshop ECE and ECRH, Gut Ising (1993) p. 549.
10. Petty, C.C., *et al.*, Proc. 13th Top. Conf. on Applic. RF Power to Plasmas, Annapolis (1999).
11. Ikezi, H., *et al.*, Rev. Sci. Instrum. **70**, 1994 (1999).
12. Ohkubo, K., *et al.*, Proc. T 10th Joint Workshop on Electron Cyclotron Emission and Electron Cyclotron Heating, T. Donne and T. Verhoeven, eds. (World Scientific, 1997) p. 597.
13. Ohkubo, K., *et al.*, Int. J. Infrared and Millimeter Waves **18**, 23–41 (1997).
14. Doane, J.L., Infrared and Millimeter Waves **13**, 123 (1985).
15. Raisky, B.V., Tsimring, S.E., IEEE Trans. Plasma Sci. **24**, n3 (1996).
16. Andronov, A.N., *et al.*, Proc. 20th Int. Conf. Infrared and Millimeter Waves, Orlando (1995) p. 141.
17. Kuftin, A.N., Zapevalov, V.E., Proc. 23rd Int. Conf. Infrared and Millimeter Waves, Colchester (1998) p. 426.
18. Luce, T.C., *et al.*, "Generation of Localized Non-Inductive Current by Electron Cyclotron Waves on the DIII-D Tokamak," submitted to Physical Review Letters.
19. Forest, C.B., *et al.*, Phys. Rev. Lett. **73**, 2244 (1994).

REVIEW OF ECR HEATING AND CURRENT DRIVE IN THE RTP TOKAMAK

F.C. Schüller, R.W. Polman for the RTP-team

FOM-Institute of Plasma Physics, 3430BE Nieuwegein, The Netherlands;
Association Euratom-FOM; partner in the Trilateral Euregio Cluster

The modest size RTP ($R=0.72\text{m}$; $a=0.164\text{ m}$; $B_t < 2.5\text{ T}$; $I_p < 150\text{kA}$) was dedicated to the study of anomalous electron turbulent transport in tokamaks. The electron transport was manipulated with an ECRH/CD system comprising two 60 GHz gyrotrons of 200 kW, 100 ms (10-mode LFS and 1X-mode HFS) and one 110 GHz gyrotron of 400 kW, 200 ms (2X-mode LFS) with tiltable launchers. The overall EC-power exceeded the ohmic input power with a factor up to 40. The deposition volumes could be made as small as $2\times 2\times 2\text{ cm}^3$. The results can be summarized as follows: the strongly localized heat-deposition together with high-resolution electron diagnostics revealed that the heating efficiency was strongly influenced by the relation between the deposition radius and position of thermal electron barriers. These barriers turned out to be located near rational q -surfaces: $1/1$, $4/3$, $3/2$, $2/1$, $5/2$, $3/1$, etc. Some of these have been found on larger tokamaks as well. Current-drive and heating changes the j -profile directly or indirectly via the resistivity profile. The resulting change in the q -profile causes a change of barrier positions and, hence, of the T_e -profile. Since heating and current-drive efficiencies are strong functions of T_e , the response becomes highly nonlinear and this makes the derivation of CD efficiencies difficult. Analysis is still going on invoking inductive j -profiles derived from neoclassical resistivity, bootstrap-currents and total j -profiles derived from q -profiles. The overall CD efficiency for the co-drive was reasonably close to theoretical expectations, whilst the one for the counter-drive was close to zero. However, a strong modification of the j -profile with the counter-drive has been observed. An explanation for this paradox has been found in synergistic effects between the parallel E-field and EC-generated suprathermals. A few examples of MHD-control by ECRH/ECCD are discussed.

1. Introduction

In September 1998 the Dutch tokamak RTP has been closed down in order that FOM could participate in a new collaboration between FZ-Jülich (Germany), KMS (Belgium) and FOM (Holland), the so-called Trilateral Euregio Cluster (TEC) around the TEXTOR tokamak in Jülich.

The RTP Programme in the 7 years of its existence has been dedicated to the study of turbulent electron transport and non-linear electron dynamics of tokamak plasmas under the influence of strong ECR-waves.

The analysis is still going on; therefore this review should be regarded as a snapshot on where we are now. First results on TEXTOR ECRH/ECCD can be expected in the spring of the year 2000.

2. The Experimental Set-up

General parameters:

RTP parameters for these ECRH experiments can be described by the following: $R = 0.72$ m; $a = 0.165$ m; $1.9 < B < 2.4$ T; $43 < I_p < 140$ kA; $5 \cdot 10^{+18} \text{ m}^{-3} < n_{\text{cav}} < 5 \cdot 10^{+19} \text{ m}^{-3}$.

ECR-systems:

The ECRH systems (see Fig.1) comprised two 60 GHz gyrotrons of nominal power 200 kW and 100 ms pulse length. One was used for 1O-mode LFS launch and the other, for 1X-mode HFS launch with variable launching angles. The results obtained with these systems were reported before [1]. In this presentation the results with a 400 kW, 200 ms, 110 GHz Gycom gyrotron will be described. The microwaves were launched as the second harmonic 2X-mode from the LFS with variable toroidal and poloidal launching angle via a periscope type of launcher. The elliptical polarisation of the beam could be varied, as well as the focal length. The latter made it possible to reduce the volume of heat deposition to a cubicle of $2 \times 2 \times 2 \text{ cm}^{-3}$, in which 99 % of the power was deposited.

The toroidal launching angle was varying in the range between +35 and -35 degrees. ECCD efficiencies could therefore be measured without changing the polarity of the plasma current.

The gyrotron power could be put under feedback for instance to keep the electron temperature evolution on a required waveform as illustrated by Fig. 2.

Pellet injector:

The injector had the capability to launch 8 pellets/discharge with variable pellet size enabling to change the averaged plasma density with $\delta n = 1 - 4 \cdot 10^{19} \text{ m}^{-3}$.

Diagnostics:

The main instrument, which yielded the most striking results, was a Thomson scattering system with a very high resolution of $\delta r/a \approx 2$ %.

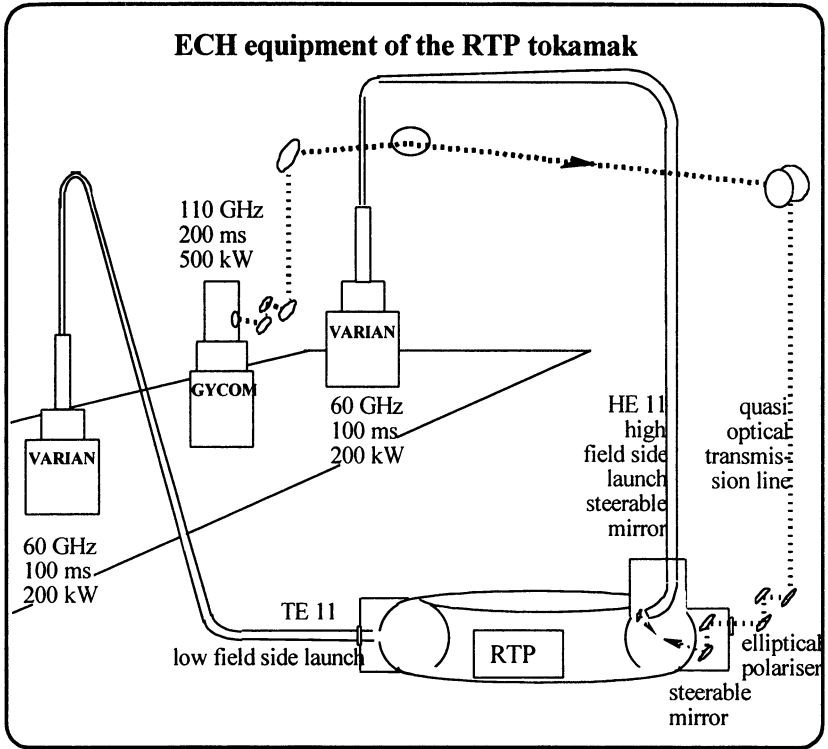


Fig. 1: The ECRH equipment of RTP. The dotted line indicates the quasi-optical transmission of the 110 GHz waves launched into the tokamak

Other advanced diagnostics comprised:

- 16-channels IR interferometer
- 20-channel superheterodyne ECE
- 5-camera=80-channel SXR
- pulse radar reflectometer
- 20-channel ECA
- various spectroscopy systems

An interesting application of the 1-O-LFS 60 GHz gyrotron system for diagnostics were the transmission measurements of the 60 GHz waves with 9 horns at the HFS opposite to the perpendicular launcher. The 9 horns were distributed in the poloidal and toroidal direction to measure the effect of refraction and scattering in both O- and X-mode.

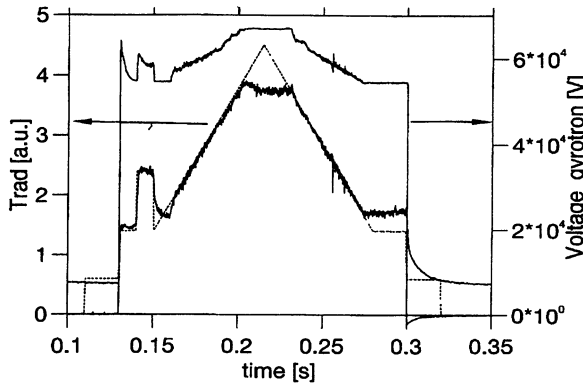


Fig. 2: T_e -feedback by gyrotron anode-voltage control
 Sensor: Heterodyne ECE-channel measurement
 (left vertical axis; continuous line)
 Required waveform (dotted line);
 Actuator: Anode-voltage modulator (right vertical axis)

3. Heating Aspects versus Electron Transport

It should be noted that in these experiments ions were heated only by collisional energy transfer from the electrons. Most experiments were done at densities around $\langle n \rangle \approx 2 \cdot 10^{19} \text{ m}^{-3}$. This means that energy exchange time between electrons and ions was longer than the energy confinement time. In other words: the electron heat loss was by far the most important transport mechanism and ions could be neglected in the analysis.

Ohmic heating power levels without EC were typically between 100 - 250 kW. During ECRH/ECCD with 320 kW the Ohmic power level dropped to 8-80 kW, therefore $P_{EC} / P_{\Omega} = 4-40!$ This means that these experiments can be described as a balance between pure electron heating and electron transport.

With a plasma volume of 0.4 m^{-3} the volume-averaged power density reached 1 MW/m^3 . By focusing the deposition volume reduced to $2 \times 2 \times 2 \text{ cm}^{-3}$, which means that inside the deposition volume $Q_{EC} / Q_{\Omega} \approx \approx 100.000!!$ The huge parallel electron heat conduction causes near-instantaneous equilibration inside the toroidal flux tube going through the deposition volume. Therefore, a more honest comparison yields a still impressive $Q_{EC} / Q_{\Omega} \approx 500$.

In conclusion: the results described in the following sections are experiments in non-linear electron dynamics.

4. Turbulent Electron Transport

In Fig. 3 an example of a T_e -Profile as measured with Thomson scattering ($\delta r/a \approx 1\%$) during ECRH is given. From this picture three very distinct features can be noticed:

- very high peaks of up to 1 keV in the centre, which are called filaments;
- steep gradients at $r = 40$ mm, i.e. thermal barrier;
- irregularities outside this barrier.

Such observations have been made in the past (PDX in 1984, Hsuan et al. [2]) and recently, inspired by the RTP results, in TEXT with ECE (Cima et al. [3]). The spatial resolution of the first one was $\delta r/a \approx 4\%$ and in the latter, about 7%.

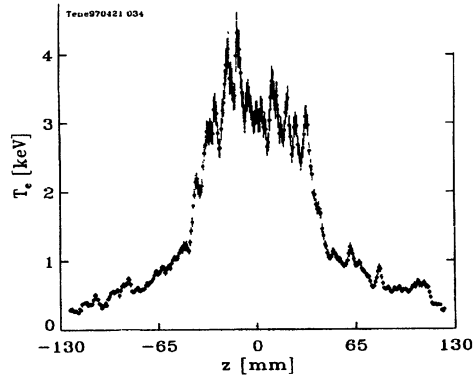


Fig. 3: An example of a T_e -profile in RTP as measured with Thomson scattering during a 300 kW EC heating pulse in a low density ($n_{eav} = 1 \cdot 10^{19} \text{ m}^{-3}$) discharge

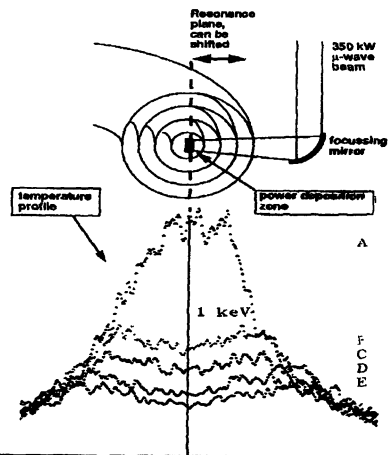


Fig. 4a: The central electron temperature as function of the ECRH deposition radius and the discrete T_e -profiles belonging to the range in radius during which no change in profiles were observed indicated by A, B, ... E

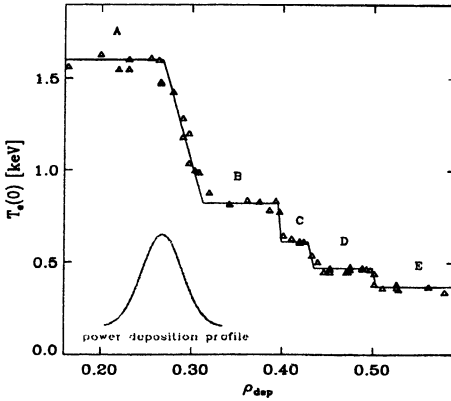


Fig. 4b: The central electron temperature as function of the ECRH deposition radius. The discrete Te-profiles of Fig. 4a are again indicated by A, B, ... E

In order to check the issue of thermal barriers experiments with off-axis heating were performed with changing the toroidal field in small steps corresponding to changes in the deposition radius of $\delta r/a \approx 1\%$ (Hogeweij et al. [4]). It turned out that over certain ranges in minor radius the plasma profiles remained identical. However, at very critical values of r/a the profile changed radically. Examples of these discrete profiles and the ‘quantum leap’ between them as a function of deposition radius are given in Fig. 4.

The observed transitions between the discrete profiles turned out to be related to the local q -value. Tuning the B-field close to each of the transition radii and then changing the plasma current has proven this. A change of 1% in current could cause the transition not to take place or to take place at a 1% different magnetic field, i.e. it was the ratio B/I , which determined, at which deposition radius the transition would take place. Calculation of the q -profile with neoclassical resistivity and bootstrap-current revealed that the transitions were related to rational q -values. For example, A-to-B was related to $q=1$, B-to-C to $q=2$, etc. Closer inspection of the A-to-B transition revealed sub-transitions close to $4/3$ and $3/2$. The calculated q -profiles were in good agreement with the mode numbers of magnetic islands always observed close to transitions and at the predicted radius. That this was really associated with thermal barriers was proven with heat-pulse propagation induced by modulated ECRH (Mantica et al. [5]). As should have been expected, the heat waves changed drastically in amplitude and phase when crossing these critical q -surfaces close to each of the transition radii and then changing the plasma current.

5. Empirical shell model

Based on the observations above the RTP-team developed an empirical transport model for the electrons only. The so-called ‘shell model’, in which it is assumed that the plasma consists of nested shells with alternative good and bad thermal isolation. The electron heat diffusivity, χ_e , is a discontinuous function of $q(r)$. The thermal barriers with low χ_e are put near rational q -surfaces: 1, 4/3, 3/2, 2, 5/2, 3, etc., irrespective at which radius these q -values may come. The model was benchmarked with a very limited set of experimental profiles under steady state conditions and since then the function $\chi_e[q(r)]$ has not been changed. The function is shown in Fig. 5.

The model was introduced as a subroutine in the usual transport models including ion-heat conduction, current-diffusion, etc. A very good agreement with all RTP observations was found under very different conditions, like:

- ohmic heating only
- ECRH on-axis
- ECRH off-axis
- pellet-cooling
- dynamic sweeps of B_r - and I_p .

Various examples of so-called ‘non-local’ transport, i.e. changes in local transport behaviour on a time scale faster than the energy confinement time itself, could be explained by subtle changes in the q -profile by which thermal barriers suddenly appeared or disappeared. An example of a dynamic sweep of the toroidal field simulated by the shell-model is shown in Fig. 6. It should be noted that the simulation tracks very well the experimental curve in amplitude as well as transition times between A, B, C, D, and E levels.

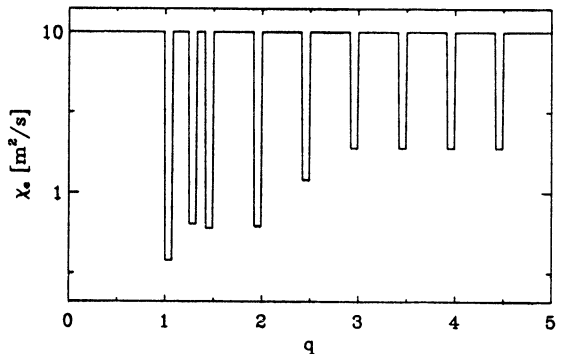


Fig. 5: The function $\chi_e[q(r)]$ as determined from a limited set of experimental profiles in steady state

6. Tentative explanation

The explanation of the shell model could go in two directions. If one favors electrostatic turbulence, one can think of thermal barriers caused by zonal flows shredding the turbulent eddies at certain radii. However it is not so clear from the developing theory of zonal flows why these zones should occur close to rational q -values. One has to wait for further evolution of this theory.

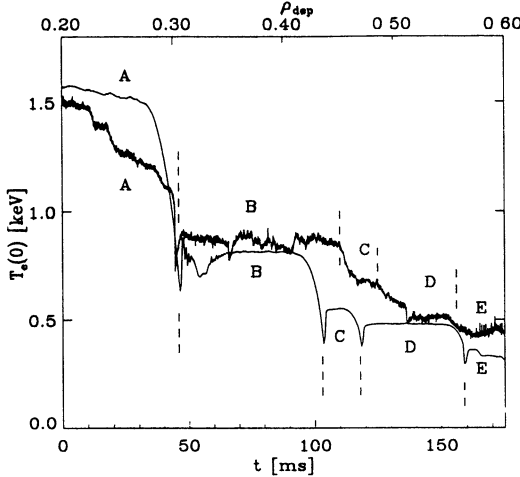


Fig. 6: Comparison between the experimental curve $T_e(0,t)$ and the simulated one calculated with the shell-model of fig. 5 combined with a transport code. In this example the toroidal magnetic field was swept over 10 % in 150 ms

Another possible explanation goes in the direction of the magnetic topology. As magnetic field lines are divergence-free, the field line equations can be written as a two-dimensional Hamiltonian. Kolmogorov, Arnold and Moser [6] have shown that the phase-space of such Hamiltonian in case of minor coupling between the two degrees of freedom, can be easily split in three distinct areas (see Fig. 7):

- islands where phase-space trajectories (or here field lines) bite in their own tail;
- unbroken surfaces, i.e. KAM-tori (or here undamaged magnetic surfaces);
- chaotic zones between the islands and the unbroken KAM-tori.

The KAM-theorem reveals the extreme vulnerability of magnetic surfaces. Perturbations of the magnetic field of the order of 10^{-5} are already

sufficient to cause such break-ups of the paradigm of unbroken nested magnetic surfaces (Montvai, de Rover [7]).

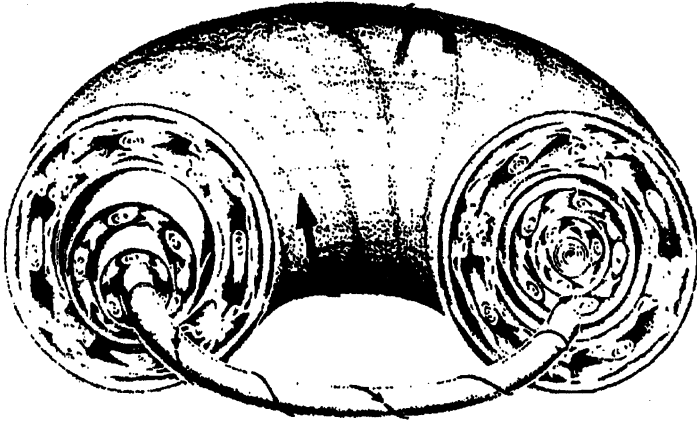


Fig. 7: The phase-space of a two-dimensional Hamiltonian with a slight coupling between the two degrees of freedom according to Kolmogorov, Arnol'd and Moser [6]

Even if electrostatic drift modes are the prime reason for tokamak turbulence, they will cause temperature fluctuations. For instance, in TEXT (Deng et al. [8]) one observed fluctuations of $\delta T / T \approx 1\%$ and rather small poloidal and radial wavelength (2 cm). Since the frequency $\approx 50 - 100$ kHz it means that the lifetime of such temperature perturbations is long enough for current penetration. Therefore, current density fluctuations will be present and even so, magnetic fluctuations. Accurate field-line calculations (de Rover et al. [7]) indicate that such current density fluctuation is enough to cause break-up of the magnetic topology. The observations in RTP: magnetic islands, thermal barriers and very high heat diffusivity between those appear to fit very well with the KAM-theorem.

7. Filaments

In Fig. 3 the attention was drawn to the very hot 'filaments' that could be observed in the central zone of the ECR-heated plasmas. A number of characteristics have been found:

- the filaments are stretched along magnetic field lines;
- they are closed on themselves and rotate with the same toroidal velocity as magnetic islands;

- they only occur in areas with low shear they mainly occur in cases of intense electron heating;
- the confinement inside the filament is very good and heat-diffusivities are comparable to those of the thermal barriers;
- their lifetime is long (0.3 ms), considering their cross-section of about one centimeter;
- therefore current will be fully penetrated in these areas of low resistivity.

The RTP-team (Beurskens [9]) explains these self-organized structures in the following way:

1. Magnetic flux-tubes close to rational q -surfaces in areas of very low shear will close at least partially on themselves;
2. If these flux-tubes pass through ECRH deposition zones with power densities of tens of GW/m^3 the electron energy-density will be pumped up to very high values even when such flux tube rotates toroidally and contact with the deposition zone is lost after some tens of microseconds;
3. Current density will increase due to the low electrical resistivity in the flux-tube;
4. The surplus of current density in comparison with the surrounding is large enough to fulfil the condition of Mirnov [14] to form 'positive islands' or 'hot snakes' which will then fully close on themselves;
5. The filaments can then survive as they are contained in the thermal isolation of their self-organized thermal barrier, i.e. they become KAM-tori;
6. Regularly the filaments pass the deposition zone so that their energy is pumped up again;
7. Areas between filaments will have stochastic magnetic field lines with very poor confinement, which can explain why the electron temperature in these areas is equal to the temperature at the top of the thermal barrier within which the filaments float;
8. The examples shown in Fig. 3 are of the $q=1$ type, i.e. slender rings floating inside the $q=1$ surface, but there have been observations of $q=2$ filaments in case of strong off-axis heating.

If one accepts such an explanation, it would mean that magnetic field fluctuations in the order of 10^{-2} have to be expected when filaments will be present. Microwave scattering theory predicts that mode conversion from O-to-X- or from X-to-O-mode can only take place in plasmas with

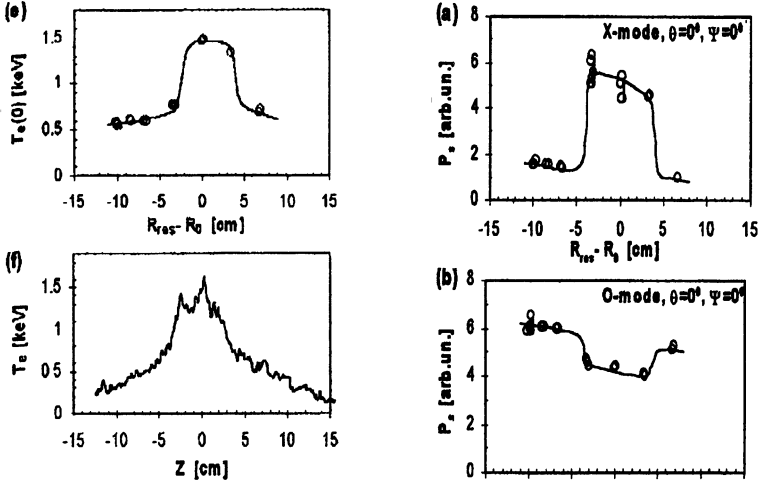


Fig. 8: Observation of anomalous O-to-X-mode conversion of 60 GHz microwaves launched from the LFS coinciding with the appearance of filaments when the EC-deposition is swept through the $q=1$ surface. (Stepanov et al. [10])

magnetic field fluctuations. In RTP the transmission or conversion of 60 GHz gyrotron radiation launched as O-mode from the LFS has been measured by horns at the HFS (Stepanov et al. [10]). When the deposition radius is swept through the plasma by a slight ramp of the toroidal magnetic field, conditions for filament formation are reached, when the deposition area is inside the $q=1$ radius as can be seen in Fig. 8. Coinciding with the appearance of filaments one can notice a sudden upsurge of anomalous X-mode radiation at the HFS. This confirms the strong magnetic field perturbations expected when filaments exist.

8. Current Drive Experiments

One of the most urgent tasks in ECCD is to determine the current drive efficiency and to compare it with numerical predictions from Fokker-Planck codes. From such comparison one can then predict how much current can be driven in a tokamak fusion reactor and if a fully non-inductive current can be reached.

The results of Fokker-Planck code calculations can be described as:

$$j_{tot} = \sigma_{neo} E_{par} + \eta_{cd} P_{EC} + \gamma_{syn} P_{EC} E_{par} + j_{bootstr} \quad (1)$$

in which the first term represents the inductive current drive with neo-classical conductivity, the second one the real ECCD, the third one the

synergetic drive caused by EC induced suprathermals in the presence of an inductive E-field and the last term is the bootstrap current.

In RTP experiments with ECCD have been undertaken with the 110 GHz gyrotron. Situations could be reached in which 55% of the current has been driven (see Fig. 9).

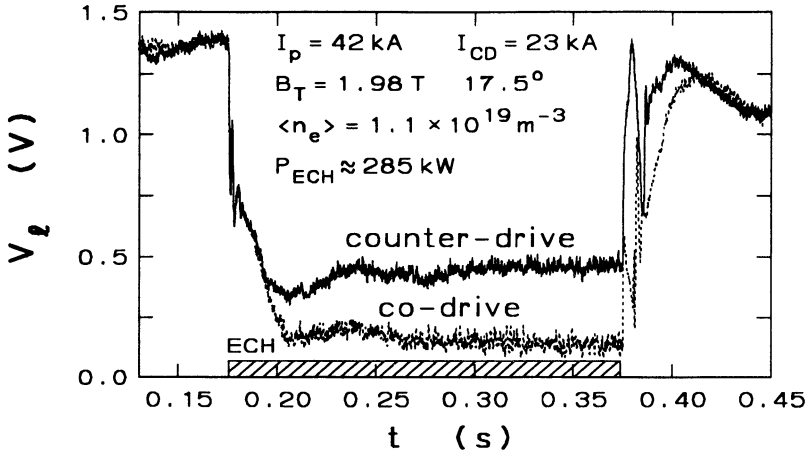


Fig. 9: The difference in loop-voltage between co- and a counter-drive launched EC-waves acting on a high q_a ($=9$) discharge under optimal conditions. An estimated 23 kA out of 42 kA total is EC-driven

If one plots the observed loop-voltage in the steady state as a function of the launching angle at the optimum magnetic field it appears that the dependance is symmetric around perpendicular injection (heating only gives $V_{\text{loop}} \cong 0.35 \text{ V}$) as co-drive at the launching angle of $+17^\circ$ degrees gives $V_{\text{loop}} \cong 0.20 \text{ V}$ and counter-drive at -17° degrees gives $V_{\text{loop}} \cong 0.50 \text{ V}$ (see Fig. 10).

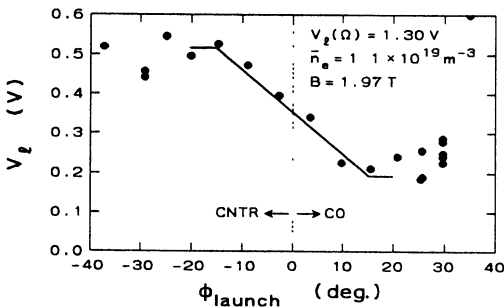


Fig. 10: The loop voltage measured during ECCD as function of the launching angle in toroidal direction. The ohmic loop voltage before the EC-puls was 1.3 V. Zero angle corresponds to perpendicular injection and therefore pure ECRH

This result appears to justify a simplified expression for the amount of driven current:

$$I_{cd} = I_p \cdot (V_{cnt} - V_{co}) / (V_{cnt} + V_{co}), \quad (2)$$

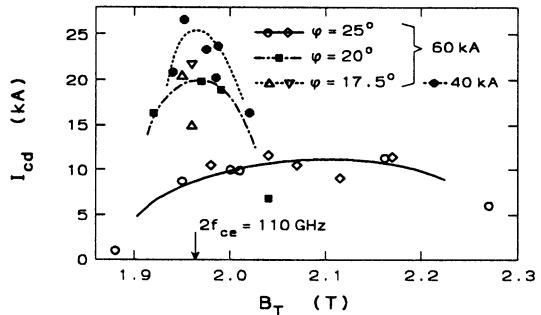
in which the $V_{co/cnt}$ indicates the steady-state measured loop voltage for co- and counter-drive for plasmas with equal current and density. The simplification in respect to eq. (1) is clear and can only be justified if:

- the neoclassical conductivity profile is equal for co- and counter-drive;
- the pressure profile is the same, so that the contribution by bootstrap currents is the same;
- the cross-term representing the synergy between E-field and EC-power can be neglected.

Under these assumptions ECCD has been studied as a function of various parameters (Fig. 11):

- Variation of the magnetic field means variation of the EC deposition radius. At the optimum launching angle it was found that I_{cd} reduced to 1/e within the displacement of 3 cm, i.e. within the $q=1$ radius. At a larger launching angle I_{cd} had a very broad and low profile. This can easily be explained by the existence of the $q=1$ thermal barrier: all heat deposited within $q=1$ leads to an appreciable temperature enhancement and current drive efficiency increases strongly with temperature. At large launching angle the beam does not reach the $q=1$ radius and so the efficiency will be low.
- Variation of EC-power causes a nearly linear increase of I_{cd} as can be expected with an only marginal increase in temperature with power.
- Variation in density reveals an inversely proportional dependence of I_{cd} with density as expected for constant T_e .

Fig. 11a: The amount of current driven according to Eq. (2) as function of the toroidal field/deposition radius. It indicates the strong drop in efficiency for off-axis current drive at the optimal launching angle. At larger angle the efficiency dependence on position is weaker



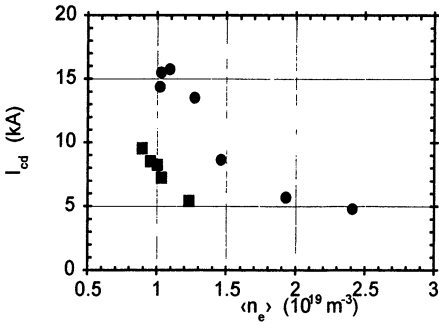


Fig.11b: The amount of current driven according to Eq. (2) as function of P_{EC} . The arrow indicates the improvement made by launching in the right elliptical polarisation.

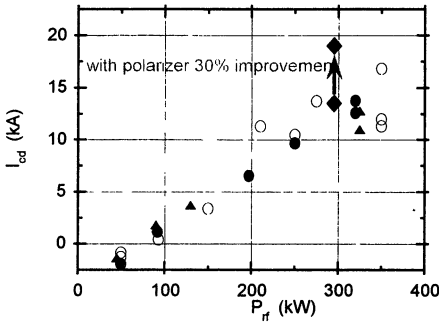


Fig.11c: The amount of current driven according to Eq. (2) as function of $\langle n_e \rangle$. The dots indicate high q_a ($=6.7$) operation. The squares indicate $q_a=4$.

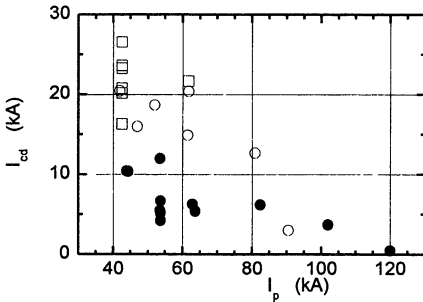


Fig. 11d: The amount of current driven according to Eq. (2) as function of I_p . The open symbols indicate pulses with $\langle n_e \rangle$ about $1.5 \cdot 10^{19} \text{ m}^{-3}$. The closed symbols stand for $\langle n_e \rangle$ about $1.5 \cdot 10^{19} \text{ m}^{-3}$.

d. Variation in total current leads to a lower efficiency at higher current. This is somewhat unexpected, as the temperature stays more or less constant. An explanation could be sought in the increase of sawteeth activity with increasing current. In general there is the tendency that sawteeth diminish the current drive efficiency.

9. Effect of ECCD on profiles

All the above reasoning has been based on the assumption of the validity of Eq. (2). However, all three underlying assumptions are not true for strong EC-power: the temperature (and, therefore, the conductivity), as well as the pressure profiles, are very much different between the co- and counter-drive (see Fig. 12) and Fokker-Planck code calculations show that the synergistic term is as large as the first two terms in Eq. (1).

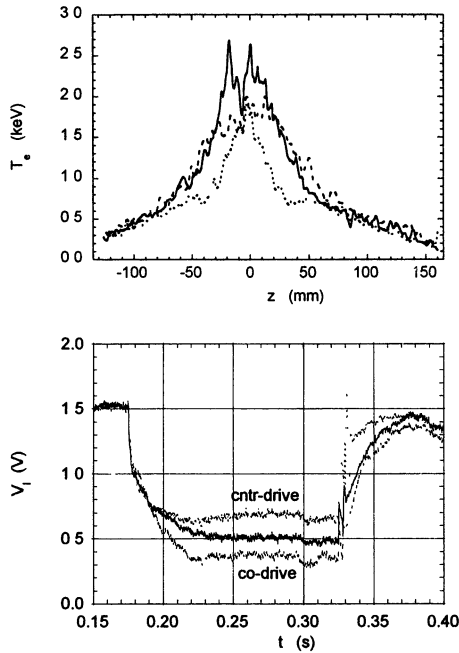


Fig. 12: An example of three identical target plasmas EC-heated at 3 different injection angles corresponding to the co-drive (broken line), heating only (full line) and counter-drive (dotted line). Whilst the loop voltage behaviour suggests a symmetry between co- and counter-drive, the temperature profiles are very much different.

Figure 12 shows an example of a set of 3 discharges with an identical target plasma. Once again it shows nicely symmetric loop voltage behaviour of the co- and counter-drive relative to perpendicular injection. Equation (2) gives a driven current of 30 %, i.e. 18 kA. However, it is clear that the neoclassical conductivity profiles are very different, as will be the contribution by the bootstrap current. In other words, the conditions for the validity of Eq. (2) are not fulfilled.

For that reason a more sophisticated modeling of these three discharges has been undertaken including Fokker-Planck calculations. The results of the analysis will be presented on EC-11 (Westerhof et al. [11]). The following can be reported as preliminary results:

Perpendicular launch with no ECCD often gives the highest temperatures, probably because the deposition width is very small and all the deposition is within the $q=1$ thermal barrier whilst, launching at 17 degrees leads to partial deposition outside the $q=1$ barrier.

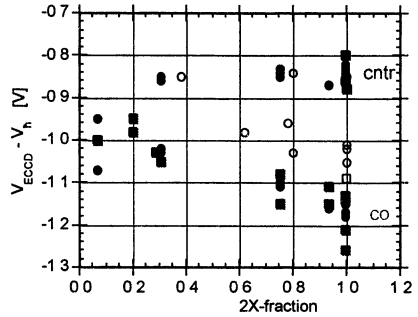
For the co-drive case the inductively driven neoclassical current is indeed about 15 kA less than the total current, i.e. not far from the 18 kA found from Eq. (2). According to the Fokker-Planck code this current is about 50:50 driven by direct ECCD and by the synergetic effect.

With counter-drive an unexpected result was obtained: no net driven current at all! The loop voltage gives with the neoclassical conductivity the total current. According to the Fokker-Planck calculations this can be explained by the synergistic term: the relatively high loop voltage gives with the large suprathreshold electron population a boost to the inductively driven current, which cancels the direct ECCD counter-drive. However, this cancellation is global not local. The on-axis counter-drive is compensated by an off-axis synergistic co-drive both leading to a dramatic flattening of the j -profile whilst the net current is close to zero. The thermal barrier close to the centre is according to this analysis *not a $q=1$ barrier but a $q=2$ barrier*.

In order to get satisfactory agreement between Fokker-Planck codes and experimental results it is necessary to assume a reduction of loop voltage inside the $q=1$ surface even in semi-stationary conditions to mock up the effects of sawteething.

A difference between co- and counter-drive has also been found in the effect of polarisation. With a series of plasmas with identical external parameters the fraction of 2X-mode in the total EC-power varied between zero (pure O-mode) and 100 % (Fig. 13). It was surprising that a low X-mode content gave, nevertheless, a good heating effect although not as good as 100 % X-mode. Probably this can be explained by repetitive wall reflections, which caused mode scrambling, and in the end 100% absorption but with a broad deposition profile. The co-drive ECCD efficiency was poor at a low X-mode fraction but improved with increasing X-fraction as expected. Counter-drive gave already at an X-mode fraction of 0.4 an appreciable higher loop voltage, which did not change at higher X-mode fractions. Analysis of this has still to be undertaken.

Fig. 13: The lowering of the loop voltage during ECRH/ECCD compared to the ohmic loop voltage with 300 kW EC-power for various values of the X-mode fraction in the total EC-power. Standard Ohmic loop voltage at these $q=6$ discharges was 1.6 V. Open symbols indicate perpendicular launching (heating) closed symbols stand for ECCD with launching angles of 17 degrees.



10. The effect of ECRH/ECCD on MHD

In RTP ECRH and ECCD have been used to control two examples of MHD activity with some success: sawteeth and high density radiation induced disruptions.

Sawteeth

The simplest method to stabilize sawteeth crashes, initiated by $m=1/n=1$ instabilities at the $q=1$ surface, is to remove the $q=1$ surface all together. Reduction of the central current density combined with an increase off-axis can be done either by counter-drive on axis or co-drive off-axis. Both methods work but the most interesting results were obtained by counter-drive on-axis, as also the heat-deposition remained on-axis. The effect of central co- and counter-drive on sawteeth is illustrated in Fig. 14. It is remarkable that the central temperature for the case with stabilizing counter-drive is higher than the co-drive, whilst one could argue that with the disappearance of the $q=1$ thermal barrier the temperature should be lower. Inspection of the profiles showed that another barrier at a higher q -value takes over still without inducing higher-order sawteeth although with strong $m=2/n=1$ activity. The latter points to the drawback of this type of stabilisation: the amount of ECCD is critical in relation to the q -profile without ECCD. For instance the same amount of counter-drive at a $q_a=6$, instead of the $q_a=4$ example shown, brings the $q=2$ surface at the position where without ECCD the $q=1$ surface would have been. This spoils the process with the result that $q=2$ sawteeth initiated by $m=2$ instabilities. These results with counter-drive illustrate once more that although the net current contribution is small or even slightly positive, the effect on the current-density distribution is dramatic. The counter-drive on-axis is more than compensated by a synergistic positive current contribution off-axis.

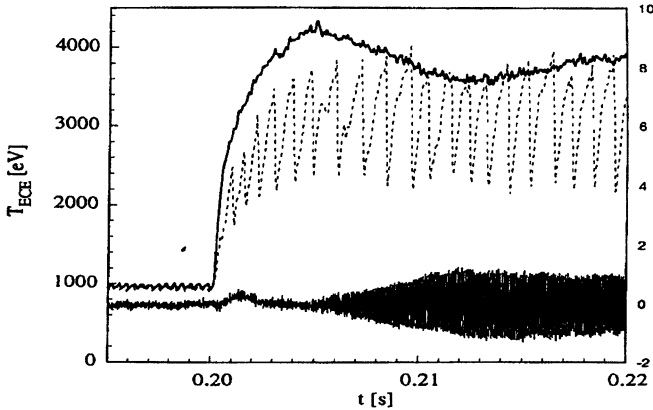


Fig. 14: The excursion of the central ECE radiation temperature in response to a modest ECCD (about 4 kA in co-drive with 90 kA total plasma current) in counter-drive (full line) and co-drive (broken line). The value of $q_a=4.3$. The bottom-line shows the $m=2$ instability growing for the counter-drive case (Westerhof et al. [11])

Radiation induced high density disruptions

Disruptions are normally caused by an excessive growth of the $m=2/n=1$ tearing mode at the $q=2$ surface. There are several different processes, which can lead to such instability [12]. The most common one is that the radiative loss in the edge region outside the $q=2$ surface becomes as large as the input power. This will result in a very cold plasma bordering at the $q=2$ surface. The latter is still acting as a thermal barrier with the result that there is a strong ∇j inside $q=2$ and $\nabla j=0$ outside. Such a situation drives the tearing mode. The tearing mode manifests itself as magnetic islands, i.e. a perturbation of flux surfaces, as has been described in Section 6. The magnetic field topology is maintained by current density inside the island, which is lower than in the surroundings. This is consistent with a lower temperature in the island caused by lower ohmic dissipation and higher radiative loss. Increase of the radiation will cause the islands to grow until they reach the width of around 15 % of the minor radius. At such magnitude the islands starts to overlap with minor islands more inside and the $m=1/n=1$ perturbation at the $q=1$ surface. This leads to a sudden stochastication of the magnetic field lines between $q=1$ and $q=2$ and a total loss of confinement: the disruption.

Remedies against such disastrous chain of events by means of ECRH/ECCD are two-fold: either one restores the energy balance by simply increasing the input power or one tries to fight the islands themselves by heating them (ECRH) or by driving extra current inside the islands

(ECCD). The latter has not been tried as the typical island temperature for these cases is below 100 eV, which means that the current drive efficiency is extremely low. ECCD of so-called ‘neoclassical tearing modes’ could well be successful as this type of islands occur at much higher temperatures.

Simple restoration of the energy balance by increasing the input power with ECRH helps to avoid the disruption or to postpone it to a higher density limit as illustrated in Fig. 15 (Salzedas [13]). The ECRH is switched on when a magnetic signal, composed to give the $m=2$ perturbation amplitude, reaches a critical level. After some time delay the mode is stabilized until at higher density a disruption follows: The time delay is caused by the time it takes to get a healthier temperature distribution and, more important, to restore a sufficient ∇j outside the $q=2$ surface. As can be expected, the deposition-radius of the ECRH was not important provided that it was placed anywhere inside or about the $q=2$ radius typically at 0.67 of the minor radius. Heating very much outside of $q=2$ was not effective, as ECR absorption in the very low temperature radiation belt was poor.

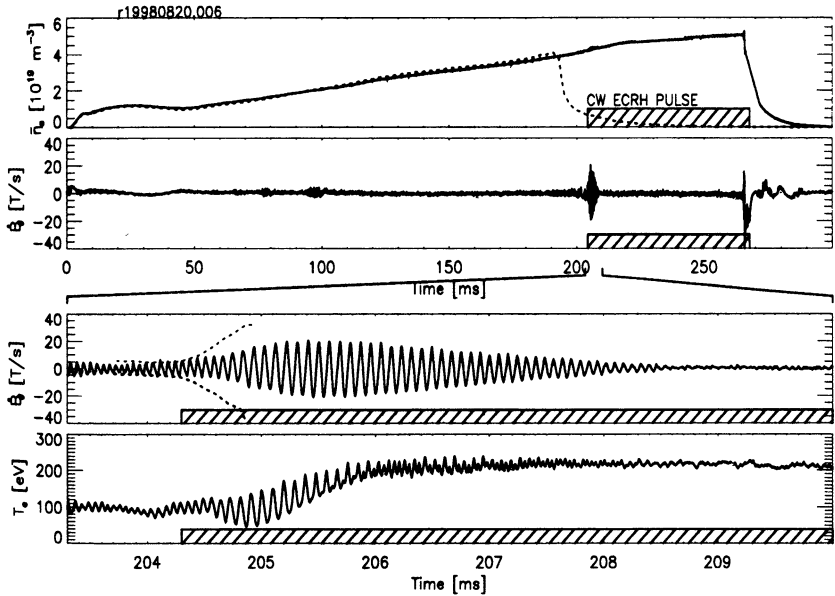


Fig. 15: Disruption control by continuous EC power. The ramping density (top trace) caused a disruption without EC-power (broken line) at $\langle n_e \rangle = 4.10^{19} \text{ m}^{-3}$. With 320 kW EC-power and continuous ramping $\langle n_e \rangle = 5.6.10^{19} \text{ m}^{-3}$ was reached. Further shown are the magnetic perturbation by the $m=2$ mode and the temperature modulation varying more or less sinusoidal between O-point/island (low) and X-point (high temperature). The broken line in the magnetic signal trace shows the mode evolution in case no ECRH is applied. The shaded area gives the time that ECRH is switched on. (Salzedas [13])

The second remedy was tried by switching on the ECRH system only when the toroidally rotating island was in front of the EC wave launcher. Rotation acceleration or deceleration could be followed electronically as not only the amplitude but also the phase of the $m=2$ magnetic detection system was used to control the EC power output. The duty cycle was chosen closely to 50 %. The result (see Fig. 16) was disappointing. No stabilisation was found. In hindsight this can be explained by the fact that inside the island the temperature was very low, such that the cooling down time by radiation is much shorter than the rotation time. The island cooled down immediately in the 50 % timespan of no ECRH. Moreover, the absorption inside the island was low because of the low temperature such that a good part of the EC-power was shining through the island.

In conclusion, one can say that at least for radiation-induced tearing modes ECRH has no advantages above other heating mechanisms.

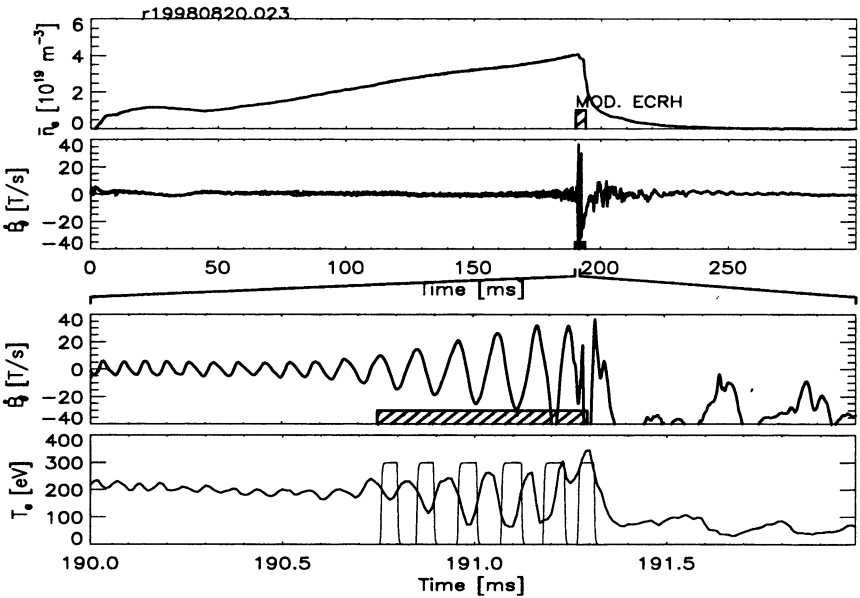


Fig. 16: An example of a try-out of mode stabilization by modulated EC-power such that only the low temperature islands received a heating pulse. The figure is further identical to the previous one (Salzedas [13])

Disruption amelioration

Another application of ECRH could be amelioration of disruptions. In reactor-sized machines like ITER disruptions can be damaging. If all

ways to control MHD fail and the plasma is heading for disruption despite the efforts, it could be helpful to postpone and soften the current-quench following the energy-quench caused by stochastization of magnetic field. The current-quench is caused by the fact that the poloidal field systems in large-sized tokamaks cannot maintain the current inductively when the resistivity of the plasma is so suddenly increased with orders of magnitude nor can the position- and shape-control be maintained. Massive ECRH could be used to keep the plasma temperature sufficiently high that further cooling by radiation after the energy quench can be avoided. Therefore, the resistivity will increase less dramatically and the current decay-rate can be reduced such that position-control can be maintained and an orderly shutdown or ‘soft-landing’ ensured. This has been tried in RTP (Salzedas [13]) with some success as can be seen in fig. 17. However, this was achieved with 0.5 MW/m^3 . For application on ITER much lower power densities should be reached to make it a practicable solution.

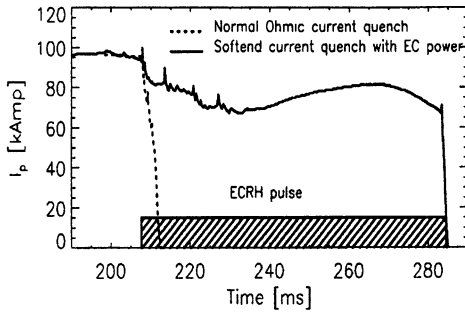


Fig. 17: An example that ECRH started just after the energy-quench of a disruption can postpone the subsequent current-quench

11. Conclusions

1. ECRH/ECCD discharges at RTP are dominated by non-linear electron dynamics in which ions do not play an important role.
2. ECRH/ECCD is easily put under feedback control and with quasi-optical means the power deposition can be variable and highly localized, which makes it an ideal tool for profile control of fusion plasmas.
3. Intense electron heating reveals that the magnetic topology of supposedly nicely nested surfaces can be easily broken and probably is always broken to some extent even in non EC-heated tokamaks.

4. The resulting empirical shell/barrier-model can explain many observations in RTP.
5. ECRH-induced filaments are identified as ‘hot snakes’ or ‘positive islands’ floating in areas with stochastic magnetic field at low shear and they cause strong magnetic field fluctuations as shown by anomalously high X-to-O mode conversion.
6. Second harmonic X-mode ECCD has led to discharges with more than half the current driven and with efficiencies of $\eta_{CD} \geq 10^{18}$ A/Wm².
7. Elliptical polarisation improves η as predicted.
8. The interpretation of ECCD results is complicated by the combination of:
 - The existence of electron thermal barriers.
 - The strong dependence of η on the electron temperature.
 - The generation of suprathermals which escapes observation by Thomson scattering but cause a strong synergistic contribution to the ECCD.
 - The effect of sawteeth on the distribution of parallel electric field.
9. Notwithstanding these difficulties the co-drive results can be understood reasonably well.
10. Counter-drive is especially difficult to analyze as there always will be an electric field causing by synergy a strong co-drive compensating partially or totally the effect of direct counter-drive.
11. Sawtooth stabilisation has been demonstrated with only 5% counter-drive.
12. Bulk ECRH around $q=2$ can postpone disruptive density-limits and can ameliorate the current-quench of a disruption.

12. Acknowledgements

The authors want to thank the many members of the RTP-team for the many experimental results obtained and in particular Dr. A.A.M.Oomens and Dr. J.Lok. Prof. N.J.Lopes Cardozo and Dr. Hogeweyj are thanked for their transport analysis, and Dr. Westerhof, for his ECCD analysis. This work was done as part of the Association Euratom-FOM programme supported by the Netherlands research organisation NWO and Euratom.

13. References

- [1] Schüller F.C., Westerhof E., Barth C.J., Box F.M.A., Da Cruz D.F., Donné A.J.H., Van Gelder J.F.M., Heijnen S.H., Hogeweyj G.M.D., Hugenholtz C.A.J., Ingesson L.C., Konings J.A., Lok J., Lopes Cardozo N.J., Oomens A.A.M., Peeters A.G., Pe-

- ters M., Polman R.W., Rommers J.H., Rutteman R.H., Schokker B.C., Smits F.M.A., Verhoeven A.G.A., Verreck M., Wilbers A.T.M. Proc. 14th Int Conf. Plasma Physics and Contr. Fus. Res., Würzburg 1992, Vol 1, 609-616, IAEA, Vienna, 1993.
- [2] Hsuan H., Bol K., Bowen N., Boyd D., Cavallo A., Dimits A., Doane J., Elder G., Goldman M., Grek B., Hoot C., Johnson D., Kritz A., LeBlanc B., Manintveld P., Polman R.W., Sesnic S., Takahashi H., Tenney F. Invited paper 4th Int. Symp. Heating in Toroidal Plasmas, Rome, Italy, 1984, pg 809-833 also as report PPPL-2114.
- [3] Cima G., Gentle K.W., Wootton A., Brower D.L., Zeng L., Deng B.H., Domier C.W., Luhmann N.C. Plasma Phys. Control. Fusion 40, 1998, 1149.
- [4] Hogewij G.M.D., Lopes Cardozo N.J., De Baar M.R., Schilham A.M.R. Nuclear Fusion 38, 1998, 1881.
- [5] Mantica p., Peters M., De Luca F., De Laurie A., Gorini G., Hogewij G.M.D., Jacchia A., Lopes Cardozo N.J., RTP team Nuclear Fusion 36, 1996, 1317.
- [6] Kolmogorov A.N., Arnold V.I., Moser J., various articles, see for instance: Russian Math. Surv. 18, 1963, 9-36; Memoirs Am. Math. Soc. 81, 1968, 1-60; drawing from Abraham R. and Marsden J.E., 'Foundations of Mechanics' 2nd ed. Benjamin/Cummings Publ., Reading, Mass., USA 1978.
- [7] De Rover M., Schilham A.M.R., Montvai A., Lopes Cardozo N.J. Physics of Plasmas 6, 1999, 2443.
- [8] Deng B.H., Brouwer D.L., Cima G., Domier C.W., Luhmann N.C., Watts C. Physics of Plasmas 5, 1998, 4117.
- [9] Beurskens M.N.A., 'Filamentation of Tokamak Plasmas' Thesis Technische Universiteit Eindhoven 1999, submitted to Physics of Plasmas See also: Lopes Cardozo N.J. et al. Phys. Rev. Lett. 73, 1994, 256.
- [10] Stepanov A.Yu., Colas L., Donné A.J.H., Gusakov E.Z., Oomens A.A.M., Schüller F.C., RTP-team: 25th EPS Conf. Contr. Fus. Plasma Phys., 1998, Paper P3.032, Prague, Czech Republic.
- [11] Westerhof E., Polman R.W., Hogewij G.M.D., Lok J., Min E., Oomens A.A.M., Schüller F.C. and the RTP team: contributed paper TCM on ECRH Phys. and Techn. and EC-11, Oh-arai, Ibaraki, Japan, Oct. 1999.
- [12] Schüller F.C., Plasma Phys. Contr. Fusion 37, 1995, A135-A162, Review paper 22nd EPS Conf. Contr. Fus. Plasma Phys., Bournemouth, UK, 1995.
- [13] Salzedas F. Thesis Utrecht University to be defended early 2000.
- [14] Mirnov S., 17th IAEA Conf. Plasma Phys. and Contr. Nucl. Fus. Res., Yokohama, Japan, 1998.

HIGH DENSITY LOWER HYBRID CURRENT DRIVE EXPERIMENTS ON FTU TOKAMAK

S. Podda, V. Pericoli-Ridolfini, E. Barbato, H. Kroegler, L. Panaccione, F. Alladio, B. Angelini, M.L. Apicella, G. Apruzzese, L. Bertalot, A. Bertocchi, M. Borra, G. Bracco, G. Buceti, P. Buratti, A. Cardinali, C. Centioli, R. Cesario, S. Ciattaglia, V. Cocilovo, F. Crisanti, R. De Angelis, F. De Marco, B. Esposito, D. Frigione, L. Gabellieri, G. Gatti, E. Giovannozzi, C. Gourlan, F. Gravanti, M. Grolli, F. Iannone, M. Leigheb, G. Maffia, G. Maddaluno, M. Marinucci, G. Mazzitelli, P. Micozzi, F. Mirizzi, F.P. Orsitto, D. Pacella, M. Panella, L. Pieroni, G.B. Righetti, F. Romanelli, F. Santini, M. Sassi, S.E. Segre, E. Sternini, O. Tudisco, V. Vitale, G. Vlad, N. Tartoni, B. Tilia, A.A. Tuccillo, V. Zanza, M. Zerbini, F. Zonca*

Associazione Euratom-ENEA sulla Fusione, Centro Ricerche Frascati, C.P.65 - 00044
Frascati, Rome, Italy

*INFN and Dipartimento di Fisica, II Università degli Studi di Roma, "Tor Vergata"
Roma, Italy

Current drive (CD) experiments have been carried out on the FTU tokamak with 8 GHz lower hybrid waves up to line averaged plasma density $\bar{n}_e > 1 \cdot 10^{20} \text{ m}^{-3}$. Efficiencies, larger than $0.16 \cdot 10^{20} \text{ m}^{-2} \cdot \text{A/W}$ are obtained which can be extrapolated to $0.22 \cdot 10^{20} \text{ m}^{-2} \cdot \text{A/W}$ for clean plasma conditions, with no significant degradation as the density is increased up to the accessibility limit. The CD efficiency follows the well known ordering with the electron temperature and this ordering fit well with the results of other tokamaks. No harmful impurity influx has been observed to limit the machine operations up to the maximum coupled power of 1.7 MW.

The main mission of the Frascati Tokamak Upgrade FTU is to demonstrate the generation of toroidal current in tokamak plasmas with Lower Hybrid (LH) radiofrequency waves at high density with large efficiency. It is widely acknowledged that the use of LH waves is one of the best tools for controlling the current profile shape to attain advanced plasma scenarios in a fusion reactor. The achievement of a large efficiency in the plasma density regimes foreseen for next step experiments [1] is of primary importance since it determines the amount of the required power and hence it has a great impact on the project of a reactor.

The experiments on FTU have been devoted to provide detailed experimental information on this issue and in particular on the behaviour of the LH current drive (LHCD) efficiency in the plasma density regimes of the order of $\bar{n}_e \approx 1 \cdot 10^{20} \text{ m}^{-3}$. In the past, only Alcator C [2] has explored such high plasma densities. Defining the current drive (CD) efficiency as $\eta_{\text{CD}} = I_{\text{LH}} \cdot n_e \cdot R / P_{\text{LH}}$ [$10^{20} \text{ m}^{-2} \cdot \text{A/W}$], where I_{LH} is the LH driven current and R is the tokamak major radius, a rather low figure of $\eta_{\text{CD}} \approx 0.12$ for toroidal magnetic field $B_T = 10 \text{ T}$ had been quoted. This has to be compared with that achieved on the largest tokamaks, as JET [3] or JT-60 [4], where $\eta_{\text{CD}} \approx 0.3$, but at much lower densities $\bar{n}_e \approx 0.2 \cdot 10^{20} \text{ m}^{-3}$.

On FTU, at density and magnetic fields close to those of Alcator C, an efficiency of $\eta_{CD} \approx 0.2$ has been attained. The observed favourable ordering of η_{CD} versus $\langle T_e \rangle$, the volume averaged electron plasma temperature, can explain the better results [2, 5].

The high magnetic field of the FTU experiment and the LH frequency, $f_0 = 8$ GHz, can further explain the reduction of the negative effects on the CD efficiency found previously in high density regimes [6, 7].

In the present paper we report the results of LHCD experiments on FTU with line density in the range of $0.3 \leq \bar{n}_e \leq 1.15 \cdot 10^{20} \text{ m}^{-3}$, LH power $0.2 \leq P_{LH} \leq 1.1$ MW, plasma current $0.22 \leq I_p \leq 0.7$ MA, and toroidal field $4 \leq B_T \leq 7.1$ T. Phasing of the LH launching grill of 65° , 75° , 90° and 120° have been used which correspond to peak values of the launched $N_{||}$ (index of refraction parallel to B_T) spectrum of 1.32, 1.52, 1.82, 2.43, respectively. Transmitted power density at the grill mouth larger than 10 kW/cm^2 for times longer than 0.7 s are routinely and safely run. In this condition no impurity influx has been observed to limit the plasma operation even at the highest P_{LH} up to now achieved, i.e. $P_{LH} = 1.7$ MW. At higher density $\bar{n}_e > 1 \cdot 10^{20} \text{ m}^{-3}$ the value of the effective ion charge Z_{eff} during the LH phase is similar to the ohmic (OH) value ($Z_{eff} \leq 1.3$). In the lower density range $\bar{n}_e \leq 0.5 \cdot 10^{20} \text{ m}^{-3}$ it increases typically from nearly 2 to about 3 as expected on a machine with entirely metallic walls [8] upon an increase of the total input power from approximately 0.45 MW to more than 0.9 MW.

Fig. 1 shows the time evolution of relevant plasma quantities in a shot with full CD phase. The plasma current (350 kA) is steadily sustained by LH power for 0.5 s at $\bar{n}_e = 0.45 \cdot 10^{20} \text{ m}^{-3}$, central density $n_{e0} = 0.7 \cdot 10^{20} \text{ m}^{-3}$, and produces $T_{e0} \geq 4$ keV, upon stabilisation of the sawtooth activity. The estimated inductive time scale $\tau_{L/R}$ is ≤ 0.4 s.

The limited LH power routinely available so far has allowed to achieve a full CD phase only for $\bar{n}_e \leq 0.5 \cdot 10^{20} \text{ m}^{-3}$. At density $\bar{n}_e = 0.9 \cdot 10^{20} \text{ m}^{-3}$ ($n_{e0} = 1.2 \cdot 10^{20} \text{ m}^{-3}$) only partial CD is obtained with a drop up to 50% of the loop voltage with $T_{e0} > 2$ keV.

Fig. 2 shows the behaviour of loop voltage drop as function of the parameter $P_{LH}/I_p \cdot \bar{n}_e \cdot R$ for the entire database of discharges with LH, compared with CD analysis method developed for PBX [10]. Apart from the points at very high density the behaviour of the quantity is linear, within the experimental errors, showing that even at partial CD regimes the effect of the residual electric field on the suprathermal electron tail is small, allowing the evaluation of η_{CD} quite reliably.

The apparent saturation at low density can be removed taking into account the impurities effect on CD [9]. The efficiency for a clean plasma η_{cd} can be inferred from the linear law, derived from the definition of the CD efficiency:

$$\frac{I_{LH}}{I_p} = h \cdot \eta_{CD} (Z_{eff} = 1), \quad (1)$$

where:

$$h = \frac{P_{LH}}{n_e \cdot I_p \cdot R} \cdot \frac{6}{Z_{eff} + 5} \left[\frac{W}{A \cdot 10^{20} m^{-2}} \right]. \quad (2)$$

The quantity h includes the effect of the impurities and can be easily measured. In Fig. 3 the ratio I_{LH}/I_p is plotted versus the parameter h . Only quasi steady states are considered, where the internal inductive effects are negligible and the electric field is almost radially uniform. Only $N_{||0}=1.52$ and 1.82 have been considered and all the data with low accessibility have been discarded in order to have a homogeneous database.

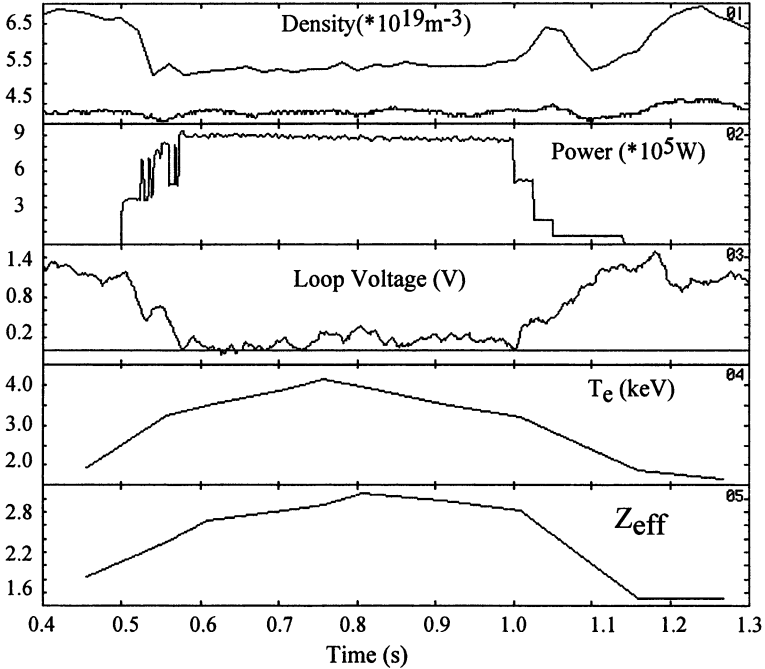


Fig. 1. Temporal evolution of the main plasma quantities during a full CD phase at low density

The right evaluation of the ratio I_{LH}/I_p may be not easy. We calculated I_{LH}/I_p from the change in the LH phase of the loop voltage and of the bulk conductivity σ , which is simply proportional to the volume average $\langle T_e^{3/2} \rangle$ and inversely to Z_{eff} , but we neglected the effect of the residual electric field on the fast electron tail, i.e:

$$\frac{I_{LH}}{I_p} = 1 - \frac{V_{i,LH}}{V_{i,OH}} \cdot \frac{\langle T_{e,LH}^{3/2} \rangle}{\langle T_{e,OH}^{3/2} \rangle} \cdot \frac{Z_{effOH}}{Z_{effLH}} \quad (3)$$

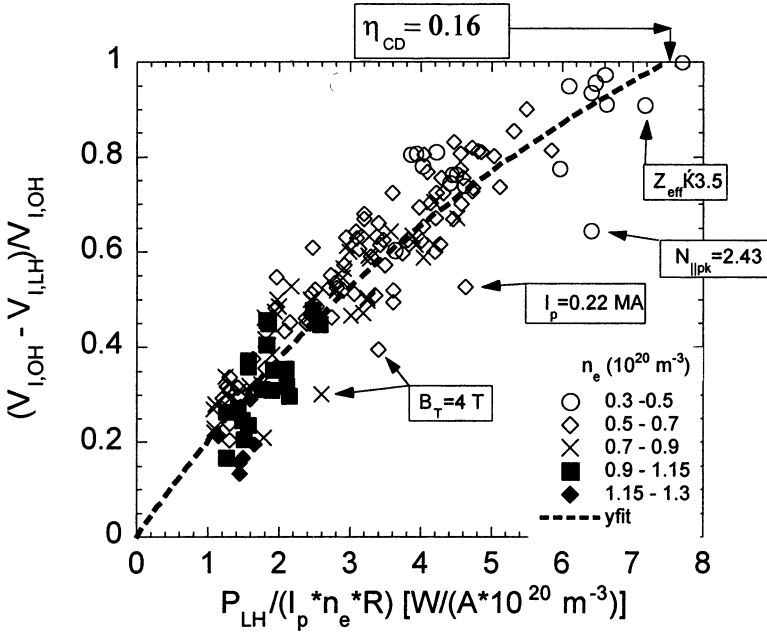


Fig. 2. Plot of the relative loop voltage drop versus the inverse of η_{CD} . Different symbols refer to different densities (see inset). The dashed line represents a fit function define in the text

The good linearity of the data presented shows, within the experimental uncertainties, that these choices are correct. The error estimated for η_{CD} is close to 20 %.

Theoretical estimates of the hot electron contribution to η_{CD} in FTU, have carried out taking into account just the experimental data. Following the CD analysis method developed for PBX [10], and from the evaluation of the collision operator according to simple 1-D models the experimental evidence of negligible effect of the residual electric field is further supported. The choice of these models, in turn is supported by preliminary data on hard X ray fluxes, giving a fast electrons slowing down time in agreement with the Asdex density scaling [11].

In conclusion the linear extrapolation to $I_{LH}/I_p = 1$ and the corresponding value for $\eta_{CD} \approx 0.22$ in full CD operation turns out to be correct. No deviation from linearity results on the basis of the density in the limits of measurement accuracy.

The discussion of accessibility questions is referred to the recent paper in Ref. [20].

While the data do not show any negative trend with n_e , an increase of η_{CD} with $\langle T_e \rangle$, above the experimental uncertainties has been observed. This is evidenced in Fig. 4 where the FTU η_{CD} data are plotted versus $\langle T_e \rangle$.

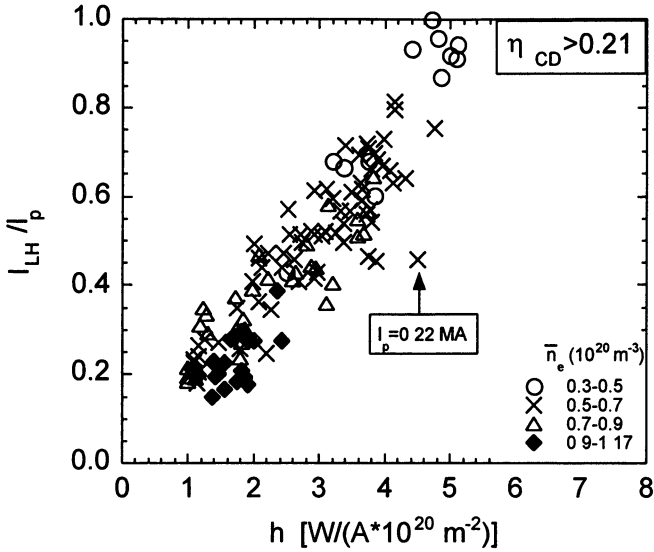


Fig. 3. Plot of the ratio of the LH driven current to the total current versus the quantity h defined in the text. Different symbols refer to different densities (see inset). Note how a fraction of about 50 % has been driven at $n_e \approx 0.9 \cdot 10^{20} \text{ m}^{-3}$ and how the points at high density are indistinguishable from the low density ones

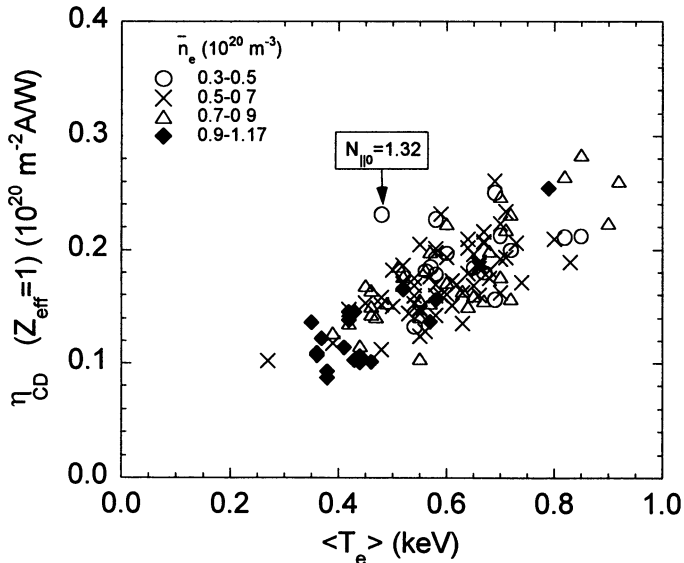


Fig. 4. Plot of the estimated CD efficiency corrected for Z_{eff} and $\langle T_e \rangle$ versus the volume averaged electron temperature. Different symbols refer to different densities (see inset)

The same data are summarized as the average of four values of $\langle T_e \rangle$ inside the spanned range 0.36 - 0.92 keV and compared, in Fig. 5, with those from other tokamaks [3, 10, 12, 13, 15, 16] extrapolated to clean plasma conditions ($Z_{\text{eff}}=1$).

The plot includes the largest $\langle T_e \rangle$ interval available in the literature, from the coldest (HT-6B [16]) to the hottest (JET [3]) device. The highest reported efficiencies in the range $1.7 \leq N_{\parallel 0} \leq 1.9$ are considered, except for Alcator C for which η_{CD} is taken at $n_e \approx 1 \cdot 10^{20} \text{ m}^{-3}$. For the data outside the range of $N_{\parallel 0}$ the correction for the different LH phase velocity according to Fisch's formula has been applied. The conclusion is: the favourable scaling with $\langle T_e \rangle$ applies to all tokamaks, and not only to single devices [3, 4].

The main mechanism, in our opinion, for the enhancement of η_{CD} rely on effect of electron temperature on LH deposition profile which can change, in turn, the fraction of the LH absorbed power as observed in JET [6]. The theory suggests other different mechanisms for this enhancement [17, 18]. Similar effects have been recently observed in preliminary experiments of combined LHCD plus electron cyclotron heating experiments [19].

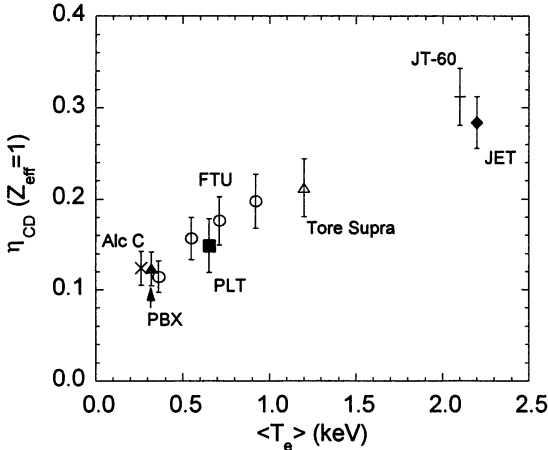


Fig. 5. Comparison of the highest values of the CD efficiency on various tokamaks as a function of the volume averaged electron temperature $\langle T_e \rangle$. For Alcator C the result for $n_e = 1 \cdot 10^{20} \text{ m}^{-3}$ is considered. The vertical bars indicate the range of results obtained for the given $\langle T_e \rangle$

To conclude, the high frequency (8 GHz) LH system on FTU has demonstrated to be able of reaching a good efficiency of current drive, $\eta_{\text{CD}} \approx 0.2 \text{ A} \cdot 10^{20} \text{ m}^{-2}/\text{W}$ at line averaged plasma density in excess to $1 \cdot 10^{20} \text{ m}^{-3}$, in a quasi steady state conditions for times longer than the skin time. The higher FTU electron temperature explains the higher efficiency reached in comparison with Alcator C. This statement is further

supported from the FTU results which show an increasing ordering of the CD efficiency versus the electron temperature, in agreement with the results of other tokamaks. This confirms the possibility to attain comparable CD efficiencies at higher densities than the ones in JET and JT-60; an encouraging result in view of the application of the LH waves on ITER like devices. Density affects η_{CD} only through the LH waves accessibility. On the other hand, onset of parametric decay instabilities, significant spectral pump broadening and generation of fast ion tails, have not been observed in the range of explored density. Fast electron tails are well detected even beyond the first pass accessibility limits at $n_e \approx 1.35 \cdot 10^{20} \text{ m}^{-3}$. The influx of impurities occurring during correct operations of both plasma and LH grill up to the so far maximum coupled power of 1.7 MW does not limit the tokamak operation.

References

1. Tomabechi K. et al., Nucl. Fusion, **31**, 1135, (1991).
2. Porkolab M. et al., Phys. Rev. Lett., **53**, 450, (1984).
3. Ekedhal et al. Proc 23rd EPS Conf. on Plasma Phys. and Controll. Fusion, Kiev, Ukraine, **20C**, Part II, 969, (1996).
4. Watari T., Plasma Phys. Controll. Fus., **35**, A181, (1993).
5. Knowlton S. et al., Phys. Rev. Lett., **57**, 587, (1986).
6. Pericoli Ridolfini V. et al., Plasma Phys. Controll. Fus., **39**, 1115, (1997).
7. Pericoli Ridolfini V. et al., Nucl. Fusion, **32**, 286, (1992); R. Cesario et al., *ibid.*, 2127.
8. Apicella M. L. et al., Nucl. Fusion, **37**, 381, (1997).
9. Fisch N. J., Rev. Mod. Phys., **59**, 175, (1987).
10. Giruzzi G. et al., Nucl. Fusion, **37**, 673, (1997).
11. Bartiromo R. et al., Nucl. Fusion, **33**, 1483, (1993).
12. Leuterer F. et al., Nucl. Fusion, **31**, 2315, (1991).
13. Stevens J. E. et al., Nucl. Fusion, **28**, 217, (1988).
14. Fischer et al., 22nd EPS Conf. on Controll. Fusion and Plasma Phys, Bournemouth, U.K., **19C**, Part III, 361, (1995).
15. Tonon G. et al., Plasma Phys. Controll. Fus., **40**, A63, (1998).
16. Cao Y. et al., Proc. 13rd Conf. on Plasma Phys and Controll. Nucl. Fusion Research, Washington DC, USA, 1-6 Oct. 1990, **V. I**, p. 411.
17. Barbato E., Plasma Phys. Controll. Fus., **35**, A181, (1993).
18. Takase H. et al., Plasma Phys. Controll. Fus., **33**, 749, (1991).
19. Pericoli Ridolfini V. et al., Proc 24th EPS Conf. on Controll. Fusion and Plasma Phys., Berchtesgaden, Germany, **21A**, Part III, 1157 (1997).
20. Pericoli Ridolfini V. et al., Phys. Rev. Lett., **82**, 93, (1999).

ECRH/ECCD EXPERIMENTS AT 140 GHz ON FTU TOKAMAK

S. Cirant¹, A. Airoidi¹, L. Bertalot², R. Bozzi¹, A. Bruschi¹, G. Bracco², P. Buratti², G. Ciccone², G. Cenacchi³, F. Crisanti², S. Di Giovenale², B. Esposito², L. Gabellieri², F. Gandini¹, G. Granucci¹, F. Iannone², H. Krögler², E. Lazzaro¹, S. Lupini², S. Mantovani², V. Mellera¹, V. Muzzini¹, A. Nardone¹, S. Nowak¹, D. Pacella², L. Panaccione², E. Pesci², G. Ramponi¹, A. Simonetto¹, C. Sozzi¹, N. Spinicchia¹, O. Tudisco², M. Zerbini², FTU GROUP²

¹*Istituto di Fisica del Plasma del CNR, Associazione EURATOM-ENEA-CNR, Via R. Cozzi 53, Milano*

²*Centro Ricerche Energia ENEA-Frascati - Associazione EURATOM/ENEA/CNR sulla Fusione.*

³*Centro Ricerche Energia ENEA, Via Don Fiammelli 2, Bologna, Italy*

Abstract - Electron heating, profile control and current drive experiments are performed on FTU tokamak by using a four units EC system at 140, 2 MW total R.F. power. Each unit is composed by a gyrotron with 0.5 MW, 0.5 s pulse length capability, and an hybrid mirror/waveguide system allowing low-loss transmission of the millimeterwave power, with full control of the e.m. field polarization. FTU plasmas are illuminated from the low magnetic field side by four narrow gaussian beams, each one quasi-optically coupled to the correspondent waveguide. The launching system is capable of poloidal/toroidal beam steering through a set of tiltable in-vacuum mirrors, all placed outside the toroidal magnet. Up grading to 1 MW per line is under evaluation.

In the high density regime (local $n_e \approx 10^{20} \text{ m}^{-3}$ or higher), ion heating is observed through the enhancement of the neutron emission in Deuterium plasmas, and the spectroscopic broadening of soft-X Fe lines. In the lower density regime (average line density down to $0.3 \cdot 10^{20} \text{ m}^{-3}$), the highest electron heating is observed when on-axis ECRH is performed in the current ramp-up phase. In steady-state conditions, which usually are dominated by sawteeth, an accurate choice of the ECRH absorbing layer allows the achievement of temperature/current density profiles stable with respect to $m=1$ reconnections.

The microwave system

The total power of 2 MW presently considered for ECRH/ECCD experiments [1,2] on FTU tokamak [3] at 140 GHz is provided by four Gycom GLGD-140-500 gyrotrons, with 0.5 s pulse length capability. Each tube feeds an hybrid transmission line composed by a closed, metallic waveguide propagating an $HE_{1,1}$ mode, and quasi-

optical elements at both ends for optimum matching to the gyrotron and to the launching system. An outline of the system is shown in Fig.1.

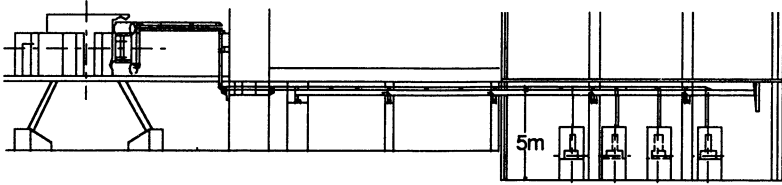


Fig.1 - Layout of the ECRH system and FTU tokamak.

Each gyrotron's output beam is filtered from spurious modes and shaped to a customer-specified waist by a Matching Optics Unit, delivered with the tube. The beam shape and polarization are then adjusted with one ellipsoidal mirror and two flat, corrugated mirrors [4] for optimum matching to the waveguide hybrid $HE_{1,1}$ mode, and for optimum coupling to the Ordinary mode into the plasma. To improve the power handling capability of the corrugated mirrors up to 1 MW per line, a pair of converging-diverging reflectors, allowing the insertion of the polarizer in a position where the beam is larger will replace the single ellipsoidal mirror. Present and improved configurations of the conditioning optics system at the gyrotron's output are shown in Fig.2.

The polarizer's surface is an array of half-cylinders on a flat ground plane [4]. Maxwell's equations for the incident and reflected e.m. field can be solved in this case analytically. Cylinder radius and spacing are adjusted for linear-to-circular ($\lambda/8$ equivalent corrugation depth) and linear-to-linear ($\lambda/4$ corrugation depth) polarization rotation. The rounded shape is also ideal for good power handling capability. The solution of e.m. scattering problem of an array of thick wires has also been used to evaluate the possibility of building cooled polarizing grids, suitable for high power operation in the millimetric wavelength region [5].

Not shown in the figure, an additional moving ellipsoidal mirror switches the beam from the main path into a local calorimetric matched load, used for power measurements and for gyrotron conditioning. The load is made of an integrating sphere with partially reflecting walls [6] coated with a mixture of Al and Ti oxides. It has a reflectivity (integrated in all directions in the half back-space) of less than 4%, and it is designed to have full 1 MW power handling capability. The diverging mirror opposite to the input aperture is fixed

in the present configuration, but it might be made flat and rotatable in the 1 MW, up-graded version.

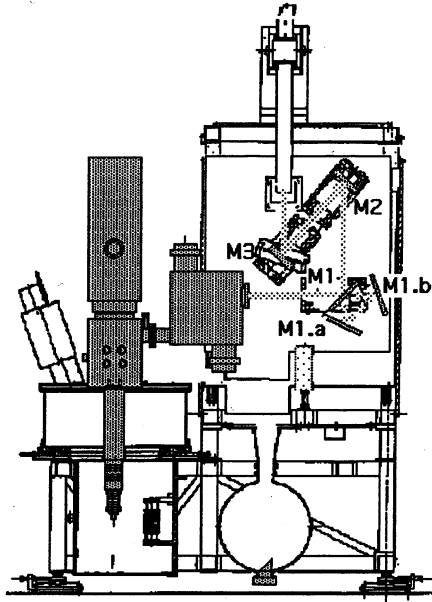


Fig.2. Conditioning optics for the gyrotron's output beam. Present configuration for 0.5 MW gyrotrons (continuous path): M1, ellipsoidal, matches the beam to the $HE_{1,1}$ mode at waveguide input; M2&M3, corrugated, match the O-mode at plasma edge. Improved configuration for 1 MW gyrotrons (outlined in the figure): M1.a&b, polarizer; M2&M3, diverging/converging for mode matching.

Each one of the four transmission lines from the gyrotrons to the launching system is composed by a circular, corrugated oversized waveguide (≈ 30 m long) propagating the $HE_{1,1}$ mode, with a diameter of 88.9 mm (3.5") large enough to allow the operation of the system, at atmospheric pressure, up to 1 MW per line [1,2]. Due to the large diameter to wavelength ratio (≈ 41.5), 90° bends can be optically accomplished with flat reflectors, with negligible conversion into dangerous edge waveguide modes. 5 bends accommodate all the necessary direction changes. A further advantage of the large diameter is that wide gaps, up to ≈ 20 mm, can be inserted without loss of transmission efficiency, for thermal expansion recovery and for easier installation/removal of each single straight section (2 m long).

Good alignment of single elements on the ideal line is essential for low loss transmission, and tilt in particular must be kept low for large

diameter waveguides. Waveguide joints, stands and the suspensions for all the components have been designed to allow alignment with an offset error less than 0.1 mm, and a tilt error less than 0.5 mm/m, which is performed according to specific procedures based on the use of standard optical alignment instrumentation [7,8].

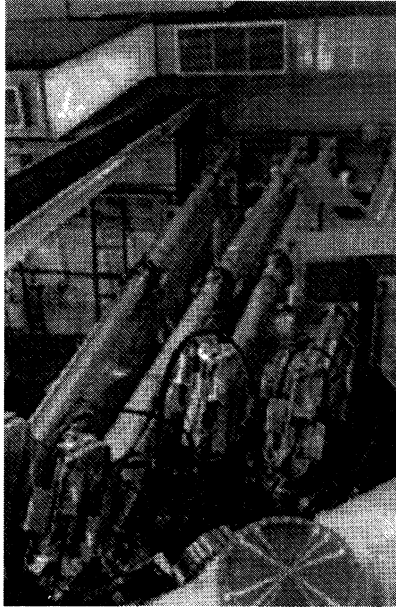


Fig.3. Waveguides at the end of the line, close to the launching system. Shown in figure: supporting beams; adjustable waveguide stands; waveguide joints (also expansion joints); bends; directional couplers.

For safety reasons all the joints in the transmission lines in areas of free access are checked against excessive r.f. leakage. A special instrument, based on the use of thermopiles as microwave detectors, has been developed to perform fast measurements as required [9].

A waveguide switch is inserted in one of the lines for feeding the antenna of a system for collective Thomson scattering experiments [10].

The launching system

Four sets of three in-vessel mirrors for each transmission line launch converging e.m. beams into the plasma [11] through the same vacuum port. The last mirror in each set is movable from shot to shot, in order to allow both vertical and horizontal beam steering. Being FTU tokamak an high field ($B_{tor,max} = 8$ T), compact machine

(major radius $R_0=0.935$ m; minor radius $a=0.33$ m), access to the vacuum chamber is limited. In particular, the maximum size of each port in the toroidal direction is 8 cm. A top view of the port used by ECRH (1 of 12) is shown in Fig.4.

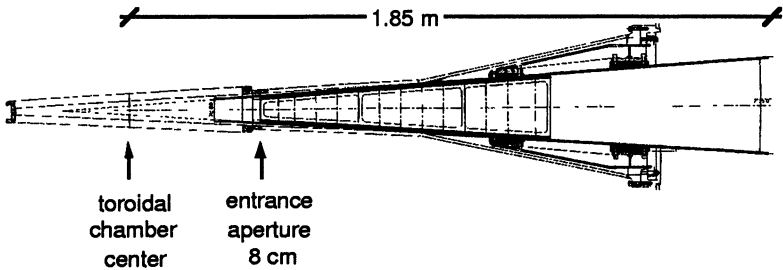


Fig.4. Top view of FTU port, connecting the toroidal chamber (on the left side in the figure) to the vacuum-tight flange (on the right). Each one of the 12 ports is fitted in a narrow space between two the 12 coils of the toroidal magnet. Two flat, vertical mirrors are inserted inside the port duct for toroidally oblique beam launch.

Due to the very narrow limiter shadow (3 cm), no object is allowed to protrude from the port duct into the toroidal chamber. Taking into account all restrictions posed by vacuum compatibility, all mirrors and mountings are positioned in a wider portion of the duct, outside the toroidal magnet. Toroidally oblique launch is achieved by reflecting each beam on flat, vertical mirrors laying against the duct walls. With this arrangement, only discrete toroidal angles (0, ≈ 10 , ≈ 20 , ≈ 30 degrees), corresponding to the number of reflections made at the vertical mirrors, are allowed (Fig.5). At all the other angles the beam is diffracted in two opposite main lobes at the entrance aperture. The flat vertical plates are made of amagnetic stainless steel for achieving adequate mechanical strength, and are gold plated in order to keep to a minimum r.f. losses at reflection. In order to maintain the beam shape at all toroidal angles, each last converging mirror rotates around the axis of the incident beam.

The launched beam quality has been accurately tested at low power [11,12], particularly in the case of toroidally oblique launch when beam shape and directivity could be affected by distortions in the surface of the vertical plates and by diffraction at the aperture. As shown in Fig.6, the beam remains gaussian still after three bounces, slightly elongated in the vertical direction because of beam truncation at the last mirror (Fig.7).

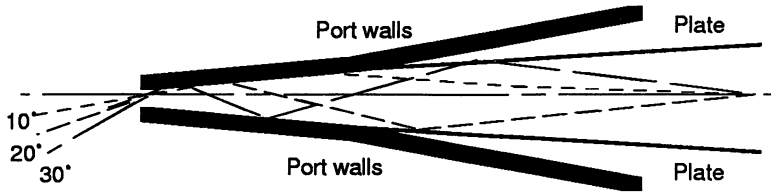


Fig.5. Scheme of oblique launch. By tilting in the horizontal plane the launching mirror, the beam is reflected n times at the flat vertical plates. It emerges undisturbed in the centre of the entrance aperture at finite toroidal angles, determined by the number of reflections and by the plate convergence.

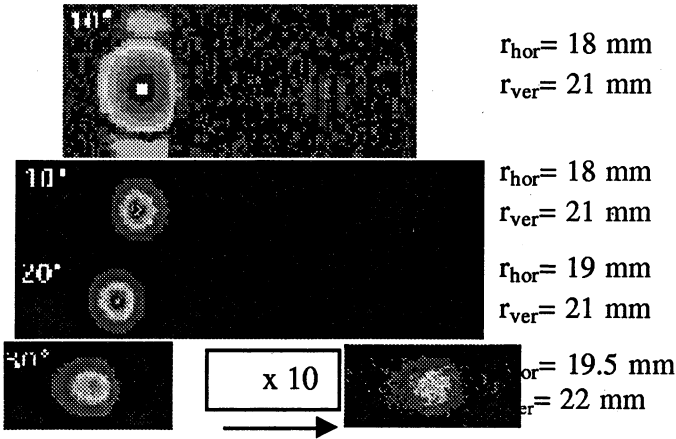


Fig.6. Beam pattern and size for toroidally oblique injection at different angles. Top pattern has a wider dynamic range, in order to show both the sidelobes and the toroidally symmetric spurious image beam; green is -25 dB .

Since the measurement is made at fixed mirror-to-detector distance, the main observable effect in case of oblique launch is a slight increase of the beam radius with increasing number of reflections, consistent with the longer beam path to the measuring point. Calculated resistive losses are $\approx 1.2 \%$ in all the cases of 1, 2 and 3 bounces. The two vertical plates reduce the entrance aperture to 70 mm, where the beam diameter is $\approx 35 \text{ mm}$.

Some interference is therefore expected also for perpendicular launch, and measured to be at a low and acceptable level (Fig.7). High resolution patterns are obtained with standard microwave techniques for beam pattern recognition (automatic scan with sensitive radiometer), but fast detection of the main beam features is made by

taking with IR camera the thermal print left by the beam on absorbing foils (Fig.6).

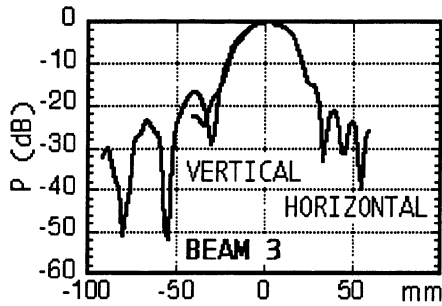


Fig.7. Typical beam pattern for perpendicular launch . Diffraction due to beam truncation at the last mirror determines the sidelobes in the vertical plane, while the interference pattern in the horizontal scan is created at the entrance port.

The amplitude of the spurious image beam generated by diffraction at the entrance varies from -25 dB for an oblique launch at 10° , 1 bounce, to -11 dB at 30° , 3 bounces. It remains therefore to an acceptable low level.

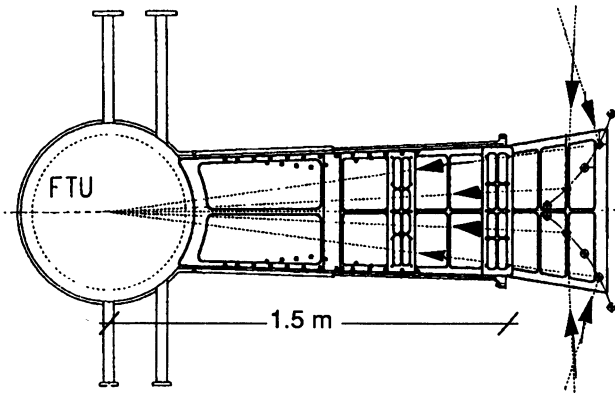


Fig.8. Side view of FTU port. The vertical plates for toroidal oblique launch, the movable launching mirrors and the four beam axes are also shown in the figure.

The vertical scan of the beams is obtained by a standard tilt of the launching mirrors, which is possible because FTU ports are narrow in the toroidal direction, but vertically they are wide enough.

Beam axis and launching mirrors are outlined in Fig.8, in a side view of the FTU port showing also the vertical plates. All mirrors are

in Aluminium or Copper. Each barrier window is a single BN disk, edge cooled, with an outer diameter of 123 mm.

Power measurements

As already mentioned, the output power from each gyrotron can be absorbed and measured by a calorimetric matched load, close to the gyrotron itself. Power measurement at any point along the transmission line, and in particular at the end, are made with a second type of load. It composed by a cylindrical cavity and an array of scattering/absorbing tubes [1], also used for circulating the cooling water. All surfaces inside the cavity, including the tubes, are covered by plasma-spray with a partially absorbing ceramic layer.

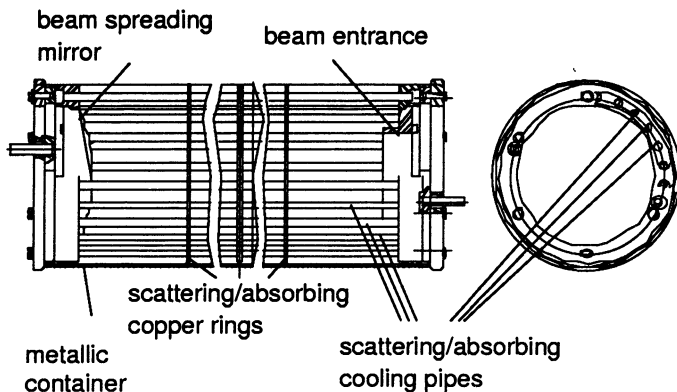


Fig.9. Scheme of the cylindrical calorimetric matched load. As for the spherical load, the surfaces inside the cavity are partially reflecting. An array of cooled tubes scatters the beam, absorbs the power and removes heat. Total length is 1.8 m.

Fast power measurements are made with quasi-optical directional couplers at the first and the last bend of each line (Fig.10). The power is directionally coupled to outside the waveguide by an array of holes in the flat mirror bend [13]. The coupled power is detected by a pair of horn antennas, one for each polarization, one pair for each incident and reflected directions, positioned close to the array and inside a shielded enclosure. Internal shielding has been accurately designed and tested for maximum directivity and minimum polarization cross-talk. Holes are in cut-off, and the measured average coupling coefficient is 62 dB. The average directivity is 20 dB, and polarization cross talk is also ≈ 20 dB. A set of fiber optics is inserted

inside each bend, looking in both the input and output waveguides, which is used to detect arcs in the transmission line [8].

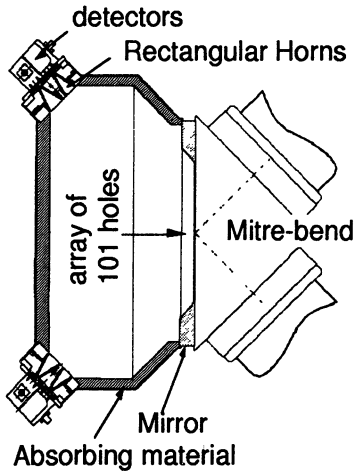


Fig. 10. Waveguide directional coupler. Incident and reflected power is directly coupled to outside the waveguide through an array of holes in cut-off, drilled in the mirror of a mitre bend [12]. The shaping of the detector enclosure and the appropriate position of absorbing materials, decouple the incident and the reflected measuring arms.

Experimental results on ECRH/ECCD and MHD activity

Two gyrotrons have been used for ECRH/ECCD experiments, with a total launched power of 0.8 MW for 0.3 s, aimed mainly at profile control and energy confinement studies by localized electron heating.

ECRH was performed both at flat top, with a plasma current of $350\div 400$ kA ($q_a \approx 6$), and during the current ramp-up at a rate of $1\div 5$ MA/s [14]. This last experimental scenario was chosen for studying confinement in regimes with low or reversed central magnetic shear [15,16]. At flat top, the impact of MHD activity on core confinement was studied, with particular attention to the effects of the presence of $q=1$ resonant magnetic surface. Since most of FTU discharges have sawtooth activity at current flat-top, the experiments were also oriented at the study of the $m=1$ mode dynamics with localized ECRH.

The sawtooth period during ECRH depends on the radial position of the absorbing layer [14, 17]. In particular, the period can be strongly increased if EC absorption at r_{abs} is near the inversion radius [14, 18] (Fig.11). ECCD at $r_{abs} \approx r_{inv}$ along with the ohmic current also extends the sawtooth period, while counter current drive has an overall moderate or negligible effect [19]. Stabilization occurs on a fast time scale, which is consistent with a local distortion of the

current density profile [18], but it is short with respect to the current diffusion time over $r_{q=1}$.

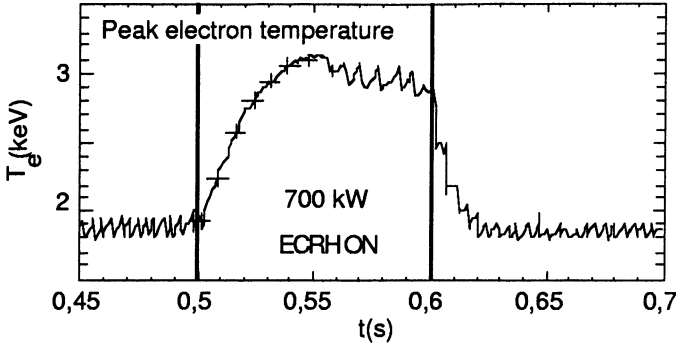


Fig.11. Central electron temperature during ECRH with $r_{ris} \approx r_{inv}$, shot #14549, showing a strong increase of the sawtooth period in these conditions. Profiles taken during temperature rise (marks) are shown in Fig.12. $P_{ecrh}=700$ kW; $P_{oh}=400 \Rightarrow 200$ kW; $n_{e,line}=0.5 \cdot 10^{20} \text{ m}^{-3}$.

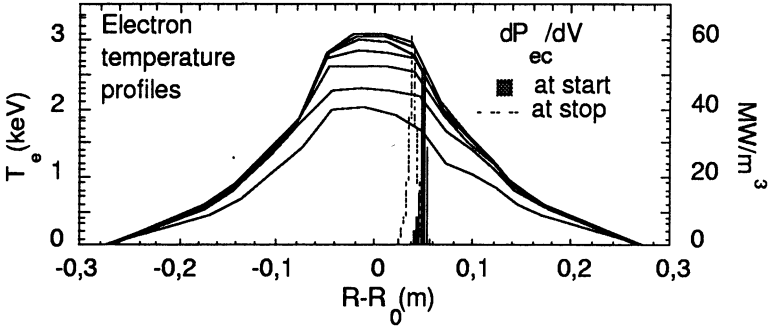


Fig.12. Electron temperature profile evolution during ECRH with $r_{ris} \approx r_{inv}$, shot #14549. The relative position of the absorbing layer moves during ECRH according to the Shafranov shift. $P_{ecrh}=700$ kW; $P_{oh}=400 \Rightarrow 200$ kW; $n_{e,line}=0.5 \cdot 10^{20} \text{ m}^{-3}$.

All these features of sawtooth reaction to localized ECRH/ECCD fit with [19, 22] the assumption that the magnetic reconnection depends on the value of the magnetic shear at the $q=1$ radius. The physical basis for this dependence is the stabilization of the internal kink mode by diamagnetic effects, which can be effective only if the local shear s_1 at $r_1=r_{q=1}$ is lower than a critical value depending on plasma parameters. In particular, stabilization occurs if the kink mode

growth rate $\gamma_p(s_1, T_e/T_i, \rho_i, r_1, \tau_A, S)$ is lower than a critical value $\gamma_{crit} \approx c\sqrt{(\omega_{dia,e} \omega_{dia,i})}$, depending on the electron and ion diamagnetic frequencies [20, 21]. ρ_i, τ_A, S are respectively the ion Larmor radius, the Alfvén time and the magnetic Reynolds number.

ECRH and CO-ECCD localized around $r_{q=1}$ tend to flatten the current density profile, delaying in time the growth up to disruption of the internal kink mode.

By implementing this model into a 1-D transport code, including flux conserving relaxations in accordance to the Kadomtsev complete reconnection model, and triggered by the overcoming of the critical shear at the calculated $q=1$ surface, the effect of ECRH on the sawtooth repetition rate has been correctly reproduced [19].

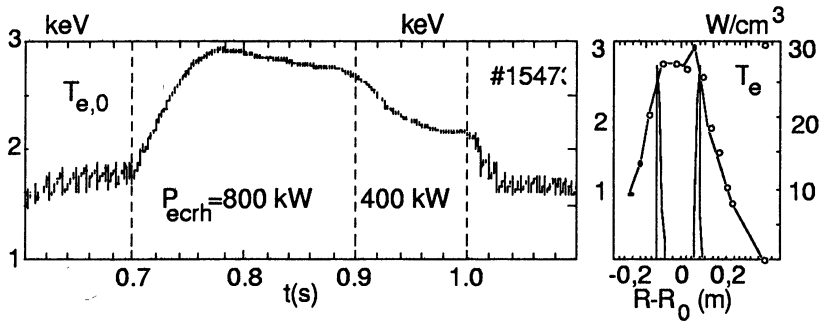


Fig.13. Electron temperature dependence with time (left) and radius(right) in case of ECRH with $r_{abs} \approx r_{inv}$ and high electron density ($n_{e,line} = 0.8 \cdot 10^{20} \text{ m}^{-3}$). Full sawteeth suppression is achieved in these conditions.

The electrodynamic reaction to a strong reduction in the electric resistivity, localized around the EC absorption layer, enhances the current density profile reshaping in the transient phase following the switching ON or OFF of the ECRH power [19]. The enhancement vanishes in times in the order of one current diffusion time over $r_{q=1}$ (≈ 20 ms), and in fact the strongest effect on the sawteeth period is observed immediately after the application of ECRH (Fig.11).

Complete sawteeth stabilization can be obtained with ECRH localized at $r_{abs} \approx r_{inv}$ in an high density plasma. The drop in the central ohmic heating power density and the e-i energy exchange produce a flat-hollow electron temperature profile with off-axis ECRH [24]. Simulations show that sawteeth suppression is due, in this case, either

to the achievement of $q_0 \approx 1$, or to a shrinking of $r_{q=1}$ inside a region with very low thermal gradients [19]. Mixing is frequent in this case, but with negligible effects on the temperature profile.

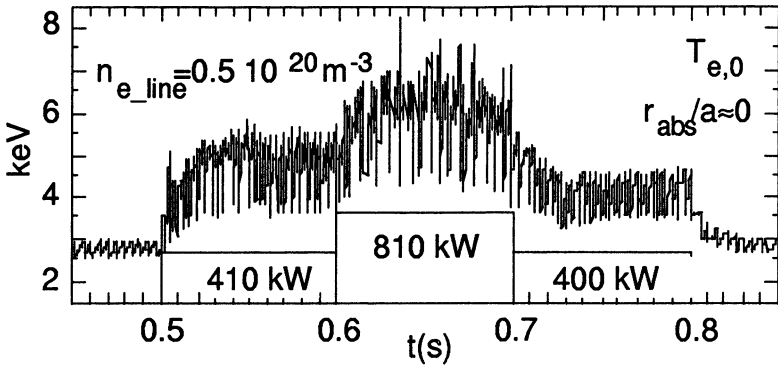


Fig.14. Central electron temperature (ECE diagnostic) during nearly on-axis ECRH at different power levels, shot #14971 .

Central ECRH has different effects on sawtooth activity, sensitively dependent on the exact position of the directly heated volume, and on the total absorbed power. At moderate EC heating power, $P_{\text{ecrh}} \approx P_{\text{oh}}$, or with absorption inside the inversion radius r_{inv} but not exactly at center, the effect is in general to speed up profile evolution towards magnetic reconnection of the $m=1$ mode, thereby increasing the sawtooth frequency [18]. As an example, Fig.14 shows that with $P_{\text{ecrh}} \approx 400$ kW, $P_{\text{ecrh}} \approx 330$ kW, central heating, the sawtooth period is about half the ohmic value. However, with $P_{\text{ecrh}} \approx 800$ kW on top of $P_{\text{oh}} \approx 250$ kW, and when the average electron temperature rises above 6 keV, the reconnection repetition rate is clearly slowed down.

Calculations, with the 1-D transport-diffusion code, of the current density re-distribution following a strong and peaked increase of the electron temperature, show in fact that also the current density peaks to the center and the magnetic shear at $r_{q=1}$ increase. However, at high electron temperature also the threshold of the critical shear increases. As a result, the global effect of central ECRH on sawteeth is a trade-off between the effective shear increase at $r_{q=1}$, and the increase in the local threshold for reconnection.

In the case of central ECRH, when the peak temperature can rise up to ≈ 8 keV with $P_{\text{ecrh}} = 800$ kW ($n_{e,0} \approx 0.8 \cdot 10^{20} \text{ m}^{-3}$) as a result of the very localized power deposition in a small plasma volume, saturated oscillations of odd order appear [22, 23]. The peak temperature rise is

interrupted during oscillations, which can continue until the next crash, or it can vanish (Fig.16) within the sawtooth period. In the last case T_{e0} rises again until reconnection occurs.

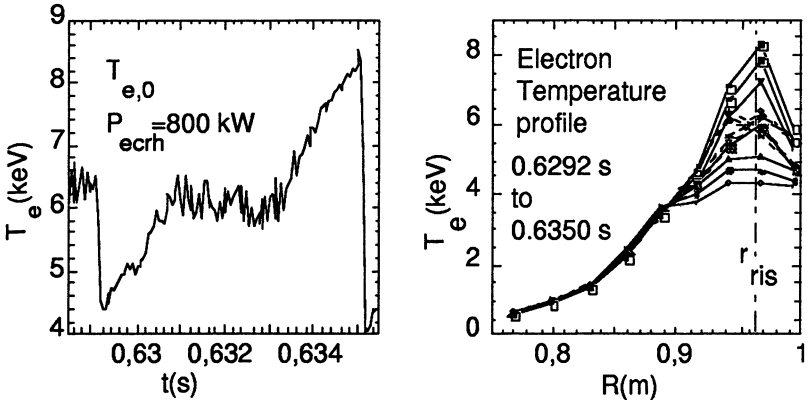


Fig.15. Peak electron temperature (left) and temperature profile (right) evolution within a single sawtooth during nearly on-axis ECRH at 800 kW, high average temperature. $n_{e,line}=0.5 \cdot 10^{20} \text{ m}^{-3}$, shot #14971.

The central temperature increase is limited by fluctuations because of de-localization of the heating power deposition (core plasma oscillates, but the resonance position remains fixed), because of re-distribution by convection of the heat inside the volume perturbed by the instability, and likely because of a loss of confinement commonly associated with MHD oscillations [24].

Magnetic reconnection at each sawtooth crash is a very fast event, occurring within 50÷100 μs , or less than one $m=1$ period, in ohmic or ECRH plasmas, with central or off-axis heating, with or without saturated $m=1$ oscillations. The crash is not anticipated by a growing or large $m=1$ oscillation. Fig.16 clearly shows the collapse of the temperature profile occurring at magnetic reconnection, which flattens the temperature inside the mixing radius on a collisionless time scale.

All the experiments performed point out that profile shaping (temperature, current density), and its effects on MHD activity, are very sensitive to the localization of the EC wave absorbing volume. This is usually calculated by beam tracing computing codes, performed taken into account the measured plasma magnetic geometry, and the electron density and temperature profiles [26].

The experimental estimate of the EC power deposition profile is obtained by fast measurements of the local pressure change during transients in the applied EC power.

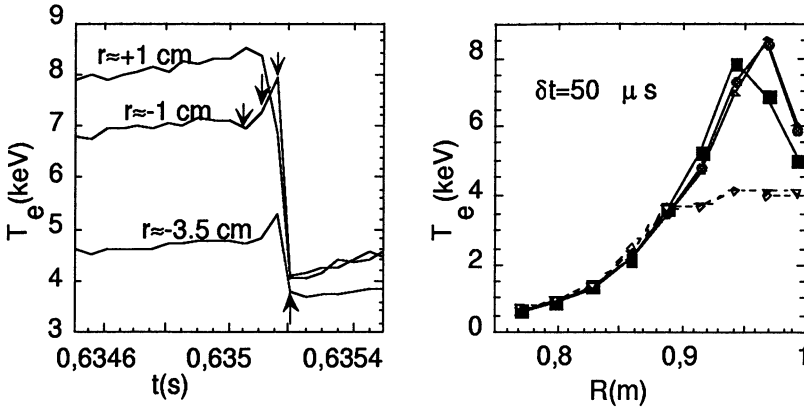


Fig.16. Sawtooth crash at $P_{ecrh}=810$ kW, with on axis resonance, shot #14971. Although reconnection is usually preceeded by $m=1$ oscillations, it takes place in this case even before a single half oscillation is completed, on a collisionless time scale. Temperature profile)are taken at the instants marked by arrows.

If P_{ECRH} is modulated in time, the heating profile is given by the spatial distribution of the amplitude of thermal oscillations at the modulation frequency with the minimum phase lag with respect to the EC power source [27]. In all cases, the distribution of the absorbed power density can be estimated at the switching ON or OFF of the ECRH power, by detecting the jump in the local rate of change of the electron energy density [28, 29]. Although the calculated and measured position of the peak in the power deposition profile are well in agreement, measured profiles are broader than calculated ones, which are usually very narrow in hot plasmas illuminated with small size, focused E.C. beams. Heat diffusion [30] and finite spatial resolution of the local temperature measurement [29] are, in most cases, the main cause for the apparent absorption profile broadening. Beam-tracing and wave damping calculations are therefore used for modelling ECRH effects in profile shaping and heat transport analysis [25].

Ion heating during ECRH at high electron density

ECRH with $B_{tor} \approx 5$ Tesla, fundamental resonance, can be performed in plasmas with an electron density high enough to allow collisional

electron-ion heat transfer, the cut-off density being $n_{e,\text{cut-off}} = 2.4 \cdot 10^{20} \text{ m}^{-3}$. This has been shown previously to be important for profile shaping with off-axis ECRH.

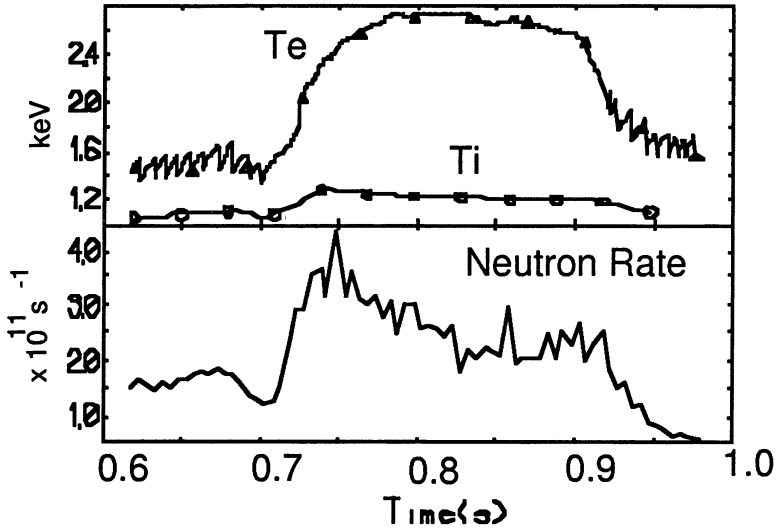


Fig.17. Ion heating during ECRH at $n_{e,\text{line}} = 0.8 \cdot 10^{20} \text{ m}^{-3}$, $n_{e,0} = 1.3 \cdot 10^{20} \text{ m}^{-3}$, shot #14977.

As a result of collisional coupling, ion heating is observed through the enhancement of D-D neutron emission from Deuterium plasmas. Fig.17 shows that neutron rate increases by a factor ≈ 3 with $P_{\text{ecrh}} = 800 \text{ kW}$, $P_{\text{oh}} \approx 250 \text{ kW}$, and $n_{e,0} = 1.3 \cdot 10^{20} \text{ m}^{-3}$, corresponding to $\approx 25\%$ increase in the central ion temperature.

The power balance on all species, and in particular the heat flow into the ions, is estimated with the aid of a time-dependent heat transport code. In order to correctly describe the observed waveform of neutron emission and ion temperature increase, both in the transient phase and at steady-state, an ion thermal diffusivity $\chi_i = 2.8 \chi_{i,\text{Chang-Hinton}}$ must be used in the code. The electron-ion heat transfer flow $Q_{e,i}$, determining the observed ion temperature rise time, is the one given by classical predictions.

The classical nature of collisional energy transfer from the electrons to the ions is confirmed by the observed scaling, at a fixed ECRH power and EC resonance position, of the ion heating efficiency $T_{i,\text{ecrh}}/T_{i,\text{oh}}$ with the plasma density (Fig.18). At low electron density e-i collisionality is strongly decreased, also because of the very large T_e/T_i ratio determined by the strong electron heating at low electron

heat capacity. As predicted by collisional theory, if the ratio T_e/T_i becomes larger than ≈ 3 the heat transfer $Q_{e,i}$ is reduced by a further increase in T_e , and ions cool during ECRH.

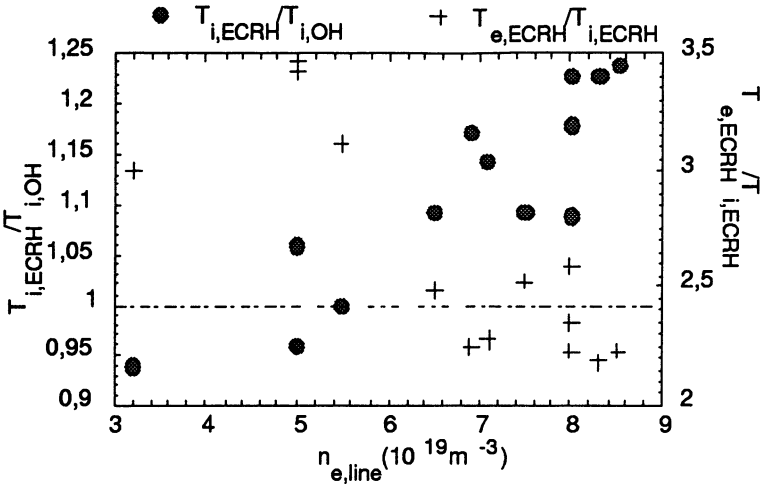


Fig.18. Ion heating efficiency during ECRH at 800 kW increases with the electron density. Because of e-i decoupling at low density, high T_e , ions in fact can be cooled during ECRH.

The cut-off density gives the upper limit of the density range useful for ECRH. At densities close to cut-off plasma refraction reduces the central heat deposition by spreading the EC beam, and the small electron-ion temperature gradient further limits ion heating. There is therefore a density for optimum ion heating efficiency, which is observed to be $n_e \approx 1.5 \cdot 10^{20} m^{-3} = 0.62 n_{e, cut-off}$ at $P_{ecrh} = 800$ kW [31], and it is expected to be closer to cut-off at full 1.6 MW ECRH power.

ECRH during current ramp-up

ECRH was performed also during the current ramp-up, in times shorter than the resistive diffusion time when the current density profile may be hollow. Furthermore, this phase is sawtooth free since $q_0 > 1$. As shown in Fig.19 and Fig.20, the response is quite different if the transient target plasma has a flat/hollow or a peaked profile in the temperature and, likely, in the current density. In the case of a low/reversed central shear, Double Tearing Modes are destabilized due to the presence of a pair of m/n resonant surfaces [32]. This causes strong internal disruptions, which affect energy content and electron temperature in the plasma core. With peaked profiles, high core

temperature and energy content are maintained until the appearance of sawteeth.

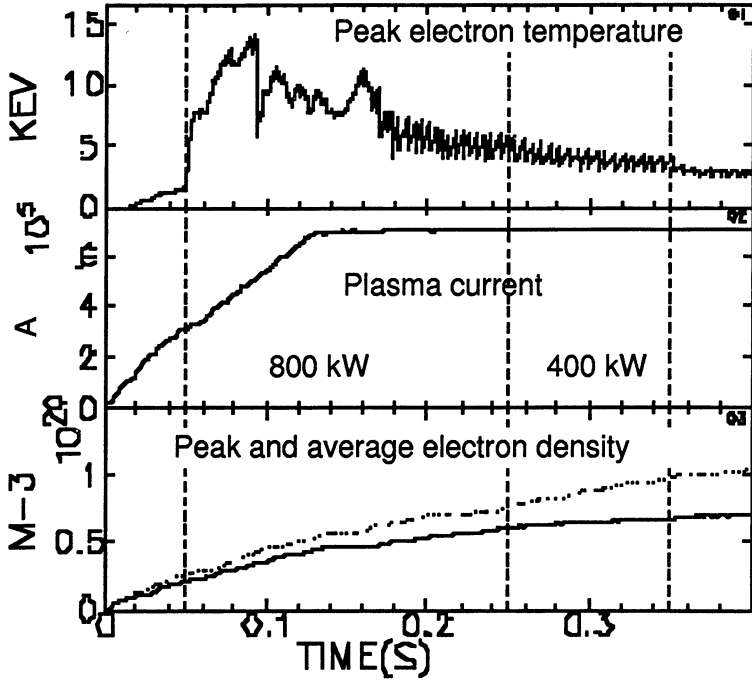


Fig.19. Peak electron temperature, plasma current and electron density during on-axis ECRH in a discharge with an initially hollow temperature (current density) profile.

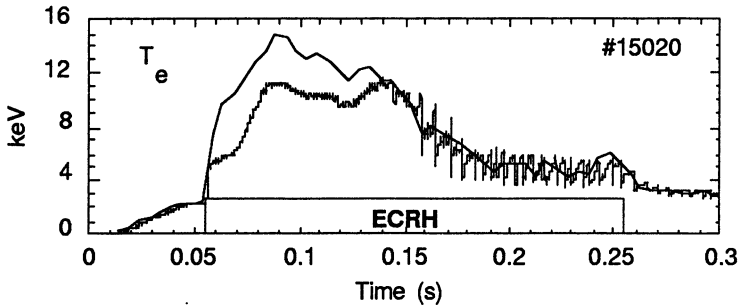


Fig.20. Peak electron temperature during on-axis ECRH in a discharge with an initially peaked temperature (current density) profile .

The highest electron temperatures have been achieved in this scenario and with central ECRH deposition, with non-negligible kinetic effects on the ECE spectra [33].

By analyzing the power balance with the aid of a time dependent transport and diffusion code, the electron heat diffusivity χ_e is found to be in the range between 0.2 and 0.4 m²/s in the plasma core, without significant degradation with high peak electron temperature and large temperature gradients [16]. The global confinement time during ECRH is in fair agreement with ITER89P scaling law [25].

Conclusions

Localized ECRH at 800 kW has been shown to be effective in shaping the profiles of FTU plasmas at $B_{tor} \approx 5$ Tesla, $n_{e,0} \approx 10^{20}$ m⁻³. This capability has been used to study MHD physics, and the associated impact on energy transfer.

In particular, sawteeth behaviour has been explored, and it has been shown that the overcoming of a critical shear at r^* is a possible cause for destabilization of the kink mode, and for magnetic reconnection. The whole reconnection process is fast, occurring on a collisionless time scale, and it is not necessarily anticipated by any precursor. By including the threshold condition into a 1-D transport and diffusion code, with an associated flux conserving mixing of plasma parameters, the observed dependence of the sawteeth period with ECRH power, resonance position and ECCD features, is satisfactorily reproduced.

Saturated or partially saturated sawteeth are observed with on-axis ECRH. In addition to the $m=1$ mode, slowly evolving accordingly to a non-linear growth rate, mode coupling might cause the appearance of higher order, higher frequency MHD instabilities.

During operation at high electron density ($\geq 10^{20}$ m⁻³) ions are included in the power balance. This contributes to profile shaping and sawtooth suppression with ECRH localized at $r \approx r_{q=1}$, and causes ion heating in agreement with neoclassical predictions.

References

- 1 S.Cirant, R.Bozzi, A.Bruschi et al, Proc.of 10th Joint Workshop on ECE Emission and ECRH, T.Donne and Toon Verhoeven Editors, 369 (1997).
- 2 C.Sozzi, B.Berardi, R.Bozzi et al., 13th Topical Conf. "Applications of RF power to Plasmas"- Apr. 12-14,1999 -Annapolis, Maryland
- 3 R. Andreani et al., Fusion Technology (Proc. 16th Symp. London 1990), Vol. 1, North-Holland, Amsterdam (1990) 218.
- 4 A.Bruschi, S.Cirant, G.Granucci et al., International Journal of Infrared and Millimeter Waves, vol.15, n°8, 1413 (1994).
- 5 Argenti L., Bruschi A., Cirant S. et al., 17th Int.Conference on Infrared and Millimeter Waves, Richard J.Temkin, Editor, Proc.SPIE 1929, 108 (1992).
- 6 L.Argenti, A.Bruschi, S.Cirant et al., 18th Int.Conference on Infrared and Millimeter Waves, Colchester 1993, J.S.Birch, T.S.Parker ed., Proc.SPIE 2104, 596 (1993).
- 7 S.Cirant, A.Bruschi, G.Granucci et al., Proc.9th Joint Workshop on Electron Cyclotron Emission and Electron Cyclotron Resonance Heating, Borrego Springs CA (USA), John Lohr Editor, World Scientific Publishing, Singapore, 1995
- 8 G.Granucci, C.Sozzi, B.Berardi et al., Proc.20th Symposium on Fusion Technology,

- Beaumont, P.Libeyre, B.de Gentile, G.Tonon Editors, p.399, 1998
- 9 A.Simonetto, V.Muzzini, A.Bruschi et al., *Rev.Sci.Instrum.* **67**, 4333 (1996)
 - 10 F.Orsitto, A.Brusadin, Yu.Brodsky et al., *Rev. Sci. Instrum.*, **70**, 1158 (1999)
 - 11 A.Bruschi, R.Bozzi, S.Cirant et al., *Proc.20th Symposium on Fusion Technology*, Beaumont, P.Libeyre, B.de Gentile, G.Tonon Editors, p.379, 1998
 - 12 A.Simonetto, A.Bruschi, R.Bozzi et al., *Proc 23rd International Conference on Infrared and Millimeter Waves*, Colchester, UK, Sept 7-11, 1998, Eds. T.J. Parker, S.R.P. Smith, ISBN 09533839 0 3, page 122
 - 13 W. Kasparek, *Proc.of 8th Joint Workshop on ECE and ECRH*, ed. by H.J.Hartfuss and V.Ereckmann (IPP III/186), Max -Planck Insitut fr Plasma Physick, Garching p. 423 (1993)
 - 14 S.Cirant, A.Airoldi, A.Bruschi et al., *Proc.17th IAEA Fusion Energy Conference*, Yokohama, 1998
 - 15 P.Buratti, E.Barbato, G.Bracco et al., *Phys. Rev. Lett.* **82**, 3 (1999) 560
 - 16 F. Alladio, B. Angelini, M.L. Apicella et al., (25th EPS Conference on Controlled Fusion and Plasma Physics, Praga, July 1998) *Plasma Phys. Control. Fusion* **41** (1999) A323-A332
 - 17 R.T.Snider, D.Content, R.James et al., *Phys. Fluids B1* (2) (1999) 404
 - 18 S.Cirant, A.Airoldi, L.Bertalot et al., *13th Topical Conference on Applications of Radio Frequency Power to Plasmas*, Annapolis, April 12-14,1999
 - 19 G.Ramponi, A.Airoldi, A.Bruschi et al., *13th Topical Conference on Applications of Radio Frequency Power to Plasmas*, Annapolis, April 12-14,1999
 - 20 Porcelli F. et al., *Plasma Phys. Contr. Fusion*, **38**, 2163, (1996)
 - 21 Sauter O. et al., *Proc. of Theory of Fusion Plasmas*, 403, (1998)
 - 22 E.Lazzaro, A.Airoldi, A.Bruschi et al., *26th EPS Conference on Controlled Fusion and Plasma Physics*, Maastricht, June 1999
 - 23 Z.A. Pietrzyk, A.Pochelon, T.P. Goodman et al., *Nuclear Fusion* **39**, 5 (1999) 587
 - 24 S.Cirant, A.Airoldi, L.Bertalot et al , *26th EPS Conference on Controlled Fusion and Plasma Physics*, Maastricht, June 1999, to be published on *Plasma Phys. Contr. Fusion*
 - 25 A.Bruschi, C.Sozzi, A.Airoldi et al., *26th EPS Conference on Controlled Fusion and Plasma Physics*, Maastricht, June 1999
 - 26 S.Cirant, S.Nowak, A.Orefice, *J.Plasma Physics*, **53**, 345 (1995)
 - 27 U.Gasparino, V.Ereckmann, H.J. Hartfuss et al., *Proc.of 10th Joint Workshop on ECE Emission and ECRH*, T.Donne and Toon Verhoeven Editors, 411 (1997).
 - 28 A.Bruschi, S.Cirant, F.Gandini et al., *Proc.22nd EPS Conference on Controlled Fusion and Plasma Physics*, B.E.Keen, P.E.Stott, J.Winter Editors, 1995, v.19C, part IV, p.369
 - 29 G.Granucci, A.Bruschi, S.Cirant et al., *Proc.22nd EPS Conference on Controlled Fusion and Plasma Physics*, B.E.Keen, P.E.Stott, J.Winter Editors, 1995, v.19C, part I, p.361
 - 30 F.Leuterer, F.Ryter, M.Beckmann et al., *2nd Europhysics Topical Conference on Radio Frequency Heating and Current Drive of Fusion Devices*, Brussels, January 1998, *Europhysics Conference Abstracts*, **22A**, p.233
 - 31 S.Cirant, A.Airoldi, L.Bertalot et al., *Proc.25th EPS Conference on Controlled Fusion and Plasma Physics*, Praga, July 1998
 - 32 P.Buratti, F.Alladio, P.Micozzi et al., *Plasma Phys. Conytol. Fusion* **39** (1997) B383
 - 33 O. Tudisco, G. Bracco, P. Buratti et al., *26th EPS Conference on Controlled Fusion and Plasma Physics*, Maastricht, June 1999

RECENT RESULTS IN ECH AND ECCD EXPERIMENTS IN THE TCV TOKAMAK

*M.A. Henderson, T.P. Goodman, R. Behn, S. Coda, J-P. Hogge, Y. Martin,
Y. Peysson*, Z.A. Pietrzyk, A. Pochelon, O. Sauter, M.Q. Tran,
and the TCV Team*

Centre de Recherches en Physique des Plasmas,
Ecole Polytechnique Fédérale de Lausanne
Association EURATOM-Confédération Suisse,
CH-1015 Lausanne BPFL, Switzerland

* CEA/Cadarache, 13108 Saint Paul-Lez-Durances Cedex, France

The ECH system on the tokamak TCV (Tokamak à Configuration Variable) has reached completion of the first of three stages of auxiliary heating installations with the operation of the first cluster of three 82.7 GHz gyrotrons each of 0.5 MW, 2.0 s pulse length second harmonic X-mode (X2). The overall ECRH project is to have 3.0 MW of X2 (six gyrotrons at 82.7 GHz) and 1.5 MW (three gyrotrons at 118 GHz, capable of 210 s pulse lengths but to be operated up to 2.0 s at CRPP) at the third harmonic X-mode (X3). During the past operational campaign a variety of experiments have been performed using the available ECH power of 1.5 MW. Some of these include: commissioning of the launching antenna, studies of confinement as a function of plasma shape and assisted L to H-mode transitions. Also studies with non-zero toroidal launch angles have been performed including scans of toroidal injection angle with co- and counter-ECCD, up-down asymmetry associated with an inherent off-axis ECCD component, and full inductive current replacement. This report will give a brief description of the X2 and X3 systems and relevant diagnostics on TCV in Section 1, followed by a description of the experimental results which have been obtained over the past experimental campaign. These results are divided into two groups: Section 2 will summarize the results of the ECH experiments (zero toroidal launch angle) and Section 3 will describe the ECCD experiments.

1. SYSTEM OVERVIEW

The TCV tokamak has a vacuum vessel elongation $\kappa=b/a=3$, major radius $R=0.89$ m, minor radius $a=0.25$ m and a maximum vacuum magnetic field of $B_\phi=1.43$ T at the chamber axis. The machine is equipped with 16 independently controlled poloidal field coils allowing the production of plas-

mas with various elongations ($\kappa_a=1-2.58$ achieved), with negative and positive triangularities ($\delta_a=-0.7$ to 1), and at various positions in the vessel. All of these parameters can be changed independently during a shot. This provides a very flexible tool for the study of shaped plasmas.

In view of the wide range of plasma configurations on TCV, a highly flexible auxiliary heating system is required. An ECH system was chosen in light of this requirement owing to its localized heating and steerable beam capabilities. The TCV-ECH system [1] will consist of nine gyrotrons of 0.5 MW each. Six gyrotrons will operate at the second harmonic frequency (X2) of 82.7 GHz and three at the third harmonic frequency (X3) of 118 GHz. The gyrotrons are grouped in clusters of three, with each cluster operating on a single Regulated High Voltage Power Supply (RHVPS) [2].

X2 system

Each X2 gyrotron [3] is connected to a matching optics unit (MOU) for optimum coupling into the evacuated corrugated waveguide and absorption of stray radiation from the gyrotron. Incorporated in the MOU is a Universal Polarizer providing the full range of all possible polarizations. Connected to each MOU is an evacuated transmission line (approximately 30 m of 63.5 mm corrugated HE_{11} waveguide) which includes two DC breaks, in-line bellows, power monitor miter bend, vacuum compatible switch and calorimetric load, in-line pumping-tee and a launching antenna (launcher).

The X2 launcher (shown in Figure 1) is designed to direct the microwave beam at any radial location within the wide range of plasma shapes achievable on the TCV tokamak as shown in Figure 2. For each cluster of X2 gyrotrons there is one launcher mounted in an

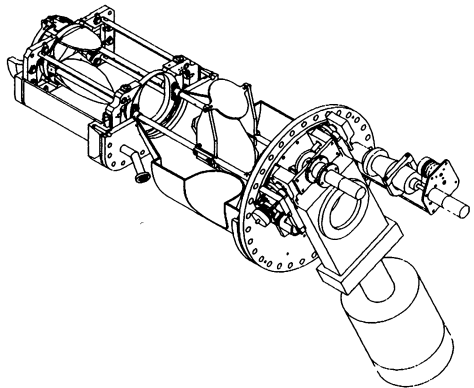


Figure 1. Drawing of the X2 Launcher with all-metal vacuum gate valve and external motors. The launcher has two degrees of freedom, the beam can be steered within a chosen plane during a shot, and the launcher can be rotated about the port axis between shots to change that plane.

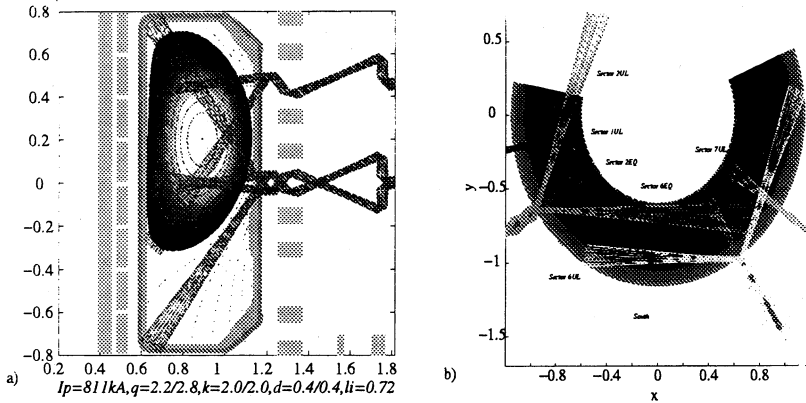


Figure 2. The accessibility of the X2 launchers in the (a) poloidal and (b) toroidal viewing planes. The 2 launchers of the first cluster gyrotrons are located in upper lateral ports and one in an equatorial port.

equatorial port (L1) and two launchers (L2 and L3) mounted in upper lateral ports. Each launcher has 2 degrees of freedom, one of which provides steering of the beam in a fixed plane during a shot (realized by rotating the last mirror), while the other allows that plane to be rotated about the axis of the launcher port between shots. Each gyrotron can be independently switched to the torus or to a calorimetric load from shot to shot, such that power can be delivered from any possible combination of three launchers for a given shot.

At the present time there is one fully operational X2 cluster on the TCV tokamak. This cluster has had several full power, full pulse length pulses on TCV during the past operational campaign period. All the gyrotrons of the second cluster have passed the acceptance tests and are ready for operation on the tokamak. The associated MOUs and transmission lines are installed and have been vacuum tested. The second cluster launchers are in the process of being installed on the tokamak for operation at the end of 1999.

X3 system

Three 0.5 MW, 2 s gyrotrons [4] at the third harmonic (X3) frequency of 118 GHz are planned to be operational on TCV for the end of the year 2000. The X3 gyrotrons will only be operating at pulse lengths of 2.0 s even though the full capabilities of the tubes are 210 s for use on the Tore

Supra tokamak. The first tube has been delivered to CRPP and has successfully passed the on-site acceptance tests, including over 160 pulses of 0.5 MW, 2.0 s pulses (reliability > 99%) have been obtained with the EC power diverted to a dummy load.

The X3 launcher is mounted on a top port to launch the beam in a direction nearly tangential to the resonant surface thereby maximizing the absorption by increasing the path length through the plasma. The three beams are incident on a single mirror which can be radially displaced ($\pm a/3$) between shots to inject the beam from either the low (LFS) or high field side (HFS) of the resonance, see Figure 3. The mirror can also be rotated ($\pm 5^\circ$) during a shot to adjust the beam along the resonance surface, from any radial location. A prototype of the launcher has been completed and is undergoing mechanical testing. A fully operational launcher is planned to be installed on TCV during the year 2000, thus bringing the full auxiliary heating power available on TCV to 4.5 MW before the end of the year 2000.

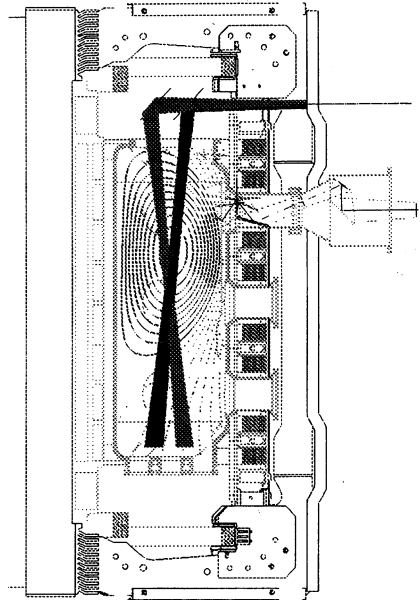


Figure 3. The X3 Launcher will inject three beams vertically into the plasma. The launcher mirror can be rotated during a shot to change the injected poloidal angle and can be displaced radially between shots.

TCV diagnostics

A brief description of some of the more relevant diagnostics used during ECH-ECCD experiments is given below. A more detailed description of these diagnostics can be found in reference [5].

The soft X-ray diagnostic provides the most direct response of the central MHD activity and is comprised of three groups of instruments:

- 1) four vertically viewing, fast diodes with a sampling rate of 250 kHz located in four toroidal positions provide high time resolution of MHD activity.

2) 180 diodes distributed in nine cameras in one poloidal cross section with sampling rate of up to 80 kHz and spatial resolution of 3.5 cm after tomographic reconstruction.

3) Four additional vertical viewing diodes for measuring the soft X-ray temperature using the two foil method.

The Thomson scattering system on TCV uses three Nd:YAG lasers (each at 20 Hz, combined in a fan and focused to a single point in the plasma) aligned in the vertical direction at a single value of the major radius. Thirty-five viewing chords are distributed on three horizontal ports providing a measure of n_e and T_e with a spatial resolution of about 4 cm along the laser beam.

A multichannel hard X-ray diagnostic system which characterizes the spectral and spatial distribution of fast electron bremsstrahlung emission has been operational on TCV [6] during part of the operating period. This diagnostic was developed for the Tore Supra tokamak [7] and was on loan to the CRPP from CEA-Cadarache, France. The system provides a spatial resolution of 2.0 cm (on the midplane) from 14 viewing chords and an energy resolution of 5-7 keV, in the range from 10-150 keV.

The LIUQE equilibrium code [8] determines the plasma position and shape from 38 magnetic probes and the plasma pressure profiles from the Thomson scattering system. These results along with the Thomson density and temperature profiles are used by the TORAY [9,10] ray tracing code to compute the beam propagation and absorption location.

2. ECRH EXPERIMENTS

X2 Launcher accuracy

A commissioning of each gyrotron/MOU/launcher is performed to ensure that a similar plasma response is observed for each system. The commissioning involves two sets of tests: an alignment test at atmospheric pressure and a plasma response test to ensure optimum coupling to the plasma and the integrity of the launcher alignment under vacuum conditions.

The alignment at atmosphere of each launcher is performed after the installation of each launcher on the torus. The launcher alignment is checked by firing the beam onto a target of liquid crystal paper attached to the vessel's central column. The target is then displaced to two other vertical locations to check the calibration of the movement of the last mirror.

The plasma response test involves the sweeping of each beam across a target plasma ($\bar{n}_e=1.4-1.9 \times 10^{19} \text{ m}^{-3}$, $I_p=173 \text{ kA}$, $\kappa=1.3$, $\delta=0.3$) as shown

in Figure 4. From previous experiments the response on the soft X-ray signal (central chord) was observed to increase/decrease as the beam deposition passed inside/outside the $q=1$ surface. The soft X-ray signals for the three launchers are shown in Figure 5. The signals for the two upper lateral launchers, L2 and L3, are identical, while the equatorial launcher, L1, is shifted in time due to differences in refraction in launching a beam from an upper lateral or an equatorial port. Large sawteeth are observed over a relatively small region during the sweep when heating near the $q=1$ surface closest to the launcher despite relatively large beam width (≈ 30 mm) [11]. Comparing the location of these large sawteeth for the two sweeps of L2 and L3 yields a relative measure of alignment of the two launchers which is found to be within $\pm 0.2^\circ$ (± 3 mm). L1 can be checked against the results of either L2 or L3 using TORAY. The angle at which these sawteeth occur is compared with the TORAY calculated angle for $q=1$ deposition. The precision for calculating

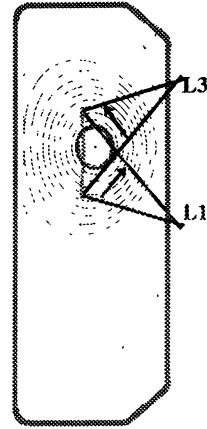


Figure 4. Swept region of the beam during the commissioning shots. Each launcher is swept from below the $q=1$ surface to above it.

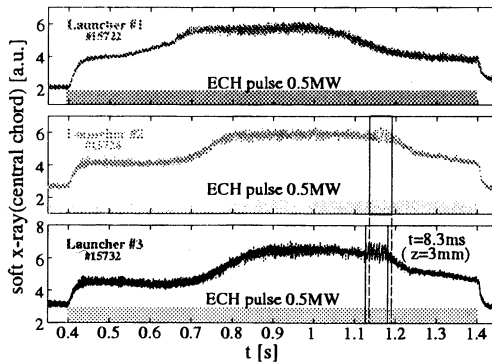


Figure 5. The soft X-ray response to each launcher sweep as shown from a central chord. The signals of Launchers 2 and 3 are shifted relative to each other by 8.3 ms in time, which corresponds to a misalignment of $\Delta Z=2.9$ mm in vertical heating location. Launcher 1 is shifted in time owing to a difference in beam refraction between the equatorial and upper lateral ports. The large sawteeth occur on the $q=1$ side nearest the swept launcher (largest power density).

the $q=1$ surface is within ± 20 mm. The TORAY calculated angle and the 'straight' ray angle both fall within the range of the calculated $q=1$ surface (i.e. refraction is insignificant for the near side $q=1$).

For both launchers 2 and 3 the realized aiming precision is $\pm 0.2^\circ$ which is the initial designed restrictions placed on the launcher. Launcher 1 can only be tested relative to the errors associated with the calculations of the $q=1$ surface from LIUQE and it gives $\pm 1.3^\circ$ (± 20 mm). Since the same pre-alignment procedure was performed for all launchers, we have the confidence that launcher 1 has the same order of precision as launcher 2 and 3.

ECH coupling

Sweeps of the ECH deposition identical to those described above, were performed with non optimal coupling of the beam by changing the X-O mode fraction via the Universal Polarizer located in the MOU. For the X-mode launch the calculated absorbed power is 100% and the coupling changes by less than 5% during the sweep of the beam [11]. The effect of the coupling scan is best seen on the soft X-ray signal as shown in Figure 6. The soft X-ray signal viewed from a central chord increases when the deposition is inside the $q=1$ surface for X-mode launch. This rise is barely apparent for the O-mode injection.

As the polarization was varied to increase the X-mode component at the plasma edge, the total stored plasma energy measured by Thomson scattering increased, (see Figure 7). Comparing the plasma's total energy during sweeps at various coupling efficiencies confirms that the optimum heating is obtained within the $q=1$ surface [5]. For X-mode launch the electron confinement time increases abruptly when deposition is within this region implying the presence of an energy transport barrier near this surface. When absorption occurs within this region the stored electron energy

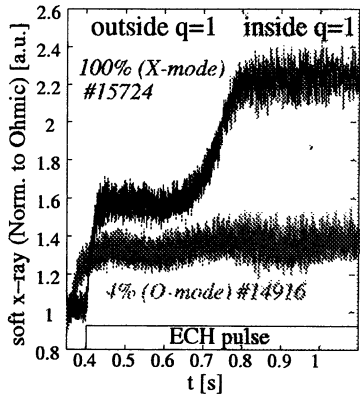


Figure 6. Difference in a central chord of the soft X-ray signal for two sweeps with X-mode and O-mode coupling respectively. When deposition is inside the $q=1$ surface the soft X-ray signal increases with X-mode percentage.

increases by 20% over deposition outside the region. Approximately the same ratio of stored energy is measured between X-mode and O-mode polarization injection cases during central deposition (see Figure 7).

In the poorest coupling case with essentially 100% O-mode coupling little difference is observed when heating inside or outside this region. This implies low first pass absorption, with the majority of the beam eventually being either absorbed in the carbon tiles of the tokamak, absorbed in the plasma after multiple reflections, or lost through vacuum windows. The total power absorbed in the plasma is represented by the following:

$$\eta_{eff} = \eta_{fp} + (1 - \eta_{fp})\eta_{mr}, \quad (1)$$

where η_{eff} is the percentage of total absorbed power in the plasma, η_{fp} is the percentage of power absorbed on the first pass, and η_{mr} is the percentage of power absorbed after multiple reflections in the torus chamber. The percentage of first pass absorption, η_{fp} , is taken from TORAY calculations. To estimate the percentage of power absorbed after multiple reflections, η_{mr} , the tokamak is modeled as a black box with holes. Radiation incident on a ‘hole’ escapes the black box. In this case the ‘holes’ are vacuum windows and the resonant surface. The amount of power ‘escaping’ (or absorbing) through the resonant surface can be represented by a sum of an infinite series:

$$\eta_{mr} = \frac{R_{wall} \cdot \frac{a_{res}}{A_{total}}}{1 - R_{wall} \cdot \left(1 - \frac{a_{res} + a_{windows}}{A_{total}}\right)}, \quad (2)$$

where a_{res} is the area of the absorbing resonant surface (both LFS and HFS), R_{wall} is the average reflection coefficient of the vessel wall, $a_{windows}$ is the sum of the surfaces of the ‘holes’ or vacuum windows on the torus,

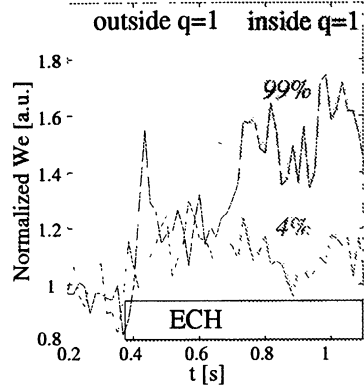


Figure 7. Total stored energy of the plasma for sweeps at various X-mode coupling percentages ranging from 0 to 100%.

and A_{total} is the sum of the areas of a_{res} , a_{windows} and the inside surface of the tokamak. In the case of randomly scattered radiation the beam is assumed to be 50% in X-mode and 50% in O-mode. Full absorption is assumed for X-mode incidence while only 12% for O-mode incidence, based on TORAY calculations for these plasmas. The non-full absorption in O-mode can be compensated by shrinking the size of the absorption surface area based on the average absorption of the two modes, thus the effective area is $0.56 \cdot a_{\text{res}}$, an average between the 100% absorption of X-mode and 12% in the case of O-mode.

Applying the above model to the TCV vacuum vessel, assuming a 95% wall reflectance, the absorbed power in the plasma is computed to be 65% of the injected ECH power. Assuming 20% of the absorbed power is inside the $q=1$ surface (based on ratio of the areas of the resonant surface inside the $q=1$ versus outside the $q=1$) from the results of the polarization scan, the total stored energy of the plasma should increase by 24% over the ohmic level. For O-mode injection (shot #14920) the average stored energy increased by $21 \pm 7\%$. This estimation of the absorbed power is useful for determining the power delivered to the plasma when first pass absorption is low because of coupling, strong refraction in the case of large injection angles, and when density cutoff is exceeded (in the later case, the region of the absorption surface inside the density cutoff region is excluded from the total a_{res}). This model should be valid when $a_{\text{res}} \ll A_{\text{total}}$.

Confinement studies

Studies of the energy confinement time in ECH discharges have been performed as a function of plasma shape in TCV [12]; to extend previous studies of confinement in Ohmic plasmas [13,14]. Steps of ECH power were used from 0 to 1.5 MW which typically represented a power ratio of $P_{\text{ECH}}/P_{\text{OH}}$ between 0 and 10 during ECH, with the power deposited within the $q=1$ surface. The shape scans were performed at two different values of the engineering safety factor $q_{\text{eng}}=1.7$ and 3 ($q_{\text{eng}} = 5abB/RI_p$, where $2.3 < q_a < 6$; $0.2 < I_p < 0.7$ MA). A fixed q_{eng} implies a nearly constant normalized radius of the $q = 1$ surface while changing the plasma shape based on analysis of the ohmic database [15]. The stored electron energy is measured during stationary periods from repetitive Thomson scattering measurements (60 Hz), typically averaged over 10 time-slices.

A general power scaling law has been obtained over the full data set

describing the dependence of the electron energy confinement time τ_{Ee} (ms) on the average line density \bar{n}_e (10^{-19} m^{-3}), total power P (MW), edge elongation κ , edge triangularity δ , and plasma current I_p (kA) using a multi-variable regression fit. The dependences on κ and I_p cannot be separately determined, owing to the strong correlation between these quantities in the present data base. The power law must therefore contain a free parameter, and takes the following form [12]:

$$\tau_{Ee} [\text{ms}] = 2n_e^{\alpha_n} P^{\alpha_p} (6I_p)^{\alpha_I} \kappa^{\alpha_\kappa} (1 + \delta)^{\alpha_\delta} , \quad (3)$$

with $\alpha_n=0.46\pm 0.2$, $\alpha_p=-0.7\pm 0.1$, $\alpha_\delta=-0.35\pm 0.3$, $\alpha_\kappa=1.4(1-\alpha_I)\pm 0.4$, where α_I remains undetermined. The uncertainties have been estimated assuming a 25% error on τ_{Ee} . Good fits are obtained with α_I in the range $0 \leq \alpha_I \leq 0.7$, an example at $\alpha_I=0.5$ is shown in Figure 8.

In spite of the unresolved confinement dependence on current and elongation, the trend toward increasing elongation for improved confinement is present. The main motivation for creating elongated discharges is indeed to increase the plasma current with the aim of increasing the energy confinement and pressure limits.

Further experiments are needed to separate the contributions of plasma current and elongation. Higher ECH power levels will be possible when the second cluster becomes available so that the ratio of additional power to the total power can be large even at high plasma current.

The general scaling obtained above can be compared with the recent scaling laws found using a multi-tokamak database, such as the ITER-98-L mode scaling, where $\alpha_n=0.40$, $\alpha_p=-0.73$, $\alpha_I=0.96$, $\alpha_\kappa=0.64$ [16], as shown in Figure 9. Within the uncertainties, the exponents, α_n and α_p found in TCV are in agreement with those of the ITER-98-L scaling; however, α_κ and α_I are not both compatible with the ITER-98-L scaling.

An improvement in confinement with negative triangularities is responsible for the

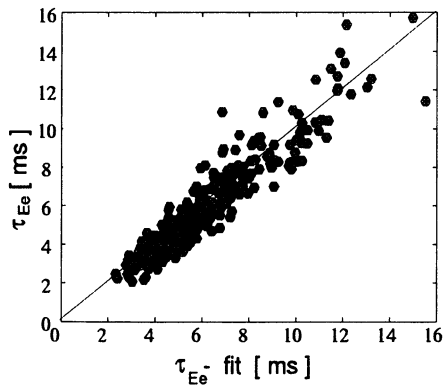


Figure 8. Empirical scaling law for TCV ECRH data set, in the representative case $\alpha_I=0.5$ [12].

spread in the comparison with the ITER-98-L modes scaling (ITER-98-L does not include a triangularity dependence). The improvement, however, becomes less pronounced at higher powers (lower τ_{Ee} on Figure 9).

L-H mode transition

Ohmic H-mode plasmas are regularly obtained in TCV (limited or diverted, single or double null, $3 < \bar{n}_e < 9 \times 10^{19} \text{ m}^{-3}$, $1.1 \leq B \leq 1.5 \text{ T}$, $1.05 \leq \kappa \leq 2.05$, $-0.2 \leq \delta \leq 0.7$, $2.05 \leq q_{95} \leq 4$). Since L-H transitions are rarely observed in low density plasmas ($\bar{n}_e \leq 4 \times 10^{19} \text{ m}^{-3}$), the goal of this experiment was to find out if H-mode could be accessible with a low density ECH target plasma.

Central deposition with 1.5 MW tends to result in a disruption. This was avoided by spreading out the deposition region along the plasma minor radius (vertically).

The low density limit of H-mode accessibility was lowered with the addition of ECH power [17]. An example of such a discharge is shown in Figure 10. The transitions were obtained in 3 successive ramps of the ECH

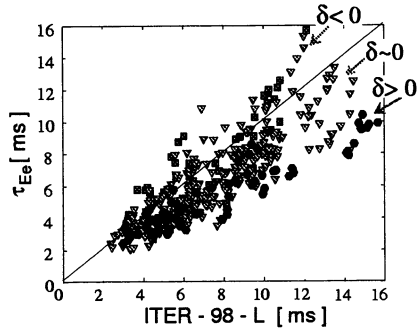


Figure 9. Fit to ITER-98-L mode scaling law. Since triangularity does not appear in ITER-98-L, it is explicitly indicated by the symbols: negative δ appear favourable (red squares: $\delta < 0$, green triangles: $0 < \delta < 0.3$, blue hexagons: $\delta > 0.3$) [12].

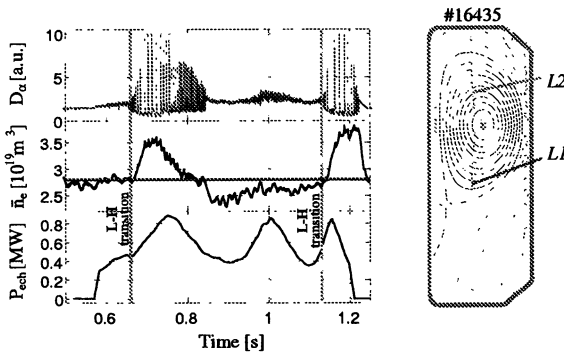


Figure 10. Time evolution of a discharge with L-H transition induced by ECH. The Two L-H transitions which occur during this particular discharge are identified by the vertical lines. The plasma poloidal cross section at the time of the first L-H transition is shown at right [17].

power. The occurrence of the L-H transition varied with ECH power depending on the plasma parameters. The absorbed ECH power was calculated from the sum of first pass absorption from TORAY and multi-pass absorption from the modified black-box model described previously.

A clear demonstration of the improved range of H-mode accessibility is shown in [17].

Figure 11: whereas, previous Ω -H transitions were limited to line average densities above $3.5 \times 10^{19} \text{ m}^{-3}$, the density threshold is lowered by 28% to $2.5 \times 10^{19} \text{ m}^{-3}$ with the addition of the ECH power. Within this extended regime the power required to initiate a transition increases with decreasing density in contradiction of ITER power scaling laws [16]. This inverse dependence was also observed on COMPASS in ECH assisted L-H transition [18]. These independent observations tend to confirm the discrepancy between heating schemes acting on ions and those acting on electrons in terms of H mode accessibility.

The limited data base of L-H transitions showed no noticeable change of $P_{\text{Threshold}}$ with the plasma shaping.

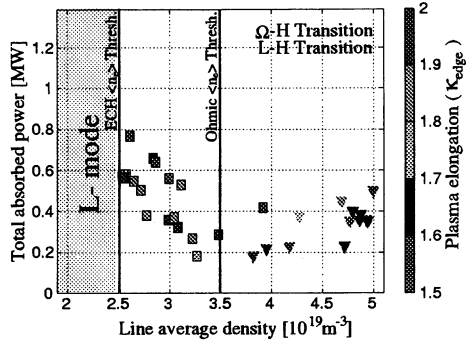


Figure 11. L-H transition threshold power in ohmic (triangles) and ECH (squares) plasmas

3. ECCD EXPERIMENTS

Toroidal Launch Angle Scan

A scan of the launcher's toroidal injection angle has been performed over a range from -35° (counter-ECCD) to $+35^\circ$ (co-ECCD) with ECH power of 1.5 MW ($\bar{n}_e = 1.4 - 1.9 \times 10^{19} \text{ m}^{-3}$, $I_p = 173 \text{ kA}$, $\kappa = 1.3$, $\delta = 0.3$). At each toroidal angle the plasma was displaced in vertical position during the shot so that there were two periods of on-axis deposition and one intermediate period of off-axis. Typically, the on-axis heating produced centrally peaked T_e profiles throughout the scan while off-axis heating yielded broader profiles with lower central temperatures as shown in Figure 12 [19]. The highest central electron temperatures of $\sim 10 \text{ keV}$ were achieved with counter-ECCD at -14° .

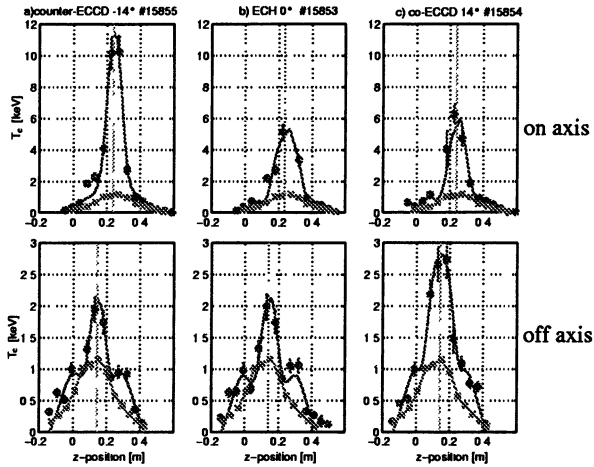


Figure 12. Electron temperature profiles from Thomson scattering for on- and off-axis ECCD and ECH discharges. Highest observed temperatures (10 keV) have occurred at -14° counter-ECCD. On-axis heating yields centrally peaked profiles while off-axis heating results in broader, lower temperature profiles [19].

The product of the loop voltage and the volume average of the $Te^{3/2}$ dependency on the toroidal injection angle is plotted in Figure 13 for on-axis deposition. During co-ECCD V_s continues to decrease with increasing injection angle. This differs from initial calculations which predicted optimization of the co-ECCD between 25 and 30° using non-linear Fokker-Planck calculations [20]. At large toroidal angles the beam undergoes

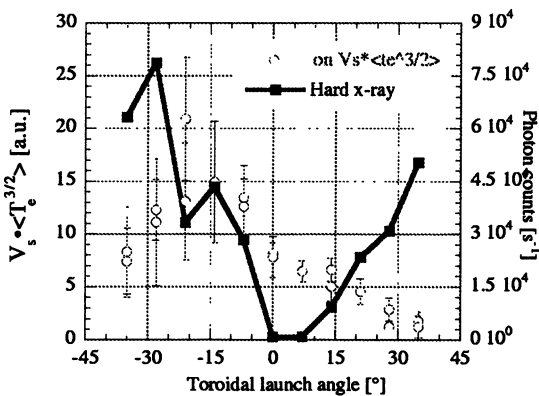


Figure 13. Plasma loop voltage for on-axis deposition and photon counts (between 40-50 keV, on axis deposition) [6] dependence on the toroidal launch angle.

strong refraction and first pass absorption becomes less than 100%, TORAY results calculate $\approx 70\%$ for the case of $\phi=35^\circ$ at these densities. Since the electron temperature is lower off axis, the driven current can be expected to decrease as the deposition moves off-axis. This was seen in the difference of the loop voltage between the on- and off-axis heating phases of the discharge. The results of this scan imply that the optimum current drive occurs at larger than predicted toroidal angles, $\phi \geq 35^\circ$.

The spectral distribution of the fast-electron bremsstrahlung emission was measured during the scan of the toroidal angle by the multichannel hard X-ray diagnostic system on loan from CEA, France [7]. The photon counts from the bremsstrahlung emission increased at all energy levels as the toroidal angle increased in both the co- and counter- directions, see Figure 13. The results from the spectral distribution during the launch at $\phi=0^\circ$ were Maxwellian and agreed with the electron temperatures measured by Thomson scattering. As a non-zero toroidal angle was introduced, a non-Maxwellian suprathermal tail developed [6]. This is consistent with theoretical expectations for ECH and ECCD discharges. During ECH, the lowest energy electrons are in resonance with the full power of the beam: attenuation of the beam leads to less power being available to heat the higher energy electrons. During ECCD, conversely, the higher energy electrons are in resonance first. With a non-zero toroidal angle the beam preferentially heats electrons on the low field side of the cold resonance which have a finite parallel velocity, due to the Doppler-shift. This results in the generation of a suprathermal tail in the electron velocity distribution.

Up-Down Asymmetry

An up-down asymmetry has been observed during launcher sweeps similar to those shown in Figure 4 [21]. This asymmetry is most pronounced in the behavior of the sawtooth shape and period when the deposition is near the $q=1$ surface. Even though the sweep of the beam was kept in a poloidal plane (no toroidal injection angle), the asymmetry has been shown to be a result of a small current drive component arising from the non-zero projection of the wave vector \mathbf{k} on the magnetic field for off-axis heating - thereby producing Doppler-shifted absorption. This is portrayed in Figure 14. The direction (co/counter) and magnitude of ECCD will depend on the absorption location, launch direction (HFS versus LFS) and toroidal field direction but not on the plasma current direction. The

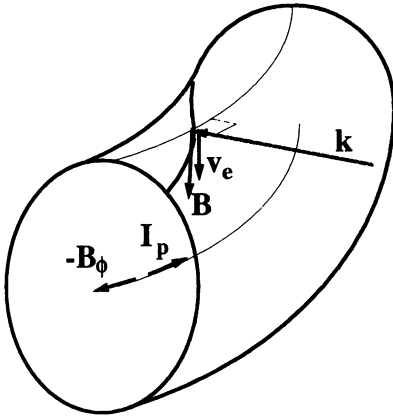


Figure 14. Sketch of \mathbf{k} and \mathbf{B} vectors with off-axis deposition. There is an inherent ECCD component due to a non-zero projection of \mathbf{k} onto \mathbf{B} arising from the poloidal magnetic field (\mathbf{v}_e is the electron velocity vector).

poloidal field and the plasma current producing it have the same sign: therefore simply reversing the plasma current will not change the relative direction of the ECCD (e.g. co-ECCD will remain co-ECCD). Because it is the poloidal field that creates the asymmetry, the effects are seen only during off-axis absorption. This effect is confirmed by TORAY calculations which show linear current drive efficiencies changing sign when heating below or above the plasma midplane. The ECCD direction can be reversed by reversing B_ϕ [11].

Initial ECCD experiments on TCV showed a change in the behavior of the sawteeth shape (co-produced large triangular sawteeth, counter-produced humpbacks) and period between co- and counter-ECCD which occurs even at low ECCD efficiencies at equivalent levels as calculated by TORAY for the off-axis ECH case described above.

Numerous effects of sweeping the deposition across the $q=1$ surface are seen; these include: a) density pump-out, b) rise in central temperature, c) increase in line-integrated X-ray emission (as viewed from central chords), d) the sawtooth period and amplitude increase at the transition from outside to inside, e) the width of the transition region is larger when passing from inside to outside (rather than outside to inside), f) the amplitude of the peak in sawtooth period increases with co-ECCD and decreases with counter-ECCD (produced by intentionally introducing small toroidal angles).

The $q=1$ transition region is of particular interest because it allows the confirmation that ECCD is responsible for the non-axisymmetric plasma response. Large roughly triangular sawteeth appear only when heating near the upper $q=1$ surface with the upper lateral launcher (L3) and not with the equatorial launcher (L1). Non-triangular, but nevertheless large, sawteeth occur when heating near the lower $q=1$ surface with L1 and not L3. When B_ϕ is reversed, these results are reversed as well, with L1 play-

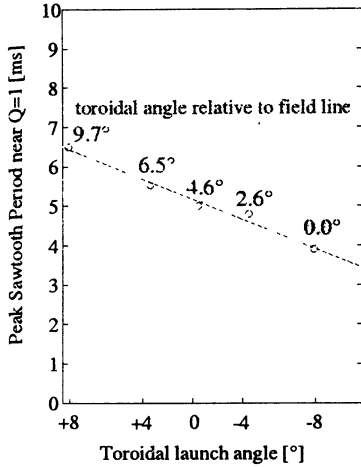


Figure 15. The sawtooth period about the $q=1$ surface with the launching plane rotated $\pm 8^\circ$ about the poloidal plane. The co-ECCD component has been eliminated on the $q=1$ surface with the introduction of a counter-ECCD toroidal angle [11].

shown in Figure 15. Positive angles decrease (with reversed B_ϕ) the ECCD component: $+4^\circ$ corresponds to pure ECH. Large triangular sawteeth only occur with a co-ECCD component and when the absorption occurs over a narrow extent in minor radius. Similarly, large triangular sawteeth can be created by over-compensating the inherent counter-ECCD offset leading to co-ECCD. The narrow range in which the large sawteeth occur allows the determination of the beam absorption region as was performed for the alignment tests mentioned previously. If the location of the large sawteeth can be proven to be a physical relevant location of interest, such as the $q=1$ surface, it could provide a useful tool for testing models describing the sawtooth instability. Tokamaks with ECH but not equipped to measure the q -profile could then find this location by sweeping the heating location and constrain equilibrium reconstruction codes accordingly.

Full current replacement with ECCD

The principal aim of this experiment was to obtain a fully non-inductive stationary scenario using three 0.5 MW gyrotrons [22]. From previous

ing the role of L3 and vice versa. This leads to the conclusion that the sawtooth shape strongly depends on the driven current direction [11] when the deposition is on or near the $q=1$.

In another experiment, the beam deposition on the transition region was kept constant while the beam power was increased, thus varying the power density. Resulting sawteeth do not change shape but become larger with power density. The period increases linearly with power. The large sawteeth can be eliminated or enhanced with the intentional addition of a toroidal angle of the launched beam. The resulting peaks in sawtooth period as well as the sawtooth shapes are

experiments of scanning the toroidal launch angle the optimum toroidal angle was found to be $\geq 35^\circ$. For this study a toroidal injection angle of 35° was chosen. The deposition profile to maximize the sustainable driven plasma current.

To obtain the maximum driven current the three launchers were aimed at near central deposition where highest efficiency occurs owing to highest temperatures. It was possible to obtain 153 kA of fully non-inductive current for 15 ms ($n_{e0}=2.0 \cdot 10^{19} \text{ m}^{-3}$, $T_{e0}=4.5 \text{ keV}$), before the discharge disrupted. The width of the power deposition was small (10-20% of minor radius) resulting in peaked current and temperature profiles. MHD modes became unstable and caused the disruption. Neoclassical tearing modes were also destabilized and degraded the performance of the discharge. To avoid these modes the power deposition of the three gyrotrons was then spread out over the minor radius such that the overall power deposition profile resembled the current density profile, as shown in Figure 16, with $\rho=0., 0.3, 0.55$. This results in a lower central temperature ($T_{e0}=3.5 \text{ keV}$) and smaller driven current ($I_p=123 \text{ kA}$) but achieved a stable fully non-inductive current for 1.9 s ($n_{e0}=1.5 \cdot 10^{19} \text{ m}^{-3}$), see Figure 17. The current in the ohmic transformer was held constant which is the most sensitive measurement of full current replacement. The loop voltage quickly decreased to zero at the turn on of ECCD, while the equilibrium profile (κ and i_j) evolved over 0.5 s. Once the profile reached equilibrium the discharge was maintained for 1.4 s, approximately three times the period for achieving equilibrium.

The shots were repeated with $I_p=112 \text{ kA}$ and 127 kA to demonstrate the exact control of the driven current. In the first scenario the transformer was charging up during the discharge implying the current was driven in excess while in the second case the transformer discharged implying insufficient current replacement. The current drive efficiency is consistent for the three shots (taking into account the change in density between shots) at $I_p=123 \text{ kA}$ and $I_p-I_{CD}=11 \text{ kA}$ for $|V_s|=0.02 \text{ V}$. TORAY calculations are in agreement with a

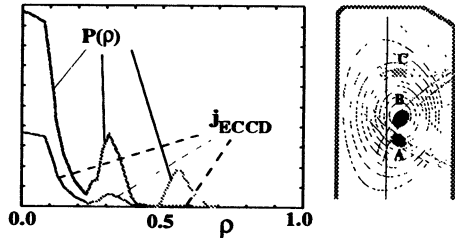


Figure 16. The power and current density profiles from Toray for the fully non-inductive current replaced discharge. The deposition of the beam projected in a poloidal plane is depicted at right [22].

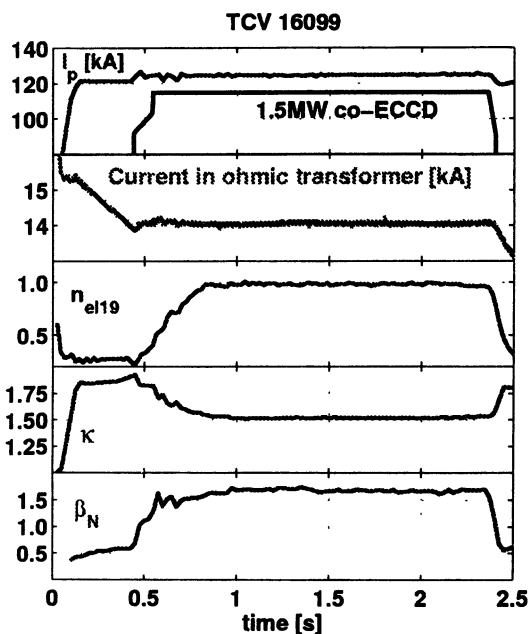


Figure 17. Steady-state fully non-inductive discharge for 1.9 s using 1.5 MW of co-ECCD with the power distribution depicted in Figure 16. Note that the equilibrium profiles require 0.5 s to settle [22].

beam 'C' (Figure 16) is calculated from TORAY as 2.5 kA, near $\rho=0.55$. This beam is important for broadening the pressure and, possibly, the current profile: this is tested by keeping the deposition location the same but removing the toroidal injection angle (ECH rather than co-ECCD). The feedback plasma current is then decreased until $V_s=0$. The difference in plasma current is 7-9 kA which confirms the results obtained on DIII-D [24] that more current can be driven off-axis than predicted.

SUMMARY

The first 1.5 MW of the ECH system on TCV has been operated with up to 2.0 s pulse lengths during the latest operational campaign. The second 1.5 MW of ECH power (X2) is planned to be operational by the end of the current year bringing the total auxiliary power available in TCV to 3.0 MW. The X3 system implementation is progressing with the delivery and successful acceptance of the first gyrotron. A preliminary design of

driven current of 120 kA ($\eta_{\text{ECCD}}=0.08$ A/W).

The peaked profile of these discharges leads to a non-negligible bootstrap current of 25 kA as calculated in reference [23]. Taking the bootstrap current into account TORAY overestimates the driven current by about 20%, which is within the error bars of the injected power and the density and temperature profiles used in the calculation.

As previously stated, the amount of current driven decreases as the beam is moved off axis. The amount of driven current from the

the X3 launcher has been made and is under test. First planned operation with the X3 system should occur by the end of the following year.

A variety of experimental programs have been performed during this period. During the ECH related studies: the launching antenna system alignment on TCv has been measured to be accurate to within ± 3 mm during a poloidal sweep; the dependence of the confinement has been shown to favor increased elongation and negative triangularities; and successful L-H transitions have occurred below the previous ohmic H-mode density threshold ($3.5 \times 10^{19} \text{ m}^{-3}$), down to a density of $2.5 \times 10^{19} \text{ m}^{-3}$.

Results of the ECCD experiments include: demonstration that the observed up-down asymmetry is due to an inherent ECCD component when heating off-axis in a nominally ECH scenario; highest TCv central electron temperatures of ≈ 10 keV have been achieved with -14° counter-ECCD; the presence of a non-Maxwellian suprathermal electron tail during ECCD has been measured with the hard X-ray diagnostic system, consistent with preferentially heating electrons at a Doppler-shifted resonance on the LFS; for maximum driven current the optimum toroidal injection angle is $\geq 35^\circ$, higher than initial predicted range of $25\text{-}30^\circ$; and full non-inductive current replacement of 123 kA for 1.9 s has been achieved. The discharge was sustained for over $400 \cdot \tau_{Ee}$ and four current diffusion times.

ACKNOWLEDGEMENTS:

This work was partially supported by Swiss National Science Foundation.

REFERENCES

- [1] T.P. Goodman et al., Proc. 19th SOFT, Lisbon vol. 1 (1996) 565.
- [2] G. Besson et al., SOFT 1994, vol. 1, p.517-520.
- [3] Bogdanov et al., Strong Microwaves in Plasmas 1993, vol. 2, p.830-835.
- [4] C. Tran et al., Proc. of 23rd Int. Conf. on Infrared and Millimeter Waves, Colchester, UK, (1998) edited by T.J. Parker and S.R.P. Smith, ISBN 0 9533839 0 3.
- [5] Z.A. Pietrzyk et al., Nuclear Fusion **39** (1999) 587.
- [6] S. Coda et al., Proc. of 26th EPS Conf. on Contr. Fusion and Plasma Physics, Maastricht, 1999.
- [7] Y. Peysson and R. Arslanbekov, Nucl. Instr. and Methods, **380** (1996) 423.
- [8] F. Hofmann and G. Tonetti, Nucl. Fusion **28** (1988) 1871.
- [9] K. Matsuda, IEEE Trans. Plasma Sci. **17** (1989) 6.
- [10] R.C. Meyer et al., Nucl. Fusion **29** (1989) 2155.
- [11] T.P. Goodman et al., Proc. of 26th EPS Conf. on Contr. Fusion and Plasma Physics, Maastricht, 1999.
- [12] A. Pochelon et al., 17th IAEA Fusion Energy Conf. 1999, CN-69/EX8/3, to appear in

Nuclear Fusion, Yokohama Special Issue (1999).

[13] J-M. Moret et al., Phys. Rev. Lett. **79** (1997) 2057.

[14] H. Weisen et al., Nucl. Fusion **37** (1997) 1741.

[15] H. Weisen et al., Plasma Phys. Control. Fusion **40** (1998) 1803.

[16] K. Thomsen et al., 17th IAEA Fusion Energy Conf. 1998, CN-69/ITER/3-ITERP1/97.

[17] Y. Martin et al., Proc. of 26th EPS Conf. on Contr. Fusion and Plasma Physics, Maas-tricht, 1999.

[18] A.W. Morris, IAEA 1998, CN-69/EXP2/04.

[19] R. Behn et al., Proc. of 26th EPS Conf. on Contr. Fusion and Plasma Physics, Maas-tricht, 1999.

[20] A. Pochelon et al., Bull. Am. Phys. Soc. **41** (1996) 1514.

[21] T.P. Goodman et al., Proc. of Joint ICPP 1998 and 25th EPS Conf. on Contr. Fusion and Plasma Physics, Praha 1998, ECA **22C** (1998) 1324.

[22] O. Sauter et al., Proc. of 26th EPS Conf. on Contr. Fusion and Plasma Physics, Maas-tricht, 1999.

[23] O. Sauter et al., to appear in Phys. Plasmas **6**(7) (1999) 2834-2839.

[24] T.C. Luce et al., General Atomics Report (1999) GA-A23018.

ECRH EXPERIMENTS IN ASDEX Upgrade

*F. Ryter, F. Leuterer, R. Wolf, O. Gruber, S. Günter,
H.-U. Fahrbach, H. Meister, M. Münich, G. Pereverzev,
J. Stober, J. Schweinzer, W. Suttrop, ASDEX Upgrade Team
and ECRH-Group from IPF**

Max-Planck-Institut für Plasmaphysik, EURATOM Association,
D-85740 Garching

* Institut für Plasmaforschung, Universität Stuttgart, D-70569 Stuttgart

This paper presents transport investigations with ECRH power modulation and results with ECCD in internal transport barrier where both T_i and T_e are above 10 keV.

An ECRH system (4×0.5 MW / 2s, at 140 GHz, 2^{nd} harmonic X-mode) was built at ASDEX Upgrade ($R = 1.65$ m, $a = 0.5$ m, $\kappa = 1.7$). The power is injected into the tokamak with 4 separate narrow-focused Gaussian beams, permitting localised deposition ($\Delta r \leq 5$ cm). A mirror system allows deflection in the poloidal and toroidal direction for pure heating (ECRH) and current drive (co or ctr ECCD). So far, three ECRH lines were in operation, providing a maximum of 1.25 MW deposited in the plasma. Experiments with ECRH power modulation to study electron transport and ECRH or ECCD in NBI-heated discharges with internal transport barrier are presented.

Transport investigations with power modulation

Complementary to power balance analysis, ECRH modulation is useful to investigate energy transport physics, because the diffusivities deduced from power balance (χ^{PB}) and from modulation (χ^{HP}) are of different nature [1].

The results are based on ECRH on/off power modulation experiments in Ohmic or NBI heated plasmas ($P_{NBI} \leq 5$ MW) at densities around $4 \cdot 10^{19} m^{-3}$. The working gas was either hydrogen or deuterium.

Amplitude and phase of the T_e modulation (from Fourier transform) allow to determine directly the electron heat diffusivity for heat pulses (χ_e^{HP}) using a slab model approximation with corrections for geometry and density profile effects [2]. This provides a quick analysis of

the heat pulse propagation, with acceptable accuracy. In addition we used the ASTRA transport code [3] for power balance analyses and for time-dependent modelling including ECRH modulation. Amplitude and phase of the modelled T_e are compared with the experimental ones. This yields a precise comparison with data, confirms χ_e^{HP} from Fourier analysis and allows to test physics models. As example, the amplitude and phase of T_e in an L-mode shot with 3 MW of total heating power, are shown in Fig. 1.

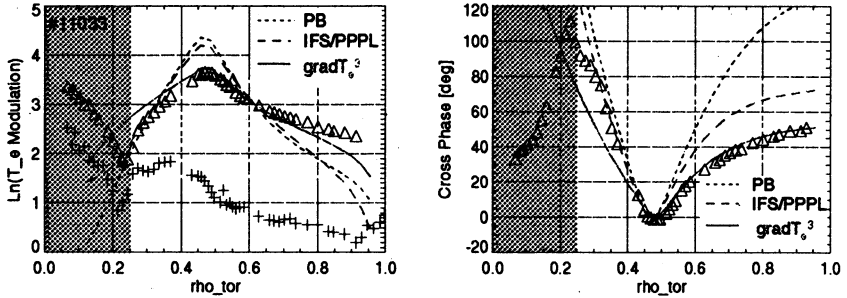


Figure 1: Amplitude (natural log) and phase of T_e versus ρ_{toroidal} , at modulation frequency (45 Hz). Triangles are data, lines models as described in the text. The ECRH deposition is at $\rho_{\text{toroidal}} \approx 0.47$. The crosses in the left figure indicate the noise, shadow where the sawtooth noise is strong. Otherwise the signal to noise ratio is good.

A striking feature of this figure is the strong asymmetry between the regions $\rho < \rho_{\text{ECRH}}$ and $\rho > \rho_{\text{ECRH}}$ of both amplitude and phase data. The analysis yields $\chi_e^{HP} \approx 1 \text{ m}^2/\text{s}$ in the region $\rho < \rho_{\text{ECRH}}$ and $\chi_e^{HP} \approx 7 \text{ m}^2/\text{s}$ for $0.6 < \rho < 0.8$. Whereas the former is close to χ^{PB} , the latter is about $4 \times \chi^{PB}$. Other shots indicate that the asymmetry and the values of χ_e^{HP} for $\rho > \rho_{\text{ECRH}}$ clearly increase with total heating power. The propagation of sawteeth exhibits properties similar to the ECRH cases $\rho > \rho_{\text{ECRH}}$, with higher values of χ_e^{HP} .

To interpret these results we made simulations with different models, indicated with the lines in Fig. 1. The reference simulation is made using χ^{PB} . The agreement with the data is poor. As physics-based model we used the IFS/PPPL [4] model based on ITG physics which is a stiff transport model for ions. The agreement with experimental time-averaged temperature profiles (not shown here) is satisfactory, however with a trend to provide flatter T_e and T_i profiles, the difference in the central temperatures being 10 % to 30 %, depending

on the conditions. In the comparison between modulation simulations, it is important to keep the time-averaged χ equal to χ^{PB} . For this model we reduced both χ_e and χ_i by 20%. For the phase the agreement between data and IFS/PPPL model is better than using χ^{PB} , however the asymmetry is not reproduced with the desired magnitude. This model is expected to describe the ion physics but probably does not include all properties of the electron transport. We also investigated the effect of a ∇T_e^α dependence of χ_e : $\chi_e = \chi_e^{PB} \times (\frac{\nabla T_e}{\langle \nabla T_e \rangle})^\alpha$, where $\langle \nabla T_e \rangle$ is the time-averaged gradient. This assumption yields $\chi_e^{HP} = (1 + \alpha)\chi_e^{PB}$ [5]. Adjusting α allows to reproduce phase and generally amplitude with a good accuracy in the region $\rho > \rho_{ECRH}$ (Fig. 1.), but the asymmetry is not reproduced. Note also that the amplitude at the ECRH deposition is well reproduced. The ECRH power was not adjusted but taken according to the experiment. The value of α must be increased with heating power from ≈ 1 in the Ohmic case to ≈ 5 with 5 MW NBI.

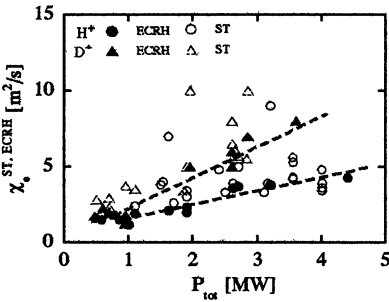


Figure 2: χ_e^{HP} versus heating power for ECRH and sawteeth (ST) in H^+ and D^+ .

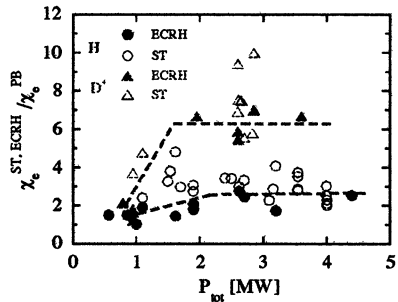


Figure 3: χ_e^{HP}/χ_e^{PB} versus heating power for ECRH and sawteeth in H^+ and D^+ .

Our results for χ_e^{HP} in the region $\rho > \rho_{ECRH}$ ($0.6 \leq \rho_{tor} \leq 0.8$) for several shots are summarised in Fig. 2 and 3. They clearly show the increase of χ_e^{HP} for both ECRH modulation and sawteeth with heating power, as well as that of χ_e^{HP}/χ_e^{PB} . The lines are supposed to only guide the eye. Some values for sawteeth at high heating power reaching 30 are outside the frame of the figures. Figures 2 and 3 also show that χ_e^{HP} is lower in hydrogen plasmas than in deuterium plasmas, in contradiction to the well-known isotope effect and to our power balance results. Correlated with the lower values of χ_e^{HP} , the

asymmetry is weaker in hydrogen than in deuterium. These results support the indications that heat pulse propagation does not directly reflect the power balance χ .

Internal transport barriers with ECRH and ECCD

Internal transport barriers (ITB) have been observed in various experiments in which current rise and heating were controlled to produce low or reversed central shear. This has been successful in two extreme regimes, in which ion temperature gradient driven (ITG) modes should be either stable, or relatively easy to stabilize by rotation shear, namely with pure electron heating (e.g. [6]) and cold ions, or with strong ion heating and $T_i \geq T_e$ [7, 8]. Internal transport barrier with $T_i \approx T_e$ were obtained on JET transiently [9].

We report on first experiments in ASDEX Upgrade, in which central ECRH or ECCD was applied during the ITB phase of NBI heated plasmas. An ECRH power of 1.25 MW was launched so as to produce, in addition to electron heating, also co or ctr ECCD in L-mode limiter discharge. Current profile is measured with Motional Stark Effect on the NBI.

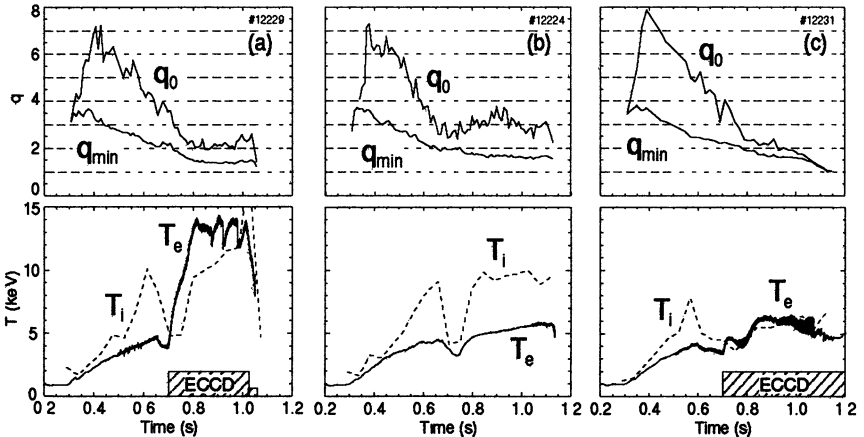


Figure 4: Comparison of the cases: (a) NBI and ctr-ECCD, (b) reference case with NBI only, (c) NBI and co-ECCD. Above: evolution of central and minimum q , the difference of which reflects the amount of shear reversal. Below central T_i (CXR) and T_e at $\rho_{tor} = 0.2$.

In these discharges a central reversed shear is attained by applying 5 MW of NBI during the current ramp-up at densities $2-3 \times 10^{19} m^{-3}$ to

reduce current diffusion [10]. The resulting shear is strongly reversed in the plasma center with initial q_0 values exceeding 6 and $q_{min} \approx 4$. However, due to the reduced but still continuous current diffusion, q evolves towards a monotonic profile with q_0 finally approaching one, if MHD instabilities do not terminate the discharge earlier. Without ECRH an ITB is formed, which is reflected in central T_i values in excess of 10 keV corresponding to an ion thermal diffusivity χ_i at neoclassical level, while T_e is a factor of two to three below T_i in the plasma core. When q_{min} reaches 2 a (2,1) mode develops which transiently deteriorates the confinement properties, resulting in a sharp drop of T_i . MHD Analysis predicts (2,1) double tearing modes to become unstable, [11].

In our experiments we applied central ECCD (co or ctr) at a time when q_{min} approaches 2, either to support the shear reversal or accelerate its decay. For ctr-ECCD (Fig. 4.a) the electron temperature, even at 0.12 m from the center, reaches a value of 13 keV (confirmed by Thomson scattering) and is higher than the central value of the ions. The large drop of T_i before ECRH pulse is due to the (2,1) mode mentioned above. Ray-tracing calculations indicate an ECR deposition at $\rho_{tor} \leq 0.2$. The calculated driven current rises from initially 82 kA to 134 kA due to the strong increase of T_e . The corresponding current density is of the order of the total current density measured with the MSE diagnostic in the plasma center. The temporal evolution of the central and minimum q slows down when ctr-ECCD is applied. At 1.06 s the discharge is terminated by a disruption triggered by the accidental tripping of two gyrotrons.

Figure 4.b shows the equivalent traces for a reference discharge without ECRH power, in which T_i reaches a similarly high value, but the maximum T_e remains at 5 keV. The behaviour of the measured q -profile is comparable. However, the slope of the central MSE polarization angles, which is a measure of q_0 , shows a small but visible difference suggesting a larger q_0 with counter-current drive.

With co-ECCD (Fig 4.c) the (2,1) mode, which disappeared in the other two cases, develops into a continuous mode (seen on T_e) which inhibits the recovery of the ITB. T_i and T_e remain low. 300 ms after the switch-on of co-ECCD, both q_0 and q_{min} start to drop finally reaching unity. Two main effects may contribute to the faster decay of the reversed shear: i) the central current density is increased by

co-current drive; ii) the boot strap current is reduced because of the lower pressure gradient.

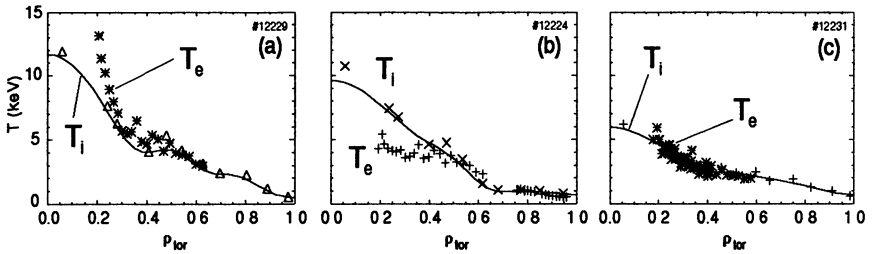


Figure 5: Temperature profiles at 0.97 s for the three discharges with heating in the current ramp-up phase: (a) NBI+ctr-ECCD, (b) reference with NBI only, (c) NBI+co-ECCD. The strong electron temperature gradient is only seen in case of ctr-ECCD.

The temperature profiles of the three cases are shown in Fig. 5, evidencing the strong electron temperature gradient with ctr-ECCD. Without ECRH the electrons are mainly heated through the ions and do not follow the increase of T_i at this low density.

The toroidal rotation velocities of ctr-ECCD and NBI only cases do not exhibit marked differences

References

1. LOPES CARDOZO, N. J., Plasma Phys. Contr. Fusion **37** (1995) 799
2. JACCHIA, A. et al., Phys. Fluids **B 3** (1991) 3033
3. PEREVERZEV, G. V. et al., IPP report 5/42 (1991)
4. KOTSCHENREUTHER, M. et al., Phys. Plasmas **2** (1995) 2381
5. STROTH, U. et al., Plasma Phys. Controlled Fusion **38** (1996) 611
6. BURATI, P. et al., Phys. Rev. Lett. **82** (1999) 560
7. LEVINTON, F. M. et al., Phys. Rev. Lett. **75** (1995) 4417
8. RICE, B. W. et al., Phys. Plasmas **3** (1996) 1983
9. SÖLDNER, F. X. et al., Nucl. Fusion **39** (1999) 407
10. WOLF, R. et al., Invited Paper at 26th EPS Conf., Maastricht 1999, to be pub. Plasma Phys. Contr. Fusion
11. GÜNTER, S. et al., Invited Paper at 26th EPS Conf., Maastricht 1999, to be pub. Plasma Phys. Contr. Fusion

THE STABILISATION OF NEOCLASSICAL TEARING MODES BY ECCD IN ASDEX UPGRADE

H. Zohm, G. Gantenbein, G. Giruzzi, S. Günter⁺, F. Leuterer⁺,
M. Maraschek⁺, J.P. Meskat, W. Suttrop⁺, Q. Yu⁺, M. Zabiégo**

Institut für Plasmaforschung, Pfaffenwaldring 31, D-70569 Stuttgart, Germany

*CEA Cadarache, F-13108 St.-Paul-lez-Durance, France, EURATOM Association

⁺MPI für Plasmaphysik, D-85462 Garching, Germany, EURATOM Association

The stabilisation of β -limiting neoclassical tearing modes by injection of ECRH and ECCD into the magnetic islands associated with this instability is discussed. Experiments in the ASDEX Upgrade tokamak show that complete stabilisation can be obtained using ECCD at the resonant surface at a power level of typically 10 % of the total heating power, corresponding to a driven current of 1-2 % of the total plasma current. The stabilisation efficiency sensitively depends on the deposition radius of the EC waves, thus indicating the need for an on-line control of the deposition radius. Theoretical modelling of the stabilisation well describes the experimental results obtained in ASDEX Upgrade.

Introduction

The economic use of fusion energy generated by a reactor based on magnetic confinement requires operation at sufficient $\beta = 2\mu_0\langle p \rangle / B^2$, where $\langle p \rangle$ is the averaged plasma pressure and B the confining magnetic field. In tokamaks, the limit to the achievable values is usually set by MHD instabilities. Ideal MHD predicts a β -limit of $\beta \propto I / (aB)$, where I is the plasma current and a the minor radius [1]. Therefore, the achieved β -values are often expressed in terms of 'normalised beta', $\beta_N = \beta / (I / (aB))$. This ideal β -limit is observed in experiments which aim for a transient high value of β [2].

However, in stationary discharges at β -values significantly below those predicted by ideal MHD, a different type of MHD instability often occurs: with finite resistivity, magnetic islands due to tearing modes can occur [3], [4], [5], [6]. These islands lead to a local flattening of the temperature profile due to a largely enhanced heat conductivity across the island and thus result in a degradation of confinement. Although β can usually still be increased in the presence of these islands by increasing the heating power, the loss in confinement is generally too high to be acceptable for a future reactor. An example is shown in Fig. 1:

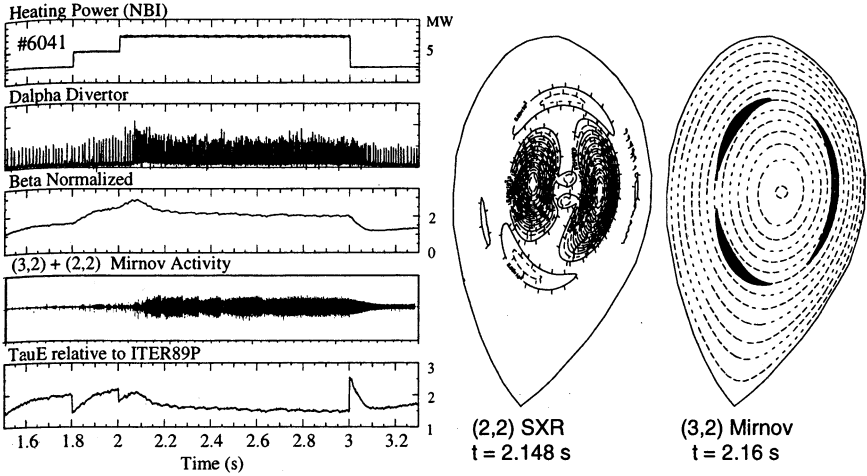


Fig. 1: The occurrence of β -limiting magnetic islands in ASDEX Upgrade. The value of follows the increase of the heating power until magnetic islands, indicated by the occurrence of a magnetic perturbation, occur. The islands result in a degradation of confinement as expressed by the normalised confinement time.

Magnetic islands as shown in the poloidal cross-section of the ASDEX Upgrade tokamak in Fig. 1 occur on magnetic surfaces where the value of the safety factor q , i.e. the number of toroidal turns that a fieldline completes until it completes a poloidal turn, has a rational value. In this case, force free perturbation currents can flow along the field lines and produce the island. The island is characterised by its width W , which is the maximum radial expansion of the island structure. The point where this maximum expansion occurs is also referred to as the island O-point, whereas the point of minimum (zero) expansion is referred to as X-point. The mechanism that drives the currents in the cases considered here can be understood as follows: consider a magnetic island opened up at a rational surface. This will lead to a flattening of the pressure profile due to the enhanced heat conductivity across the island, where different radii are connected by fieldlines and the heat and particles are transported from one radius to the other parallel to B . This flattening will in turn locally reduce the bootstrap current due to the pressure gradient. Therefore, a helical defect current within the island develops that will lead to an even bigger island. Thus, an unstable situation may develop if

the loss of bootstrap current overcomes other helical currents that tend to resist tearing. A special feature of these modes is that they are usually triggered by other MHD events that produce the initial island, the so-called 'seed-island' [7]. Due to its origin from the bootstrap current, which is an effect of neoclassical transport, this type of tearing mode has been called 'neoclassical tearing mode' [3].

Amongst the possible remedies against neoclassical tearing modes, the control of their amplitude or even the complete stabilisation by local current drive at the resonant surface has been identified as a very promising approach [8], [9]. With this scheme, several stabilisation mechanisms exist: the current developing due to the local change in resistivity or directly driven by ECCD can change the equilibrium current profile and thus change the stability against tearing. In addition, a helical current in the island O-point will tend to replace the lost bootstrap current and thus reduce the island size. The latter effect should be best accessible by phased ECCD that only generates a co-current in the island O-point (AC-scheme). Contrary, the generation of a co-current (with respect to the total plasma current) in the X-point should lead to a destabilisation, so that one may expect that DC injection should, on average, not lead to a stabilisation. However, at finite deposition width, even DC injection will be stabilising, because near the island X-point, a large fraction of current is deposited outside the island and rapidly equilibrates on the open field lines, thus not contributing to destabilisation.

In the remainder of the paper, we will first discuss the description of the dynamics of the neoclassical tearing mode by analytical theory. Then, experiments on the stabilisation by ECCD in the ASDEX Upgrade tokamak [10], [11] are reviewed. Finally, numerical modelling of these experiments is presented.

Theoretical Considerations

The growth of a magnetic island can be described by the balance of the helical currents on the resonant surface at radius r_s . If we perturb the flux surfaces outside the island with the helicity of the island, we can calculate the poloidal magnetic field on the left and right borders of the island by use of the force-free condition. This can be done integrating the so-called tearing mode equation

$$\Delta\psi + \frac{\mu_0 dj(r)/dr}{B_\theta(1-n/mq(r))} \psi = 0, \quad (1)$$

where m and n are the poloidal and toroidal mode numbers, $j(r)$ is the equilibrium current density profile and ψ is the helical magnetic perturbation flux. From ψ , the components of the perturbed helical field can be calculated by $B_\theta = d\psi/dr$ and $B_r = -m\psi/r$. From Ampère's law, the difference between the poloidal components of the helical field across the island can be related to δI , the helical perturbation current inside the island:

$$B_\theta(r_s^+) - B_\theta(r_s^-) \propto \delta I = I_{Ohm} + I_{bs} + I_{ECCD}, \quad (2)$$

where r_s is the radius of the resonant surface and we have assumed that the helical current consists of three relevant contributions, namely the ohmic current I_{Ohm} related to the resistive generation or dissipation of helical flux, I_{bs} , the helical component of the perturbed bootstrap current and I_{ECCD} , the helical component of the current driven by EC waves. The ohmic current is given by

$$I_{Ohm} \propto j_{Ohm} W \propto \sigma E W \propto \sigma d\psi/dt W \propto \sigma dW/dt W^2, \quad (3)$$

where E is the helical electric field, σ the conductivity and we have made use of the relation $\psi \propto W^2$. The bootstrap current is

$$I_{bs} \propto j_{bs} W \propto -\frac{\nabla p}{B_\theta} W \propto -\beta_p W, \quad (4)$$

where the poloidal beta, β_p , has been introduced and the minus sign is due to the fact that it is a defect current.

We must take into account that only the helical component of the current driven by ECCD *within* the island contributes to stabilisation, so that for $d > W$, only the fraction $I_{ECCD} W/d$ can be accounted. Inserting into (2), rearranging the terms and introducing the quantity $\Delta' = (B_\theta(r_s^+) - B_\theta(r_s^-)) / \psi$, we obtain

$$\tau_{res} \frac{dW}{dt} = a_1 \Delta' + a_2 \frac{\beta_p}{W} - a_3 f(W) \frac{I_{ECCD}}{W^2}, \quad (5)$$

where the function

$$f(W) = \begin{cases} 1 & \text{for } d < W \\ W/d & \text{for } d > W \end{cases} \quad (6)$$

and the resistive timescale $\tau_{res} \propto \sigma a^2$ have been introduced. Eqn. (5) is the so-called Rutherford equation. From the definition of Δ' , it can be seen that it is determined by the perturbation of the flux surfaces outside the island. It can be shown that Δ' determines the stability of the equilibrium configuration against tearing: for $\Delta' < 0$, the plasma resists tearing at the particular resonant surface whereas for $\Delta' > 0$, the magnetic energy associated with the equilibrium can be lowered by forming an island. In the latter case, a magnetic island will form spontaneously (so-called current gradient driven tearing mode). However, in the case of neoclassical tearing modes, the plasma usually resists tearing and hence $\Delta' < 0$ and the free energy has to come from the pressure gradient.

The Rutherford equation given above is valid at finite island widths, but has a deficiency for $W \rightarrow 0$: in the absence of an ECCD current, the equation will always predict instability due to the diverging form of I_{bs} . This is clearly unphysical and has been resolved by introducing two changes: The finite ratio of parallel to perpendicular heat conductivity introduces a lower bound W_0 to the values of W for which the temperature is completely flattened across the island. For $W < W_0$, the parallel and perpendicular heat fluxes become comparable, the temperature is not flattened and hence the bootstrap current is not decreased in the island [12]. In addition, the motion of the island through the plasma leads to a polarisation current that, in toroidal geometry, tends to stabilise the mode [13]. This term is again only important for small island widths, because it enters in the Rutherford equation proportional to W^3 . Taking these terms into account, the Rutherford equation reads

$$\tau_{res} \frac{dW}{dt} = a_1 \Delta' + a_2 \frac{\beta p W}{W^2 + W_0^2} - a_3 f(W) \frac{I_{ECCD}}{W^2} - a_4 \frac{\beta_p}{W^3}. \quad (7)$$

This equation can be evaluated for $dW/dt = 0$ to give the value of I_{ECCD} needed to hold the island of width W stationary. A plot of I_{ECCD} using the ITER reference parameters from [9] as function of W and d is shown in Fig. 2:

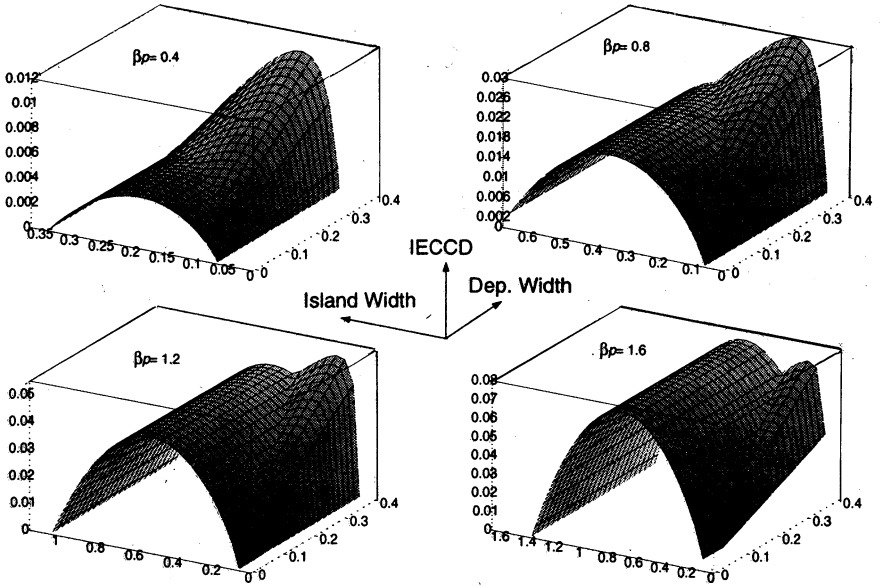


Fig. 2: The ECCD current (expressed as fraction of total current) needed to hold a neoclassical tearing mode of island width W stationary as function of W and deposition width d . The sequence corresponds to an increase of β_p . At low β_p , the absolute maximum can be decreased by a decrease in d , whereas for high β_p , it is independent of d .

It can be seen that the required current has in general two local maxima as function of W and d , one in the region $W < d$ and one in the region $W > d$. The β -scaling of these maxima is different, because at $d < W$, I_{ECCD} / W^2 has to balance β/W (see Eqn. (5)) and thus $I_{ECCD} \propto W\beta \propto \beta^2$ (the saturated island width of a neoclassical tearing mode is proportional to β). On the other hand, for $d > W$, $I_{ECCD} d / W$ has to balance β/W (see Eqn. (5)) and thus $I_{ECCD} \propto d\beta$. Thus, for low β , the requirement for $d > W$ sets the absolute maximum, whereas for high β , the requirement for $d < W$ determines the absolute maximum. Conversely, for low β , the maximum can be decreased by decreasing d , whereas at high β , it is independent of d . From these analytical considerations, it thus follows that it is beneficial to maximise I_{ECCD} / d if $d > W$ holds. For complete stabilisation, this will always occur for sufficiently small island size.

Experimental Set-up

The experiments reported here were carried out in the ASDEX Upgrade tokamak (major radius $R_0 = 1.65$ m, minor radius $a = 0.5$ m) in a lower single null X-point configuration with elongated plasma cross-section and modest triangularity ($\kappa = 1.7$, $\delta = 0.1$). At a line-averaged density of $n_e = 5\text{-}6 \cdot 10^{19} \text{ m}^{-3}$, we inject 10 MW of NBI heating power to provoke a neoclassical tearing mode with poloidal mode number $m = 3$ and toroidal mode number $n = 2$ at $\beta_N = 2.3\text{-}2.5$. At lower density, also (2,1) modes are observed, but stabilisation of this mode was not studied so far. All discharges are operated in the type I ELMy H-Mode regime.

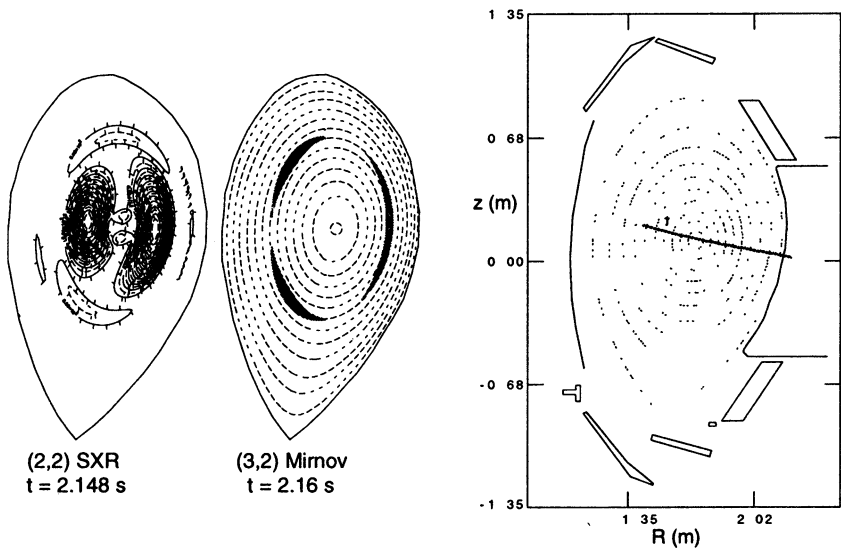


Fig. 3: Ray tracing calculation for ASDEX Upgrade stabilisation experiments. The deposition is at the position of the $q = 1.5$ surface.

Stabilisation experiments were carried out using 1-3 gyrotrons, each delivering about 400 kW of absorbed RF power to the plasma at 140 GHz. Injection is done in X-mode and absorption occurs at the 2nd harmonic (2.5 T). For ECCD, the injection is done under a toroidal angle of 15° . Although this value does not provide the maximum driven current, it leads to a good localisation at still reasonable current. Absorption is on the high field side, where the current drive efficiency is

maximum. Calculations with the TORAY code [14] yield a driven current of 10-15 kA in this scenario with a deposition width of $d = 0.04$ m, which is small compared to the usual saturated island width of $W_{sat} = 0.08$ m. The result of such a ray-tracing calculation is shown in Fig. 3.

For phased injection, a trigger signal is generated from an $n = 2$ combination of Mirnov probes. The RF beams from different gyrotrons are injected from different ports, so that there is a toroidal angular distance between them. We vary the poloidal injection angle to compensate this difference. Field line maps of the resonant surface are used to check if the gyrotrons deposit on the same field line; from ray tracing calculations, we can find out if the beams are also absorbed on the same flux surface. This is illustrated in Fig. 4, where a map of field lines on the $q = 1.5$ surface is shown together with several rays launched under different poloidal angles. The poloidal launch angle, θ_{ECR} , is converted into a geometrical poloidal angle θ , measured with respect to the plasma centre.

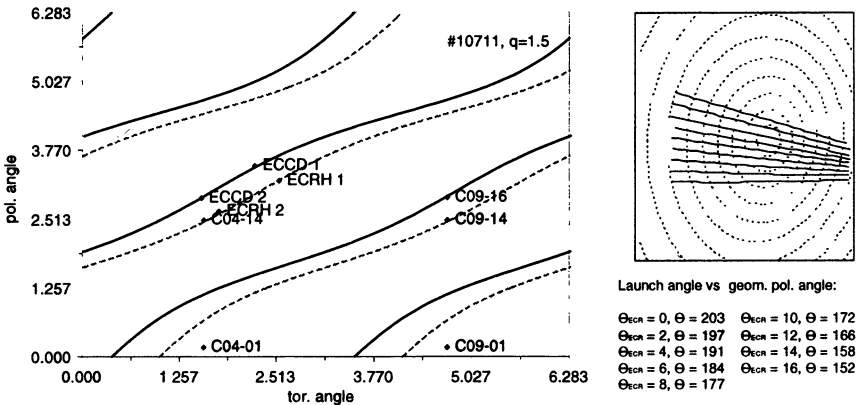


Fig. 4: Map of the fieldlines on the $q = 1.5$ surface (left part). It can be seen that the two gyrotrons deposit on the same field line for heating or current drive (ECRH 1 and 2 or ECCD 1 and 2). In addition, Mirnov probes that probe the same field line can be identified (C04-14 or C09-16). From ray tracing (right figure), two poloidal injection angles under which absorption is on the same flux surface are identified ($\theta_{ECR} = 2^\circ$ and $\theta_{ECR} = 12^\circ$).

Using this system, it is possible to inject either into the O-point or the X-point of the magnetic islands. No feedback could be applied to match

the radial position of the deposition during the shot. Thus, we fine-tuned B_r from discharge to discharge to find the optimum position. However, we found, from ECE measurements of the magnetic island, that the resonant surface moved from shot to shot by 1-3 cm and optimum deposition could thus not be ensured. Therefore, a B_r -ramp was applied, where we changed B_r on a timescale of 1.5 s by 5 %, changing the EC resonance position by 0.08 m. The typical growth time for a (3,2) neoclassical tearing mode in ASDEX Upgrade is of the order of 100 ms, so that the change of the EC resonance was always slow compared to the growth rate. This technique of ramping B_r in a small range has been very successful in matching the deposition and led to an appreciable reduction of the time needed to accomplish the experiments.

Experimental Results: O-Point versus X-Point Injection

We first describe the experiments carried out using phased injection as described before. Fig. 5 shows the behaviour of two discharges, one with phased injection into the O-point and one with phased injection into the X-point of the magnetic island. In both cases, 0.8 MW of ECCD was applied as described above and the current was in the co-direction, i.e. stabilising for O-point injection and destabilising for X-point injection. It can be seen that O-point injection results in a decrease in mode amplitude and in an increase in β . However, it is not a smooth decrease of the mode amplitude, but rather a switch to a different state. Closer analysis shows that not only the (3,2) amplitude decreases, but also the sawtooth frequency is prolonged, pointing towards the importance of the non-linear coupling between (3,2) and (1,1) modes. In the case with X-point injection, there is hardly any change in mode amplitude visible. There is indeed a drop in β , as one would expect for a destabilising current, but its magnitude is of the order of the natural fluctuations of β . We thus conclude that O-point current drive is more effective than X-point current drive. This can be understood taking into account the fact that around the X-point, the island is so narrow that for finite deposition width, we will always deposit a noticeable fraction of the current outside the island, whereas in the O-point, for our conditions, $W > d$ is fulfilled at least for the saturated island.

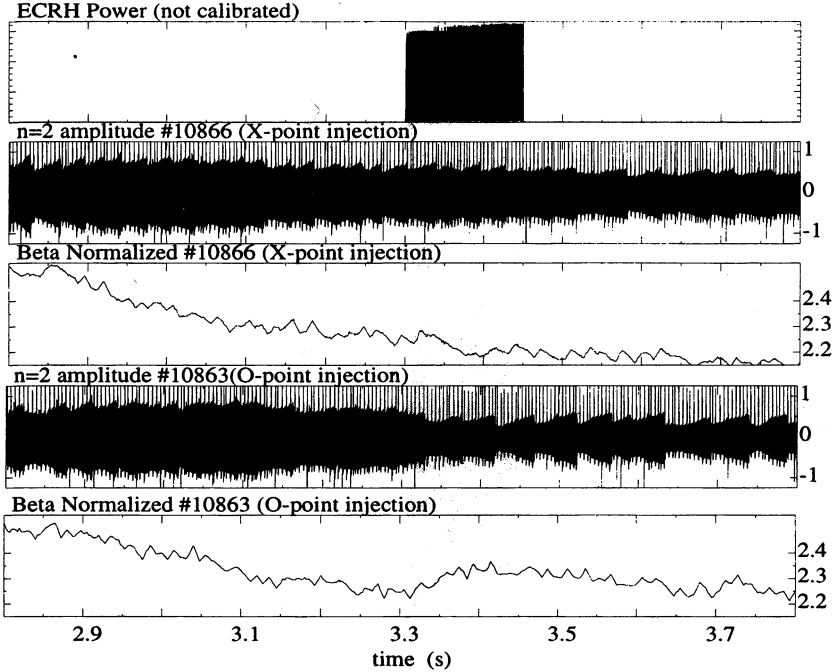


Fig. 5: Phased injection into the O-point results in a decrease in mode amplitude and an increase in β . Phased X-point injection hardly shows an effect.

The situation becomes clearer in discharges where no or only infrequent sawteeth are present. An example is shown in Fig. 6. Here, a smooth decrease of the mode amplitude on the resistive timescale is seen. In addition, we again notice an increase in β . In this discharge, the trigger failed to produce trigger pulse at reduced mode amplitude, so there is an effective switch from AC to DC injection after about 50 ms of ECCD. It can be seen that there are no dramatic changes in the decrease of the mode amplitude, indicating again that the destabilisation efficiency of X-point injection is low, so that AC and DC effectively have the same stabilisation efficiency. This has been found before in the experiments where current gradient driven modes were stabilised (see [15] and references therein).

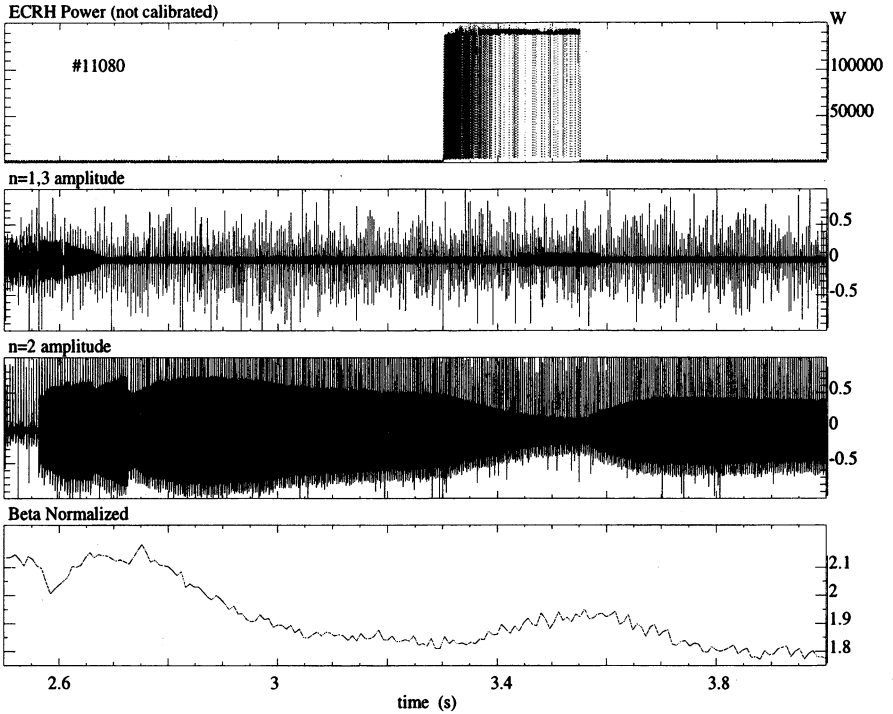


Fig. 6: Stabilisation experiment in which the trigger unit fails at low mode amplitude and switches from phased AC injection to DC injection. There is hardly any difference visible between the stabilisation efficiency of the two schemes.

Motivated by this experimental result, we carried out further experiments using DC ECCD. In these experiments, a B_t ramp as described above was used to vary the position of the EC resonance during the shot. Fig. 7 shows an example of such a discharge, but at a too high density, so that no mode occurs.

It can be seen here, that during ECCD, the stored energy actually decreases, inspite of the additional heating power. This can at least partly be explained by the observation that ECRH tends to decrease the density (so-called 'ECRH pump-out' of particles) and, because the line averaged density is kept constant by gas puff via feedback control, the gas puff is increased during ECRH. This leads to a deteriorated confinement that is probably responsible for the drop in stored energy. In the following, we will use this discharge as a reference.

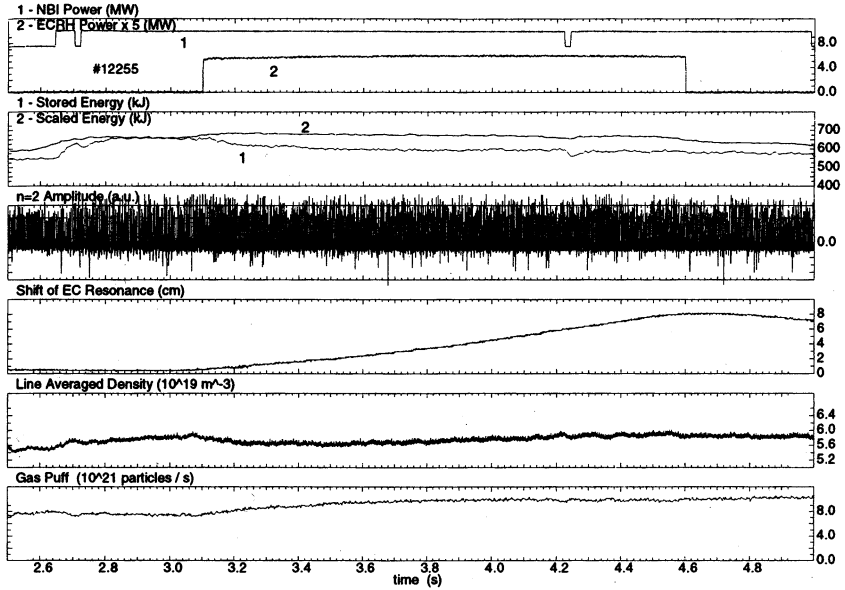


Fig. 7: Reference discharge with 1.2 MW ECCD and a slow B_r -ramp but without a neoclassical tearing mode.

Fig. 8 shows an experiment where 1.2 MW of ECCD power were injected DC into a discharge where a neoclassical tearing mode occurred at $\beta_N = 2.4$. As the EC resonance is slowly moved towards the resonant surface by the B_r -ramp, the mode amplitude decreases and finally goes to zero. The timescale for the stabilisation is thus given by the ramp, not by the resistive timescale, i.e. the island width parametrically follows the increase of ECCD current driven inside the island. The decrease of mode amplitude is accompanied by an increase in β . As explained above, due to the deteriorated confinement in the ECRH phase, β does not recover to the value at the onset of the mode. However, as can be seen from the β -trace of the reference discharge also shown in Fig. 8, the complete stabilisation leads to the same value as in the case without mode at all. This means that at $\beta_N = 2.4$, the mode can be fully stabilised by injection of an RF power that amounts to only 10 % of the total heating power. This result can be obtained reproducibly, provided the radial localisation is correct, as e.g. ensured by the B_r -scan.

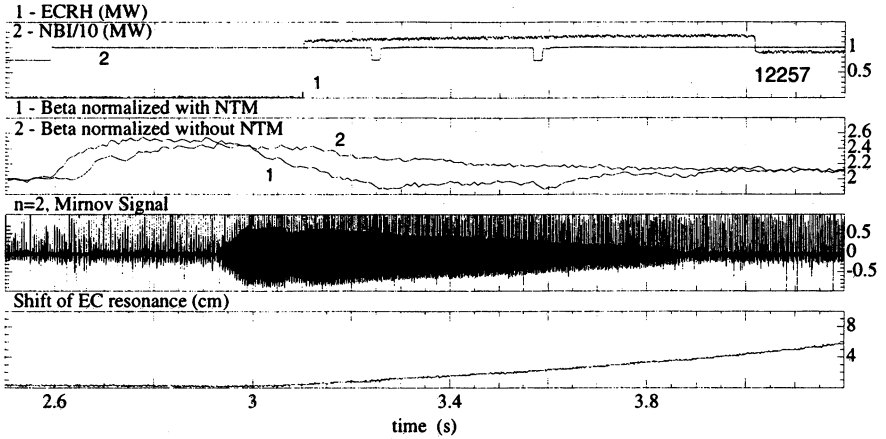


Fig. 8: DC stabilisation experiment using ECCD and a slow B_r -ramp. The mode is completely stabilised with 1.2 MW ECCD power.

One should also note that the mode does, in the present experiments, not come back after ECCD is switched off. Although the complete stabilisation can be understood by the fact that the mode is nonlinearly stable if the island width is smaller than the seed island width, one would expect the next sawtooth to trigger the mode again. However, due to the confinement degradation mentioned above, β is lower after stabilisation than at the mode onset. This may explain why the mode is not triggered again. In addition, there is also a change in sawtooth behaviour and it is not clear if seed island of sufficient size are produced in the time interval after stabilisation.

Experimental Results: ECCD versus ECRH

In Fig. 8, we have shown an experiment where complete stabilisation occurs with 1.2 MW of ECCD. As was pointed out above, there are two contributions to the helical current generated by ECCD, namely one from the decreased resistivity due to local heating that will increase the ohmic component and one due to the current directly driven by the ECCD effect. In order to separate the two effects, we performed an experiment where all parameters were kept constant with respect to the co-case, but the toroidal injection angle was reversed. Now, the ECCD current is destabilising, whereas the current due to ECRH is still stabilising. The

result is shown in Fig. 9:

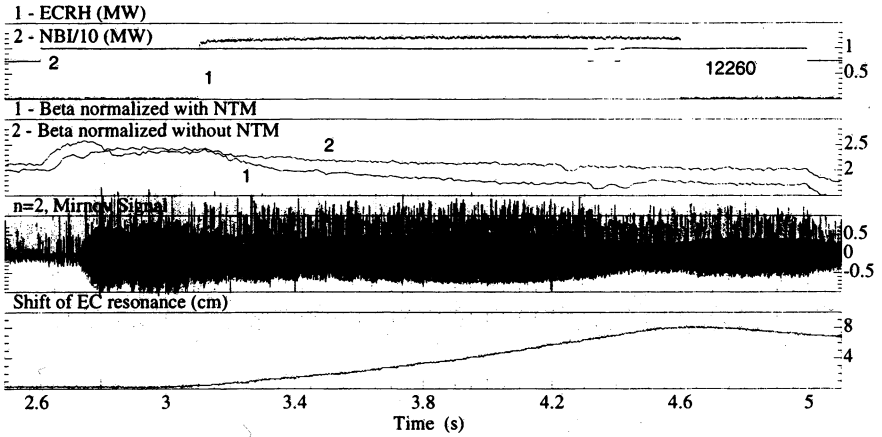


Fig. 9: DC stabilisation experiment using the same parameters as shown in Fig. 8, but with the toroidal injection angle reversed. Now, there is only a small effect on the mode amplitude, indicating the importance of the ECCD current in the stabilisation process.

There is only a small effect on the mode amplitude, although with co-ECCD, the mode had been completely destabilised in this case. From the temporal behaviour of the mode amplitude, it is not clear if a slightly destabilising effect is first seen. In the later phase of the scan, there is a small stabilising effect, but it is not comparable to that seen in Fig. 8. This small stabilisation might actually be due to either a change in Δ' , because in the late phase of the B_t -ramp, a counter current is driven at $r < r_s$, or to a helical component driven so far off the resonance, but still inside the island separatrix, that it actually corresponds to a ctr-current in the X-point. We can however clearly conclude that ECCD is at least important, if not dominant, in the stabilisation process.

Experimental Results: Localisation Requirements

Another important question is the sensitivity on the mismatch between the ECCD deposition radius r_{dep} and r_s . During the B_t -ramp, r_{dep} starts outside r_s and then moves across r_s to smaller radii. Thus, one expects the stabilising effect to increase as r_{dep} approaches r_s , have a maximum somewhere around the point $r_{dep} = r_s$ where the island is eclipsed by the RF beam, and then to decrease again. Experimentally,

such a behaviour can only be verified when the mode is present, i.e. not completely stabilised. We therefore carried out a B_r -ramp at lower ECCD power (0.4 MW). The result is shown in Fig. 10:

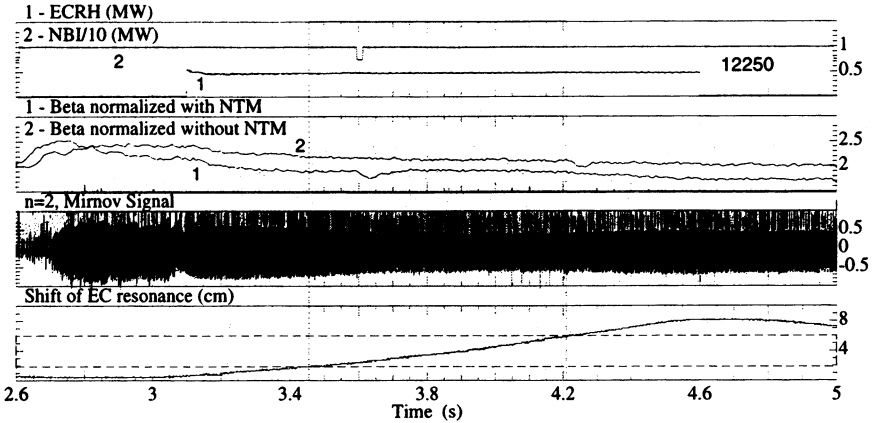


Fig. 10: DC stabilisation experiment using ECCD and a slow B_r -ramp at lower power (0.4 MW). From the time interval in which a stabilising effect is seen, the localisation requirement is inferred to be 0.04 m.

Here, we can in fact see the expected behaviour: stabilisation sets in at a certain value of B_r , noticeable by the stop of the β -decrease at still decreasing mode amplitude (this is in contrast to the global decrease in amplitude due to the β -drop induced by the mode, which leads to a smaller saturated island size). At a later time, one can see that β starts to decrease again, accompanied by an increase in mode amplitude. From the B_r -values at which this occurs, one can deduce that the requirement for localisation is about 0.04 m. This is close to both the island half width and the deposition width. It is therefore at the moment not possible to decide if this is due to the fact that for $|r_{dep} - r_s| > d$, the current is deposited too far away from the resonant surface, but still within the island, or that at $|r_{dep} - r_s| > W/2$, too much current is deposited outside the island.

Modelling of the Experimental Results

We finally describe the theoretical interpretation of our results. In order to calculate the current driven by ECCD, a time dependent Fokker-Planck Code is used [16]. This code takes into account the finite poloidal localisation when the power is modulated. As a result, a helical current density is obtained. This can be inserted into the Rutherford equation [16]. However, if we want to correctly describe also the effect of the local island heating and the effect of the change in equilibrium when the mode grows, a 2D non-linear MHD code is better suited. Thus, the results obtained from the Fokker-Planck code have been inserted into such a code [17]. In addition, this code correctly models the transport of heat and particles across the island. It also takes into account the radial transport of the fast particles that carry the ECCD current. The results are presented in the following section.

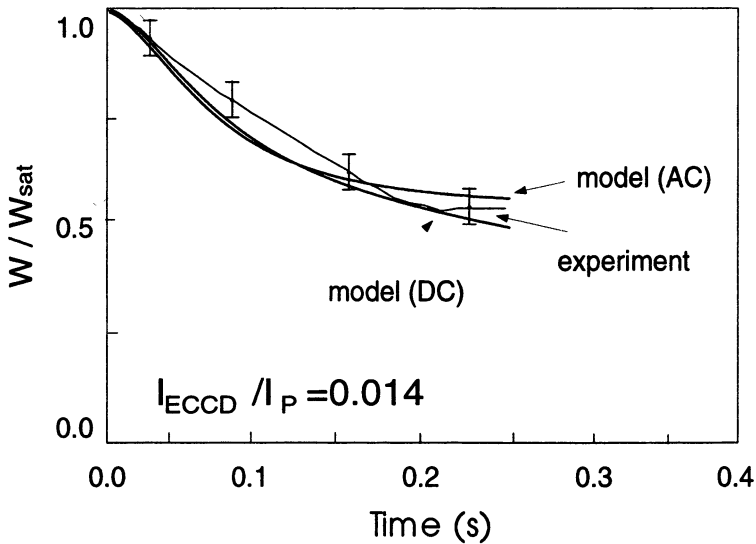


Fig. 11: Modelling of the experiment shown in Fig. 6. The curves are calculated for AC and DC injection.

First, we model the experiment where the stabilisation scheme changed from AC to DC and a reduction of the mode was observed (discharge 11080, shown in Fig. 8). The result of the code calculation is shown in Fig. 11.

It can be seen that the experimental data are very well modelled by the code calculations. In particular, the timescale of the stabilisation can be identified to be the resistive timescale of the mode. Also, the experimentally observed fact that there is hardly a difference between AC and DC scheme is found in the modelling. An analysis of the helical currents shows that the major part of the (3,2) helical current is driven by ECCD. For large island size, local heating also plays a role, but its effect diminishes when the island gets smaller.

With this method, we can also analyse a case where the mode was completely stabilised during the B_r -ramp, e.g. discharge 12257 shown in Fig. 8. The results of a scan which was started 1.5 cm off the resonant surface and the resonance moved by 2.5 cm / s are shown in Fig. 12:

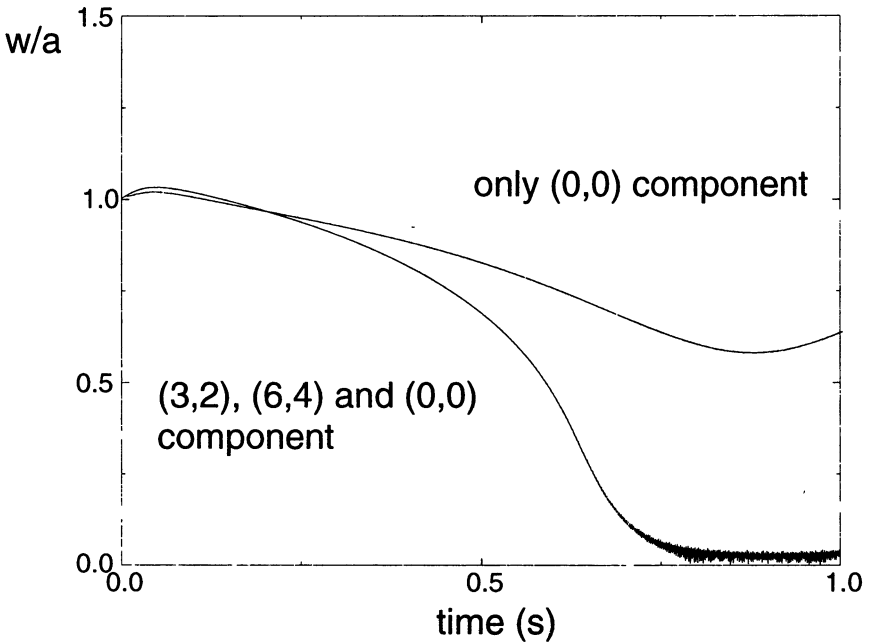


Fig. 12: Modelling of the experiments shown in Fig. 8 (co-ECCD with B_r -ramp). In addition to the result obtained using all relevant Fourier components, the effect of only the (0,0) component of the driven current is also shown.

It can be seen that again, the main trends of the experimental result are well reproduced. The mode amplitude now decreases on the

timescale of the scan, not on the local resistive timescale. In addition, it is possible to separate the effect of the non-linear $\Delta'(W)$ by decomposing the driven current into Fourier harmonics and analysing their effect on the mode. In Fig. 12, we also show the effect of the (0,0) component alone (by artificially setting the other components to zero in the code). This corresponds to the pure change in the equilibrium profile and thus to the change in $\Delta'(W)$. It can be seen that this change indeed is slightly stabilising, but it has a much smaller effect than the sum of all components, indicating the importance of the helical currents driven in the island.

It is interesting to note that in the modelling, one finds a small destabilising effect when the deposition is not well centred. This occurs when the current is driven close to, but inside the island separatrix. In this case, the (3,2) helical current mainly develops as co-current in the X-point region, i.e. as a destabilising current. Furthermore, a (0,0) co-current inside the separatrix at $r > r_s$ is also destabilising. These effects are small compared to the stabilising effect at correct deposition, so that they are difficult to verify in the experiment. They may however offer an explanation for the small stabilising effect of the ctr-ECCD experiment as discussed in the context of Fig. 9.

Summary and Conclusions

Experiments in ASDEX Upgrade demonstrate the possibility to completely stabilise neoclassical tearing modes by ECCD at a power level of only 10 % of the total heating power. If less power is available, the mode amplitude can still be reduced substantially. The removal of the magnetic island is accompanied by a recovery of β to a value comparable to that reached without the mode present. Although these experiments do not result in an effective increase of the global β -limit so far, they do show that the β -limit set to long pulse discharges by resistive MHD can be increased, thus ensuring safe operation at reasonable β and good confinement. This is especially important for ITER, where operation at $\beta_N = 2.4$, i.e. well below the ideal limit but close to the resistive limit is envisaged.

The experiments indicate that the helical current driven by ECCD is important in the stabilisation process; theory predicts that this will be even more the case for a reactor [17]. We have shown that with the same available installed gyrotron power, AC and DC injection have a

comparable stabilisation efficiency. Although the average power used in the AC scheme is then only half the power used in the DC scheme, DC injection is technically much easier since it does not require any phase feedback and is thus the preferred method in ASDEX Upgrade.

So far, no feedback on the radial position was applied. A B_r -ramp of 5% was used to ensure correct positioning at some point during the ramp and provided a method to reliably remove the mode. However, this method will not be applicable in future devices with superconducting coils. Alternatively, one can use a scan of the poloidal injection angle if the antenna provides this flexibility. This method is difficult to apply in small experiments, because it requires steering of mechanical elements as e.g. mirrors on the 100 ms timescale. This constraint will be relaxed in a reactor-scale machine, where the resistive timescale of the mode is in the region of 10 s of seconds. Finally, one can also consider the use of step-tunable gyrotrons, provided their availability. Short pulse experiments have recently demonstrated the possibility to operate a gyrotron in frequency steps of about 3.7 GHz between 114 and 166 GHz [18]. These frequency steps of about 2.5 % will, at an aspect ratio of 3 result in radial steps of 7.5 % of the minor radius. For typical island widths of 10 to 20 % of the minor radius, this indicates that a finer spacing would be favourable, but a certain control will be possible even at this value. A finer spacing can in principle be obtained by operating the gyrotron cavity at higher volume modes.

In summary, ECCD stabilisation has been proven to be a very attractive candidate for neoclassical tearing mode stabilisation, but the fully feedback controlled extension of the tokamak operational space by this method still has to be demonstrated experimentally. Further experiments in ASDEX Upgrade will focus on this goal.

Finally, the good agreement between theoretical modelling and experimental results will allow a reliable extrapolation to future reactor-scale experiments such as ITER and may be used as a guideline for designing an ECCD system especially dedicated to the stabilisation of neoclassical tearing modes.

References

- [1] Troyon, F. et al., Plasma Phys. Control. Fusion **26**, 209 (1984)
- [2] Ferron, J.R. et al., Phys. Fluids B **5**, 2532 (1993).
- [3] Chang, Z. et al., Phys. Rev. Lett. **74**, 4663 (1995).
- [4] Zohm, H. Plasma Phys. Control. Fusion **37**, A313 (1995).
- [5] Gates, D.A. et al., Nucl. Fusion **37**, 1593 (1997).
- [6] La Haye, R. et al., Nucl. Fusion **37**, 397 (1997).
- [7] Gude, A et al., Nucl. Fusion **37**, 127 (1999).
- [8] Hegna, C.C. et al., Phys. Plasmas **4**, 2940 (1997).
- [9] Zohm, H., Phys. Plasmas **4**, 3433 (1997).
- [10] Zohm, H. et al., Nucl Fusion **39**, 577 (1999).
- [11] Zohm, H. et al., 26th EPS Conference on Control. Fusion and Plasma Physics (1999).
- [12] Fitzpatrick, R., Phys. Plasmas **2**, 825 (1995).
- [13] Wilson, H. et al., Plasma Phys. Control. Fusion **38**, A149 (1996).
- [14] Kritz, A. Proc. 3rd Varenna-Grenoble Sympos., Vol. 2, CEC, Brussels, 707 (1982).
- [15] Lloyd, B., Plasma Phys. Control. Fusion **40**, A119 (1998).
- [16] Giruzzi, G. et al., Nucl. Fusion **39**, 107 (1999).
- [17] Yu Q. et al., Plasma Phys. Control. Fusion **40**, 1977 (1998).
- [18] Dammertz, G. et al., Proc. of the EC-10 workshop, World Scientific, 483 (1997).

EXPERIMENTS ON ECRH POWER MODULATION IN THE L-2M STELLARATOR

*D. Akulina, G. Batanov, M. Berezhetskii, G. Gladkov,
S. Grebenshchikov, L. Kolik, N. Larionova, A. Meshcheryakov,
K. Sarksyian, I. Sbitnikova, O. Fedyanin, N. Kharchev, Yu. Kholnov;
T. Estrada*, K. Likin*, Elena de la Luna*, J. Sanchez**

General Physics Institute, Russian Academy of Sciences, Moscow
*CIEMAT, Spain, Madrid

In ECRH power modulation experiments, the absorption region of the ECR heating radiation and the thermal diffusion coefficient were determined by analyzing a change in the amplitude and phase of ECE and SXR signals. It was shown that the absorption region has a nonlocal character and depends on the value of the magnetic field. The estimated value of the electron thermal diffusion coefficient turns out to be higher than expected.

Introduction

Recently, the interest in heat transport processes in magnetic confinement systems has increased noticeably [1, 2]; however, much remains to be done to clear up a nature of processes occurring in plasma. As an example, the reasons for an increase in heat transport which is observed with increasing the heating power or decreasing the plasma density to 10^{13} cm^{-3} as well as a number of other effects have not been consistently explained up to now. The method of modulation of heating power at the electron cyclotron resonance frequency with subsequent analysis of the amplitude and phase of signals measuring the spatial and temporal distributions of the electron temperature (such as electron cyclotron emission and multi-chord signals from soft X-ray detectors) is widely used in the electron heat transport studies. Analysis of the amplitude and phase of the modulated signals at various ECRH modulation frequencies allows one to determine both the heating power absorption region and rates of transport processes in plasma.

The aim of this paper is to report on the first results of the ECRH modulation experiments in the L2-M stellarator [3] ($R = 1 \text{ m}$, $a_p = 11 \text{ cm}$, $\iota(0) = 0.18$, and $\iota(a_p) = 0.8$, number of field periods is 14). Figure 1 shows a "standard" cross section with contours of constant field values. A focussed microwave beam from a gyrotron (the gyrotron frequency was 75 GHz; its power reached 200 kW) was transmitted through a

quasi-optical mirror transmission line and launched through an outer horizontal port situated in the equatorial plane from the low-field side (LFS) as X-mode wave. The ECRH power modulation frequency was 1-4 kHz; modulation amplitude was 20%. For the gyrotron frequency $\omega = 2\omega_{ce}$, the resonance magnetic field is $B_{res} = 1.34$ T. The plasma radius could be varied with a graphite limiter from 11.5 to 8 cm in order to reduce the plasma-wall interaction. The average electron density was $n_e = (1-2) \cdot 10^{13} \text{ cm}^{-3}$; the electron temperature was $T_e = 0.7-1.2$ keV, the global energy confinement time measured from diamagnetic signals was $\tau_e = 1.5-2$ ms. A multichannel ECE receiver and multichannel soft X-ray detectors [4, 5] were used to measure the evolution of the electron temperature. ECE was received from high-field side (HFS) (Fig. 1). One channel (71 GHz) was positioned in the “non-standard” cross section in which a resonance region for this frequency lied almost at the plasma boundary; this channel was used to observe the emission from “suprathermal” electrons which present at any operating conditions of the L-2M [6]. The array of SXR detectors was positioned in the vertical port and allowed measurements in the plasma core up to $r/a = 0.6$.

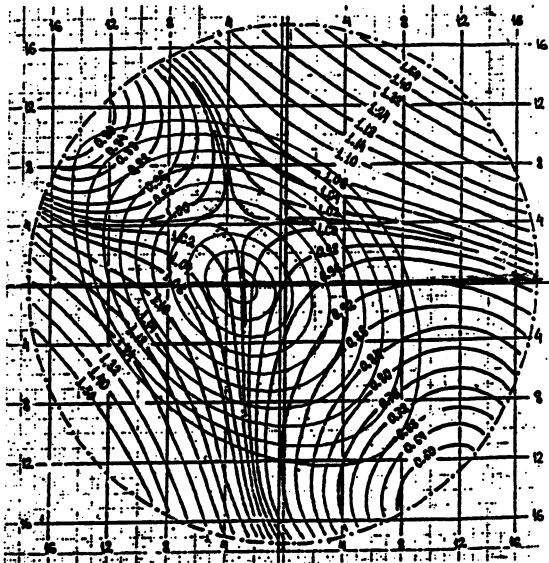


Fig. 1. Magnetic field contours ($B = \text{const}$) and magnetic surfaces in the “standard” cross section of the L-2M stellarator.

Experimental Results

Power deposition profiles in the L-2M are obtained so far from a ray-tracing code [7], based on the assumption of Maxwellian electron energy distribution function, having regard of the shape of radial profiles $T_e(r)$ and $n_e(r)$ and actual geometry of the magnetic field and beam. Along with these calculations, the analysis of the ECRH power modulation experiments is to estimate the absorption region from the time-dependent electron temperature measurements. It is well known that in a free-absorption region the amplitude of modulated temperature falls exponentially with radius, and the temperature perturbation damping length (λ) depends on the thermal diffusion coefficient (χ) and the modulation frequency of the ECRH power f_{mod} :

$$\lambda = (2\chi/3\pi f_{mod})^{1/2} \quad (1)$$

As the modulation frequency increases, the damping length decreases and becomes of the order of the size of the absorption region [8], [1].

Figure 2 shows the temporal behavior of some signals for a ECRH power modulation frequency of 1 kHz. The modulation is clearly seen in the ECE signals, the derivative of diamagnetic signal (P_{abs}), P_{in} and others. Figure 3 illustrates typical signals from the alternating components of P_{in} and ECE at various frequencies from 76.5 to 81 and 71 GHz for a modulation frequency of 1 kHz. It is seen from this figure that the signal amplitude decreases substantially as the distance from the heating point (corresponding to 75 GHz) increases. It should be noted that the 71 GHz signal represents emission from the “suprathermal” electron component.

The experiments were carried out at various ECRH power modulation frequencies (1, 2, and 4 kHz) and various values of the magnetic field on the axis $R = 1$ m (1.31; 1.34 and 1.36 T). The contours of constant value of the magnetic field (see Fig. 1) were used to identify the spatial location of the ECE signals and to refer these signals to the plasma radius. The resulting profiles are demonstrated in Fig. 4 for $B = 1.34$ T and Fig. 5 for $B = 1.36$ T. It is seen from these figures that the amplitude of the modulated signal ΔT_e decreases nearly by 2-fold at $a/r = 0.3$ for $B = 1.34$ T and at $a/r = 0.2$ for $B = 1.36$ T. It should be noted that both profiles demonstrate a strong broadening of the absorption region. A similar broadening of the absorption region was obtained for the W7-AS stellarator [2]. Theoretical calculations presented in [10] have shown that appearance of suprathermal “tails” and broadening of the absorption region can take place in the L-2M as well. Moreover, an intricate

topology of the magnetic field in the L-2M leads to extended power-deposition profiles (see, e.g., Fig. 6). It is likely that this factor can also contribute to broadening of experimental profiles of the absorbed power.

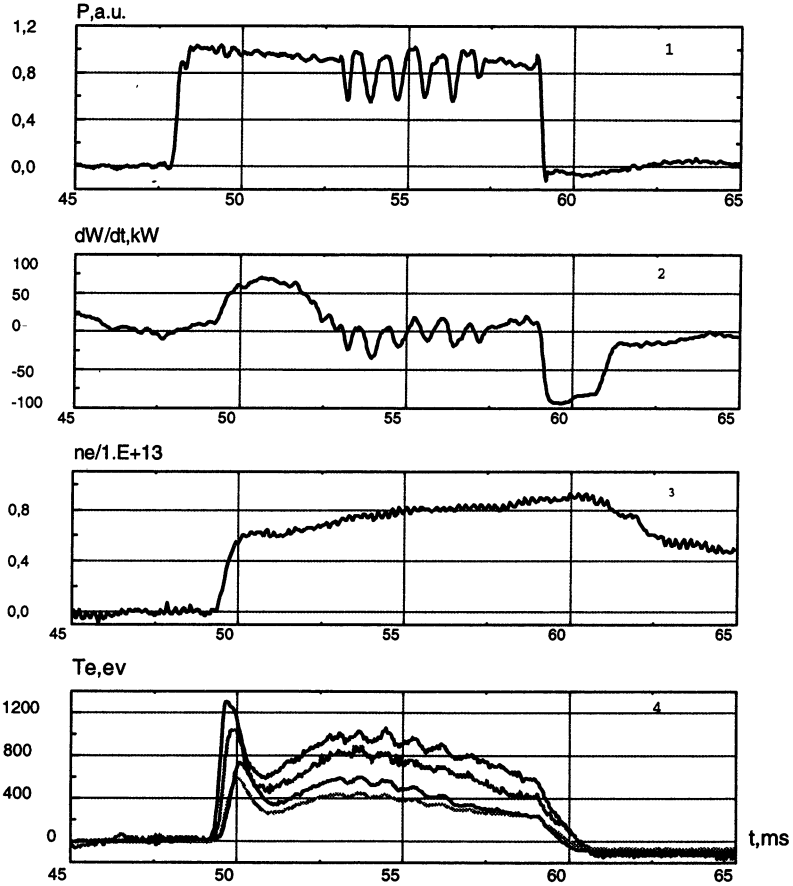


Fig. 2. Typical waveforms of the discharge: 1 - ECRH power (P_{in}), 2 - dW/dt (absorbed power, P_{abs}), 3 - average density, 4 - ECE signals.

Our previous ECRH experiments [4, 9] have shown that increasing the magnetic field to $B = 1.38$ T was not accompanied by a decrease in the central electron temperature as expected for the “off-axis” heating conditions. This effect has been attributed to the Shafranov shift of the magnetic surfaces center. The SXR measurements of the profiles $T_e(r)$ also show that at $B < B_{res}$ (Fig. 7a), the profile $T_e(r)$ flattens,

and the central temperature decreases as compared to the resonance case (Fig. 7b). On the contrary, at $B > B_{res}$ (Fig. 7c), no broadening of the profile $T_e(r)$ and no decrease in the central temperature was observed up to $B = 1.38$ T. These experiments conflict with the ray-tracing calculations of the power deposition profile (Fig. 6) which predict the off-axis displacement of the absorption region for higher magnetic fields.

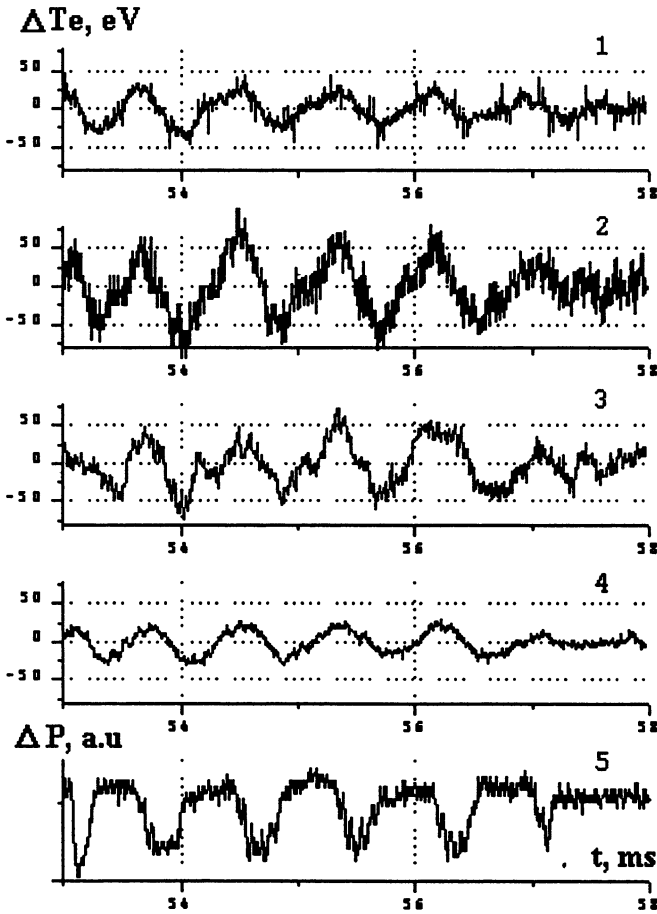


Fig. 3. Amplitude-modulated signals: 1 - 71 GHz, 2 - 76.5 GHz, 3 - 78 GHz, 4 - 81 GHz, 5 - ECRH.

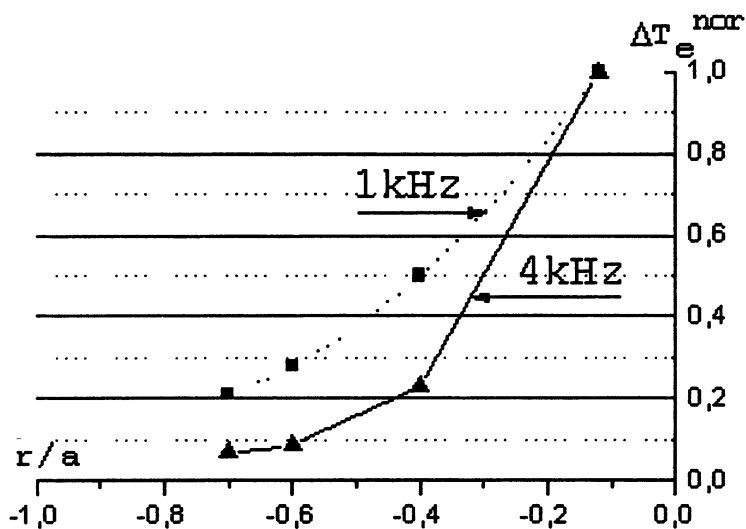


Fig. 4. ΔT_e as a function of r/a for a modulation frequency of 1 and 4 kHz. Magnetic field is $B = 1.34$ T.

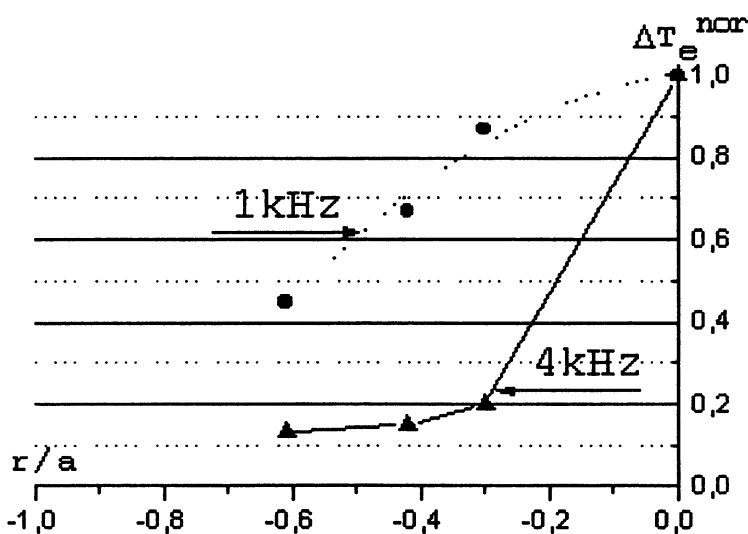


Fig. 5. ΔT_e as a function of r/a for a modulation frequency of 1 and 4 kHz. Magnetic field is $B = 1.36$ T.

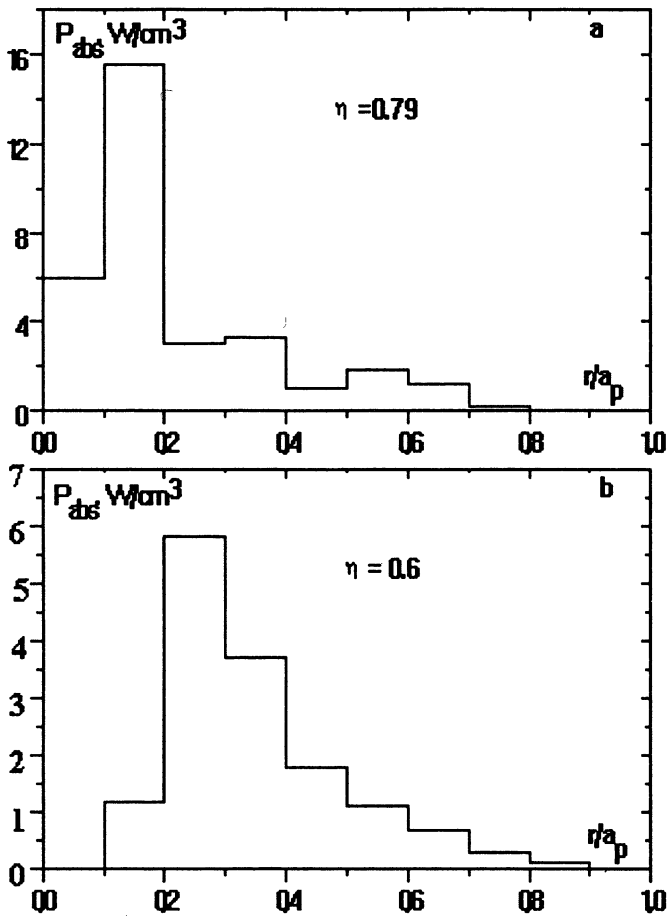


Fig. 6. The ray-tracing of absorbed power profile for the two cases at average density $n_e = 10^{13} \text{ cm}^{-3}$, the center of magnetic surfaces is $R_{ax} = 100 \text{ cm}$; *a* - $T_e(0) = 1 \text{ keV}$, $B = 1.34 \text{ T}$, $R_{gyr} = 100 \text{ cm}$; *b* - $T_e(0) = 1,2 \text{ keV}$, $B = 1.36 \text{ T}$, $R_{gyr} = 102,5 \text{ cm}$.

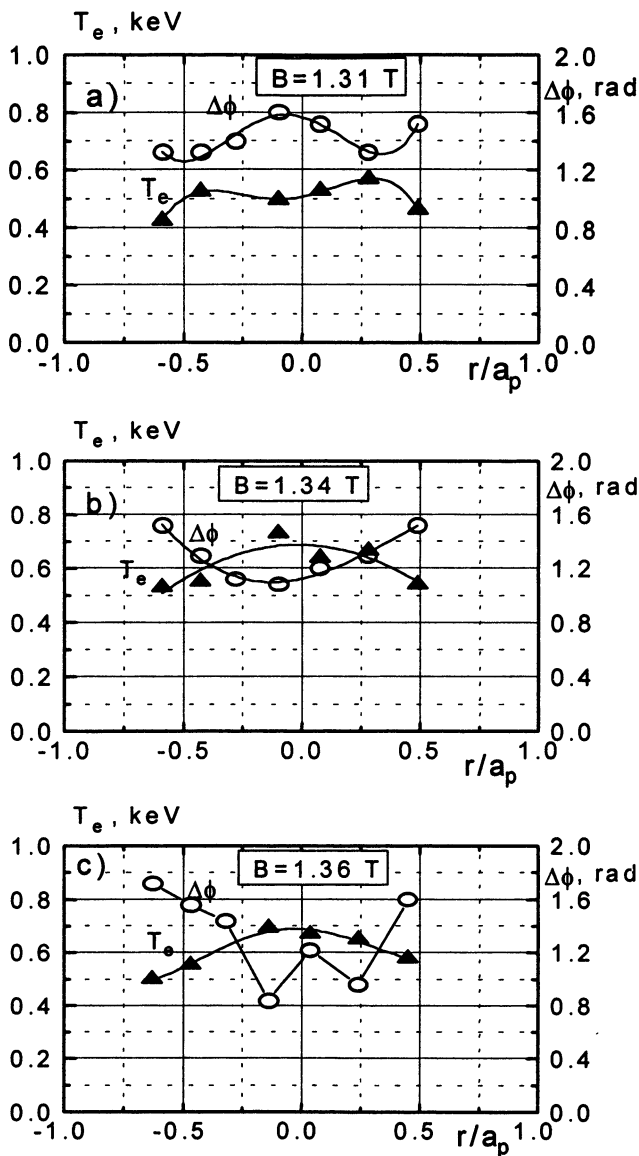


Fig. 7. Soft X-ray data on the profile $T_e(r)$ and phases for different magnetic fields: a) $B_{res} > B = 1.31$ T; b) $B_{res} = B = 1.34$ T; c) $B_{res} < B = 1.36$ T.

Phase Shifts of Modulated Signals

The ECRH power modulation causes the periodic heat flux perturbations due to periodic variations in the gradients. Propagation of the perturbed temperature signal through the ECRH power absorption region was investigated in many devices with the time-dependent ECE and soft X-ray signals and was used to determine the plasma heat conductivity. However, despite the simplicity of the experiment statement, the experimental results, not always, can be described by available theoretical models based on diffusion processes only [1, 2, 11-13].

In the experiments, we used a conventional Fourier analysis, and the phase values were obtained from the crosscorrelation function of ECRH, ECE and SXR signals. As is known, the minimum phase is observed in the microwave power absorption region. Figure 7 shows the phase of SXR signals as a function of the mean plasma radius for three values of the magnetic field. It is seen that, for $B = 1.31$ T, the absorption region is shifted from the center (see Fig. 7, *a*) to the radius $r/a \sim 0.5$, whereas for $B = 1.34$ T, this region lies in the center, which coincides with the ray-tracing calculations. At the same time, it is evident from Fig. 7, *c* that, for $B = 1.36$ T, the absorption region lies near the center, contradicting the ray-tracing calculations. Figs. 8, 9 show the phase as a function of the ECE frequency for two modulation frequencies of 1 and 4 kHz and two magnetic field of 1.34 and 1.36 T. As is seen from these figures, the minimum phase is observed for the 71 GHz signal, which indirectly indicates that this emission originates in the heating region (the gyrotron frequency is 75 GHz). As the modulation frequency increases, the minimum phase increases and exceeds $\Delta\phi > \pi/2$. In accordance with [13], this evidence suggests that the plasma thermalization does not occur instantaneously, in which case the kinetic effects in the process of energy absorption should be taken into account [12]. Figs. 10, 11 show the phase as a function of the plasma radius. In this case, the points corresponding to a ECE frequency of 71 GHz are tentatively referred to the radius of the resonance region. For $B = 1.34$ T, the resonance region is situated at $R = 100$ cm (which is the magnetic axis radius - R_{ax}); for $B = 1.36$ T, this radius is $R = 102.5$ cm.

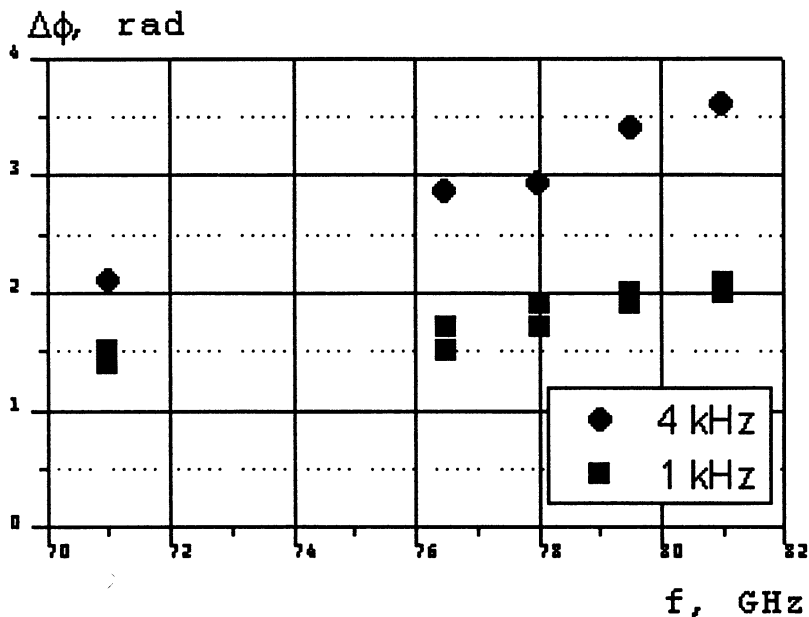


Fig. 8. ECE data on the phase for a modulation frequency of 1 and 4 kHz. Magnetic field is $B = 1.34$ T.

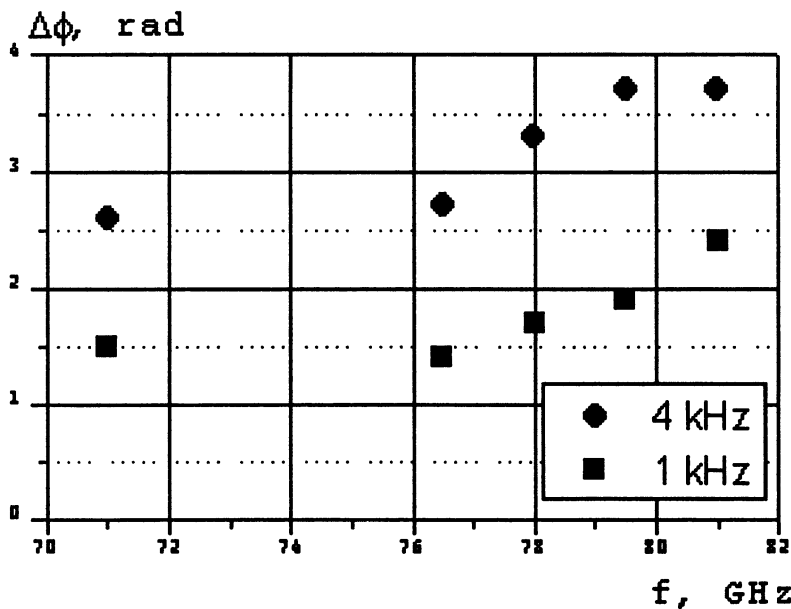


Fig. 9. ECE data on the phase for a modulation frequency of 1 and 4 kHz. Magnetic field is $B = 1.36$ T.

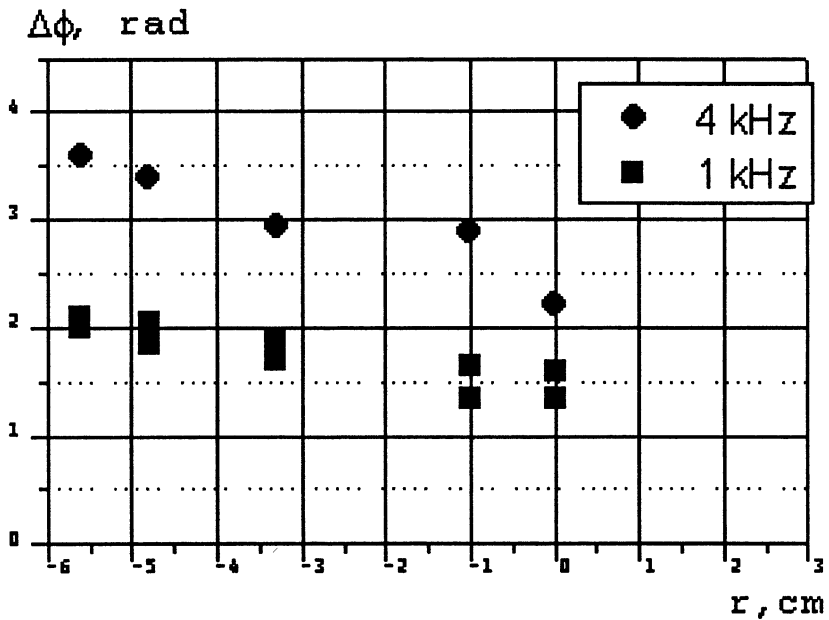


Fig. 10. ECE data on the phase as a function of radius for $B = 1.34T$.

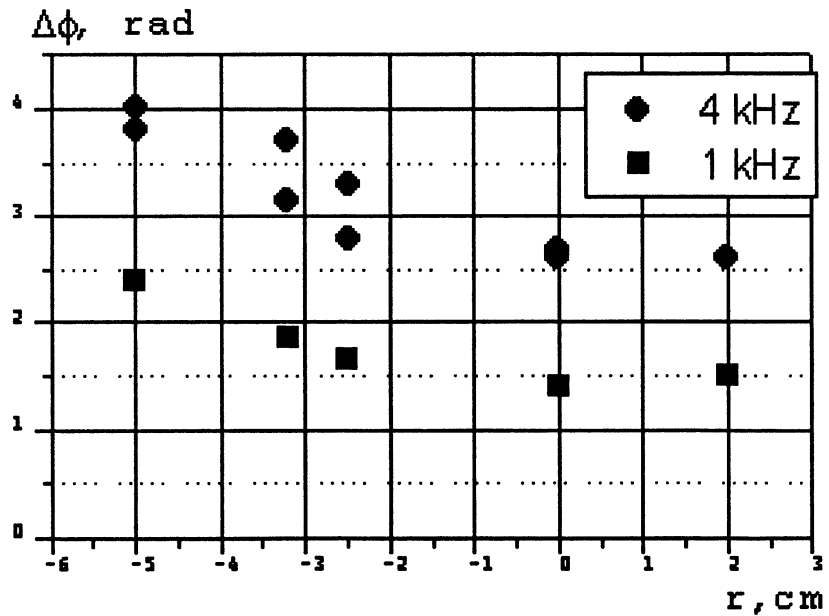


Fig. 11. ECE data on the phase as a function of radius for $B = 1.36T$.

The phases φ and amplitudes of a harmonic component of the electron temperature perturbation ΔT_e , observed for the 1 kHz modulation frequency, were used to estimate the electron heat diffusivity by the simplified formula [11]

$$\chi = 3\omega/4\varphi'(\Delta T_e' / \Delta T_e + 1/2r), \quad (2)$$

which gives the value of the electron heat diffusivity outside the beam absorption region. The values $\chi \sim 2.5 \cdot 10^5 \text{ cm}^2/\text{s}$, obtained for $r = 3-5 \text{ cm}$, turn out much higher than the estimates that follow from simple calculations of electron heat conductivity on a basis of the power balance or neoclassical calculations for simple types of the power deposition profiles [14, 15]. The experimentally observed features in plasma heating and power absorption region should be taken into account in constructing a more exact model consistent with the experiment.

Conclusion

1) First ECRH power modulation experiments in the L-2M have been carried out, and data on $\Delta T_e(r)$ and $\varphi(r)$ have been obtained with the ECE and SXR diagnostics.

2) The absorption region has determined for various values of the magnetic field. Comparison with the ray-tracing calculations shows that the experimentally obtained location of the heating region is consistent with the calculated ECRH power deposition profiles for $B \leq B_{res}$, but not for $B > B_{res}$.

3) The observed phases of modulated signals support the conclusion of [12] that their value can exceed $\varphi > \pi/2$, which indicates that in studies of the wave absorption in plasma it is necessary to take into account kinetic effects.

4) The estimated value of the electron heat diffusivity turns out be higher than the expected values, in which case it seems reasonable to modify the available code by including realistic processes occurring in the region of energy release.

References

1. Lopes Cardozo N.J. Plasma Phys. Control. Fusion 1995, 37, 799.
2. Gasparino U., Erckmann V., Hartfuss H.J., et al., Proc. 10th Joint Workshop on ECE and ECRH, Ameland, 1997, 411.
Hartfuss H.J., Maassberg H., et al., Nucl. Fusion 1986, 26, 678.
- Rome M., Erckmann V., Gasparino U., Hartfuss H., Kuhner G., Maassberg H., Marushchenko N. Plasma Phys. Control. Fusion 1997, 39, 117.

3. Abrakov V., Akulina D. et al., Nucl. Fusion, 1997, 37, 233.
4. Akulina D., Batanov G. et al., Proc. 10th Joint Workshop on ECE and ECRH, Ameland, 1997, 341.
5. Meshcheryakov A., Grebenshchikov S., et al., J. Plasma and Fusion Res. Series, 1998, 1, 350.
6. Akulina D., Gladkov G., et al., Plasma Phys. Rep., 1997, 23, 28.
7. Likin K., Ochirov B. Sov. J. Plasma Phys. (Engl. Transl.), 1992, 18.
8. H. Hartfuss, V. Erckman et al., Proc. EC-9, Bornego Springs, 1995, 445.
9. Grebenshchikov S., Akulina D., et al., J. Plasma and Fusion. Res. Series, 1998, 1, 41.
10. Tereshchenko M., Sakharov A. Proc. 1998 Congress of PP and 25th EPS Conf. on CF and PP, paper P2.092.
11. Gorini G., Mantica P., et al., Phys. Rev. Lett., 1993, 71, 2038.
- Jacchia A., et al., Phys. Fluids B 3, 1991, 11, 3033.
- Peters M., Hartfuss H., et al., Proc. 23rd Europ. Conf. on PP and CF, Montpellier, 1994, 18B, p.1, 158.
12. Giruzzi G., Se`gui Y., et al., Phys. Rev. Lett., 1995, 74, 550.
13. Elena de la Luna, Krivenski V., J. Plasma and Fusion Res. Series, 1998, 1, 354.
14. Akulina D. Andrukhina E., Batanov G., et al., Proc. Intern. Conf. on PP and CF, Washington, 1990, (IAEA, Vienna, 1991), 2, 693.
15. Grebenshchikov S., Danilkin I., Mineev A., Plasma Phys. Rep., 1996, 22, 609.

RECONSTRUCTION OF THE ECRH POWER DEPOSITION AND ELECTRON HEAT CONDUCTIVITY FROM SXR INTENSITY EVOLUTION AFTER SHUT-OFF ECRH IN T-10

A.V.Sushkov, V.F.Andreev, Yu.N.Dnestrovskij, K.A.Razumova

RRC 'Kurchatov Institute', Moscow, Russia

Introduction

The ECRH system of T-10 tokamak ($R=1.5$ m, $a=0.3$ m) consist of 4×0.4 MW gyrotrons at 140 GHz (2-nd harmonic, X-mode). The EC waves launching to the plasma from the low field side with the angle 21° to the major radius of the torus. Variation of the toroidal magnetic field allows to make ECCD experiments with on-axis or off-axis deposition. Determination of the EC power deposition profile is important for the analysis of the experimental results.

The power deposition can be determined from the time derivative of the electron temperature variation after switch-on or switch-off of the ECRH. However time derivative of the electron temperature can not be determined for short enough time due to noise of the experimental signals. Therefore calculated deposition profile are always wider then real one because of broadening of the electron temperature perturbation with time due to the heat diffusion [1].

In this paper we determine the ECRH power deposition profile from the time variation of the electron temperature by solving the inverse problem for transport equations and reconstructing the transport coefficients and the heat source. The inverse problem is formulated for transients process with switch-on or switch-off the additional heating power. This process is considered on a small temporal interval, thus the change of integral plasma parameters can be neglected.

Statement of the problem

The dynamic process, which happens during the gyrotrons switch-off or switch-on, can be described as follows. The heat conductivity equation for the steady-state electron temperature $T^S(r, t)$, (with index 's') before switch-off can be written as :

$$\frac{3}{2} \frac{\partial}{\partial t} (n^S T^S) = \frac{1}{r} \frac{\partial}{\partial r} \left(r K^S \frac{\partial T^S}{\partial r} \right) - \frac{1}{r} \frac{\partial}{\partial r} (r V^S T^S) + P_{OH}^S + Q^S + P_{EC}^S, \quad (1)$$

$$\frac{\partial T^S}{\partial r} (r=0, t) = 0, \quad T^S(r=1, t) = T_0, \quad 0 < r < 1, \quad t = t_S,$$

and heat conductivity equation for the electron temperature $T(r, t)$, corresponding to the transient process after the gyrotrons switch-off (without index) is

$$\frac{3}{2} \frac{\partial}{\partial t} (nT) = \frac{1}{r} \frac{\partial}{\partial r} \left(rK \frac{\partial T}{\partial r} \right) - \frac{1}{r} \frac{\partial}{\partial r} (rVT) + P_{OH} + Q, \quad (2)$$

$$\frac{\partial T}{\partial r} (r=0, t) = 0, \quad T(r=1, t) = T_0, \quad T(r, t=t_S) = T^S(r), \quad 0 < r < 1, \quad t > t_S.$$

Here $n^S(r, t)$ and $n(r, t)$ are the electron densities, t_S is the time instant, when the gyrotron is switched-off, T_0 is the boundary temperature, $K^S = n^S \cdot \chi_e^S$ and $K = n \cdot \chi_e$ are the heat conductivities, $V^S = n^S \cdot u_e^S$ and $V = n \cdot u_e$ are the heat pinch velocities, P_{OH}^S, P_{OH} are the ohmic heating powers, Q^S, Q are another heat losses before and after the gyrotron switch-off, P_{EC} is the additional heating power. During the transient process the electron temperature $T(r, t)$ can be presented as the sum of its steady state value $T^S(r, t)$ and an increment $\Delta T(r, t)$, i.e.

$$T(r, t) = T^S(r, t) + \Delta T(r, t).$$

We subtract Eq. (1) from Eq. (2) and expand the ohmic heating power P_{OH} and heat loss power Q relatively ΔT , omitting the second order terms $O(\Delta T^2)$. Thus we obtain the following equation:

$$\begin{aligned} \frac{3}{2} \frac{\partial}{\partial t} (n\Delta T) = & \frac{1}{r} \frac{\partial}{\partial r} \left(rK \frac{\partial \Delta T}{\partial r} \right) - \frac{1}{r} \frac{\partial}{\partial r} (rV\Delta T) - P_{EC} + P_{OH}(T^S) \cdot \Delta T + Q(T^S) \cdot \Delta T \\ & + \left\{ \frac{3}{2} \frac{\partial}{\partial t} [(n-n^S)T^S] + \frac{1}{r} \frac{\partial}{\partial r} \left[r(K-K^S) \frac{\partial T^S}{\partial r} \right] - \frac{1}{r} \frac{\partial}{\partial r} [r(V-V^S)T^S] \right\}. \end{aligned} \quad (3)$$

We assume that the steady state temperature gradients are much less than the dynamic temperature gradients, therefore as a first approximation, we do not take into account the terms describing the change of transport coefficients. In the report we study shots where the

ohmic heating power P_{OH} and heat loss Q are considerably less than the deposited power P_{EC} , therefore we can also omit the terms describing the change of P_{OH} and Q . As a result, we obtain the approximate linear equation for ΔT :

$$\frac{3}{2} \frac{\partial}{\partial t} (n\Delta T) = \frac{1}{r} \frac{\partial}{\partial r} \left(rK \frac{\partial \Delta T}{\partial r} \right) - \frac{1}{r} \frac{\partial}{\partial r} (rV\Delta T) - P_{EC}, \quad (4)$$

$$\frac{\partial \Delta T}{\partial r} (r=0, t) = 0, \quad \Delta T(r=1, t) = 0, \quad \Delta T(r, t=t_0) = 0.$$

Numerical algorithm of the solution

Let we know the experimental values of increments of the electron temperature f_i^k , measured in N radial points: $i = 1, \dots, N$, and in M temporal points: $k = 1, \dots, M$, also we know the global parameters: the total current, ohmic heating power, major and minor radii. The discrepancy functional can be written as:

$$J = \frac{1}{2} \sum_{k=1}^M \sum_{i=1}^N \gamma_k \left[\Delta T(\rho_k, t_i) - f_i^k \right]^2 / \sum_{k=1}^M \sum_{i=1}^N \gamma_k \left[f_i^k \right]^2. \quad (5)$$

where γ_k are the weight factors, which are selected in accordance with the reliability of measurements in the every channel.

The inverse problem is formulated as follows. We should find the additional heating power P_{EC} , heat conductivity K and heat pinch V such as the solution $\Delta T(r, t)$ of equation (4), provides the minimum of the functional (5).

We expand the unknown functions K , V and P_{EC} over some given basis [2,3]:

$$K(r) = \sum_{j=1}^{M_K} k_j \cdot \varphi_j^K(r), \quad V(r) = \sum_{j=1}^{M_V} v_j \cdot \varphi_j^V(r), \quad (6)$$

$$P_{add}(r) = A \cdot \exp \left[- \left(\frac{r - r_0}{2w} \right)^\alpha \right],$$

where $\varphi_j^K, \varphi_j^V = \{1, x, x^2, x^3, \dots\}$ are the polynomial, r_0, w are the position of the centre and e-fold width of the additional heating profile,

A and α are the constants. Thus the solution of the inverse problem is reduced to the finding of the unknown parameters $P = \{k_j, j = 1, \dots, M_K, v_j, j = 1, \dots, M_V, A, r_0, w, \alpha\}$ from the condition of the functional (5) is minimum.

We use the method of iterational regularization [4] for the solution of the inverse problem, which is as follows:

- 1) we set the initial vector of parameters to be found $P^S, s = 1$, and solve the equation (4);
- 2) we calculate the gradient of the discrepancy functional (5), ∇J^S , and the vector of depth of descent, h^S ;
- 3) we find the new approximation of parameters to be found from the relation $P^{S+1} = P^S + h^S \cdot \nabla J^S$.

The minimum of functional (5) gives the solution of the inverse problem (4)-(6).

Results of numerical calculations

As the ECE channels on T-10 not allows measured electron temperature profile with good enough spatial resolution we use the SXR intensity measurements for determination of $T_e(r, t)$. On T-10 the SXR intensity I_{SXR} was measured along 40 chords with the spatial resolution $\Delta r = 1-1.5$ cm and temporal resolution $\Delta t = 40 \mu s$. After Abel reconstruction of local SXR intensity $I_{SXR}(r)$ the electron temperature variation determines from variation of $I_{SXR}(r)$ in accordance with relation:

$$I_{SXR} \propto f(Z_{eff}) \frac{n_e^2}{\sqrt{T_e}} \int_0^{\infty} \exp\left(\frac{-E}{T_e}\right) \eta(E) dE. \quad (7)$$

In (7) the $\eta(E)$ is the energy dependence of the SXR-detector sensitivity and Maxwell distribution of electrons is suggested. We also assume that the electron density and Z_{eff} profiles not changed for the short time interval which we use for calculations. The electron temperature profile measured by Thomson scattering diagnostic before the EC power switch-off is used for calibration of SXR channels.

The results of calculations for T-10 shot #23281 ($I=75$ kA , $B=2.35$ T) with of-axis EC power deposition are presented on figures 1-4.

Figure 1 presents time traces of the SXR intensity for some various chords after gyrotrons switch-off. Time $t=800.5$ ms corresponds to gyrotrons switch-off.

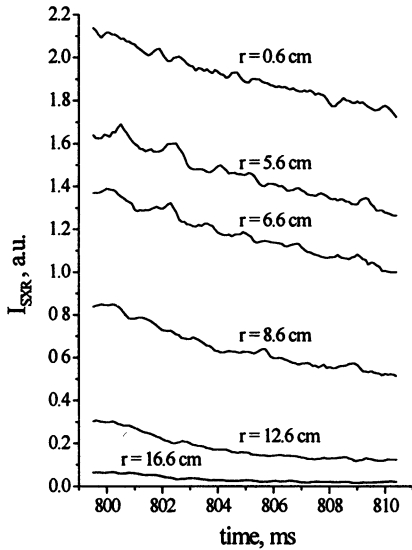


Fig.1. Time dependence of SXR intensity signals for various chords. Time $t=800.5$ ms corresponds to gyrotron switch-off.

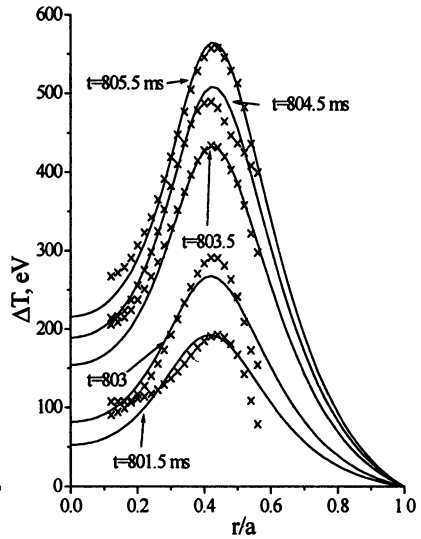


Fig.2. Increment of the temperature for some time instants. Solid lines are the solution of the inverse problem, crosses are experimental temperature.

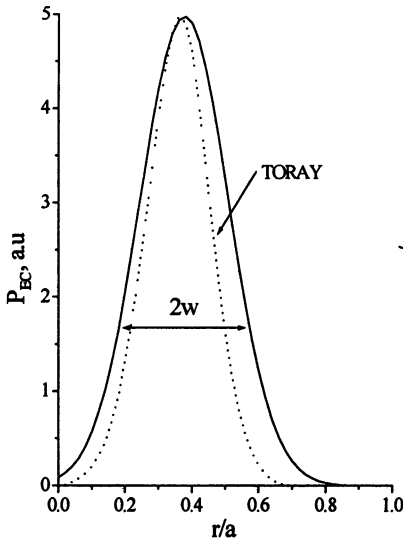


Fig.3. Deposition profile of EC power with parameters $r_0=0.113$ m, $w=0.048$ m, $\alpha=2$. Dashed line shows ray tracing calculation.

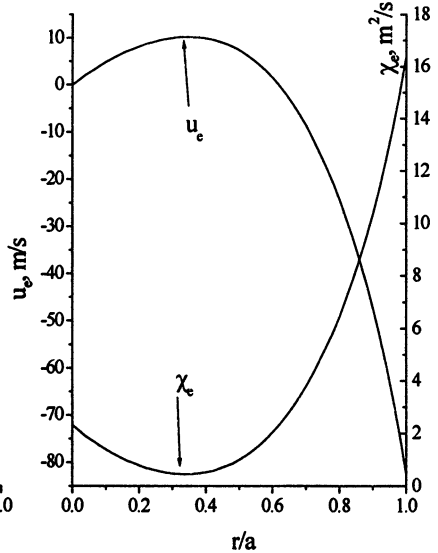


Fig.4. Radial dependences of the heat diffusivity $\chi_e(\rho)$ and heat pinch velocity $u_e(\rho)$.

Figure 2 presents the increments of the electron temperature $\Delta T(r, t)$ at different time instants. The crosses correspond to the experimental values of the temperature, the solid lines show the solution of the inverse problem (4)-(6).

Figure 3 shows the power deposition profiles versus normalized radius. The solid line shows the obtained profile of deposited EC power with following parameters:

$$P_{EC}=0.65 \text{ MW}, \quad r_0 = 0.113 \text{ m}, \quad w = 0.048 \text{ m}, \quad \alpha = 2.$$

The dashed line shows the results of ray tracing calculations [5].

In Figure 4 the calculated heat diffusivity $\chi_e(r)$ and heat pinch velocity $u_e(r)$ are shown.

Conclusion

A new method of reconstruction of the ECRH power deposition profile from SXR intensity evolution after shut-off ECRH, based on solution of inverse problem is proposed. It takes into account a broadening of the electron temperature perturbation with time due to the heat diffusion. This allows to use the experimental data from not very small time interval and to determine the power deposition profile with a high accuracy. This method allows us to find the heat conductivity and heat pinch velocity profiles also.

This work was supported by Russian Basic Research Foundation Grant № 98-02-16277.

References

1. Leuterer F. et al., 24-th EPS Conf. Contr. Fus. and Plasma Phys. Part IV, (1997), 1533.
2. Andreev V.F., Dnestrovskij Yu.N., Popov A.M., Nucl. Fusion, v. 33 (1993) p. 499-504.
3. Andreev V.F., Dnestrovskij Yu.N., Razumova K.A., Sushkov A.V., 24-th EPS Conf. Control. Fusion and Plasma Phys. Part II, (1997), 937.
4. Alifanov O.M., Artjuhov E.A., Rumjantsev S.V. Extremal Method of the Solution of Ill-posed Problems, Nauka, Moscow, 1988. (in Russian)
5. Cohen R. H. Effect of trapped electrons on current drive. Phys. Fluids, 30(8) 1987, 2442.

MEASUREMENT OF PLASMA TRANSMITTED EC-WAVE POWER IN MAGNETIC FIELD MAGNITUDE SCANNING EXPERIMENT IN CHS

Y. Yoshimura, N. Sueoka, H. Idei, S. Kubo, K. Ohkubo,
M. Isobe, T. Minami, S. Nishimura, M. Osakabe,
K. Tanaka, C. Takahashi, S. Okamura, K. Matsuoka

National Institute for Fusion Science, Toki, Japan

Transmitted EC-wave power through plasmas has been measured at the opposite port to an EC-heating wave injection antenna. Electric field components in two orthogonal directions are measured through rectangular waveguides. The property of wave polarization is changed and the waves are absorbed at resonance layers during their propagation in plasmas. The results from the transmitted power measurement as a function of magnetic field magnitude are analyzed by using numerical calculation. Dependence of the total transmitted power on the magnetic field magnitude can be roughly explained, though the components of the total transmitted power in vertical and toroidal directions have discrepancies with the calculation.

I. Introduction

Absorption of heating EC-wave in plasmas has been investigated theoretically, for example, by Bornatici *et al.* [1] Theoretically, the best absorption for second harmonic EC-wave of normal injection to magnetic flux surface is obtained when the electric field direction is perpendicular to the magnetic field direction (second harmonic X-mode resonance). Evolution of injected EC-wave in plasmas has also been studied. Both of the X- and O-mode waves vary their electric field direction according to a change in the magnetic field direction (magnetic shear) during their propagation. It is also pointed out that those two modes do not propagate independently, affected by the magnetic shear [2,3].

For localized heating, study of location-dependent relation between the directions of the electric field of the wave and the magnetic field is important. For this purpose, stellarators or torsatrons which make their rotational transform by external coils are favorable devices. The vacuum magnetic field is definitely given and plasma current has no essential effect on plasma confinement. Low plasma current does not modify the externally given magnetic field structure.

II. Experimental Setup

CHS is a heliotron/torsatron type device with low aspect ratio ($R/a = 1.0/0.2 = 5$). Its helical-coil winding is characterized by $l=2 / m=8$. The ECH system has two injection ways. One is for horizontal injection to horizontally elongated plasma cross section, and the other for vertical injection to vertically elongated plasma. All the data used

in this paper were obtained with the horizontal injection of EC-wave power and with the radius of plasma axis, R_{ax} , of 0.92 m. Setting R_{ax} as 0.92 m is standard for CHS operation so that plasma ignition and sustenance are most manageable. In Fig. 1, the vacuum magnetic field direction to the toroidal direction is shown as a function of the distance from the plasma axis along the horizontally injected wave path. A distribution of magnetic field magnitude B is also plotted. The B -distribution in heliotron/torsatron type device varies with two factors. One is the major radius, like tokamaks. The other is a distance from helical coils. Because of the pitch modulation of the helical coil windings, the peak of B -distribution along the wave injection path is placed at $R = 0.85$ m. Here, the peak is 7 cm inside from the plasma axis when $R_{ax} = 0.92$ m.

In horizontally elongated plasmas with $R_{ax} = 0.92$ m, the last closed magnetic flux surface (LCFS) extends from - 27 cm to 23 cm measured from the plasma axis. Here, minus sign means outside from the plasma axis. At the outer cross point of the LCFS and the wave path, the angle between the vacuum magnetic field and the toroidal direction is 30 degrees, and at the inner cross point - 40 degrees. Magnetic field component along the wave path is negligibly small in this configuration, so that the wave feels rotating magnetic field vector in the plane normal to the wave path. Here, the wave path is supposed to be linear, which is justified by that the path is almost parallel to density gradient and that the line-averaged density is less than one third of the cut-off density of the 53.2 GHz wave at $B = 0.95$ T.

The EC-wave power is generated by a gyrotron with a frequency of 53.2 GHz and maximum output power of 300 kW. The wave power is transmitted through a transmission line which is composed of plane and focusing mirrors, one polarizer, and waveguides. From an antenna system at an outer port of the vacuum vessel the power is injected into plasmas. The injection direction can be changed both toroidally and poloidally. For this transmitted power measurement experiment, the direction is fixed so that the waves propagate through the plasma axis. The polarizer in the transmission line can change the property of injected waves such as polarization direction and ellipticity.

At the opposite port to the horizontal injection antenna, two receivers which are composed of V-band rectangular waveguides, attenuators and shotkey-barrier diodes are installed to detect transmitted power through a sapphire vacuum window. Transmitted power components in vertical and toroidal directions corresponding to respective electric fields are measured simultaneously.

III. Magnetic Field Magnitude Scanning Experiment

Transmitted power was measured when the magnetic field magnitude was scanned in CHS. Keeping the basic distribution shown in Fig. 1, the B -distribution can be varied proportionally by changing

a parameter so called Bt . One plotted in Fig. 1 is of the case with $Bt = 0.88$ T. The EC-wave power comes from the left side of the figure. With $Bt = 0.875$ T, one of two positions of the 2nd harmonic resonant magnetic field magnitude, $B = 0.95$ T for 53.2 GHz EC-wave, is at the plasma axis and the other is about 14 cm apart from the plasma axis inwardly. Increasing Bt up to 1.0 T makes both the $B = 0.95$ T points further from the axis. One is 10 cm outside and the other 20 cm inside from the axis. On the other hand, decreasing Bt makes these two points nearer and with Bt of 0.845 T they come together at the peak point of the B -distribution. Decreasing Bt much more, there is no $B = 0.95$ T point on the first path of the wave, that means there is no resonance on the first path.

Figure 2 shows a set of typical waveforms in the experiment. Figure 2A shows the time sequence of heating powers. An ion Bernstein wave (IBW) power is applied from $t = 20$ ms to 53 ms for plasma ignition. From $t = 40$ ms, a neutral beam injection (NBI) with 500 kW is superposed on the IBW and during the NBI the plasmas are sustained. Two ECH pulses are injected. One is from $t = 11$ ms to 14 ms, and the other from 55 ms to 65 ms. The polarizer rotation angle is chosen so that the injected vertical power component is largest. The injected wave is approximated to be linearly polarized and its electric field is oscillating in the vertical direction. The multi-reflected component is evaluated to be less than 7 % from another measurement, and its effect is not taken into account here. There is no plasma when the first ECH pulse is injected so that it represents the injected EC-wave power. The second pulse is injected into low density, low temperature plasmas. The transmitted powers of the two pulses are compared to investigate the absorption and modification of the EC-waves by plasmas. The stored energy measured with a diamagnetic loop is presented in Fig. 2B and the line-integrated electron density on the center chord in Fig. 2C.

Typical examples of the measured transmitted power are shown in Fig. 3. The ordinate is the power in arbitrary unit but the ranges of the figures are same to be compared each other. Figure 3A and 3B show the measured powers of the electric fields oscillating in the vertical and toroidal directions with $Bt = 0.850$ T, respectively. Fig. 3C and 3D the powers in the vertical and toroidal directions with Bt of 0.806 T. As noted above, with $Bt = 0.850$ T EC-waves encounter 2nd-harmonic resonant areas, while with $Bt = 0.806$ T there is no resonant area on their first path. With $Bt = 0.850$ T, the sum of the transmitted vertical and toroidal components of the EC-wave power is much smaller than that of the injected components. The wave power is considered to be absorbed at the 2nd-harmonic resonances. With $Bt = 0.806$ T, the transmitted vertical component is smaller than the injected one (Fig. 3C), however, the transmitted toroidal component is larger than the injected one (Fig. 3D). Both the decrease in the vertical

component and the increase in the toroidal component should be attributed to the modification of the wave characteristics during the propagation in plasmas.

The experimental results are summarized in Fig. 4. The abscissa is Bt in tesla. The value of Bt was set to be 0.80 T, 0.835 T, 0.85 T, 0.875 T and 1.0 T. The ordinate is for the measured plasma transmitted power components in the vertical and toroidal directions, and they are normalized by the respective total injected powers. The closed circles depict the transmitted vertical component, transmitted toroidal component and the sum of these two components. Due to fluctuations on the raw data, averages during the pulse duration are plotted.

Each of the transmitted vertical component, toroidal component through the plasmas and the sum of them has its minimum with $Bt \approx 0.85$ T. With $Bt = 0.85$ T, the B -distribution near the resonant magnetic field magnitude 0.95 T has very small gradient so that the wave is under the resonant condition longer along its path. With Bt of 0.875 T, magnetic field at the plasma axis is 0.95 T. Having the EC-resonance at the plasma axis makes temperature profile peaked and the peak temperature high. The high temperature results in a good absorption with $Bt = 0.875$ T. With $Bt \approx 0.80$ T, that is, without resonance along the wave first path, the total transmitted power is about unity which means there is no absorption of the wave power. With $Bt \approx 0.835$ T, the wave path has no resonance either. However, the wave power of about 30 % is absorbed. With $Bt \approx 1.0$ T, the resonant areas come to considerably outer region of the plasmas where the electron density and temperature are lower, so that the absorption is not good.

IV. Discussion Using Numerical Calculation

The results in B -scanning experiment are qualitatively explained at the last part of section III. In this section, the results are examined by using numerical calculation. The framework of the calculation is the same with recent article by Nagasaki *et al.* [4] The evolutions of parallel (O-mode) and perpendicular (X-mode) components of the electric field to the magnetic field direction, E_{\parallel} and E_{\perp} , along the wave path are calculated by the following coupled equations,

$$\begin{aligned} \frac{d^2 E_{\parallel}}{dx^2} + \left(\frac{\omega^2}{c^2} N_o^2 - \eta^2 \right) E_{\parallel} &= 2\eta \frac{dE_{\perp}}{dx} + \frac{d\eta}{dx} E_{\perp}, \\ \frac{d^2 E_{\perp}}{dx^2} + \left(\frac{\omega^2}{c^2} N_x^2 - \eta^2 \right) E_{\perp} &= -2\eta \frac{dE_{\parallel}}{dx} - \frac{d\eta}{dx} E_{\parallel}, \end{aligned} \quad (1)$$

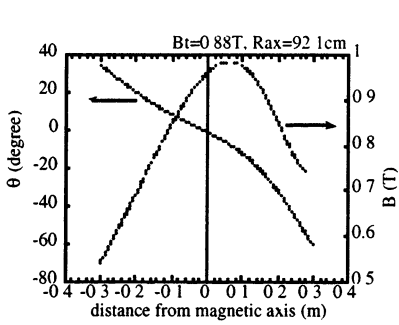


Fig. 1 Angle between the magnetic field direction and the toroidal direction as a function of distance from magnetic axis. The magnitude of magnetic field is also plotted.

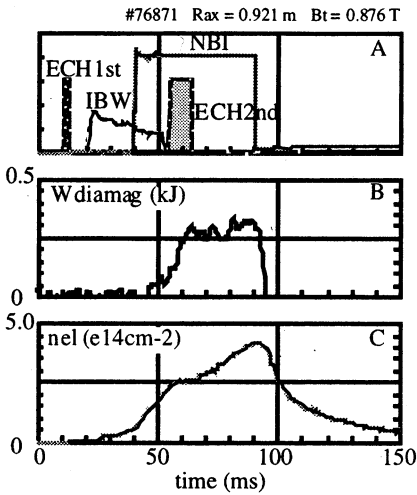


Fig. 2 Typical waveforms in the experiment. A: heating powers, B: stored energy and C: line-integrated electron density.

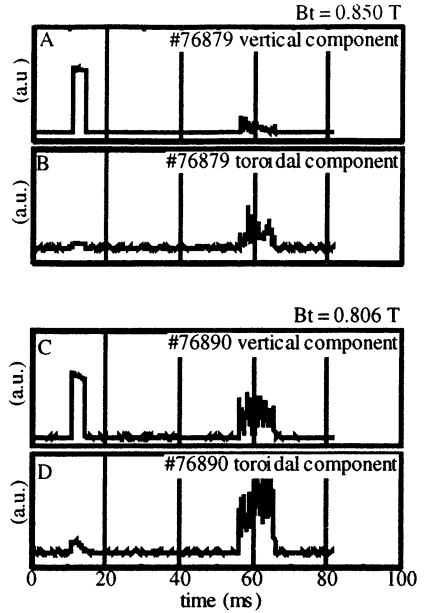


Fig. 3 Typical examples of the measured transmitted power. The ordinate is the power in a.u. but the ranges of the figures are same to be compared each other.

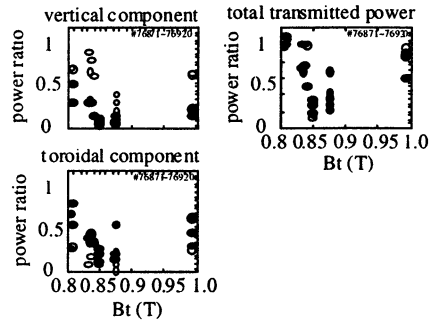


Fig. 4 Measured and calculated results.

where N_o and N_x denote the refractive indices of O- and X-mode waves, and η magnetic shear, respectively. Theoretical power absorption of X-mode component under the resonance condition is combined with the equations. All the region where the wave propagates (vacuum region outside the plasma, thin peripheral plasma and the core plasma) can be dealt with this procedure.

The total power is calculated as $N_o E_{//}^2 + N_x E_{\perp}^2$ and it is normalized to unity at the beginning of the injection. Electric field components in the vertical and toroidal directions, E_v and E_t are composed of $E_{//}$ and E_{\perp} using the angle θ between the magnetic field direction and the toroidal direction as

$$\begin{aligned} E_v &= E_{//} \sin \theta + E_{\perp} \cos \theta, \\ E_t &= E_{//} \cos \theta - E_{\perp} \sin \theta. \end{aligned} \quad (2)$$

The calculations are carried out for each plasma shots using respective measured parameters such as B_t , ne and Te . The results are plotted in Fig. 4 for comparison with the measured powers. In general, the dependence of the total transmitted power on B_t is explained by the calculation. Concerning with the vertical and toroidal components, difference between the calculation and the measurement is large. Most of this discrepancy might be attributed to the sensitivity of the calculated results to the magnitudes and profiles of ne and Te .

For example, with $B_t \approx 0.80$ T, setting ne for the calculation 20 % smaller than the measured value can change both the ratios of the calculated vertical and toroidal components to be about 0.5. The ratio as a function of position x are modified by the accumulation of phase

difference between the X- and O-modes, $2\pi \int (N_o - N_x) dx / \lambda$, and

coupling of these two modes due to the magnetic shear. The accumulation of phase difference causes a largest modification in the ratio calculated at the outside of the plasma after the transmission, while the modification in the ratio at the core plasma region is smaller. Absorption of X-mode component in the core plasma region diminishes the influence of the sensitivity. As a whole, the calculation roughly explains the total transmitted power while the discrepancies are large for the vertical and toroidal components especially with no or weak absorption cases.

References

1. M. Bornatici et al., Nucl. Fusion **23** (1983) 1153
2. I. Fidone et al., Nucl. Fusion **11** (1971) 133
3. A. Airoidi et al., Phys. Fluids B **1** (1989) 2143
4. K. Nagasaki et al., Phys. of Plasmas **6** (1999) 556

ECRH AND ECCD FOR THE STELLARATOR W7-X

*W. Kasperek**, *V. Erckmann***, *H.P. Laqua***, *E. Borie****,
*G. Dammertz****, *L. Empacher**, *W. Förster**, *G. Gantenbein**,
*S. Illy****, *G. Michel***, *G. Müller**, *B. Piosczyk****, *M. Thumm****,
*D. Wagner**, *M. Weißgerber***, *H. Zohm**, *W7-X and W7-AS Teams at*
*IPP Garching***, *W7-X Team at IPF Stuttgart**, *W7-X Team at FZK*
*Karlsruhe****.

*Institut für Plasmaforschung, Univ. Stuttgart, D-70569 Stuttgart, Germany

**Max-Planck-Institut f. Plasmaphysik, EURATOM Ass., 85748 Garching, Germany

***Forschungszentrum Karlsruhe, PMW, EURATOM Ass., D-76021 Karlsruhe, Germany

ECRH is the main heating system for steady state operation of the stellarator W7-X which is presently under construction at IPP Greifswald. A brief description of the W7-X Stellarator and predicted plasma parameters are presented. These predictions are based on ECRH and ECCD results from W7-AS. Several applications for the ECRH system are foreseen like: plasma start-up, electron heating with O-mode and X-mode, transport investigations, stimulated heat wave propagation, current drive, density and impurity control by profile shaping, studies of trapped/passing particle physics by ECCD methods, and diagnostics. To meet these objectives, a flexible, powerful and reliable electron cyclotron heating and current drive system is being developed with a total power of 10 MW CW at 140 GHz. At present, a 1 MW CW gyrotron with high efficiency due to a single-stage depressed collector is being developed. The main power for the electron beam is delivered by a HV switched power supply (< 65 kV); the acceleration voltage is precisely controlled by differential HV amplifiers. The microwave transmission from the gyrotrons to the plasma will be performed with purely optical elements including beam matching and polarising units and two multiple-beam waveguide systems. 12 individual launchers allowing a scan of the beam in poloidal and toroidal direction will be installed at different toroidal positions to provide the required high experimental flexibility for heating and current drive.

1. Introduction

The stellarator concept is investigated in many laboratories as an attractive approach in nuclear fusion research with magnetic confinement. In contrast to the tokamak, the magnetic field structure, which is required for equilibrium and stability of the confined plasma is generated by external coil currents only and stellarators therefore have an inherent steady-state capability. Electron Cyclotron Resonance Heating (ECRH) plays a key

role in stellarator research [1], because it provides net current free plasma start up from the neutral gas and efficient heating of the plasma. The capability to drive currents in the plasma (electron cyclotron current drive, ECCD) by oblique launch of the microwaves is an additional interesting option for physics investigations. The development of ECRH is thus very closely linked to the development of stellarators and their needs. One of the key issues for next step stellarators is the demonstration of continuous operation, with the consequence, that ECRH must have CW capability also. As an RF-heating method, ECRH decouples particle fuelling from energy transfer, which is of crucial importance for CW operation. In the stellarator line of IPP Garching, which comprises several generations of experiments, a significant progress in both, stellarator and ECRH development was achieved in a tight mutual interaction. A particular advantage for the development of the ECRH physics and technology is, that both, the W7-AS stellarator [2], which is in operation since 1988 and the W7-X stellarator, which is presently under construction, operate at the same magnetic induction of 2.5 T and consequently the ECRH systems have the same frequency of 70 (1st harmonic) or 140 GHz (2nd harmonic). At W7-AS, which is equipped with a strong and flexible ECRH system, the basic physics phenomena as well as technological concepts could be investigated and provide the basis for the ECRH system of W7-X. This installation is presently constructed and will provide a CW power of 10 MW at 140 GHz, and, at a later stage, additionally 2 MW at 70 GHz. In the following, the concept and goals of W7-X are described. The underlying physics will be highlighted with some illustrative results from W7-AS. In the main part, the ECRH system including gyrotrons, power supplies, millimetre wave transmission and in-vessel components is discussed.

2. The Stellarator W7-X

The physics goals for W7-X can be formulated as follows and have direct consequences for the design of W7-X and the heating systems:

1. demonstration of quasi steady-state operation in a reactor relevant plasma parameter regime, with temperatures $T_e = 2 - 10$ keV, $T_i = 2 - 5$ keV and densities $n_e = 0.1 - 2 \cdot 10^{20} \text{ m}^{-3}$
2. demonstration of good plasma confinement to improve the data base for reactor extrapolation
3. demonstration of stable plasma equilibrium at a reactor relevant nor-

malised plasma pressure $\beta \approx 5 \%$

4. investigation and development of a divertor to control plasma density and impurities

The physics objectives are achieved by a proper architecture of the magnetic configuration [3,8,9] introducing the concept of Advanced Stellarators (AS) [4,5,6]. Such advanced magnetic configurations are generally of 3-D nature and can be generated by modular twisted coils, which carry both, the required helical and toroidal current components [7]. The advanced stellarator concept with a modular coil system was successfully inaugurated with the construction of the partially optimized W7-AS stellarator, which is working at IPP Garching since 1988 and will remain operational until the year 2001.

W7-X will be housed in a new branch of IPP in Greifswald, Germany, the mechanical completion is scheduled for 2005. This device is a **HELICAL** Advanced Stellarator (HELIAS) [8,9] with strongly varying plasma cross section, 5 field periods (as was W7-A and W7-AS) and low shear. The major radius is 5.5 m, the averaged aspect ratio is about 10.

The modular coil system of W7-X is shown in Fig. 1a. 50 non-planar coils generate the confining magnetic configuration, the flux surfaces show a variation from a strong intended elongation (bean shape) in the $\Phi = 0^\circ$ plane to a triangular shape in the $\Phi = 36^\circ$ plane. The standard configuration has a 'built in' profile of the rotational transform with $\iota = 0.86$ on axis and 0.99 at the edge. A separate set of planar coils can be independently powered and allows a variation of the rotational transform from 0.75 to 1.01 on axis and 0.83 to 1.25 at the edge. Low and high shear configurations can be realised.

The reduction of the Pfirsch-Schlüter-currents is a key issue to reduce the Shafranov shift, thus the equilibrium becomes robust against high- β effects. This is seen in Fig. 1b,c, which shows the cross sections of the vacuum magnetic surfaces at 3 poloidal planes within one half field period, i.e. at a toroidal angle of $\Phi = 0^\circ$, 18° and 36° , respectively, for the vacuum configuration (Fig. 1b) and for $\langle \beta \rangle = 5 \%$ (Fig. 1c). The magnetic surfaces and the magnetic axis show a very small deviation from the vacuum configuration in the high- β case.

The modulus of the magnetic field varies along the toroidal direction such, that maxima occur at $\Phi = 0^\circ$, therefore the density of trapped particles is low at these planes.

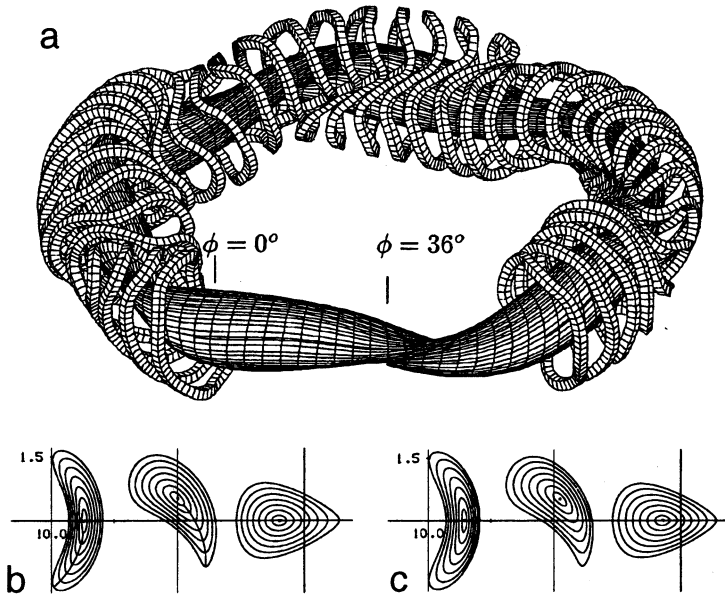


Fig. 1: a) The modular coil system of W7-X comprising 50 nonplanar coils (the additional 20 planar coils foreseen for experimental flexibility are not shown).
 b,c) Flux surfaces at three positions ($\Phi = 0^\circ$, $\Phi = 18^\circ$ and $\Phi = 36^\circ$) along one half magnetic field period for $\langle \beta \rangle = 0$ (b) and 5% (c), respectively.

The quasi steady-state operation of up to 30 min asks for a superconducting coil system, a divertor capable of high heat loads and a continuously operating heating system. Details on the design of the coils, the cryostat and the divertor can be found in [7].

3. ECRH and ECCD for W7-X

ECRH was chosen as the basic heating system for steady-state operation in the reactor relevant long mean free path (l.m.f.p.) transport regime. 10 MW of heating power are required to meet the envisaged plasma parameters, the operation frequency is 140 GHz, which corresponds to a resonant magnetic induction of 2.5 T at second harmonic. The standard heating scenario is 2nd harmonic extraordinary-mode (X2), launched perpendicularly to the confining magnetic field from the low field side. This scenario

always has complete absorption of the irradiated microwaves in a single transit through the plasma at all relevant plasma parameters ($T_e > 0.2$ keV) and provides safe plasma start-up. The plasma density,

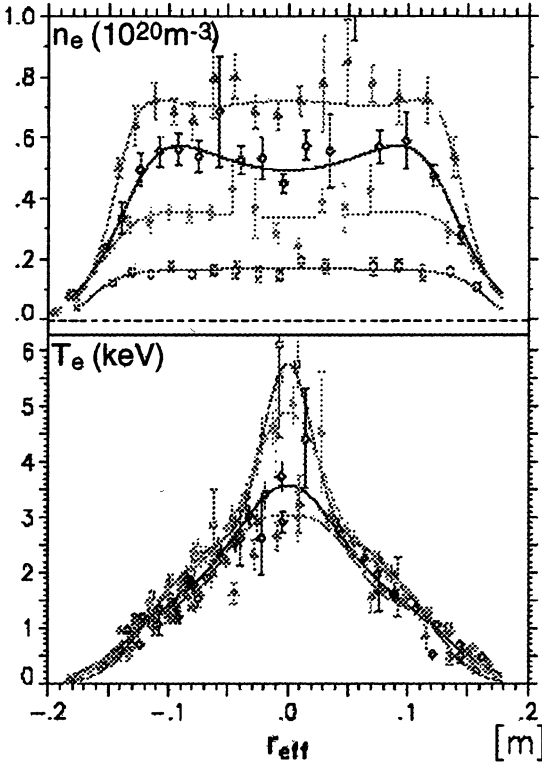


Fig. 2: Electron density n_e (top) and temperature T_e (bottom) as a function of the effective plasma radius r_{eff} for 1.3 MW ECRH power at 2nd harmonic X-mode with perpendicular launch obtained in W7-AS. The resonant magnetic induction is $B_0 = 2.5$ T, the ECRH frequency is 140 GHz.

however, is restricted with this heating scenario by the cut-off density of $1.2 \cdot 10^{20} \text{ m}^{-3}$. The power is deposited very localised around the resonance layer [10], which was proven experimentally at W7-AS [11].

As an example, radial profiles of the electron temperature and density for a constant ECRH power of 1.3 MW with X2-mode launch from the low field side are shown in Fig. 2. The underlying transport physics is discussed in [12]. As can be seen from Fig. 2, the electron temperature ranges from 3 keV at high densities of $n_e = 0.7 \cdot 10^{20} \text{ m}^{-3}$ to 5.7 keV at low electron densities of about

$0.15 \cdot 10^{20} \text{ m}^{-3}$. The central narrow power deposition and the resulting high power density is one reason for the strongly peaked temperature profiles. Predictive calculations [13] of the electron temperature in W7-X as a function of the ECRH-power for 3 different densities are shown in Fig. 3.

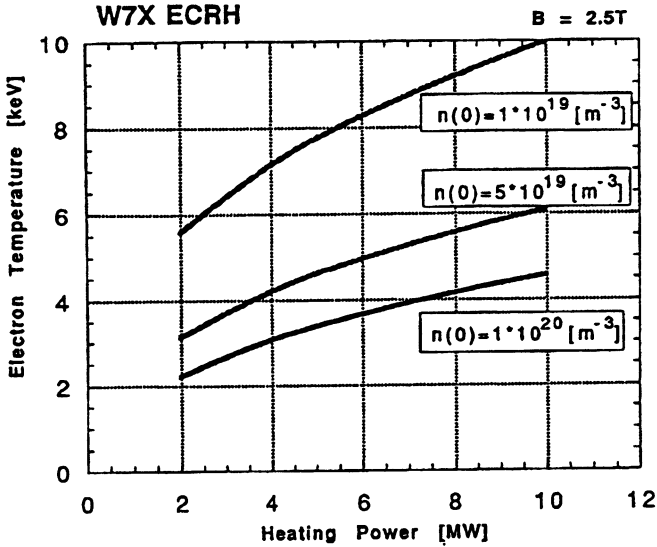


Fig. 3: Transport code predictions for the central electron temperature at W7-X as a function of the ECRH-power for 3 different central densities of 0.1 , 0.5 and $1.0 \cdot 10^{20} \text{ m}^{-3}$.

The maximum electron density in the calculations is compatible with the cut-off restrictions for X2-mode launch. Further extension of the density is possible using oblique launch at 2nd harmonic O-mode (O2) with a cut-off density of $2.5 \cdot 10^{20} \text{ m}^{-3}$. The plasma is, however, not optically thick at the W7-X parameters for this scenario. The single-pass absorption as calculated by ray-tracing is shown in Fig. 4 as a function of the density for several toroidal launch angles. The electron temperature profile was kept constant with an central electron temperature of 4 keV for the scan.

The single-pass absorption displays a broad maximum in the angular range $10^\circ < \varphi < 20^\circ$ and depends strongly on the electron temperature. As a consequence the O2-mode is not applicable for plasma start up and scenarios have to be developed, were the plasma is started with X2-heating while changing both the polarisation and the toroidal angle once the plasma is established and has reached sufficiently high electron temperature. Due to the incomplete single pass absorption, especially at high densities, one has to rely on multi-pass absorption [14]. Therefore it is neces-

sary to redirect the beam in a controlled way (e.g. mirrors) from the inner torus wall and, particularly in CW operation, to install special wall protections with appropriate heat removal to avoid structural damage.

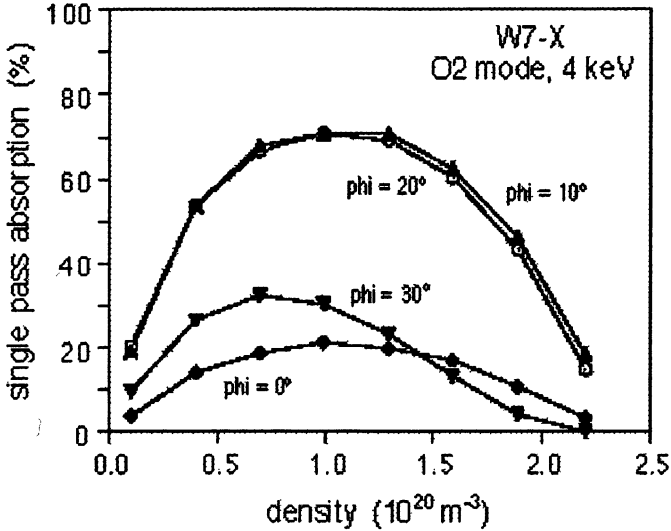


Fig. 4: Single pass absorption for 2nd harmonic O-mode in W7-X as a function of the central density for different toroidal launch angles ϕ assuming a central electron temperature of 4 keV.

Recently experiments with mode conversion heating via the Ordinary-Extraordinary-Bernstein (O-X-B) Mode conversion were successfully performed at W7-AS. This scenario works above the O-mode cutoff and has no density limit [15]. Efficient heating depends on the efficiency of the conversion process, which is very sensitive on the RF-beam quality and the density gradients of the plasma. This scenario is nevertheless of high importance, because it would allow to operate ECRH in combination with Neutral Beam Injection Heating (NBI) for high- β experiments in high density plasmas and low magnetic fields.

As there is no OH-transformer foreseen for W7-X, ECCD is a valuable tool to modify the internal current density distribution and operate with plasma net-current to investigate the physics of the rotational transform and shear as well as the current drive physics. Intense studies were per-

formed at W7-AS with ECCD [16], and up to 18 kA are driven at optimum launch angles of typically 20° . The maximum ECCD-efficiency $\eta_{\text{ECCD}} \equiv 15 \text{ A/kW}$ corresponds to a normalised efficiency of $\gamma_{\text{ECCD}} = n_e I_{\text{ECCD}} R / P_{\text{ECRH}} \equiv 0.0075 \cdot 10^{20} \text{ A/Wm}^2$. Both the absolute numbers of the driven current and the location of the maxima are well described by linear theory taking into account trapped particle effects and the measured profiles of T_e and n_e . At experiments with high (flux surface averaged) power densities of 50 MW/m^3 , hints for a degradation of the CD-efficiency have been found. As seen from Fig. 5 (right), fairly good agreement with linear theory is observed at these extremely high power densities for launch angles in counter direction; however, for launch angles in co-direction, some deviation occurs. These results from W7-AS will influence the launcher design for W7-X such that lower power densities will be used, at least for the majority of the antenna beams.

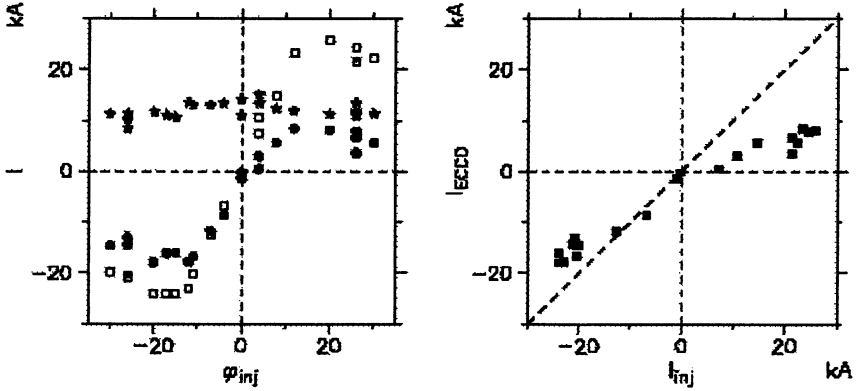


Fig. 5: Left: Theoretical (open squares) and data from current balance of the EC-driven current (dots) together with the bootstrap current (stars) as a function of the launch angle. Right: EC-driven current from current balance versus linear prediction.

Further applications foreseen for the EC system are investigation of trapped particle physics, measurement of electron transport via heat-wave propagation and collective Thomson scattering diagnostics [17].

4. The ECRH System for W7-X

4.1 General overview

It is evident, that the physics requirements and the different envisaged heating scenarios ask for an ECRH system with high flexibility, i.e. the system must be capable of

- arbitrary toroidal launch (current drive, O-mode, O-X-B conversion)
- arbitrary poloidal launch (on- and off-axis heating)
- arbitrary wave polarisation (linear for perpendicular launch, elliptical to circular for oblique launch)
- good power control (variation of temperature and density)
- AM capability (heat waves and switching experiments)

The system is thoroughly modularised and based on the idea, that each gyrotron can be operated separately from all others and without affecting the operation of other gyrotrons to increase the reliability of the overall system. This design also minimises the costs, because series production of identical modules is possible, and maximises the experimental flexibility.

A principle sketch of the ECRH system consisting of the millimetre-wave generator with high-voltage power supplies, the optical beam matching and polarising units, the long distance optical transmission line and the independently steerable plug-in launchers is shown in Fig. 6.

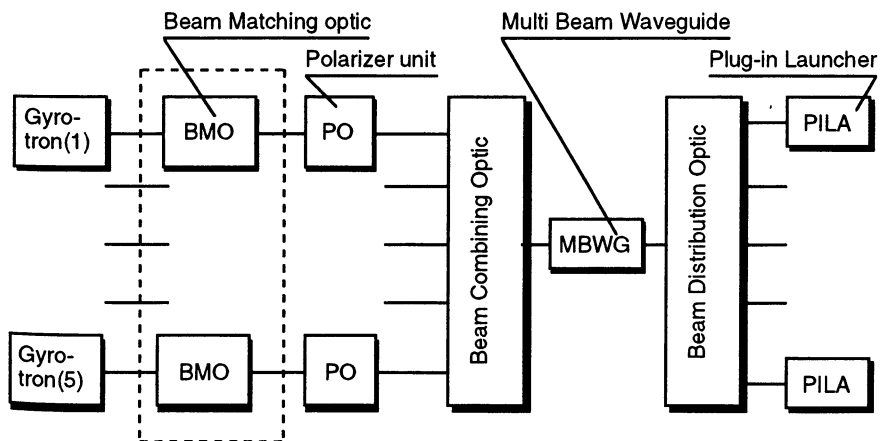


Fig. 6: Block diagram of the ECRH system

The arrangement of the gyrotrons and the transmission system in the ECRH building is seen from Fig. 7. The total ECRH power is generated by 10 gyrotron oscillators at 140 GHz with 1 MW output power in CW operation each. Two subgroups of 5 gyrotrons are arranged symmetrically to a central beam duct in the ECRH hall [18]. The ECRH building is prepared to house two additional 70 GHz gyrotrons in a later state of the experiment. These gyrotrons will be installed to ensure reliable start-up for NBI-heated high- β plasmas at reduced magnetic field of 1.25 T.

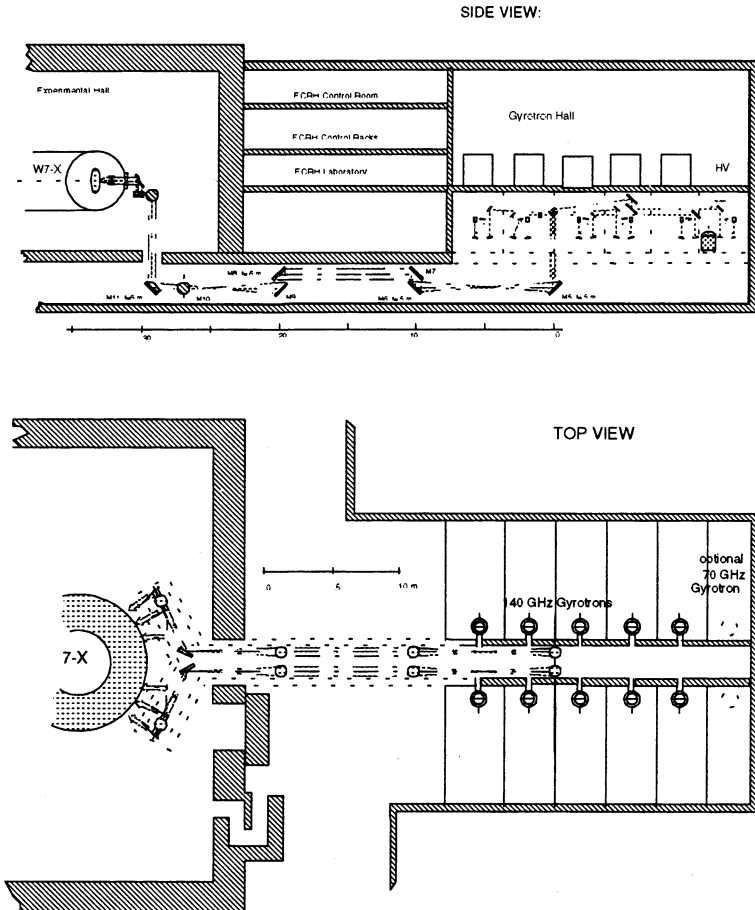


Fig. 7: Side view and top view of the ECRH system on W7-X.

4.2 Gyrotrons

The gyrotron for W7-X should be highly efficient, therefore voltage depressed collector techniques will be used. At present, the 140 GHz gyrotron are being developed with industries in Europe [19] and United States. The gyrotrons are equipped with a magnetron injection gun (MIG) of diode type. The European development aims at a gyrotron with an electron beam having an electron velocity ratio of $\alpha = v_{\perp}/v_{\parallel} = 1.3$. The electrodes of the MIG have been shaped to provide a low dispersion of $\Delta\alpha/\alpha = 1.2\%$ required for high efficiency interaction and low probability of mirroring. The cavity mode is $TE_{28,8}$ with a nominal quality factor of 1100 (calculated by self-consistent codes), the expected peak wall loading of the cavity is $\leq 2\text{kW/cm}^2$. A careful optimisation of the cavity was performed to keep the influence of possible deformations during heat-up reasonably low, i.e. to minimise the resulting frequency chirp, the increase of quality factor and the reduction of output power. Mode conversion is reduced by use of angle roundings and of a non-linear output taper. The resulting mode purity is calculated to be 99.9% (instead of 98.5% with no roundings and linear uptaper).

The RF beam is separated from the electron beam by a highly efficient quasi-optical mode converter, consisting of a rippled-wall waveguide launcher [20] followed by a quasi-elliptical mirror and two toroidal focusing mirrors which match the beam to the window size. The waist of the Gaussian beam (waist radius of $w_0 = 22\text{ mm}$) lies 220 mm outside the window. The launcher employs an improved perturbation structure leading to optimum phasing of the mode mixture and suppression of spurious oscillations. The calculated ohmic losses in the launcher and on the three mirrors are around 3.2%, the theoretical diffraction losses are only 1.1%. The output vacuum window unit uses a single, edge-cooled CVD diamond disc with an outer diameter of 106 mm, a thickness of 1.8 mm ($4\lambda/2$) and a clear aperture of 88 mm. Thermal finite element calculations show, that for a power of 1 MW at 140 GHz and a loss tangent of $4\cdot 10^{-5}$, the temperature rise of the window centre will be about 60 °C, the absorbed power will be only 700 W. Thus the total internal losses of the tube are expected to be about 8%.

The tube will have a single stage depressed collector for electron beam energy. The collector body together with the mirror box and the window unit are at ground potential. At a depression voltage of 30 kV, the cathode runs at -50 kV and the cavity at + 30 kV. To reduce the peak loading of

the collector, DC and AC axial magnetic fields are employed for beam sweeping. 1 MW output power at an overall efficiency of 47 % and a retarding voltage of 26 kV is expected. A preliminary prototype gyrotron has been constructed now and tests will start in September 1999.

The gyrotrons are operated in a super-conducting magnet with an induction of 5.56 T and a warm bore of 220 mm. In the final gyrotron generator, liquid helium is supplied via transport dewars from the liquefier of the stellarator. The liquid Nitrogen is refilled automatically from a storage tank. Each gyrotron is equipped with an individual cooling circuit including heat exchanger and pumping unit.

4.3 High-voltage Power Supplies

The main power supply for the gyrotrons will be a pulse step modulated (PSM) power supply with modular units, each module will be capable of -65 kV/50 A in continuous operation. The power supply is designed as a

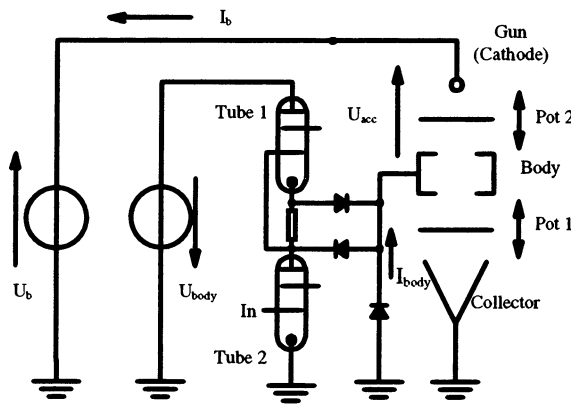


Fig. 8: Principle sketch of the HV power supplies and the differential control for the Gyrotrons on W7-X. U_b = main power supply, U_{body} = body power supply.

multiple-user supply and meets also the requirements of the other heating systems NBI and ICRH (which need inverse polarity). In combination with a low power body supply of up to +45 kV / 0.3 A [21] an acceleration voltage in the range of 80-90 kV as needed for the gyrotron is available with some margin. This combination minimises the cost of power supplies and allows to ground

both supplies together with the collector. For modulation of the gyrotron power (e.g. for heat wave excitation), in principle only the voltage of the body supply is varied (For strong reduction of the output power, where the

efficiency drops, also the cathode voltage must be reduced to limit the power dissipation of the collector). However, to control this voltage, the sum of the voltages of the main power supply and the body supply is used. The HV circuit to feed the gyrotron together with this differential control scheme is shown in Fig. 8. Operational experience of a body supply with differential control [21] was obtained together with a prototype gyrotron from Russia (GYCOM-NN) with depressed collector which is installed at W7-AS. This tube delivers an output power of 0.8 MW at 140 GHz for a pulse duration of 1 s and has an efficiency of 51 %.

The body supply is located in close vicinity of each gyrotron in the gyrotron hall (Fig. 7). Furthermore, the heater supply, which is on cathode potential and the crowbar circuit (thyratrons) are installed here on an air insulated floating deck device to ease maintenance.

The individual modules of the main power supply are located in a separate building and are connected with the ECRH hall via triaxial HV lines having an approximate length of 30 m. Snubber circuits assist in handling the stored energy in the long HV cable in case of a breakdown. In the event of tube breakdown the current through the gyrotron is limited by the snubber circuits. A second snubber which normally provides a residual resistance in parallel of the crowbar, which is needed for triggering the thyatron can be omitted due to a new design of the thyatron system.

4.4 Transmission System

The W7-AS ECRH installation (5 gyrotrons) was used as a test bed to investigate several options for the transmission of high power microwaves [22]. Long distance transmission was done in oversized HE11 waveguides (140 GHz, 0.5 MW per line, 3 lines) [23], in mixed HE11 waveguide and mirror systems including dual beam transmission in an optical line as well as two frequency dual beam optical transmission (70 GHz and 140 GHz, 0.5 MW each). Based on the excellent experience with a 35 m long fully optical transmission line at W7-AS (140 GHz/0.9 MW) [24] an optical transmission line for W7-X was chosen. It turned out to be the most simple, reliable and cost effective solution. In contrast to waveguide transmission matching sections between the gyrotron output beam and the waveguide and back to the optical launcher in the plasma vessel are avoided. The beam waveguide is especially characterised by a low power density and inherent mode filtering properties due to out-scattering (diffraction loss) of unwanted higher-order free-space modes, which leads

to a very high power capability and low risk of arcing. Additional features are broadband transmission, simple polarizers [25], no need for special sections for compensation of thermal expansion of the line and movements of the plasma vessel. The transmission efficiency is high owing to the low Ohmic losses of the optical elements and the low diffraction loss of high-power designs. Major alignment and stability problems were not found in the W7-AS installations. For W7-X, the long-distance transmission will be performed via two multiple-beam waveguides, which further reduces the complexity of the system essentially.

The principle elements are sketched in Fig. 6, the arrangement in the building is shown in Fig. 7. All optical elements are installed in a concrete duct leading from the gyrotron building to the experimental hall. This duct is used simultaneously as a stable support for the optics, screening of the microwaves and basis for installation of dummy loads, calorimeters, absorbers for stray radiation for cooling pipes etc.

In order to match the gyrotron output beam to a stigmatic Gaussian beam with appropriate beam waist two phase correcting mirrors are located in the beam duct close to the gyrotron window. These mirrors are the only elements which have to be adapted to the individual gyrotron output and can be designed and built at a late stage of the installation without affecting the layout of the overall system. The polarisation of each beam can be chosen individually by using two polarising grooved mirrors close to the entrance of the beam combining optics. The main transmission is performed by two multi-beam waveguides (MBWG), each combining 5 beams at 140 GHz, 1 beam at 70 GHz and a spare beam channel on common mirrors. At the input and the output of the MBWG, plane mirror arrays match the individual beams which are used near the gyrotrons and near the stellarator.

The MBWG is a confocal system [18, 26] consisting of four focusing mirrors (and additional three plane mirrors to straighten the beam path), which must simultaneously offer a low-loss propagation of all (on-axis and off-axis) beams and a correct imaging from the input to the output plane. The principle is illustrated in Fig. 9, where one unit consisting of 2 mirrors in Z-configuration is sketched.

Mirrors for a single beam waveguide can be designed straightforward, but for a compact MBWG design the beams overlap on the mirrors, so that no optimisation of partial mirror surfaces is possible. Additionally, for W7-X,

the central on-axis beam will have a frequency of 70 GHz, which requires the full mirror surface due to the larger beam divergence at the longer wavelengths. To fulfil all requirements, 3-dim. diffraction calculations with Gaussian beam mode analysis were performed [25]. The codes were bench-marked by experiments on a small scale which confirm the numerical results. The investigations showed that simple elliptical paraboloids lead to minimum mode conversion losses. Furthermore, the studies showed, that the remaining mode conversion on the curved surfaces cancels after four mirrors, if these mirrors are installed in the proper orientation [25]. This is shown in Fig. 10, where the power distribution and the mode analysis with respect to the

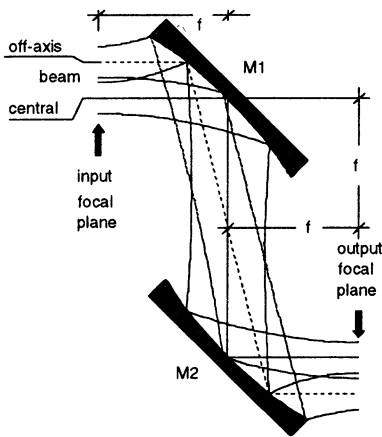


Fig. 9: Principle sketch of a confocal 2-mirror MBWG system (Z-configuration)

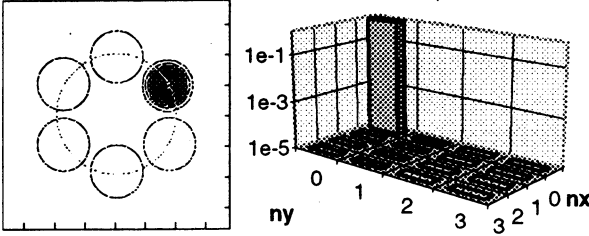
ideal beam is plotted for a representative beam at different positions. At the input plane of the MBWG, the 140 GHz beams are closely packed and parallel, a pure gaussian beam is assumed. In the focal plane after the first mirror, the beams cross the optical axis. In the focal plane after the second mirror, the initial beam pattern is nearly recovered, the mode analysis however yields a purity of 96.1 %. After four mirrors, the spurious modes have cancelled and the beams cross the output plane exactly perpendicular in the nominal position, which is documented by a mode purity of 99.8%.

At present, the detailed design of the transmission system is underway

including the design of water-cooled mirrors.

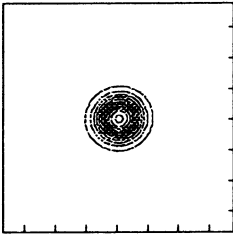
Measurement systems are built up to measure ohmic loss of mirrors, and to develop the alignment system based on reflectometry from shallow diffraction gratings in first-order Littrow-mount [26, 28] machined on the mirror surfaces. In parallel, a test-facility is constructed at IPF Stuttgart to investigate the performance of the transmission system and to test components prior to the series production and installation of the system at Greifswald.

At the starting plane is a pure fundamental mode:

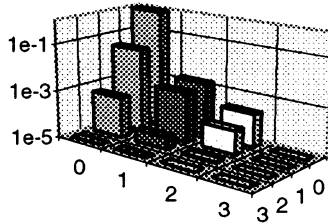
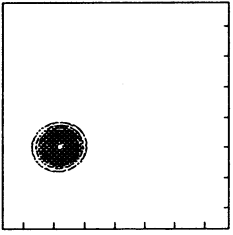


At the output plane of the MBWG, a plane mirror array separates the individual beams, and two further mirrors distribute the beams to the launchers.

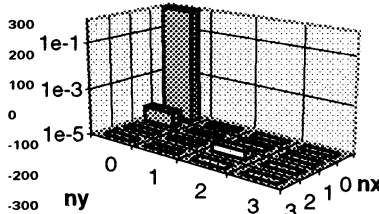
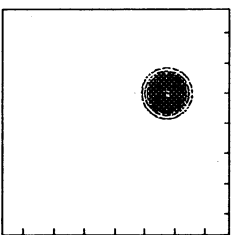
Cross-section after 1st mirror:



Cross-section after 2nd mirror: TEM₀₀-content 96.1%



Cross-section after 4 mirrors: TEM₀₀ content 99.8%



4.5 Launchers

The launchers are designed as plug-in units (PILAs) and include the diamond vacuum window with similar design as the gyrotron window, a vacuum valve, a fixed focusing and a plane movable mirror as well as the necessary structure and cooling lines. Each antenna will be independently steerable, thus a wide variety of deposition profiles can be realised. Both on- and off-axis heating is achieved by steering the beams in the poloidal plane. Electron cyclotron current drive (ECCD)

Fig. 10: Numerical calculation of beam pattern and mode content for one of the 140GHz-beams in the ECRH-system for W7-X at different cross-sections (see figure)

is possible by directing the beams in toroidal direction.

10 launchers will be installed in the planes where the plasma shows a bean-shaped cross-section and the modulus of the magnetic induction is maximum (c.f. Fig. 1b). Thus, heating and current drive are not influenced remarkably by trapped particles. A cross-section through the vacuum vessel, a port with three of the launchers and the plasma in the plane $\Phi = 0^\circ$ are shown in Fig. 11. Two further launchers will be installed at $\Phi = 22^\circ$, where the density of trapped particles is high and thus their influence can be studied. Switching between the antennas is performed by movable mirrors in the transmission system.

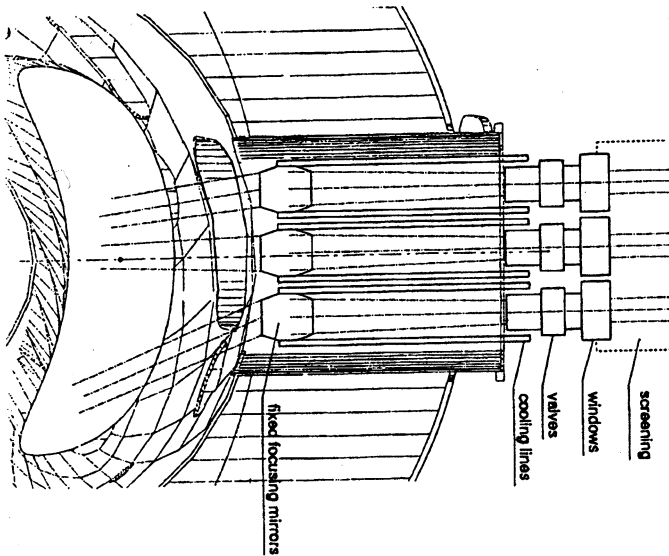


Fig. 11: Cross-section through the vacuum vessel showing the arrangement of three PILAs in an A-type port and the plasma in the plane $\Phi = 0^\circ$.

The antenna beams will be optimized to get a sufficiently narrow power deposition profile in the plasma with a tolerable power density on the vessel walls. Inside the vessel reflectors will be installed to redirect the non-absorbed fraction of the beams back into the plasma. For most areas exposed to the millimetre waves, cooled graphite tiles with a reflection coefficient of typically 94 % can be used. This design is appropriate for X2-mode heating, where the single-pass absorption is nearly total. Heating of high-density plasmas in O2-mode with lower absorption (c.f. Fig. 4) is

planned with a fixed geometry (launch angle about 20°). For this case, metallic mirrors with high reflection will be installed to limit the thermal load. For an efficient absorption in the second pass, the angle with respect to the magnetic field as well as the correct (elliptical) polarisation of the reflected beam must be conserved. To fulfil these requirements, grating surfaces [28] have to be applied for the design of the internal reflectors. Pick-up waveguides will be integrated into the in-vessel structures to monitor the single-pass absorption as well as the beam characteristics. Additionally, cameras will be installed to diagnose any problems.

5. Conclusions

Stellarators were continuously developed towards optimized magnetic field configurations, which led to the concept of helically advanced stellarators with a significant improvement of neoclassical transport properties and stability. W7-X is a superconducting device, which is based on this concept and is presently being constructed. The physics results obtained with ECRH at the predecessors of W7-X, i.e. the W7-A and W7-AS stellarators guided the design of a strong ECRH system with 10 MW in CW operation at 140 GHz. Advanced gyrotrons with energy recovery and an efficiency of about 50 % will be used. The RF-transmission from the gyrotrons towards the stellarator ports is performed by two purely optical transmission systems, which handle 5 MW each in CW operation. Launching of the 10 individual microwave-beams is provided by in-vessel mirrors, which allow to steer each beam towards arbitrary poloidal (for on-and off-axis heating) and toroidal (for oblique launch, ECCD) launch angles. The power of each gyrotron and the polarisation of the emitted microwave beam can be controlled independently from all others to guarantee experimental flexibility and optimum absorption for all scenarios. The W7-X ECRH system combines the most advanced technologies in high power microwave sources (e.g. depressed collector schemes, diamond windows etc.), power supplies and microwave transmission and control techniques.

References

- [1] V. Erckmann and U. Gaparino: " Electron cyclotron resonance heating and current drive in toroidal fusion plasmas", *Plasma Phys. Control. Fusion* **36** 1869 - 1962, (1994)
- [2] V. Erckmann, U. Gasparino, H.J. Hartfuß, W7-AS Team, NI-Team (W7-AS) and

- ECRH Group (IPF Stuttgart): "Electron cyclotron resonance heating experiments at the W7-AS stellarator", *Fusion Eng. Des.* **26**, 141 - 152, (1995)
- [3] G. Grieger et al.: HELIAS stellarator reactor studies and related European technology studies, *Fusion Engineering and Design* **25**, p. 73 (1994)
- [4] G. Grieger et al.: Physics Optimization of Stellarators, *Physics of Fluids B* **4** (7), p. 2081 (1992)
- [5] C. Beidler, G.Grieger, F.Herrnegger, E.Harmeyer et al.: Physics and Engineering design for W7-X, *Fusion Technology* **17**, p. 148 (1990)
- [6] H. Wobig: The theoretical basis of a drift optimized stellarator reactor, *Plasma Phys. Control. Fusion* **35**, p. 903 (1993)
- [7] V. Erckmann et al.: The W7-X project: Scientific Basis and Technical Realization, Proc. 17th IEEE/NPSS Symposium on Fusion Engineering, San Diego, USA (1997). (Ed.) IEEE, Piscataway, NJ 1998, 40 - 48
- [8] J. Nührenberg and R. Zille: Stable stellarators with medium β and aspect ratio, *Phys. Lett.* **114A** (3), p. 129 (1986)
- [9] J. Nührenberg and R. Zille: Quasi-helically symmetric toroidal stellarators, *Phys. Lett.* **129A** (2), p. 113 (1988)
- [10] M. Romé, V. Erckmann, U. Gasparino, N. Karulin: Electron cyclotron resonance heating and current drive in the W7-X stellarator, *Plasma Phys. Contr. Fusion* **40**, p. 511 (1998)
- [11] U. Gasparino, V. Erckmann, H.J. Hartfuß, H. Maaßberg, M.Romé: Transport analysis through heat waves driven at different radial positions, *Plasma Phys. Contr. Fusion* **40**, p. 233 (1998)
- [12] H. Maaßberg et al, this conference
- [13] H. Wobig, I. Ott: Plasma parameters in W VII-X, Proc. of the 4th workshop on Wendelstein 7-X, Schloß Ringberg, Germany, IPP Report 2/313, p.112 (1991)
- [14] V. Erckmann, N. Karulin and H. Wobig: High density operation with 140 GHz ECRH: Experiments at the W7-AS stellarator, prospects for the W7-X stellarator, Proc. 21st EPS Conference on Controlled Fusion and Plasma Physics **18B**, Part II, p. 1008 (1994)
- [15] H.P. Laqua, V. Erckmann, H.J. Hartfuß, H. Laqua, W7-AS Team, and ECRH Group, Resonant and nonresonant Electron Cyclotron Heating at Densities above the Plasma Cutoff by O-X-B Mode Conversion at the W7-AS Stellarator, *Phys. Rev. Lett.* **78**, 3467 (1997)
- [16] V. Erckmann, U. Gasparino, H. Maaßberg: Current drive and bootstrap current in stellarators, *Plasma Phys. Controlled Fusion* **34**, 1917 (1992)
- [17] E.V. Suvorov, A.B. Burov, Y.A. Dryagin, S.E. Fil'chenkov, A.A. Fraiman; L.M. Kukin, A.V. Kostrov, L.V. Lubyako, D.A. Ryndyk, A.M. Shtanyuk, N.K. Skalyga, O.B. Smolyakova, V. Erckmann, H. Laqua, T. Geist, M. Kick, M. Rust, WVII-AS Team, ECRH Team, NBI Team, E. Holzhauer, W. Kasperek: "Collective Thomson Scattering at W7-AS", *Plasma Phys. and Control. Fusion*, **39** (1997) B337-B351
- [18] L. Empacher et al: "Conceptual design of the 140 GHz/10 MW CW ECRH system for the stellarator W7-X", Proc. of the 19th Symp. on Fusion Technology, Fusion

Technology 1996, p. 541, Elsevier, Amsterdam (1997)

- [19] M. Thumm et al.: 140 GHz / 1MW CW Gyrotron with depressed collector, Proc. of the 24th Int. Conference on Infrared and Millimetre waves, Monterey, California, September 1999
- [20] G.G. Denisov, M.I. Petelin and D.V. Vinogradov: Effective conversion of high order modes to Eigenwaves of open mirror lines, in 17th Int. Conf. on Infrared and Millimetre waves, R.J. Temkin, ed., Proc. SPIE 1929, 124 (1992)
- [21] G.A. Müller, W. Förster, V. Erckmann and H.P. Laqua: Voltage Regulator for power modulation of a gyrotron with voltage depressed collector. In: Proc. of the 20th Symp. on Fusion Technology, Marseille 1998, (Ed.s.) B. Beaumont, P. Libeyre, B. de Gentile, G. Tonon. Assoc. EURATOM-CEA, Saint-Paul-lez-Durance 1998, 877
- [22] M. Thumm, W. Kasperek, „Recent advanced technology in electron cyclotron resonance heating systems“, Fusion Engineering and design, **26** (1995), 291 - 317.
- [23] L.Empacher Förster, W., Gantenbein, G., Graubner T., Kasperek, W., Kumric, H., Müller, G.A., Schüller, Wagner, D., Erckmann, V., Geist, T.: „Millimetre wave technology and performance of the 2 MW/140 GHz ECRH system on the Stellarator W7-AS.“ In Fusion Technology 1994, Elsevier Science Publishers B.V. (1991), 1142
- [24] Henle, W., A. Jacobs, W. Kasperek, H. Kumric, G.A. Müller, P.G. Schüller, M.Thumm, V. Erckmann, "Microwave technology of the quasi-optical 140 GHz system on the advanced stellarator W7-AS", Fusion Technology 1990, Elsevier Science Publishers B.V. 485 - 488 (1995)
- [25] K.W. Kopp, W. Kasperek and E. Holzhauer, "Microwave reflection properties of grooved metallic mirrors", Int. J. Infrared and Millimeter Waves, **13** (1992), 1619.
- [26] G. Gantenbein, L.Empacher, V.Erckmann, F.Hollmann, W. Kasperek, M. Weißgerber, H. Zohm, "Simulation and Experiments on a Multi-Beam Waveguide ECRH Transmission System", Proc. of the 20th Symp. on Fusion Technology, Marseille 1998, (Ed.s.) B. Beaumont, P. Libeyre, B. de Gentile, G. Tonon. Assoc. EURATOM-CEA, Saint-Paul-lez-Durance 1998, 423 - 426
- [27] L.Empacher and W. Kasperek: Analysis of a multiple-beam waveguide for free-space transmission of microwaves, submitted for publication to IEEE Transactions on Antennas and Propagation (1999)
- [28] R.Petit (ed.): Electromagnetic theory of gratings, Springer, Berlin 1980

28 GHZ ECH SYSTEM FOR H-1NF HELIAC

*K. Nagasaki¹, M. G. Shats, H. Punzmann, H. B. Smith, M. Sato**

Plasma Research Laboratory, Research School of Physical Sciences and Engineering,
The Australian National University, Canberra, ACT 0200, Australia

*National Institute for Fusion Science, Toki, Japan

Abstract

Electron cyclotron heating system has been designed and is being installed for the H-1NF heliac device. The main purpose is to produce and heat currentless plasmas for studying the particle and heat transport of high temperature plasmas in advanced helical devices. In this paper, the 28 GHz ECH system is overviewed and the low power measurement results are presented. A theoretical study on power absorption using a ray tracing numerical code is also shown.

1. Introduction

Recently many of the new generation of fusion experiments use configurations from the stellarator family, which are called variously advanced stellarators, heliotrons, and heliacs. The experimental devices under operation or construction are, for example, LHD in Japan, TJ-II in Spain, Heliotron J in Japan, W7-X in Germany, HSX in USA, and H-1 NF heliac in Australia. The common feature is that they form nested flux surfaces for plasma confinement without ohmic current. The ECH is recognized as an important heating tool in these devices, because high temperature plasmas are produced and heated mainly by ECH.

H-1 NF is a helical axis stellarator in the Plasma Research Laboratory of the Australian National University, Canberra [1]. Parameters of magnetic surfaces are major radius, $R=1.0$ m, mean minor radius, $a=0.2$ m, rotational transform, $\iota=0.6-2.0$ and low magnetic shear ($\Delta\iota/\iota=0.03-0.06$) [2]. Low temperature plasma experiments have been performed at low magnetic field. The H-1NF device is now being upgraded to increase the magnetic field from its present operating value of 0.2 T to its design value of 1 T. An ECH system has been designed and is being constructed as a part of the device upgrade.

Physics advantage of the ECH application to H-1 NF plasma is to localize the power absorption in the desired region by scanning the beam

¹ Permanent address: Institute of Advanced Energy, Kyoto University, Uji, Kyoto 611-0011, Japan
e-mail address: nagasaki@iae.kyoto-u.ac.jp

direction and the magnetic field strength. The main purposes of physics studies in ECH plasmas are 1) transport physics study related to the radial electric field, which may be controlled by ECH, 2) electron temperature profile shaping, probably also electron density profile shaping, and 3) heat wave propagation experiments to measure the local thermal conductivity. At the first stage, ECH experiment in H-1 NF will be performed at the second harmonic at $B=0.5$ T with an X-mode launched from a low magnetic field side. Then the fundamental O-mode ECH will be carried out when increasing the magnetic field to 1.0 T.

In this paper, we overview the 28 GHz ECH system for H-1 NF, and show low power measurement results on the waveguide transmission line and quasi-optical antenna system. A ray tracing numerical code has also been developed for heliac configurations. The calculation results on the power absorption are shown.

2. 28GHz ECH System for H-1NF

Figure 1 illustrates a schematic view of the 28 GHz ECH system. The system mainly consists of a gyrotron microwave source, in-waveguide converter, waveguide transmission line, ceramic window and quasi-optical launching mirrors. High power microwaves are generated by a

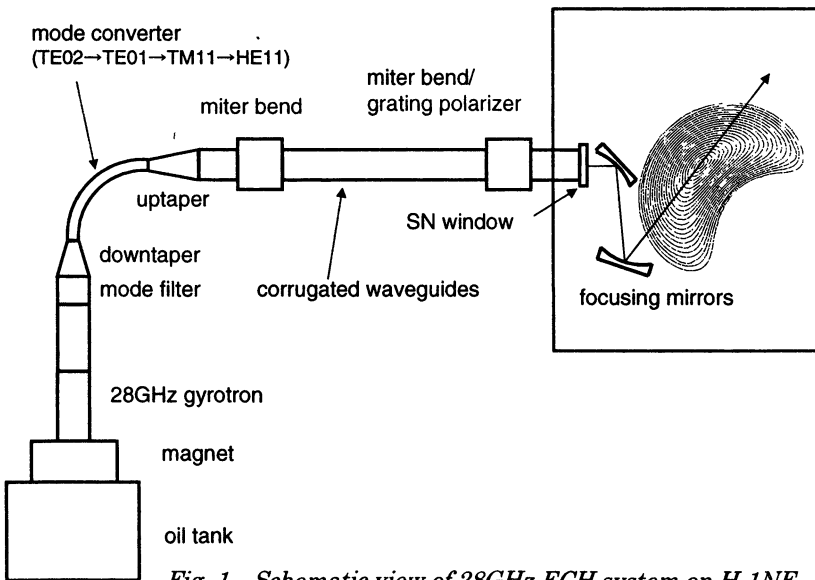


Fig. 1 Schematic view of 28GHz ECH system on H-1NF

gyrotron that was manufactured by Varian (CPI). The gyrotron and its power supply are loaned from Institute of Advanced Energy, Kyoto University / National Institute for Fusion Science. The maximum output power is 230 kW, and the output mode is TE_{02} axisymmetric mode. The pulse length is up to 40 msec, which is long enough to obtain quasi-stationary plasmas. The beam voltage and current are 80 kV and 8 A, respectively, corresponding to the efficiency of 36 %. The gyrotron system is placed at the downstairs of the H-1NF room, which is 5 m below and 10 m away horizontally from the H-1NF device.

Since the TE_{02} mode is not suitable from the viewpoint of localized plasma heating and effective power transmission, it is converted into a linearly polarized mode through an in-waveguide converter that has been designed and manufactured by General Atomics. The waveguide of 2.5 inch is tapered down into the one of 1 inch, then the TE_{02} mode is converted into the HE_{11} waveguide mode through the following process; $TE_{02} \rightarrow TE_{01} \rightarrow TM_{11} \rightarrow HE_{11}$. After the conversion into the HE_{11} mode, the waveguide is up-tapered, and then it is connected to a corrugated waveguide of 63.5 mm. The groove depth is determined to minimize the ohmic attenuation loss, that is, the slot depth and pitch of grooves are 2 mm, and 4.2 mm, respectively. The ratio of width to pitch is 0.33.

The corrugated waveguides are totally about 10m long. Two 90deg miter bends are used to change the waveguide direction. The corrugation is continued up to the reflecting mirror, which reduces the mode conversion loss by one-half compared to the case without corrugations. The Gaussian beam is launched from the outside horizontal port of H-1NF vacuum chamber through a silicon nitride, single-disk window of 2.5-inch diameter. Two mirrors are set up in the vacuum chamber to focus the Gaussian beam and to control the beam direction. The focused beam is launched from the bottom of the plasma.

A waveguide with a relatively large diameter has the advantage of low transmission loss and broad frequency range [3]. The loss is caused by ohmic attenuation, mode conversion and some imperfections in the waveguide line. The calculated losses are as follows; ohmic attenuation in waveguides, 4.6×10^{-4} dB, radius offset, 6.9×10^{-4} dB, radius change, 7.5×10^{-3} dB, elliptical offset, 2.3×10^{-3} dB, tilt, 4.9×10^{-4} dB, unintentional curvature, 1.1×10^{-3} dB, ohmic attenuation in miter bends, 8.0×10^{-3} dB, and mode conversion in miter bends, 0.17 dB. These indicate that the main transmission loss occurs at the miter bends due to the diffraction. Including the power loss at the in-waveguide converter, window and

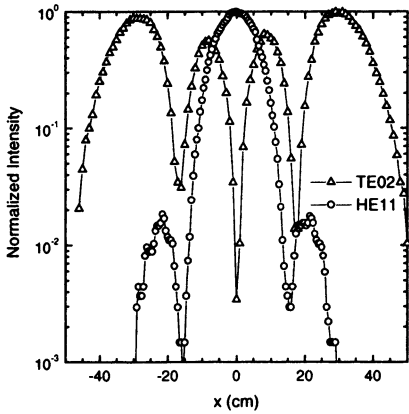


Fig. 2 Radial Profiles of TE_{02} and HE_{11} modes

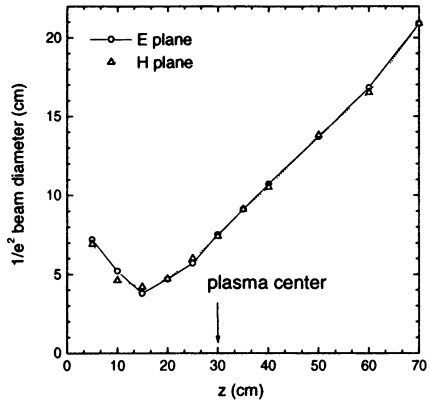


Fig. 3 $1/e^2$ beam radius as a function of the distance from the mirror.

launching antenna, the total transmission efficiency is estimated about 80 %. The waveguide system will be operational without evacuation, because the transmitted power, 200 kW, is lower than the upper limit of 1 MW, and the pulse length is short.

The transmission line has been bench-tested using equipment of a low power TE_{02} mode source. Figure 2 shows the radial profile of TE_{02} and HE_{11} modes radiating from the waveguide. The TE_{02} mode is well converted into the HE_{11} mode, and the HE_{11} mode is effectively transmitted in the waveguide line. No strong deformation due to higher harmonics is visible within the measurement accuracy. The beam pattern after the last focusing mirror is also measured. The beam is circular, and the beam waist is 4 cm as shown in Fig. 3.

Two polarizers with sinusoidal grooves, which are assembled on the miter bends, control the polarization of launched waves. A wide range of polarization from a linear to a circular polarization is available by choosing the groove depth and controlling the rotation angle of grooved mirrors. The measured polarization parameters are in good agreements with numerical calculation results in which the groove shape are taken into account [4].

3. Ray Tracing Calculation

A new ray tracing code for H-1NF configuration, 'H-Ray', has been developed, based on a ray tracing code for Heliotron E [5]. The conventional ray equations using geometrical optics approximation are

solved to trace a bundle of rays. The number of rays is determined to obtain the numerical accuracy to simulate the Gaussian beam profile. The number of rays are taken as 16×16 in the azimuthal and radial directions, respectively. The flux surfaces are assumed to be helically symmetric, that is, to have the same beam shape at any toroidal cross-section, which is a good approximation for H-1NF configuration. Multi-reflection is not considered in this code, because the vacuum chamber is located so far from the plasma that the reflected waves hardly return back to the plasma confinement region. Two cases are considered as starting points of the rays according to the experimental set up; (a) bottom launch from the final mirror and (b) horizontal launch directly from the corrugated waveguide.

Figure 4 shows an example of the ray trajectory. The calculation results show that the 28 GHz ECH is promising for heating plasmas although the electron density is rather low due to the low cut-off density. The bottom launching is more advantageous for single pass absorption and controlling the power deposition profile. The single pass absorption rate reaches 90 % at the second harmonic X-mode heating if the launching angle is properly adjusted. As shown in Fig. 5, the absorbed power profile can be shifted from on-axis to off-axis by scanning the magnetic field strength with keeping the total absorption rate more than 70 %. This suggests that the plasma profile shaping experiment would be possible at the second harmonic ECH. Accessible plasma parameters

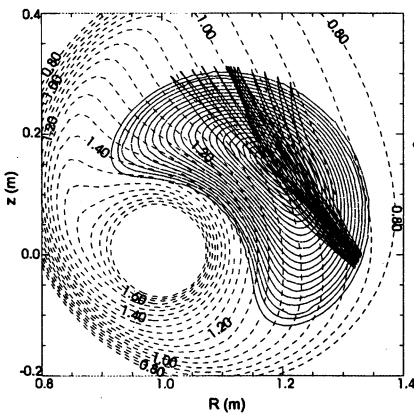


Fig. 4 Ray trajectory of second harmonic X-mode at $n_e(0)=0.2 \times 10^{19} \text{ m}^{-3}$, $B=0.5 \text{ T}$.

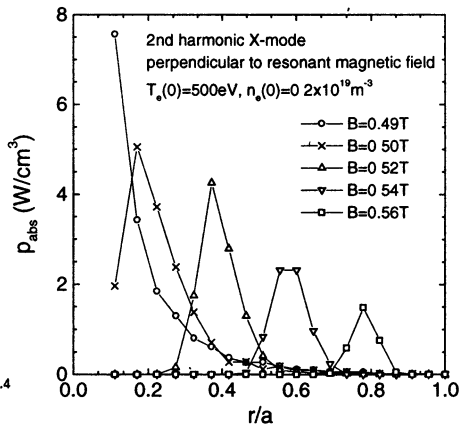


Fig. 5 Single pass absorption profile of second harmonic X-mode

predicted in combination with ISS95 energy confinement scaling law [6] are $n_e(0) < 0.4 \times 10^{19} \text{ m}^{-3}$, $T_e(0) \leq 500 \text{ eV}$ and $\tau_E \leq 3 \text{ msec}$. On the other hand, the total absorption rate is low $\sim 20 \%$ for the fundamental O-mode ECH due to low absorption coefficient, although the accessible density is doubled. Some schemes are required to improve the absorption, such as installation of a reflecting mirror and mode conversion to the electron Bernstein wave.

4. Conclusion

The 28 GHz ECH system has been designed and fabricated as a part of the upgrade of H-1NF heliac. Microwaves generated from a gyrotron are transmitted in the waveguide line and launched by the quasi-optical antenna system. Low power measurement showed that the transmission components had a good performance as designed, and the microwave beam was well focused in the desired region of core plasma. A ray tracing code for H-1NF three-dimensional configurations has been developed using geometrical optics approximation. The calculation results indicate that the second harmonic X-mode ECH at $B=0.5 \text{ T}$ is promising even at low density. A high power test and application to H-1NF for plasma production and heating will be done in the middle of 1999 after the magnet field power supply for H-1NF is operational.

Acknowledgements

Authors would like to thank H-1NF staff for continuous discussions. Encouragement by Prof. T. Obiki and Prof. J. H. Harris is appreciated. One of the authors (K. N.) was supported by the overseas research fellowship of the Japanese Ministry of Education, Sports and Culture during his stay at ANU.

References

1. Hamberger S. M., et al., Fusion Technol., 1990, **17**, 123.
2. Shats M. G., et al., Nucl. Fusion 1994, **34**, 1653.
3. Nagasaki K., et al., Fusion Technol., 1997, **32**, 287.
4. Nagasaki K., et al., Int. J. Infrared and Millimeter Waves, 1999, **20**, 823-843.
5. Zushi H., et al., Nucl. Fusion, Nucl. Fusion, 1988, **28**, 1801.
6. Stroth U., et al., Nucl. Fusion, 1996, **36**, 1063.

DESIGN OF THE LOWER HYBRID HEATING AND CURRENT DRIVE TRANSMISSION LINE SYSTEM FOR A NEXT STEP DEVICE

*Ph. Froissard, S.V. Kuzikov**

Association Euratom CEA, CEA Cadarache, St-Paul-Lez-Durance Cedex, France

*Institute of Applied Physics, Russian Academy of Sciences, Nizhny Novgorod, Russia

Abstract: A LHCD System for Next Step Tokamaks like ITER will rely on many high power sources located between 50 and 100 m to the Tokamak. Standard transmission lines cannot be used since their power density is limited and their loss is too high. A new design based on oversized circular transmission lines has been studied for ITER which recombines power from several sources. The design of the Splitting and Recombining Network has been investigated. Several concepts of circular bends have been considered. Two types of mode filters have been studied in order to avoid spurious resonance in the transmission line. The analysis of all RF components in the transmission line shows that a good efficiency is achieved as the diffraction loss does not exceed 10 % for a 70 m long line with 6 bends and 3 mode filters.

Introduction

The successful experiments carried out in large Tokamaks in recent years have demonstrated perspectives for Lower Hybrid Heating Current Drive (LHH&CD) on Next Step devices like ITER. A LHH&CD system has been designed and integrated in the ITER EDA [1]. The LHH&CD system operates at 5 GHz and couples a minimum of 50 MW using two ITER ports. Each antenna is fed by 8 Main Transmission Lines, each composed of a splitting network to feed 6 mode converters, one oversized size C7 Circular Transmission Line operating in the axisymmetrical TE_{01} mode and a Recombining Network to mix power produced by 4 klystrons (upgradable to 6). This kind of transmission is attractive due to low-loss attenuation as well as breakdown safety. Taking into account technical constraints, the transmission line has to include 4-6 bends as well as mode filters. All these components are analysed in this paper.

Transmission Line Bends

Bends Based on Curved Waveguides

The simplest way to bend a circular transmission line is to use a waveguide of circular cross-section, uniformly curved in one plane [2]. The mode behaviour in curved waveguides are accurately described by means of coupling mode formalism [3, 4]. In this case 11 most important modes are taken into account. The choice of the bending radius is dictated by the angle of the bend (90° in our case). For a bending radius a between 106 and 108 mm, an efficiency of 99 % is reached for very large bends only (total length ~ 10 m).

In order to reduce the total length of the waveguide bend, an optimisation, based on varying the bending radius along the distance, was carried out. Sinusoidal profile for the curvature was used and the best achieved efficiency is of 98.3 % for a bending radius varying from $R_{max}=4.83$ m to $R_{min}=3.91$ m and a total length of 6.6 m.

Waveguides with elliptic cross-section have also been studied as they reduce the degeneration between TE_{01} and TM_{11} modes, thus, reaching a higher efficiency for the same bending radius. Such waveguides with an ellipticity amplitude of 3 mm are found to have a rather high efficiency (98.1 %) for a compact geometry: $a=102$ mm; $R_{max}=2.8$ m; $R_{min}=2.2$ m and a total length=3.8 m.

Mitre Bends

Mitre bends are also frequently used in oversized transmission lines [5]. Their efficiency increases for large waveguide diameter and for $a=300$ mm, the efficiency is ≈ 70 % only. However, using an improved mitre bend based on so-called quasi-optical principles can increase this efficiency [6].

The incident TE_{01} mode is converted into a wavebeam which could propagate through the free space section without losses. An axisymmetrical mode converter, forming a converging wavebeam with the waist, being precisely in the middle of the free space section (Fig.1) produces this wavebeam. The second part of the converter has to be the exact symmetry of the first part, in order to reconvert the wavebeam into the initial operating TE_{01} mode.

Calculations are done in two steps. At first, the field distribution at the open end of the pre-converter is calculated. The next step, based on

Kirchhoff approach, is the calculation of the wavebeam propagation through the free space. The best efficiency is 99 % (including losses into free space and mismatching between field structures); the power reflection is ~ 0.1 %.

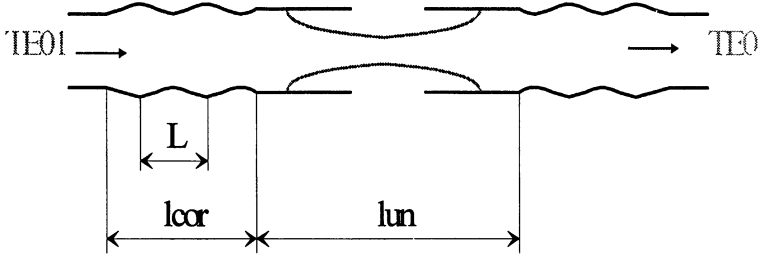


Figure 1: Quasi Optical mitre bend model

The mode behaviour calculated with this model as a function of the distance is indicated in Fig. 2 for modes TE_{02} and TE_{03} . The final mode content for the given wavebeam at the input of the free space section is 77.7% for TE_{01} , 20.8% for TE_{02} and 1.4% for TE_{03} . The efficiency remains above 99% for a frequency range of $5 \text{ GHz} \pm 10 \text{ MHz}$.

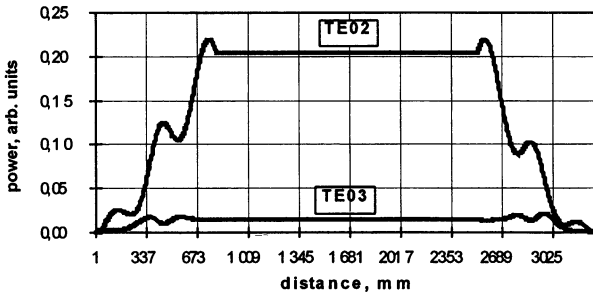


Figure 2: Mode behaviour in the Quasi Optical mitre bend

Splitting/Recombining Network

In order to combine the powers of several coherent RF sources the standard rectangular waveguides are transformed adiabatically into sectorial waveguides, feeding a common circular waveguide. A section of coaxial waveguide before the final circular cross-section waveguide is also used to complete the assembly (Fig. 3). The central metallic rod should suppress the possible excitation of other higher axisymmetrical

modes like TE_{0n} (where $n>1$, note that TE_{61} mode is also evanescent for this geometry).

The excited TE_{01} mode in the coaxial waveguide has to be launched into the transmission line through a special up-taper. It provides a low-loss transition from a small enough input diameter, used for pure TE_{01} mode excitation, to a large operating diameter in the transmission line (C7).

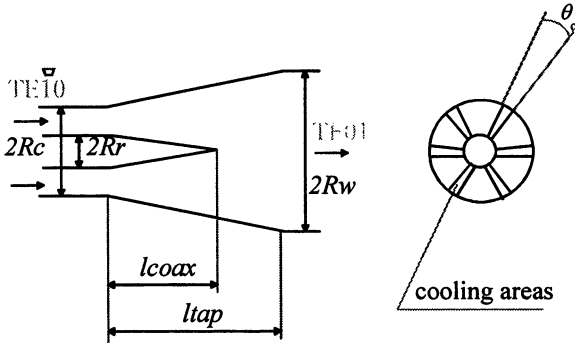


Figure 3: Splitting Network model

Interface zone

The losses caused by the excitation of spurious modes are approximately proportional to the surface of cooling.

The desired TE_{01} mode can be excited purely (a section of coaxial waveguide has to be used before an up-taper), but it is necessary to take into account reflection back from the open end. The estimated power reflection is less than 3% if the angle describing the cooling area does not exceed $\theta_c = 15^\circ$.

Table 1

Input Amplitudes (a.u.)	Input Phases (deg)	TE_{01} mode content
1,1,1,1,1,1	0,0,0,10,10,10	99.26%
1,1,1,1,1,1	0,10,0,10,0,10	99.24%
0.95,0.95,0.95,1,1,1	0,0,0,0,0,0	99.92%
0,1,1,1,1,1	0,0,0,0,0,0	84,1%

A code was written in order to simulate arbitrary configurations of phases and amplitudes of waves in the sectorial waveguides. This code is based on the accurate modelling of coaxial mode excitation. It allows, by

changing the incident field structure, to observe the resulting mode content in the coaxial waveguide. Some typical «non-ideal» cases, calculated for the proposed design are given for $\theta_c=15^\circ$ in Table 1. In conclusion, it is shown that the splitter sensibility to phase variation is rather not critical.

Up-taper

The up-taper starts from a diameter $\varnothing 140$ mm to finish at a diameter $\varnothing 300$ mm. The longer the taper the better is the efficiency, because the scattering into any spurious mode is proportional to the angle of the conical section. Two possible shapes were tested numerically. The first profile tested is based on a linear expansion of external radius under linear narrowing of the rod so that the lengths of the external and linear parts are strictly identical. An efficiency of 99 % is achieved for $l \sim 1000$ mm. For the second profile the lengths of the external and internal transitions are allowed to be independent. This model was computed for two values of inner rod length: $l_{COAX}=200$ mm and 300 mm. For 200 mm, a rather high efficiency (~ 99 %) is achievable for shorter distances $\sim 700 - 800$ mm.

Mode filters

Mode filters are needed along the transmission line in order to avoid spurious resonance, which spoil the VSWR parameter of the line and increase the electric fields. The mode filters reduce also the power reflected from the plasma and propagating back to the klystrons as part of the reflected power is only contained into the TE_{01} mode.

One of the classic mode filters is based on corrugated waveguides filled by absorber [7]. Unfortunately, mode filters, based on absorbing waveguide with impedance corrugation are insufficient to suppress other axisymmetrical TE_{0n} modes. Therefore, another type of the filter is also suggested. The same principle as for the mitre bend is applied in this case: the operating TE_{01} mode is converted into a wavebeam propagating with negligible losses through a free space section, and behind the free space section, it is reconverted into the incident TE_{01} mode. All other TE_{0n} modes propagate with some losses through the free space, which is filled by absorber. The proposed filter provides losses of TE_{02} mode – 12.8 %, TE_{03} mode – 74.0 %, TE_{04} mode – 63.5%, while the loss of the operating mode TE_{01} is 0.5 %.

Summary

The results of the calculations done for each component are summarised in Table 2, where the diffraction and ohmic losses are given. This table corresponds to the proposal at 5 GHz for the LHH&CD transmission line on ITER. Two concepts of bends are analysed. The mitre bend design is much more attractive in comparison with the waveguide bend designs. An efficient splitting/recombining network, based on coaxial junction in a waveguide of reduced cross-section, has been suggested and calculated. Two versions of mode filters are suggested. The first one is designed for nonsymmetrical modes suppression; while the second one is designed to suppress higher axisymmetrical modes. An analysis of all RF components shows that a satisfactory efficiency of LH transmission line is achieved for both «ideal» and «non-ideal» cases.

Table 2

Component	Number	Diffraction losses	Ohmic losses
Recombiner	1	1.5%	0.5%
Main Waveguide	50 m	0	0.2%
Mitre bend	6	1%	0.01%
Corrugated mode filter	2	<0.01%	0.3%
Quasi-optical mode filter	1	0.5%	0.01%
Splitter	1	1.5%	0.5%
Total		9.5%	1.8%

References

1. Froissard P. et al., Proc. of 20th Symposium on Fusion Technology, 7-11 September 1998, Marseille, France.
2. Jouguet M., Effets de la courbure dans guide a section circulaire, Cabl. et Trans. Vol.1, No.2, 133, 1947.
3. Kerzhentseva N.P., Radiotekhnika i Elektronika, 1958, No. 5, p. 650-659 (in Russian).
4. Katsenelenbaum B.Z., Theory of Nonuniform Waveguides with Slowly Varying Parameters, Moscow: Akad. Nauk SSSR, 1961 (in Russian).
5. Marcatili E.A., Waveguide Elbow / US Patent 3.090.931.C1.333-98; Filed Mar.8, 1962.
6. Belousov V.I. et al. New Components for TE01 Transmission Lines. Abstracts of IV Int. Workshop Strong Microwaves in Plasmas, 2-9 August 1999, S47.
7. Thumm M. et al. Very High Power MM-Wave Components in Oversized Waveguides. Microwave Journal, Vol.29, No.11, 103-121.

THE NEW LOWER HYBRID COUPLING STRUCTURES FOR FTU

*F. Mirizzi**, *Ph. Bibet*[°], *Ph. Froissard*[°], *F. Kazarian*[°], *A. Marra**,
*M. Roccon**, *A.A. Tuccillo**

*Associazione EURATOM-ENEA, C. R. Frascati, Frascati (Rome), Italy
°Association EURATOM-CEA, Département de Recherches sur la Fusion Contrôlée,
Centre d'étude de Cadarache, St Paul lez Durance, France

Abstract

In the frame of a collaboration between CEA-Cadarache and ENEA-Frascati, a conventional Multijunction (MJ) and a Multijunction with passive waveguides (PAM) are under construction to be used on the Lower Hybrid (LH) system for FTU. The aims are to overcome the severe limitations on power handling capability deriving, on the actual FTU LH grills, from the maximum allowable electric field on the "multiwindows" and to test in a real scenario the PAM conceptual studies. In a successive step all the technologic solutions of the PAM will be tested in a full rated experiment on Tore Supra.

Introduction

In the LH system for FTU the "multiwindow", a titanium alloy frame incorporating 48 alumina (Al_2O_3) bricks (cross section 28×3.6 mm² and thickness 12 mm) put about 20 cm far from the plasma, separates the pressurized grill from the vacuum vessel.

It is the most critical component in the RF transmission lines being able to withstand a maximum E-field of only 5 kV/cm.

This is a severe limitation in experiments with intrinsically transient phenomena such as "advanced tokamak scenarios", where the MHD activity affects the plasma density in the scrape-off layer modulating the reflected LH power beyond the threshold level of the on line protections (40% of the maximum available incident power) that in turn switch off the RF pulse.

More over during the last few years has become compelling the need for robust coupling structures able to withstand the strong thermal loads foreseen for the new generation of tokamaks (heat load = 0.5 MW/m², neutron flux = 10 MW/m³). In this respect the PAM, proposed by CEA-Cadarache [1], seems a good solution combining optimum coupling properties with the possibility of an effective cooling through holes drilled in the thick vertical walls between active waveguides.

The CEA-ENEA Collaboration

To test a conventional MJ and a PAM on FTU a collaboration has been undertaken between CEA-Cadarache and ENEA-Frascati.

The main objective is the first experiment of a PAM on plasma [2] to measure the coupling properties and the power directivity of this launcher for a direct comparison between theory and experiment.

The collaboration consists of two steps:

- 1st step: design, assembling and test of a 8 GHz PAM on FTU to validate the theory.
- 2nd step: design, assembling and test on Tore Supra of a 3.7 GHz PAM to asseverate all the related technological solution.

The test on FTU permits to abridge costs and times of the set up due to the compactness of this machine; on the other hand, the high plasma density and high magnetic field of FTU make this test significant for the development of PAM for ITER-like machines.

The collaboration has been extended to the design, assembling and test of a conventional MJ on FTU to evaluate an alternative solution to the actual LH grills that eliminates the multiwindows.

Preliminary Design

To introduce only minor changes in the RF power distribution section of the existent LH modules, both the new launchers will have the same overall configuration of the actual grill: 48 rectangular waveguides arranged in four poloidal rows and twelve toroidal columns.

Therefore the actual lay-out of the LH module [3] will remain unchanged up to the RF power primary division. The twelve output WR 137 waveguides will be arranged in a 4 rows by three columns array; each one of them will feed one out of the twelve elementary MJ/PAM module.

Three different set of constraints influence the design of these new coupling structures.

From the mechanical point of view the cross section of the FTU port (420×80 mm) defines their maximum overall dimensions.

The maximum admissible E-field in the waveguides gives the maximum power density at the mouth; extrapolation of data available from the existing LH systems for FTU and for Tore Supra indicates $E_{max} = 6 \text{ kV/cm}$ as a safe value to limit arching probability. According to this constraint the diagram in Fig. 1, specific for the FTU new coupling structures at 8 GHz, indicates a maximum power density of about 8 kW/cm^2 at a maximum reflected power of 20%.

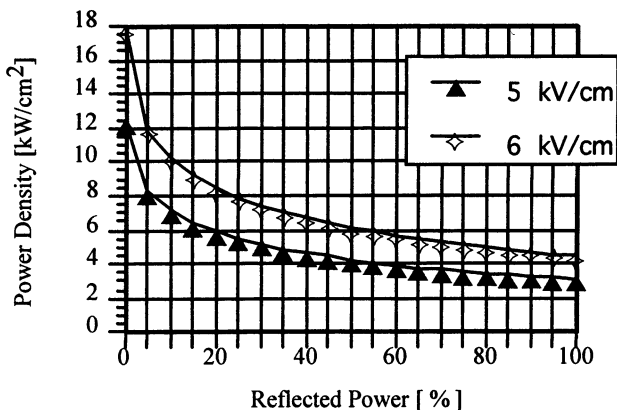


Fig. 1. MJ/PAM for FTU: Maximum available Power Density

The diagram in Fig. 2 defines the pitch between active waveguides at the antenna mouth for a given value of $N_{||0}$ at $f = 8$ GHz; the curves are obtained at a built-in phase shift of 90° for the MJ and 270° for the PAM.

The available experimental data indicate $N_{|| \text{ peak}} = 1.6 \div 2.4$ as the optimum range according to the FTU plasma characteristics; from the diagram, a pitch of 5 mm for the MJ and 5.8 mm for the PAM gives respectively $N_{||0} = 1.9$ and $N_{||0} = 2.4$, well in agreement with the desired values allowing a comparison at the same $N_{||}$ value (2.2) when the phase shift between module is changed.

To assure a good mechanical stiffness of the whole structure, a vertical wall thickness of 0.8 mm at the mouth has been chosen.

By fixing the waveguides height to 28 mm as for the extant grill, the

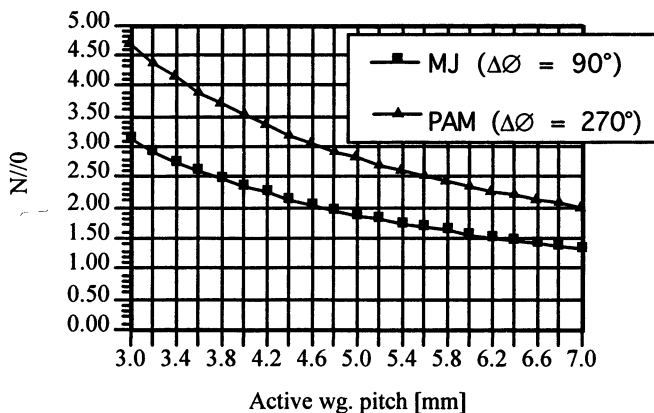


Fig. 2. MJ/PAM for FTU: $N_{||0}$ vs. wg pitch

conclusive dimensions of the elementary waveguides for the two structures are therefore:

- MJ 28×4.2 mm
- PAM 28×5 mm.

The MJ/PAM module lay-out

To properly fit the new coupling structures, the WR 137 waveguide cross section is tapered to 28×22.2 mm.

A first E-plane bijunction (Fig. 3/a) splits the resulting waveguide in two 28×10.6 mm waveguides with an output phase shift between them fixed to 90°; the vertical wall thickness is set to 1 mm.

This component, in common to both MJ and PAM, is made by copper to reduce the rf insertion losses.

In the case of the MJ, two E-plane bijunctions follow (Fig. 3/b) with inner phase shift 0°, 90°, 90°, 180° in the four output waveguides to have a phase periodicity of 90° at the module mouth.

The cross section of the waveguides at the mouth is reduced to 28×4.2 mm and the vertical wall thickness to 0.8 mm. The total active cross section of the MJ is therefore about 56.5 cm² and the maximum allowable incident power is about 450 kW.

For the PAM each waveguide resulting from the first bijunction is followed by an E-plane down-taper to thicken the vertical wall up to 5.8 mm (Fig. 3/c); passive waveguides (optimum depth = 0.25 λ_g) are dug in the thick walls at the PAM mouth. A 180° phase shift is achieved in one of the two active waveguides to have a total phase shift at the module output of 270°. The total active cross section of the PAM is 33.6 cm² and then the maximum allowable incident power at the mouth is about 270 kW.

The two terminal pieces are made by stainless steel, endowed of good mechanical stiffness, gold plated on the inner surfaces to reduce the RF losses; this material is more efficiently machined and less expensive than glidcop; moreover its electrical resistivity is forty times the copper resistivity.

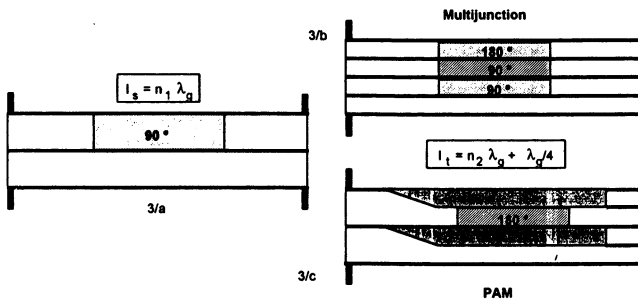


Fig. 3. MJ/PAM for FTU: Schematic layout of a module

This lay-out gives the possibility to test both the structures on FTU by simply changing this second piece and, in addition, to test in the future different launchers, e.g. the hyperguide.

The above analysis shows the need of reduced level of RF power, also for the initial conditioning of both the structures; according to the experience earned in the LH system exploitation, the gyrotron assembled in the module no. 6 has been chosen as the more versatile rf source to use in this test.

The numerical analysis

The two structures have been verified by numerical codes based on the "Method of Moments" (MoM) to calculate their scattering matrix, while the interaction with the plasma has been ascertained by "SWAN" (Slow Wave ANtenna), a specific and experimentally validated code developed in Cadarache.

In this code the plasma is modeled as an electron density step in the radial direction plus a density gradient; a reference plasma density $n_e = 1.6 \times 10^{12} \text{ cm}^{-3}$ (two times the FTU cut-off density) and a gradient density $\nabla n_e = 1.6 \times 10^{12} \text{ cm}^{-4}$ have been chosen for the preliminary computation.

In these hypothesis the mechanical dimensions of the two structures have been first optimised for the best power directivity at a working frequency of 8.015 GHz.

The successive analysis, achieved for variation of phase shift between modules in the range $-135^\circ \div 180^\circ$, have investigated the performances of both MJ and PAM with respect to frequency, plasma density and density gradient.

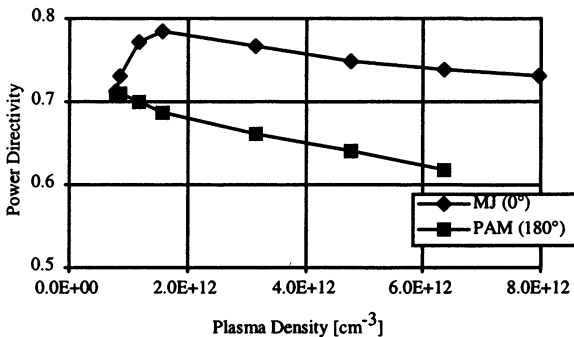


Fig. 4. Computed power directivities of MJ/PAM for FTU

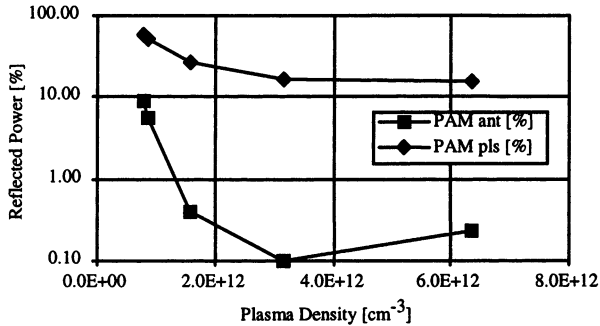


Fig. 5. Computed reflected powers in the PAM for FTU (ant : at the input, pls : at the plasma antenna interface)

The results confirm the optimum directivity of these launchers at low plasma density (Fig. 4) and their excellent coupling property due to the multijunction effect, furtherly improved by the passive waveguides in the PAM (Fig. 5); the density gradient has instead a limited influence on the performances.

Time shedule

The final design of both MJ and PAM have been achieved; the MJ construction has started by the beginning of last June and its delivery is foreseen by the end of January 2000.

In the meanwhile the design of the RF measurement facilities and of the connection between the extant RF distribution system and the new coupling structures are in progress. These items are in common with the PAM.

The final assembly of the MJ on FTU is foreseen for the next year summer shut-down.

References

1. Bibet Ph., Litaudon X., Moreau D.: Principle of a retroreflecting LH antenna. Conf. IAEA 1994: LHCD in ITER (IVA-LH)
2. Mirizzi F., Bibet Ph. et al.: Toward an active-passive waveguide array for Lower Hybrid application on ITER. Proc. of the 20th SOFT, Marseille, France, 1998
3. Mirizzi F. et al.: Commissioning of the 8 GHz, 1 MW, gyrotron of the FTU LH system; Proc. of the 3rd Int. Workshop: Strong microwaves in plasmas, Nizhny Novgorod, Russia, 1996.

SPHERICAL TOKAMAKS CONCEPT AND STATUS

V.K. Gusev

A.F.Ioffe Physico-Technical Institute, RAS
194021 Polytechnicheskaya st. 26, St.Petersburg, Russia

Introduction

The success of tokamak research program during the last decade, resulted in demonstration of controlled fusion reaction and significant fusion power production, had confirmed the leading role of tokamaks in magnetic fusion approach development. Recently international thermonuclear experimental reactor (ITER) detailed design was completed and that if built, it will operate successfully and produce necessary conditions for ignition and burning of D-T plasma.

To improve performance and minimize cost of future reactors it is necessary to continue tokamak physics research program. Among principal problems to be solved on this way the problem of plasma global and local stability seems to be one of the main. The existing scaling for D-T reactor operation requires to operate at maximum possible plasma current (minimum safety factor) to increase confinement time (τ_E). Also it's favorable to maximize plasma density to increase plasma $\beta=2\mu_0\langle p\rangle/B^2$ and fusion gain respectively, here: $\langle p\rangle$ - volume averaged plasma pressure, B - toroidal magnetic field. This leads to minimizing of auxiliary heating power ($\sim 1/\tau_E$) and maximizing of fusion power ($\sim \beta^2$).

The marginal stability of plasma column in such regimes is limited by ideal magnetohydrodynamics (MHD) stability limit and is the principal limit for plasma current and pressure increase. Troyon scaling predicts the ideal β - limit at the experimental value of $\beta(\%) \leq \beta_N (I_p/aB_T)$, where: $\beta_N \approx 3.5$ for conventional tokamaks, I_p - plasma current in MA, a - minor plasma radius in m, B_T - toroidal magnetic field in T. Recently neoclassical beta limits was discovered. The uncontrolled growth of magnetic islands width at rational magnetic surfaces leads to loss of confinement and stability, decreasing the effective β limit well below the ideal MHD limit. ITER will operate at the value of $\beta_N \approx 2.2$ only, to provide 90% disruption free discharges.

There are other significant confinement, stability and current drive problems to be solved for high performance, safe and low cost reactor

operation, among which important are: (i) disruption physics investigation, as the stored plasma column energy in reactor is very large, (ii) investigation of novel class of reactor instabilities (e.g. produced by superalfvenic particles), (iii) internal and external transport barriers creation and control, (iiii) controlled and safe heat and particle exhaust and plasma fueling, (iiiii) stationary regimes achievement with high fraction of plasma self-generated currents, etc.

It is clear, that physics of high β plasma in marginally stable regimes, with emphasis on conditions for nearly steady-state operation achievement will be at the focus of tokamak investigation program in the near future.

Among high β systems under attention now spherical tokamaks play a significant role. The idea was pioneered by Peng and Strickler in the 80'th. As it was pointed out in [1], when the aspect ratio $A=R_o/a$ of the plasma column (here R_o is the major radius) is substantially reduces with respect to conventional tokamak range of $A \approx 3 \div 4$, there is a significant increase of plasma column stability properties. Fig.1 illustrates such a reduction of aspect ratio, by depicting the path of a magnetic field line on the plasma periphery. In conventional tokamak, - left side of the figure, - magnetic

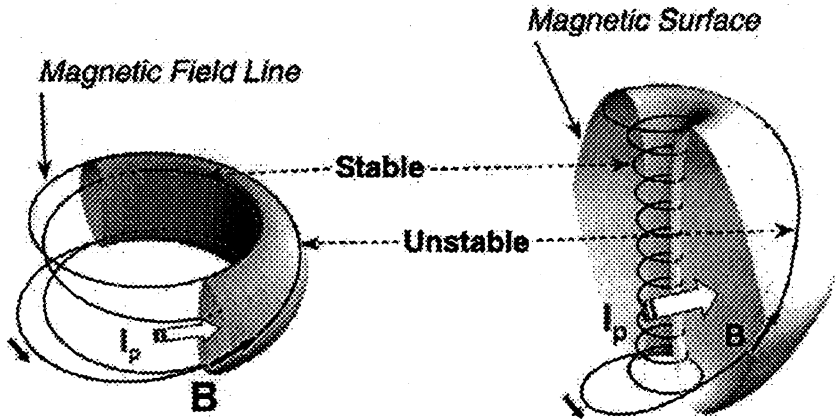


Fig.1 Magnetic field lines structure in the cases of conventional tokamaks (left, $q_a=4$) and small aspect ratio tokamaks (right, $q_a=12$)

field line has comparable lengths in the regions of favorable (inner stable region) and unfavorable curvature of magnetic field (outer unstable region). Variation of magnetic field across the plasma is small or moderate. In the case of spherical or small aspect ratio tokamak, - right side of the figure, - the field line path in the inner, stable region is significantly higher

than in the outer, unstable region and the field line is mostly spines around central bore of plasma column, where toroidal magnetic field is high and curvature is favorable. The magnetic field gradients in the plasma column are high. The most straightforward result of aspect ratio decrease is the increase in plasma column MHD stability, which permits either to increase significantly the plasma current, or to decrease magnetic field strength without global and local stability deterioration. Lower magnetic field operation reduces reactor cost ($\sim B^4$).

Spherical tokamak parameters domain

High toroidal plasma current in low magnetic field is the key feature of spherical tokamak (ST) parameters domain. The edge safety factor against global kink mode instability could be approximately represented as follows:

$$q_a \approx \{5a^2 B_T / I_p R_o\} \times \{ [1+k^2(1+2\delta^2-1.2\delta^3)]/2 \} \times 1/(1-1/A^2)^{3/2}, \quad (1)$$

where: k - vertical elongation of plasma column, δ - triangularity. The first term in braces is so called cylindrical q for circular column shape (q^{cyl}). The second term is shaping correction and the third one is toroidicity correction factors. The minimum value of q_a , corresponding to maximum possible plasma current, is $q_a = 2 \div 3$ for conventional (high aspect ratio, $A > 3$) tokamaks. For the case of conventional tokamak significant are first

two terms. Equation 1 can be rewritten for the normalized current $I_N = I_p / a B_T$, as the function of A , which is plotted at Fig.2. For constant, a and B_T - values the normalized current is the strong function of A , due to the principal contribution of the toroidicity correction factor of eq.1.

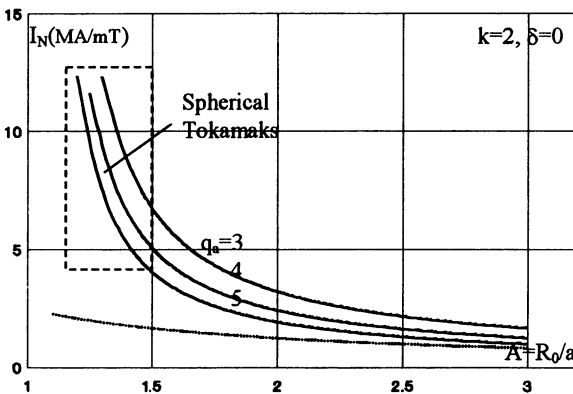


Fig.2. Dependence of normalized current I_N , from aspect ratio A for different values of edge safety factor q_a and elliptical cross-section of plasma column ($\delta=0$) with vertical elongation $k=2$. Dotted curve represents conventional tokamak approximation

Dotted line represents conventional tokamak approximation. The values of $q_a = 3, 4, 5$ are used as parameters for $I_N(A)$ dependence. The simple plasma shape with elliptical cross section ($\delta=0$) and elongation $k=2$ was chosen. Significant increase of I_N with respect to conventional tokamaks approximation is the characteristic of ST domain $1.2 < A < 1.5$. High normalized current leads to significant increase in plasma $\beta = \beta_N I_N$, according to Troyon scaling.

Dense and hot, high beta plasma to be obtained in new ST with strong plasma current in low magnetic field. Theory predicts that at such conditions plasma will have some properties different from conventional aspect ratio plasmas. Among main are: high edge magnetic shear, very high pressure gradients, low value of Alfvén velocity and high dielectric constant ($\omega_{pe}^2 / \omega_{ce}^2 \approx 10^2$). Some favorable predictions for this new parameter range could be made already. Well known is the role of high magnetic shear at the plasma edge in stabilization of peripheral MHD instabilities, which could help in beta limit increase. Very high pressure gradients are the drivers for self generated plasma currents and for $E \times B$ strongly sheared plasma flows, stabilizing microturbulence by creating transport barriers. High fraction of superalfvenic particles is expected to be generated during neutral beam injection or ICRH in moderate temperature, low magnetic field plasma, which could be very helpful in experimental modeling of reactor instability conditions (e.g. studying of TAE modes). High dielectric plasma constant resulted in low phase velocity of electromagnetic waves makes possible effective electron heating in the ion cyclotron waves frequency range by use of high harmonic fast wave heating (HHFW) scenario [2]. Strong poloidal inhomogeneity of plasma provides necessary conditions for externally launched lower hybrid waves absorption in the range of $\omega \approx 10 \omega_{LH}$ [3]. Other methods of auxiliary plasma heating and current drive (CD) currently used in spheromaks and field reverse configuration devices could be tested in ST (e.g. helicity injection, rotation of magnetic field, etc.) [4,5].

Should be mentioned that other plasma dimensionless parameters used in tokamak physics study change significantly in ST's, i.e. particle trapping edge fraction and normalized ion gyroradius are increased, normalized connection length and normalized radius of field line curvature are decreased. This gives opportunity to verify existent theory and computational models to new parameters range.

Equilibrium and stability issues of spherical tokamaks

In addition to ST plasma properties described above there are many poorly investigated phenomena which should be studied in the frames of ST research program. Among main are other strong toroidicity effects, low disruptivity, “natural” divertor configuration and unusual plasma behavior in scrape of layer, new types of particle orbits, high normalized Larmour radius effects, high density limits and other, which makes research program of ST very existing and helpful for deeper insight into magnetic confinement physics [6]. Many of these phenomena are the consequence of ST equilibrium properties. High curvature of the field lines, high plasma current and strong gradient of toroidal magnetic field, resulting in high magnetic shear, have a strong influence on plasma column stability also. This allows considering some issues of equilibrium and stability in ST jointly.

In ST configuration one can not more use conventional tokamak approximation $B_T/B_{pol} \gg 1$, as at the outer plasma column boarder (see Fig.1) the poloidal magnetic field is dominating. Result is high outboard pitch angle of the field line. When moving into the plasma core the field line pitch angle is quickly decreases, producing high magnetic shear $\{r/q\} \times \{dq/dr\} \gg 1$, which has strong stabilizing effect. At the inner plasma column boarder, contrary, the toroidal magnetic field is much higher than poloidal one, and the field line has mostly toroidal direction.

Several important consequences arise from equilibrium properties of ST. First - the vertical elongation of plasma column increases in uniform vertical field [1]. Increased vertical elongation enhances plasma column kink stability, by increasing the poloidal circumference of column (decreasing edge B_p). In accordance with formula 1, edge safety factor increases with elongation, $q_a \sim (1+k^2)/2$.

Second - high I_{pol} component of plasma current is responsible for paramagnetic effect, as the magnetic field produced by this component adds the vacuum toroidal field enhancing it. As it was pointed out in [7] the diamagnetic effect of high β plasma counters the paramagnetic effect of high plasma current and an absolute magnetic well can appear. The example of magnetic surfaces reconstruction indicating magnetic well existence in NBI heated START discharge is shown in Fig.3. The magnetic well appearance inside plasma column improves stability, modify particle orbits reducing trapping and therefore increase current drive efficiency.

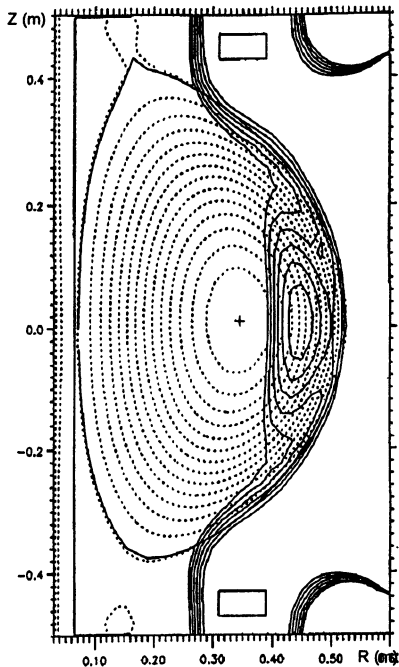


Fig.3. START magnetic surfaces reconstruction in high beta shot. Solid lines represent surfaces of $|\mathbf{B}|$. Magnetic well at $\sim a/2$ position appears.

Third consequence of ST equilibrium is weaker influence of current density profile shape on safety factor spatial distribution. Field lines at the plasma periphery at the inboard surface of plasma column have mostly toroidal direction, as toroidal field is much higher than poloidal one in this region. Overall kink stability of plasma column is provided by big number of toroidal field line transits at the plasma periphery (in the region of high magnetic field) and doesn't depend so much on current density distribution as in conventional tokamaks. This effect results in "decoupling" of $q(r)$ and $j(r)$ profile shapes [6], which is not the case in conventional tokamaks, and gives rise to new class of stationary current density distributions, including hollow current

density profiles, stable for kink and double tearing modes. The example of such equilibrium simulations for Pegasus spherical tokamak [8] is shown on Fig.4. Stationary equilibrium current density profiles variety means that

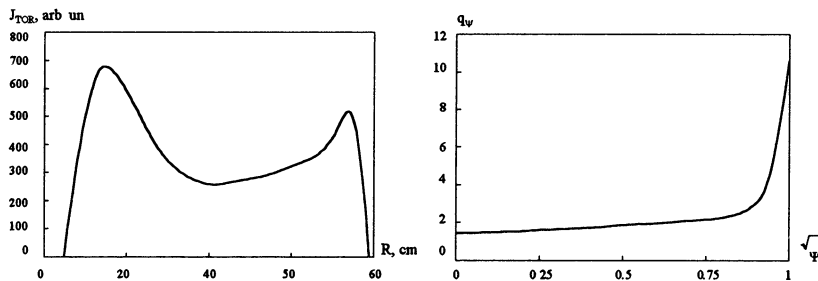


Fig.4. Left – toroidal current density j_{tor} versus major radius R distribution simulations for Pegasus high β discharge. Right – edge safety factor q_w versus flux coordinate ψ for this discharge

for the same total plasma current the internal inductance of plasma column l_i , which is the measure of profile peakedness, could change in wider range than that appropriate for conventional aspect ratio tokamaks. As the equilibrium vertical field, providing an inward force to balance the outward hoop force of the plasma current, is linearly dependent on l_i [9], it must be taken into account in the design of plasma column control system.

In addition to equilibrium simulations MHD stability analysis is desired to ensure the obtained $p(r)$, $j(r)$ profiles are stable with respect to pressure gradient and current gradient driven modes. This becomes more actual in ST case, as the class of equilibrium profiles is much broader including flat and hollow profiles, producing very strong peripheral gradients $\nabla j(r)$, $\nabla p(r)$. Such analysis was performed in [10] for the case of NSTX geometry and high β , high β_p conditions. It was found that, (i) broader pressure profiles are better for stability and that, (ii) stable equilibrium with very high fraction of pressure gradient driven currents exists. The spatial distribution of current density is strongly influenced by high components of locally generated peripheral Pfirsch-Schluter and diamagnetic currents. Overall net contribution of these components averaged over the flux surface is zero. Main component of toroidal current is bootstrap current (I_{bootst}) and the current density distribution is hollow. High β , high β_p regimes are of great importance for future tokamak-reactor, providing high gain, steady state, and low auxiliary power operating scenario, which is impossible to realize in conventional tokamak geometry. As fusion gain is limited by finite value of $\beta \sim \langle p \rangle / B_T^2$, whereas bootstrap current value is proportional to $\beta_p \sim \langle p \rangle / B_p^2 \sim \langle p \rangle / I_p^2$. Combining $\beta\beta_p$, we have $\beta\beta_p \sim \langle p \rangle^2 / (B_T^2 I_p^2) \sim \beta^2 B_T^2 / I_p^2$. If Troyon scaling holds in reactor ($\beta = \beta_N I_p / a B_T$), we have $\beta\beta_p \sim \beta_N$, and the only way to increase fusion gain and bootstrap current simultaneously is to increase β_N . It's impossible to do in conventional tokamaks due to trade off between β and β_p . Their product is limited by Troyon coefficient $\beta_N \leq 3.5$ (ideal beta limit), or lower value, due to soft beta limit. As it was shown in [11], there are stable equilibrium conditions for ST with $\beta_N \leq 10$ and $I_{bootst} \approx 0.99 I_p$. The description of such a scenario in ST reactor is a question, which is out of the scope of this paper, and one could look into [12].

Different issue is nonideal MHD modes. Principal limitation of tokamak reactor performance is so called soft beta limit, caused by uncontrolled growth of neoclassical tearing modes (NTM). Flattering of in-island pressure profiles lead to vanishing of bootstrap current inside

magnetic islands and nonlinear increase of islands widths. This destroys magnetic surfaces and deteriorates magnetic thermoizolation of entire plasma column. To saturate the island width growth at the finite value, the missed in-island current could be substituted by ECD externally driven one [13]. Theoretical analysis applied for ST conditions showed that unstable NTM's could be avoided due to unique features of ST equilibrium. Large Phirsch-Schluter currents in such equilibrium, represented by stabilizing "Glasser" term prevent island width growth [14], providing conditions for NTM's stabilization.

There are favorable predictions for microturbulence suppression in ST. In conditions of high beta, low aspect ratio plasma, losses caused by ion microturbulence activity could be effectively reduced, or even suppressed by sheared flow in crossed $E_r \times B_T$ fields. Radial electric field value in tokamak can be estimated from the expression [15]:

$$E_r = \nabla p / e z n_i + V_T B_p - V_p B_T, \quad (2)$$

where: e - unit electric charge, z - effective plasma charge, n_i - ion density, V_T , V_p - toroidal and poloidal flow velocities. In the case of spherical tokamak the pressure gradient could reach extremely high value, making the first term dominating in equation 2 and an extreme high value of electrical field could be reached. Corresponding shearing flow rate, $\omega_{E \times B} \approx (RB_p/B_T) \times d\{E_r/RB_p\}/dr$ could be as high as $\omega_{E \times B} \approx 10^6$ 1/sec, which is approximately one order of magnitude higher than microinstability growth rate increment [12]. Fig.5 illustrates the result of simulations

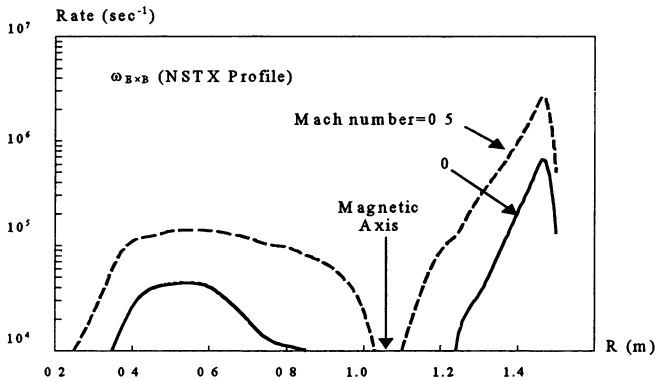


Fig.5. Simulations of shearing flow rate $\omega_{E \times B}$ for NSTX conditions. Solid line – distribution of $\omega_{E \times B}$ along plasma radius without momentum transfer to the plasma column. Dashed line the same with moderate momentum transfer ($M=0.5$). The conventional tokamak range is $\omega_{E \times B} < 10^5$.

for NSTX conditions. Plasma energy losses are minimized down to classical ion transport losses across big region of plasma column.

Status of research

There are few comprehensive review papers summarizing experimental and theoretical results of ST's research during the last years, for more details one could look in [6,7,16].

Few selected results, experimentally observed and theoretically explained, seem to be underlined once more, in spite of analysis made in the papers referred above. First is the confirmation of spherical tokamak equilibrium properties, basically predicted in [1]. Experiments on START (Culham lab.), CDX-U (PPPL), Medusa (Wisconsin university) had confirmed that high plasma current could be achieved in weak magnetic field and this is typical for spherical tokamaks. Other details of the ST equilibrium were demonstrated. It was shown that experimental configurations of plasma column with flat or hollow, low internal inductance $j(r)$ profiles exist with monotone, high shear $q(r)$ profiles ensuring ballooning, and kink stability of the column. It was shown also, that vertical stability of plasma column is conserved up to significantly higher vertical elongations of plasma column than that appropriate for conventional tokamaks. Very small values of dangerous halo currents, accompanying vertical displacement events were demonstrated. The paramagnetic effect caused by big poloidal component of plasma current was recorded.

In addition few novel features of ST equilibrium and stability were observed. High beta shots, obtained in START machine, were characterized by very low edge safety factor value, which initially were regarded as unstable. Successful were double null configuration discharges with $q_{95} \approx 2.3$. The enhanced, low q stability of plasma column couldn't be explained by existent theoretical models developed for conventional tokamaks, especially taking into account kink modes coupling due to high toroidicity effects. New method of plasma MHD stability analysis, based on the principal role of separatrix current in providing enhanced stability of ST plasma column, predicts even lower limit of kink stability ($q_{95} \approx 1.1$) [17]. As the toroidal field in START was order of magnitude lower than in conventional tokamaks, the normalized current, $I_N = I_p/aB_T$ could reach high values (about 7 in START) before the edge q decreases below 2. Another reason for high beta regimes achievement in START was overcoming of conventional tokamaks soft ($\beta_N \approx 2$) and ideal ($\beta_N \approx 3.5$) beta

limits. It was demonstrated that high power NBI heated regimes with $\beta_N < 6$ were stable, theoretical analysis shows even higher limits for β_N [10,11]. This helps in achievement of high toroidal beta in accordance with Troyon scaling. Toroidal beta up to 40% were recorded for beta defined as, $\beta_T = 2\mu_0 \langle p \rangle / B_T^2$, where B_T - axial vacuum toroidal field strength. Fig.6 shows the dependence of average β_T on normalized current value [7].

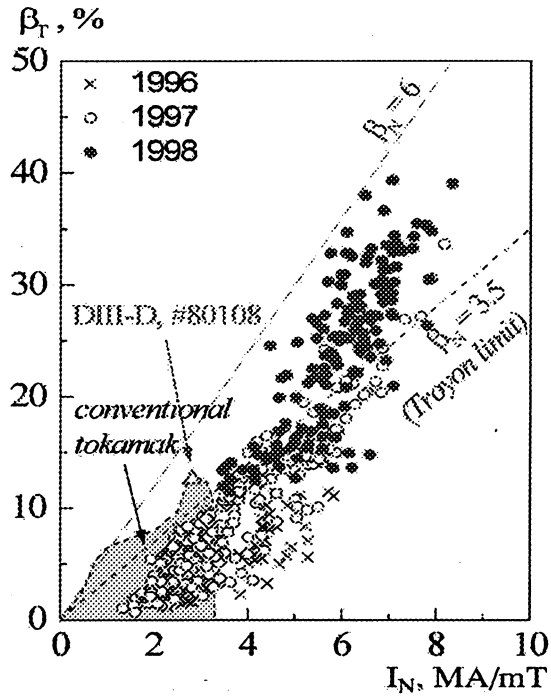


Fig.6. Beta toroidal β_T versus normalized current dependence in START spherical tokamak. Conventional tokamak range is shown by dashed area. Ideal conventional tokamak limit is represented by $\beta_N = 3.5$ line

One more example of unexpected phenomenon observation was disruption resilience demonstration. In early START experiments (until 1995) there was no hard plasma current disruption event recorded for plasma with $A < 1.8$. Instead of disruptions, at the conditions close to stability limit, the MHD activity event, called internal reconnection (IRE) of magnetic field lines was registered. Such event, characterized by MHD precursor and thermal energy quench, has much in common with hard disruption event, except current quench phase. The phenomenology of this event is discussed in [7] and declared that the main reason for current disruption immunity was the existence of free space beyond the plasma column in START. This allows plasma column to expand freely in vertical direction after current profile fluttering and drop of l_i , increasing the edge safety factor with column elongation, in accordance with formula 1. Plasma survives, conserving significant part of thermal and current en-

ergy. Such picture was confirmed by recording IRE's also in CDX-U and Medusa [8,18], but no disruption immunity was registered due to the vertical space limit. Later on, after divertor coils installation, limiting the vertical plasma size, START plasma also lost disruption immunity.

Important are other experimental data, described elsewhere, confirming other features of ST. High density limits, in accordance with Greenwald scaling were achieved ($n \sim \langle j \rangle$). Superalfvic particles driven instabilities were recorded. The favorable features of HHFW heating in the ion cyclotron range of frequency and NBI assistant current drive were observed.

Significant part of the work performed in the previous time interval was connected with theoretical and computational analysis of experimental data and making prospects for the new machines parameter range. One of the principal tasks of next step machines program is how to realize favorable configurations of plasma column predicted theoretically and simulated numerically? In other words, how to create necessary $j(r)$ and $p(r)$ profiles? In ohmically driven ST's toroidal current density profile will be peaked on-axis and monotonic, once the current profile relaxed. To achieve distributions described in [8,10,11] the externally driven current is necessary.

Auxiliary heating, current drive and profile control methods are the key instruments for this task solution. Spherical tokamaks parameter range makes possible the application of unusual current drive and auxiliary heating schemes and more effective usage of well known schemes. Interesting possibility of high frequency current drive will be tested at Globus-M. Severe accessibility criteria make the usage of conventional lower hybrid frequency range current drive ineffective for high density, low magnetic field plasma, as the electromagnetic waves only with high $N_{\parallel} > 8$ could penetrate into plasma. But, as it was firstly pointed out in [3], the accessibility for the higher frequency waves, with the frequency $\sim 10 \omega_{LH}$ simplifies, if the waves are launched from plasma periphery with slowing down in the poloidal direction. Note, that conventional tokamak scenario for lower hybrid CD implies the toroidal direction slowing down of the waves. In scenario proposed for spherical tokamak, grill must be rotated 90° around the axis of symmetry ($N_\theta \neq 0$, where θ is poloidal angle). The simulated efficiency of the waves absorption is dependent on the plasma current amplitude and current drive efficiency could reach the value of $\eta \approx 4 \cdot 10^{18} \text{ A/W} \cdot \text{m}^2$. Fig.7a shows the power deposition as the function of

plasma minor radius for different plasma current amplitudes. Fig.7b represents the driven current dependence with respect to total plasma current.

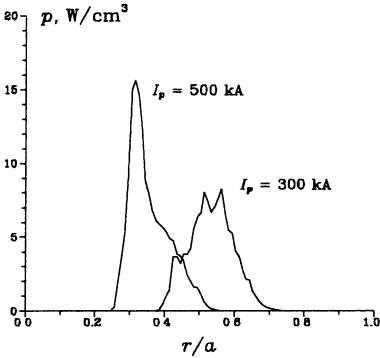


Fig.7a. Simulation results of power deposition at the frequency 2.45 GHz for different plasma currents. The slowing down is in poloidal direction ($N_\phi = 0, N_\theta \neq 0$)

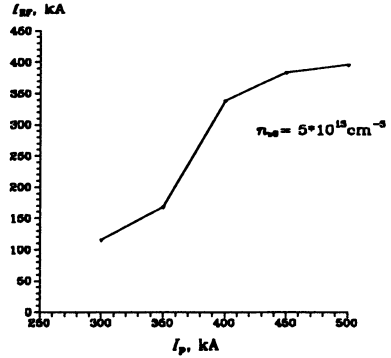


Fig.7b. The dependence of RF driven current from total plasma current amplitude for the Fig.7a scenario. The central electron density is $5 \cdot 10^{13} \text{ cm}^{-3}$

Mentioned above was HHFW heating and current drive scenario in the ion cyclotron frequency range, which is the main method for the NSTX tokamak [19]. Ion cyclotron heating at fundamental frequency in light atomic mass minority scenario, as well as HHFW heating are planned to be used at Globus-M spherical tokamak as the main methods. Simulations performed in the conditions of high toroidicity, high magnetic shear and paramagnetic effect, showed high single pass absorption and narrow central power deposition zone [20], which makes the heating more effective than in conditions of conventional tokamaks of comparable size. Fig.8 illustrates the energy flux variation and absorbed power distribution inside plasma column.

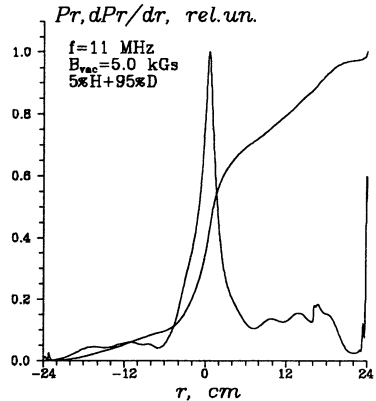


Fig.8. Energy flux (smooth curve) and absorbed power distribution simulations in Globus-M spherical tokamak in hydrogen minority IC heating scenario. $r=0$ indicate the axis of vacuum vessel.

still a big deficit of data to provide complete theoretical analysis and to establish selfconsisting database for all phenomena observed. Another reason sophisticating theoretical and computational data analysis is that all experimental data were obtained in rather cool, collisional plasma in conditions of typically pulsed machines with an extreme influence of transient processes. The more significant is the success of experimental and theoretical work performed, which demonstrated the spherical tokamaks remarkable features and more intriguing is the expectations for the results from bigger scale, higher performance machines.

Program and plans for spherical tokamaks research

Features and advantages of ST approach, i.e. high current in low magnetic field and high plasma column stability resulted in record β values, woke up the interest among the world fusion community for spherical tokamak investigation program. There are few old and several new experiments around the world (totally more than 10) continue and start operation now. They can be tentatively divided into two groups with respect to machine performance and expected plasma parameters, as proof of principal and concept exploration devices. The map with spherical tokamaks distribution around the world is shown on Fig.9, parameters of several spherical tokamaks are summarized in the Table.

Research programs of new spherical tokamaks will be concentrated

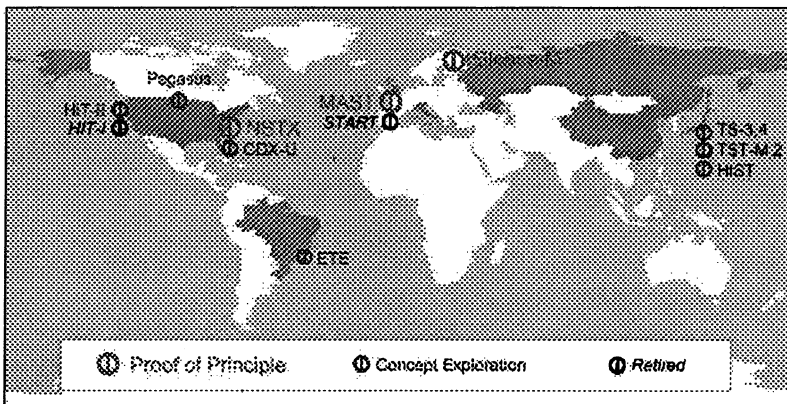


Fig.9. Existing and retired ST experiments in the world.

around investigation of novel physical phenomena caused by ST plasma properties and existing tokamak data base extension to the new parameters

Table. Parameters of spherical tokamaks

Device	START	CDX-U	ETE	Pegasus	Globus-M	NSTX	MAST
Country	UK	USA	Brazil	USA	Russia	USA	UK
Location	Culham	PPPL	INPE	Wisc. Univ.	Ioffe Institute	PPPL	Culham
R_0 (m)	0.3	0.34	0.3	0.45	0.36	<0.85	<0.85
a (m)	0.25	0.22	0.2	0.4	0.24	<0.68	<0.65
A	>1.2	>1.5	1.5	1.1-2	1.5	>1.25	>1.3
k	<4	<1.6	1.6-1.8	1.5-3.7	1.5-2.2	1.5-2.5	1.5-2.5
I_p (MA)	0.31	0.15	0.22/0.4	0.3	0.5	1	2
B_T (T)	0.3	0.2	0.4/0.8	0.15	0.65	0.3/0.6	0.63
Additional heating	0.8 MW NBI 0.2 MW ECRH	0.3 MW HHFW	Awaits funds	2 MW ICRH	2 MW ICRH 1 MW HHFW 1 MW LHCD 1 MW NBI	6 MW HHFW 5 MW NBI	5 MW NBI 1.5 MW ECRH
Pulse length (s)	<0.04	<0.05	<0.2	0.05	<1	<5	<5

range. It should be noted, that spherical tokamaks can operate in two distinct regimes, one being similar to conventional tokamaks (high aspect ratio regime) and another (low aspect ratio regime), which is completely different from conventional tokamaks data domain, allowing generalization of existent scaling laws and the development of new ones.

Investigation programs of different spherical tokamaks, as well as their experimental possibilities allow crosschecking of results from one hand and complementary from another. There are different auxiliary heating methods planned for use in MAST, NSTX and Globus-M machines, referred as proof of principal devices. As it could be seen, NBI and HHFW heating methods could be checked in conditions of different machines. Another example is the complementary design principals, which could help to make the proper choice for future big scale and costly ST machines. MAST is constructed, as the big tank, with all poloidal coils

placed inside and have big ballast volume, but more space beyond plasma. NSTX and Globus-M has more close fitting vessels with lower ballast volumes and lower space beyond plasma. MAST and NSTX have bigger plasma sizes and higher plasma currents, but Globus-M has higher current density and B/R ratio, both favorable for operation at higher plasma density [21]. These machines capabilities variety will help to scan scaling laws in maximum possible parameter range and extend significantly existing tokamak data base. Now these machines are at the very beginning of the research programs. First plasma results were reported. First plasma traces in Globus-M tokamak are shown at Fig.10. Experimental possibilities of the proof of principal machines and their research programs are described in [22,23,24].

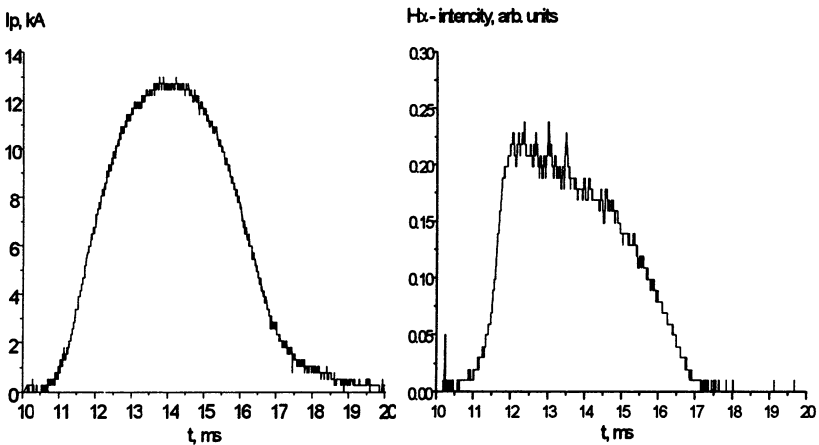


Fig.10. First plasma in Globus-M tokamak. The left trace – the plasma current, the right trace – the intensity of hydrogen Balmer alpha line

Physics investigation of marginally stable regimes with high I_N and β_N values, study of disruption physics and physics of new classes of plasma instabilities, creation of stable transport barriers, physics research of divertor and scrape of layer, development of CD and auxiliary heating methods for $j(r)$ and $p(r)$ profile control, achievement of low auxiliary power regimes with high selfgenerated plasma currents, technology and engineering development - are the key tasks of new spherical tokamaks research programs.

Conclusions

Spherical tokamaks, combining properties of tokamaks, such as high stability and confinement, with compactness of spheromaks and high betas appropriate for field reversed configurations, many of which were experimentally demonstrated, should be regarded now as very important branch of magnetic confinement research which could contribute a lot into fusion science and development of neutron sources and power plants.

Unusual plasma parameters domain, expected in spherical tokamaks, with high pressure and current density spatial gradients, high magnetic shear, severe toroidicity effects gives impetus for modification of existing tokamak theoretical models, computational tools and creation of new. Experimental verification of such models must help in: (i) understanding of basic physical processes in high performance (hot, low collisionality) ST plasma with contributions into the development of selfconsistent theory of tokamak plasma and in (ii) making a significant step in approaching to advanced tokamak concept regime characterized by high confinement, low auxiliary power, steady state operation.

Acknowledgment

I would like to acknowledge A. Sykes, M. Peng, W. Morris and other colleagues, who had provided material, N. Sakharov and J. Menard for discussions, V. Minaev and A. Novokhatskii for the help in preparation of the manuscript.

References

1. Peng, Y-K.M., et al, Nuclear Fusion, v.26, N.6, 769, 1986
2. Ono M. Phys. Plasma, v.2, 4075, 1995
3. Esterkin A.R., et al, Proc. Int. Workshop on Spherical Tori, S. Petersburg, v.1, 265, 1997
4. Jarboe T.R., et al, Fusion Energy, v.2, 243, 1996
5. Knight A.R., et al, Plasma Phys. and Contr. Fusion, v.32, 575, 1990
6. Morris A.W. invited paper, 26 EPS conf on Contr. Fusion and Plasma Phys., Maas-tricht, 1999
7. Sykes A., Technical Physics, v.44, N9, 1047, 1999
8. Fonk R.J., Proc. of Spherical Tori and US-Japan Workshop for low aspect ratio tokamaks, Culham, v.1, 40, 1996
9. Wesson J.A., Tokamaks, Clarendon Press, Oxford, 73, 1987
10. Menard J.E., et al, Nuclear Fusion, v.37, N.5, 595, 1997
11. Miller R.L., et al, Phys. Plasma, v.4, N.4, 1062, 1997
12. Stambaugh R.D., et al, Fusion Technology, v.33, 1, 1998

13. Zohm H., This conference
14. Kruger S.E., et al, Phys. Plasma, v.5, 455, 1998
15. Zarnstorff M.C., Invited Report on Symp. devoted to 80th anniversary of A. F. Ioffe institute, S.Petersburg, 1998
16. Robinson D.C., Plasma Phys. and Control Fusion, v.41, A143, 1999
17. Medvedev S., Proc. 25th EPS conf. on Contr. Fusion and Plasma Phys., Pregue, 741, 1998
18. Ono M., Proc of 16th IAEA Fusion Energy conf., Montreal,v.2, 71, 1996
19. Jaeger E.F., et al, Proc of 24th EPS conf. on Contr. Fusion and Plasma Phys., Berchtesgaden, v.21A, p.II, 917, 1997
20. Irzak M.A., et al, Plasma Physics Reports, v.25, N.7, 1999
21. Gusev V.K., et al, Technical Physics, v.44, N.9, 1054, 1999
22. Ono M., Proc of IAEA TCM on Spherical Tori and 4th International orkshop on Spherical Tori, Tokyo, 214, 1998
23. Morris A.W., Proc of IAEA TCM on Spherical Tori and 4th International Workshop on Spherical Tori, Tokyo, 194, 1998
24. Gusev V.K., Proc of IAEA TCM on Spherical Tori and 4th International Workshop on Spherical Tori, Tokyo, 232, 1998

PROPAGATION OF WEAKLY DIVERGENT MICROWAVE BEAMS IN TOKAMAK PLASMAS

A.D.Piliya, A.N.Saveliev

A.F.Ioffe Physico-Technical Institute, St.Petersburg, Russia

An approach which treats microwave beam as a superposition of wide "virtual" beams unaffected by diffraction is proposed. A code based on this method is developed.

Calculation of the microwave fields radiated by a wave-guide antenna in tokamak plasmas is a difficult problem not fully solved up to now. Since equilibrium plasma parameters vary little over a wavelength in the microwave frequency region, the multidimensional WKB theory seems to be a suitable tool for treating the beam propagation. However, the WKB method ignores effect of diffraction, and, for this reason, breaks down in the wave zone at a distance $L \geq (\omega/c)D_a^2$ from the antenna, where D_a is the antenna diameter. In large tokamaks, the wave zone may occupy a noticeable part of the plasma volume. Then direct application of the WKB method is inadequate. Since these limitations are related to the beam diameter value D_a , we could avoid them by representing the actual narrow beam as a superposition of much wider beams whose diameter D satisfies $(\omega/c)D^2 \gg a$, where a is the minor radius. These virtual beams are unaffected by diffraction within the plasma and may be treated using the WKB theory. Their initial phases and amplitudes must be adjusted in such a way that the superposition as a whole satisfies the boundary conditions. The actual beam is a result of interference of the virtual beams. The interference pattern changes as these beams travel through the plasma, describing evolution of the real beam.

Assume that the electric field on the plasma boundary at $\rho=l$ is given in the form.

$$\vec{E}(\theta, \varphi) = \vec{E}^b = \vec{\varepsilon}(\theta, \varphi) U(\theta - \theta_0, \varphi - \varphi_0) \exp\{i\sigma [n_2(\theta - \theta_0) + n_3(\varphi - \varphi_0)]\} \quad (1)$$

Here (ρ, θ, φ) are flux surface related co-ordinates, ε is a unity polarisation vector, $\sigma = (\omega a/c) \gg 1$, n_2 and n_3 are constants of the order of unity and (θ_0, φ_0) are co-ordinates of the amplitude U maximum. Now, Fourier transforming the amplitude U , present the field on the boundary surface as

$$\vec{E}^b = \int \vec{E}_\chi^b(\theta, \varphi) d\vec{\chi} , \quad (2)$$

where χ is a vector with covariant components $\{0, \chi_2, \chi_3\}$. The amplitude spectral width $\Delta\chi_2$ is related to the beam angular size $\Delta\theta \approx D_0/a$ by $\Delta\chi_2 \Delta\theta \approx 1/\sigma$. For certainty we assume the ordering $\Delta\theta \approx \Delta\chi_2 \approx \sigma^{-1/2} \ll 1$. We present the beam electric field everywhere in the plasma in the form

$$\vec{E} = \int \vec{E}_\chi(\vec{r}) d\vec{\chi} \quad (3)$$

The virtual beams $\vec{E}_\chi(\vec{r})$ are the solutions of the wave equation satisfying $\vec{E}_\chi(\vec{r})|_{\rho=1} = \vec{E}_\chi^b(\theta, \varphi)$. According to the above consideration they can be found using the WKB approximation. In the simplest case with no wave reflection or mode conversion

$$\vec{E}_\chi = \vec{e}_\chi(\vec{r}) A_\chi(\vec{r}) \exp\{i\sigma S_\chi(\vec{r})\} , \quad (4)$$

where \vec{e}_χ , A_χ and σS_χ are the unity polarisation vector, the amplitude and the eikonal, respectively. Further we ignore weak χ -dependence of \vec{e}_χ . The ray approach is used to find the virtual beams. In the phase space $\{\rho, \theta, N_2\}$ rays map the line $N_2 = n_2 + \chi_2$ given at the surface $\rho = 1$ into a continuous curve $M_\chi(\rho, \theta)$ at any surface $\rho = \text{const}$ they reach. Suppose that the value $\Phi_\chi(\rho)$ of the function S_χ is known at the point $P\{\rho, \theta_0^{(\rho)} + \delta\theta, \varphi_0^{(\rho)} + \delta\varphi\}$, which is the map of the point $P^0\{\rho=1, \theta_0, \varphi_0\}$. Then

$$S_\chi(\vec{r}) = \Phi_\chi(\rho) + \int_{\theta_0^{(\rho)} + \delta\theta}^{\theta} M_\chi(\rho, \theta') d\theta' + (n_3 + \chi_3)(\varphi - \varphi_0^{(\rho)} - \delta\varphi) \quad (5)$$

Equation (5) implies that M_χ is an unambiguous function of the poloidal angle. This is the case only close enough to the antenna, at larger distances it typically has an S-like form. This means that three different rays come to the same spatial point here. The points θ^* , where $\partial M_\chi / \partial \theta \rightarrow \infty$, form continuous curves in the (ρ, θ) plane which are known as caustics for given mode χ (Fig.1,2). The caustics are similar to the mode conversion surface in the 1D WKB theory. In their neighbourhood Eq.(4) is modified to give in the propagation region

$$\vec{E}_\chi = \vec{e} \left[A_\chi^I \exp(i\sigma S_\chi^I) - i A_\chi^R \exp(i\sigma S_\chi^R) \right] , \quad (6)$$

and $E_{\chi}=0$ in the evanescent region. Here superscripts I and R denotes incident and reflected waves and $S_{\chi}^{I,R}$ are given by Eq.(5) with the integration limit θ belonging to the different brunches of $M_{\chi}(\theta)$.

To find the χ -dependence of M_{χ} note that displacement of the phase trajectory resulting from small perturbations of the initial conditions $n_i \rightarrow n_i + \chi_i$ depends on the perturbations linearly:

$$\delta\theta(\rho, \vec{\chi}) = \alpha_i \chi_i, \quad \delta\varphi(\rho, \vec{\chi}) = \beta_i \chi_i, \quad \delta M(\rho, \vec{\chi}) = \mu_i \chi_i \quad (7)$$

The coefficients α_i, β_i, μ_i are slowly varying functions of the initial poloidal angle and can be considered constant over the beam. Then, $M_{\chi}(\theta) = M_0(\theta - \delta\theta) + \delta M$ at small χ and reference phase $\Phi_{\chi}(\rho)$ at the point $P\{\rho, \theta_0^{(\rho)} + \delta\theta, \varphi_0^{(\rho)} + \delta\varphi\}$ is given by

$$\Phi_{\chi}(\rho) = \Phi_0(\rho) + M_0(\rho, \theta_0^{(\rho)}, \varphi_0^{(\rho)}) \delta\theta + n_3 \delta\varphi + \frac{1}{2} \lambda_{ik} \chi_i \chi_k, \quad (8)$$

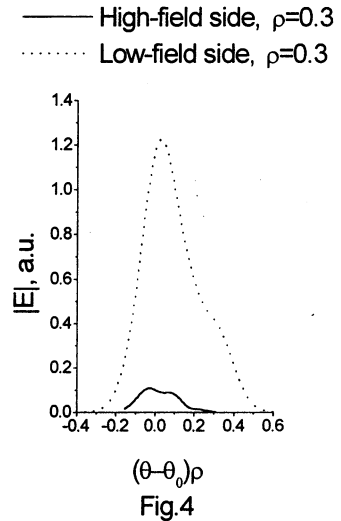
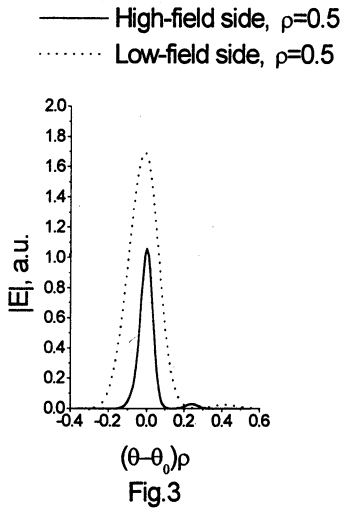
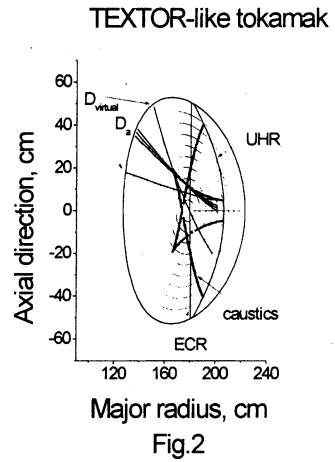
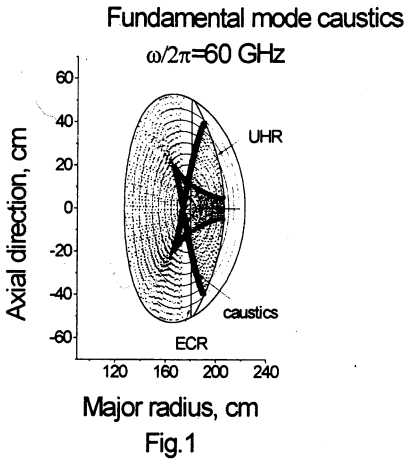
where $\lambda_{ik}(\rho), (i, k = 2, 3)$ are quantities of the order of unity. The amplitude A_{χ} of the virtual beam can be obtained from the Poynting theorem applied to a bundle of rays. Its variation is due to change in the group velocity, the effect of convergence or divergence of the bundle and the wave damping. Ignoring, for lack of place the last factor, the amplitude can be presented similarly to the function M_{χ} in the following form:

$$A_{\chi}^{I,R}(\vec{r}) = U_{\chi} G_0^{I,R}(\rho, \theta - \delta\theta) \quad (9)$$

Close to the caustics, $G_{\chi} \propto |\theta - \theta^*|^{-1/4}$ at $\theta \rightarrow \theta^*$ in the allowed region and equal zero in evanescent region. Substituting obtained expressions for the eikonals and amplitudes into Eqs.(6,4,3) and assuming the Gaussian boundary conditions with $U_{\chi} = C \exp(-b_{ik} \chi_i \chi_k)$, one integration in Eq.(3) can be performed analytically with the use of a proper change of variables. This reduces calculation of the beam electric field to evaluation of a 1D integral whose integrand involves the ‘‘fundamental’’ virtual beam E_0 and elementary functions.

Using the above approach a numerical code calculating microwave beam electric field in tokamak plasma has been developed. In this code all necessary functions entering Eqs.(6,7,8,9) are calculated directly from

the ray data without using the perturbation theory. Numerical examples (Fig.3,4) and illustrations (Fig.1,2) are given for a TEXTOR-like tokamak with the parameters: $R_0=1.75\text{m}$, $a=0.48\text{m}$, $B_{T0}=2.2\text{T}$, $n_{e0}=1.5\cdot 10^{19}\text{m}^{-3}$, $T_{e0}=1\text{KeV}$, $\omega/2\pi=60\text{GHz}$. The temperature and density profiles are parabolic and the antenna is on the high-field side of the tokamak off the equatorial plane (Fig.2).



MODELING OF THE COULOMB COLLISIONS FOR KINETIC DESCRIPTION OF ECR PLASMA HEATING

A.G. Shalashov, E.V. Suvorov

Institute of Applied Physics, Nizhny Novgorod, Russia

ECR plasma heating is analyzed basing on 2D kinetic equation for electron distribution function with Landau collision integral and an operator of quasilinear diffusion being taken into account. Two approaches for simplified account of a collision term are tested for a model problem. Numerical solutions obtained indicate the similar dynamics of the total electron energy for both types of collision integral under consideration. For the regime of quasistationary ECR heating the qualitative analytical approximation is developed.

Under cyclotron resonant plasma heating distribution function of the resonant electrons can deviate from the Maxwellian. This is significantly more pronounced in low-density high power ECRH condition where kinetic effects modify rf-power absorption rate. Combined action of resonant rf-field and Coulomb collisions with non-resonant particles results in the change of the whole electron distribution function displaying as heating of bulk electron component in the long run. Such a situation is usually described by a kinetic equation in which there is a collision term as well as quasilinear diffusion term representing an interaction with EC waves

$$\frac{\partial f}{\partial t} = \hat{L}_c[f] + \hat{L}_{qi}[f]. \quad (1)$$

The well-known representation of a collision term \hat{L}_c is Landau collision integral (or its modifications). However, in a case of ECR plasma heating, when the distribution function can be distorted in the region of thermal energies, including of full Landau collision integral in a kinetic model is related to substantial numerical difficulties and requires a lot of computational time for complex multidimensional situations. Thus, different approaches for simplified account of a Landau collision term are of interest. Two widely spread possibilities of such a simplification adopted for the description of heating in the main body of a distribution function are considered below.

That is, first, the linearized collision term obtained from Landau collision integral assuming that deviations of electron distribution function interact with “background” distribution specified as being Maxwellian:

$$\hat{L}_c[f] = \hat{L}_c^{ee}[f_M, f] + \hat{L}_c^{ei}[f_M^i, f], \quad (2)$$

where f_M and f_M^i – Maxwellian distributions of electrons and ions. The problem is, however, that within this approximation, the electron-electron collisions do not satisfy the energy conservation law in general. For example, assuming that energy losses are absent and the temperature of the background electron distribution f_M is constant, one can obtain a steady-state solution of a kinetic equation in which absorption of rf-power is nonzero. To model cyclotron heating of bulk electrons we suggest in our simulations that all the absorbed rf-power is immediately transmitted to the background electron distribution, more exactly, that the background temperature $T_e(t)$ is increasing in time according to the “balance” equation

$$\frac{3}{2} \frac{d}{dt} N_e T_e = P_{abs} = \int \frac{1}{2} m_e v^2 \hat{L}_{qt}[f] dv, \quad (3)$$

where $P_{abs}(t)$ is total rf-power absorbed by resonant electrons.

The second approach analyzed is based on a "truncated" nonlinear integral, corresponding to the zero-order Legendre harmonic of a pitch-angular expansion of Landau collision kernel. The operator can be obtained if isotropic function appropriate to pitch-angle averaging of a real electron distribution function is used as a background distribution:

$$\hat{L}_c[f] = \hat{L}_c^{ee}[\langle f \rangle, f] + \hat{L}_c^{ei}[f_M^i, f], \quad \langle f \rangle = \int_{-1}^1 f(v, \mu) d\mu, \quad (4)$$

with μ being a cosine of an electron pitch-angle. In this case, e-e collisions conserve the total energy automatically (to satisfy the momentum conservation one should include the next-order Legendre harmonic). This approximation becomes exact in the limited case of strong isotropization of a distribution function, for example, due to the strong collisions with multi-charged ions.

Both approaches (2), (3) lead to the same form of collision operator:

$$\hat{L}_c[f] = \frac{1}{v^2} \frac{\partial}{\partial v} v^2 \left(D_{ee} \frac{\partial f}{\partial v} + F_{ee} f \right) + (v_{ee}^\mu + v_{ei}^\mu) \frac{\partial}{\partial \mu} (1 - \mu^2) \frac{\partial f}{\partial \mu}. \quad (5)$$

Diffusion coefficients D_{ee} , v_{ee}^μ , v_{ei}^μ and collision friction force F_{ee} are given in explicit form in Appendix. Note that electron-ion energy exchange is neglected, so the ion part results in a pitch-angle scattering only.

To test the collision operators under ECRH conditions a model situation has been considered when spectrum of a heating radiation is given and has noise nature in a finite frequency bandwidth

$$I_{\omega} = \begin{cases} I_0 & \text{if } \omega \in (\omega_1, \omega_2) \\ 0 & \text{if } \omega \notin (\omega_1, \omega_2) \end{cases} \quad (6)$$

This can describe monochromatic heating on a single magnetic surface in a toroidal geometry, when effective broadening of a heating spectrum corresponds to cyclotron frequency variation on a magnetic surface. Heating by EC mode propagating transverse to the magnetic field is analyzed. In this case quasilinear diffusion occurs over transverse velocities and results in the following expression (see e.g. Ref.[1]):

$$\hat{L}_{qi}[f] = \frac{1}{v_{\perp}} \frac{\partial}{\partial v_{\perp}} \left(v_{\perp} D_{qi} \frac{\partial f}{\partial v_{\perp}} \right) \Big|_{v_{\parallel} = \text{const}}, \quad v_{\perp} = v \sqrt{1 - \mu^2}, \quad v_{\parallel} = v \mu. \quad (7)$$

This term is nonzero in the limited resonant region $v_0 - \Delta v < v < v_0 + \Delta v$ in a velocity space where cyclotron resonance condition is fulfilled:

$$\omega_{res} = s \omega_H \sqrt{1 - v^2/c^2} \in (\omega_1, \omega_2) \Rightarrow D_{qi} \neq 0 \text{ if } |v - v_0| < \Delta v. \quad (8)$$

To be definite we investigate ECR heating at the second harmonic by extraordinary mode ($D_{qi} \approx v_{qi} v_{\perp}^2$). The evolutions of initial Maxwellian distribution with natural boundary conditions ($f|_{v=0}$ and $f|_{\mu=1}$ are limited, $f|_{v=\infty} = 0$, $\partial f / \partial \mu|_{\mu=0} = 0$) will be compared for both collision models.

Numerical simulations demonstrate that there are two different stages in the evolution of a distribution function within kinetic equation (1). First stage is characterized by fast quasilinear plateau formation without significant variation of the total electron energy. The next more slow stage is a stage of quasi-stationary heating when substantial growth of the bulk electron temperature occurs.

The first stage is illustrated in fig.1 in the most interesting case when quasilinear plateau formation time $t_{qi} \sim \Delta v^2 D_{qi}^{-1}$ is smaller than e-e collision time in a resonant region $\nu_{ee}^{-1}(v_0)$. Linearized collision integral is used; it should be noted, however, that using "truncated" nonlinear collision integral yields quite the same results. Initially distortions arise in the localised resonant region in a velocity space (see curves 1-2). Then, collisions with non-resonant particles result in a slight modification of the whole electron distribution function when quasilinear operator acting in a narrow resonant region pumps electrons from low to high energies (curves 3-4). After all, this effect results in the growth of total electron energy in the next stage of quasi-stationary heating (curves 5-7).

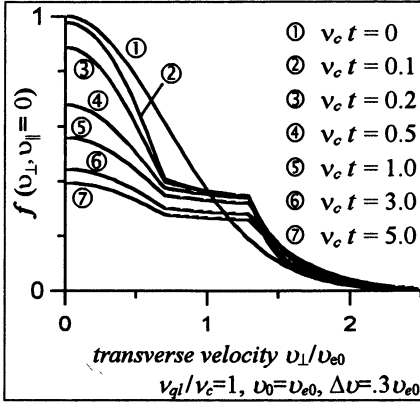


Fig.1. Formation of distorted distribution function (linearized collision term). Here v_{e0} and $v_c \equiv v_{ee}(v_{e0})$ – initial thermal velocity and initial thermal e-e collision frequency

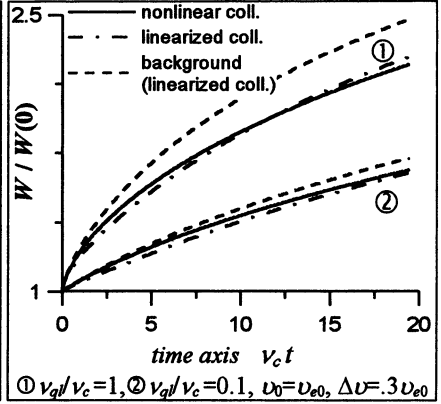


Fig.2. Evolution of total electron energy (1D model)

To check the validity of presented technique for the description of heating process we consider first the 1D kinetic equation obtained by pitch angular averaging in the presence of strong isotropization mechanism

$$\frac{\partial f}{\partial t} = \frac{1}{v^2} \frac{\partial}{\partial v} v^2 \left\{ (D_{ee} + \langle D_{q1} \rangle) \frac{\partial f}{\partial v} + F_{ee} f \right\}, \quad \langle D_{q1} \rangle = \int_0^1 \frac{v_{\perp}^2}{v^2} D_{q1}(v, \mu) d\mu. \quad (9)$$

For isotropic distribution function, nonlinear collision operator (4) is exact. In 1D case, we performed direct comparison of solutions obtained with the exact nonlinear collision integral (4) and with linearized collision integral (2).

As an example, two curves for evolution of total electron energy

$$W(t) = \int \frac{m_e}{2} v^2 f dv \quad (10)$$

obtained from strict nonlinear and linearized 1D models are presented in fig.2; the background electron energy obtained from balance equation (3) for linearized model is also presented. One can see that the linearized model is rather accurate. However, there is a slight difference between total and background energies, but their time derivatives are equal in the quasi-stationary stage. It means that linearized model for e-e collisions conserve a total energy asymptotically. For 2D case, we have approximate solutions only, but the figures obtained are quite similar to the 1D case – asymptotic conservation of energy is established in quasi-stationary stage for linearized model, and this provides self-consistent description of heating both

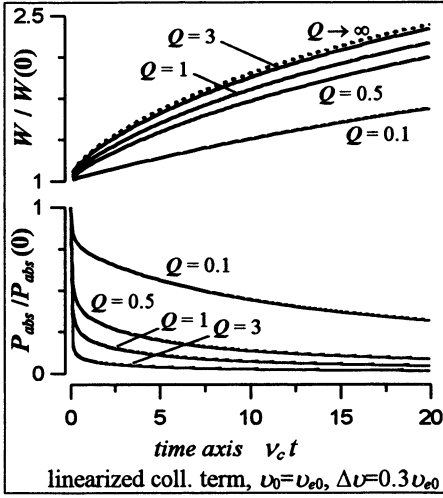


Fig.3. Heating process depending on $Q = v_{q1}/v_c$

for linearized and “truncated” nonlinear collision operators.

The dynamics of the total energy and the power absorption for different heating intensities is presented in fig.3. Absorption drops in time due to the quasilinear plateau formation, and this effect becomes stronger with input power increase. On the other hand, total energy evolution tends to universal one with the heating intensity increase, i.e. absorbed RF power is independent of the input power at high values of input power.

The latter effect came understood in a following way. Absorption of rf-power (3) is proportional to the input power multiplied by velocity derivative of the distribution function in the resonant region: $P_{abs} \sim D_{q1} \partial f / \partial v$. Starting, for simplicity, from the stationary 1D kinetic equation and assuming that the distribution function remains close to the Maxwellian:

$$(D_{ee} + \langle D_{q1} \rangle) \frac{\partial f}{\partial u} + F_{ee} f \approx 0 \Rightarrow \frac{\partial f}{\partial u} \approx - \frac{F_{ee}}{D_{ee} + \langle D_{q1} \rangle} \cdot f_M, \quad (11)$$

one can obtain the total rf-power absorbed by resonant electrons:

$$P_{abs} = P_{abs}^{max} \cdot \frac{1}{D_{ee} / \langle D_{q1} \rangle + 1}, \quad P_{abs}^{max} \approx 8\pi m_e v_0^3 \Delta v F_{ee}(v_0) f_M(v_0), \quad (12)$$

where P_{abs}^{max} depends on the temperature of bulk electrons, but not on the input power explicitly. Hence, no dependence on input power is expected when input power is high $\langle D_{q1} \rangle / D_{ee} \gg 1$. Substituting $P_{abs}^{max}(T_e)$ into the energy balance equation (3) yields the universal temperature evolution indicated in fig.3:

$$T_e(t) = \frac{m_e v_0^2}{2} G^{-1}(t/t_{heat} + G(u_0^{-2})), \quad (13)$$

where $t_{heat} = v_0 v_{e1}^{-1}(v_0) / \Delta v$ is the characteristic time of quasi-stationary evolution; $u_0 = v_0 / \sqrt{2T_{e0} m_e^{-1}}$ defines the initial electron temperature; uni-

versal function $G(\theta)$ is obtained using Eq. (A2) for collision friction F_{ee} :

$$G(\theta) = \frac{3\pi}{128} \int_1^\theta y^{3/2} e^{1/y} \left(\int_0^{y^{-1/2}} s^2 e^{-s^2} ds \right)^{-1} dy; \quad (14)$$

and $G^{-1}(x)$ – inverse function to $G(\theta)$. Approximation (12) is valid when variation of the distribution function in a resonant region is small $\Delta f \ll f_M(v_0)$ (i.e. $\Delta v \ll v_e^2/v_0$), and the time t_{heat} is much greater than the plateau formation time $t_{ql} \sim \Delta v^2 D_{ql}^{-1}$ and the collision time $\nu_{ee}^{-1}(v_0)$.

Presented results demonstrate that quasilinear modification of electron distribution function and related to it variation of energy deposition profile can be described using approximate linearized collision integral with electron temperature of the background Maxwellian distribution varying according to the calculated absorption of rf-power obtained, in general, using an energy transport model. The work is supported by Russian Foundation for Basic Research Grant #98-02-17204.

Appendix

For electron velocities significantly greater than ion velocities the collision frequency of electron-ion pitch-angle scattering is (Z is ion charge number)

$$\nu_{ei}^\mu(v) = \frac{1}{2} Z \nu_{ee}(v), \quad \nu_{ee}(v) = 4\pi e^4 N_e \ln \Lambda_e / m_e^2 v^3. \quad (A1)$$

Electron-electron part of a collision term (2) linearized with $f_M = N_e \pi^{-3/2} v_e^{-3} \exp(-w^2)$, $w = v/v_e$, $v_e(t)$ – thermal velocity of bulk electrons, is defined by the coefficients:

$$F_{ee}(v) = \nu_{ee}(v) v \frac{4}{\sqrt{\pi}} \int_0^\infty e^{-s^2} s^2 ds, \quad D_{ee}(v) = \frac{v_e^2}{2v} \cdot F_{ee}(v), \quad (A2)$$

$$\nu_{ee}^\mu(v) = \nu_{ee}(v) \frac{1}{\sqrt{\pi}} \left(w e^{-w^2} + (2 - w^{-2}) \int_0^\infty e^{-s^2} s^2 ds \right), \quad (A3)$$

Coefficients for "truncated" nonlinear Landau collision term (4) are

$$F_{ee}(v) = \nu_{ee}(v) \frac{1}{N_e} \int_0^v u^2 \langle f \rangle du, \quad D_{ee}(v) = \nu_{ee}(v) \frac{4\pi}{3N_e} \left(\int_0^v u^4 \langle f \rangle du + v^3 \int_0^v u \langle f \rangle du \right) \quad (A4)$$

$$\nu_{ee}^\mu(v) = \nu_{ee}(v) \frac{4\pi}{N_e} \left(\frac{1}{2} \int_0^v u^2 \langle f \rangle du - \frac{1}{6v^2} \int_0^v u^4 \langle f \rangle du + \frac{v}{3} \int_0^v u \langle f \rangle du \right). \quad (A5)$$

These expressions have been obtained, for example, in Ref. [1].

References

1. Dnestrovskij Yu.N., Kostomarov D.P. Mathematical Modeling of Plasma, Nauka, Moscow, 1993.

ABOUT THE GEOMETRICAL OPTICS OF EC-WAVES IN SUBRELATIVISTIC PLASMA

M.D.Tokman, E.Westerhof , M.A.Gavrilova*

Institute of Applied Physics of the Russian Academy of Sciences, Nizhny Novgorod,
Russia

* FOM-Instituut voor Plasmafysica, 'Rijnhuizen', Trilateral Euregio Cluster,
Associatie EURATOM-FOM, Postbus 1207, 3430 BE Nieuwegein, The Netherlands

A modified expression of the wave energy flux and a new expression
for the ray Hamiltonian in anisotropic dissipative media are proposed.

As is well known, there are no general phenomenological expressions for such characteristics as the wave energy density and flux or the group velocity in case of media with dissipation [1]. The situation becomes far more complicated if apart from absorption one also has to take into account the spatial dispersion. Exactly such a situation is characteristic for electromagnetic wave propagation in plasma near the zone of electron-cyclotron resonance (i.e. for the so-called EC-waves). In the latter case this problem is closely connected to the problem of the correct development of ray-tracing in the ECR zone. The problem is that near the ECR the Hermitian and anti-Hermitian parts of the dielectric permittivity tensor ($\epsilon_{pm}^{(H)}$ and $\epsilon_{pm}^{(aH)}$) are of the same order of magnitude. Though the dispersion equation

$$D(\omega, \mathbf{k}) = \det \|\mathbf{D}_{pm}\| = \det \|\delta_{pm} k^2 - k_p k_m - \frac{\omega^2}{c^2} \epsilon_{pm}\| = 0$$

has solutions for real ω with weak dissipation (i.e. $|\text{Re } \mathbf{k}| \gg |\text{Im } \mathbf{k}|$), nevertheless, the real and imaginary parts of derivatives $|\text{Re}(D'_r, D'_k)| \propto |\text{Im}(D'_r, D'_k)|$ are of the same order of magnitude in the center of the electron-cyclotron absorption lines which appears to require the determination of ray traces in complex space. Moreover, also the standard expression for the wave energy flux

$$\mathbf{S} = \mathbf{S}_e + \mathbf{S}_p = \frac{c^2}{16\pi\omega} \mathbf{E}_p^* \mathbf{E}_m \frac{\partial \mathbf{D}_{pm}}{\partial \mathbf{k}}$$

(where $\mathbf{S}_e = \frac{c^2}{8\pi\omega} \text{Re}[\mathbf{E}^*[\mathbf{k}\mathbf{E}]]$) is the pure electromagnetic component (the

Poynting vector) and $\mathbf{S}_p = -\frac{\omega}{16\pi} \mathbf{E}_p^* \mathbf{E}_m \frac{\partial \epsilon_{pm}}{\partial \mathbf{k}}$ is the kinetic component (the

energy carried with plasma particles, i.e. the so-called «sloshing» flux) becomes complex in this zone. Note, that the quasi-standard expression for the energy flux (with the substitution $\epsilon_{pm} = \epsilon_{pm}^{(H)}$) remains true in some special case (see, e.g. [2]).

In the present work these problems are solved by the determination of a modified expression for the wave energy flux (for stationary wave field $e^{-i\omega t}$) in anisotropic dissipative media and by the development of the corresponding expression for the ray Hamiltonian that determines the ray traces along this modified flux.

In accordance with the routine procedure let us start from the Poynting theorem in general media:

$$\operatorname{div} \mathbf{S}_e = -\frac{1}{2} \operatorname{Re}(\mathbf{j} \mathbf{E}^*) \quad (1)$$

(where $\mathbf{j} = \hat{\sigma} \mathbf{E}$ is the current generated in plasma by the wave field \mathbf{E} .)

For wave fields $\mathbf{E} = \mathbf{E}_o(\mathbf{r}) \exp(-i\omega t + i \int \mathbf{k}_o \cdot d\mathbf{r})$ with «slowly varying»

complex amplitude ($E_o^{-1} \frac{\partial E_o}{\partial \mathbf{r}} \ll k_o$) it sometimes is possible to separate from the right hand side of (1) a term in the form of a divergence of a vector and then add this vector to the Poynting flux in left hand side of (1). The resulting vector may be regarded as the full wave energy flux including both the electromagnetic component and the sloshing flux.

Now let us, for simplicity, carry out this procedure for anisotropic media without spatial dispersion:

$$\operatorname{div} \mathbf{S} = -Q \quad (2)$$

$$Q = i \frac{c^2}{8\pi\omega} D_{pm}^{(aH)} E_p^* E_m$$

(where \mathbf{S} is the standard expression for the wave energy flux with $D_{pm} = D_{pm}^{(H)}$). Due to the fact that in anisotropic media wave polarization depends upon the wave propagation, i.e. the RF-field amplitude may be represented in the form [2]:

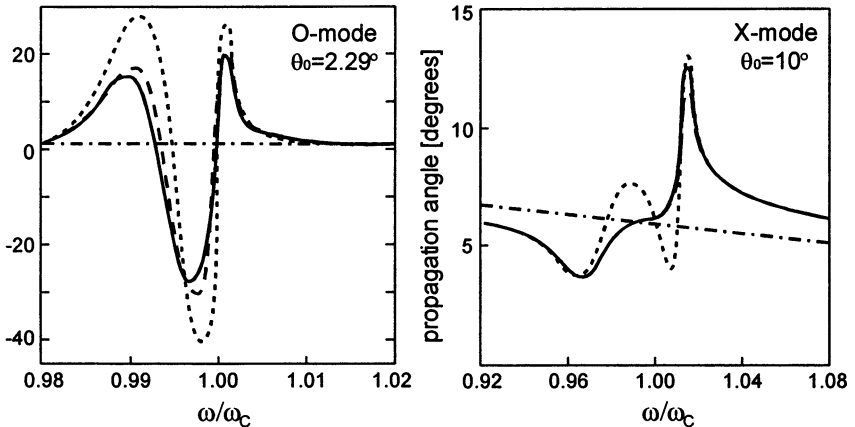
$$\mathbf{E}_o(\mathbf{r}) = [e\mathbf{A}(\mathbf{r}) - iA_r' e_{\mathbf{k}}']_{\mathbf{k}=\mathbf{k}_o}$$

where $|A|$ is the scalar wave amplitude (the square root of the intensity), $\arg|A|$ is the wave phase and $e(\mathbf{k})$ is the polarization vector which is also the eigenvector of the tensor D_{pm} corresponding to its zero eigenvalue. The source term Q in (2) depends correspondingly on the width of the spatial Fourier-spectrum of the wave field, so, $Q \propto \partial |A|^2 / \partial \mathbf{r}$. The

account boths of the spatial dispersion and dissipation [2] adds in (2) the additional term $q \propto \frac{\partial \epsilon_{pm}^{(aH)}}{\partial \mathbf{k}} |A|^2 \frac{\partial \arg A}{\partial \mathbf{r}}$. As a result, due to the presence of divergence terms in Q and q in the quasi-optical limit after some cumbersome mathematical manipulation (taking into account the relation $D_{pm}^{(H)} \mathbf{e}_m = -D_{pm}^{(aH)} \mathbf{e}_m$) one can rewrite the Poynting theorem (2) with the additional term q again in standard form $\text{div} \mathbf{S}_M = -Q_M$ with a modified source term (just the change of the central wave vector \mathbf{k}_0 to the current wave vector $\mathbf{k} + \nabla \arg A$) and a modified wave energy flux

$$\mathbf{S}_M = \frac{c^2 |A|^2}{16\pi\omega} \frac{\partial}{\partial \mathbf{k}} (\mathbf{e}_p^* \mathbf{e}_m D_{pm}^{(H)})$$

where the polarization vector depends on $D_{pm}^{(aH)}$ (it is obvious that in case $D_{pm}^{(aH)} = 0$ this expression is equivalent to the standard one). In dissipative media both expressions differ from each other only by the presence in the modified flux of the derivatives of wave polarization vector along the wave vector \mathbf{k} . So, one may draw the conclusion that this difference becomes most significant for situations with strong dependence of the wave polarization on the wave vector. Exactly this situation is characteristic of EC-waves. This is illustrated in the next figure [3]:



Propagation angle depending on frequency for $T_e=1$ keV, $(\omega_p/\omega)^2 = 0.7$

In the picture the angle of wave propagation with respect to the normal of the magnetic field is given (the straight thin dotted lines correspond to the «cold plasma» approximation; the dotted lines the standard wave energy

flux; dashed lines the modified energy flux and full lines are the wave traces calculated on the basis of the «group trajectory» method [2,3])

It is clearly seen that the differences between the direction of the standard flux and the direction of the modified flux or the actual wave beam trajectory is most significant in the vicinity of the ECR zone where wave polarization vectors are most sensitive to wave vector variations. Note, that the expression for the modified wave energy flux includes under the derivative along \mathbf{k} the expression $\mathbf{e}_p^* \mathbf{e}_m D_{pm}^{(H)} = \text{Re } \lambda$ (where λ is the eigenvalue of the tensor D_{pm} , $\mathbf{e}_p(\lambda)$ is the eigenvector of D_{pm} corresponding to the $\lambda = 0$ which satisfies the dispersion relation). Thus, this $\text{Re } \lambda(\mathbf{k}, \mathbf{r})$ may be regarded as the ray Hamiltonian for EC-wave ray-tracing. Determined in such a way ray traces are automatically consistent with both the «group trajectories» and modified wave energy flux as the previous picture shows.

The small remaining difference between the modified flux and the group trajectory for the O-mode case is due to the assumption of small absorption ($|\text{Re } \mathbf{k}| \gg |\text{Im } \mathbf{k}|$) which is only marginally satisfied for this case. Almost exact agreement between the two curves would be obtained when the imaginary part of wave vector is taken into account. The imaginary part may be determined, for instance, by some auxiliary relation.

The work has been performed under support of the Russian Foundation of Basic Research (the grant No. 98-02-17204).

Reference

1. Agranovich V.M., Ginzburg V.L. *Spatial Dispersion in Crystal Optics and the Theory of Excitons*, Wiley, New York, 1967.
2. Tokman M.D., Smirnov A.I. *Sov. Phys.-JETP*, 1996, **83**, 294.
3. Westerhof E. *Plasma Phys. Controll. Fusion*, 1997, **39**, 101.

MODIFICATION OF ECE SPECTRA DUE TO THE QUASILINEAR EFFECTS AT ECR HEATING IN TOROIDAL PLASMA

A. G. Shalashov, E. V. Suvorov

Institute of Applied Physics, Nizhny Novgorod, Russia

We consider an opportunity of diagnostics for ECRH driven quasilinear modification of electron distribution function in the case of transverse low-field side injection of heating rf beam. The diagnostics is based on measurements of ECE spectra of toroidal plasma in the vicinity of a heating frequency. As an example, numerical simulations for quasilinear disturbances of ECE spectra are performed for low-density high power ECRH regime of W7-AS stellarator.

Modification of electron distribution function under cyclotron resonant condition in toroidal plasma is well pronounced for HFS injection or oblique launch typical of ECCD experiments, when EC waves interact with energetic electron populations. In the opposite case of a transverse LFS injection in ECRH experiment in optically thick plasma, cyclotron waves are absorbed presumably by low energetic electrons, so ECRH driven quasilinear effects are strongly suppressed by Coulomb collisions. Under these circumstances quasilinear effects result only in small shift and expansion of rf-power absorption region. However, this may be of importance in suppression of MHD instabilities when fine localization of energy deposition profile is needed.

In the present communication, we discuss a possibility of ECE diagnostic of quasilinear effects when rf-power is deposited to low energetic electrons and no substantial tail formation is expected in the electron distribution function. The diagnostic is based on the increase of ECE level around the resonant frequencies due to effect of quasilinear degradation of EC absorption coefficient.

Specific feature of ECR heating in toroidal geometry is that even for monochromatic radiation heating process is of stochastic nature due to rotational transform – every electron moving over the magnetic surface crosses rf field region with randomly different detuning between the frequency of heating radiation and local gyrofrequency. This results in effective broadening of heating radiation spectrum from the point of view of electron distribution function modification.

Following [1] we model this situation by slab geometry in which magnetic field is monotonously varying in the direction transverse to it, all other plasma parameters being constant and heating radiation with noise δ -correlated frequency spectrum is launched transverse to the magnetic field from the low-field side. To be definite we take linear dependence of magnetic field \mathbf{B} on z -coordinate

$$\mathbf{B} = \mathbf{B}_0 \cdot (1 + z/L_H), \quad \mathbf{B}_0 \perp \mathbf{z}_0, \quad (1)$$

which is applicable in the localized rf-power absorption zone. With the heating radiation propagating in z -direction ECR condition is also z -dependent due to magnetic field inhomogeneity:

$$\omega_{res} = s\omega_c(z)\sqrt{1 - (v/c)^2}, \quad \omega_c(z) = eB(z)/m_e c. \quad (2)$$

Evolution of the electron distribution function $f(v_\perp, v_\parallel, z, t)$ is governed by a kinetic equation in which a collision term and a quasilinear diffusion term are included:

$$\frac{\partial}{\partial t} f = \hat{L}_c[f] + \hat{L}_{ql}[f]. \quad (3)$$

Quasilinear operator \hat{L}_{ql} for a fixed z depends on effective spectral density of rf-energy, which satisfies the radiation transfer equation

$$\frac{\partial}{\partial z} I_\omega^{eff} = -\mu^{EC} I_\omega^{eff}, \quad (4)$$

where $I_\omega^{eff}(\omega, z, t)$ is the effective intensity of the heating radiation. Cyclotron absorption coefficient μ^{EC} is calculated with taking into account the quasilinear modification of electron distribution function, so there are two coupled equations – the initial problem (3) for the electron distribution function and the boundary problem (4) for the spatial distribution of the heating radiation spectrum.

A steady-state plasma condition is investigated, so linearized Landau collision term with the “background” Maxwellian electron distribution and constant electron temperature T_e is used for simulations [2]. Numerical calculations are continued until stationary solution has been established.

The solutions obtained are used for the calculation of disturbed ECE spectra using the radiation transfer equation for the effective radiation temperature T_r of EC emission:

$$\frac{\partial}{\partial l} T_r = A_\omega^{EC} - \mu^{EC} \cdot T_r, \quad (5)$$

where both the emissivity A_w^{EC} and the absorption coefficient μ^{EC} are defined by the calculated electron distribution function (3).

Note that normal waves and ray trajectories for heating radiation (4) and emission radiation (5) are different in general. However, maximum disturbances are expected for ECE spectra at the same harmonic as the heating radiation when the ray-trajectories of the detected emission coincide with those of the heating rf beam. In this case, at each z -point ECR conditions for ECE and for the heating radiation are the same, so deviations from thermal ECE are located exactly in the frequency band corresponding to the effective heating spectrum. For the emission at other harmonics these deviations are less pronounced, so they are of minor interest. To be definite we consider X-mode heating at the second harmonic and EC emission in the same mode. A full dimensionless formulation of the problem one can see in Appendix. There are three parameters in the problem: 1) the effective ratio of quasilinear to collision terms $q \sim \hat{L}_{ql} / \hat{L}_c$ which is proportional to the injected rf-power, 2) the optical depth τ_0 of initial thermal plasma layer, and 3) the normalized spectral width of the heating radiation (see Eq. (A9) for more details).

Before going to the results of numerical calculations, we make a few evident remarks clarifying the dependence of the level of ECE distortions on the parameters. If ECRH power is so high that Coulomb collisions can be neglected with respect to quasilinear diffusion (i.e. $q \rightarrow \infty$), than plateau formation results in zero EC absorption when resonant condition agrees with resonant heating condition, and the value of EC emission escaping from the whole plasma layer may be estimated as

$$T_r = \int_{-\infty}^{\infty} A_w^{EC} dl \approx \tau_0 \cdot T_e. \quad (6)$$

This is obtained under assumption that emissivity is close to the thermal one (number of resonant electrons does not vary substantially) and defined by Kirhgooff's law: $A_w^{EC} \approx \mu_{th}^{EC} \cdot T_e$. The same is true for optically thin plasma layer ($\tau_0 \ll 1$) independently of all other conditions. For LFS injection into optically thick plasma layer ($\tau_0 \gg 1$) the main part of rf-power is deposited into low-energetic particles being subjected to strong Coulomb collisions ($\nu_c \sim \nu^{-3}$). This results in thermal EC emission just as for collision dominated case. For intermediate case $0 < \tau_0 < \infty$ there should be optimal va-

lue of optical depth at which the deviation of ECE from the thermal level is maximal.

The summarizing results of numerical calculations are shown in fig. 1. Higher optical depths correspond to ECRH driven "transparent" regions, which are more shifted to the low-field side. This causes different dependencies of emission to high and low field directions on optical depth: the maximum possible distortion is for emission to HFS, but in optically thick plasma emission to LFS prevails (see the figure).

Example of simulation corresponding to ECRH heating in low-density discharges of W7-AS (when ray trajectories may be approximated by strait lines) is presented below. The heating rf-power is injected into the plasma cross-section with tokamak-like magnetic geometry. In order to increase the width of effective noise spectrum the direction of rf beam launch is assumed to be inclined with respect to the equatorial plane (see fig.2). The effective spectrum of heating radiation is obtained from geometrical considerations (see [1] for more details) under assumption of step-like distribution of rf-power over the beam cross-section. ECE spectra are calculated for the radiation escaping from the plasma in two opposite directions: (I) in the direction of the heating rf beam propagation¹ and (II) backward direction. Generally, both quasi-linear perturbations of ECE signal and its variation within the beam cross-section are of the same order, so the observed antenna response should be obtained by integrating over set of rays modelling the antenna radiation pattern. We present below results of calculation

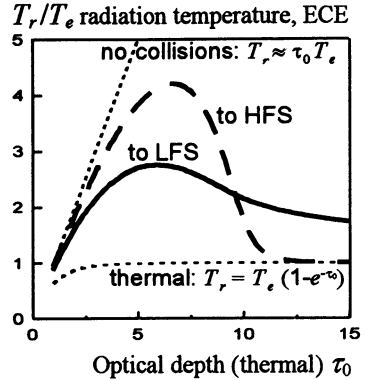


Fig. 1. Solid line – EC emission to LFS, dashed line – to HFS

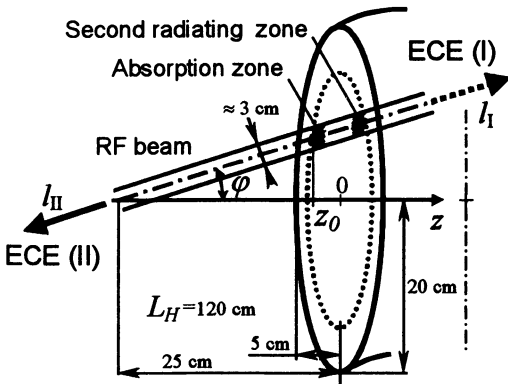


Fig.2. W7-AS ECRH experiment (X2 140 GHz)

¹ It should be kept in mind that due to rotational transform the system of ECE registration can be shifted toroidally to avoid the direct light of heating rf-power.

of ECE radiation temperature along the central ray, having in mind that effect of finite receiving antenna radiation pattern results in some broadening of registered spectrum without its significant modification near the central line.

The maximum perturbations are expected for EC emission from the power absorption region, but they are localized in the vicinity of the heating frequency, where its registration is complicated due to a strong background of stray-radiation. So, calculation of shifted ECE spectra, which are formed at the same magnetic surfaces for other values of a toroidal magnetic field (see fig.2), is included also.

Calculated stationary ECE spectra are presented in fig.3a for more or less standard experimental conditions. In this case about 50% increase of ECE level in the main peak may be achieved for emission to the backward direction, and emission to HFS direction (i.e. along the heating beam propagation) is suppressed. The minor peak at $f \sim 1.5$ GHz is formed by radiation from the zone, which is "opposite" to the power absorption zone.

To demonstrate the most pronounced influence of quasilinear effects we simulate the case close to the optimal point in fig.1, which corresponds to enhanced level of ECRH power and low-density operational regime (see figs. 3b, 3c).

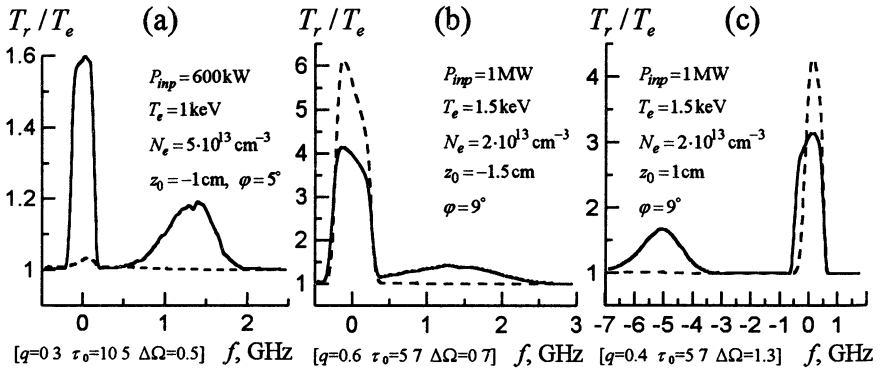


Fig.3. ECE spectra (X2) for W7-AS. Solid line – emission to LFS direction, dashed line – emission to HFS direction. Zero f corresponds to the heating frequency. Plots (a) and (b) correspond to the case shown in fig.2, plot (c) corresponds to the case in which "absorption zone" and "second radiating zone" mutually change their positions.

Going to conclusion we note again that discussed mechanism of ECE modification does not rely on generation of energetic electron tail, but it is sensitive to deformations in the main (thermal) body of the electron distribution function. The results obtained for the realistic plasma parameters

show that registration of such distortions requires well enough spectral resolution of the detection system and is possible in principle for some specific operational regimes of W7-AS for example.

The work is supported by RFBR grant #98-02-17204.

Appendix. Formulation for X2-mode, transverse LFS injection

Using variables $\mu = \cos \theta$, $u = v/v_e$, $\Omega = (\omega - \omega_0)/\omega_0\beta_e^2$, $Z = (z - z_0)/L_H\beta_e^2$, where v and θ – electron velocity modulus and pitch-angle, v_e – electron thermal velocity, $\beta_e = v_e/c$, ω_0 – frequency of monochromatic heating, one can perform Eq. (1)-(5) as

$$\frac{\partial}{\partial t} f(t, Z, u, \mu) = \hat{L}_{ql} f + \hat{L}_c f, \quad \frac{\partial}{\partial Z} J(t, Z, \Omega) = -\mu^{sc} J, \quad (A1)$$

$$f(0, Z, u, \mu) = \exp(-u^2), \quad J(t, 0, \Omega) \equiv 1, \quad 0 < \Omega < \Delta\Omega, \quad (A2)$$

$$\hat{L}_{ql} f = \frac{q}{u^2} \left\{ \frac{\partial}{\partial u} \left(Q \frac{\partial f}{\partial u} \right) - \frac{\partial}{\partial u} \left(\frac{\mu}{u} Q \frac{\partial f}{\partial \mu} \right) - \frac{\partial}{\partial \mu} \left(\frac{\mu}{u} Q \frac{\partial f}{\partial u} \right) + \frac{\partial}{\partial \mu} \left(\frac{\mu^2}{u^2} Q \frac{\partial f}{\partial \mu} \right) \right\}, \quad (A3)$$

$$\begin{cases} Q = u^4 (1 - \mu^2)^2 J(\Omega_{res}) & \text{if } 0 < \Omega_{res} = Z - u^2/2 < \Delta\Omega \\ Q = 0 & \text{outside the resonant region} \end{cases}, \quad (A4)$$

$$\hat{L}_c f = \frac{1}{u^2} \frac{\partial}{\partial u} \left\{ B \left(\frac{1}{2u} \frac{\partial f}{\partial u} + f \right) \right\} + C \frac{\partial}{\partial \mu} (1 - \mu^2) \frac{\partial f}{\partial \mu}, \quad (A5)$$

$$B = \frac{4}{\sqrt{\pi}} \int_0^u e^{-s^2} s^2 ds, \quad C = \frac{1}{u^3} \left(\frac{1}{2} Z_{ef} + \frac{1}{\sqrt{\pi}} \left(u e^{-u^2} + (2 - u^2) \int_0^u e^{-s^2} s^2 ds \right) \right), \quad (A6)$$

$$\mu^{sc} = -\tau_0 \frac{1}{\sqrt{\pi}} \int_0^1 \int_0^1 u^4 (1 - \mu^2)^2 \left(u \frac{\partial f}{\partial u} - \mu \frac{\partial f}{\partial \mu} \right) \delta(\Omega_{res} - \Omega) d\mu du, \quad (A7)$$

$$A_w^{sc} = 2T_e \tau_0 \frac{1}{\sqrt{\pi}} \int_0^1 \int_0^1 u^6 (1 - \mu^2)^2 f \delta(\Omega_{res} - \Omega) d\mu du, \quad (A8)$$

where

$$q = \frac{\pi^2 e^2 n}{c^3 m_e^2} \frac{P_{in}}{S \cdot \Delta\omega} v_e^{-1}, \quad \tau_0 \equiv \frac{\pi n \omega_p^2 L_H}{2 c \omega_e} \beta_e^2, \quad \Delta\Omega = \frac{\Delta\omega}{\omega_0 \beta_e^2} \quad (A9)$$

– parameters of the system, P_{in} – injected rf-power distributed over the magnetic surface with area S , $\Delta\omega = 2\Delta\omega_e$ – spectral width of the heating radiation defined by variation $\Delta\omega_e$ of gyrofrequency in power absorption zone, $v_e = 4\pi e^4 N_e \ln \Lambda_{ee} / m_e^2 v_e^3$ – thermal e-e collision frequency, n – refraction index, ω_p – Lengmuir frequency, Z_{ef} – effective ion charge.

References

1. Suvorov E.V., Tokman M.D. Plasma Phys., 1983, **25**, 723.
2. Dnestrovskij Yu.N., Kostomarov D.P. Mathematical Modeling of Plasma, Nauka, Moscow, 1993.

DETERMINATION OF ABSOLUTE H-ION LOCAL DENSITY FROM CTS MEASURED CHARACTERISTICS OF LH TURBULENCE

E.V. Suvorov

Institute of Applied Physics, Nizhny Novgorod, Russia

In some operation regimes of W7-AS stellarator injecting into the plasma of diagnostic hydrogen neutral beam is accompanied by essential increase in the level of small-scale lower-hybrid turbulence. Under these conditions Collective Thomson Scattering (CTS) technique provides unique possibility of determination the local concentration of hydrogen ions.

Electron density distribution in toroidal plasma is one of the most reliably measurable quantities. Essentially more difficult task is a direct measurement of plasma ion composition which is formed due to combined action of great variety of not well enough investigated processes. In particular hydrogen isotope content in fusion toroidal plasma is formed in a rather complicated manner due to such processes as hydrogen or deuterium gas-puff combined with the injection into the plasma of neutral hydrogen or deuterium neutral beams used for NBI heating, recycling etc.

We would like to draw attention to a rather unique possibility of the local absolute hydrogen ion density determination practically independent of all impurity and deuterium ion concentrations from CTS measurements of LH turbulence characteristics. This opportunity may be realized in some specific operation regimes of W7-AS stellarator.

It was discovered [1] that injecting into the plasma with electron temperature considerably above the ion temperature of weak diagnostic hydrogen neutral beam results in the triggering of enhanced level of small scale (around 1 mm) narrow-band electron density fluctuations. These fluctuations were detected in CTS experiment using 140 GHz gyrotron as a

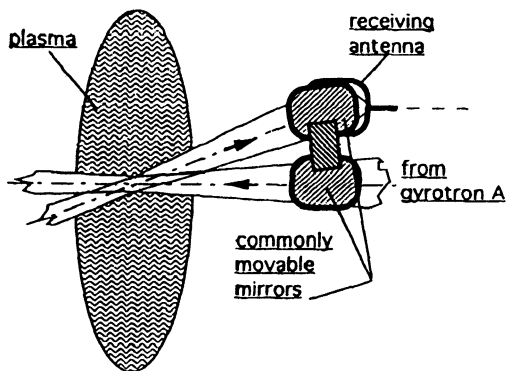


Fig. 1. CTS geometry for measurements of LH turbulence

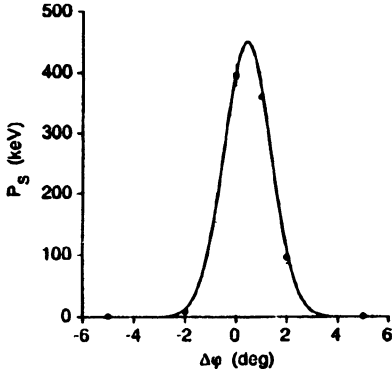


Fig.2. CTS signal from LH turbulence vs. toroidal angular scan in equatorial plane

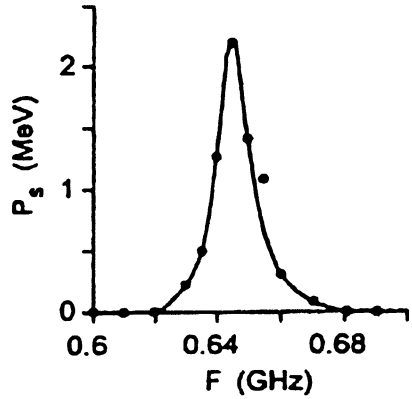


Fig.3. Typical LH turbulence spectrum measured with enhanced resolution

source of probing radiation in practically back-scattering geometry shown schematically in Fig.1. This fixed scattering geometry allowed angular scanning in both horizontal and vertical directions. Density dependence of the detected signal frequency definitely points that discovered electron density fluctuations can be specified as being related with LH turbulence. LH waves are propagating in a very narrow angular range transverse to the toroidal magnetic field (see Fig.2) and possess an extremely narrow frequency spectrum (Fig.3) in spite of practically absent spatial resolution in CTS geometry under consideration. These specific features of observed LH turbulence characteristics are explained in detail within theoretical model based on the idea of LH wave instability excited by transverse ion beam (resulting from trapping of diagnostic neutral beam atoms) under so called double-resonance condition (see [2] for more details). An important conclusion from theoretical model (supported also by experimental evidence) is practically transverse propagation of excited LH waves with respect to the magnetic field.

This was tested additionally in a special experimental investigation of LH turbulence distribution in vertical and horizontal directions by corresponding scanning with rigid emitting-receiving antenna block shown in Fig.1. Distribution over directions from which signal scattered by LH turbulence comes is presented in Fig.4. Antisymmetric deviation in toroidal direction for up and down shifted positions of antenna block is naturally explained by the influence of poloidal magnetic field component, while up and down asymmetry of presented plot is due to the fact that the scattering geometry is not exactly back-scattering ($\theta_s \approx 160^\circ$).

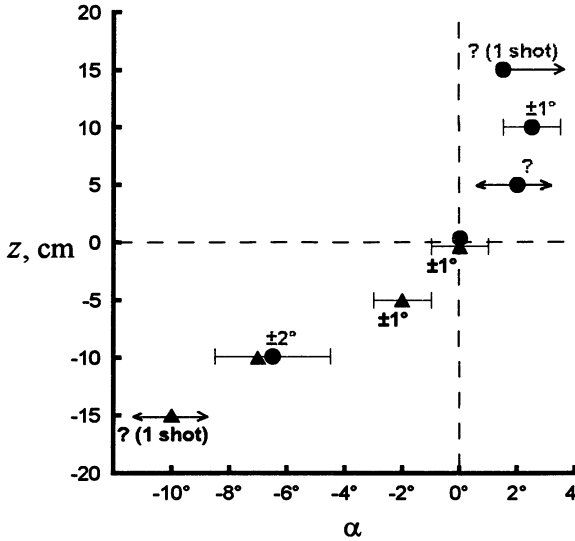


Fig.4. Distribution of LH turbulence in z - α plane

Let us assume that the local value of LH frequency is measured, which is possible in principle in 90° scattering geometry provided that there is an enhanced level of LH waves propagating transverse to the magnetic field. With taking into account all ion species LH frequency is determined by the well known relation:

$$f_{LH}^2 = \frac{e^2 N_e}{\pi m_p} \cdot \frac{1}{1 + \frac{\omega_{pe}^2}{\omega_{ce}^2}} \cdot \left(X_H + \frac{X_D}{2} + \sum_{\alpha} X_{\alpha} \frac{Z_{\alpha}^2}{M_{\alpha}} \right), \quad (1)$$

where e is electron charge, m_p is the mass of proton, N_e is electron density, ω_{pe} and ω_{ce} are electron Langmuir and gyro- frequencies respectively, X_{α} is the density of α -th ion specie normalized to the electron density, Z_{α} and M_{α} are their charge and mass numbers respectively. Correction to the LH frequency due to finite thermal velocity may be easily taken into account, but they are negligibly small for W7-AS plasma parameters under consideration.

Assuming that local values of the magnetic field and of the electron density are well defined and taking into account natural normalization condition for the electron and all ion densities:

$$X_H + X_D + \sum_{\alpha} Z_{\alpha} X_{\alpha} = 1, \quad (2)$$

after eliminating X_D from Eqs. (2) and (3) one can easily yield for the absolute hydrogen density (normalized to the electron density) the following:

$$X_H = 0.46(f_{LH}GHz)^2 \cdot \left(1.46 \left(\frac{2.5T}{B_0} \right)^2 + \frac{10^{14} cm^{-3}}{N_e} \right) - 1 + \sum_{\alpha} X_{\alpha} Z_{\alpha} \left(1 - 2 \frac{Z_{\alpha}}{M_{\alpha}} \right) \quad (3)$$

where LH frequency, magnetic field and electron density are normalized to the natural values for W7-AS operating regimes and corresponding numbers are introduced. It should be noted that for fusion plasma with electron temperature in keV range, plasma density higher than $10^{13} cm^{-3}$ and life time in tens millisecond range practically all reasonable ions (up to masses of Fe or even higher) are fully stripped and with high accuracy satisfy the equality $M_{\alpha} = 2Z_{\alpha}$. Under these conditions Eq.(3) without the last term defines the absolute value of hydrogen ion density which is practically independent of all other ion specie content.

Preliminary attempt of absolute H ion density determination was performed basing on CTS results in the back-scattering geometry. The first idea was to localize the scattering volume by following the path of probing beam and to find the point on it where k-vector of LH turbulence, defined by scattering geometry, is strictly transverse to dc magnetic field in the plasma. Unfortunately the first attempt to exploit this idea was not successful with taking into account the finite width of both probing and receiving antenna radiation patterns (diameters of both quasi-optical beams in the plasma center about 4 cm).

Nevertheless in some special low density plasma shots with rather flat density profile (see Fig.5) exact localization of the scattering volume is of minor importance. Unfortunately for these shots with similar density profiles absolute density values obtained from Thomson scattering are regu-

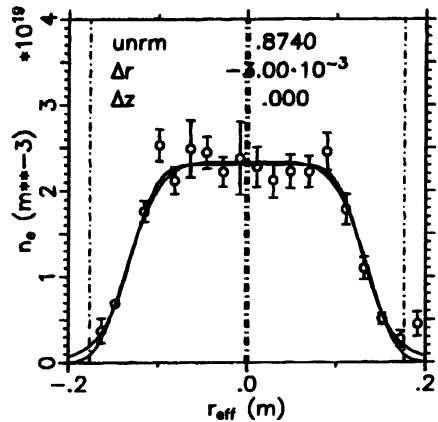


Fig.5. Radial profile of electron density distribution

larly higher than those obtained from multi-channel interferometer by approximately 25 %. Determination of absolute content of hydrogen ions was performed for ECR supported plasma shots with deuterium gas-puff after few tens of more or less identical shots which may be considered as chamber cleaning. The results of «local» hydrogen density determination for 3 different vertical positions of emitting-receiving antenna block are summarized below:

Shot # 43300	$f_{LH} \approx 0.64 \text{ MHz}$	
(vertical shift -10cm)	$N_{Th} \approx 2.3 \cdot 10^{13} \text{ cm}^{-3}$	$\Rightarrow X_H \approx 0.12$
	$N_{MCI} \approx 1.8 \cdot 10^{13} \text{ cm}^{-3}$	$\Rightarrow X_H \approx 0.35$
Shot # 43316	$X_H \text{ (MCI)} \approx 0.40$	
(vertical shift +10cm)	$X_H \text{ (Th)} \approx 0.12$	
Shot # 43310	$X_H \text{ (MCI)} \approx 0.36$	
(no vertical shift)	$X_H \text{ (Th)} \approx 0.08$	

It should be noted that in spite of rather preliminary and «qualitative» character of presented estimates data based on the Thomson scattering diagnostics seem to be more close to expected reality.

Author is greatly indebted to W7-AS team for friendly support and fruitful discussions.

The work was supported by German Bundesministerium für Bildung, Wissenschaft, Forschung und Technologie, and by Russian Foundation for Basic Research, Grant #99-02-16230.

References

1. Suvorov E.V., Erckmann V., Holzhauer E. *et.al.* Plasma Phys., Controlled Fusion, 1995, **37**, 1207-1213
2. Suvorov E.V., Holzhauer E., Kasperek W. *et.al.* Nuclear Fusion, 1998, **38**, 661-671.

3D FOKKER-PLANCK MODELLING OF ECR HEATING AND CURRENT DRIVE IN RC ITER PLASMA

V. L. Vdovin

RRC “Kurchatov Institute”, Institute of Nuclear Fusion, Moscow

Introduction

We have upgraded our 2D non linear code STIF [1], solving for electron distribution function in tokamaks in two velocity space coordinates as well as time, to 3D code incorporating radial transport in axisymmetric tokamaks and describe it. This 3D code solves 3D electron non linear Fokker-Planck equation for an arbitrary shaped axisymmetric tokamak, with the effects of collisions, ECR and Ohmic heating, radial transport through ad hoc diffusion plus convection term, and electron banana trapping all included. Electron heating and current drive is treated through quasilinear operator and gives velocity space diffusion. RF diffusion coefficients are calculated from ray tracing data. The launched RF spectrum is modelled by a bundle of rays (~ 100) which are followed by solving the ray tracing equations, and at each step on each ray parameters such as wave polarization, k -parallel and Δk -parallel are stored. Then RF diffusion coefficients are constructed in velocity space for each flux surface radius from these ray data.

The radial diffusivity and pinch speed are input by the user. They are frequently adjusted to keep a constant in time density profile. As for tokamak plasma equilibrium we make use VMEC code equilibrium, Solov'ev equilibrium or elliptical plasma equilibrium (for debugging).

Our goal is to study the influence of radial transport on kinetic effects in tokamaks. The preliminary modelling is performed for RC ITER plasma parameters [2]. Among several interesting scenarios we plan to investigate the localisation of current drive close to a rational surface which might be used to suppress tearing activity in ITER. Preliminary calculations have shown that that driven current profile is broadened significantly if a level of radial transport is comparable with the bulk thermal conductivity, while current drive efficiency is not changed significantly with or without transport of electrons.

Main code features are as follow:

STIFOK - 3D Fokker-Planck code

- non linear relativistic Fokker-Planck code conserving momentum and energy with self consistent ray tracing support

- 2D velocity space and 1D real space
- transport and trapping effects in real magnetic geometry (from MHD code)

We used bundles of rays (half - width 3°) with Gaussian power distribution Low Field Side O-mode fundamental harmonic ECRF wave injection.

RC ITER and PLASMA PARAMETERS

The main plasma and machine parameters used in the modelling are close to the present reduced cost RC-ITER (IAM and LAM) design reference scenario ones [2] and shown in Table:

	IAM	LAM
Major radius, R	6.20 m	6.45 m
Minor radius, a	1.90 m	2.20 m
Plasma elongation, κ	1.67	
Plasma triangularity, δ	0.32	
Nominal plasma current, I_p	13 MA	17 MA
Toroidal field, B_0	5.51 T	4.23 T
MHD safety factor, q_ψ	3.0	
$n_{e0}(10^{20}m^{-3})$	0.89	1.09

The chosen plasma profiles were as follow:

$$T_e(s) = (T_{e0} - T_{ea})(1 - s^2/a^2) + T_{ea},$$

$$n_e(s) = (n_{e0} - n_{ea})(1 - s^2/a^2)^{0.15} + n_{ea},$$

$$T_{e0} = 20 \text{ keV}, \quad T_{ea} = 0.5 \text{ keV},$$

$$Z_{\text{eff}} = 1.8$$

So one may attempt to scale basic RF parameters of ECR system to new reduced size and new magnetic field of the machine. On a first glance scaling from 170 GHz FDR (ITER Final Design Report, $B_0 = 5.74 \text{ T}$, $R_0 = 8.14 \text{ m}$, $a = 2.8 \text{ m}$, $I_p = 17 \text{ MA}$) according to change in B_0 gives:

$$f \sim 160 - 165 \text{ GHz LAM}$$

$$f \sim 120 - 125 \text{ GHz IAM}$$

But this simple approach is not sufficient because:

- Higher $f \rightarrow$ may give higher current drive efficiency,
- Lower $f \rightarrow$ may lower frequency cut – off.

So it is needed to perform detailed Fokker - Planck modelling. Usually modelling calculates Current Drive (CD) efficiency:

$$\eta = \frac{I_{CD} \langle n_{20} \rangle R}{P_{RF}}$$

and power deposition and driven current profiles.

3D F-P code modelling of high aspect ratio IAM ITER option for O-mode fundamental harmonic EC outside injection gives global CD ECRF efficiency dependence over toroidal angle radiating beam steering shown on Fig. 1 for frequencies 150, 170 and 200 GHz. One can see efficiencies $\eta = 0.22-0.25 \text{ A/W/m}^2$.

The observed optimal frequency to maximise CD efficiency is connected with parasitic second (2-d) harmonic absorption at outer ITER plasma boundary where driven EC current flows in opposite direction (due to Doppler effect). It is shown in Fig. 2. It limits possibilities to use higher frequencies.

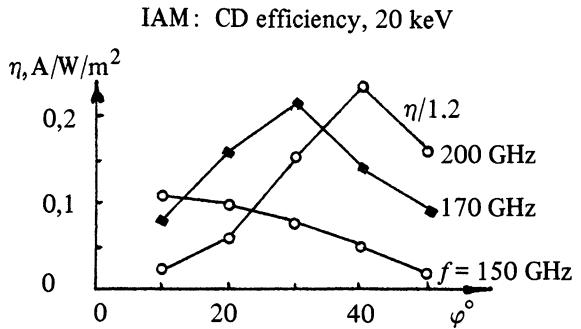


Fig. 1

3D code modelling of low aspect ratio LAM ITER option gives global CD ECRF efficiency dependence over toroidal angle radiating beam steering shown on Fig. 3 for frequencies 120, 150 and 170 GHz. The observed efficiencies are $\eta = 0.22-0.25 \text{ A/W/m}^2$. The upper frequency limit again is due to second harmonic absorption as shown in Fig. 4.

IAM: 2D Harmonic Absorption vs Frequency,
 $T_{e0} = 20 \text{ keV}$, injection angle, $\varphi = 20^\circ$

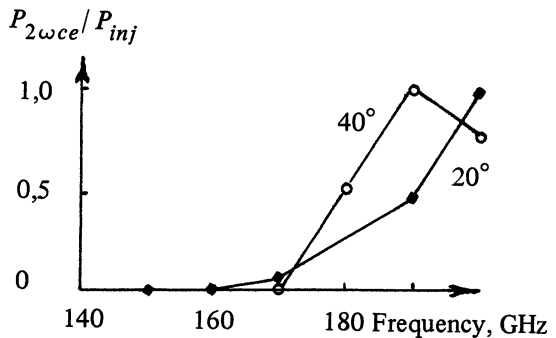


Fig. 2

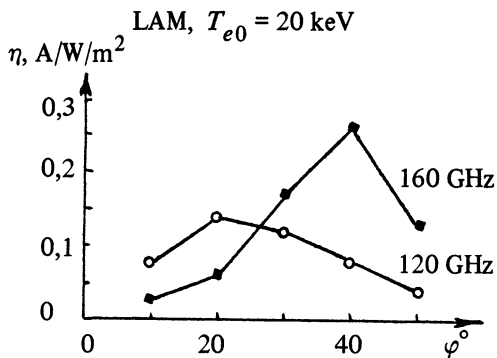


Fig. 3

LAM: Second Harmonic Absorption, $T_{e0} = 20$ keV,

$\varphi = 40^\circ, 30^\circ, 10^\circ$

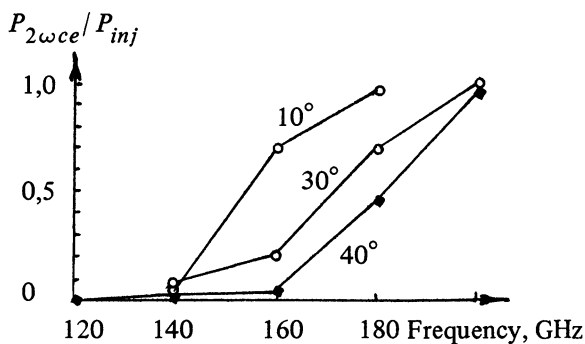


Fig. 4

HAM is better than for FDR and worse in LAM.

Far off-axis EC current drive on the High Field Side with LFS O-mode launch will be strongly diminished due to second harmonic absorption in plasma core.

In this preliminary modelling an influence of radial transport effects on driven current profile was not investigated. These effects can strongly modify expectations of EC waves in tearing modes stabilisation in ITER.

Conclusions

Preliminary modelling of EC heating/CD in RC ITER designs with mid-plane Low Field Side power injection shows comparable behaviour and performance predicted earlier by experts and JCT for FDR ITER.

For LAM and HAM designs, higher frequencies provide higher CD efficiencies in plasma core but impose reduced flexibility and increased role of deleterious absorption at second harmonic. With regard to parasitic second harmonic damping situation for

References

1. Alikae V., Vdovin V. Sov. Jour. Plasma Phys. 9, 538 (1983).
2. Point Design Meeting on Reduced Cost/Reduced Objective ITER, Naka (Japan), October 1998.



**MICROWAVE
DISCHARGES**

ELECTRODE MICROWAVE DISCHARGES. PHENOMENOLOGY, PROBE AND OPTICAL MEASUREMENTS

Yu.A. Lebedev, M.V. Mokeev, A.V. Tatarinov

A.V. Topchiev Institute of Petrochemical Synthesis RAS, Moscow, Russia

The paper summarizes results of experimental study of non-equilibrium non-uniform microwave discharges which can be generated near the antenna placed in a metal chamber filled up by H_2 , N_2 at pressures 0.5-15 Torr. The discharge dimensions were much less than the chamber dimensions (chamber diameters were 8 and 14 cm). Antennas of different shapes and dimensions were tested. The structure of discharges was studied by the integral plasma emission with spatial resolution and double probe method. A discharge in molecular gases has non-uniform structure with pronounced sharp ball shape periphery and bright thin region surrounding the exciting electrode-antenna. Slight increase in boundary layer intensity was also observed in H_2 . Physical explanations for the part of observed phenomena are discussed. This type of discharge have been successfully used in the plasma chemistry for diamond growth and CN_x films deposition.

Introduction

It must be noted that the investigations of microwave discharges are now aimed primarily at studying electrodeless discharges excited in various devices and even in free space [1]. This line of investigations are also motivated by multiple applications, e.g., plasma chemistry. The absence of electrodes is considered to be one of the important advantages of such discharges, because, in this case, it is possible to avoid the contamination of a plasma and plasma-treated surfaces by the products of electrode erosion.

At the same time, electrode discharges have some merits. The electrode discharges permit the plasma to be created at a low microwave power. These discharges can be classified as initiated discharges with one peculiarity: electromagnetic energy is transmitted to the system along the initiator-antenna. The plasma can be created in a given region, which can be located close to the treated surface, thus allowing to avoid difficulties connected with the transport of active particles to this surface. As a rule, the electrode discharge plasma is inhomogeneous. On the one hand, the non-homogeneity facilitates the transportation of active particles to the treated surface, and, on the other hand, it is an additional source of the plasma non-equilibrium. At present, the latter factor is almost unstudied.

Recent experiments indicate that the risk of contamination might be overestimated [2]. In experiments on the diamond film deposition on a

silicon substrate in a microwave electrode-discharge plasma under fairly severe conditions (the electrode was heated to the red-heat temperature, and the temperature of the substrate located at a distance of 1 cm from it was 1000 °C), ESCA analysis showed no traces of the products of electrode erosion in plasma-treated substrates.

The absence of erosion was related to the fact that the plasma was produced by microwave electromagnetic waves. This problem has been studied extensively for RF discharges (see, e.g., [3]). As the field frequency increases, the thickness of the electrode sheath and the energy of the ions bombarding the electrode decrease. In the microwave range, the sheath conductivity is low, and the current continuity is provided by the displacement current through the sheath. In this case, the role of the electrode in generation of charged particles is negligible (γ -processes associated with the secondary electron emission from the electrodes can be neglected), and the discharge exists in the form of an α -discharge, in which the processes of volume ionization are of importance. Our experiments indicated the DC voltage of several volts between the antenna and floating probe placed at distance of 3 mm from it. Presumably, the electrode only determines the structure of the electromagnetic field. The lack of data on the parameters of electrode discharges substantially restricts the possibility of studying the physical-chemical processes occurring in plasma. Some results of plasma chemical applications of such discharges are presented in [2,4,5].

The main goal of this paper is to summarize some experimental results to describe the phenomenology and general properties of electrode microwave discharges and to attract attention of specialists in different areas of the plasma and gas discharge physics to this insufficiently studied gas discharge and revealed unusual features.

Experimental set-up

Two types of similar discharge cameras which differed in the cylinder diameters of discharge vessels ($R_1=7$ cm and $R_2=4.2$.cm) have been used for experiments [6-8]. Plasmas in both arrangements revealed similar features, so the properties of the described plasmas seems to be typical for the electrode microwave discharge systems.

The discharge chambers were the stainless steel cylinders excited by an antenna at the butt-end of a chamber (Fig. 1). The antenna was an element of a coaxial-to-waveguide converter, which could be tuned with the shorting pistons in the waveguide transmitted lines. The lower end of one of discharge chambers was a movable shorting piston that provided

an additional possibility of tuning the system and changing the position of substrates immersed to plasma (this piston was used as a heated substrate holder). Another chamber had unchangeable internal dimensions.

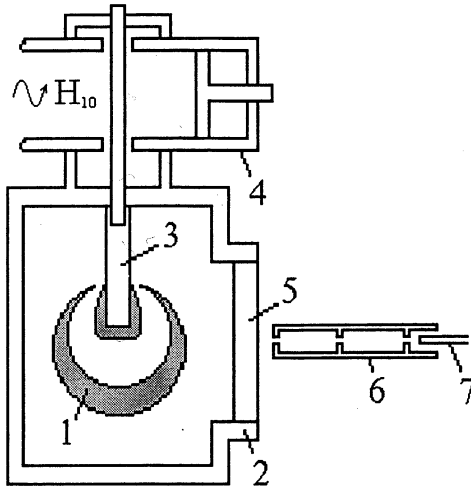


Fig.1. Experimental device.

- 1 – plasma, 2 – discharge chamber,
- 3 – antenna, 4- waveguide-to-coaxial converter, 5 – optical window, 6 – collimator, 7 – optical fiber

A cylindrical tube and solid electrodes with diameters of 0.5-6 mm manufactured from stainless steel and copper and of different shapes have been used for studying dependencies of discharge properties on the shape of the antenna (Fig. 2).

Most of results has been obtained when the discharge was ignited at the end of exciting electrode (antenna). Plasma dimensions were much less than that of the discharge camera so these discharge systems can be attributed to single-electrode systems (the second one is the metal discharge camera). This is one of fundamental differences from conventional discharges where the plasma volume is strongly defined by the discharge vessel. This discharge property defines peculiarity both the electrodynamics of discharge and correlation of external and internal plasma parameters. Some information on the electrode microwave discharge initiated between the electrode and close placed metal plane or metal lug has been presented in Ref. [6].

The sizes of discharge chambers were not specially chosen. The system can be considered as a non-regular coaxial line (regularity is disturbed by a break of the central conductor) loaded on the plasma

column produced at the end of the central electrode. Since the radii of the outer electrodes (camera) were high enough to satisfy the inequality $\lambda(r+R) > 1$ (where r and R are the inner and outer radii of the coaxial line and $\lambda = 12.4$ cm is the of the electromagnetic radiation wavelength in vacuum), not only the transverse TEM mode, but also the upper spatial modes (e.g., H-modes) could propagate in such systems. The transformation of the electromagnetic field structure occurred exactly inside in the region occupied by plasma due to both the presence of plasma and break up of the electrode. And vice versa plasma is created as a result of the action of the set of electromagnetic field modes.

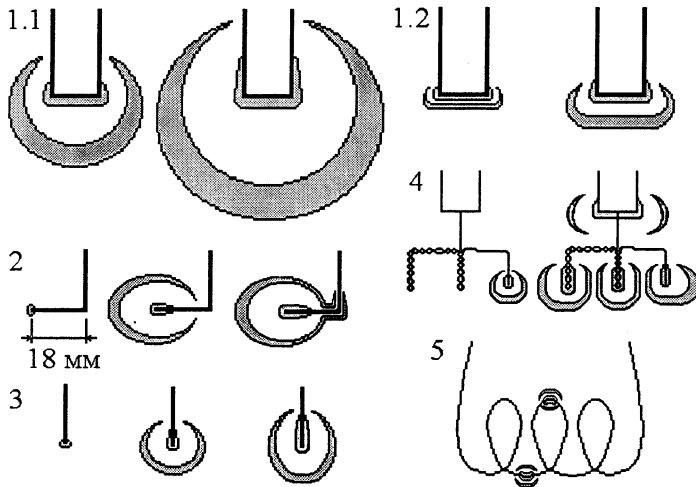


Fig. 2. Shapes of electrodes and dependencies of discharge shapes on geometry of electrodes and plasma conditions. 1 – thick cylinder electrode at low (1.1) and high (1.2) pressure, 2 – thin bent electrode, 3 – thin direct electrode, 4 – trident electrode, 5 – spiral electrode.

The set-up was equipped with the system of optical measurements. Integrated over the spectrum plasma emission with spatial resolution was used for studying discharge structure. Spatially integrated or with spatial resolution signals were used to characterize the emission properties of plasma in the spectral range 400-800 nm. The spatial resolution of measurements was provided by a collimator (spatial resolution was not worst than 1 mm) which could be moved parallel to the antenna axis or in the perpendicular directions. The optical plasma emission was directed

through the optical fiber to the photomultiplier or to the input slit of the monochromator, according to the needs of experiment.

Parameters of electron plasma component were measured with the help of a double electric probe. The details of these measurements were described in [9]. The tungsten probes of a diameter of 100 μm in the quartz capillaries were introduced through the orifice in the lateral surface of the chamber and could be moved along the radius of the discharge column. The length of the open part of the probes was of 1 mm, and the distance between them was 3-4 mm. Each of the probes was covered by a metal shield. The measurements were performed in the plane perpendicular to the axis of the antenna and located at distance, which exceed the thickness of high luminosity of the sheath observed near electrode. Resistive filters (20 k Ω) were used to decrease the possible influence of a microwave field on the voltage-current characteristic of the probe.

The charged particle density can be estimated from the ion saturation current from the well-known relation

$$I_i = 0,61 N_i e S_p v_i, \quad (1)$$

where N_i is the density of charged particles, e is the electron charge, $S_p = \pi dl = 4,7 \cdot 10^{-7} \text{m}^2$ is the probe surface, $v_i \approx 10^4 (T_e/A)^{1/2}$ is the average ion velocity (with the ion acceleration in the pre-sheath taken into account), and A is the ion mass number. The values of the ion saturation current presented below correspond to the 50 V probe bias and are averaged over both branches of the double probe characteristic. In some cases, a single-probe scheme was also used in which the metal discharge chamber served as a reference probe. The ion current was measured within 10% accuracy. In calculation of the charged-particle density, it is necessary to know the ion composition of plasma. In hydrogen plasma, for the degree of dissociation below 50 %, the most abundant ions are H_3^+ ions, which are produced as a result of the ion conversion [10]. An order of magnitude of the charged-particles density can be estimated from the ion saturation current using the relation $N_i [\text{cm}^3] \approx 2 \cdot 10^9 I_i [\text{mA}]$ (here we assumed $T_e \sim 3$ eV) can be used. In nitrogen plasma, assuming N_2^+ as the major ion, the electron concentration can be estimated as follows: $N_i [\text{cm}^3] \approx 6.4 \cdot 10^9 I_i [\text{mA}]$. The electron temperature was determined from the current-voltage characteristics of the double probe at the floating potential.

Plasma gases were Ar, Ne, H₂, N₂, O₂, CH₄, C₂H₂, air, and their mixtures. Gas flow systems were used. The total gas flow rate was less than 1000 cm³/min under the normal conditions (sccm). Results for H₂ and N₂ are presented in this paper.

Microwave power (2.45 GHz) was transmitted from the magnetron generators with output powers of 2.5 kW or 150 W. In last case the stabilized DC power supply was used to feed the magnetron. The power absorbed in the system was measured by a directional couplers by subtracting the reflected power from the incident one. It should be noted that the absorbed power can not be attributed completely to the plasma due to power losses in the discharge camera walls, the coaxial-to-waveguide converter and feeders. The share of these losses is unclear in general case [11].

The aspects of plasma chemical applications of electrode microwave discharge for surface processing were studied using the set-up with large chamber diameter in the Angstrom Laboratory, Uppsala University (Sweden). This discharge device was used for the diamond growth [2] in hydrogen and hydrogen-methane mixtures (1-8%) at 1-15 Torr and to deposit CN_x films in N₂+C₂H₂ mixtures [5]. The composite of nanotubes oriented perpendicular to the substrate surface was also obtained [5].

Phenomenology of the discharge

Distinctive feature of the electrode microwave discharges is that they exist at high levels of reflected power (the standing wave ratio is changed between 5 and 15). This property of the discharge is probably a result of peculiar self-consistence of plasma and discharge system electrodynamic. This property distinguishes the discharge which possess the described phenomena from known discharges, e.g. in coaxial line. It can be used as an indicator of belonging of the discharge to the type of electrode microwave discharge (see below).

The discharge is spatially non-uniform, and the structure of its luminosity depends on the microwave power and gas pressure. In the regimes under study, the discharge with large content of molecular gases has the following characteristic features (see Fig.2):

1. Tube and rod antennas

- The discharge is ignited at the end of antenna and it partially covers it.
- The less the antenna diameter the less is the ignition and maintenance microwave field. The discharge could be ignited at incident powers of 2 W with 0.5 mm diameter antenna.

The discharge could appear just at the place, where the antenna is introduced to the vacuum camera and could be moved to the end of antenna by adjusting the shorting pistons of the matching system.

As microwave power is increased up to certain threshold level, which is defined by the pressure and electrode diameter, the discharge runs away towards the microwave generator along the antenna. It can be moved back by matching the adjusting elements in microwave system but this leads to the decrease of absorbed power. Thus in the particular configuration of the gas discharge system it is impossible to generate the plasma at the top of antenna with absorbed power, which exceeds some threshold value. In this case the discharge can simultaneously exist (depending on the power level, pressure, and plasma gas) at the end of antenna, along it and at the place of an antenna input of the discharge chamber. The last one is the "main" discharge and it strongly reduce the electromagnetic wave penetration into the camera. The reflected power is decreased in the feeder and almost all incident power is absorbed. These regimes were not of our interest because in those cases the pure electrode discharge placed at the end of antenna is only small supplementary discharge.

At lower incident microwave power the discharge can be ignited by the use of external initiators, e.g. the Tesla-coil.

The luminosity of the discharges has non-uniform structure. For all values of power and pressures at which the discharge exists, the end of the exciting electrode was covered with a thin (< 1 mm) bright luminous sheath. Its thickness decreases with pressure and the area of the electrode covered by the discharge weakly increases with power. Increase in incident power leads to growth up of the sheath along the antenna. From the butt-end of the antenna the sheath looks like a ring-shaped bright region along its periphery. The bright near-electrode sheath was also observed in the electrode-plane system [6].

The bright plasma sheath is surrounded by plasma region with weaker luminosity having a sharp external boundary. At low pressures this region has a ball shape with the diameter larger than that of the antenna. When pressure or incident power are such that the sizes of plasma region and electrode are comparable, the shape of plasma follows the shape of the electrode (the case of a thin plasma region). Slight increase in the plasma emission in periphery regions was observed at some conditions.

The dumbbell-like structures of the discharge were obtained in H_2 and N_2 : two balls stringed the antenna with one placed at the end of

antenna and the other placed at distance of $\lambda/4$ upward the antenna. Both balls were connected by weak plasma slab which covers the antenna. The observed structure differed from the conventional standing-wave shape: balls had the sharp boundary from both the side of microwave generator and the opposite side. The whole system had the symmetry plane placed between the balls centers.

The plasma ball exhibits properties of medium with the elastic boundary: when the probes touch the boundary and move further the boundary layer was bent inside. At certain moment the plasma covers the probes and the boundary returns to its initial position. In the reverse motion of the probes the boundary was bent outside moving together with the probes. Finally the plasma loses contact with the probes. Several oscillations in shape and diameter of the plasma occur before it come to the state of equilibrium with an initial diameter of the ball.

2. Trident electrode.

Firstly the discharge is ignited near the top of one end of the trident. The structure of the plasma region is the same as described above. When the incident power is increased the other ends are covered by the same plasma. The diameters of plasma balls are increased with increase of the incident power but the balls never overlap and the dark region exists between plasma regions at any power. The shapes of the balls are changed to ellipse with increased power.

3. Spiral electrode.

The ball-shaped plasma formations are generated at several points of the spiral. Positions of this points are changed with the incident power. The structure of all discharges is the same as described above: the spiral surface was partly covered by a bright sheath surrounded by the plasma ball.

Thus the general feature of electrode microwave discharge is the presence of bright plasma near the electrode sheath and less luminous plasma region with sharp external boundary. As usual this region is ball-shaped.

Results of optical study

Figures 3-8 show distributions of the integrated over the spectrum intensity of plasma emission along the axis of the rod antenna with diameter of 6 mm. Absorbed power in the system was ranged between 10 and 30 W in the interval 20-90 W of the incident powers. One can see a bright near-electrode plasma sheath surrounded by a plasma region with

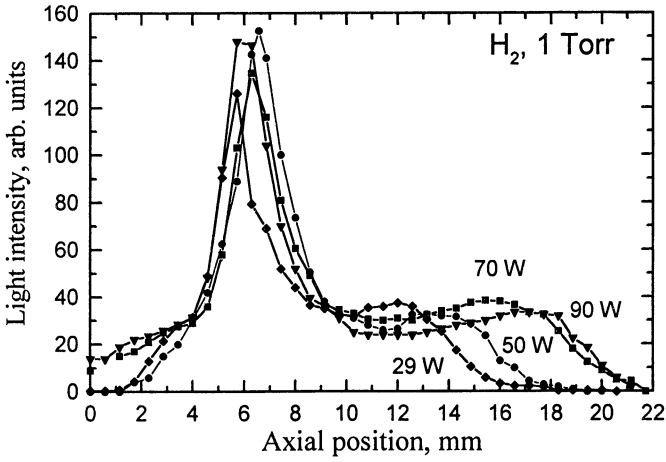


Fig.3. Axial profiles of light-of-sight plasma emission in H_2 . Numbers near the curves correspond to the incident power.

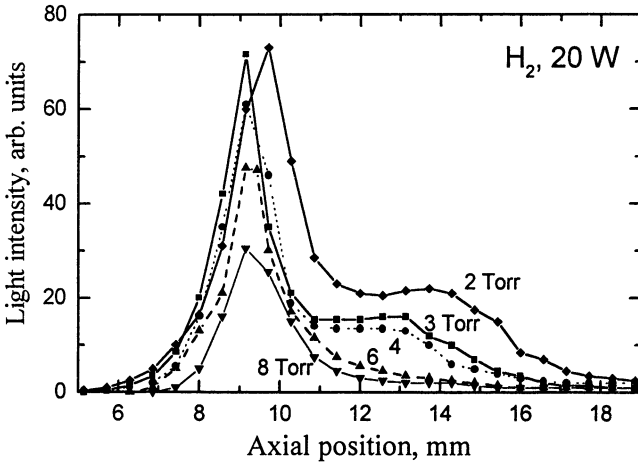


Fig.4. Axial profiles of light-of-sight plasma emission in H_2 at incident power 20 W.

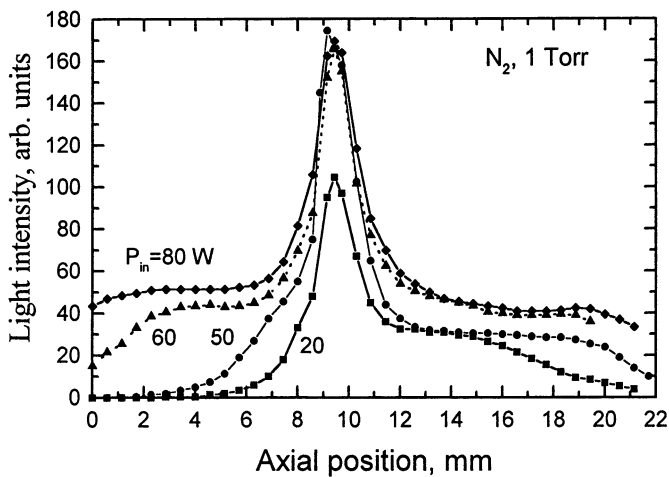


Fig.5. Axial profiles of light-of-sight plasma emission in N_2

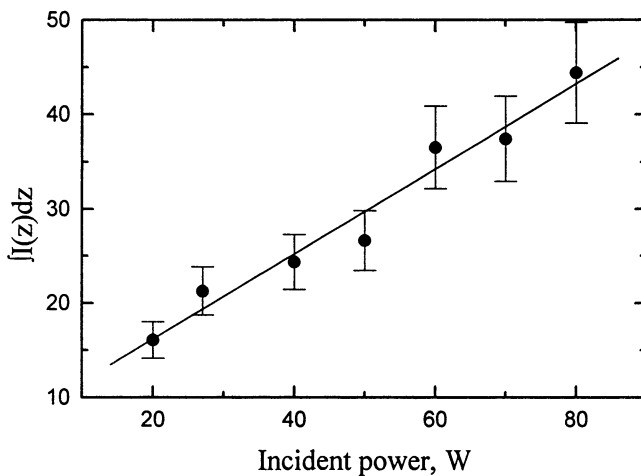


Fig.6. Integrals of curves presented in Fig.5

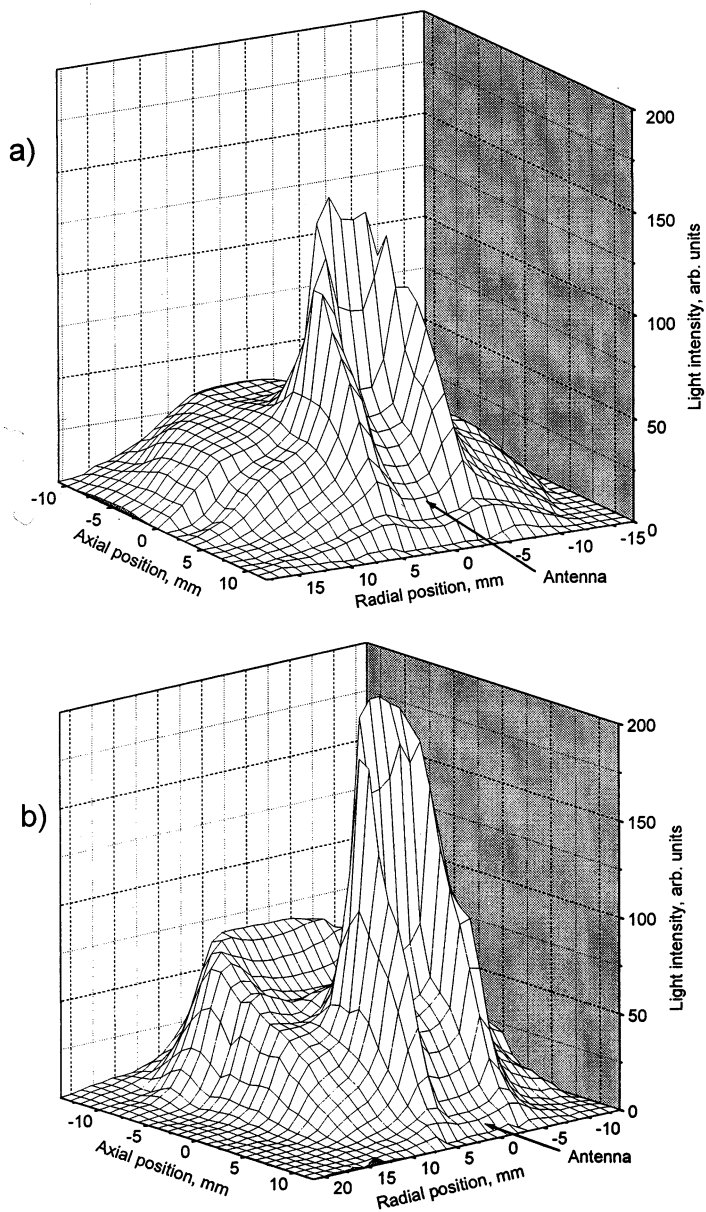


Fig.7. Structure of emission of the electrode microwave discharges in nitrogen (a) and hydrogen (b) at pressure 1 Torr and incident microwave power 90 W.

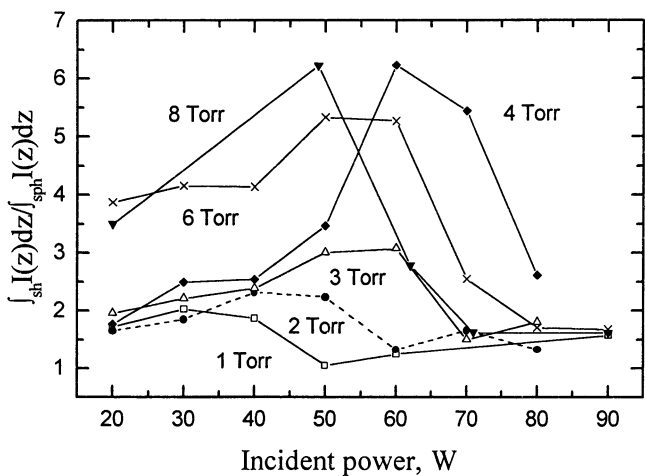


Fig.8. Ratio of integral intensity of sheath emission to that for sphere

weaker emission. As a rule, the total discharge emission is the linear function of microwave power. The growth of plasma brightness near the discharge boundary was observed in hydrogen discharge.

One feature can be noted in comparing H₂ and N₂ discharges (Fig. 3, 5): the discharge in N₂ is more symmetric with respect to the end of antenna, i.e. is more better covered by the plasma ball region for N₂ than in H₂ discharge. This difference can be related to differences in mechanisms of plasma emission excitation in both gases. It is known that in the hydrogen discharge the ionization and excitation of heavy particles occurs due to direct electron impact. As high energy part of the electron energy distribution function is sensitive to the electric field strength, the visible structure of discharge is defined by spatial distributions of the electron density and field.

In the nitrogen discharge these processes go along with a participation of excited particles and by means of secondary processes. This means that the plasma can exist in regions with weaker electric field strength.

Thus the structure of external region of the electrode discharge seems to be related to mechanisms of ionization and excitation.

Figure 8 shows that two regions can exist in the discharge (i.e. the plasma sheath and plasma ball-sphere) and the ratio of intensities of this regions depends on microwave power and pressure. It is important that in

spite of small thickness of the sheath, the major part of plasma emission is attributed exactly to this region.

The nature of near-electrode plasma sheath can be explained as follows.

Since the intensity of plasma emission is related to the absorbed power, the conclusion can be made that the specific absorbed power in the near-electrode sheath is several orders of magnitude higher than that of the plasma sphere. Thus the plasma density in the sheath region can be estimated under the assumption that the whole power is absorbed in the plasma sheath. Using the results of numerical simulation [10], this estimation gives $n_e \sim 10^{13} \text{ cm}^{-3}$ for the pressure 1 Torr in hydrogen plasma. It can be also showed that the volume dissociative recombination is the main channel for the loss of charged particles. This means that the plasma density profile should follow the field profile.

There are several reasons for radial change of the microwave field strength in plasma. The first one is the skin-effect. Other mechanism was presented in [12], where the change in the component of the electric field normal to the surface of an electrode have been analyzed in the case when this component was parallel to the gradient of electron density. Both mechanisms give the same thickness of the sheath. This thickness corresponds to the observed one (about 1 mm). This means that these mechanisms can not be separated but there are physical reasons, which can explain the presence of bright near electrode sheath.

The sharp decrease of the electric field should exist in this region together with the sharp change in plasma emission. As the electron density decreases towards the plasma boundary, the electromagnetic field gradient should decrease and parameters of the discharge in this region (e.g., sphere) slowly changes. All these is agreed with the observed results (Fig. 3-7).

Results of probe measurements

a) Space outside luminous plasma region.

Figures 9-11 show some characteristics of this region. The space outside the plasma region is spatially uniform and double probe voltage-current characteristics pass through zero current at $\Delta U_p(I_p=0)=0$.

Estimations have shown that the characteristic length of electron energy losses in collisions with heavy particles is much less than the observed length (Fig.10). This means that Fig.10 illustrates the heating effect of electromagnetic field. Thus the electric field strength distribution can be determined with the help of the Boltzmann equation

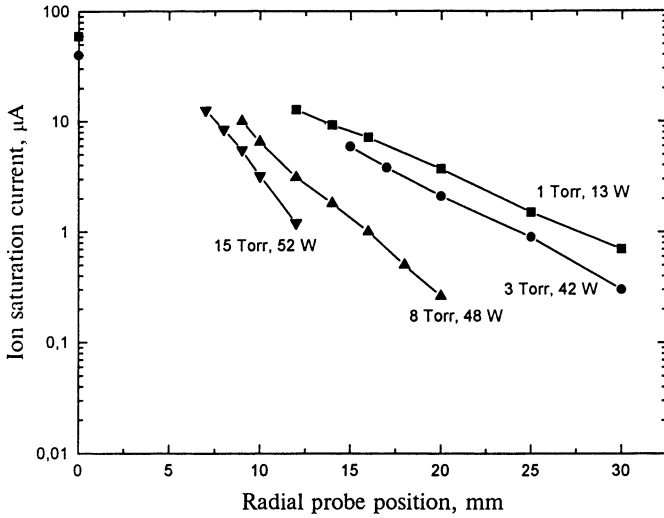


Fig.9. Ion saturation current in the space outside the hydrogen electrode discharge. Numbers near the curves correspond to the absorbed power in the system.

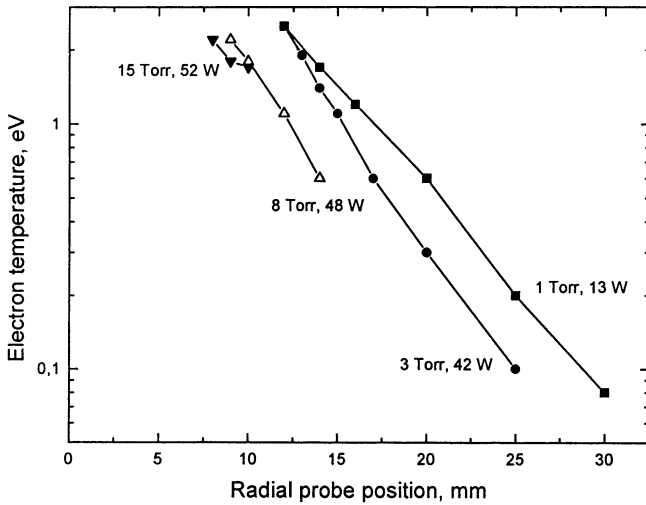


Fig.10. Electron temperature in the space outside the hydrogen electrode discharge.

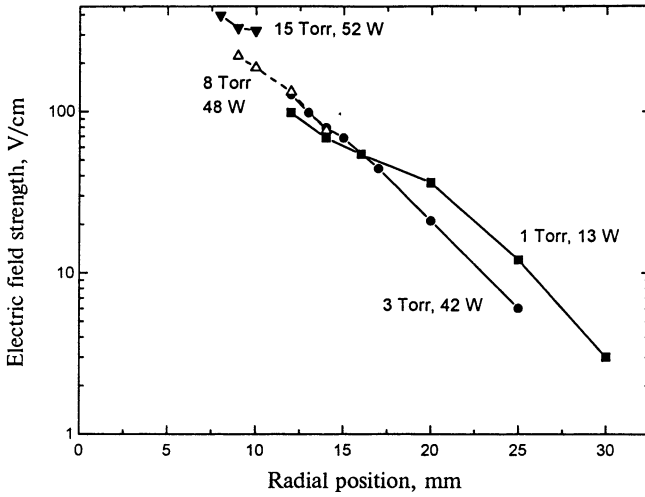


Fig.11. Electric field strength in the vicinity of the hydrogen electrode discharge.

and measured values of electron temperatures. It is possible to match the electric field strength in such a way that the solution of the Boltzmann equation gives the electron energy distribution function with the mean electron energy corresponding to the measured value.

Results of such calculations are shown in Fig.11. It is seen that the electric field strength exponentially decays with radius. The only wave mode with such a structure is a surface wave [13]. This wave spread along the plasma boundary and can cause the increase of intensity of plasma emission as it was observed in experiments (Fig. 3,7). The role of the surface wave in maintenance of the electrode discharge is unclear at present: is it necessary factor of discharge existence or simply result of transformation of the wave mode?

b) Internal space of the discharge.

Figures 12-14 show radial distributions of plasma characteristics measured by a double probe method in the internal region of nitrogen electrode microwave discharge. Measurements showed that the voltage-current characteristics of double probe system passes through the zero

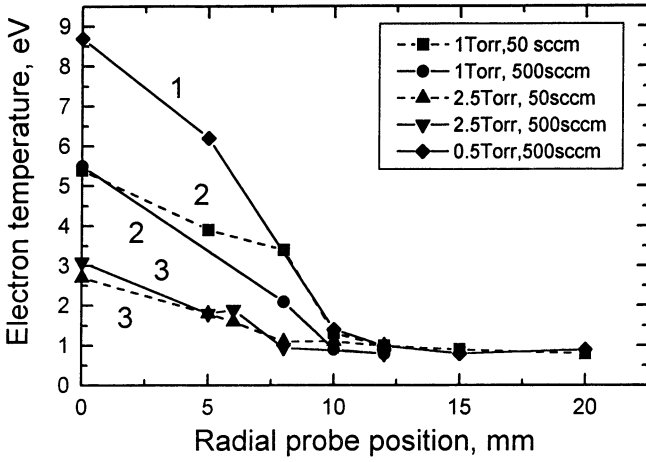


Fig.12. Electron temperature in luminous plasma sphere region in nitrogen. Incident power 200 W, absorbed power 20 W.

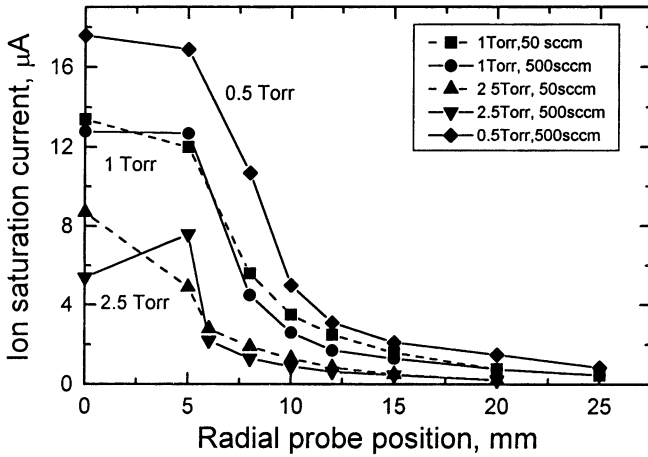


Fig.13. Probe ion saturation current in luminous plasma sphere region in nitrogen. Incident power 200 W, absorbed power 20 W.

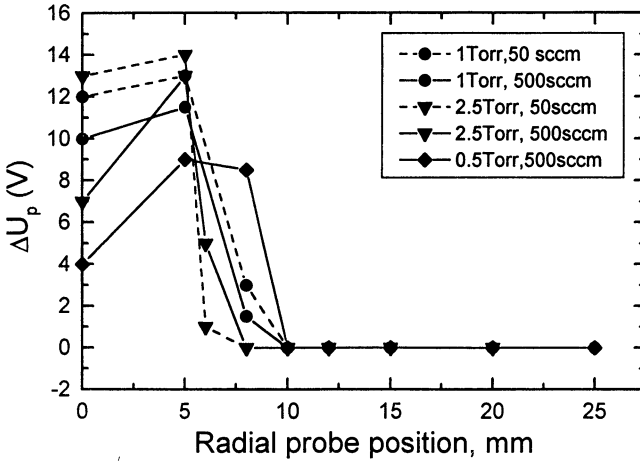


Fig.14. Difference of floating potentials in double probe system in luminous plasma sphere region in nitrogen. Incident power 200 W, absorbed power 20 W.

current at a certain DC voltage difference between the probes $\Delta U_p(I_p=0)$. This means that the internal space of the discharge is non-uniform.

It is seen that the electron temperature monotonously decreases with radius while the ion saturation current and $\Delta U_p(I_p=0)$ decreases abruptly at the boundary. The last one falls down to zero in the external region of the discharge. The estimated electron density exceeds the critical value inside the plasma sphere.

At present a simple interpretation of these results is hardly possible. Some comment should be done on the nature of $\Delta U_p(I_p=0)$. There are several origins of the DC voltage. The first one is the well-known rectification effect of microwaves on non-linearity of the probe-to-plasma sheath. In the case of strong non-homogeneous plasma differences in amplitudes of the microwave field strength in the points where the probes were placed leads $\Delta U_p(I_p=0) \neq 0$.

This reason is very important and it is considered as a disturbing factor for probe measurements. But if it does really exist, $\Delta U_p(I_p=0)$ can be used as an indicator of non-uniformity of the microwave field. In this case Fig.14 shows the distribution of microwave

field in the discharge chamber with plasma. The field outside the plasma is negligibly small.

The difficulty of probe measurements in plasma with alternating fields lies in the fact that the probe method does not contain direct criterion of absence of voltage-current disturbances by the AC field [14]. It is only possible to conclude about bigger or smaller extent of such influence. Note that we have used the resistive filter to suppress the influence of ac field, which was successfully used in other plasma measurements [14]. The indirect evidences should be taken into account.

Experiments showed that the increase of the electron temperature was accompanied by the decrease in $\Delta U_p(I_p=0)$. In the recombination controlled discharge the increase of the electron temperature is caused by the increase of electric field and the behavior of $\Delta U_p(I_p=0)$ should be inverse. Increase of the gas flow rate decreases the $\Delta U_p(I_p=0)$ value. This effect is accompanied by a small change of electron temperature and decrease of the electron density. The decrease of the electron density leads to the increase of the plasma-probe sheath reactance. This should increase the influence of the microwave field on the probe characteristics.

All these seem to give the evidence that the DC voltage really exists in the plasma.

Nonlinear interaction of electromagnetic waves with the overcritical plasma (the critical value of plasma density is reached at the boundary of the plasma) accompanied by the frequency transformation can be the origin of appearance of $\Delta U_p(I_p=0)$. In this case the DC field has the structure of electrostatic trap (Fig. 14). It can be supposed that the DC fields play the key role in the electrode discharge physics.

Indirect evidence of the role of the DC fields in the formation of plasma ball structures can be found in literature. It was experimentally shown that positively biased electrostatic probe in the RF plasma was surrounded by a plasma sphere [15]. Spherical structures were obtained in the DC discharge in the discharge system similar to ours if the internal electrode was used as anode [16]. Note that the ball structures have been also observed in the inductively coupled RF discharge [17] and in the microwave discharge at pressures of 100 Torr [18].

Conclusion

Results of the study of electrode microwave discharges by optical and double probe methods at pressures 0.5-15 Torr in hydrogen and nitrogen have been described. This type of discharges can be attributed to the class of so-called "initiated" discharges but with the initiator used as an

element of microwave feed system (the coupling antenna). General features and peculiarities of electrode microwave discharge can be formulated as follows.

- Electrodes (antennas) having different shapes can be used to ignite the discharge. In systems with the rod electrode the discharge exists at the top of it.
- The discharge dimensions are much less than those of the discharge chamber.
- The discharge exists at a high level of reflected power.
- The discharge consists of two regions:
 - a) Bright thin plasma sheath placed close to the electrode (antenna). In this region high electron density, large gradients of electromagnetic field and plasma density exists and main absorption of electromagnetic energy occurs.
 - b) Main body of the discharge, which often has the shape of a ball with sharp boundary. In this region gradients of plasma parameters are small.
- The discharge is controlled by the volume recombination of charged particles.

The electrode microwave discharges can be successfully used in the plasma chemistry, e.g. for surface treatment.

Some advantages of the electrode microwave discharges are:

- Generation of plasma at extremely low incident power.
- Exact localization of the plasma region.
- Generation of active plasma particles very close to the treated substrate.
- Absence of the electrode erosion.

Experimental results on physical parameters of the electrode microwave discharges and the phenomenological picture of discharge have been presented. Unfortunately the obtained results produce more questions than answers. And this is not surprising since the study of the electrode microwave discharges is in its initial stage. Additional efforts are necessary to understand the physical nature of the observed phenomena. One of the problems to be solved is the explanation of the sharp external boundary of the discharge.

Acknowledgments

Authors would like to thank L. Bardos for collaborations and interest to applied aspects of electrode microwave discharges. This work was partly supported by NWO (the Netherlands) Grant 047.011.000.01 and the Scientific Exchange Program of the Royal Swedish Academy of Sciences.

References

1. Lebedev Yu. A. J. Phys. IV France 1998, 8, 369.
2. Bardos L, Barankova H, Lebedev Yu.A., Nyberg T., Berg S. Diamond and related materials, 1997, 6, 224.
3. Raizer Yu.P., Shneider M.N., Yatsenko N.A. Radio Frequency Capacitive Discharge. CRC Press. Boca Raton, Tokyo, London, 1995.
4. Brovkin V.G., Kolesnichenko Yu.F., Khmara D.V. Appl. Phys. (Russ.), 1994, N4, 5.
5. Bardos L, Barankova H, Lebedev Yu.A. Proc. 42-nd Ann. Conf. of Soc. of Vac. Coaters, Chicago, 1999, paper E-7.
6. Bardos L., Lebedev Yu.A. Plasma Phys. Reports, 1998, 24, 956.
7. Bardos L., Lebedev Yu.A. Technical Physics, 1998, 43 , 1428.
8. Lebedev Yu.A., Mokeev M.V. Tatarinov A.V. Plasma Phys. Reports, 1999 (accepted for publication)
9. Lebedev Yu.A. High Temperature, 1995, 33, 846.
10. Lebedev Yu.A., Epstein I.L. J. Moscow Phys. Soc. 1995, 5, 103.
11. Lebedev Yu.A. Plasma Sources Sci.&Technol. 1995, 4, 4740.
12. Gildenburg V.B., Gol'tsman V.L., Semenov V.E. News of high school, Radiophysics (Rus), 1974, 17, 1718.
13. Moisan M., Shivarova A., and Trivelpiece A.W. Plasma Phys., 1982, 24, 1331.
14. Ivanov Yu.A., Lebedev Yu.A., Polak L.S. Methods of contact diagnostics in nonequilibrium plasma chemistry. Moscow, Nauka, 1981.
15. Ivanov S. T., Thomae R. W., Klein H., Hilschert F. H., Nikolaev N. I. Bulgarian Journal of Physics 1998, 25, 49.
16. Nerushev O.A., Novopashin S.A., Radchenko V.V., Sukhinin G.I. Preprint N 285-97, Inst. of Thermophysics, Siberian Branch RAS, 1997.
17. Gildenburg V.B., Markov G.A. Pisma v JTPH (Russian). 1982, 8, 1245.
18. Brovkin V.G., Kolesnichenko Yu.F., Khmara D.V. In "Ball lightning in the laboratory", Chemistry (Moscow, Russia) 1994, 119.

THE PINCH EFFECT IN MICROWAVE RESONANT STREAMER DISCHARGE AND ITS POSSIBLE APPLICATIONS

L. P. Grachev, I. I. Esakov, K. V. Khodataev

Moscow Radiotechnical Institute RAS, Moscow, Russia

The work is devoted to experimental and theoretic study of a streamer discharge in the focus of microwave radiation in the open resonator. The observations show that if a gas pressure more than 0.1 atmosphere the single streamer discharge appears in the focus. When the resonant length of the streamer is achieved, the all energy storage of resonator is adsorbed by the streamer with very high efficiency. The simulations show that if gas pressure is quite enough the pinch force of the current inducted in the resonant streamer compress the discharge plasma. The small scale of phenomena and the device size, very high efficiency of the energy utilization, absence of electrodes and surfaces contacting with the hot plasma, direct pumping of energy to the ion heating allows us to hop that forecasted high plasma parameters really can be achieved and be applied not only for design of a gamma or neutron sources but for creation of a fusion reactor.

Introduction

The electrodeless microwave discharges in a gas of high pressure demand appropriately high level of the electromagnetic field. For example the normal pressure air breakdown needs the microwave radiation specific energy flow 1 MW/cm^2 . The high amplitude microwave field can be achieved in a focus of a radiation beam. Even in the case when the focusing system has a short focus so that the area of the focus cross section equals approximately wave length squared the needed generator power for 10 cm wave length is 100 MW with pulse duration more than few microseconds. It is difficult to provide so high power during some microsecond in a laboratory. But the field level needed for breakdown of a gas with high pressure (more than some atmosphere) can be achieved in a resonator because the resonator quality can be very high.

The open resonator created by two spherical copper mirrors was used in our experiments [1]. The resonator allows us to create a discharge in air and other gases with pressure which does exceed one atmosphere. A high-pressure discharge in the focused traveling-wave radiation beam represents a net of the thin hot strings (connected among themselves), consistently appeared one from another (of course if the radiation inten-

sity in the focus and pulse duration are enough). But the discharge in the resonator represents the single hot string. The string is a single because the stored energy in resonator is finite. Usually the all stored energy is adsorbed by one resonant streamer. The length of developed streamer is close to half of wave length. It is electrodynamic resonance. Appropriately the high current is inducted in the streamer. The inducted current heats the streamer plasma up to high temperature because the streamer diameter is very small. The heating up specific power related to the gas density is proportional to gas pressure because the breakdown electric field (and inducted current) is proportional to one. If the gas density is quite enough the magnetic pressure force of inducted current is able to compress the plasma in streamer. The pinch instability in central part of the resonant streamer can cause strong local dissipation of energy in the pinch region. The attributes of this phenomena are observed in our experiments as a bright core. The courageous estimations clearly show that very high temperature (up to thermonuclear temperature) can be achieved in the resonant streamer if the gas pressure is more than some decades of atmosphere [2]. We will show the key experimental and simulation results and discuss extrapolating estimations based on simplified theory of a resonant streamer discharge.

Experimental data

The scheme of experimental installation is shown on Fig. 1.

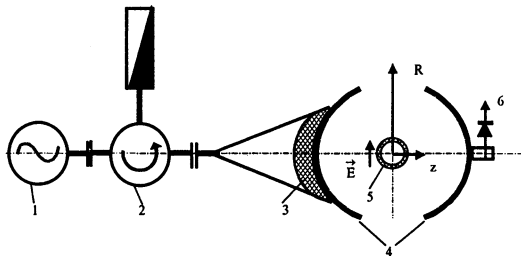


Fig. 1. The scheme of the experimental installation. 1 – magnetron generator, 2 – circulator, 3 – lens, 4 – spherical mirrors of the open resonator, 5 – quartz retort, 6 – field probe

The open resonator 4 consists from two spherical copper mirrors displaced along common axis z . The curve radius a_s , diameter $2a_m$ and distance between them L_0 equal 35 cm, 55 cm and 51.7 cm correspondingly. The quartz retort 5 fulfilled by a gas is displaced in the center of

resonator. The retort represent the quarts long tube with the inner diameter equaled to 8 cm and has the optical windows on the ends. The gas pressure in the retort can be varied from small value up to several atmosphere. The magnetron generator feed the resonator through wave guide with circulator 2 and reactive attenuator 3 with the feeding coefficient $\sim 10^{-3}$. The output power of generator is 10 MW with pulse duration 40 μ s. Wave length of radiation λ is 8.9 cm. The repetition frequency is less than 1 Hz. The amplitude envelop of field in resonator is monitored by the probe 6.

The resonant distance between mirrors along the resonator axis z is defined by the resonance equation [3]

$$\frac{2 \cdot L_0}{\lambda} - \frac{2}{\pi} \cdot \arcsin\left(\sqrt{\frac{L_0}{2 \cdot a_s}}\right) = h, \quad (1)$$

where h – mode number, odd integer.

The distribution of the electric field amplitude near resonator center is described by the known rate [4]

$$E = E_0 \frac{\left| \cos\left(\frac{2 \cdot \pi}{\Lambda} \cdot z\right) \right|}{\sqrt{1 + \left(\frac{2 \cdot z}{k \cdot a_f^2}\right)^2}} \cdot \exp\left(\frac{-\left(\frac{r}{a_f}\right)^2}{1 + \left(\frac{2 \cdot z}{k \cdot a_f^2}\right)^2}\right), \quad (2)$$

where $\Lambda = \frac{2 \cdot L_0}{h}$ – wave length in resonator, $k = 2\pi/\lambda$ – wave number, z – distance from the resonator center, a_f – focus radius

$$a_f = \sqrt{\frac{L_0}{k}} \cdot \sqrt{\left(\frac{2 \cdot a_s}{L_0} - 1\right)}. \quad (3)$$

The surface current induced in the mirrors has the Gauss distribution with dispersion radius a_c

$$a_c = \frac{\sqrt{2 \cdot a_s}}{\sqrt{k \cdot \sqrt{\left(\frac{2 \cdot a_s}{L_0} - 1\right)}}}. \quad (4)$$

The measurements show that $\Lambda = 9.4$ cm, $h = 11$ and $a_f = 9$ cm.

The excited mode in the resonator is TEM linear polarized standing wave with the electric field vector oriented transversally z axis and the retort axis.

For the feeding of resonator one of the mirrors must be semi-transparent. The microwave energy from generator, passing through wave-guide, circulator, horn and focusing lens, penetrates into the resonator from back side of the semi-transparent mirror.

One can see that the transparence coefficient α is optimal if

$$\alpha = \alpha_{opt} \equiv 2 \cdot \sqrt{1 - \operatorname{Re}(R)}, \quad (|1 - \operatorname{Re}(R)| \ll 1), \quad (5)$$

where $\omega = k \cdot c$ – circle frequency, c – light velocity, σ_m – electrical conductivity of the mirrors, R – the mirror reflection coefficient taking into account diffraction losses of the open resonator

$$R = \frac{\sqrt{1 + i \cdot \frac{4 \cdot \pi \cdot \sigma_m}{\omega}} - 1}{\sqrt{1 + i \cdot \frac{4 \cdot \pi \cdot \sigma_m}{\omega}} + 1} \cdot \sqrt{1 - \exp \left[-2 \cdot \left(\frac{a_m}{a_c} \right)^2 \right]}. \quad (6)$$

If the resonator is tuned and (5) is satisfied the field E_f in the focus of the tuned resonator rises as

$$E_f = E_m \cdot \frac{\tau \cdot (1 - e^{-t/\tau}) - \tau_g \cdot (1 - e^{-t/\tau_g})}{\tau - \tau_g}, \quad (7)$$

$$\tau = \frac{2 \cdot h \cdot \pi}{\omega \cdot 4 \cdot \sqrt{1 - \operatorname{Re}(R)}}, \quad (8)$$

$$E_m = \frac{4}{a_f} \cdot \sqrt{\frac{P_{gen}}{c}} \cdot \frac{1 + \operatorname{Re}(R)}{2 \cdot \sqrt{1 - \operatorname{Re}(R)}}, \quad (9)$$

where τ_g – the front time of the generator, τ – the resonator constant of time, E_m – maximum field in resonator in stationary regime, P_{gen} – the generator power.

The application of the resonator allows to increase the field in the focus in η times

$$\eta = \sqrt{\frac{c \cdot \tau}{L}}. \quad (10)$$

The measurements show that the used resonator has $\tau = 5 \mu s$. It means that in our case $\eta = 52$.

The most part of experiment was performed in air and hydrogen.

The main results of experimental study of microwave discharge in a gas of high pressure ($p > 0.2$ atm) in the open resonator can be formulated by following [5, 6, 7].

The electron avalanche starts from one electron and represents the expanding the immovable in average spherical electron cloud with increasing electron number and radius. The streamer evolution is shown by Fig. 2.

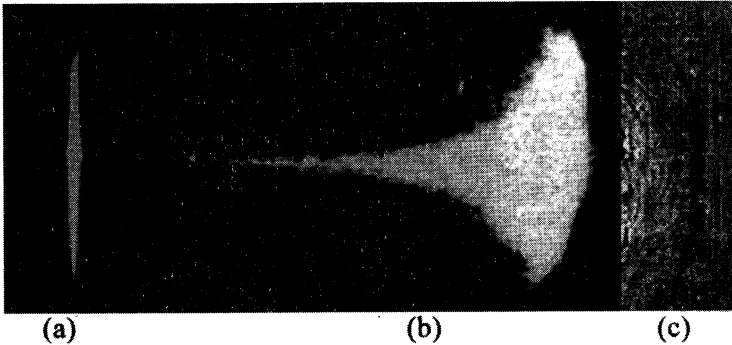


Fig. 2. The streamer development. (a) – the photo of the streamer by the exposed lens, (b) – the scanned image of the streamer (the total time durance is 70 ns), (c) – the shadow of the shock wave, generated by the exploded streamer. The vertical size of the plot is 5 cm

When the electron number in avalanche is quite enough the electron cloud starts to transform to a string which is oriented along vector of electric field. It is streamer (Fig. 2a and Fig. 2b). The speed of the streamer arising can exceed 10^8 cm/s if the pressure is quit enough [8].

When the streamer length achieve the resonant value (near half wave length) the field in resonator breaks down and farther exists on a small level. The streamer development is stopped.

After breakdown the shock wave runs out from the streamer (see Fig. 2c) [9]. The measured shock wave parameters show that the streamer adsorbs almost all energy stored by resonator and explodes.

If gas pressure equals or more than 0.5 atm the bright core is observed in central part of the resonant streamer (see Fig. 2a and Fig. 3). In hydrogen some times two bright cores can arise near center of the streamer. One can suppose that the most part of stored energy is adsorbed in the core. It is important to note that the hard boundary on gas pressure exists between state with the core and without one.

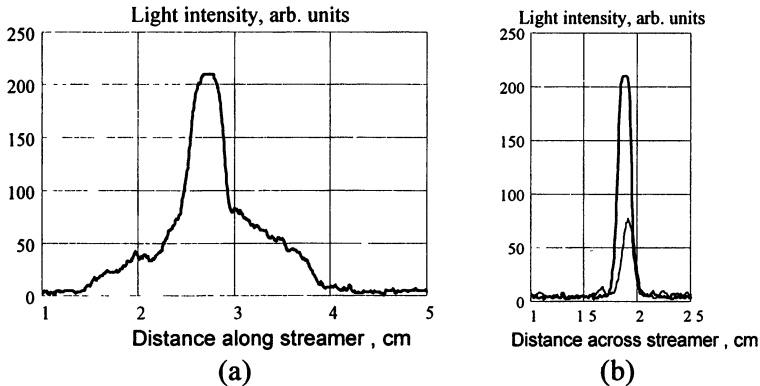


Fig. 3. The measured light intensity of the streamer, (a) – distribution along the streamer axis; (b) – distribution across the streamer, solid line – across the corn ($z = 2.7$ cm at (a)), dot – aside the corn ($z = 3.0$ cm at (a))

The simple theoretical model of the discharge

The streamer development is the very complicated nonlinear process. Its adequate theory description can be performed by modeling only. The complete model is too complicated for the brief investigation. The simple model is taking into account the main factors of the process but several suppositions allow to describe it by the system of the simple differential equations.

Let us suppose that the streamer discharge plasma is the conducting cylinder with the diameter $2a$ and length $2b$, oriented along external microwave electrical field. It allow to use for calculation of the current inducted in the cylinder the elements of theory developed for a wire antenna. This cylinder can be described as a series contour which consists from inductance, capacity and resistance. The impedance of the circuit equals approximately

$$Z(\sigma, a, b) = R_w(b) + R_{om}(\sigma, a, b) + i \cdot \frac{\Lambda}{c} \cdot \left(\frac{b_r}{b} - \frac{b}{b_r} \right), \quad (11)$$

where Λ – logarithmic form-factor, R_w , R_{om} – wave and Ohm resistance, b_r – resonant value of the streamer half-length, σ – electrical conductivity of the streamer plasma,

The current inducted in the middle of the cylinder can be defined as

$$J(E, \sigma, a, b) = \frac{E \cdot 2 \cdot b}{Z(\sigma, a, b)}, \quad (12)$$

where E – the microwave field amplitude at the focus of resonator.

The evolution of the cylinder length is defined by the ionization front velocity [10], that defined by the local values of electric field on the ends of the streamer and unperturbed gas density and temperature.

$$\frac{db}{dt} = 2 \cdot \text{Re} \left(\sqrt{D(\rho_0, T_{e_{\text{end}}}) \cdot v(\rho_0, T_0, T_{e_{\text{end}}})} \right), \quad (13)$$

where $v(\rho, T, T_e) = v_i(\rho, T, T_e) - v_a(\rho, T, T_e)$, $D = D(\rho, T_e)$ – electron diffusion coefficient, taking into account the exchange the free diffusion on ambipolar diffusion [11], $v_a = v_a(\rho, T, T_e)$ – electron attachment frequency, $v_i = v_i(\rho, T, T_e)$ – electron ionization frequency.

The modeling by means of more complicated model allows us to approximate the electron temperature dependence on electric field by the rate

$$T_{e_{\text{end}}} = T_0 + T_{\text{ccr}} \cdot \frac{E_{\text{end}}}{E_{\text{cr}}}, \quad (14)$$

where E_{cr} – the critical value of electric field for unperturbed gas. The field E_{end} on the end of the streamer is defined by the charge continuous equation

$$E_{\text{end}} = E \cdot \left| 1 + \frac{i}{k \cdot a} \cdot \frac{\pi}{c \cdot Z} \right|. \quad (15)$$

The radius of the streamer in its middle is defined by the ionization front velocity from one side and gas dynamics from other side as result of the streamer heating. The Sedov's theory of a point explosion in the gas with a finite pressure is used for simulation of the radial dynamics of the streamer. The estimations show that at high unperturbed gas pressure the pinch force of the inducted current can be more than the discharge plasma pressure gradient thus the pinch force is included in the movement equation (17):

$$\frac{da}{dt} = 2 \cdot \frac{D(\rho_0, T_e)}{a} + V, \quad (16)$$

$$\frac{dV}{dt} = \frac{2}{a} \cdot \left(\frac{(p_0 - p)}{\rho_0} - V^2 - \left(\frac{2 \cdot J}{c \cdot a} \right)^2 \cdot \frac{1}{8 \cdot \pi \cdot \rho} \right), \quad (17)$$

$$\frac{dp}{dt} = \frac{1}{\rho \cdot C_v(p, T, n, T_e)} \cdot \frac{\operatorname{Re}(Z) \cdot |J|^2}{\Omega_{\text{str}}}, \quad (18)$$

where p , ρ – total pressure, total density of plasma mixture, T – temperature of molecules, atoms and their ions, n , T_e – number density and temperature of the plasma electrons, $\Omega_{\text{str}} = 2 \cdot b \cdot \pi \cdot a^2$ – the volume of the streamer. C_v – thermal capacity.

The electron temperature in the middle of the streamer also is defined by the gas temperature and electric field in the middle

$$T_e = T + T_{\text{ecr}} \cdot \frac{E_{\text{mid}} \cdot \rho_0}{E_{\text{cr}} \cdot \rho}, \quad (19)$$

where the field in the middle of the streamer is defined by usual Ohm law

$$E_{\text{mid}} = \frac{J \cdot \sigma}{\pi \cdot a^2}. \quad (20)$$

The calculated state equation (21), thermal capacity in (18) and electric conductivity (22) for diatomic molecular gas for wide diapason of a temperature and the electron continuity equation (23) for the not equilibrium ionization pretends to be near to realty:

$$\rho = \rho(p, T, n_e, T_e), \quad (21)$$

$$\sigma = \sigma(p, T, n_e, T_e), \quad (22)$$

$$\frac{dn}{dt} = v(\rho_0, T_0, T_{e_{\text{end}}}) \cdot n - \beta(\rho_0, T_e) \cdot n^2 + G(p, T). \quad (23)$$

The MW generator provides the energy to the resonator but refraction and heat losses decrease the stored energy. Both factors is took into account in differential equation for electric field at the resonator focus

$$\frac{dE}{dt} = \frac{E_m - E}{\tau} - \frac{4 \cdot \pi}{\Omega_{\text{res}}} \cdot (R_w + R_\sigma) \cdot \left(\frac{2 \cdot b}{|Z|} \right)^2 \cdot E, \quad (24)$$

where $\Omega_{\text{res}} = \pi \cdot \frac{a_f^2}{2} \cdot L$ – equivalent volume of the resonator.

It is supposed that resonator is tuned in resonance with generator frequency.

The evolution of the microwave streamer discharge is described by the system of the differential equations (13), (16), (17), (18), (23), (24) and functions (11), (12), (14), (15), (19), (20), (21), (22).

The task parameters are the wave length and power of generator, the resonator parameters, the gas pressure and the moment of appearance of initial free electron.

The simulation results and its comparison with experimental data

The task parameters was the same that in the experiment: maximum field in resonator in stationary regime $E_m = 35 \text{ kV/cm}$, time constant of resonator $\tau = 5\mu\text{s}$, the initial free electron appears in the focus of resonator when electric field in the focus achieves the critical value depending on gas pressure. The gas pressure was varied from 50 Torr up to 760 Torr.

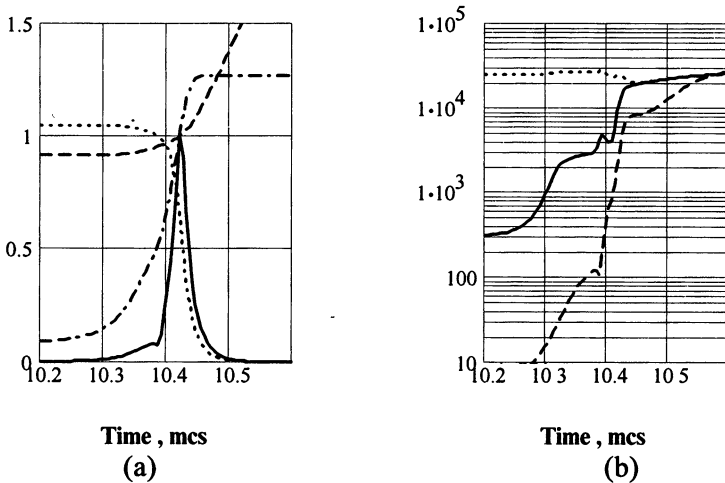


Fig. 4. The example of simulation. Gas pressure is 760 Torr. (a) The solid line – induced current $J/J(t_1)$, dot – electric field in the resonator E/E_{cr} , dash – streamer radius $a(t)/a(t_1)$, $J(t_1) = J_{max}$, dash-dot – length of the streamer $b(t)/b_r$, t – the time after switching the generator. (b) The solid line – the gas temperature $T(t)$, K, dot – the electron temperature $T_e(t)$, K, dash – electric conductivity $4\pi\sigma(t)/\omega$

The simulation shows that independently on the gas pressure if electric field exceeds the critical value the electron avalanche starts to develop and transforms into the streamer. The streamer length, electric conductivity and induced current rise up to maximum value limited by finite energy stored by resonator. Electric field in the resonator decreased quickly, it is breakdown. The streamer radius rises initially up to value limited by ambipolar process and after heating rises quickly because of the explosion. Fig. 4a demonstrates this process on the case of the gas

pressure 760 Torr. One can see that after heating the electron temperature T_e and gas temperature T is the same and achieve the value 30,000 K (see Fig. 4b).

The Fig. 5–6 show the dependencies on the pressure. One can see that dependencies are very strong. The maximum induced current and maximum velocity of streamer ends are near the theoretic limit if the pressure is quit high (see Fig. 5a and Fig. 5b). The current is limited by the radiation resistance of an ideal resonant vibrator in the critical external field E_{cr} . The ends velocity is limited by the product of the free electron diffusion and maximum ionization frequency. The product almost do not depends on the gas pressure.

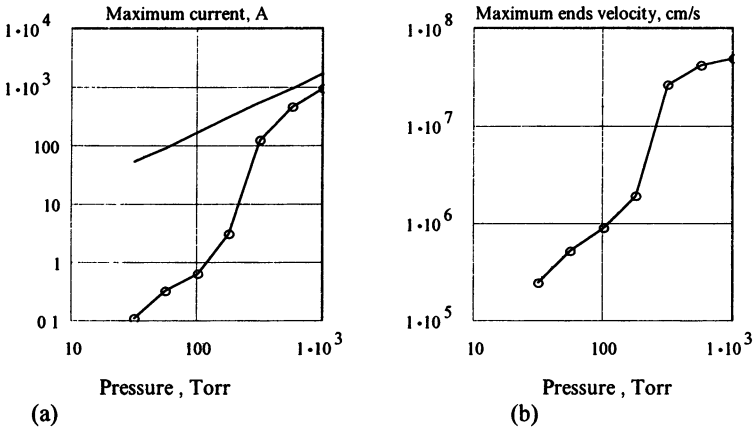


Fig. 5a. Maximum induced current J_{max} dependence on the pressure. The solid line – simulation data, dot – theoretic limit, current in resonant ideal vibrator if $E = E_{cr}$.

Fig. 5b. Maximum velocity of the streamer ends dependence on the gas pressure simulation data

The maximum gas temperature exceeds 0.5 eV if the pressure is more than 500 Torr (see Fig. 6). The streamer has the maximum temperature at the its middle only. It means that the light intensity of the middle of the streamer must be strongly higher than one of the streamer branches. The observing bright corn at the middle of the streamer can be explained by the high gas temperature at the middle. Is clear why the corn arises if the pressure is more than 500 Torr.

The calculated and measured values of the streamer radius are compared on the Fig. 7. The bottom branch is the streamer radius at the mo-

ment when the inducted current is maximum; the top branch is the radius after the streamer explosion. The experimental data are got from the streamer photo and shadow method correspondingly. One can see the quit good agreement. It give us some assurance that designed model has relation to the realty. This assurance gives us a good possibility to forecast the discharge parameters by means of designed simple model if the pressure is much more 1 atm. The calculated ratio of magnetic pressure created by inducted current to discharge plasma total pressure is shown on Fig. 8 (solid line).

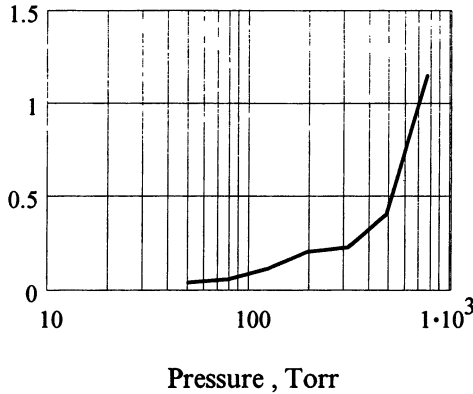


Fig. 6. The maximum gas temperature T , eV, dependence on the gas pressure

The several suppositions lay in the basis of estimation:

- inducted current is maximum when the streamer has the resonant length,
- Ohm resistance of the streamer is less than the radiation resistance, (it means that at this moment the gas in the streamer is fully ionized and has Coulomb conductivity),
- the streamer radius is limited by the ambipolar process,
- plasma has the identical electron and ion temperature.

The avalanche starts to develop when the MW field exceeds the critical value. The ambipolar field limits the discharge radius on the avalanche stadium. Using the noted suppositions one can write the rate for limited avalanche radius

$$a_{\text{limit}} = \sqrt{2 \cdot D \cdot \sqrt{2 \cdot \ln \left(\frac{T_{e0} \cdot a_{\text{limit}}}{3 \cdot e^2} \right) \cdot \frac{2 \cdot \tau}{v_a \cdot \beta} \cdot \frac{E_{\text{cr}}}{E_m - E_{\text{cr}}}}, \quad (25)$$

where $\beta = \frac{\left(\frac{E}{N}\right)_{cr}}{v_i} \cdot \frac{\partial v_i}{\partial \frac{E}{N}}$ (usually it is accepted $\beta=5.3$), T_{e0} – electron temperature if the electric field is the critical one.

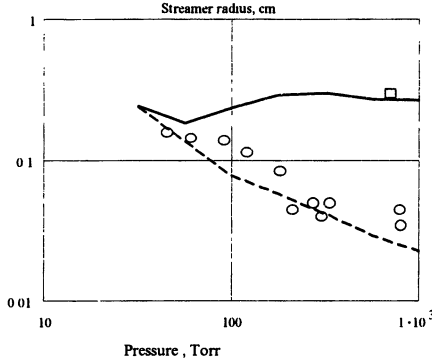


Fig. 7. The streamer radius dependence on gas pressure. Circles – the measured values from photo of the streamer by exposed lens, box – usual value of the streamer radius measured by shadow method, lines – the simulation result: solid – the streamer radius after expanding caused by explosion, dash – the radius at moment when induced current (and correspondingly light radiation of the streamer) is maximum

The discharge temperature must be more than

$$T_{\min} = \left(\frac{\omega}{4 \cdot \pi \cdot 1.3 \cdot 10^{13} \cdot k^2 \cdot a_{\text{limit}}^2} \right)^{2/3} \quad (26)$$

The ratio of magnetic pressure and gas pressure is defined now as

$$\Phi = \left(\frac{2}{c \cdot a_{\text{limit}}} \cdot \frac{E_{cr} \cdot 2 \cdot b}{R_w} \right)^2 \cdot \frac{1}{8 \cdot \pi \cdot 4 \cdot N \cdot k_B \cdot T_{\min}} \quad (27)$$

where a_{limit} and T_{\min} are defined by (25) and (26). The estimation (27) are compared with the simulation data on Fig. 7. One can see that that the estimation helps as to understand the simulation data. Both show that Φ is proportional to the gas pressure and if the gas pressure is more than 10 atm, the magnetic pressure is able to exceed the plasma pressure so the pinch effect can be observed [12]. The simulation by means of more advanced complete model of the process at gas pressure 10 atm confirms this conclusion. The Fig. 9 demonstrates the simulation result.

At the moment of resonance the plasma density is rising instead of usual decreasing at lower gas pressure. It is consequence of the pinch

effect. Also one can see that at resonance the ion temperature is near to the electron one. Estimations show that the temperature increases proportionally to gas pressure. If the gas pressure will be increased up to some tens of atmosphere the temperature some keV can be achieved. The

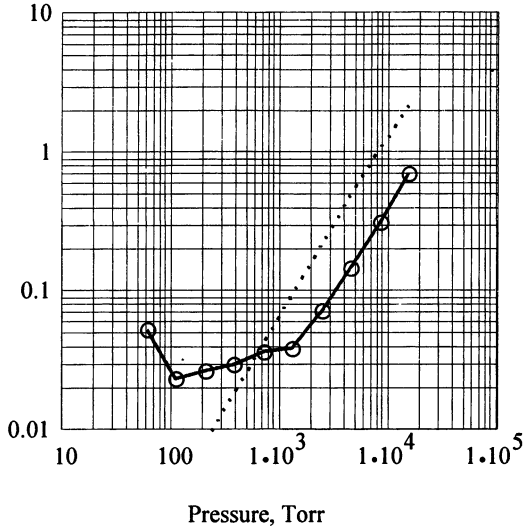


Fig. 8. The rate Φ of magnetic pressure of induced current J to plasma pressure at the middle part of the streamer when the current is maximum in dependence on gas pressure: solid line – data calculated by means of the simple model, dot – estimation (27)

pinch influence is important both for density increasing and for ion heating. If plasma temperature is high the electron-ion relaxation time is comparable with time of the process so as electrons do not able to heat ions through Coulomb collisions. But MW pinch effect generates the strong shock wave every half period of MW oscillations. The shock waves are dissipated by ion component and ions are being heated directly during the pinch time.

Of course the discharge at the pressure about several atm needs the significantly deeper experimental and theoretic study than it is performed here.

Possible applications

The experimental results simulation and theory data specify the possible ways of the MW discharge streamer discharge in an opened resonator. This type of discharge has the important peculiarities.

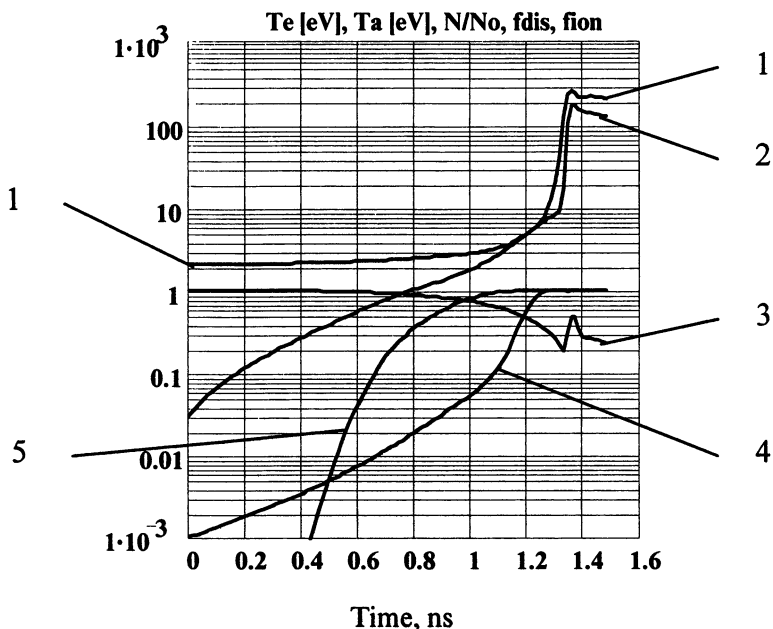


Fig. 9. The simulation result achieved by means of complete model for discharge at 10 atm. 1 – electron temperature T_e , 2 – gas temperature T , 3 – plasma density ρ/ρ_0 , 4 – dissociation coefficient, 5 – ionization coefficient

The simulations show that if gas pressure is quite enough the average pinch force of the current inducted in the resonant streamer strongly compress the discharge plasma. The dense very hot plasma can be created for a short time about several nanoseconds. The pinched plasma can have the parameters up to needed for fusion in DT mix if the mix pressure is more than 40 atmosphere. At the compress stage the gas dynamic time of plasma is compared with period of microwave field. In this condition the pinching force generates the periodical shock waves which are cumulated at the axis of the filament. Thus the work of the pinch force is transformed into ions temperature directly. This discharge need not electrodes and arises far from the walls of device chamber. It means that only work gas takes part in the process without any impurities.

The small scale of phenomena and the device size, very high efficiency of the energy utilization, absence of electrodes and surfaces contacting with the hot plasma, direct pumping of energy to the ion heating allows us to hop that forecasted high plasma parameters really can be achieved and applied not only for design of a gamma or neutron sources

but for creation of a fusion reactor. It is the nearest possibilities. We also dream that the Lawson criteria will be exceeded at a high pressure of DT mix and may be the resonant streamer discharge is one of the possible realistic ways to create the nuclear fusion reactor.

References

1. Grachev L.P., Esakov I.I., Mishin G.I., Khodataev K.V. Tech. Phys. 39(2), February 1994, pp. 130-136.
2. Grachev L.P., Esakov I.I., Mishin G.I., Khodataev K.V. Preprint of LFTI im. A. F. Joffe, 1992, № 1577.
3. Wineshtein L.A. Open resonators and open waveguides. «Sov. radio», Moscow, 1966.
4. Vinogradova M.B., Rudenko O.V., Sukhorukov A.P. Wave theory. Moscow. «Nauka», 1979.
5. Grachev L.P., Esakov I.I., Mishin G.I., Khodataev K.V., Tsyplyakov V.V. Pis'ma v JTF, 26 November 1992, v. 18, № 22, pp. 34-38.
6. Grachev L.P., Esakov I.I., Khodataev K. V. JTF, 1998, т. 68, № 4, pp. 33-36.
7. Grachev L.P., Esakov I.I., Mishin G.I., Khodataev K. V. JTF, 1996, v. 66, № 7, pp. 32-45.
8. Khodataev K. V. Proc. XXIII ICPIG, Contributed papers, IV-24.
9. Khodataev K.V. Proc. of the ICPIG-XX (Pisa, 1991), Invited papers 1991, pp. 207-217.
10. Vikharev A.L., Gildenburg V.B., Kim A.V., Litvak A.G., Semionov V.E. Proc. Of scientific works «High frequency discharge in the wave fields», Gor'kiy, 1988, pp. 41-135.
11. Khodataev K.V., Gorelik B.R. Fizika Plasmy. 1997, v. 23, № 3, pp. 236-245.
12. Khodataev K.V. Abstracts of the XXVI Zvenigorod conference on plasma physics and control thermonuclear fusion (5-9 April 1999, Zvenigorod), II-C2-26.

MICROWAVE BREAKDOWN IN AIR-FILLED RESONATORS

*U. Jordan, D. Anderson, M. Lisak
T. Olsson*, V. E. Semenov**, M. Åhlander****

Chalmers University of Technology, Göteborg, Sweden

*Allgon System AB, Täby, Sweden

**Institute of Applied Physics, Nizhny Novgorod, Russia

***Ericsson Radio Systems AB, Stockholm, Sweden

Microwave breakdown in air-filled rotationally symmetrical resonators is considered analytically, numerically and experimentally, with emphasis on experimental results. Comparisons are made between numerical calculations and experimental data.

Microwave breakdown is a much studied problem. The recent rapid development in the field of mobile telecommunications has renewed the interest for the problem, since some components are best constructed using resonators, but the power handling capability is often limited by microwave breakdown. Air is an important dielectric in these applications thus this work is focused on air-filled resonators.

Physical model

Plasma generation by microwave breakdown is described by a simple model using Maxwell's equations and the equation of continuity for the electron density:

$$\frac{\partial n}{\partial t} = D\nabla^2 n + (\nu_i - \nu_a)n, \quad (1)$$

where n denotes the electron density, t the time, D the diffusion coefficient, ν_i the ionisation frequency, and ν_a the attachment frequency. Here losses due to recombination are neglected. This model assumes that the electron density is high enough for a continuum description. When the background density of electrons is very small there will be a statistical delay until a first electron appears and the breakdown avalanche can develop.

The breakdown threshold for continuous wave (CW) is obtained with $\partial n/\partial t=0$ in the equation of continuity. For time dependent problems, the breakdown condition has to be formulated in terms of the electron density needed to significantly change the wave propagation characteristics.

To obtain the threshold it often suffices to solve Maxwell's equations (ME) without free charges, since they become important only near the threshold. Considering the correspondingly determined microwave fields as given, the steady state solution for the electron density can be found from eq. (1) as an eigenvalue problem.

Analytical approach

The eigenvalue problem, which determines the breakdown threshold, can be solved exactly only in situations involving certain simple idealised geometries. For more complicated geometries resort must be taken either to approximate analytical methods or to full numerical computations. A convenient approach for approximate analysis of the eigenvalue equation is direct variational methods based on trial functions and subsequent Raleigh-Ritz optimisation. This approach has been used in the present problem to find simple analytical approximations for the breakdown threshold as it depends on geometrical parameters for some nontrivial geometries. The result clearly demonstrates the importance not only of the direct geometrical dimensions but also of the scale length of the inhomogeneous mode structure of the electric field. However, for the complicated geometry of a commercial resonator design, the only option for obtaining accurate predictions is numerical computations.

Numerical calculations

For comparison with experimental data the CW-breakdown threshold is calculated numerically, with the simplifications stated above.

For the dominant mode in a rotationally symmetric structure ME become:

$$\begin{aligned} \nabla^2 H_\varphi - H_\varphi/r^2 + \omega^2 \mu \varepsilon H_\varphi &= 0, \\ H_\varphi &= 0, \quad r=0, \end{aligned} \quad (2)$$

$$\hat{n} \bullet \nabla H_\varphi + \frac{n_r}{r} H_\varphi = 0, \quad \text{on the boundary,}$$

where r is the radial coordinate and \hat{n} is the outward normal vector to the boundary. The E_r and E_z components are readily calculated from H_z .

The CW-breakdown condition can then be formulated as:

$$\begin{aligned} D \left[\frac{\partial^2 n}{\partial z^2} + \frac{1}{r} \frac{\partial}{\partial r} \left(r \frac{\partial n}{\partial r} \right) \right] + (v_i - v_a) n &= 0, \\ n(z, r) &= 0, \quad \text{on metal boundaries,} \end{aligned} \quad (3)$$

where the dependencies of D , v_i , and v_a on the electric field strength and pressure are given by semi-empirical expressions, cf. [1, 2].

The solution yields the electric field strength needed for breakdown and also the electron density. The electric field strength can be related to the input power by the coupling at the ports and the losses in the resonator.

Experiments

Breakdown thresholds for different signals have been measured using a set-up that permits measuring incident and reflected average power and peak to average ratio for the signal.

The peak equivalent power (PEP) is defined as the average power of a sinusoid with the same amplitude as the peak of the considered signal. The peak to average ratio (PF) is defined as the ratio between PEP and average power (P_{av}) for the signal:

$$PF = \frac{P_{PEP}}{P_{av}}. \quad (4)$$

The measurements were done by keeping the average power constant and lowering the air pressure in the component until breakdown occurred, at which point the pressure was recorded. Three different kinds of signals were used:

- 1) single carrier (sinusoid)
- 2) multicarrier (varying number of sinusoids)
- 3) modulated (one carrier with information modulated on it, according to the IS95 standard).

Results

The numerically calculated CW-threshold is plotted together with the experimental points for the different experiments.

For the case with single carrier signal, one can observe the following features, see Fig. 1:

- Large spread: the pressure sweep can continue far into the region where breakdown is expected before breakdown takes place. This is due to the statistical waiting time for a first electron to appear in the breakdown region and to start the electron avalanche.
- The numerically calculated CW-breakdown threshold gives a good estimate of the “worst” performance of the component.

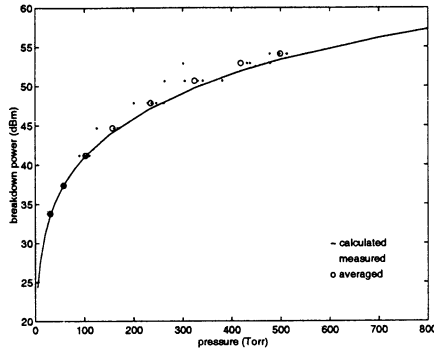


Figure 1: Breakdown threshold for single carrier experiment.

In the multicarrier experiment the number of carriers were varied between one and seven, with the power equally divided between the carriers, but the relative phases between the carriers were not fixed. In Fig. 2 the CW-breakdown threshold is plotted together with, in (a) the average power, and in (b) the peak equivalent power for each signal versus pressure at breakdown. From Fig. 2 it is seen that:

- The picture that the device can not handle full average power due to the interference peaks of the signal is confirmed.
- The spread among the measured points is increased as compared to the single carrier case.

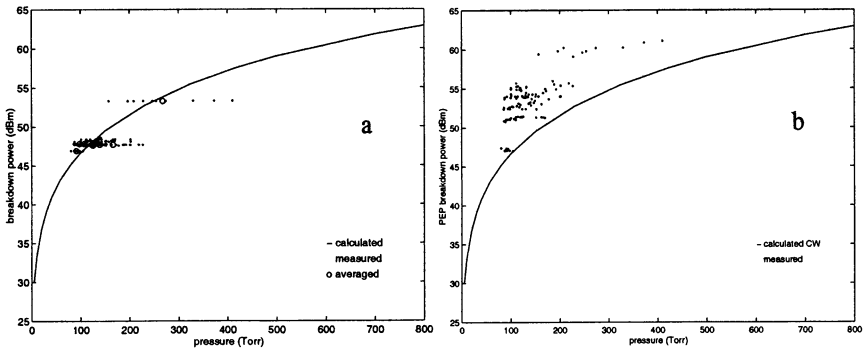


Figure 2: Breakdown threshold for the multicarrier experiment, (a) average power versus pressure, (b) peak equivalent power versus pressure.

The modulated carrier experiment shows essentially the same features as the multicarrier experiment, as can be seen from Fig. 3. The points are less spread out in Fig. 3b as compared to Fig. 2b, because the

modulated signal has a less varying peak to average ratio than the multi-carrier signals that were used.

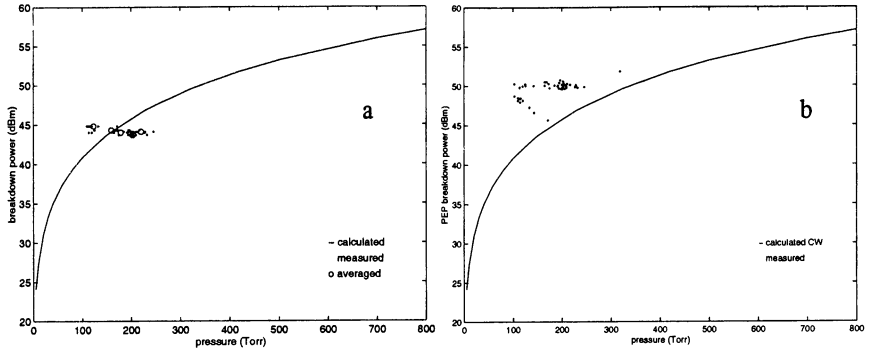


Figure 3: Breakdown threshold for the modulated carrier experiment, (a) average power versus pressure, (b) peak equivalent power versus pressure.

Conclusions

Good agreement is found between numerical simulations and experimental data.

The large spread and the tendency for the resonator to sustain more power than the predicted threshold in many of the experimental points lead to the conclusion that care must be taken when trying to verify the performance of a given component experimentally. This is more important if a signal with time-varying envelope, such as a pulsed signal, is used since the high power interval must coincide with the occurrence of a seed electron.

References

1. W. Woo and J. S. DeGroot, Microwave absorption and plasma heating due to microwave breakdown in the atmosphere, *Physics of Fluids*, 1984, **27**, 475.
2. W. C. Taylor, W. E. Scharfman and T. Morita, *Advances in Microwaves*, Vol.7, Editor: L. Young, Academic Press, New York 1971.

LARGE DIAMETER MICROWAVE PLASMA EXCITED AT 2450 MHZ IN ARGON AND OXYGEN GASES

*Y. Lahmar-Mebdoua, K. Henda and Ph. Leprince**

Laboratoire des Plasmas Centre de Développement des Technologies Avancées,
Alger, ALGERIE

*LPGP, Université Paris XI, Orsay, France

This work is focused on the study of the large diameter microwave discharge (120 mm) excited at 2450 MHz in argon and oxygen gases (low pressure), then compare the main results with those obtained in the small radii plasma. In such a large diameter plasma, the description of the spatial electromagnetic field distribution as well as the species distribution is performed by non-intrusive diagnostics. The results show that several plasma modes can propagate simultaneously in the plasma which is mainly maintained by the hexapolar plasma mode TM_{30} . The actinometry technique yields the relative atomic oxygen densities and their spatial distribution; it is about 1% of the neutral density.

1. Introduction

Industrial need for the development of large area microwave plasma has grown in several fields: surface modifications etching and deposition of thin films, because of samples greater at each time.

The main advantages of the microwave plasma excited at 2450 MHz are the high production of the active neutral particles and the higher energetic electron than those obtained with lower frequency plasma. These properties are of interest for plasma chemical process. They are also electrodeless and can be operated over a wide pressure range [1, 2].

Our work is focused on the study of the large diameter microwave plasma sustained by surface waves at 2450 MHz, for which the free space wavelength is 12.24 cm; and compare the main results with those obtained in the small radii plasma; particularly the excited mode in plasma, the ground state atomic oxygen densities and their spatial distribution.

2. Wave propagation

In the case of a small radii plasma, the widely assumption of a flat radial electron density profile, constitute a satisfactory approximation for determining the propagation constant [3, 4].

In the large diameter plasma the electromagnetic field components and the dispersion relation are expected to depend on the radial electron density profile. So, we have to solve the following set of Helmholtz equations [5, 6]:

$$\bar{\nabla}_T^2 E_z + k_p^2 E_z + \frac{\gamma^2}{k_p^2} \cdot \frac{d\varepsilon_p/dr}{\varepsilon_p} \cdot \frac{\partial E_z}{\partial r} = -j\omega \mu_0 \frac{\gamma}{k_p^2} \cdot \frac{1}{r} \cdot \frac{d\varepsilon_p/dr}{\varepsilon_p} \cdot \frac{\partial H_z}{\partial \varphi},$$

$$\bar{\nabla}_T^2 H_z + k_p^2 H_z - \frac{k_0^2 \varepsilon_p}{k_p^2} \cdot \frac{d\varepsilon_p/dr}{\varepsilon_p} \cdot \frac{\partial H_z}{\partial r} = j\omega \varepsilon_0 \varepsilon_p \frac{\gamma}{k_p^2} \cdot \frac{1}{r} \cdot \frac{d\varepsilon_p/dr}{\varepsilon_p} \cdot \frac{\partial H_z}{\partial \varphi},$$

$$E_r = -\frac{\gamma}{k_p^2} \cdot \frac{\partial E_z}{\partial r} - j\omega \frac{\mu_0}{k_p^2} \cdot \frac{1}{r} \cdot \frac{\partial H_z}{\partial \varphi},$$

$$E_\varphi = -\frac{\gamma}{k_p^2} \cdot \frac{1}{r} \cdot \frac{\partial E_z}{\partial \varphi} + j\omega \frac{\mu_0}{k_p^2} \cdot \frac{\partial H_z}{\partial r},$$

$$\text{where} \quad k_p^2 = k_0^2 \varepsilon_p + \gamma^2, \quad k_0 = \frac{\omega}{c},$$

E_i, H_i are the components of respectively electric and magnetic field, ε_p – plasma permittivity, $\gamma = \alpha + j\beta$, with α the attenuation coefficient and β the wave number.

Pasquiers and Darchicourt have shown that the radial electron density profile has an increasing influence in the range of low electron density (less than $8 \cdot 10^{11} \text{ cm}^{-3}$) [7].

According to our experimental conditions, our computations have been performed for a wave frequency $f=2450 \text{ MHz}$, inside and outside plasma tube diameters respectively equal 120 and 125 mm, with an external metallic cylinder diameter of 188 mm.

In these conditions the electron density is about 10^{12} cm^{-3} . This value allows us to take again the assumption of a flat radial electron density profile [8]. Thus, the radial variation of the plasma relative permittivity vanishes; we find again the case of a small radii plasma [5]. We proceed with the same manner as in the case of the small radii plasma. The solutions of the Helmholtz equations are combinations of two Bessel functions of first and second kind [5]. The continuity of the tangential electromagnetic field components yields the dispersion relation. These computations predict that several modes can be excited in this plasma. We find that at low electron density (10^{10} cm^{-3}), the seven first guide

modes have their cut-off frequency smaller than the excitation frequency (2450 MHz); at higher electron density ($>10^{11} \text{ cm}^{-3}$), the cut-off frequencies of these guide modes become greater than the excitation frequency and only five plasma modes (the fundamental plasma mode TM_{00} , the dipolar mode TM_{10}^* , the quadrupolar mode TM_{20}^* , the hexapolar mode TM_{30}^* and the octapolar mode TM_{40}^*), all these modes can propagate simultaneously with a close value of the attenuation coefficient α .

Thus, we conclude from theoretical computations that our plasma is sustained simultaneously by five plasma modes, contrarily of small radii plasma, where the fundamental plasma mode can be selected alone [5].

3. Experimental set up

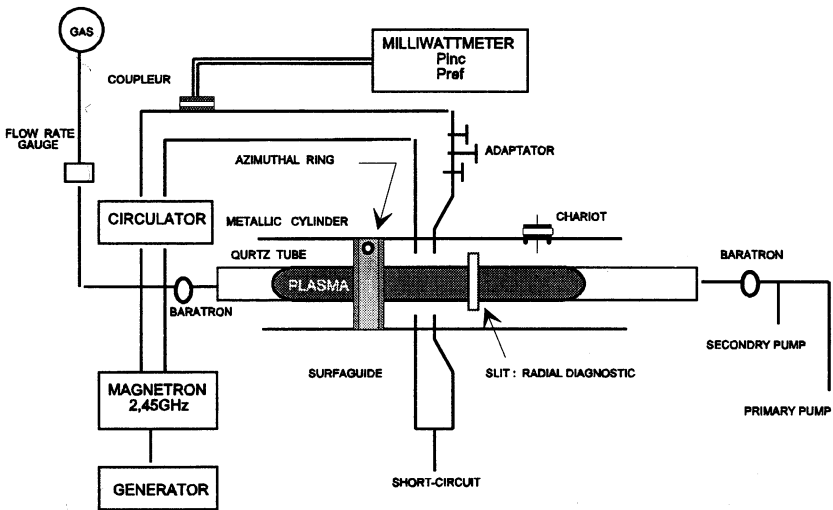


Figure 1: Experimental set up

As shown in figure 1, the plasma is created in the quartz tube (inner diameter 120 mm) surrounded by a metallic cylinder (188 mm diameter). The plasma is excited at the gap by a microwave power (0.8 – 3 kW) at an industrial frequency of 2450 MHz in Ar and O_2 gazes mixtures at low pressure (0.1 – 5 Torr) with a flowrate of about 200 sccm. For a microwave power around 1 kW, total plasma length range from 15 – 20 cm in pure oxygen to 120 cm in pure argon. The higher the percentage

of O_2 , the lower the plasma length and the electron densities. Nevertheless, the electromagnetic behaviour is always the same.

The description of the spatial electromagnetic field distribution and the species density distribution are performed by non-intrusive diagnostic : electrical antenna and emission spectroscopy.

4. Results

Electromagnetic aspect

We have plotted in figure 2, the longitudinal evolution of the emission intensity of the argon line (750.4 nm) which exhibit modulations. These ones are explained by a simultaneous propagation of several plasma modes, among others the hexapolar hybrid plasma mode TM_{30}^* .

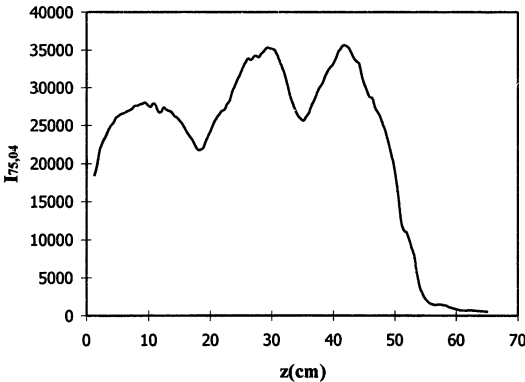


Figure 2: Spectroscopic measures of the argon line in pure argon p=1 Torr, P=1200 W

In figure 3, we present the electrical signal azimuthally collected by an antenna; it shows the predominance of the hexapolar plasma mode TM_{30}^* . The plasma is mainly sustained by the hexapolar plasma mode.

But, it seems that the calculated beat wavelengths of the hexapolar mode and the others propagating modes are largely greater than the measured ones, which are of the order of 18 cm.

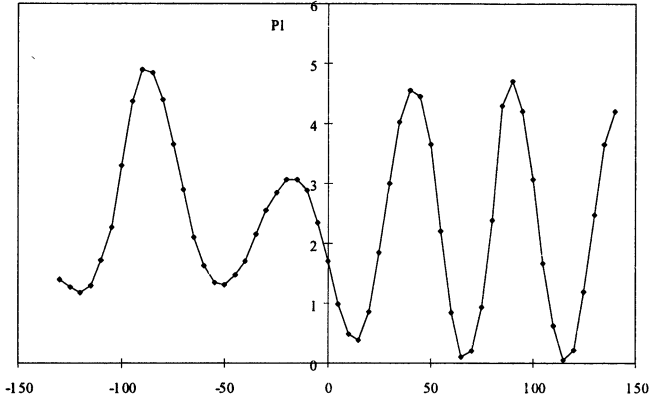


Figure 3: Azimuthal evolution of the electric antenna measures in pure argon, $p=1$ Torr

$$\lambda_{B_{30}} = \frac{2\pi}{\Delta\beta_{30}} = 36 \text{ cm,}$$

$$\text{where } \Delta\beta_{30} = \beta(TM_{30}^*) - \beta(TM_{00}),$$

$$\lambda_{B_{31}} = \frac{2\pi}{\Delta\beta_{31}} = 40 \text{ cm,}$$

$$\text{where } \Delta\beta_{31} = \beta(TM_{30}^*) - \beta(TM_{10}^*),$$

$$\lambda_{B_{32}} = \frac{2\pi}{\Delta\beta_{32}} = 61 \text{ cm,}$$

$$\text{where } \Delta\beta_{32} = \beta(TM_{30}^*) - \beta(TM_{20}^*).$$

This discrepancy is possibly due to the fact that the calculated beat wavelengths are obtained from the resolution of the dispersion equation in which we consider a flat radial electron density profile.

The radial electron density profile has to be taken into account in the computation of the propagation constant.

Scaling laws

Different experimental results of the discharge characteristics (ν , θ , E_{eff}) in small plasma radii at low pressure have been expressed in terms of similarity laws, they are written as follow :

$$X/N = f(N \cdot a),$$

where $X = \nu$, θ , E_{eff} ; a – represents the plasma radius. For a given gas, these expressions are only dependent on the product Na , where N is the neutral density, and are independent on the electronic density and the excitation frequency. In plasma, where there is no neutral density gradient, these quantities have to be constant and thus, they characterise the plasma. These laws have theoretically established by Ferreira [9] and

verified then in several works. In the case of large diameter plasma, the experimental results constitute a coherent set; thus the plasma characteristics are only dependent on the neutral density and the plasma radius. But it seems that the values of the e-neutral collision frequency present a similar variation to the results obtained for another tube smaller than 120 mm, but they are three times greater. This could be due to the values of the electron density which is obtained by the hyperfrequency diagnostic.

Density of species

Our interest bears also on the ground state atomic oxygen densities and their spatial distribution for their efficiency in some treatments.

This density is provided by the ratio $I(O)/I(Ar)$. This technique called actinometry is valid under the following conditions:

- the radiating excited states have to be directly created by electron impact from the atomic ground state.
- they have to be lost by radiative de-excitation.

These conditions are verified in situations similar to our experimental conditions; this technique is used in order to measure the relative density of the ground state atomic oxygen, which is given by:

$$[O]/N = C * I(O)/I(Ar),$$

where N is the neutral density [10, 11, 12].

Longitudinal and azimuthal distribution of $[O]/[Ar]$ are plotted in figure 4 and 5. They present a homogenous profile; this ratio is about 1% of the total neutral density. It is also about 1% in the case of small radii plasma.

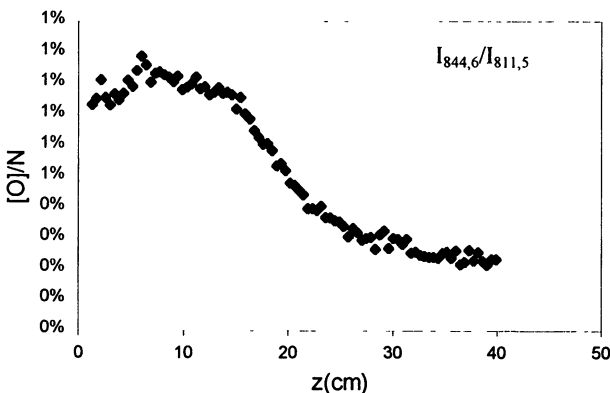


Figure 4: Longitudinal evolution of the relative atomic oxygen density,
 $P=2200$ W, $p=0.5$ Torr Ar/O₂ = 2/98 sccm

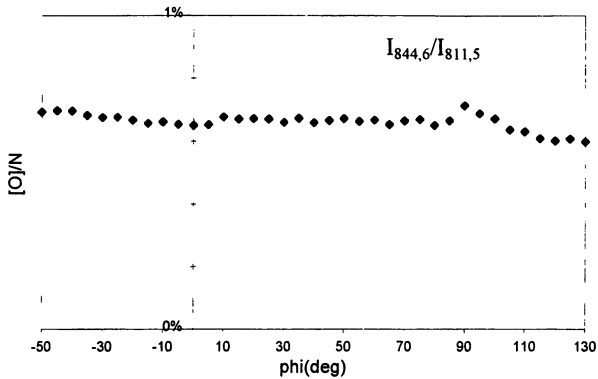


Figure 5: Azimuthal evolution of the atomic oxygen percentage,
 $P=2200\text{ W}$, $p=0,5\text{ Torr}$, $\text{Ar}/\text{O}_2=2/98\text{ sccm}$

This relative density increases by increasing the microwave power then decreases in the plasma end, where all the curves reach the same non-vanished value as presented in figure 6. The same result has been obtained in the case of the small radii plasma; thus we can conclude that the atom sources is independent of the microwave power in the plasma whatever the plasma radius.

This result is very interesting for surface treatment applications.

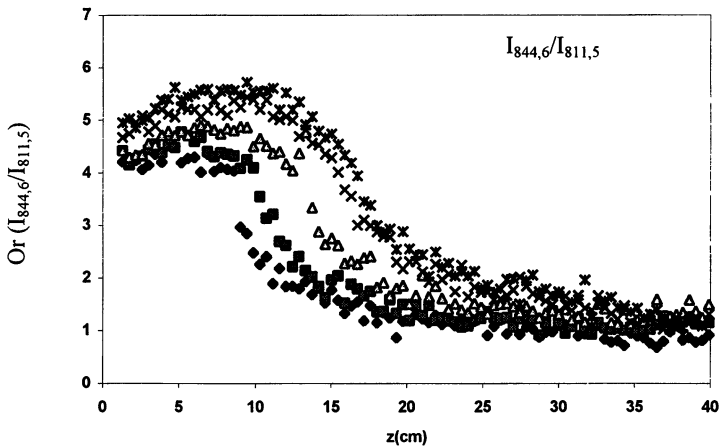


Figure 6: Evolution of the microwave atomic oxygen density
with the microwave power at $\text{Ar}/\text{O}_2=2/98\text{ sccm}$

Conclusion

We have shown in this study that a large diameter plasma (120 mm) excited at 2450 MHz is mainly maintained by an hexapolar plasma mode ($m = 3$) contrary to a small radii plasma where the plasma could be maintained only by the selected fundamental plasma mode TM_{00} .

Spectroscopic measures show also that several plasma modes can propagate simultaneously with a predominance of the hexapolar plasma mode.

The density of the ground state atomic oxygen is homogeneous in the two directions; it is about 1% of the total neutral density.

We have also concluded that the radial electron density profile has to be taken into account in the computation of the propagation constant, this is the main discrepancy between the two ranges of diameters (small and large).

References

1. Caroline Boisse-Laporte and al, «Microwave discharges produced by surface waves in Argon gas», J. Phys. D., 1987, **20**, 197.
2. A. Granier, «Microwave plasma in Argon produced by a surface wave. Study of the effect of pressure on the optical emission and the potentiels for analysis of gaseous sample», Spectrochemica Acta 1988Vol. **43 B**, n° 8, 963.
3. C. M. Ferreira, «Theory of a plasma column sustained by a surface wave», J. Phys. D: App. Phys, 1981, **14**, 1811.
4. C. M. Ferreira and M. Moisan, «Microwave discharges: Fundamentals and Applications», NATO series b: Physics vol. 302, Plenum Pub. (1993).
5. Caroline Boisse-Laporte, thèse de doctorat, Université de Paris-Sud Centre d'Orsay, «Etude du transfert d'énergie d'une onde à un plasma. Application aux décharges basses pressions créées par onde de surface» (1989).
6. Karim Henda, thèse de magister, laboratoire des plasmas C.D.T.A. «Etude d'une décharge créée par onde de surface à 433 MHz et 2450 MHz dans O_2 et O_2-N_2 en flux. Application à l'optimisation d'une source d'espèces actives pour les traitements de surface» (1992).
7. S. Pasquiers, «Plasma waves in a bounded plasma, influence of the electron density inhomogeneity», J. Phys. D: App. Phys., 1988, **21**, 293.
8. Eric Bluem, thèse de doctorat ès sciences, Université Paris XI Orsay, «Caractérisation d'une décharge microonde de grand diamètre» (1995).
9. C. M. Ferreira, «Modelling of a low pressure plasma column sustained by a surface wave», J. Phys. D: App. Phys., 1983, **16**, 1673.
10. J. W. Coburn and M. Chen, J. App. Phys., 1980, **51**, 3134
11. R. E. Walkup, J. Chem. Phys., 1986, **84**, n° 5, 2668.
12. A. Granier, J. Appl. Phys., 1994, **75**, 104.

SELF-CONSISTENT MODEL OF THE PULSED SW-DISCHARGE IN HYDROGEN

O.A.Ivanov, V.A.Koldanov

Institute of Applied Physics, Russian Academy of Sciences,
Nizhny Novgorod, Russia.

This paper present self-consistent model of the surface waves discharge in the hydrogen.

Introduction

Earlier experimental investigations of plasma degeneration in hydrogen and hydrogen-methane mixture demonstrated significant influence that processes of ion conversion have on ion composition of such plasma. Such conversion results in a change in ionization-recombination balance, which, in its turn, influences chemical activity and parameters of the discharge plasma. Thus, the experiments showed that in the degenerating plasma, as a rule, a certain type of ions prevails. Due to the processes of ion recharging “primary” H_2^+ ions in hydrogen are converted fast into H_3^+ ions. The above peculiarities stimulated our interest for studying pulse SW discharge in hydrogen. The main attention was given to construction of a self-consistent model of an SW discharge with various kinetic processes in hydrogen plasma taken into account. The interest to such plasma is caused by its wide range of application in plasma technologies for film deposition and material etching.

Numerical model and discussion of results

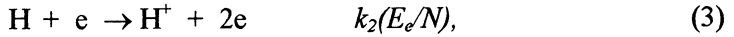
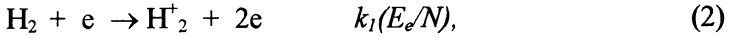
The system of basic equations that describe dynamics of the SW discharge was analogous to that used earlier for modeling the motion of the SW ionization front in air [1, 2]. This system included electrodynamic and kinetic parts.

Evolution of electromagnetic field in plasma in an azimuth-symmetric SW was determined by solving Maxwell equations by the FDTD method[3]. Maxwell solutions were written down in the cylindrical system of coordinates for TM mode. The current density in plasma, $\mathbf{j} = z_0 j_z + r_0 j_r$, was determined by formula

$$\vec{\partial}/\partial t = e^2 N_e \mathbf{E} / m - \nu \mathbf{j} \quad (1)$$

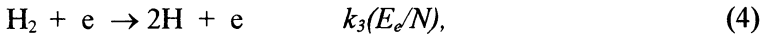
where ν is frequency of electron-molecule collisions.

The system of Maxwell equations and equation (1) was complemented with balance equations for electrons, ions H^+ , H_2^+ , H_3^+ and hydrogen atoms. The main ionization processes in the discharge are reactions that lead to formation of ions H_2^+ and H^+ :

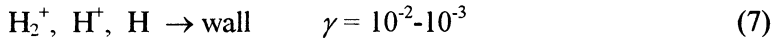
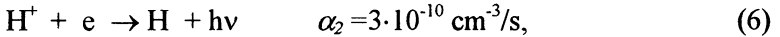
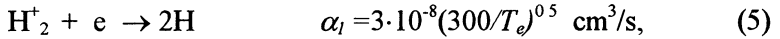


where k_1 and k_2 are constants of reactions (2) and (3) and functions of parameter E_e/N . Here $E_e = E_0 \cdot v / (v_2 + \omega_2)^{1/2}$ is efficient electric field, N is density of neutral gas, and E_0 is amplitude of the field in the surface wave.

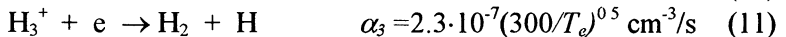
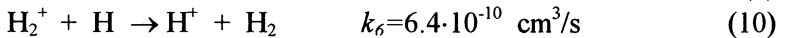
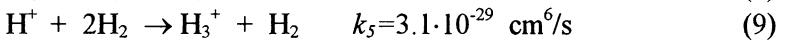
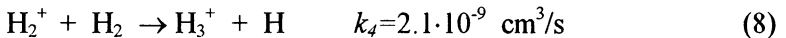
Hydrogen atoms are formed in the discharge as the result of hydrogen molecule dissociation:



The main processes, in which charged particles perish at the discharge stage, were assumed to be electron-ion recombination and diffusion of particles to the walls of the discharge tube with consequent recombination:



Analysis of the kinetics of charged particles and the experiments performed showed that a significant role in hydrogen plasma is played by ion-molecule reactions that lead to a change in ion composition of the plasma. Therefore, the above kinetic scheme was supplemented with fast reactions of ion conversion and reactions with participation of newly formed ions:



This model did not take into account reactions with complex ions H_5^+ , because density of these ions is not high at low and average pressure.

The constants of processes (2)-(11) that were used in the calculations were determined basing on the data given in [4-8]. The constant of process (3) was determined from the section of the corresponding process [9] under the assumption about the Maxwell function of EEDF. This assumption is justifiable at high densities of electrons, $N_e \sim 10^{14} \text{ cm}^{-3}$, that are achieved in SW discharge, when a significant role in EEDF formation is played by electron-electron collisions. By that, the relation between electron

temperature T_e and parameter E_e/N was determined basing on the data from [10]. The calculations used also the data on diffusion coefficients for different ions from [4] and [8].

The initial data for calculations were the pressure and temperature of the gas mixture, tube radius, and duration and power of the microwave pulse.

Dynamics of the spatial distribution of the electron density N_e and the E_z component of the electric field along the tube axis at different time moments are shown in Fig. 1. It indicate the effect of strong increase of the electric field in the region of the plasma resonance at the leading the front of the discharge. The amplitude of the peak of the electric field slowly decrease along the discharge tube.

It's seen also that powerful electric field penetrates into the region of the neutral gas at the SW front, which confirm the mechanism of the ionization front motion based on the breakdown wave.

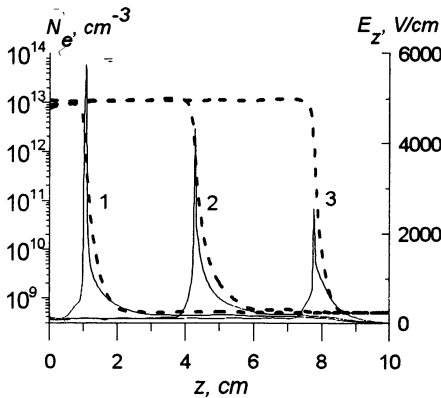


Fig. 1. Dynamics of the spatial distribution of the electron density and E_z component of the electric field along the tube axis. $P=30$ kW, $p=1.5$ Torr, $T=600$ K, $R_{\text{tube}} = 6$ mm; 1 – $t=0.2$ μs , 2 – 0.7 μs , 3 – 1.3 μs .

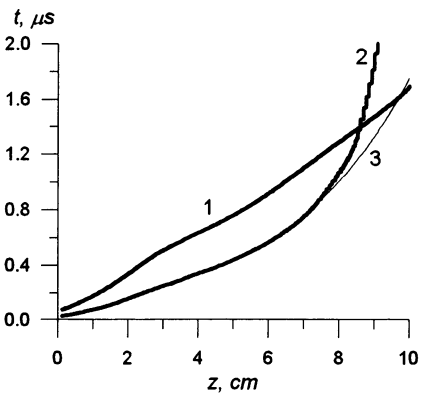


Fig. 2. The time-dependence of the ionization front coordinate. $P=30$ kW, $T=600$ K, $R_{\text{tube}} = 6$ mm; 1 – $p=1.5$ Torr, 2 – $p=5$ Torr, 3 – approximations for curve 2: $Z_f \sim \ln(t)$.

The time-dependence of the ionization front coordinate is shown in Fig.2. It's seen that near the launcher ionization front velocity decrease exponentially with z . But after certain distance for high pressure this velocity decrease sharply.

Characteristic dependencies density distribution for electrons, ions and hydrogen atoms along the radius of the discharge tubes in pulses with different duration are shown in Figs. 3-4.

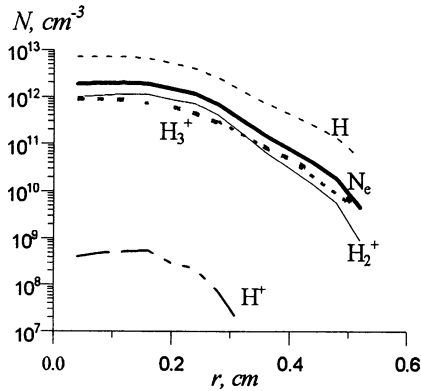


Fig.3. Radial distribution of density of different particles (Simulation conditions: P=30 kW; p=1.5 Torr; T=600 K; R_{tube}=6 mm; time moment t=0.7 μs).

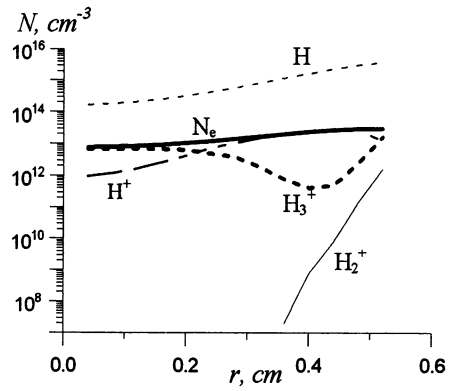


Fig.4. Radial distribution of density of different particles (Simulation conditions: P=30 kW; p=1.5 Torr; T=600 K; R_{tube}=6 mm; time moment t=3.5 μs).

Calculations show that at the initial discharge stage (at the leading edge of the surface wave) the highest density of particles is achieved near the axis of the discharge tube. This stage is characterized by prevalence of primary H_2^+ ions and H_3^+ ions formed in fast reaction (8). Density of H^+ ions is not high. After some time distribution of density of main particles along the radius becomes more homogeneous. By that, H_3^+ becomes the main ion, and H^+ ions are found only in the near-wall region. Besides, intense dissociation of H_2 molecules in the discharge takes place and, correspondingly, density of H atoms becomes higher.

The calculations showed that formation of the quasi-stationary structure characteristic for the surface wave under the considered pressures happens in several hundreds of nanoseconds after the ionization front appeared in the given section of the discharge tube. By that, high values of the amplitude of the electric field near the tube walls lead to an increase in the density of the majority of the particles from the tube center to its periphery. The degree of hydrogen association reaches 10-15% already after several microseconds. Note that high efficiency of the SW discharge as a source of hydrogen atoms was stated already in [11]. As the result of dissociation, the role of reaction (4) becomes more significant, and, correspondingly,

density of H^+ ions increases. At the same time, density of H_3^+ ions in this region becomes lower due to the decrease of H_2 concentration and higher (as compared to H^+) recombination coefficient. Near the tube center the H_3^+ ion remains prevalent.

The dynamics of density for different particles along the tube axis at the difference time moments are shown in Fig.5, 6. Simulation conditions: P=30 kW; p=1.5 Torr; T=600 K; tube radius 6 mm.

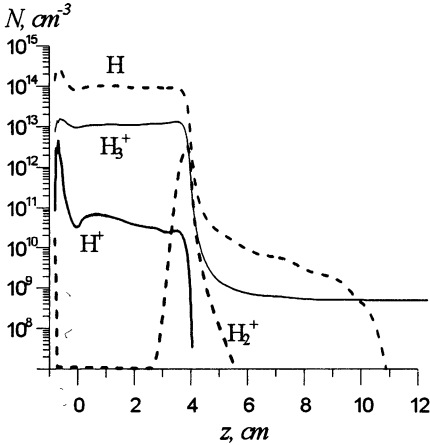


Fig. 5. Longitudinal distribution of density of different particles (Simulation conditions: P=30 kW; p=1.5 Torr; T=600 K; $2R_{\text{tube}}=6$ mm; time moment $t=0.7 \mu\text{s}$).

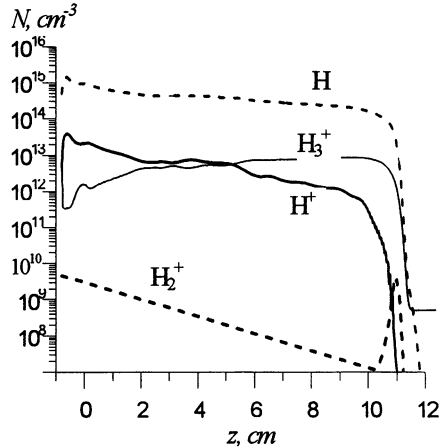


Fig. 6. Longitudinal distribution of density of different particles (Simulation conditions: P=30 kW; p=1.5 Torr; T=600 K; $2R_{\text{tube}}=6$ mm; time moment $t=3.5 \mu\text{s}$).

It is seen that H_2^+ ions are generated in a wide region at the leading edge of the surface wave. These ions are converted into H_3^+ ions very fast as they collide with H_2 molecules. As the result, the main ions at the leading discharge edge become ions H_2^+ and H_3^+ . In the quasi-stationary stage (when the length of the discharge becomes much longer) densities of N_e , H^+ and H decrease smoothly along the axis of the discharge tube. By that, near the SW exciter, where density of H atoms is high, H^+ ions are prevalent, and density of H_3^+ ions becomes somewhat lower.

Kinetic processes in a discharge under higher pressures run in a similar way. However, in this case the prevalent ion in a larger part of the discharge volume becomes the H_3^+ ion. Higher densities of H^+ are reached only in a narrow region near the tube walls.

Basic results

- Density of electrons in SW discharge produced by pulse microwave radiation exceeds the critical value for 3-cm wavelength band by more than an order of magnitude and reaches values of $N_e \cdot 10^{13} \text{ cm}^{-3}$.
- The pulse SW discharge is a very efficient H atom source.
- Velocity of the SW front is significantly dependent on the effect of the plasma resonance at the leading front of the discharge.
- The calculation performed show that under the experimental conditions a significant role is played by ion-molecular reactions that lead to ion conversion.

Acknowledgment

This work was partly supported by the Netherlands Organization for Scientific Research (NWO).

References

- [1] Ivanov O.A., Koldanov V.A. // Proc. XXIV Intern. Conf on Phenomena in Ionized Gases. Warsaw, Poland, July 11-16, 1999, **1**, 193.
- [2] Ivanov O.A., Koldanov V.A // Advanced Technologies Based on Wave and Beam Generated Plasmas. Edited by Schluter H and Shivarova A., Kluwer Academic Publishers 1999, NATO Science Series, High Technology **67** , 511
- [3] Tan. W., Grotjohn T.A. // J. Vac. Sci. Technol. 1994. A12(4). P.1216
- [4] Lebedev Yu.A., Epshtein I.L // High Temperature (in Russian) 1998, **36**, 534
- [5] Brovikova I.N., Galiaskrov E.G., Ribkin V.V., Bessarab A.B. // High Temperature 1998, **36**, 706 (in Russian)
- [6] Rousseau A., Granier G., et.al. // J. Phys.D: Appl. Phys. 1994, **27**, 1412
- [7] Gordiets B., Ferreira C.M., et.al. // Plasma Sources Sci. Technol. 1998, **7**, 363
- [8] Smirnov B.M. // Complex Ions, Moscow, Nauka, 1983, 150 (in Russian)
- [9] Kieffer L.J., Dunn G.H. // Reviews of Modern Physics 1966, **38**, 1
- [10] Loureiro J., Ferreira C.M. // J. Phys.D: Appl. Phys. 1989, **22**, 1680
- [11] Rousseau A., Tomasini L , et.al.. // J. Phys. D: Appl. Phys. 1994, **27**, 2439

TWO-DIMENSIONAL ELECTRON BOUNCE AVERAGED FOKKER-PLANCK MODEL WITH SELF-CONSISTENTLY CALCULATED ION PARAMETERS FOR ECR DISCHARGE IN PLASMA SOURCES

A.B. Shmelev, A.P. Smirnov

Moscow State University, faculty of Computational Mathematics and Cybernetics

It is generally assumed and recognized, that plasma sources are of great interest due to their numerous and multifarious technological applications.

We have assumed the following experimental conditions. A pipe, filled with rarified gas (in our case argon) is placed into longitudinal magnetic field and is affected with a microwave heating at a EC resonance frequency. This causes partial ionization. Part of the electrons leave the trap, causing an ambipolar potential to appear, the other part becomes trapped and causes further ionization.

We have developed a 2-D bounce averaged Fokker–Planck model of rarified gas ionization for Electron Energy Distribution Function (EEDF) [1]. We have taken into account the following effects:

- ECR heating in quasilinear approximation
- Ionization and excitation of neutral
- Elastic scatter on the neutrals
- Linearised Coulomb collisions operator
- Self-consistent ambipolar potential

For EEDF the following equation can be written:

$$\frac{\partial f}{\partial t} = L_{ec} + L_{ion} + L_{Coul} + L_0 \quad (1)$$

EEDF is considered to be a function of the following constants of motion:

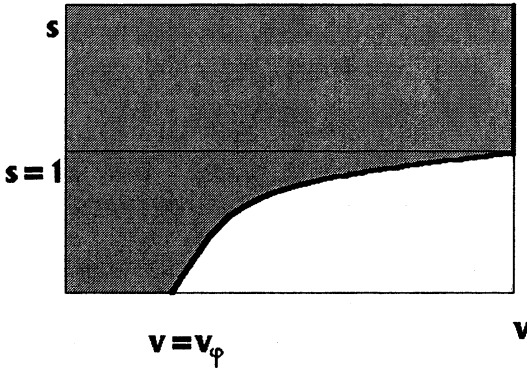
$f = f(v, s, t)$, here v is magnitude of the velocity of an electron,

$s = \frac{v_{\perp}^2 B_0}{v^2 B(x)}$, ($B(x)$ is magnetic field, x axis coincides with the axis of

symmetry of the device and t is the time. For obtaining this equation we used an averaging procedure over a standard Fokker-Planck equation. Due to axial symmetry of the device only perpendicular and longitudinal components of velocity should be used and we consider that only x axis,

which coincides with the device symmetry axis is important. We changed the set of variables in a way, that all the variables would be constants of motion except for the x . Afterwards we integrated the Fokker-Planck equation over the x axis from $-x_0$ till x_0 and from x_0 till $-x_0$.

The equation is written for the particles, that are trapped. In the (v, s) space, the domain of the trapped particles has the following appearance:



Domain of the equation

The boundary, which is shown with the strong curve corresponds to the condition, that the function is equal to zero. Thin line corresponds to the condition that the flow of the function through the boundary is equal to zero, as it is also the boundary of the phase space. Maxwell low temperature distribution was used as an initial condition.

Ambipolar potential is taken into account in the boundary condition. For $s < 1$ maximum value of v is determined by the formula

$$v_{\max}^2(s) = \frac{v_\phi^2}{1-s}. \text{ Here } v_\phi \text{ is a parameter, reflecting the value of the}$$

ambipolar potential. Its value can be found from a condition of the plasma quasineutrality. The consequence of this condition is the fact that at the stationary the flow of ions through the bound is equal to the flow of

electrons through the bound. Thus $\frac{dN_e}{dt} = \frac{dN_i}{dt}$. Total electron flow can

be found as integral over the $v = v_{\max}(s)$ curve of the vector of electron flow, that can be found from the main equation. Ion flow can be

determined as $\frac{dN_i}{dt} = \frac{N_i}{\tau_i}$, here τ_i is the ion characteristic time, that determines the average ion living time in the device. The idea of this paper is to suggest a method of self-consistent determination of this characteristic time. This allows to create a fully self-consistent model of the discharge.

The idea of the method is to use the results of the electron model for finding the electric field and the ion source distribution in the device for the ion problem.

Firstly we need an electron field distribution. We used the following equation for its calculation:

$$\frac{\partial}{\partial x}(N_e(x) \langle v_{\parallel}^2 \rangle) = qE(x)N_e(x) + N_e(x)\mu\nabla B(x). \quad (2)$$

Here q is electron charge, $E(x)$ – electric field, $B(x)$ – magnetic field, $\mu = \frac{m_e v_{\perp}^2}{2B(x)}$ – magnetic momentum, $N_e(x)$ – electron density. Though equation (1) is averaged over the x axis, it is possible to obtain integral characteristics for the x axis. Thus

$$N_e(x) = 2L \int_0^{\infty} v^2 dv \int_0^{s_{\max}} f(v, s, t) \frac{1}{\sqrt{1 - sB(x)/B_0}} ds. \quad (3)$$

Here L is the length of the device. By solving the equation (2) one can obtain the electric field distribution over the x axis. Thus we can solve a problem for a single ion

$$\begin{cases} m_i \ddot{x}(t) = qE(x) \\ x(0) = x_0 \\ \dot{x}(0) = v_0 \end{cases} \quad (4)$$

Here m_i is the ion mass and q is its charge. By solving the problem (4) for the given initial conditions x_0 and v_0 , we can find the amount of time needed for the ion to leave trap with the length L . We will denote this time as $T = T(x_0, v_0)$.

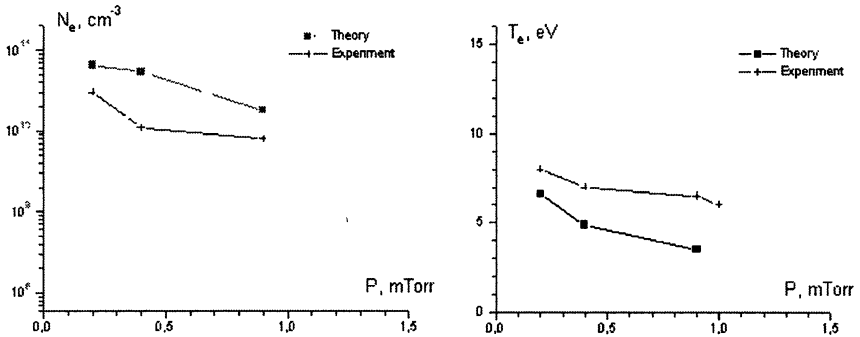
For the whole ion problem we consider that the ion density along the x axis has the same form as the electron one (due to quasineutrality of the plasma), and that the ions have Maxwell distribution in the velocity space. Thus we can write the following formula for the ion time:

$$\tau_i = C \int_{-L}^L dx_0 \int_0^{\infty} dv_0 T(x_0, v_0) N_e(x_0) \exp\left(-\frac{v_0^2}{v_i^2}\right) \quad (5)$$

Here C is a normalizing constant, v_i is a thermal ion velocity. For our calculations it was taken to be equal to “normal” conditions of 300K. This method is equivalent to the solution of a kinetic equation for the ions by a characteristic method.

During the calculations we fixed the value of the τ_i , iterated till the function $f(v,s,t)$ reached the stationary and then self-consistently changed the value of the τ_i . This procedure had to be repeated until the next iteration of the τ_i gave a value, that differed from the previous approximation less than for ϵ .

One can see the results of the calculations and the experimental data [2] at the picture:



Here electron density and temperature are shown versus gas pressure.

References

1. Smirnov A.P., Suetin N.V., Shmelev A.B. Two-dimensional bounce averaged Fokker-Planck modelling of an electron cyclotron resonance plasma source. J. Plasma Physics, vol. 59, part 2, pp 243-257.
2. Gulyaev K.S., Kasheev A.V., Kovalev A.S., Suetin N.V. and Vasilieva A.N. Investigation of in-resonator gas breakdown for electron cyclotron resonance conditions. J. Phys. D. Appl. Phys 27 2349-2353.

NUMERICAL MODELING OF MICROWAVE DISCHARGE IN THE CVD DIAMOND DEPOSITION REACTOR

A.M. Gorbachev, V.A. Koldanov, A.L. Vikharev

Institute of Applied Physics, Russian Academy of Sciences,
Nizhny Novgorod, Russia

The paper presents the results of numerical simulation of the microwave CVD reactor operating in CW and pulse regimes. Dependencies of discharge parameters on the pressure and microwave power have been studied. The possibility to use the pulse-periodic regime of discharge maintenance for deposition of diamond films has been analyzed.

Recent years have seen intense studies of diamond film deposition by the CVD (chemical vapor deposition) method [1]. Different types of CVD reactors are used, in which hot filament, RF, DC and microwave discharges, and flame are used. The microwave discharges reactors have the following advantages: absence of electrodes, high specific power contribution, high densities of excited and charged particles, relatively large area and high homogeneity of the film.

A successful type of the microwave-based reactor was proposed in [2]. This reactor is made as a cylindrical resonator excited at the TM_{013} mode by means of a coaxial waveguide connected to the resonator at the center of the end wall. At the other end wall of the reactor a quartz dome is situated, which limits the discharge volume. The upper wall of the resonator can be moved. This provides tuning of the resonator to the resonance frequency. This reactor operates at the frequency 2.45 GHz at microwave power in the range from 1 to 5 kW. It provides growth of diamond film with their area of several tens of square centimeters at the rate of several micrometers per hour.

This paper offers a simplest numerical model of a discharge in such a reactor. It makes it possible to reveal basic regularities characteristic for such a discharge and estimate the quality and growth rate of diamond films.

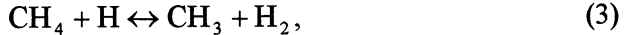
Growth rate and quality of diamond films are determined by a complex set of volume and surface reactions. However, the growth rate is essentially dependent on the density of atomic hydrogen at the substrate surface. According to Goodwin's results [3], the growth rate may be estimated by the following formula:

$$G \propto \frac{[\text{CH}_3][\text{H}]}{3 \cdot 10^{15} \text{ cm}^{-3} + [\text{H}]}, \quad (1)$$

Relative defect density that determines film quality can be estimated as

$$X_{def} \propto \frac{G}{[\text{H}]^K}, \quad K \approx 2. \quad (2)$$

Here $[\text{H}]$ is atomic hydrogen concentration and $[\text{CH}_3]$ is methyl concentration near the surface. Often the gas-phase reaction,



is rapid and near equilibrium. The methyl concentration is coupled chemically to atomic hydrogen. Thus, in order to estimate the film quality and growth rate, we have to determine density of atomic hydrogen near the substrate surface. That is why the model proposed includes calculations of the electric field in the reactor; of electron density; temperature, density and velocity of the gas; of the density of atomic hydrogen in the reactor volume and near the substrate surface.

Distribution of the electromagnetic field in the resonator was found from the Maxwell equation by the FDTD method (Fig. 1). The microwave electric field interactions with the plasma discharge are described using a finite-difference solution of the equation for electron current [4].

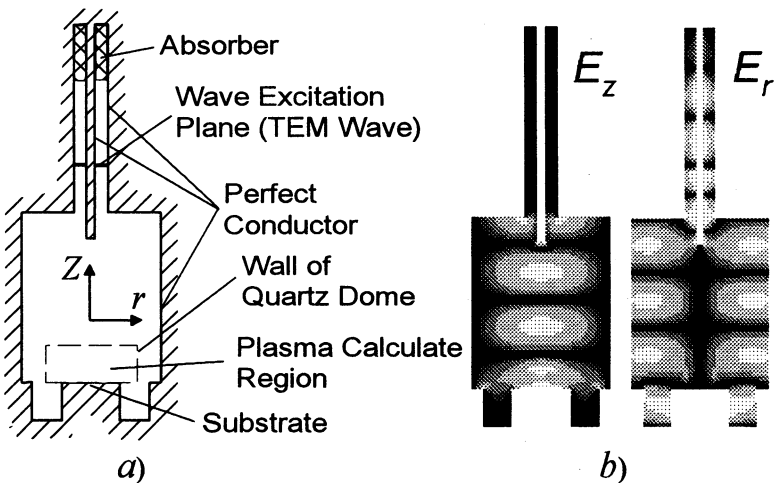


Fig.1. Microwave cavity plasma reactor configuration used for numerical simulation (a) and spatial distributions of electric field components in the resonator (b).

Density of electrons, N_e , was found from the equation of ionization-recombination balance with account for ambipolar diffusion of electrons:

$$\frac{dN_e}{dt} = \nu_i \cdot N_e - \alpha \cdot N_e^2 + \nabla(D_a \nabla N_e), \quad (4)$$

where ν_i is ionization frequency, α is recombination coefficient, D_a is diffusion coefficient.

Density N , temperature T and velocity U of the gas were found by solving the gas dynamic equations of the ideal gas in the isobaric approximation with an external heat source σE^2 :

$$\begin{cases} \frac{\partial N}{\partial t} + \nabla(N\vec{U}) = 0 \\ \gamma p \cdot \nabla\vec{U} = (\gamma - 1)[\sigma E^2 + \nabla(\lambda \nabla T)], \end{cases} \quad (5)$$

where $p = kNT$ is gas pressure, γ is adiabatic constant, σ is plasma conductivity and λ is coefficient of the gas heat conductivity.

For calculation of density of atomic hydrogen [H] we take into account the processes of hydrogen dissociation, diffusion and transport with gas flows:

$$\frac{d[\text{H}]}{dt} = k_d \cdot N \cdot N_e + \nabla(D_H \nabla[\text{H}]) - \nabla(\vec{U} \cdot [\text{H}]), \quad (6)$$

where k_d is dissociation constant, D_H is diffusion coefficient. The density of atomic hydrogen near the surface, $[\text{H}]_{\text{sur}}$, was found from the relation between the diffusion flow and the rate of surface recombination of atomic hydrogen [4]:

$$D_H \left. \frac{d[\text{H}]}{dz} \right|_{\text{sub}} = \gamma_H \frac{[\text{H}]_{\text{sub}} \bar{c}_H}{4}; \quad (7)$$

here γ_H is recombination coefficient, \bar{c}_H is mean thermal speed of H atom.

The following results of the numerical modeling of continuous wave (CW) discharge were obtained. Figure 2 shows maximum density of electrons (N_e) and gas temperature (T), specific power ($\eta = \sigma E^2$) and effective plasma volume ($V = W / \eta$), the maximum density of atomic hydrogen $[\text{H}]_{\text{max}}$ and its density near the substrate surface $[\text{H}]_{\text{sur}}$ versus pressure (p) at a constant power level ($W = 2$ kW). It is seen from Fig. 2 that as the pressure grows, the specific power increases and the plasma volume decreases. Correspondingly, electron density and gas temperature also increase. The density of atomic hydrogen near the surface grows proportionally to specific power and gas pressure. Thus, higher gas

pressure results in the growth of atomic hydrogen density and higher rate of film growth. However, by that, the plasma volume and the deposition area is smaller.

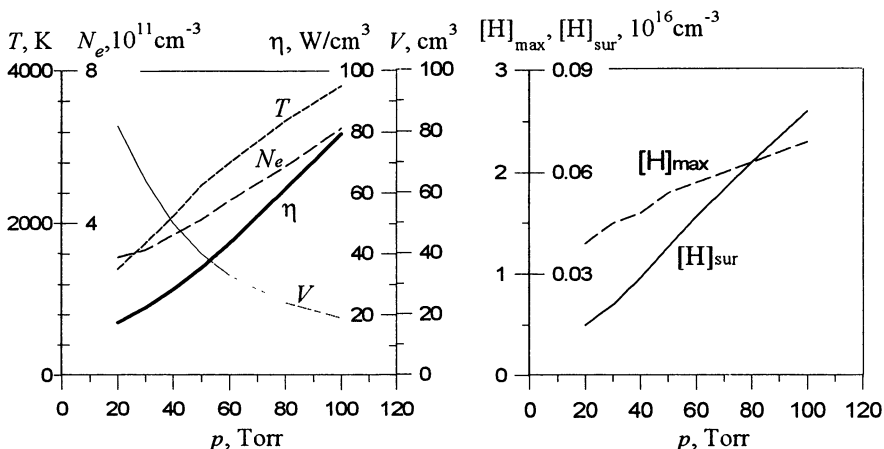


Fig. 2. Pressure dependence of the parameters of the CW discharge at constant power level.

Power dependence is shown in Fig. 3. It is seen that higher microwave power under constant pressure leads mainly to a larger plasma volume. The electron density, gas temperature and specific power stay the same. The density of atomic hydrogen insignificantly increases. Thus, higher microwave power leads mainly to a larger deposition area.

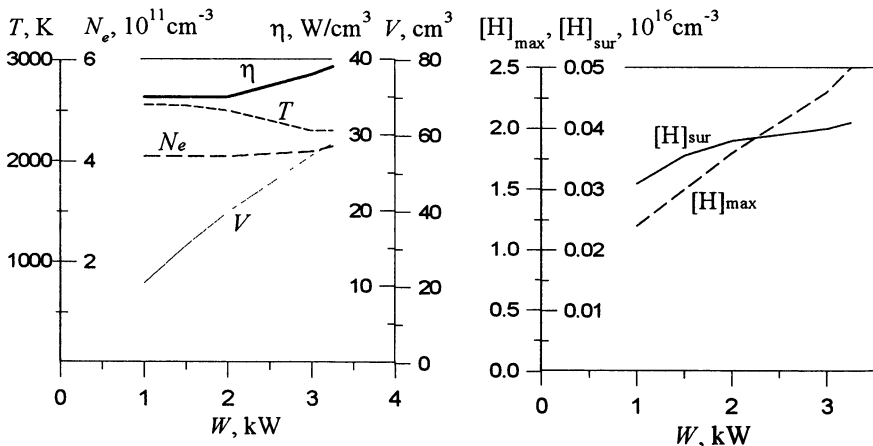


Fig. 3. Dependence of the parameters of the CW discharge on microwave power at constant gas pressure.

However, the power can be increased only to a certain limit. It is seen in Fig. 4. that when the power reaches some threshold, the discharge plasma becomes significantly inhomogeneous. At high levels of microwave power the homogeneous plasma can be obtained at higher pressures. However, by that the plasma volume becomes smaller and, correspondingly, the dimensions of the film decrease.

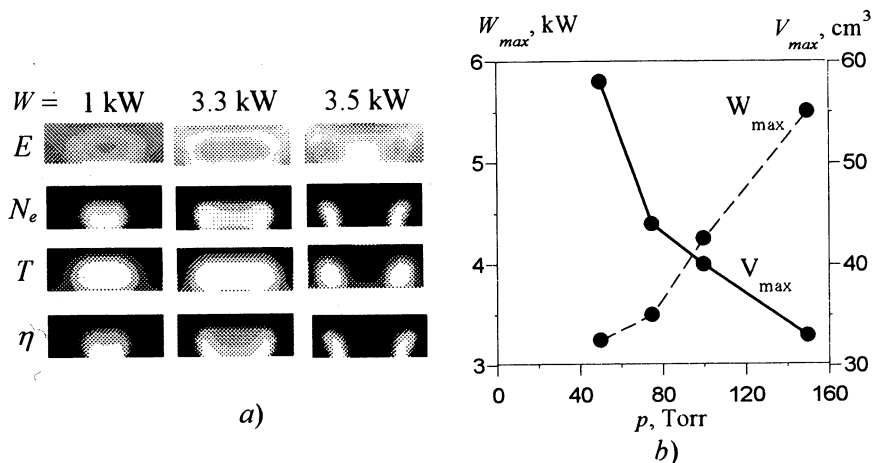


Fig. 4. Spatial distributions of the discharge parameters at various power level (a) and pressure dependencies of the maximum power (W_{max}) and volume of the plasma (V_{max}) achievable in a homogeneous microwave discharge in the continuous regime.

The discharge passes over to the inhomogeneous state in a certain time. Therefore, the use of the pulse-periodic regime of discharge maintenance with pulse duration shorter than the time of inhomogeneous discharge formation makes it possible to obtain a large-size homogeneous discharge. Numerical modeling showed that the use of pulses with pulse repetition rate of several kHz makes it possible to obtain large-volume homogeneous plasma at a high level of power. The value of atomic hydrogen density in the pulse regime approximately equals to the density in the continuous regime at the same values of specific power.

The use of the pulse regime at a relatively low pulse repetition rate may be also useful for improving quality of the films (Fig. 5). The Table 1 shows parameters of CW (1) and pulse (2,3) regimes. It is seen that at the same pressure the pulse regime leads to lower mean specific power and mean density of atomic hydrogen (curve 2). This is explained by higher peak power in the pulse regime, and, consequently, a larger plasma volume

at the constant mean power. In the third case, the pressure in the pulse regime is greater than in the continuous regime. Plasma volume and mean specific power are same, as in the continuous discharge. But, the value of the mean density of atomic hydrogen squared is greater than in the continuous regime. The expressions determined the growth rate (1) and quality of the films (2) show that in this case the growth rate approximately does not change, and the quality of the film improves.

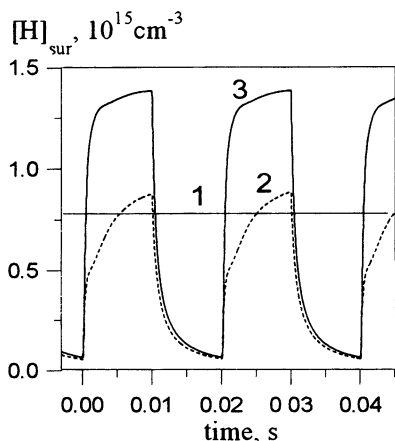


Fig. 5. Time dependence of the atomic hydrogen density near the surface in the continuous (1) and pulse regimes (2,3) at pulse repetition rate of 50 Hz.

Thus, the numerical analysis performed for the regimes of microwave discharge maintenance in the CVD reactor revealed the basic regularities of its operation. It was shown that the pulse-periodic regime of discharge maintenance can be used for generation of homogeneous plasma at high pressures and for improvement of the growth rate of diamond films.

This work was supported by CRDF under grant RE1-352.

References

1. Handbook of industrial diamonds and diamond films, ed. by M.A.Prelas, Marcel Dekker Inc., New York-Basel-Hong Kong, 1997.
2. Asmussen J., in High density plasma sources, ed. O.A.Popov, Park Ridge, NJ: Noyes, 1995, 251.
3. Goodwin D.G. J. Appl. Phys., 1993, **4**(11), 6888.
4. Tan W. And Grotjohn T.A. J.Vac.Sci.Technol. A, 1994, **12**(4), 1216.
5. Goodwin D.G. J. Appl. Phys., 1993, **74**(11), 6895.

Table 1

Curve	p , Torr	$\langle [H]_{sur} \rangle$, cm^{-3}	$\langle [H]_{sur}^2 \rangle$, cm^{-6}
1	100	$7.8 \cdot 10^{14}$	$6.1 \cdot 10^{29}$
2	100	$4.5 \cdot 10^{14}$	$3.0 \cdot 10^{29}$
3	150	$7.5 \cdot 10^{14}$	$8.8 \cdot 10^{29}$

GENERATION AND STUDY OF Cs-Xe DISCHARGE PLASMA SLABS FOR NONLINEAR MICROWAVE QUASIOPTICAL EXPERIMENTS

N.A. Bogatov, M.S. Gitlin, D.A. Dikan

Institute of Applied Physics RAS, Nizhny Novgorod, Russia

Nonlinear microwave quasioptical devices such as antennas with all-microwave gain control, phase conjugate mirrors, power-controlled switches, power-dependent phase shifters, etc. can be used in radar, navigation, microwave communications, beamed microwave power transmission [1]. However, the lack of appropriate nonlinear volumetric media for microwaves is considered a bottleneck in achieving potential of the field. Plasma of the positive column of a DC gas discharge in the Cs-Xe mixture was shown to provide a fast and effective volumetric nonlinear medium for microwaves [2]. This paper is concerned with generation and study of Cs-Xe discharge plasma slabs for microwave quasioptical experiments.

Figure 1 shows top view of experimental setup used for generation of a slab of the positive column of the Cs-Xe DC discharge and investigation of interaction of microwaves with it. The plasma was produced in

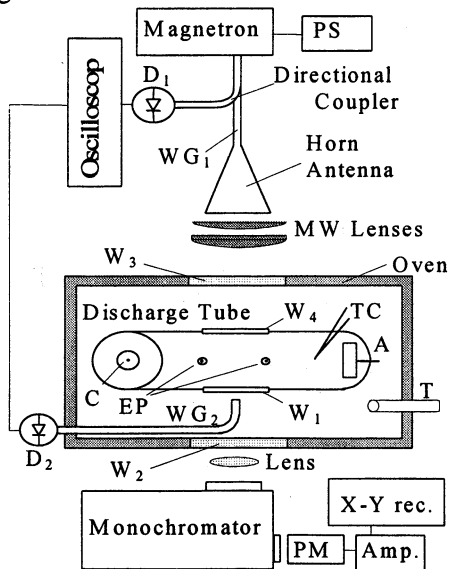


Fig. 1

a sealed cylindrical glass gas-discharge tube with a heated cathode C. The big bend of the L-shaped gas discharge tube of length 40 cm and internal diameter 4.8 cm was placed horizontally, and the distance between cathode C and anode A was 38 cm. For transmission of microwave beams and creation of a plasma slab two parallel plane quartz windows W_1 and W_4 were built in the tube in the middle between the anode and the cathode. The distance between inner surfaces of the windows was 4 cm, and their diameter was 5 cm. Gas discharge tubes filled with xenon were

generally used in the experiments reported here. Xenon pressure at the room temperature was 30 Torr. The discharge tube had a sidearm, in which a drop of cesium was placed. To obtain the required density of cesium vapor, the gas-discharge tube was heated in a special oven with hot air supplied through tube T. The temperature of the discharge tube wall, T_w , was controlled by means of thermocouples TC with accuracy 2 degrees. Two single cylindrical probes EP were built in the gas discharge tube. They were placed at the tube axis and spaced 5 cm apart. The longitudinal electric field E in the positive column of the discharge was determined by the difference of potentials between the two probes using a high-impedance voltmeter or oscilloscope. The emission of the positive column of the gas discharge was sent to a monochromator through quartz windows W_1 and W_2 and a lens. The light was detected with photomultiplier PM. The 35 GHz magnetron produced microwave radiation with maximum output power 10 W in CW mode and 20 W in the long pulse mode (pulse duration is 0.1 s). The microwaves were fed to the transmitting horn antenna by means of rectangular waveguide WG_1 . The pyramidal horn antenna was 50 cm long and its aperture dimensions were 8 cm x 6 cm. Its output was coupled to a plane-convex spherical lens 20 cm in diameter, to create a plane wavefront. Plane-convex cylindrical lens with dimensions 20×15 cm and focal length 60 cm focused microwaves in the positive column. In the focal plane the beam width (FWHM) was 2.5 cm and height 10 cm. A microwave beam was fed into the discharge tube through plane-parallel quartz windows W_3 and W_4 perpendicular to the tube axis and focused between probes EP on the positive column of the discharge. Waveguide directional coupler served to branch a small part of the microwave radiation to calibrated microwave diode D_1 which was used to control the power of millimeter waves. The microwaves that passed through the tube were received by the open end of rectangular waveguide WG_2 connected on the other side to calibrated diode detector D_2 . The open end of the waveguide was located at the microwave beam axis just behind quartz window W_1 .

The electron temperature in the positive column of the discharge was deduced from the emission spectrum of radiative recombination of electrons and cesium atomic ions Cs^+ with formation of a cesium atom in the state 6P (6P-recombination continuum of cesium) [3, 4]. The absolute value of electron density in the positive column of discharge was determined from discharge current J by measuring of E , T_e and d as

$$N_e = 4J / \pi d^2 \mu(T_e) E, \quad (1)$$

where $\mu(T_e)$ is electron mobility in the longitudinal electric field, which have been calculated as a function of the electron temperature for the momentum transfer cross-section of the electron-xenon atom collision as given in [5]. Small relative variation of electron density and electron mobility under the action of the microwaves could be found from (1) by the relative variation of longitudinal electric field in the region, where microwave beam cross the plasma column as $\Delta E/E_0 = -(\Delta N_e/N_{e0} + \Delta\mu/\mu_0)$, here E_0 , N_{e0} and μ_0 are the longitudinal electric field, the electron density and electron mobility in the absence of the microwave field.

Studies of the DC Cs-Xe discharge have shown that at a preset value of the discharge current there is a range of tube temperatures about some degrees, in which the positive column of the discharge is deconstricted and spatially uniform. The deconstriction of the positive column of the Cs-Xe discharge is a result of considerable depletion of ground state cesium atoms in the region of the current density maximum. The reason of depletion the cesium atoms is their excitation and ionization [2]. The study of the spatial distribution of electron density in the positive column of the discharge was performed using movable single cylindrical probes and emission of the 6P-recombination continuum of cesium. It showed that the spatial distribution of electron density in the nonconstricted positive column of the Cs-Xe discharge is nearly uniform and its width (FWHM), d , reaches 0.8 of the tube diameter.

The action of microwaves on the plasma of the nonconstricted positive column of the Cs-Xe discharge was studied at discharge current 1.5A at the tube wall temperature 368 K. For such conditions $E_0=0.6$ V/cm, $T_{e0}=0.32$ eV, and the electron density is $4 \cdot 10^{12}$ cm⁻³ which is about a quarter of the critical plasma density, N_c , for microwaves with $\lambda=8.5$ mm.

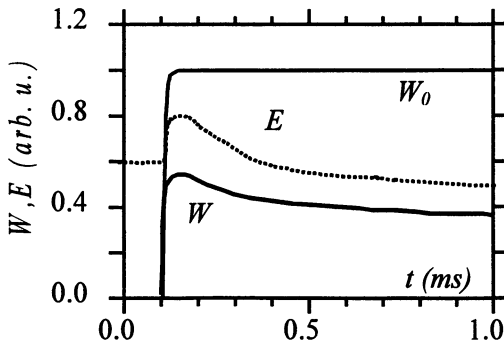


Fig. 2

The ratio of the mean electron-xenon atom collision frequency for momentum transfer, ν_m , to the angular frequency of the microwave field, ω , equals $\nu_m/\omega=0.1$. The measured value of linear intensity absorption coefficient in the plasma at these experimental conditions is 0.2 cm⁻¹, and

the reflection coefficient of the microwave beam from the plasma boundary is less than 1 %. Considerable variations of longitudinal electric field, transmissivity of the plasma, intensity of the 6P-recombination continuum of cesium were observed for incident microwave intensity, W_0 , more than 0.1 W/cm². Figure 2 shows time history of the longitudinal electric field in the region of the microwave beam, intensities of incident and transmitted through the plasma microwaves after switching on the microwave source instantaneously for incident microwave intensity $W_0=0.5$ W/cm². As seen from the oscillogram, after switching microwaves on sharp growing up of the longitudinal electric field takes place, which is caused evidently by decreasing of electron mobility in xenon due to electron heating. Thereafter, a decrease of the longitudinal electric field and transmissivity of the plasma due to electron density growing under the action of the microwaves occurs during several hundreds of microseconds. Since electron temperature and electron mobility would reach the new quasi-stationary value for the time of elastic recoil electron energy losses which is of the order of ten microseconds [8], the variation of electron density in the plasma is equal to $\Delta N_e(t) = -N_{e0} \Delta E(t)/E_m$, where E_m is maximal value of the longitudinal electric field after switching microwaves on. As the result of additional ionization of cesium atoms due to the electron heating under the action of microwaves [6] electron density varies as a function of time according to relation $\Delta N_e(t) = -(N_e^{st} - N_{e0}) [1 - \exp(-t/\tau)]$, where N_e^{st} is quasi-stationary value of the electron density in the presence of the microwaves, τ is characteristic time of electron density variation. Hence, as may be observed from the oscillogram, the ionization nonlinearity response time of such a plasma

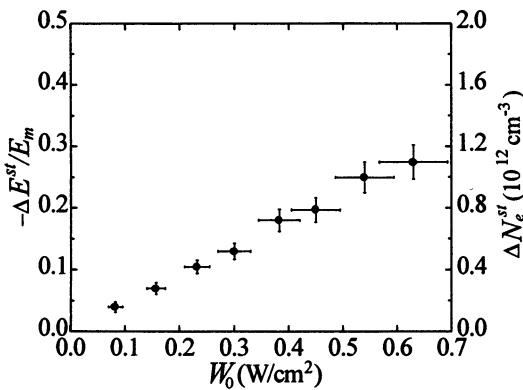


Fig. 3

medium determined as the time of plasma density variation, τ , is less than a millisecond. Figure 3 shows the plots of the relative variation of longitudinal electric field, $-\Delta E^{st}/E_m \equiv -(E^{st} - E_m)/E_m$, and variation of electron density in the plasma, $\Delta N_e^{st} \equiv N_e^{st} - N_{e0} = -N_{e0} (E^{st} - E_m)/E_m$ as a function of the incident microwave intensity,

here E^{st} is quasi-stationary value of E in the presence of the microwaves. It follows from this plot that variation of the electron density is approximately in direct proportion to the incident microwave intensity $\Delta N_e^{st} = q \cdot W_0$, where coefficient q equals $2 \cdot 10^{12} (\text{W} \cdot \text{cm})^{-1}$. The real part of intensity-dependent refractive index, $n(W_0)$ [7], for plasmas in the limit $\nu_m \ll \omega$ is much greater of imaginary one and is equal to $n(W_0) = (1 - N_e(W_0)/N_c)^{1/2} = (n_0^2 - \Delta N_e/N_c)^{1/2}$ [8], here n_0 is linear refractive index of the plasma. When $\Delta N_e \ll N_c n_0^2$, plasma intensity-dependent refractive index equals $n(W) = n_0 + n_2 \cdot W$, where n_2 is nonlinear refractive index of the plasma. The quasi-stationary value of n_2 of the positive column Cs-Xe discharge is $n_2^{st} = -q/(2N_c n_0) = -0,07 \text{ cm}^2/\text{W}$.

Experimental investigation of four-wave mixing (FWM) and selfaction of microwave beams requires generation of a uniform slab of nonlinear medium with its dimensions much larger than the wavelength of the microwaves. We have developed the method for generation of the Cs-Xe discharge plasma slab with its volume of several liters and aperture about 10 cm. In order to solve this problem, we used a sealed cylindrical glass gas-discharge tube 40 cm long and 12 cm in diameter. Its design is shown in Fig. 4. The tube was equipped by anode A shaped as a disk with its area about 80 cm^2 was, and two cylindrical heated cathodes C mounted in the bottom part of the tube. The use of two cathodes improved uniformity of the discharge in the tube. The distance between the cathodes and the anode was 31 cm. Two $20 \times 10 \text{ cm}$ plane quartz plates QP were set in the tube parallel to each other and tube axis. The distances from plates to the tube axis were 3.5 cm. Lateral barrier between quartz plates and tube wall prevented discharge ignition on the outer sides of the plates and the discharge burned between the quartz plates. Thus, a slab of plasma was generated.

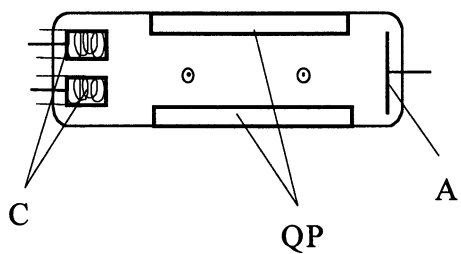


Fig. 4

Analysis of spatial distribution of the 6P-recombination continuum of cesium showed that such a plasma medium is highly uniform. Under the pressure of xenon 30 Torr, tube temperature 368 K and discharge current 6 A the values of plasma parameters (E , T_e , N_e) coincided approximately with the above plasma parameters for the case of a gas discharge tube 4.8 cm in diameter at current 1.5 A.

The generated nonlinear plasma medium can be used, e.g. as phase conjugate mirror for the microwaves. We estimated CW phase conjugate (PC) reflectivity via FWM in the created slab of the positive column of the Cs-Xe discharge at xenon pressure 30 Torr and the electron density $N_{e0}=4 \cdot 10^{12} \text{ cm}^{-3}$. PC power reflectivity of microwaves with $\lambda=8.5 \text{ mm}$ for equal intensities of the pump waves 0.1 W/cm^2 and measured value of the nonlinear refractive index $-0.07 \text{ cm}^2/\text{W}$ should be about 10 %.

Thus, our study has shown that the plasma of the positive column of DC discharge in the cesium-xenon mixture provides a stationary, uniform nonlinear medium for microwaves with dimensions much larger than the microwave wavelength, a high nonlinear refractive index, and a fast response time. Such a plasma slab may be used in various nonlinear microwave quasi-optical devices.

References

1. Bogatov N.A., Gitlin M.S. Bull. Russian Acad. of Sci., Physics, 1999, **63**, No.12.
2. Bogatov N.A., Gitlin M.S., Dikan D.A., et al. Phys. Rev. Lett., 1997, **79**, 2819.
3. Sayer B., Jeannot J.C., Lozingot J., et al. Phys. Rev. A, 1973, **8**, 3012.
4. Wetzler J.M. Physica, 1984, **C123**, 247.
5. Hunter S.R., Carter J.G., Christophorou L.G. Phys. Rev. A., 1988, **38**, 5539.
6. Novichkov D.N., Glebov V.V. High Temp. (USSR), 1970, **8**, 391
7. Boyd R.W. Nonlinear Optics, (Academic Press, London, 1992).
8. Raizer Y.P. Gas Discharge Physics, Springer, Berlin, 1991.

MEASURING HYDROGEN PLASMA PARAMETERS IN PULSED MICROWAVE DISCHARGE BY OPTICAL EMISSION SPECTROSCOPY

R.A. Akhmedzhanov, A.L. Vikharev, A.M. Gorbachev, D.B. Radishev

Institute of Applied Physics, Russian Academy of Science,
Nizhny Novgorod, Russia

Introduction

A microwave discharge in hydrogen with minor admixture of a carbon-containing gas is widely used to obtain diamond films from the gaseous phase. Efficiency of diamond film synthesis depends significantly on the temperature and dissociation degree of the gaseous mixture. Due to this, development of methods for measuring and controlling gas temperature is currently given much attention. The results of measuring gas temperature by observing radiation spectra of different bands of hydrogen molecules are often contradicting [1, 2]. That is why it is interesting to compare experimentally different methods for measuring gas temperature in hydrogen plasma. This paper presents the results of measuring gas temperature by radiation spectra of hydrogen and nitrogen molecules and by the width of the spectral line of hydrogen atoms.

Experimental setup and measurement methods

The scheme of the experimental setup is described in full detail in [3]. Microwave radiation of the magnetron (power 100 kW, wavelength 3 cm, radiation duration up to 10 μ s) was fed via an emitting horn into a chamber filled with hydrogen or the mixture of hydrogen with minor (~5%) admixture of nitrogen. The linearly polarized microwave radiation was intercepted by a spherical mirror and directed backwards, opposite to the wave beam. As the result, two opposite wave beams formed a standing electromagnetic wave. A spatially localized microwave discharge was ignited in one central antinode of the electric field. Total pressure in the chamber varied from 40 to 120 Torr. The experiments were performed in two regimes: at pressures below 50 Torr and at pressures, at which the discharge had the filament structure as the result of evolution of an ionization-

overheating instability that arose due to mutual amplification of perturbation of electron density and gas temperature. Thus, during a microwave pulse the gas temperature changed fast from the room temperature to 1500 °C. The wide dynamic range of gas temperature variation made it possible for us to test different methods of measuring it.

The spectral composition of radiation of microwave plasma in the range 300-900 nm in hydrogen and a nitrogen-containing mixture was analyzed by means of a monochromator (focus distance 300 mm, grids 1200 and 2400 lines/mm were used). As a receiver, photoelectron multipliers were used. Spectral resolution of the tools was 0.5 Å, and temporal resolution was 0.5 μs. Sensitivity of the registration system was calibrated by the standard method: by means of a source with the known spectral distribution of radiation intensity. Distribution of relative intensities of rotational lines R in branch (0-0) of $d^3\Pi_u \rightarrow a^3\Sigma_g^+$ (Fulcher band) and $G^1\Sigma_g^+ \rightarrow B^1\Sigma_u^+$ bands of H_2 molecules was used to measure the gas temperature.

The reverse life time, ν , of top levels in the both bands is actually the same and equals $4 \cdot 10^7 \text{ s}^{-1}$ for $d^3\Pi_u$ and $3 \cdot 10^7 \text{ s}^{-1}$ for $G^1\Sigma_g^+$ [4]. The frequency of neutral collisions is estimated as $\nu_{\text{coll}} = 8 \cdot 10^6 \text{ P s}^{-1} \text{ Torr}^{-1}$ [5], that is why under the conditions of our experiments $\nu < \nu_{\text{coll}}$. That means that the rotational temperature is in equilibrium with the gaseous one.

According to [6] the rotational temperature for $G \rightarrow B$ was determined by lines R0, R5, R7, R8 and R10. Lines R1–R4 were not resolved by the used tools, lines R6 and R9 were excluded since they were perturbed strongly by other levels [6]. The rotational temperature of the Fulcher band was determined by lines R0–R5.

The gas temperature was measured also by analyzing how intensities of rotational lines in band 0–2 of the $C^3\Pi_u \rightarrow B^3\Pi_g$ electron transition were distributed. Special experiments showed that small (up to 5%) addition of nitrogen do not cause variation of the distribution in the rotation structure of hydrogen bands.

In order to change the profile of the H_a absorption line the method of intracavity laser spectroscopy (ICLS) was used [7]. The ICLS method is a modification of the multi-pass absorption spectroscopy. However, unlike the latter method, in which the number of passes rarely exceeds several tens due to losses at optical elements, the method of intracavity laser spectroscopy uses the resonator of a multi-mode laser as a multi-pass cell.

The idea of a method is, that when a narrow-band absorber $\gamma(\lambda)$ is put into the cavity of a broad-band laser, spectral intensity of modes inside $I(\lambda)$ and outside I_0 of absorption region is determined by following equation.

$$\frac{I(\lambda)}{I_0} = \frac{1 - e^{-\gamma(\lambda)}}{\gamma(\lambda)},$$

where $\gamma(\lambda) = \frac{c\tau}{L} \kappa(\lambda)$, τ is the pulse duration, and $\frac{l}{L}$ - is ratio of absorber length to the laser cavity length. $\frac{c\tau}{L}$ is the multiplier, showing

the sensitivity gain of ICLS over traditional absorption spectroscopy. An apparent advantage of the ICLS method is the possibility to use tools with high spectral resolution and ignore inevitable losses in light power, since the information about parameters of the absorbing medium is carried by intense laser radiation.

In our experiments we used an organic-dye laser with generation pulse duration $0.5 \mu\text{s}$ as an ICL spectrometer. Spectrum analysis and registration were performed by means of a diffraction spectrograph (focus distance 1600 mm, reverse linear dispersion 0.1 nm/mm) and optic multi-channel analyzer. The tool function of the registration system proved to be close to the Gaussian one with width 0.05 \AA . When determining the temperature of H atoms we took into consideration that line H_α consists of seven components, which are dipole transitions between levels with $n = 2$ and $n = 3$. By that, we assumed that the resonance trapping of ejected photons in the α -line of the Lyman series, strong mixing of 2S and 2P sublevels in the presence of the electric field, as well as suppression of metastable states by neutral particles equalizes life times of the metastable, 2S, and resonance, 2P, levels. The shift of the levels in the presence of the microwave field was taken into consideration in accord with [8]. The collision broadening was assumed small (0.0075 \AA under pressure of 100 Torr). The Stark broadening was taken into account by measuring density of charged particles by the method of observing the H_β line of hydrogen atoms, which are strongly subjected to the Stark broadening. For this, the experimental profile was compared to the calculated one, which was obtained as the result of convolution of the instrumental and Doppler

profiles, as well as broadening by the microwave fields and charged particles [8, 9].

Measurement results

Temporal dependencies of the rotational temperature for different pressures determined by radiation spectra of molecules of hydrogen and nitrogen are shown on fig. 1. The same figure shows time dependencies of the temperature of atomic hydrogen, measured by Doppler broadening of H_α line.

It is seen from the figure that distribution of intensities of the rotational lines in the Fulcher system corresponds to the temperature of 600-700 K and does not depend neither on the time after the microwave pulse beginning, nor on the pressure. According to the recommendations given in [10], the transition from the Holn-London factors to half-empiric values of transition probability found in the said paper lead to higher values of rotational temperature. However, that does not eliminate the absence of the dependence on time and pressure. Moreover, the temperature corresponding to distribution of intensity of rotational transitions in the $G \rightarrow B$ band of hydrogen molecules, the $C^3\Pi_u \rightarrow B^3\Pi_g$ transition of nitrogen molecules, as well as to the Doppler width of hydrogen grows after 3-4 μs at pressures over 50 Torr. This scenario of dependence is quite natural due to development of ionization-overheating instability. However, in the region of low temperatures (at low pressures or at the initial stage of the discharge) the results of measurements in the $G \rightarrow B$ band do not correspond to the temperatures obtained by observing the radiation spectra of nitrogen molecules and the profile of the H_α absorption line. Evidently, this is associated with the fact that at low gas temperatures, when $T_g < N$ (N is rotational quantum number, and B_v is rotational constant) the main part in formation of population distribution starts to be played not by R-T relaxation but by other processes.

Conclusion

Analysis of the experimental data shows that the rotational temperature determined by observing the R-branch of the $G^1\Sigma_g^+ \rightarrow B^1\Sigma_u^+$ band of hydrogen molecules "traces" variations of the gas temperature for the temperature range over 800-1000 K. These results coincide with conclusions

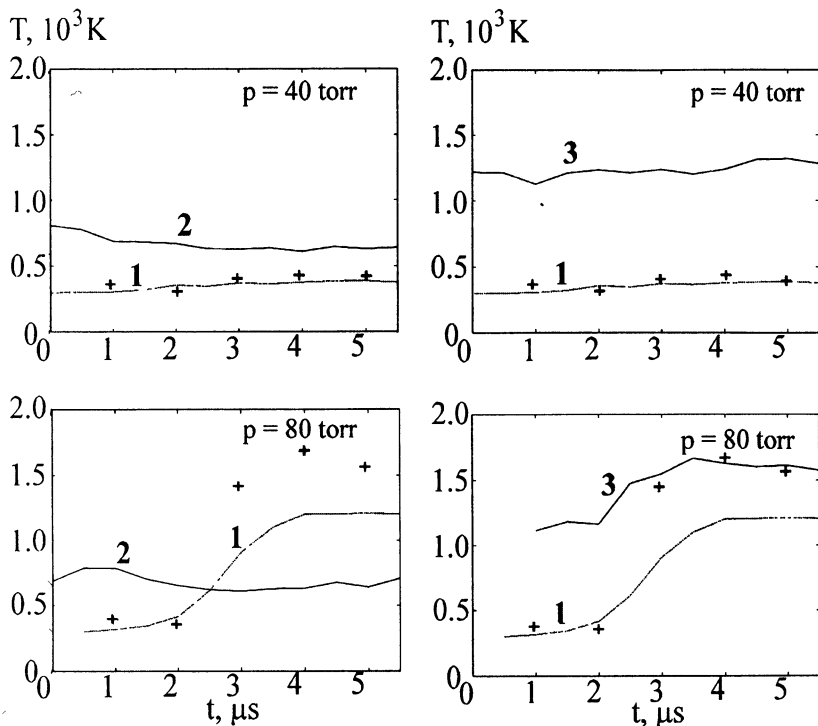


Fig.1. Results of gas temperature measurements by rotational structure of nitrogen (1), Fulcher band (2), G-B transitions (3) and Dopler broadening of atomic hydrogen (+).

given in [6]. The absence of dependence of the rotational temperature corresponding to the radiation of the Fulcher band on the pressure and time of discharge evolution proves that the Fulcher band cannot be used for measurements of gas temperature. It may be explained by strong influence of the $h^3\Sigma$ level on the $d^3\Pi_u$ level [11].

Measurements of the hydrogen atom temperature make it possible to conclude that hydrogen atoms are balanced with the molecules. That contradicts to the results given in [1], where the authors observed the difference between temperatures of H atoms and of molecules. Note that at our conditions the density of hydrogen atoms is significantly lower than that of the molecules, unlike in [1], where the share of H atoms was 40–60% (the

degree of dissociation was found from measurements by the ICLS method of density of H atoms in the $n=2$ state within the assumption that the electron energy distribution function is of the Maxwell type). That is why at our conditions “hot” atoms with energy 3.5 eV formed as the result of the $H_2 + e \rightarrow H + H + e$ reaction are efficiently “cooled” by molecules.

Acknowledgement

This work was supported by CRDF under grant RE1-352.

References

- 1 L. Tomasini, A. Rousseau, G. Gousset and P. Leprince. Spectroscopic temperature measurements in a H₂ microwave discharge. *J. Phys. D: Appl. Phys.* **29** (1996), pp 1006-1013.
- 2 A. Gicquel, K. Hassouni, Y. Breton et al. Gas temperature measurements by laser spectroscopic techniques and by optical emission spectroscopy. *Diamond and Related Materials*, **5** (1996), 366-372.
- 3 R. A. Akhmedzhanov et al: *Journal of Technical Physics* **67** (1997), N3, pp.9-18.
- 4 A. V. Phelps: *J. Phys. Chem. Ref. Data*, **19** (1990), p.653
- 5 J Van der Linde, F.W. Dalby: *Can. J. Phys.* **50** (1972), 287
- 6 A N. Goyette, W. B. Jameson, L. W. Anderson and J. R. Lawler. An experimental comparison of rotational temperature and gas kinetic temperature in a H₂ discharge. *J. Phys. D: Appl. Phys.* **29** (1996), pp. 1197-1201
- 7 E. A. Sviridenkov et al: *Quantum Electronics*, (1977), N5, pp.1028-1033.
- 8 V. V. Yazenkov, Ph. D thesis, Gorky, IAP, 1989.
- 9 H. R. Griem: *Spectral line broadening by plasmas*, 1974.
- 10 S. A. Astashkevich, B. P. Lavrov: *Optics and Spectroscopy* **77**, N3, pp.369-385
- 11 G. H. Dieke: *Phys. Rev.* **48** (1972), p. 610

SOURCES OF SOFT X-RAYS AND MULTICHARGED IONS BASED ON ECR DISCHARGE IN HEAVY GASES SUSTAINED BY HIGH-POWER GYROTRON RADIATION

*S.V. Golubev, S.V. Razin, V.E. Semenov, A.N. Smirnov,
A.V. Vodopyanov, and V.G. Zorin*

Institute of Applied Physics of Russian Academy of Sciences, Nizhny Novgorod, Russia

Dense mirror-trapped plasma heated by high power and high frequency radiation is very promising for soft X-ray generation and deeply stripped ion formation. Changing plasma parameters, one can create conditions optimal either for X-rays or for multicharged ions formation. For the electron densities exceeding 10^{13} cm^{-3} the regime of plasma confinement in a trap changes significantly, the description based on Pastukhov's formula is no longer valid, and the quasi-gasdynamic regime of plasma confinement is realized. The present work concerns experimental investigation of the quasi-gasdynamic regime of hot plasma confinement in a mirror magnetic trap and searching for optimal conditions of multicharged ions formation and soft X-rays generation in this regime.

Experiments were conducted with the use of a gyrotron with maximum power $W=130 \text{ kW}$, frequency $f=37.5 \text{ GHz}$, and pulse duration up to 1.5 ms. The simple mirror magnetic trap had the mirror ratio 3.4, length 25 cm, and the maximum magnetic field 2.5 T.

The temperature and density of the electrons were determined from spectral analysis of X-ray plasma bremsstrahlung in 2–15 keV range and from the transmission factor of diagnostic microwave radiation through the plasma. It was concluded that the quasi-gasdynamic regime of plasma confinement was realized in the experiments. Ion distribution over charge states in the quasi-gasdynamic regime was calculated and the obtained results were compared with the experimental data. A strong effect of anisotropy of the electron distribution function over energies on the efficiency of plasma confinement and formation of multicharged ions was observed.

Introduction

Dense plasma in a simple mirror trap heated by high power and high frequency radiation is very attractive from the point of view of soft X-ray generation [1, 2] and deeply stripped ion formation [3]. Changing plasma parameters, one can create conditions optimal either for X-rays or for multicharged ions formation.

Line emission of multicharged ions is the most effective mechanism of generation of plasma soft X-ray radiation in a wide range of parameters. The intensity of line emission grows proportionally to the product of electron and ion densities in the trap, while microwave power needed to sustain the electron temperature at a fixed level increases proportionally to the density of electrons. One can see that the increase of

plasma density leads to the increase in both emission intensity and efficiency of conversion of microwave radiation into X-ray radiation. The sustainment of a dense hot plasma is possible only by powerful short-wave radiation. Gyrotrons are the most promising sources for this purpose.

An increase in frequency and power of microwave radiation used for ECR plasma heating in an ion source reveals a rank of promising prospects regarding improvement of ion sources performance as well [4]. Namely, an increase in frequency and power of microwave pumping may lead to an increase in a density of a mirror-trapped plasma while the electron temperature is maintained at the optimal level for stripping of multicharged ions (MCI). The use of gyrotrons in MCI sources has made it possible to reach the plasma density $N_e > 2 \cdot 10^{13} \text{ cm}^{-3}$, which is an order of magnitude higher than in conventional ECR ion sources ($N_e \sim 10^{12} \text{ cm}^{-3}$). A regime of magnetic confinement of such a dense plasma changes from the classical [5] to the so-called quasi-gasdynamical one [6, 7]. A characteristic feature of the quasi-gasdynamical regime is that the rate of electron precipitation into the mirror loss-cone $D_p \sim v_{ei}$ exceeds the one of plasma escape through the trap plugs $D_e \sim V_s/kL$: $D_p > D_e$ (here, v_{ei} is the electron-ion collision frequency, V_s is the ion acoustic velocity, L is a trap length, and k is a numerical factor). Thus, the mirror loss-cone is filled with electrons, and plasma confinement time $\tau \sim D_e^{-1}$ is determined by the ion acoustic velocity and weakly depends on the plasma density. In this regime an increase in the plasma density is accompanied by an increase in the plasma confinement parameter $N_e \tau$ and causes a shift of the maximum of the ion charge state distribution (CSD) towards higher charge states. Moreover, MCI current, which is roughly estimated as N_e/τ , increases as the frequency of microwave pumping is increased [8].

Powerful ECR heating of a mirror-trapped plasma leads to formation of an anisotropic electron velocity distribution function (EDF) [9]: the average energy of the transverse, in respect to the magnetic field, electron motion is much greater than the energy of longitudinal motion. Theoretical studies of a mirror magnetic confinement of a multicomponent plasma with anisotropic (stretched along V_{\perp}) EDF in a simple mirror trap reveals an essential augment in multicharged ion confinement time due to the EDF anisotropy [10]. Consequently, the EDF anisotropy improves the ion CSD.

In this paper we discuss results of experimental investigation of an ECR discharge sustained by powerful pulse microwave radiation of a

gyrotron in a mirror magnetic trap. In particular, data on plasma hard X-ray emission spectrum, on the intensity of soft X-ray plasma emission, and on ion CSD are presented. Formation of the ion CSD has been explored both experimentally and numerically.

Experimental setup

The experimental setup is sketched in Fig. 1. The pulse mirror magnetic field (pulse duration is 13 ms), produced by two «warm» coils, achieved the maximum plug value of 2.5 T. The mirror ratio R and length L (the distance between the plugs) of the trap are equal to 3.4 and 25 cm, respectively. The linearly polarized gyrotron's (1) microwave radiation with the frequency of 37.5 GHz, power of 130 kW, and pulse duration of 1 ms, was focused by a dielectric lens (2) into the center of a discharge chamber (3). The trapped plasma was ECR-heated at the fundamental harmonic of the gyrofrequency. The ions, outflowing through the trap plugs along the magnetic field lines, got into the two-step five-channel ion analyzer (4). The ion analyzer enables one to investigate independently ion distribution over charge states and energy by means of electrostatic and magnetostatic analyses. The operating gas (argon) was admitted into the discharge chamber through a pulse valve (5). Exploiting a pulse gas influx, within a certain period of time (the microwave pumping was introduced at this very moment), it was possible to maintain inhomogeneous gas pressure: it amounted to $3 \cdot 10^{-5} \div 10^{-4}$ Torr in the discharge chamber, while it was considerably lower (10^{-6} Torr approximately) in the diagnostic chamber (6) and in the ion analyzer. Under such conditions an effect of the MCI beam attenuation due to ion-

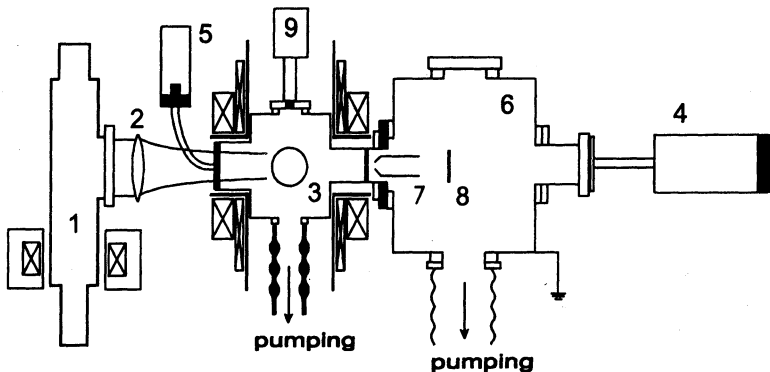


Fig. 1. Schematic of the experiment.

neutral charge exchange along the path through the diagnostic chamber to the ion analyzer is nearly inessential. For instance, relative attenuation of the Ar^{+10} ion beam was evaluated to be $\sim 6\%$.

Hard X-ray radiation of a plasma was investigated by the XR-100T analyzer (9), which was exploited as a photon counter. The spectral resolution of the analyzer amounts to 200 eV. A cooled silicon pin-diode was used as a detector. The output signal of the analyzer represents a series of peaks with a duration of 20 μs and the amplitude proportional to the energy of recorded quantum. A typical oscillogram of the X-ray analyzer signal is shown in Fig. 2, trace 1. Computer processing of recorded signals made it possible to obtain spectra as well as absolutely calibrated intensity of plasma X-ray radiation with time resolution. Using the analyzer, we carried out measurements of the intensity of X-ray plasma radiation in the region of quantum energies from 2 to 15 keV [11].

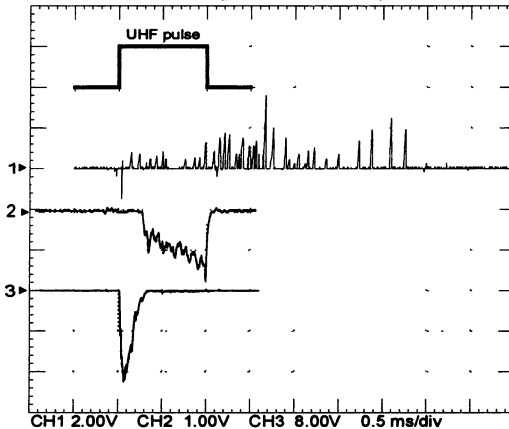


Fig. 2. Typical signals of the X-ray detector (trace 1) and ion analyzer: current of Ar^{6+} ions with energy 100 eV per ion charge (trace 2), current of Ar^{10+} ions with energy 300 eV per ion charge (trace 3). The microwave pulse is shown at the top (magnitude is not to scale).

Experimental results

In the course of measurements the ion distribution over charge states and energy was found to be strongly dependent on the power of microwave pumping and gas pressure in the discharge chamber. Unfortunately, the technique of pulse gas influx, employed in our experimental device, did not allow for obtaining a steady-state gas flux. Since the gas flux could alter significantly (twofold) within the microwave pulse, the conditions of MCI generation were changing

inevitably while the microwave power was applied. The experimental data obtained for the optimal (at least within the first 100–300 μs after the switching on of microwave pumping) rates of neutral gas flux are presented below.

At the beginning of a microwave pulse, within the first 100–300 μs after the switching on of microwave pumping, the current of highly charged ions Ar^{10+} - Ar^{11+} was observed (Fig. 2, trace 3). Right afterwards, within the time period from 500 μs to 1000 μs after the switching on of microwave pumping, the mean ion charge fell down, and the current of Ar^{5+} - Ar^{6+} ions dominated. The corresponding ion CSDs are shown in Fig. 3. Curve 1 was obtained at the beginning and curve 2 at the end (time period from 500 μs to 1000 μs after the switching on of microwave pumping) of the microwave pulse.

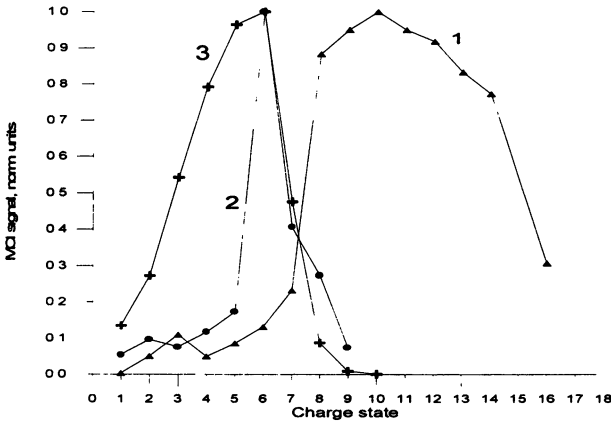


Fig. 3. The ion charge state distribution: curve 1 - at the beginning of the discharge (first 100-300 μs); curve 2 - at the end of the discharge (time period from 500 μs to 1000 μs after the switching on of microwave pumping); curve 3 - the calculated CSD for argon plasma with the parameters: $N_e=4 \cdot 10^{13} \text{ cm}^{-3}$, $T_e=300 \text{ eV}$.

Plasma X-ray bremsstrahlung measurements show (Fig. 4) that by the time the current of highly charged ions Ar^{10+} ceases to flow (see the oscillograms in Fig. 2) two fractions of electrons have been formed in a plasma: ‘warm’ electrons with mean energy $T_w \approx 300 \text{ eV}$ and density $N_w \approx 4 \cdot 10^{13} \text{ cm}^{-3}$, and the ‘hot’ ones with $T_h \approx 10 \text{ keV}$ and $N_h \approx 1.5 \cdot 10^9 \text{ cm}^{-3}$. (Observation of the cut-off of a diagnostic microwave signal at the 35.52 GHz frequency additionally confirmed the high plasma density: $N_e > N_{cr} = 1.5 \cdot 10^{13} \text{ cm}^{-3}$ [8].) Note that the temperature of the ‘warm’

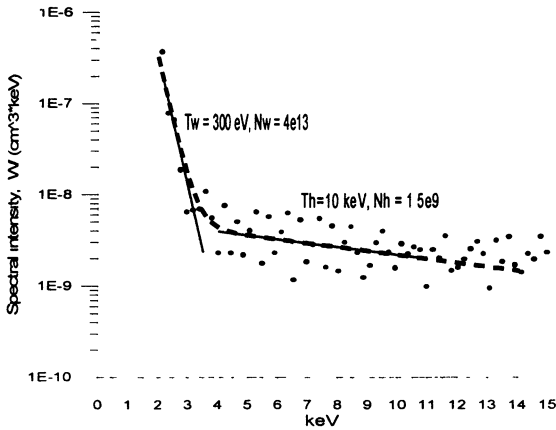


Fig. 4. Spectral intensity of plasma bremsstrahlung by the instant the current of Ar^{10+} ions ended off.

electrons is nearing the level optimal for MCI stripping. As follows from the measurements, the values of T_w at the beginning and at the end of the microwave pulse do not differ drastically from each other. Therefore, the experimentally observed shift of the ion CSD towards lower charge states can't be deemed as a result of MCI generation depression due to a possible fall in the electron temperature.

Discussion and numerical simulation

Temporal evolution of the ion CSD can be explained as follows. At the beginning of a discharge, as the plasma density is not extremely high, ECR heating of electrons proceeds more effectively than collisional isotropization of the EDF in the velocity space. Formation of the strongly anisotropic EDF results in an essential increase in the plasma confinement time τ [10]. Then, as the rate of ionization is enhanced and the electron density goes up, the frequencies of electron-ion and electron-electron Coulomb collisions increase. The EDF isotropization evokes a drop in the confinement parameter $N_e \tau$ and shifting of the ion CSD towards lower charge states. Therefore, one can speculate that the isotropization time of the EDF under given microwave power and gas flux defines the moment when the current of Ar^{10+} ions ends off.

In the second part of the microwave pulse, when the current of Ar^{5+} – Ar^{6+} ions prevails, an influence of the 'hot' electrons upon the processes of ionization and plasma confinement in the trap is virtually negligible. 'Hot' electrons do not contribute much to the total rate of ionization

because of their too high temperature T_h and fairly low density N_h . One can assume the energy of 'hot' electrons to be stocked mainly in the transverse, in respect to the magnetic field, motion as it is theoretically predicted. However, the EDF anisotropy due to the fraction of 'hot' electrons is weak: $N_h/N_w \ll 1$, i.e., the 'hot' electrons in the second part of the microwave pulse almost do not affect plasma trapping.

Thus, in the second part of the microwave pulse both the ionization process and the plasma confinement are completely determined by the fraction of 'warm' electrons. Under experimental conditions the EDF of 'warm' electrons is isotropic in the velocity space. Ref. [10] gives an estimate for the confinement time of ions of different charge states in a trap with multicomponent plasma under conditions of the quasigasdynamic regime with the isotropic (maxwellian) EDF:

$$\tau_i \approx \frac{\sqrt{e}RL}{2\sqrt{Z_i T_e / M_i}}, \quad (1)$$

where Z_i and M_i are the ion charge and mass, respectively; L and R are the trap length and mirror ratio; T_e is the mean electron energy (effective temperature), and e is the base of the natural logarithm. This formula is valid at $T_i \ll T_e$, which is a relation between electron and ion temperatures typical of ECR MCI sources. In plasmas with experimentally observed parameters: $N_e = 4 \cdot 10^{13} \text{ cm}^{-3}$, $T_e = 300 \text{ eV}$, and average ion charge $\langle Z \rangle = 6$, the product $v_{ei} \tau_e \approx v_{ei} \tau_{\langle Z \rangle} \approx 20$ (here, τ_e is the electron confinement time). Consequently, the 'warm' electrons isotropize their distribution within the plasma confinement time, and (1) can be exploited in order to evaluate the ion confinement time.

Computer simulation of ion CSD formation in the MCI source was done for Argon plasmas within the framework of a 0-dimensional nonstationary set of differential equations for ionization balance. The temperature of the 'warm' electrons was regarded to be a given parameter which can be determined experimentally. The time dependence of neutral gas pressure in a pulse was also taken from the experiment. The confinement times of ions with different charges were determined from (1). The calculated ion CSD for steady-state plasma (when ionization of operating gas is compensated by plasma longitudinal losses) is shown in Fig. 3. The results of numerical simulation agree well with the ion CSD observed in the second part of the ECR discharge.

Thus, the agreement between simulated and experimental data demonstrates realization of two sub-regimes of quasigasdynamic confinement of a dense mirror-trapped plasma: isotropic and anisotropic

ones. In the case of anisotropic confinement the average ion charge in plasma proves to be high enough – it's approximately equal to or higher than the average ion charge in the world-best ECR ion sources – but in our experiments the plasma density is much higher, which allows us to obtain much higher ion current.

Simple preliminary experiments were carried out to investigate the possibility of ion extraction with high ion current. An ion extractor (7) with an aperture of 1 mm in diameter was placed in the region of magnetic plug as shown in Fig. 1. The accelerating electrode was grounded and high ion accelerating 1 – 10 kV voltage was applied to the vacuum chamber. The current on the vacuum chamber, which was equal to the total current of ions extracted, and the current on a probe (8) placed behind the accelerating electrode were measured. Difference in these currents shows a divergence of the ion beam. Dependencies of the currents on the accelerating voltage are shown in Fig. 5. The ion current density (the extracting aperture's area was $8 \cdot 10^{-3} \text{ cm}^2$) achieved few amperes per sq. centimeter, which exceeds significantly current densities of all existing ECR multicharged ion sources.

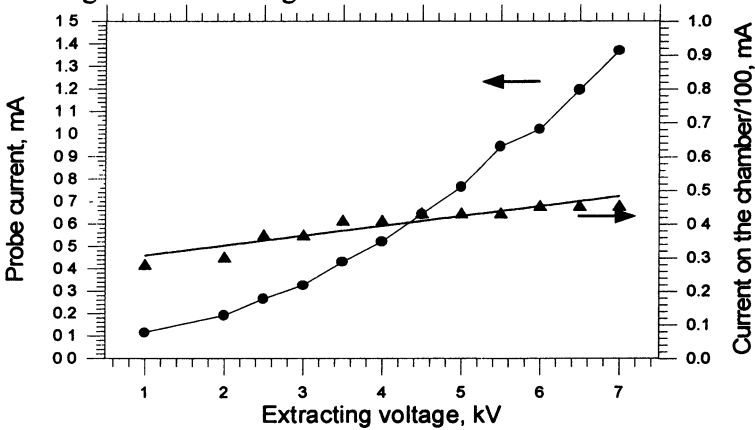


Fig. 5. Probe current and current on the chamber vs. extracting voltage.

The soft X-ray radiation intensity was measured by calibrated p-i-n diodes. Spectrum of soft X-ray plasma radiation was explored with help of a monochromator on multilayer Bragg X-ray mirrors and with the use of filter's method [11]. Under conditions of ECR discharge in argon at pressure 10^{-4} Torr when isotropic quasigasdynamic regime of plasma confinement was realized X-ray plasma radiation was found to lie almost entirely in the region of quantum energies from 90 to 185 eV.

Conversion efficiency of microwave radiation into X-ray radiation was about 10 %. Namely, the X-ray radiation power achieved approximately 10 kW. Accuracy of this estimate is not very high due to a rather big uncertainties of the X-ray spectrum and of the emissive volume determination.

Thus, it was shown experimentally that ECR discharge with pumping by powerful millimeter wave radiation is very promising as a source of both multicharged ions and soft X-rays.

References

1. Booske J.H., Aldabe F.A., Ellis R.F., and Getty W.D. Journal of Applied Physics, 1988, **64**, N 3, 1055.
2. Golubev S.V., Platonov Yu.Ya., Razin S.V., and Zorin V.G., Jour. of X-ray Sci. And Technology, 1996, **6**, 244.
3. Geller R., Rev. Sci. Instrum., 1998, **69**, 613.
4. Sortais P. Rev.Sci. Instrum., 1996, **67**(3), 867.
5. Pastukhov V.P. Nucl. Fusion, 1974, **14**, N. 3.
6. Ryutov D.D. Plasma Phys. Controlled Fusion, 1986, **28**, 191.
7. Turlapov A.V., Semenov V.E., Phys. Rev. E, 1998, **57**, 5937.
8. Golubev S.V., Razin S.V., Vodopyanov A.V., and Zorin V.G., Transactions of Fusion Technology, 1999, **35**, N. 1T, 298.
9. Golubev S.V., Semenov V.E., Suvorov E.V., and Tokman M.D., Proc. Int. Workshop on Strong Microwaves in Plasmas, (Nizhny Novgorod, 1994) v.1, 347.
10. Semenov V.E., Smirnov A.N., and Andrey Turlapov, Transactions of Fusion Technology, 1999, **35**, N. 1T, 398.
11. Golubev S.V., Razin S.V., Smirnov A.N., Vodopyanov A.V., and Zorin V.G. These proceedings.

MIRROR-TRAPPED PLASMA HEATED BY POWERFUL MILLIMETER WAVE RADIATION AS AN ECR SOURCE OF SOFT X-RAYS

S. V. Golubev, V.I. Luchin, S.V. Razin, N.N. Salaschenko*,
A.N. Smirnov, A.V. Vodopyanov, and V.G. Zorin*

Institute of Applied Physics RAS, Nizhny Novgorod, Russia

* Institute for Physics of Microstructures, Nizhny Novgorod, Russia

A series of experiments on investigation of the efficiency of generation of soft X-ray radiation by plasma confined in a mirror magnetic trap and heated by powerful millimeter wave radiation were conducted. The use of millimeter wave radiation leads to a substantial increase in electron density N_e of a hot confined plasma and, therefore, results in enhanced intensity of line ion emission $I \sim N_e N_i \sim N_i^2$ (here, N_i is the density of ions). For specific parameters of the discharge, multicharged ions of the charge state 3÷5 can dominate and their line emission belongs to the soft X-ray region.

A pulse gyrotron with maximum power $W = 130$ kW, frequency $f = 37.5$ GHz and pulse duration up to 1.5 ms was used for electron cyclotron resonance (ECR) plasma heating. Plasma was confined in a mirror trap with a mirror ratio of 3.4 and maximum magnetic field of 2.5 T. The pressure of an operating gas (argon) exceeded $3 \cdot 10^{-5}$ Torr. X-ray emission was studied by absolutely calibrated p-i-n diodes with different spectral sensitivities and a set of filters, by cooled X-ray detector XR-100T with spectrum resolution of 250 eV, and by a multi-layer mirror monochromator (Mo-B₄C and Mo-Si mirrors). Image of emissive region was also taken with help of a pine-hole camera.

Emission spectrum of ECR discharge was obtained in the 65÷170 Å range. Soft X-ray emission of the discharge lies in this spectral interval almost entirely. The measured absolute values of spectral intensity of the X-ray radiation enabled us to determine operation efficiency of the source. It was found, in particular, that up to 10% of microwave radiation can be converted into X-ray radiation of the spectral interval 80÷100 Å.

Introduction

This work is devoted to creation of a source of soft X-ray radiation. One way to obtain X-ray radiation in the photon energy range from 100 to 200 eV is to excite line emission of multicharged ions. This line emission can be produced in plasmas by heavy gas multicharged ions excited by the electron impact. Thus, plasma with multicharged ions of a heavy gas is needed with more or less high electron temperature. These conditions are fulfilled in a mirror-trapped plasma, which is ECR-heated with millimeter-wave radiation [1, 2, 3]. Line emission intensity of multicharged ions is proportional to the electron density multiplied by the ion density in

a wide range of plasma parameters. Microwave power required for maintaining sufficient electron temperature is proportional to the density of electrons. Finally, conversion efficiency (power of X-ray emission divided by microwave power supplied) is proportional to the electron density. Future prospects to increase efficiency of such a source are connected with an increase in frequency and power of microwave pumping.

Experimental setup

The scheme of the experimental setup is shown in Fig. 1. The gyrotron with maximum power of 130 kW, frequency of 37.5 GHz, and pulse duration up to 1.5 ms was used for microwave pumping. Microwave beam was focused by a dielectric lens into the center of a discharge vacuum chamber, which was set between two identical worm pulse coils producing a mirror magnetic field. Mirror ratio of the trap and the maximum magnetic field strength were equal to 3.4 and 2.5 T, respectively. A silicon p-i-n diode with a collimator and a set of filters in front of it was attached to the discharge chamber to record soft X-ray radiation. The diode was covered with a thin layer protecting it from visible and ultraviolet light. A diode of the same type was used as a detector in the X-ray spectrometer based on a multilayer Bragg mirror.

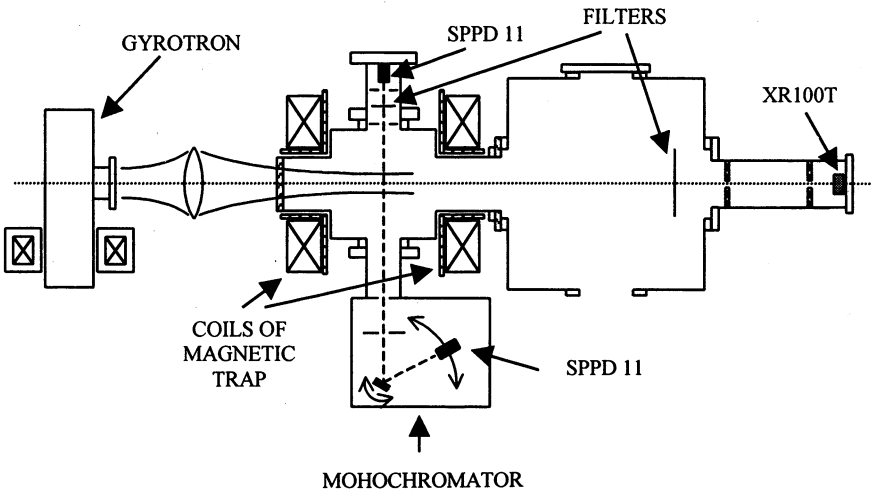


Fig. 1. Schematic of the experiment

Preliminary X-ray measurements

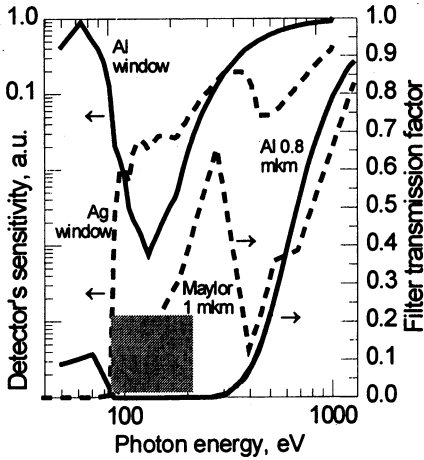


Fig. 2

In preliminary X-ray measurements we used two different detectors that had 0.13- μm protective layers of aluminium and silver, and two different filters: one of aluminium and the other of mylar with 0.8- μm and 1.0- μm thickness, respectively. Different detectors had different spectral sensitivities (see Fig. 2), because different covering layers had different spectral transmission factors. Different filters had different transmission factors as well (Fig. 2). Through combining two detectors with two different filters

it was found that the major portion of plasma radiation belongs to the region of photon energies from 80 to 200 eV. This region is marked in Fig. 2 by a shadowed rectangle.

Spectral intensity investigation

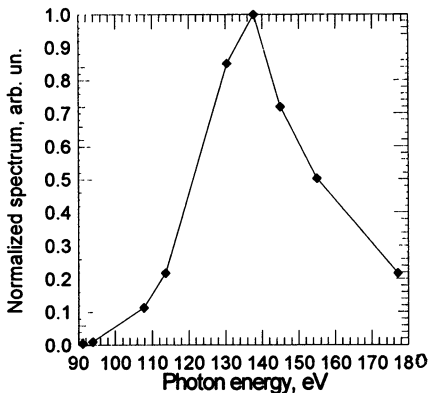


Fig. 3. X-ray spectral intensity

The X-ray monochromator on multilayer Bragg mirrors (Mo-B₄C and Mo-Si mirrors were used) was specially designed for investigation of plasma radiation spectral intensity. Its schematic arrangement is shown in Fig. 1. The monochromator has an operating range from 90 to 180 eV and spectral resolution less than 20 eV. Exploiting the monochromator, we measured more exactly X-ray spectral intensity in the previously studied spectral range and obtained

a spectrum which is presented in Fig. 3. The spectrum's maximum is at 140 eV (90 Å).

Absolutely calibrated measurements

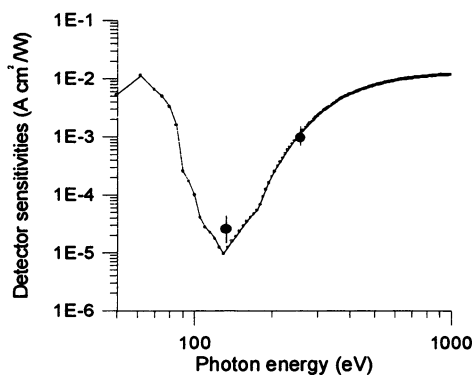


Fig. 4. Detector spectral sensitivity:
contin. curve - calculated, dots - measured

One of the silicon p-i-n diodes used in the experiments was absolutely calibrated. The calculated and measured spectral sensitivities of the calibrated diode is shown in Fig. 4. Using this calibration the total power of plasma X-ray emission at the region of photon energies from 100 to 170 eV was estimated to be equal to 10 kW, which in its turn means that the efficiency of transformation of microwave radiation into X-ray radiation is about 10%.

Measurements of plasma parameters

To determine plasma parameters we used another type of X-ray diagnostics – an X-ray detector XR-100T with cooled p-i-n diode working as a photon counter. This detector has operating range from 2 to 10 keV and spectral resolution of 250 eV. The detector was set at the installation symmetry axis at the distance of 150 cm from the plasma as shown in Fig. 1. The output signal of the detector represented a series of 20- μ s

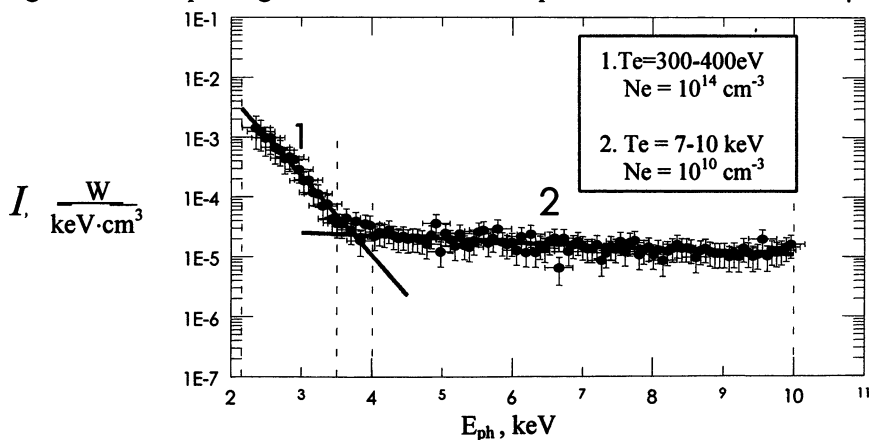


Fig. 5. Spectral intensity of plasma X-ray radiation

pulses with their amplitude proportional to the energy of recorded quanta. Computer processing of recorded signals, which took into account spectral sensitivity and transmission factor of the system, made it possible to obtain spectra as well as absolutely calibrated intensity of plasma X-ray radiation (see Fig. 5).

Estimates demonstrate that in the studied quantum energy range (2÷10 keV) plasma bremsstrahlung dominates. If electron distribution over energy in a plasma is maxwellian, spectral intensity of plasma bremsstrahlung can be written as follows:

$$dE_{\text{eff}}/dv = C \cdot N_e \cdot N_i \cdot (Z_i)^2 \cdot (T_e)^{-0.5} \cdot \text{Exp}(-hv/T_e), \quad (1)$$

where C is numerical factor, N_e is the electron density, N_i is the ion density, Z_i is the mean ion charge, and T_e is the electron temperature. The experimentally obtained dependence of spectral intensity on quantum energy in a semi-logarithmic scale (the plot in Fig. 5) can be apparently approximated by two straight lines. Exploiting eq. (1), from the slope of the line it is possible to derive the electron temperature, and from the absolute value of intensity one can determine the plasma density. Accordingly, two fractions of electrons have been found in a plasma: ‘warm’ electrons with mean energy $T_w \approx 300 - 400$ eV and density $N_w \approx 10^{14} \text{ cm}^{-3}$, and the ‘hot’ ones with $T_h \approx 7 - 10$ keV and $N_h \approx 10^{10} \text{ cm}^{-3}$.

Simulation of plasma emission

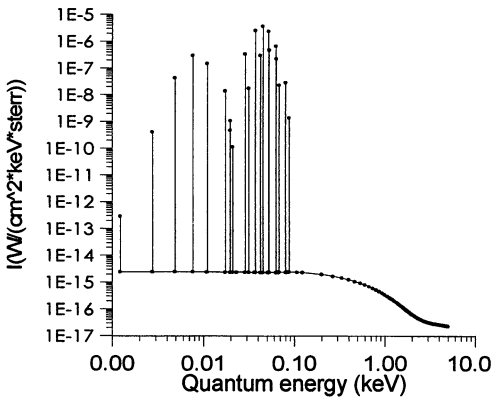


Fig. 6. Calculated spectral intensity of plasma X-ray radiation

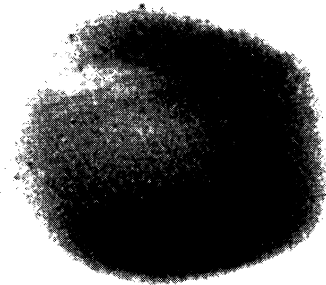
The calculation of plasma X-ray emission for the measured values of T_e and N_e was performed. The model of ion level kinetics realized in the simulation was based on the most widely used collisional-radiative approach, which takes into account the following kinetic processes: collisional-, photo- and autoionization, collisional-, photo- and dielectronic recombination, spontaneous radiation transitions between

discrete ion energy levels, process of collisional excitation and de-excitation. Plasma was assumed to be optically thin. Both line emission

and bremsstrahlung were calculated (see Fig. 6). The continuous part of the calculated spectrum is in a good agreement with the measured spectrum.

Pinhole image of the plasma

The study of spatial distribution of radiation intensity was performed by means of a pinhole camera, placed on the longitudinal axis of the magnetic trap. Fig. 7 presents the X-ray pinhole image ($0.11 < E_{\text{ph}} < 0.6$ keV quantum energy range) of an ECR plasma discharge, averaged over 20 discharge pulses at non-coaxial injection of a microwave beam that provided azimuthally inhomogeneous plasma heating.



Negative

Fig. 7. X-ray pinhole image of the discharge

Conclusion

A series of experimental results on investigation of generation of soft X-ray radiation by plasma confined in a mirror magnetic trap and heated by powerful millimeter wave radiation are presented. They convincingly demonstrate that creation of a plasma source of soft X-ray radiation with efficiency up to 10-15 % is quite feasible.

References

- [1] Booske J.H., Aldabe F.A., Ellis R.F., and Getty W.D. Journal of Applied Physics, 1988, **64**, N 3, 1055.
- [2] Walters U., Wiesemann K., Ullman F., Werner T., Zschornak G. Proc. of 14th Int. Workshop on ECR Sources. (CERN, Geneva, Switzerland, 3-6 May 1999.)
- [3] Grubling P., Holland J., and Ulm G. Proc. of 14th Int. Workshop on ECR Sources (CERN, Geneva, Switzerland, 3-6 May 1999.)

TORNADO TYPE CLOSED MAGNETIC TRAP FOR AN ECR ION SOURCE

K.B. Abramova, A.N. Smirnov, A.V. Voronin*, V.G. Zorin*

Institute of Applied Physics, Russian Academy of Sciences, Nizhny Novgorod, Russia

* Ioffe Physico-Technical Institute, St.-Petersburg, Russia

We propose to use a Tornado type closed magnetic trap for creation of a source of multicharged ions with plasma heating by microwave radiation. Plasma loss in closed traps is determined by diffusion across the magnetic field, which increases substantially plasma confinement time as compared to the classical mirror trap. The Tornado trap also possesses merits such as: an opportunity to produce high magnetic fields up to 3 T, which makes possible heating and confinement of plasma with a high density of electrons; an opportunity to use supplementary coils for ion extraction; plasma stability to magneto-hydrodynamic perturbations because the magnetic field structure corresponds to the "min B" configuration; and relatively low costs.

All estimates and calculations were carried out for the existing Tornado-322 pulse installation (maximal magnetic field 2.8 T) with plasma heating at 53 GHz frequency. The numerical simulation has shown that, by the end of the magnetic field pulse, ion distribution over charge states may reach a maximum at Ar^{+16} for the plasma density of 10^{13} cm^{-3} . The current density of ions Ar^{+16} can be varied from 10 mA/cm^2 to approximately 1 A/cm^2 .

Introduction

At present time the most widely used sources of multicharged ions (MCI) are ECR sources that exploit a mirror magnetic trap for plasma confinement and microwave radiation for plasma heating at electron gyrofrequency. Such devices sustain sufficiently high electron temperature for multiple gas ionization as well as provide a fairly long-duration plasma confinement for achievement of high ion stripping rate. In addition, they enable one to extract an ion beam, which is then transported for a few tens of meters to the consumption region. (A project of a built-in ECR MCI source is discussed in Ref. [1]. The MCI source, installed inside the cyclotron accelerator, is free from the system of ion transfer.) If ideal, plasma losses from such a trap are determined by plasma leakage along the axial magnetic field through the trap plug where an extractor is set. Longitudinal losses limit the ion life-time in a trap and, consequently, the stripping rate of multicharged ions¹.

¹ The efficiency of multicharged ions generation in a plasma is determined by the plasma confinement time, the electron temperature, and density.

The use of traps with a closed structure of magnetic field lines seems alluring for increasing plasma confinement time that can be essentially greater (as a ratio of longitudinal and transverse, in respect to the magnetic field, rates of plasma diffusion) than in a simple mirror trap. An apparent shortcoming of closed traps is complicated ion extraction. Tornado type closed magnetic traps [2] can solve this contradiction. They allow for using a supplementary coil that partially destroys the closeness of magnetic field lines but yet does not alter drastically the over-all plasma confinement time. This allows for regulation of plasma outflux by varying the magnetic field of the supplementary coil, i.e. there appears an opportunity to control a plasma flux into the extractor and govern, within certain limits, the ion confinement time.

In the present paper we propose to use a closed Tornado type trap for creation of an ECR source of MCI. We describe a scenario of cyclotron plasma heating and present the ion charge state distribution (CSD), which can be obtained in Tornado-322 trap. Tornado-322 trap has been fabricated this year and is now being tested [3].

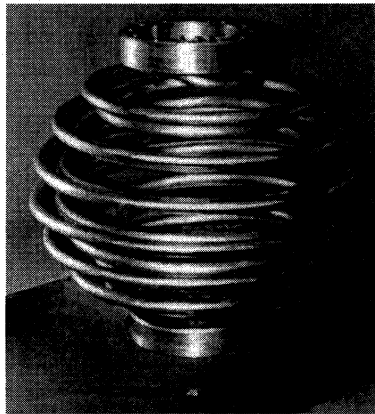


Fig. 1. External appearance of Tornado-322 trap

Tornado trap

The feasibility of creating a closed magnetic system with a magnetic field increasing towards the periphery was shown nearly 40 years ago. Then a device, which enables one to create such a magnetic field, was proposed. The magnetic structure, which was called Tornado, can be used as a magnetic trap for confinement of hot dense plasmas. The Tornado type magnetic field can be produced by two currents flowing through

a couple of concentric helical conductors connected at the poles by two jumpers (Fig. 1).

Later realization of such a field was demonstrated analytically. Its magnetic configuration has got a spherical separatrix that divides the magnetic field into two regions. The magnetic field lines inside the separatrix encircle the inner helical conductor and keep to the volume confined by the separatrix, whereas, outside the separatrix the magnetic field lines encircle the outer helical conductor and can go to the infinity. The volume within the separatrix is used for plasma confinement [2]. This volume includes a region of reduced magnetic intensity surrounded by a magnetic barrier. The magnetic field forms a regular and stable system (Fig. 2).

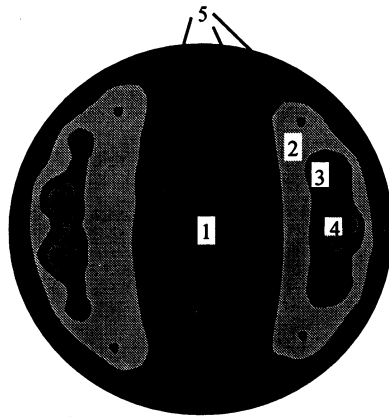


Fig. 2. Regular field - line structure inside the separatrix. 1, 2, 3, 4 - regions built of generalised magnetic lines; 5 - region built of individual magnetic lines.

A series of independent experiments on the system confinement properties have been performed. They have convincingly proved the following: the magnetic structure is closed; the plasma confinement time reaches its maximum when the values of conductors' currents meet the condition of the spherical separatrix existence; the major channels of plasma losses (for plasmas with the electron temperature of 2-5 eV) are the classical diffusion and recombination. It should be emphasized that in the present paper we assume that the latter statement is still valid over much greater electron temperatures.

At the electron density less than 10^{13} cm^{-3} the experimentally observed plasma confinement time was found to be directly proportional to the

magnetic intensity H squared and inversely proportional to the electron density N_e : $\tau_i^D \sim H^2 \cdot N_e^{-1}$. Thus, the plasma confinement time in this regime can be written as follows:

$$\tau_i^D \approx \frac{R^2}{D_{\perp}^{ef}} \approx \frac{\chi \cdot R^2 H^2 T_e^{3/2}}{AN_e(T_i + \langle Z \rangle T_e)}, \quad (1)$$

where D_{\perp}^{ef} is the transverse diffusion coefficient; R (cm) is the magnetic barrier width; T_e and T_i (eV) are the electron and the ion temperatures, respectively; $\langle Z \rangle$ is average ion charge, $A \approx 3 \cdot 10^{-4}$ is a numerical factor; H is given in Tesla; and χ is the correction factor, which accounts for the complexity of the magnetic field structure. The value of χ can be derived from comparison of (1) with results of accurate calculations. For numerical simulation χ was taken to be equal to 1/6, relying on the experience of Tornado trap handling.

Investigations conducted on Tornado-X trap verified these results for the plasma density up to 10^{14} cm^{-3} and 0.25 T magnetic field with a pulse duration up to 2 ms.

At high electron densities, the plasma confinement time, measured experimentally, was restricted by recombination. In this case we have:

$$\tau_i^R \approx (\alpha \cdot N_e)^{-1}, \quad (2)$$

where α is the recombination rate coefficient.

Thus, all the measurements performed on different Tornado devices have demonstrated the magnetic structure closeness and stability of the trap in relation to magnetohydrodynamic perturbations. However, for long-duration confinement of a hot plasma it is necessary to increase the magnetic field strength and pulse duration. None of the former models allowed both conditions to be met simultaneously. That's why a new advanced device (Tornado-322) was elaborated and fabricated. Experiments on Tornado-322 have already been started this year [3].

The confinement of relatively hot and dense plasma in Tornado-322 trap must be provided by the following characteristics: 1) The helices are assembled of two elements: a tube maintaining the helical shape of the conductors and conductors inside the tube. 2) The stainless steel tubes contain insulated current-carrying copper wires. This allows one to refuse any insulating materials inside the vacuum chamber and to lower the background pressure. 3) The current-carrying wires are cooled down with a nitrogen vapor. This decreases their conductivity approximately four-fold and increases the magnetic field pulse duration. 4) Turns of the inner helix are placed between those of the outer helix. This moderates pon-

derivative interaction between the helices' turns and provides an opportunity to raise the magnetic field strength.

The advantage of closed magnetic traps over the mirror traps in terms of plasma confinement could be evaluated as a ratio of the plasma confinement times (for a mirror magnetic trap we use an expression for the classical regime of plasma confinement [4], conventionally exploited in ECR MCI sources):

$$\frac{\tau_i^D}{\tau_i^C} \approx \frac{R^2 \cdot v_{ei}}{D_{\perp}^{ef}} \sim \frac{R^2 \cdot H^2}{T_e} \quad (3)$$

The advantage is the most apparent for high magnetic intensities. For instance, this ratio amounts to 10^5 for Tornado-322 trap (the magnetic field strength is about 2 T) with the electron temperature taken as 100 eV.

ECR plasma heating

ECR heating of the electron component is the most efficient way to produce strongly nonequilibrium plasmas with parameters optimal for MCI stripping, namely, with hot electrons having the temperature of 1-5 keV and with relatively cold ions having the temperature of several electron-volts. Unfortunately, no experiments have been conducted on microwave plasma heating in Tornado trap, relying on which we could measure the efficiency of ECR heating in this trap. The structure of magnetic field lines in the trap is fairly intricate and, therefore, a detailed analytical study of microwave radiation absorption seems impossible at the present. Nevertheless, some conclusions concerning feasibility of plasma heating can be made from general considerations.

Features of the structure of magnetic field lines do not allow longitudinal launching of microwave radiation (when a wave vector is parallel to the magnetic field). This kind of launching is the most effective in terms of radiation absorption in small laboratory devices.

Estimates have shown that at nonlongitudinal launching the one-pass absorption of cyclotron microwaves is weak (plasma is optically thin for normal waves). One might expect a considerable augment in microwave absorption due to a multi-pass effect (the trap is set into the vacuum chamber, which is a resonator) and, perhaps, under the conditions of upper-hybrid resonance absorption. Anyway, microwave radiation is believed to be absorbed in a broad range of frequencies due to a strong inhomogeneity of the magnetic field in the trap.

Formation of multicharged ions in a Tornado-trapped plasma

Pulse duration of the magnetic field in Tornado- 322 trap is less than the plasma confinement time. Thus, in order to investigate formation of the ion CSD, one has to solve a nonstationary set of differential equations for ionization balance of electrons, neutral atoms, and ions of all charge states. Density N_i of ions in the i^{th} charge state is determined by ionization, recombination, charge exchange processes, and by the rate of transverse plasma diffusion:

$$\begin{aligned} \frac{\partial N_i}{\partial t} = & (k_{i-1,i} N_{i-1} - k_{i,i+1} N_i + k_{i+1,i}^r N_{i+1} - k_{i,i-1}^r N_i) \cdot N_e \\ & + (k_{i+1,i}^{ex} N_{i+1} - k_{i,i-1}^{ex} N_i) \cdot N_0 - \frac{N_i}{\tau}, \end{aligned} \quad (4)$$

where $k_{i,i+1}$ is the electron impact ionization rate coefficient (Lotz formula [5] was employed in computations), $k_{i+1,i}^r = k_{i+1,i}^{rr} + k_{i+1,i}^{dr}$ is the sum of radiative recombination [6] and dielectronic recombination [7] rate coefficients, and $k_{i+1,i}^{ex}$ is the rate coefficient of charge exchange process [8] due to collisions with neutral atoms. In a computer simulation the time of transverse diffusion τ was assumed to be equal for ions of all charge states and was calculated from (1).

Let us suppose that the electron distribution function is Maxwellian with temperature T_e which depends on plasma density N_e and the power P of microwave radiation absorbed by a plasma. Therefore, the balance of the electron temperature is given by the equation:

$$\frac{\partial T_e}{\partial t} = \frac{P}{N_e V} - \delta \sum_i \nu_{ei} (T_e - T_i) - \sum_i k_{i,i+1} N_i (U_i + T_e). \quad (5)$$

Here, $\delta = 2m_e/M_i$; U_i is the ionization potential of an ion with the charge i ; and V is the trap volume.

Temporal distribution of the magnetic intensity in the magnetic barrier of Tornado-322 trap is shown in Fig. 3. This curve was obtained in testing experiments. As a pulse current is flowing through the trap coils, the ECR zone, which corresponds to the given frequency of microwave radiation, is moving over the trap volume. This may provide a quasi-uniform plasma heating in different internal trap regions. For simplicity's sake, the injected microwave power is assumed to be totally absorbed by a plasma if there is a zone of resonance inside the separatrix of the trap.

For Tornado-322 trap, the optimal frequency for plasma heating lies between 30 GHz and 60 GHz. Microwave radiation of this frequency range can be absorbed in the separatrix area with the magnetic field from

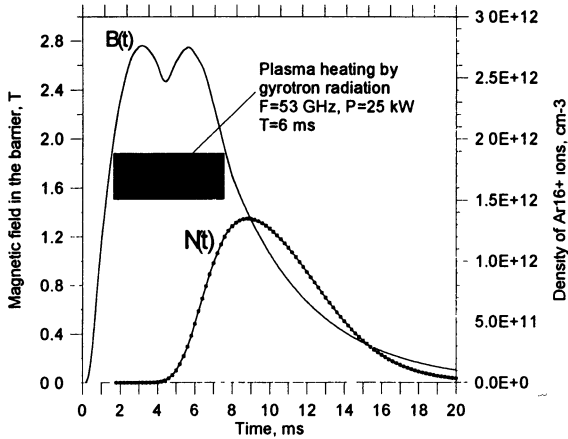


Fig. 3. $P(t)$ is a model block diagram of microwave radiation absorption, which was used in the numerical simulation. Curve $B(t)$ is a pulse of the magnetic field in Tornado-322 trap. Curve $N(t)$ is the calculated temporal evolution of the density of ions Ar^{16+} ; $P_{ini} = 6 \cdot 10^{-5}$ Torr.

1.06 T up to 2.12 T. The corresponding powerful generators – gyrotrons – are presently manufactured in IAP RAS (Appendix A). The numerical simulation was carried out for the 53 GHz frequency.

The time of plasma confinement in the trap exceeds the magnetic field pulse duration. Therefore, temporal limitation of resonance plasma heating by the pulse duration of the magnetic field is a crucial factor that determines a possibility to attain ion CSD with a high mean charge. To shorten the stage of plasma ignition while the gyrotron pumping is applied, it is proposed to produce a pre-plasma with a density of about $10^{10} \div 10^{11} \text{ cm}^{-3}$ before the switching on of a gyrotron. Calculations indicate that the pre-plasma density should be much greater than that of the background plasma. On the other hand, computed results are weakly dependent on a further rise in the initial ionization rate if the pre-plasma density exceeds 10^{10} cm^{-3} . When solving the set of equations (4) the pre-plasma density of 10^{10} cm^{-3} was taken as the initial condition. In experiments, it is suggested to produce pre-plasmas by ECR break-down of neutral gas at the 2.45 GHz frequency. Generators for this frequency exert a power up to several kilowatts at moderate device cost.

Computer simulation of ion CSD formation in Tornado trap was done for Argon plasmas. The model diagram (Fig. 3) of microwave radiation absorption at 53 GHz frequency was used in calculations. The curve $N(t)$

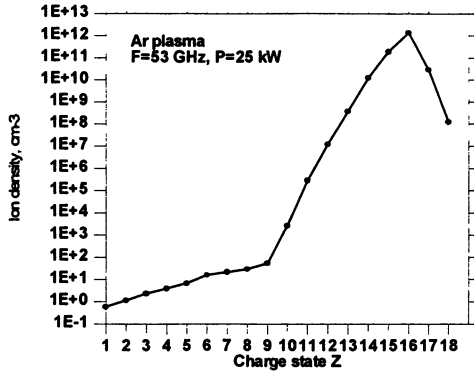


Fig. 4. Calculated ion CSD for initial parameters the same as in Fig. 3.

in Fig. 3 represents temporal evolution of the density of ions Ar^{16+} . This time dependence was obtained under the following conditions: initial pressure of neutral gas $P_{ini} = 6 \cdot 10^{-5}$ Torr and gyrotron output power $P = 25$ kW. For the same initial conditions, the ion CSD, which has the highest over time average charge, is shown in Fig. 4. This ion CSD is formed in a plasma by the instant the density of ions Ar^{16+} reaches the maximum value (Fig. 3), i.e. after the microwave pumping has been switched off. At high power absorption, the electrons gain the energy T_e of 1÷3 keV and keep stripping multicharged ions effectively for some time after the end of a microwave pulse due to a rather great plasma confinement time.

In a regime illustrated in Fig. 3 – Fig. 4, the maximum electron density in a discharge during the ECR heating is $\{N_e(t)\}_{max} \leq 2.3 \cdot 10^{13} \text{ cm}^{-3}$, which is less than the cut-off plasma density for the 53 GHz frequency ($N_c = 3.47 \cdot 10^{13} \text{ cm}^{-3}$). This, in principle, solves a problem of microwave radiation reflection from the boundary of a plasma with the density nearing the cut-off value.

The authors are grateful to Prof. M.D. Tokman for helpful comments and suggestions.

Appendix A

Most popular gyrotrons are those generating at the second gyrofrequency harmonic, which allows one to use a lower magnetic field in a generator cavity and renounce superconducting magnets that make microwave sources very costly. Gyrotrons with "hot" magnets tested at the frequencies of 24 GHz and 30 GHz may be tuned to any frequency ranging from 20 GHz to 40 GHz.

Table 1. The best Russian CW Gyrotrons [9] (updated)

Freq., GHz	Output power, kW	Mag. field, T	Type of magnet
30	25	0.55	Ns ^a
37.5	20	1.45	SCM ^b
83	20	3.2	SCM

a - Normal solenoid b - Superconducting magnet

Gyrotrons with superconducting solenoids are much more expensive in service but provide much higher frequencies. The experience of the Institute of Applied Physics RAS verified feasibility of fabricating a gyrotron with a superconducting solenoid at frequencies from 30 GHz to 140 GHz with the power of 20 kW and higher.

Gyrotrons may operate both in the CW and pulse-periodic regime. Pulsed power may be much higher than the one indicated in Table 1, but average power is limited to about 20 kW. Parameters of the pulsed gyrotrons fabricated in IAP RAS for nuclear plasma heating at ECR are listed in Table 2.

Table 2. Russian Pulsed Gyrotrons [9] (updated)

Freq., GHz	28	53	83	100	110	110	140	140	168
Output Power, kW	500	500	500	2100	1300	6000	550	500	500
Pulse duration, s	0.1	0.2	2	$3 \cdot 10^{-5}$	10^{-4}	2	3	2	0.7

Thus, available data and technologies allow for fabricating a gyrotron with a frequency in the interval from 15 GHz to 140 GHz with the power of 20 kW and higher in the CW regime and with the power exceeding 500 kW in the pulse-periodic regime.

References

- [1] Golubev S.V., Zorin V. G., Gulbekian G.G. and Kutner V.B. Proceedings of the Int. Conf. on Cyclotrons and Their Applications (Caen, France, June 1998).
- [2] Galechyan G.A. and Peregood B.P. Sov. Phys. Tech. Phys., **14**, 1272 (1970); Abramova K.B. et al, Tech. Phys., **42** (2), 134 (1997).
- [3] Abramova K.B. et al. Trans. of Fusion Technology, **35**, 263 (1999).
- [4] Pastukhov V.B. Nucl. Fusion, **14** (3), 68 (1974).
- [5] Lotz W. Zeit. fur Phys., 216, 241 (1968).
- [6] Mazzotta P. et. al. Astron. Astroph. Suppl. Ser., **133**, 403 (1998).
- [7] Shull J.M., Van Steenberg M. Astroph. J. Suppl. Ser., **48**, 95 (1982).
- [8] Muller A., Salzborn E. Phys. Lett., **62A**, 391 (1977).
- [9] Goldenberg A.L., and Litvak A.G. Physics of Plasmas, **2**, 2562 (1995).

STATIONARY LARGE VOLUME MICROWAVE DISCHARGE FOR H^- NEUTRALIZATION

A.A. Skovoroda and OGRA Team

INF RRC Kurchatov Institute, Moscow, Russia

The experiment on PNX-U installation which is the prototype of a plasma neutralizer of MeV H^- ions in ITER neutral beam injector is described. The plasma target thickness $1.8 \cdot 10^{14} \text{cm}^{-2}$ is obtained in 0.5 m^3 plasma volume at 40 kW input microwave power. The ambipolar potential plasma confinement in multicusp magnetic system is observed.

Introduction

The purpose of the present experiment consists in check of the basic properties (steady state operation; high power efficiency of the arbitrary cold plasma production by the gas ionization and plasma heating on the periphery; high ionization degree in the plasma center; small beam divergence) of a plasma neutralizer (PN), based on the low pressure microwave discharge in a multipole magnetic trap (3D magnetic wall) and proposed in [1]. The more detailed description of the PN concept, requirements and first experiments can be found in [2, 3]. The first results from PNX-U device was discussed on last Plasma MAGATE Conference [4]. In Table the modern status of PN eXperiment is shown

Device	Status	$n_e I, 10^{15} \text{cm}^{-2}$	V, m^3	P_{mw} , kW	f, GHz	B_{sz} , T	Ioniz. degree	Type of mag.system
PN-1	exp.95-96	0.03	0.07	1.5	2.45 magnetron	0.18	0.1	Perm.Mag.
PN-2	exp.07.96	0.04	0.07	1.5+0.5	2.5+7	0.18	0.1	Perm.Mag.
PNX-U	exp. 07.99	0.18	0.5	50+50	7 klystron	0.36	0.2	Copper
PNX-SU	Naka beam exp. proposal	1	1	150	7+18	1	0.3	SuperCond. +Copp.
PN-ITER	design	>2	>10	>500	>18 gyrotron	>1	>0.3	SuperCond.

Plasma Production in PNX-U

The steady state 3D magnetic wall in PNX-U device is formed by copper coils with opposite direction of currents. The magnetic field 0.36 T can be obtained in 14 slits routinely. Two steady state 50 kW klystron amplifiers with 7 GHz frequency are used to organize the microwave discharge in PNX-U. The used tangential microwave inputs system is

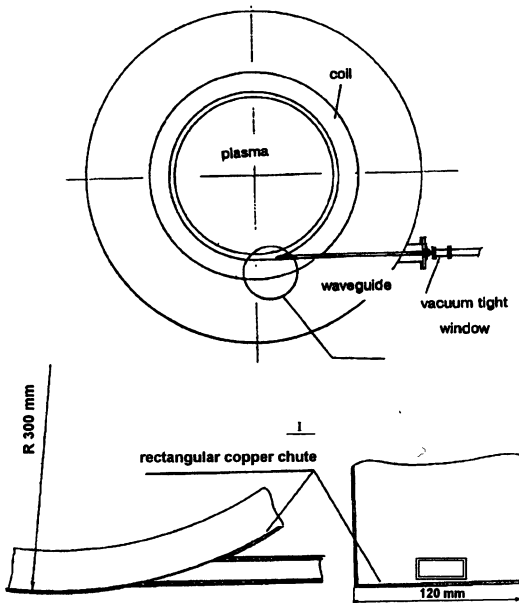


Fig. 1. Scheme of tangential microwave input system

shown on Fig. 1. Two such systems are placed symmetric along PN axis (the distance between end coils along axis is 2.2 m) and should excite the plasma - wall waveguide, formed on plasma periphery at the large plasma density (larger than cut-off density $6 \cdot 10^{11} \text{ cm}^{-3}$). The exited waves can have the large surface absorption in upper hybrid resonance conditions. This possibility was investigated theoretically [5] and experimentally in PN-1 installation [6].

The steady state or modulated microwave power can be used for plasma production in PN. For example, on Fig. 2 the oscillograms of linear density (signal of 4 mm interferometer) for meander type discharge are shown. In this case the combination of the steady state space distributed gas

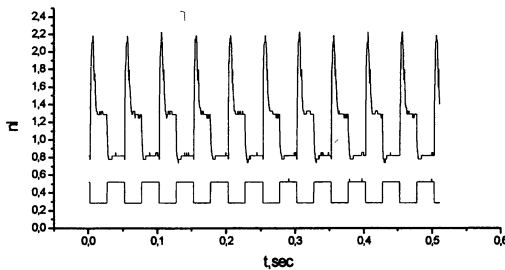


Fig. 2. Target thickness (top) and power in meander discharge, Ar, 10^{-4} torr, 40 kW

puffing with a vacuum pumping was used. The nl decreasing during the pulse duration is explained as a gas burn out. To investigate the role of additional gas puffing on increasing of the plasma density the piezovalue was installed. The oscillograms of nl at different piezovalue scenario are

shown on Fig. 3. One can see, that the density linearly increased by additional gas puffing, but at the critical value $6 \cdot 10^{11} \text{ cm}^{-2}$ the density collapse can be observed (b, c, d). Only at the special gas puffing scenario the good discharge can be obtained (a).

Such plasma behavior is connected with the plasma cut-off phenomena and the surface plasma waveguide production.

The existence of surface plasma waveguide discharge gives us the possibility to obtain density 1.5 times greater than the cut-off density. On Fig. 4 such discharge is shown. Only at additional temporary gas puffing can be obtained this form of discharge in PNx-U. The Fig. 4 shows, that the mean density $\langle n \rangle = n/L \sim 0.9 \cdot 10^{12} \text{ cm}^{-3}$ ($L \sim 2 \text{ m}$) is obtained at pressure 10^{-4} torr ($\langle n_{\text{gas}} \rangle \sim 3.5 \cdot 10^{12} \text{ cm}^{-3}$). So the mean degree of ionization is high, 25 %. In the plasma center the degree of ionization should be higher.

Fig. 4. Surface plasma - wall waveguide discharge: linear density nl (top), input microwave power P , reflected microwave power R and Ar line radiation (Ar, 10^{-4} torr , 40 kW)

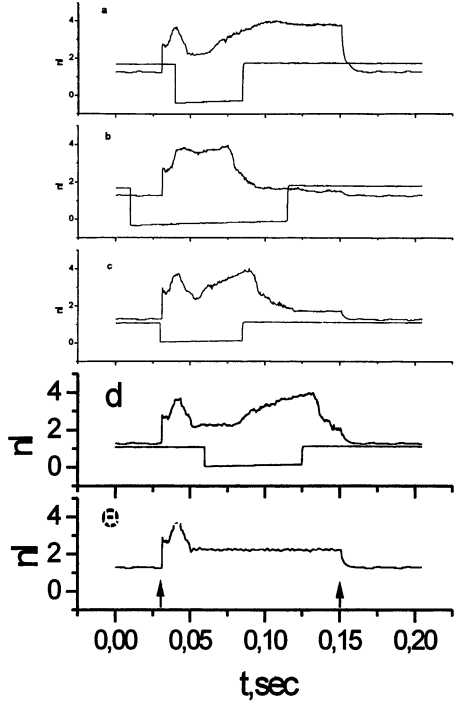
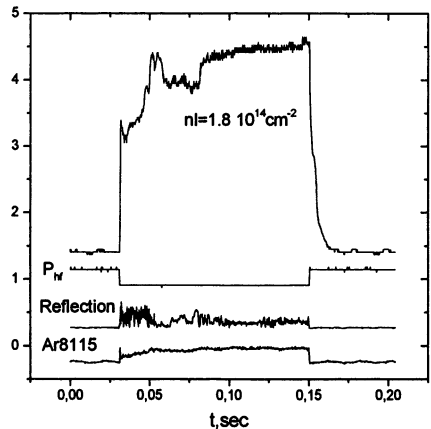


Fig. 3. nl (top) and piezovalue switch on (pointers 40 kW is on, Ar, 10^{-4} torr): (a) surface discharge, (b-d) destroying discharge, (e) without additional gas puffing



Plasma Parameters and Confinement

Fig. 4 shows that the density decay time is large $\tau = 3$ ms. The probe measurements give the decay electron temperature $T_e = 4$ eV. So the cusp particle confinement time scaling

$$\tau[s] = 3 \frac{B[T](V/LN)[m^2]}{T_e[eV]} \quad (1)$$

is good satisfied in PNX-U conditions (magnetic field in slits $B = 0.36$ T, plasma volume $V = 0.5$ m³, total slit length $LN = 50$ m). Fig. 4 shows also, that radiation disappears quickly with power switch off. So we can conclude, that the small radiated plasma in the center of the trap is consisted of the cold electrons and ions, confined with time (1) for particles and energy. The total power needed to provide this cold plasma (~ 1 kW) can be estimated from the relation

$$P = \frac{10T_e n V}{\tau} \quad (2)$$

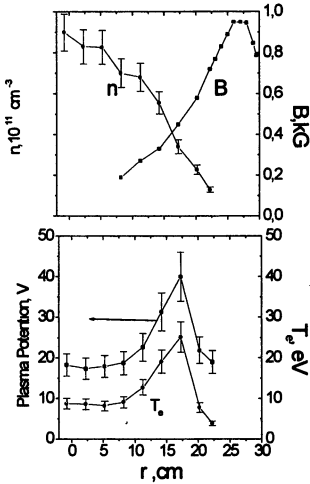


Fig. 5. Radial profiles, $r=0$ center, $r=30$ cm wall

and is much smaller, than input power 40 kW. The greater part of input microwave power is spent on the hot electron production, ionization and radiation on plasma periphery. Fig. 5 shows the radial profiles of density n , electron temperature T_e , plasma potential ϕ and magnetic field B measured by probes at low input power (5 kW) discharge in Ar at pressure $5 \cdot 10^{-5}$ torr. The measurements are carried out between two magnetic slits (normal to field lines) in PNX-U center.

One can see, that T_e reaches the maximum value ~ 25 eV on the periphery of installation and falls down to small value ~ 8 eV at the center. On the periphery the magnetic field and the magnetic mirror ratio $R_m \sim 10$ are large enough to magnetically confine hot electrons (for the conditions on Fig. 4 the hot electron density and temperature are $n_h \sim 3 \cdot 10^{11} \text{ cm}^{-3}$, $T_{eh} \sim 20$ eV) with time $\tau_{ee} \ln R_m \sim 30 \mu\text{s}$. Relation (2) gives the value $P \sim 50$ kW for hot electron volume $V_h \sim 0.15$ m³. But this estimations are rough and demonstrate only the large energy accumulation on the periphery of multipole mirrors.

The absolute values of plasma potential were tested with measurements of ion end loss energy spectrum by the multigrid analyzer (ELA). The dependence of ion current J_i on keeping potential U is shown on Fig. 6. The maximum positive plasma potential $\phi_m \sim 50$ V is detected. The ion temperature is close to the cold electron temperature. This potential value coincides with the potential magnitude, measured in the slit area by probes. On Fig. 7 the density, electron temperature and potential profiles along slit (along the field lines) are shown in same conditions as on Fig. 5. So, the measured (see Figs. 5–7) potential profile demonstrates the existence of the additional ambipolar potential plasma confinement as in ambipolar mirror traps. The potential in slits on the periphery is larger than in the center on $\Delta\phi \sim 20 \div 30$ V. This value is comparable with the hot electron energy. In such conditions the confinement time for central cold plasma should be increased by factor $\alpha = \exp(e\Delta\phi/T_{ec}) \sim \exp(20/4) = 150$ ($\tau_c = \alpha \cdot 3 \text{ ms} \sim 0.45 \text{ s}$). Note, in all our experiments we do not observe the ELA cold electron signal when microwaves are switched on. The measured positive maximum potential $\phi_m \sim 50$ V should increase confinement time for the hot electrons on the large factor

$$\beta = \exp\left(\frac{e\phi_m}{T_{eh}}\right) \sim \exp(50/20) = 12$$

($\tau_h = \beta \cdot 30 \text{ } \mu\text{s} \sim 0.36 \text{ ms}$) also. We can determine the mean total plasma confinement time as $\tau \approx \tau_h \frac{V}{V_h}$ and obtain the value $\tau \sim 1 \text{ ms}$. If we determine the loss energy per one lost particle by relation $(T_{eh} + U_{ionization} + \phi_m) \sim 100 \text{ eV}$ and use the mean total confinement time, we obtain $P \sim 8 \text{ kW} < 40 \text{ kW}$ for Fig. 4 conditions. This estimation can indicate the large role of radiation losses. The rough estimation of radiation losses on periphery ($0.05 \text{ W}\cdot\text{cm}^{-3}$) gives the comparable value $P_{rad} \sim 8 \text{ kW}$. We do not know

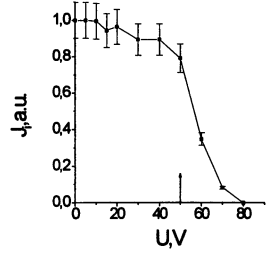


Fig. 6. ELA ion spectrum

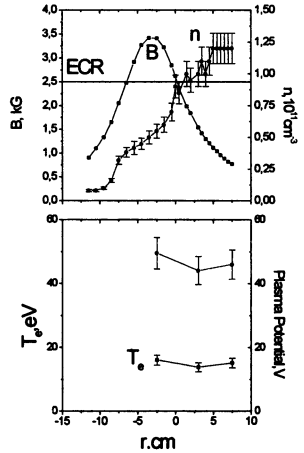


Fig. 7. Profiles along slit. $r=0$ wall, $r>0$ in plasma

the absorbed with plasma tail of input microwave power and, hence, the energy balance in resent experiment. But our preliminary consideration shows good perspective for effective plasma production by microwave discharge in multipole magnetic systems.

Discharge in H₂

The hydrogen discharges are similar to discharges in Ar. But the discharge in Ar gives the twice greater plasma density at the center, than the discharge in H₂ However, the radial plasma density profile in H₂ is much more flat, than in Ar, and the total number of charged particles in

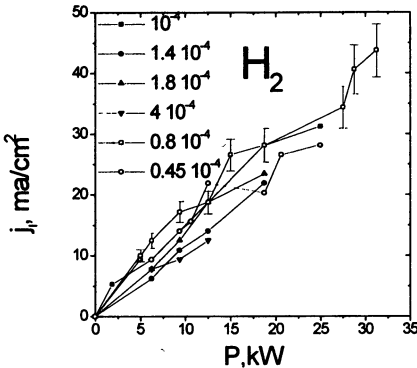


Fig. 8. Probe ion current on input power at different H₂ pressures

discharge volume is the same for both gases.

The disruptions in waveguide system (see Fig. 1) limit the power input increment. The maximum input microwave power depends on the preliminary gas pressure in the installation. As lower is the pressure as the higher microwave power can be used. Fig. 8 shows the probe saturation ion current on input power for different H₂ pressure. The curves ends indicate the beginning of disruptions.

Conclusion

The plasma in the volume 0.5 m³ with parameters: $n \sim 10^{12}$ cm⁻³, $T_{e,i} \sim 5 \div 10$ eV, $n/n_{gas} \sim 0.25$ was obtained at mean power density 0.08 W·cm⁻³.

References

1. Skovoroda A.A. Pre-print IAE-5544/6, Moscow, 1992.
2. Skovoroda A.A., Zhil'tsov V.A. Proc. of Int. Workshop "Strong Microwaves in Plasmas", Nizhny Novgorod, 1996, V. 1. P. 368.
3. Kulygin V.M., Skovoroda A.A., Zhil'tsov V.A. Plasma Devices Operations, 1998, 6, 135.
4. Zhil'tsov V.A., Klimenko E.Yu., Kosarev P.M. et al. 1998, IAEA-FI-CN-69/ITERP2/04.
5. Gildenburg V.B., Skovoroda A.A. Plasma Phys. Reports, 1998, 24, 339.
6. Zhil'tsov V.A., Kosarev P.M., Skovoroda A.A. Plasma Phys. Reports, 1996, 22, 246.

APPLICATIONS FROM TEMPERATURE PROFILE CONTROL DURING MICROWAVE PROCESSING

J.G.P. Binner

Brunel University, Uxbridge, UK

Four case studies are examined in which the temperature profile developed in ceramic bodies heated using 2.45 GHz microwave radiation was controlled. The first case study outlines the potential for combining microwaves with conventional heating to achieve a uniform temperature profile throughout the ceramic component during processing. In the following three case studies the intention was to utilise the inverse temperature profile that formed. The results indicate the importance of the dielectric characteristics of the systems under investigation.

Introduction

Direct microwave heating of materials is fundamentally different from more conventional radiant element techniques in that the energy can be deposited volumetrically throughout the material rather than relying on thermal conduction from the surface. Since power is only deposited into the ceramic, the surrounding air remains cooler than the body, which can result in the creation of an inverse temperature profile with time, i.e. a hotter interior than surface. The magnitude of the profile is dependent upon many factors such as power level, electric field intensity and material properties including lossiness, thermal and electrical conductivity, etc. Properly manipulated the nature of this energy deposition may lead to a number of opportunities being realised, including: improved product properties, reductions in manufacturing costs due to energy savings and shorter processing times and even synthesis of new materials. Before full advantage may be taken of these processing enhancements however, there are a number of technical challenges to be overcome. These include precise control of power deposition and hence temperature profile within the workpiece. This paper provides a brief overview of the potential to be gained from temperature profile control during microwave processing by examining four case studies.

Development of a Uniform Temperature Profile via Hybrid Heating

Control of the temperature profile during microwave sintering so that it is virtually uniform across the ceramic allows the use of much higher heating rates since differential expansion is not experienced. This can be crudely achieved by using the technique referred to as 'casketing', which involves surrounding the component by microwave transparent insulation and a microwave susceptor such that heat losses from the surface are minimised. However, this approach does not allow the temperature profile to be modified during processing. The alternative is to use a hybrid microwave/conventional system so that the interior and surface are heated simultaneously and independently [1]. This approach can result in the ability to heat and cool samples at much faster rates than conventionally possible, saving processing time and reducing stresses. Both batch and tunnel kilns have been developed by EA Technology in the UK and are now commercially available. Retrofitting of existing conventional kilns with microwave systems is also possible. The net result can be a significant reduction in processing costs, figure 1.

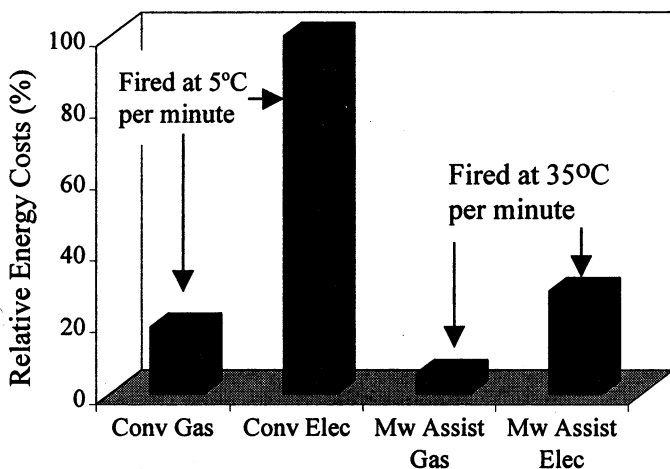


Figure 1: Relative costs in the UK for processing ceramic materials
(adapted from reference 5)

Microwave Sintering of YBCO Ceramic Superconductors

Current bulk polycrystalline ceramic superconductors suffer from the major disadvantage that only the surface layers have the correct oxygen stoichiometry and are, therefore, superconducting. This occurs because conventional sintering results in the surface densifying before the interior, cutting off the latter from the oxygen-rich atmosphere required during sintering. This effectively creates a 'shell' of superconducting phases surrounding a central core that is non-superconducting.

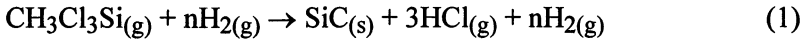
Yttrium-barium-copper oxide (YBCO) compacts were heated under a range of conditions using both 2.45 GHz microwave and conventional sintering techniques [2] and a flowing oxygen atmosphere. The magnitude of the temperature profile was controlled by a simple casketing approach that did not involve the use of susceptors but in which the degree of insulation was variable. The results indicated that microwave heating provided the ability to achieve perfectly uniform and full oxygen content ($x = 7$ in $\text{YBa}_2\text{Cu}_3\text{O}_x$) and almost full densities (98 %) throughout bulk ceramic samples. The critical transition temperatures were also higher, typically 90–91 K, and grain size was uniform and finer than in the conventionally processed samples. In addition, total processing time was approximately a factor of six faster. This was achieved by the ability to use a) shorter hold times at temperature for both the sintering and annealing part of the schedule and b) heating and cooling rates approximately a factor of four faster without the sample being damaged.

Microwave Chemical Vapour Infiltration of Ceramic Matrix Composites

In chemical vapour infiltration a porous fibre preform is heated in an atmosphere that dissociates on contact with the hot fibres to deposit a solid coating onto their surfaces. The process continues until the deposited material fills the voids between the fibres and forms a dense matrix. The advantages of this method include relatively low processing temperatures, the potential for near-net shaping and the ability to control matrix microstructures. Difficulties are the tendency to deposit preferentially near the surface leading to 'crusting'. This inhibits further densification and necessitates intermittent machining operations. As a

consequence processing times can exceed 2–3 months. Although many methods have been investigated to accelerate the process, the problems stem from the conventional heating methods used to heat the preform that rely on surface heating and conduction.

The microwave enhanced chemical vapour infiltration of SiC_f-SiC ceramic composites has been examined [3]. Methyltrichlorosilane (MTS) was used as the starting material for SiC deposition:



whilst 50 mm diameter plain weave Nicalon fabric discs were used as the preform. About 30 discs were pressed and sewn together, the average porosity was about 60 % and the average thickness about 7 mm.

As expected, deposition occurred from the centre outwards allowing much faster processing than conventionally achievable. For example, densification equivalent to an average of 70 % of theoretical was achieved after only 19 hours of infiltration at 1000°C. A similar level of infiltration would take several hundred hours using conventional CVI. The deposited area itself was sharply defined, figure 2, and near full density. The maximum bulk density of the infiltrated preform was also found to be dependent on the preparation method of the preform. The initial local porosity distribution affected both the microwave heating characteristics and the formation of non-accessible pores.

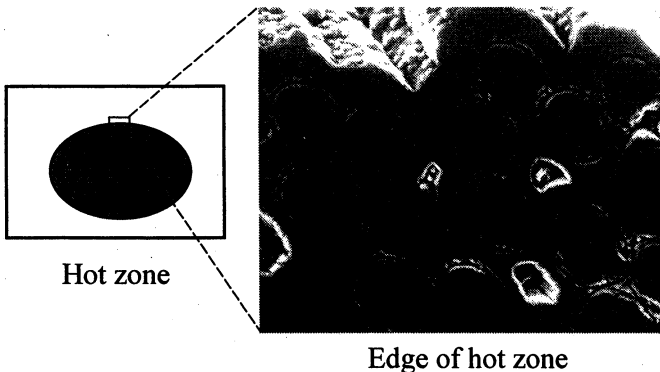


Figure 2: The hot zone developed during microwave enhanced CVI showing deposition from the centre of the component

Microwave Reaction Bonding of Silicon Nitride

Reaction bonded silicon nitride (RBSN) is a ceramic that retains its strength to high temperatures and displays very low creep rates since glassy grain boundary phases are avoided. The principle disadvantage is the inability to achieve high densities since porosity must be kept open throughout the process to allow nitrogen to permeate the silicon compact. This reduces the strength of the material and also permits internal oxidation at high temperatures if oxidising gases are present during use.

Silicon powder compacts were microwave reaction bonded in a flowing nitrogen atmosphere [4] using the same experimental arrangement used for the YBCO work. Nitridation occurred in a layered fashion however, with a thick layer just below the surface and the base of the discs being virtually phase-pure silicon nitride whilst the other areas displayed negligible evidence of reaction.

Discussion of the Use of the Inverse Temperature Profile

The reason for the success during the YBCO and CVI work and lack of success for the RBSN experiments was due to the shape of the temperature profile developed in the samples during processing. For the YBCO and CVI work an initial inverse temperature profile was developed. However, in both cases the product being formed (dense YBCO and SiC respectively) were significantly more lossy than the initial green body. This rapid increase in dielectric loss with increasing temperature and densification resulted in a severe reduction in penetration depth of the microwaves, e.g. figure 3. This in turn resulted in the microwave field being excluded from the centre of the sample and the hot zone sweeping outwards towards the surface, figure 4. Thus at any given point during processing the ceramic forming had access to the oxygen or MTS it required and near theoretical densities could be achieved without sacrificing any of the properties.

In the case of the RBSN, however, the results suggest that a complex inverse temperature profile developed, probably because the initial depth of penetration of the microwaves into the silicon compacts was too small. This will have resulted in two hot regions within the sample with the lower temperature maximum nearer the surface because of the thermally insulating effect of the sample support. In addition, the silicon nitride formed was less lossy than the original silicon. This prevented the

development of the profile as a function of time since the microwave field was not excluded from the densified areas, as was the case for the YBCO and CVI work.

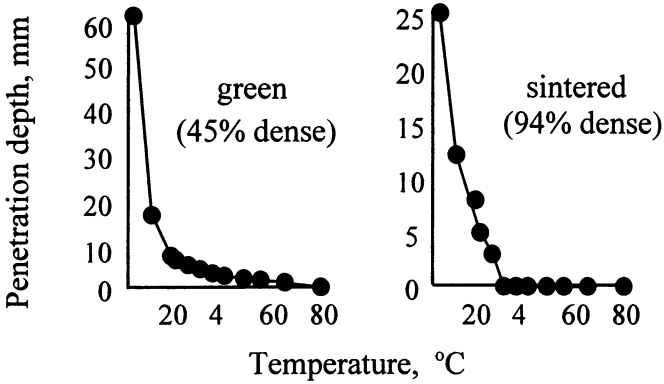


Figure 3: Change in penetration depth for YBCO as a function of temperature and densification

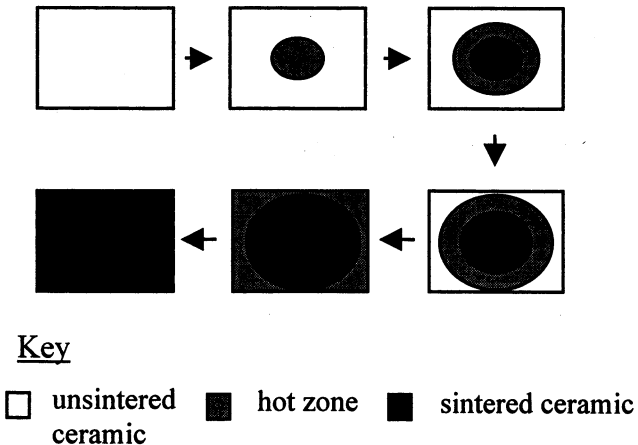


Figure 4: Model for the microwave sintering of YBCO

Conclusions

Four case studies have been examined in which attempts were made to control the temperature profile developed in ceramic bodies heated using 2.45 GHz microwave radiation. The first case study outlined the potential for combining microwaves with conventional heating to achieve a uniform temperature profile throughout the ceramic component during processing. The concept has been successfully taken to commercialisation for both batch and tunnel kilns. In addition, retrofitting of existing conventional kilns is possible. The following three case studies explored the potential for utilising the inverse temperature profile that forms during heating of dielectric materials. The results indicated the importance of the dielectric characteristics of the systems under investigation. Ideally, the green body should be relatively transparent to microwave energy, yielding a high initial depth of penetration, and should then become increasingly opaque as processing proceeds to ensure that the microwave field is excluded from the processed regions. This ensures that the microwave field effectively 'sweeps' through the material resulting in a homogeneous product.

References

1. Wroe FCR, *Ceram. Trans.*, 1993, **36**, 449-458.
2. Binner JGP and Al-Dawery IA, *Superconductor Sci. & Tech.*, 1998, **11**, 449-457.
3. Binner JGP, *Ceram. Trans.*, 1998, **83**, 433-442.
4. Binner JGP and Cross TE, *Mat. Res. Soc. Proc.*, 1992, **269**, 357-362.
5. Wroe F.C.R., personal communication.

ON A POSSIBILITY TO USE A RAY TRACING METHOD FOR CALCULATION OF MICROWAVE FIELD DISTRIBUTION INSIDE AN OVERSIZED CAVITY

*V.E. Semenov, N.A. Zharova,
V.I. Pozdnyakova*, I.A. Shereshevskii**

Institute of Applied Physics RAS, Nizhny Novgorod, Russia

*Institute for Physics of Microstructures RAS, Nizhny Novgorod, Russia

To optimize processing of materials in the microwave oven fed by millimeter wave radiation it is popular to use computer simulations based on ray tracing approach. However, this approximation is not justified rigorously in this case. To understand the possibility of using the geometric optics approach the microwave intensity distribution inside an oversized cavity of simple geometry was computed by solving scalar Helmholtz equation with appropriate boundary conditions. The obtained field patterns are compared with the results of calculations within averaged geometric optics approximation for the same problem.

For industrial applications of high temperature microwave processing of materials it is important to realize a uniform distribution of power over a large volume of microwave oven. In principle, microwave oven is a cavity fed by electromagnetic radiation of appropriate frequency. Respectively, microwave field distribution inside the oven volume is determined by its geometry and feeding scheme. To optimize the oven configuration numerical simulations appear to be preferable and this approach has received increased attention during the last decade [1-5]. For the present state of computer capabilities the problem can be solved rigorously only for a cavity with size to wavelength ratio $L/\lambda < 10$, as long as the Finite Difference Time Domain (FDTD) method can be used in this case. However the FDTD technique is not applicable for supermultimode cavity which is of main interest for applications. Therefore in the latter case the ray tracing approach is exploited for simulations [4, 5]. Unfortunately this approximation is not justified rigorously and each time a question arises: how reliable are calculations performed within geometric optics approximation. To clarify the answer a series of simulations of the field distribution has been performed for the same oven configurations both within ray tracing approach and solving scalar Helmholtz equation with appropriate boundary conditions:

$$\nabla^2 E + k^2 E = 0, \quad (1)$$

$$\frac{\partial E}{\partial n} = k \frac{2(-1+i)}{1-R} E, \quad (2)$$

where E is complex amplitude of microwave field, $k=2\pi/\lambda$ is vacuum wave number, $\partial/\partial n$ denotes a normal (with respect to the boundary) derivative on the surface enclosing the cavity volume, R corresponds to the reflection coefficient for the geometric optics ray falling normally on the cavity wall ($1-R \ll 1$).

To avoid the problems related to numerical solution of Eqn. (1) via a finite difference technique, simple rectangular and cylindrical cavities were considered. In these cases the field E can be presented as a sum of eigenmodes,

$$E = \sum_{n,m} \left\{ A_{n,m} \psi_{n,m} \exp(+ih_{n,m}z) + B_{n,m} \psi_{n,m} \exp(-ih_{n,m}z) \right\}, \quad (2)$$

whose transverse structure, $\psi_{nm}(x,y)$, propagation constants, h_{nm} , and amplitudes, A_{nm} , B_{nm} , can be found. Numerical methods are only employed to summarize the field of these modes at any specified points.

Presented below in Figs. 1-7 are some results of calculations carried out for the radiation wavelength $\lambda=1$ cm and cavity length $L=50$ cm. The exact solution of Helmholtz equation is illustrated in Figs. 1-2 where the field intensity distribution over the central cross section is shown for rectangular and cylindrical cavities and two different feeding schemes. Each of Figs. 2-6 presents these distributions (on the left) averaged over cubic cells of size 2 cm. For comparison on the right of these figures shown are the averaged field intensity distributions calculated within ray tracing approach with large number, $N \sim 5000$, of rays.

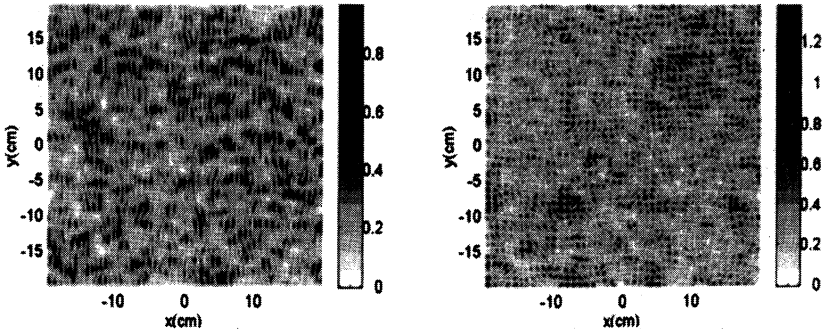


Fig. 1

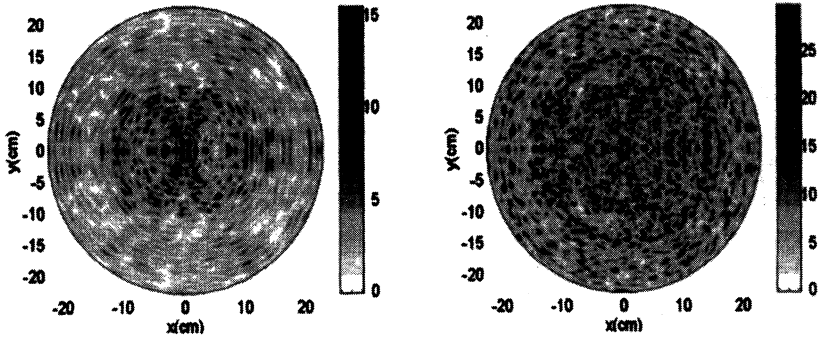


Fig. 2

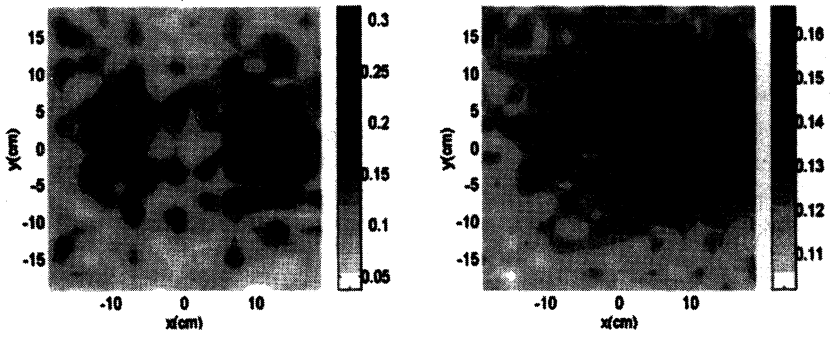


Fig. 3

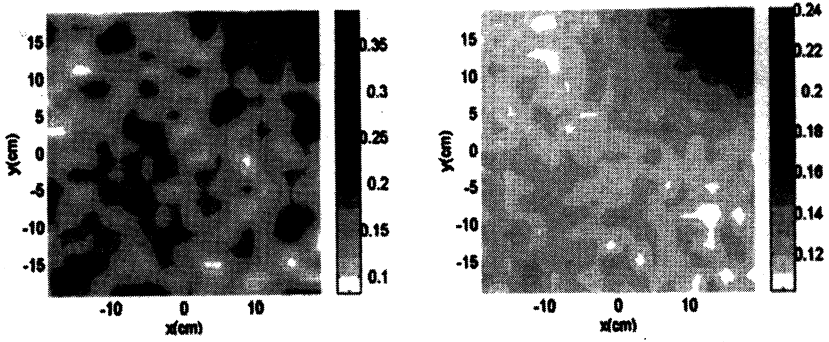


Fig. 4

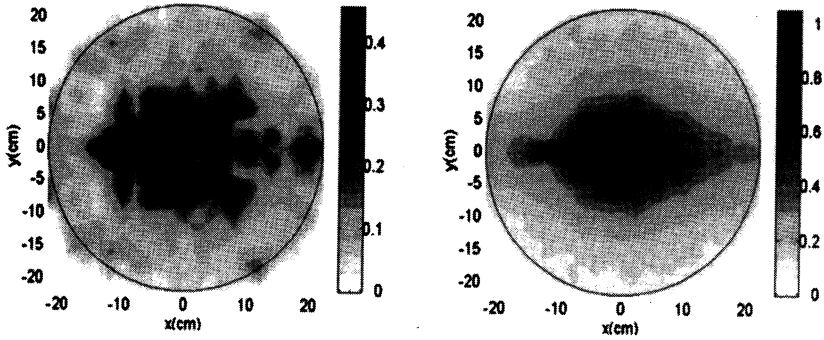


Fig. 5

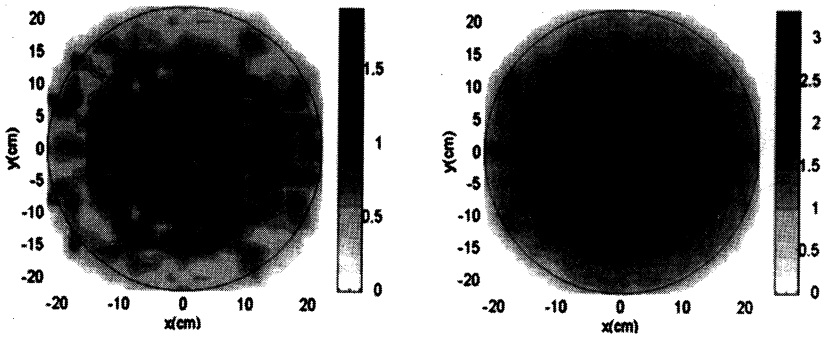


Fig. 6

The dependence of results of calculations on the cell size and number of rays is illustrated on Fig. 7 where the solution of Helmholtz equation (at the left) and results of ray tracing approach with $N=68$ (at the right) are averaged over cubic cells of size 8 cm.

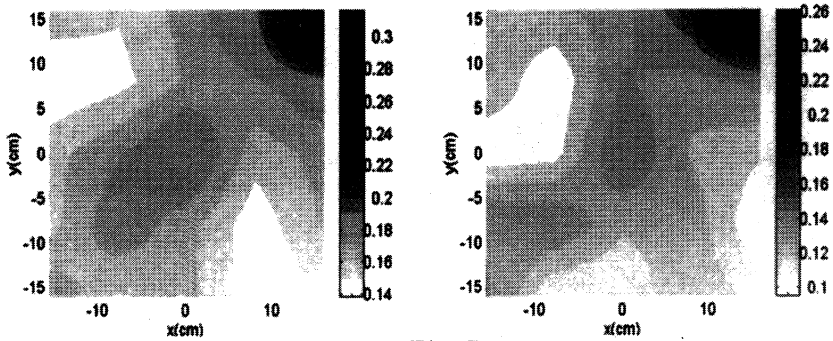


Fig. 7

A comparison of the obtained field patterns makes it possible to come to the following conclusions:

- 1) The geometric-optics approximation only reflects well the largest-scale (on the order of the cavity dimensions) nonuniformities of the microwave field intensity distribution.
- 2) The nonuniformities on the scale of the transverse section of the input microwave beam are only reflected on the qualitative level.
- 3) The results of the geometric-optics calculations are the closer to the results of exact calculations the larger is the number of modes excited within the cavity.
- 4) There exists an optimum number of rays with which the geometric-optics results are the closest to the reality. This number is about the number of modes of an oversized waveguide (whose cross-section is the same as that of the cavity) fed by the incident beam.

Acknowledgment

This research is supported in part by the Commission of the European Communities under the Cooperation with Third Countries and International Organizations programme.

References

1. E. K. Miller, 'Time-domain modeling in electromagnetics', *J. Electromagnet. Waves Applic.*, 1994, Vol. (8), pp. 1125-1172
2. M. F. Iskander, 'Computer modeling and numerical techniques for quantifying microwave interactions with materials', In *Microwave Processing of*

Materials II, W. B. Synder, W. S. Sutton, M. F. Iskander and D. L. Johnson, eds. (Material Research Society, Pittsburgh, PA, 1990), Vol. (189), pp. 149-171.

R. L. Smith, M. F. Iskander, O. Anrade and H. Kimrey, 'Computer modeling and numerical techniques for quantifying microwave interactions with materials', In *Microwave Processing of Materials II*, W. B. Synder, W. S. Sutton, M. F. Iskander and D. L. Johnson, eds. (Material Research Society, Pittsburgh, PA, 1990), Vol. (189), pp. 149-171.

L. Feher, G. Link, M. Thumm, 'Computer modeling and numerical techniques for quantifying microwave interactions with materials', In *Microwave Processing of Materials II*, W. B. Synder, W. S. Sutton, M. F. Iskander and D. L. Johnson, eds. (Material Research Society, Pittsburgh, PA, 1990), Vol. (189), pp. 149-171.

S.V. Egorov, V.V. Holoptsev, V.E. Semenov, A.A. Sorokin, N.A. Zharova, 'Computer modeling and numerical techniques for quantifying microwave interactions with materials', In *Microwave Processing of Materials II*, W. B. Synder, W. S. Sutton, M. F. Iskander and D. L. Johnson, eds. (Material Research Society, Pittsburgh, PA, 1990), Vol. (189), pp. 149-171.

MICROWAVE ABSORPTION IN A WAVEGUIDE FILLED WITH PARAFFIN

*V.D.Dougar-Jabon¹, J.C.Escobar Remolina², C.Medina Zarate²,
C.Pelaez Uribe², F.A.Pinto Siabato², V.P.Tarakanov³ and
F.A.Vivas Mejia¹*

¹Universidad Industrial de Santander, Bucaramanga, Colombia

²Instituto Colombiano de Petroleo-ECOPETROL, Bucaramanga, Colombia

³High Energy Density Research Center, Moscow, Russia

Abstract

A 3D numerical analysis of electromagnetic waves propagation in a cylindrical tube partially filled with paraffin precipitated from crude oil flow on the tube walls is studied. The calculated space distribution of the specific absorbed energy for different modes is used to estimate the degree of paraffin heating and the time necessary to heat the layer to a desirable temperature.

The simulations are made with the 2.45 GHz TE₀₁, TM₀₁ and TM₁₁ microwaves of 7 kW launched along a 16 cm diameter tube filled with paraffin in solution layer that is 4 cm thick. The calculated data on space distribution of the absorbed specific energy have permitted to estimate the time necessary to heat the layer surface up to 80°C as 15 s.

1. Introduction

Crude petroleum is a complex physical-chemical mixture of different substances in petroleum solution. In its natural state, these substances occur as emulsions, oil sand coagulants, associations with saline formations, water etc. The physical-chemical composition of crude oil is not constant, it varies from one oil field to another and it is even true for oil wells.

The gas that accompanies crude oil mainly composed of methane and the volatile dissolved in petroleum is by itself no problems for petroleum production technology, but it, however, severely affects the oil stream fluidity. The crude oil while moving to an oil well gives off the dissolved gas and the volatile follow by reduction auto-refrigeration effect. The temperature drop leads to reducing the solubility of paraffin that results

in raising the crude viscosity raise and paraffin precipitating on the tubing strings. Paraffin and other condensable constituents such as hydrates, asphaltens and sulfurs can also coagulate and settle out of crude oil especially in zones of pump and compression stations.

Paraffin accumulation inside the tubing can reduce dramatically oil production, particularly production of heavy oils. At present, some chemical methods are used to prevent plugging the tubing by paraffin and other condensable constituents. The chemical treatment has proved its efficiency but it is too costly and it causes environmental problems.

It is conceivable that physical methods of treatment of crude oil and precipitated layers can contribute to solving the problem of effective oil production. The oil industry regards the microwave technology as that will make it possible to change the crude characteristics in a desired manner. By now, the investigations in the area of improvement of the transportation conditions by microwaves are still at the initial stage and are hampered by the fact that oil composition, complex dielectric permeability, thermal conductivity and viscosity vary drastically for different crude oil types.

In this report, a three-dimensional numerical experiment on propagation of the microwaves TE_{01} , TM_{01} and TM_{11} modes in a cylindrical tube partially filled with paraffin in solution is described. Using the simulation data on space distribution of the absorbed specific energy, the efficiency of paraffin layer heating and the time required for heat the layer to the temperature of paraffin destruction is estimated.

2. Assumptions and numerical code

We study propagation of electromagnetic waves in a straight cylindrical tube of supercritical radius R partially filled with dielectric. The wave of frequency f is launched into the tube at the tube cross section with longitudinal coordinate $z = 0$. The dielectric also forms a layer of a cylindrical configuration. The inner radius of the layer decreases linearly from $r = R$ at the cross section $z=z_1$ to R_0 at $z=z_2$. The layer width is kept equal to $(R-R_0)$ along the remaining part of the tube, $z_2 < z < L$.

We assume that the dielectric layer is homogeneous and the complex dielectric permeability has only a weak dependence on the temperature. No account in our study is taken of radiate and convection heat transport. The hydrocarbon and water molecular resonance response to electromagnetic wave is outside our numerical consideration of the problem.

To compute the process of propagation, reflection, transformation and absorption of the electromagnetic waves, a 3D version of the numerical code KARAT is used [1]. This code is based on the complete system of the maxwellian equations that are determined on a rectangular 70x70x200 mesh. The electric field is adjusted continuously by the Boris leap-frog technique. Since the code KARAT is elaborated for only electrodynamics problems, the degree of dielectric heating by electromagnetic waves is calculated through a thermal balance equation.

It is significant that numerical simulations of the electromagnetic waves evolution make it possible to appreciate better the problem of preventing paraffin precipitation on the walls of the oil transportation lines and overcoming some drawbacks at designing and construting systems for electromagnetic wave heating.

3. Results and conclusions

For numerical experiments on electromagnetic waves propagation in the tubing with paraffin precipitated on the walls, we use commercially available 2,45 GHz microwaves. The microwaves travel along a cylindrical tube of 8-cm radius and 200 cm in length partially filled with paraffin in solution layer. The layer thickness is mount to 4 cm at a point $z_1 = 10$ cm to $z_2 = 25$ cm. From the point z_2 , the layer radius remains invariable.

Paraffin settled out on the tubing walls is characterized by a complex dielectric permittivity $\varepsilon = \varepsilon_1 + i\varepsilon_2$. Assuming paraffin in solution we have $\varepsilon_1 = 2,4$ and $\varepsilon_2 = \sigma/2\pi f$ where $\sigma = 0,01$ S/m is the electric conductivity. The real part, ε_1 determines reflection and transformation of the wave by the layer and the imaginary part, ε_2 is responsible for microwave energy absorption. Since different types of electromagnetic field that propagate in a waveguide with dielectric have their own specific absorption features and wave transformation on the dielectric boundary, we have chose the TE_{01} , TM_{01} and TM_{11} modes for simulations.

The evolution of the microwave structure along the tube is shown in Fig. 1. In Fig. 1a one can see the electric component structure of the TM_{11} mode at the $z = 4.2$ cm cross section. The wave structure in the region taken up by paraffin varies considerably as shown in Fig. 1b for $z = 30$ cm.

The space distributions of the energy absorbed by unit length of the paraffin layer during 20 ns for TM_{01} and TM_{11} modes are demonstrated in Fig. 2 and 3. For both cases, approximately 90% of the incident energy

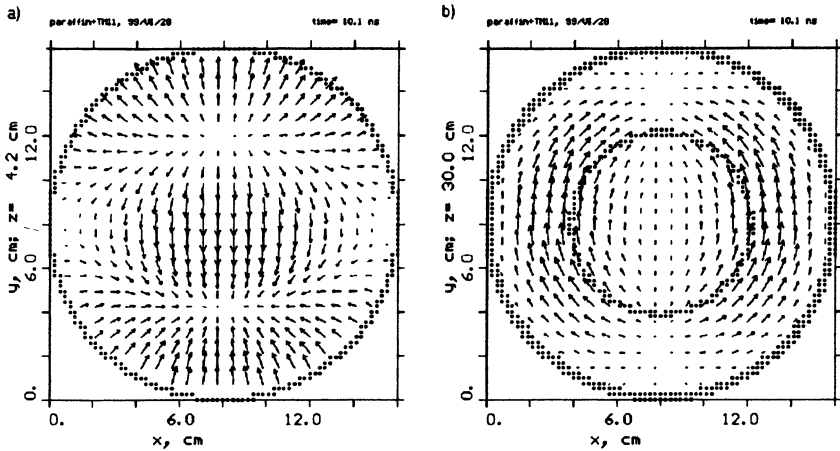


Figure 1. a) Electric component structure of the TM_{11} mode for $z = 4.2$ cm (a), for $z = 30$ cm (b).

is dissipated within a distance of 100 cm. The distinction between in the dissipated energy distributions is as follows: for TM_{01} mode, the absorption peaks near the tube walls, whereas for the TM_{11} mode energy is released largely at the air-dielectric boundary surface. Figure 4 shows the space distribution of the TM_{11} mode energy absorbed during 10 ns in the cross section $z = 30$ cm.

Heating degree is calculated using a value of 1.10^3 J/kgK for specific heat. To attain the temperature of 80°C from a level of 30°C in zones of maximal absorption, a microwave power of 7 kW is to be maintained during 15 s. In this matter there is no a difference between TE_{11} , TM_{01} and TM_{11} modes. The energy losses through the tube walls due to paraffin heat conductivity are found less than 1% of the total microwave energy.

The obtained results show that much of the microwave energy is absorbed by paraffin in solution within a short distance. It is necessary to note that the paraffin is destroyed at temperature of 80°C and it follows that the destruction zone at a fixed microwave power will move ahead and clean the tubing of precipitated paraffin. To prevent paraffin from settling out of a crude oil flow on the tubing walls, the TM_{01} mode would rather to be used.

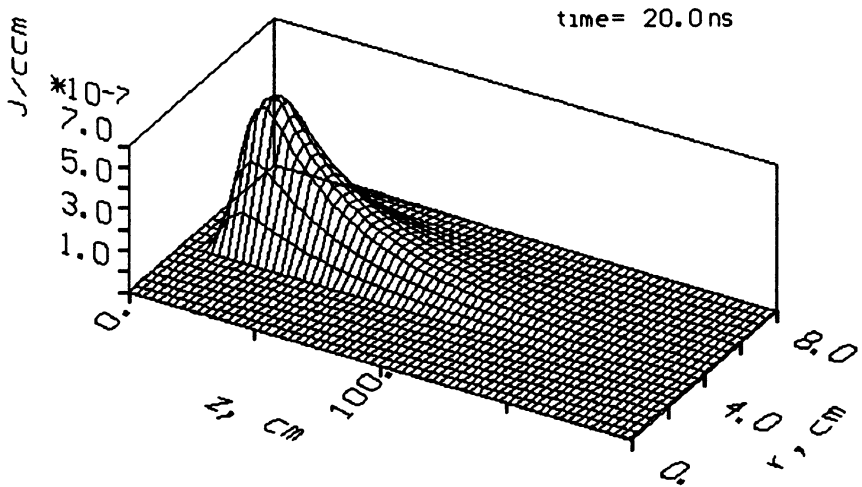


Figure 2. Space distributions of the energy absorbed by unit length of the paraffin layer during 20 ns for mode TM_{01} .

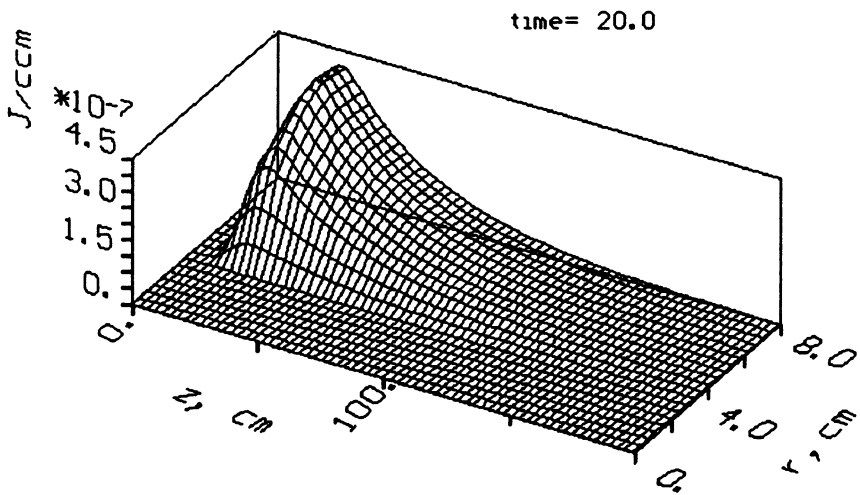


Figure 3. Space distributions of the energy absorbed by unit length of the paraffin layer during 20 ns for mode TM_{11} .

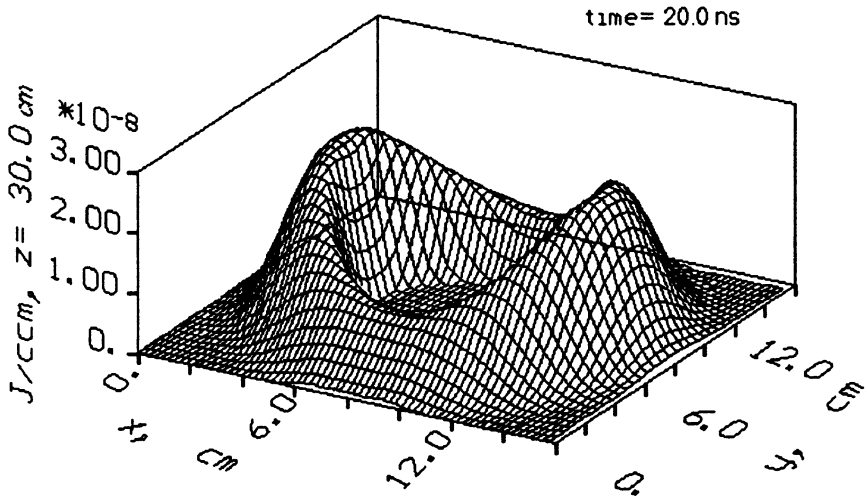


Figure 4. Space distribution of the TM_{11} mode energy absorbed during 20 ns in the cross section $z = 30$ cm.

Further work, perhaps based upon the paraffin specific parameters depending on temperature and specific melting and evaporation heat could provide better approximation to a simulation of the paraffin destruction problem.

Acknowledgement. Authors thank the Petroleum Institute of Colombia-ECOPETROL-MARESOL Ltd. and the Industrial University of Santander for support of this research.

References

1. Tarakanov V. P., User's Manual for Code KARAT, BRA Inc., V.A., USA, 1992.

CONTENTS OF VOLUME 1

<i>Editor's Preface</i>	3
CURRENT DRIVE AND HEATING OF PLASMA BY MICROWAVES IN FUSION DEVICES AND OTHER APPLICATIONS OF HIGH-POWER MICROWAVES	
ECRH and ECCD at high power density at W7-AS <i>H. Maassberg, C.D. Beidler, V. Erckmann, U. Gasparino, J. Geiger, H. Laqua, S.V. Kasilov, N.B. Marushchenko, S. Murakami and the W7-AS Team</i>	7
Electron cyclotron plasma production and heating on LHD: system and its application <i>K. Ohkubo, S. Kubo, T. Shimosuma, H. Idei, M. Sato, Y. Yoshimura, Y. Mizuno, S. Ito, S. Kobayashi, Y. Takita, O. Kaneko, K. Kawahata, A. Komori, N. Ohyabu, H. Yamada, K. Ikeda, Y. Oka, M. Osakabe, K. Takeiri, K. Tsumori, R. Kumazawa, T. Mutoh, K. Saito, T. Seki, T. Watari, N. Ashikawa, M. Emoto, P.C. de Vries, H. Funaba, M. Goto, K. Ida, S. Inagaki, M. Isobe, S. Kado, T. Kobuchi, S. Masuzaki, T. Minami, J. Miyazawa, T. Mori- saki, S. Morita, S. Murakami, S. Mutoh, Y. Nagayama, Y. Nakamura, H. Nakanishi, K. Na- rihara, K. Nishimura, N. Noda, S. Ohdachi, T. Ozaki, R.O. Pavlichenko, B.J. Peterson, A. Sagara, S. Sakakibara, R. Sakamoto, H. Sasao, M. Sasao, K. Sato, M. Shoji, S. Sudo, H. Suzuki, M. Takechi, K. Tanaka, K. Toi, T. Tokuzawa, I. Yamada, S. Yamaguchi, S. Ya- mamoto, K. Yamazaki, M. Yokoyama, K. Y. Watanabe, O. Motojima, M. Fujiwara</i>	27
Polarization measurements during electron cyclotron heating experiments on the DIII-D tokamak <i>C.C. Petty, T.C. Luce, M.E. Austin, H. Ikezi, J. Lohr, R. Prater</i>	41
The 110 GHz gyrotron system on DIII-D: gyrotron tests and physics results <i>J. Lohr, P. Cahalan, R.W. Callis, T.S. Chu, J.S. de Grassie, I. Gorelov, H. Ikezi, R.A. Legg, T.C. Luce, C.C. Petty, D. Ponce, R. Prater, D.I. Schuster, S.E. Tsimring</i>	46
Review of ECR-heating and current drive in the RTP tokamak <i>F.C. Schuller, R.W. Polman for the RTP-team</i>	65
High density lower hybrid current drive experiments on FTU tokamak <i>S. Podda, V. Pericoli-Ridolfini, E. Barbato, H. Kroegler, L. Panaccione, F. Alladio, B. Angelini, M.L. Apicella, G. Apruzzese, L. Bertalot, A. Bertocchi, M. Borra, G. Bracco, G. Buceti, P. Buratti, A. Cardinali, C. Centioli, R. Cesario, S. Ciattaglia, V. Cocilovo, F. Crisanti, R. De Angelis, F. De Marco, B. Esposito, D. Frigione, L. Gabellieri, G. Gatti, E. Giovannozzi, C. Gouylan, C. Gravanti, M. Grolli, F. Iannone, M. Leigheb, G. Maffia, G. Maddaluno, M. Marinucci, G. Mazzitelli, P. Micozzi, F. Mirizzi, F.P. Or- sitto, D. Pacella, M. Panella, L. Pieroni, G.B. Righetti, F. Romanelli, F. Santini, M. Sassi, S.E. Segre, E. Sternini, O. Tudisco, V. Vitale, G. Vlad, N. Tartoni, B. Tilia, A.A. Tuccillo, V. Zanza, M. Zerbini, F. Zonca</i>	88
ECRH/ECCD experiments at 140 GHz on FTU tokamak <i>S. Cirant, A. Airoldi, L. Bertalot, R. Bozzi, A. Bruschi, G. Bracco, P. Buratti, G. Cic- cone, G. Cenacchi, F. Crisanti, S. Di Giovenale, B. Esposito, L. Gabellieri, F. Gandini, G. Granucci, F. Iannone, H. Krögler, E. Lazzaro, S. Lupini, S. Mantovani, V. Mellera, V. Muzzini, A. Nardone, S. Nowak, D. Pacella, L. Panaccione, E. Pesci, G. Ramponi, A. Simonetto, C. Sozzi, N. Spinicchia, O. Tudisco, M. Zerbini, FTU GROUP</i>	95

Recent results in ECH and ECCD experiments in the TCV tokamak <i>M.A. Henderson, T.P. Goodman, R. Behn, S. Coda, J.-P. Hogge, Y. Martin, Y. Peysson, Z.A. Pietrzyk, A. Pochelon, O. Sauter, M.Q. Tran and the TCV Team</i>	114
ECRH experiments in ASDEX Upgrade <i>F. Ryter, F. Leuterer, R. Wolf, O. Gruber, S. Günter, H.-U. Fahrbach, H. Meister, M. Münich, G. Pereverzev, J. Stober, J. Schweinzer, W. Suttrop, ASDEX Upgrade Team and ECRH-Group from IPF</i>	134
The stabilisation of neoclassical tearing modes by ECCD in ASDEX Upgrade <i>H. Zohm, G. Gantenbein, G. Giruzzi, S. Günter, F. Leuterer, M. Maraschek, J.P. Meskat, W. Suttrop, Q. Yu, M. Zabięgo</i>	140
Experiments on ECRH power modulation in the L-2M stellarator <i>D. Akulina, G. Batanov, M. Berezhetskii, G. Gladkov, S. Grebenshchikov, L. Kolik, N. Larionova, A. Meshcheryakov, K. Sargsyan, I. Sbitnikova, O. Fedyanin, N. Kharchev, Yu. Kholnov, T. Estrada, K. Likin, Elena de la Luna, J. Sanchez</i>	160
Reconstruction of the ECRH power deposition and electron heat conductivity from SXR intensity evolution after shut-off ECRH in T-10 <i>A.V. Sushkov, V.F. Andreev, Yu.N. Dnestrovskij, K.A. Rasumova</i>	173
Measurement of plasma transmitted EC-wave power in magnetic field magnitude scanning experiment in CHS <i>Y. Yoshimura, N. Sueoka, H. Idei, S. Kubo, K. Ohkubo, M. Isobe, T. Minami, S. Nishimura, M. Osakabe, K. Tanaka, C. Takahashi, S. Okamura, K. Matsuoka</i>	179
ECRH and ECCD for the stellarator W7-X <i>W. Kasperek, V. Erckmann, H.P. Laqua, E. Borie, G. Dammertz, L. Empacher, W. Förster, G. Gantenbein, S. Illy, G. Michel, G. Müller, B. Piosczyk, M. Thumm, D. Wagner, M. Weßgerber, H. Zohm, W7-X and W7-AS Teams at IPP Garching, W7-X Team at IPF Stuttgart, W7-X Team at FZK Karlsruhe</i>	185
28 GHz ECH system for H-1NF heliac <i>K. Nagasaki, M.G. Shats, H. Punzmann, H.B. Smith, M. Sato</i>	205
Design of the lower hybrid heating and current drive transmission line system for a next step device <i>Ph. Froissard, S.V. Kuzikov</i>	211
The new lower hybrid coupling structures for FTU <i>F. Mirizzi, Ph. Bibet, Ph. Froissard, F. Kazarian, A. Marra, M. Roccon, A.A. Tuccillo</i>	217
Spherical tokamaks concept and status <i>V.K. Gusev</i>	223
Propagation of weakly divergent microwave beams in tokamak plasmas <i>A.D. Piliya, A.N. Saveliev</i>	240
Modeling of the Coulomb collisions for kinetic description of ECR plasma heating <i>A.G. Shalashov, E.V. Suvorov</i>	244
About the geometrical optics of EC-waves in subrelativistic plasma <i>M.D. Tokman, E. Westerhof, M.A. Gavrilova</i>	250

Modification of ECE spectra due to the quasilinear effects at ECR heating in toroidal plasma	
<i>A.G. Shalashov, E.V. Suvorov</i>	254
Determination of absolute H-ion local density from CTS measured characteristics of LH turbulence	
<i>E.V. Suvorov</i>	260
3D Fokker - Planck modeling of ECR heating and current drive in RC ITER plasma	
<i>V.L. Vdovin</i>	265

MICROWAVE DISCHARGES

Electrode microwave discharges. Phenomenology, probe and optical measurements	
<i>Yu.A. Lebedev, M.V. Mokeev, A.V. Tatarinov</i>	271
The pinch effect in microwave resonant streamer discharge and its possible applications	
<i>L.P. Grachev, I.I. Esakov, K.V. Khodataev</i>	291
Microwave breakdown in air-filled resonators	
<i>U. Jordan, D. Anderson, M. Lisak, T. Olsson, V.E. Semenov, M. Ahlander</i>	306
Large diameter microwave plasma excited at 2450 MHz in argon and oxygen gases	
<i>Y. Lahmar-Mebdoua, K. Henda, Ph. Leprince</i>	311
Self-consistent model of the pulsed SW-discharge in hydrogen	
<i>O.A. Ivanov, V.A. Koldanov</i>	319
Two-dimensional electron bounce averaged Fokker - Planck model with self-consistently calculated ion parameters for ECR discharge in plasma sources	
<i>A.B. Shmelev, A.P. Smirnov</i>	325
Numerical modeling of microwave discharge in the CVD diamond deposition reactor	
<i>A.M. Gorbachev, V.A. Koldanov, A.L. Vikharev</i>	329
Generation and study of CS-XE discharge plasma slabs for nonlinear microwave quasioptical experiments	
<i>N.A. Bogatov, M.S. Gitlin, D.A. Dikan</i>	335
Measuring hydrogen plasma parameters in pulsed microwave discharge by optical emission spectroscopy	
<i>R.A. Akhmedzhanov, A.L. Vikharev, A.M. Gorbachev, D.B. Radishev</i>	341
Sources of soft X-rays and multicharged ions based on ECR discharge in heavy gases sustained by high-power gyrotron radiation	
<i>S.V. Golubev, S.V. Razin, V.E. Semenov, A.N. Smirnov, A.V. Vodopyanov, and V.G. Zorin</i>	347

Mirror-trapped plasma heated by powerful millimeter wave radiation as an ECR source of soft X-rays	
<i>S.V. Golubev, V.I. Luchin, S.V. Razin, N.N. Salaschenko, A.N. Smirnov, A.V. Vodopyanov, V.G. Zorin</i>	356
Tornado type closed magnetic trap for an ECR ion source	
<i>K.B. Abramova, A.N. Smirnov, A.V. Voronin, V.G. Zorin</i>	362
Stationary large volume microwave discharge for H^- neutralization	
<i>A.A. Skovoroda and OGRA Team</i>	371
Applications from temperature profile control during microwave processing	
<i>J.G.P. Binner</i>	377
On a possibility to use a ray tracing method for calculation of microwave field distribution inside an oversized cavity	
<i>V.E. Semenov, N.A. Zharova, V.I. Pozdnyakova, I.A. Shereshevskii</i>	384
Microwave absorption in a waveguide filled with paraffin	
<i>V.D. Dougar-Jabon, J.C. Escobar Remolina, C. Medina Zarate, C. Pelaez Uribe, F.A. Pinto Siabato, V.P. Tarakanov, and F.A. Vivas Mejia</i>	390

**STRONG
MICROWAVES
IN PLASMAS**

**PROCEEDINGS
OF THE INTERNATIONAL WORKSHOP**

In two volumes

Volume 1

License № JIP 040840 of 22.08.97.

**Institute of Applied Physics,
Russian Academy of Sciences**

46 Ul'yanov Street, 603600 Nizhny Novgorod, Russia

**Printed by Printing House № 2, "Nauka" Publishers,
6 Shubinsky Pereulok, 121099 Moscow**